University of Kentucky
**UKnowledge**

University of Kentucky Doctoral Dissertations

Graduate School

2010

# NEAR-FIELD RADIATIVE TRANSFER: THERMAL RADIATION, THERMOPHOTOVOLTAIC POWER GENERATION AND OPTICAL CHARACTERIZATION

Mathieu Francoeur
*University of Kentucky*, mfran0@engr.uky.edu

**Click here to let us know how access to this document benefits you.**

## Recommended Citation

Francoeur, Mathieu, "NEAR-FIELD RADIATIVE TRANSFER: THERMAL RADIATION, THERMOPHOTOVOLTAIC POWER GENERATION AND OPTICAL CHARACTERIZATION" (2010). *University of Kentucky Doctoral Dissertations*. 58.
https://uknowledge.uky.edu/gradschool_diss/58

This Dissertation is brought to you for free and open access by the Graduate School at UKnowledge. It has been accepted for inclusion in University of Kentucky Doctoral Dissertations by an authorized administrator of UKnowledge. For more information, please contact UKnowledge@lsv.uky.edu.

# ABSTRACT OF DISSERTATION

Mathieu Francoeur

The Graduate School

University of Kentucky

2010

# NEAR-FIELD RADIATIVE TRANSFER: THERMAL RADIATION, THERMOPHOTOVOLTAIC POWER GENERATION AND OPTICAL CHARACTERIZATION

---

ABSTRACT OF DISSERTATION

---

A dissertation submitted in partial fulfillment of the
requirements for the degree of Doctor of Philosophy in the
College of Engineering
at the University of Kentucky

By
Mathieu Francoeur

Lexington, Kentucky

Director: Dr. M. Pinar Mengüç, Professor of Mechanical Engineering

Lexington, Kentucky

2010

Copyright © Mathieu Francoeur 2010

# ABSTRACT OF DISSERTATION

# NEAR-FIELD RADIATIVE TRANSFER: THERMAL RADIATION, THERMOPHOTOVOLTAIC POWER GENERATION AND OPTICAL CHARACTERIZATION

This dissertation focuses on near-field radiative transfer, which can be defined as the discipline concerned with energy transfer via electromagnetic waves at sub-wavelength distances. Three specific subjects related to this discipline are investigated, namely near-field thermal radiation, nanoscale-gap thermophotovoltaic (nano-TPV) power generation and optical characterization. An algorithm for the solution of near-field thermal radiation problems in one-dimensional layered media is developed, and several tests are performed showing the accuracy, consistency and versatility of the procedure. The possibility of tuning near-field radiative heat transfer via thin films supporting surface phonon-polaritons (SPhPs) in the infrared is afterwards investigated via the computation of the local density of electromagnetic states and the radiative heat flux between two films. Results reveal that due to SPhP coupling, fine tuning of near-field radiative heat transfer is possible by solely varying the structure of the system, the structure being the film thicknesses and their distance of separation. The coexistence of two regimes of near-field thermal radiation between two thin films of silicon carbide is demonstrated via numerical simulations and an asymptotic analysis of the radiative heat transfer coefficient. The impacts of thermal effects on the performances of nano-TPV power generators are investigated via the solution of the coupled near-field thermal radiation, charge and heat transport problem. The viability of nano-TPV devices proposed so far in the literature, based on a tungsten radiator at 2000 K and indium gallium antimonide cell, is questioned due to excessive heating of the junction converting thermal radiation into electricity. Using a convective thermal management system, a heat transfer coefficient as high as $10^5$ $\mathrm{Wm^{-2}K^{-1}}$ is required to maintain the junction at room temperature. The possibility of characterizing non-intrusively, and potentially in real-time, nanoparticles from 5 nm to 100 nm in size via scattered surface wave is explored. The feasibility of the characterization framework is theoretically demonstrated via a sensitivity analysis of the scattering matrix elements. Measurements of the scattering matrix elements for 200 nm and 50 nm gold spherical particles show the great sensitivity of the characterization tool, although an ultimate calibration is difficult with the current version of the experimental set-up.

KEYWORDS: Near-field thermal radiation, Surface phonon-polariton, Nanoscale-gap thermophotoltaic power generation, Optical characterization of nanoparticles, Scattering (Mueller) matrix

Mathieu Francoeur

July 1, 2010

# NEAR-FIELD RADIATIVE TRANSFER: THERMAL RADIATION, THERMOPHOTOVOLTAIC POWER GENERATION AND OPTICAL CHARACTERIZATION

By

Mathieu Francoeur

Dr. M. Pinar Mengüç
Director of Dissertation

Dr. James M. McDonough
Director of Graduate Studies

July 1, 2010

# RULES FOR THE USE OF DISSERTATIONS

Unpublished dissertations submitted for the Doctor's degree and deposited in the University of Kentucky Library are as a rule open for inspection, but are to be used only with due regard to the rights of the authors. Bibliographical references may be noted, but quotations or summaries of parts may be published only with the permission of the author, and with the usual scholarly acknowledgments.

Extensive copying or publication of the dissertation in whole or in part also requires the consent of the Dean of the Graduate School of the University of Kentucky.

A library that borrows this dissertation for use by its patrons is expected to secure the signature of each user.

Name Date

DISSERTATION

Mathieu Francoeur

The Graduate School

University of Kentucky

2010

# NEAR-FIELD RADIATIVE TRANSFER: THERMAL RADIATION, THERMOPHOTOVOLTAIC POWER GENERATION AND OPTICAL CHARACTERIZATION

---

DISSERTATION

---

A dissertation submitted in partial fulfillment of the
requirements for the degree of Doctor of Philosophy in the
College of Engineering
at the University of Kentucky

By
Mathieu Francoeur

Lexington, Kentucky

Director: Dr. M. Pinar Mengüç, Professor of Mechanical Engineering

Lexington, Kentucky

2010

Copyright © Mathieu Francoeur 2010

# ACKNOWLEDGEMENTS

Looking back at these last five years, I cannot believe how many hours and efforts I devoted for completing my PhD. I have to admit that I enjoyed every single minute that I spent in the Radiative Transfer Laboratory, and I have the feeling that I will regret the good time I had during these years that past so fast. Of course, this work would not have been possible without the collaboration of various people that I would like to thank.

I am of course extremely grateful to my advisor, Professor M. Pinar Mengüç. He is an unbelievable researcher and hard-worker, and I benefited a lot from his experience not only from a professional point of view, but also from a personal one. I appreciated the confidence that Professor Mengüç had in me and the level of freedom that I had in my research. This allowed me to explore subjects that were not originally in my PhD project, and this helped me to broader my horizons as a researcher. This work has also been done in close collaboration with Dr. Rodolphe Vaillon, with which I worked since my master studies. He is one of the best researchers and mentors that I had the chance to meet. His contribution during my PhD work was enormous, and I had a really good time discussing about scientific (and non-scientific) subjects with him. My career plan was to become a University Professor, and I now have the chance to realize my dream at the University of Utah as an Assistant Professor. I hope that both Drs. Mengüç and Vaillon take some credits is this endeavor, as I firmly believe that a good part of my success is related to their mentorships.

I would like to express my gratitude to Professors J. Todd Hastings, Stephen Gedney and Tingwen Wu who kindly accepted to be part of my PhD committee. Special thanks also to Professors Richard Charnigo and Cidambi Srinivasan, and Dr. Mehmet Arik with which I had the chance to work these past years. My labmates Basil T. Wong, Senthil Kumar, Mehmet Kozan, Jaime A. Sanchez, Ellie Hawes, Ozgur Bayer, Benoit Gay, Shuvo Uddin and Mustafa Aslan have been of great support during my studies. I am also grateful to Neha Nehru for preparing some samples, and to Daniel Russell for performing experimental measurements. Finally, I would like to express my deepest gratitude to my girlfriend Randee, my family and my friends for their support during all these years.

# TABLE OF CONTENTS

ACKNOWLEDGEMENTS ..... iii
LIST OF TABLES ..... ix
LIST OF FIGURES ..... x
NOMENCLATURE ..... xv

**Chapter 1 Introduction** ..... **1**

1.1 Definition of near-field radiative transfer ..... 1

1.2 Near-field radiative transfer applied to thermal radiation, thermophotovoltaic power generation and optical characterization ..... 3

1.3 Organization of the dissertation ..... 5

**Chapter 2 Fundamentals of Near-Field Thermal Radiation** ..... **8**

2.1 Fundamental processes in radiative heat transfer: Near-field versus far-field treatment ..... 12

2.2 Electromagnetic description of thermal radiation: Fluctuational electrodynamics and the stochastic Maxwell equations ..... 14

2.3 Near-field radiative heat flux ..... 20

2.4 Density of electromagnetic states ..... 21

2.5 Spatial and temporal coherence of thermal radiation ..... 22

2.6 Experimental evidences of radiative heat transfer enhancement in the near-field ..... 23

2.7 Evanescent waves and surface polaritons ..... 24
  2.7.1 Evanescent waves and total internal reflection ..... 24
  2.7.2 Surface polaritons ..... 27

2.8 Concluding remarks ..... 34

**Chapter 3 Numerical Solution of Near-Field Thermal Radiation in One-Dimensional Layered Media** ..... **35**

3.1 Description of the problem ..... 37

3.2 Dyadic Green's functions for one-dimensional layered media ..... 39

3.3 Solution for the field amplitudes via the scattering matrix approach ..... 44
  3.3.1 Scattering matrix method ..... 44
  3.3.2 Determination of coefficients ..... 47
    3.3.2.1 Case of an emitting film ..... 48
    3.3.2.2 Case of an emitting half-space ..... 51

3.4 Algorithm for solution of one-dimensional near-field thermal radiation problems ............ 52

3.5 Numerical solution of the near-field radiative heat flux ...................................................... 56
  3.5.1 Near-field radiative heat transfer involving cubic boron nitride .................................. 56
  3.5.2 Physical details of near-field radiative heat transfer between two bulks separated by a vacuum gap ........................................................................................................ 65

3.6 Concluding remarks ........................................................................................................ 72

**Chapter 4 Local Density of Electromagnetic States within a Nanometric Gap formed Between Two Thin Films supporting Surface Phonon-Polaritons ........................................ 74**

4.1 Analytical expression of the LDOS in the gap formed between two thin films .................. 76

4.2 Dispersion relation of cross-coupled surface phonon-polaritons ...................................... 80

4.3 LDOS profiles above a single thin film ............................................................................ 84

4.4 LDOS profiles within the gap formed between the two films ........................................... 93
  4.4.1 Impact of inter-film distance ......................................................................................... 94
  4.4.2 Impact of distance where the LDOS is calculated ....................................................... 96
  4.4.3 Impact of thickness of film 3 ......................................................................................... 100

4.5 Concluding remarks ........................................................................................................ 101

**Chapter 5 Near-Field Radiative Heat Transfer between Two Thin Films supporting Surface Phonon-Polaritons ............................................................................................................ 102**

5.1 Analytical expression of the near-field radiative heat flux between two thin films .......... 103

5.2 Convergence of radiative flux for different near-field thermal radiation regimes ............. 106
  5.2.1 Near-field radiative transfer between a bulk and a film ............................................. 106
  5.2.2 Near-field radiative transfer between two bulks ........................................................ 107
  5.2.3 Thermal radiation emission by a single film ............................................................... 107

5.3 Asymptotic analysis of surface phonon-polariton dispersion relation ............................... 108

5.4 Spectral distribution of radiative heat flux near surface phonon-polariton resonance ...... 110

5.5 Approximate predictions of resonant frequencies maximizing the radiative heat flux ..... 118

5.6 Coexistence of two near-field thermal radiation regimes between two thin SiC films ..... 121

5.7 Concluding remarks ........................................................................................................ 133

**Chapter 6 Nanoscale-Gap Thermophotovoltaic Power Generation ..................................... 134**

6.1 Historical overview and main components of TPV power generators .............................. 136

6.2 Basics of a p-n junction and photovoltaic effect .............................................................. 138

6.3 Nano-TPV power generators ............................................................................................ 142

6.3.1 Description of a nano-TPV energy conversion device .......... 142
6.3.2 State-of-the-art on nano-TPV power generation .......... 143
6.3.2.1 Literature on numerical modeling of nano-TPV power generation .......... 143
6.3.2.2 Literature on nano-TPV experimental works .......... 147

6.4 Modeling of coupled near-field thermal radiation, charge and heat transport in the TPV cell .......... 149
6.4.1 Near-field thermal radiation modeling .......... 149
6.4.2 Minority carrier transport modeling .......... 150
6.4.3 Modeling of heat transport in the TPV cell .......... 152
6.4.4 Evaluation of nano-TPV device performances .......... 154

6.5 Modeling of optical, electrical and thermophysical properties .......... 156
6.5.1 Dielectric functions of the radiator and TPV cells .......... 156
6.5.2 Thermal conductivity .......... 161
6.5.3 Intrinsic carrier concentration .......... 161
6.5.4 Thickness of the depletion region .......... 162
6.5.5 Diffusion coefficients and surface recombination velocities .......... 163
6.5.6 Minority carrier lifetimes .......... 163

6.6 Evaluation of nano-TPV system performances .......... 164
6.6.1 Algorithm for solving the coupled near-field thermal radiation, charge and heat transport problem .......... 164
6.6.2 Performances of nano-TPV power generation as a function of the temperature of the cell .......... 165
6.6.3 Predictions of nano-TPV power generation performances via the solution of the coupled near-field thermal radiation, charge and heat transport model .......... 176

6.7 Concluding remarks .......... 180

**Chapter 7 Characterization of Nanoparticles via Scattering of Surface Waves .......... 183**

7.1 Measurement of the state of polarization of light .......... 185
7.1.1 Polarization state of light .......... 185
7.1.2 Stokes vector .......... 188
7.1.3 Mueller (scattering) matrix .......... 190

7.2 Characterization of nanoparticles via elliptically polarized surface waves .......... 191

7.3 Sensitivity analysis of the scattering matrix elements .......... 194

7.4 Concluding remarks .......... 207

**Chapter 8 The Polarized-Surface-Wave-Scattering System (PSWSS) .......... 208**

8.1 Steps for developing the characterization procedure .......... 208

8.2 Experimental measurement of the scattering matrix elements .......... 209

8.3 Description of the PSWSS ........ 214

8.4 Experimental results ........ 217
  8.4.1 Mueller matrix of a linear polarizer ........ 217
  8.4.2 Scattering by a diffraction grating ........ 219
  8.4.3 Scattering by 200 nm gold spherical particles ........ 222
  8.4.4 Scattering by 50 nm gold spherical particles ........ 229

8.5 Concluding remarks ........ 232

**Chapter 9 Conclusions and Recommendations ........ 234**

9.1 Near-field thermal radiation ........ 234

9.2 Nanoscale-gap thermophotovoltaic power generation ........ 238

9.3 Optical characterization of nanoparticles via scattered surface waves ........ 242

**Appendix A Solution of the Stochastic Maxwell Equations via the Method of Potentials .. 246**

**Appendix B Models for Dielectric Functions of Metals and Polar Crystals ........ 251**

**Appendix C Sipe's Unit Vectors ........ 253**

**Appendix D Validation of Near-Field Thermal Radiation Simulations ........ 256**

D.1 Far-field thermal radiation emission from thin films ........ 256

D.2 Near-field radiative heat transfer between two bulks of cubic boron nitride ........ 258

D.3 Near-field radiative heat transfer between two bulks of silicon carbide ........ 259

D.4 Near-field radiative heat transfer between two films of silicon carbide ........ 260

**Appendix E Length Scale of Transition from the Near- to the Far-Field Regime of Thermal Radiation between Two Dielectric Bulks ........ 262**

**Appendix F Derivation of the Near-Field Radiative Heat Flux between Two Films ........ 268**

**Appendix G Numerical Solution and Validation of the Nanoscale-Gap Thermophotovoltaic Model ........ 274**

G.1 Discretization equations ........ 274

G.2 Validation of the coupled near-field thermal radiation and charge transport model ........ 279

**Appendix H Database of Scattering Matrix Elements** ........ **287**

H.1 Modeling of agglomerates of spherical nanoparticles ........ 287

H.2 Construction of a database of scattering profiles ........ 288

**Appendix I Technical Details of the PSWSS** ........ **290**

I.1 Feasibility and stability of measuring the scattering matrix elements via the six intensity method ........ 290

I.2 Components of the PSWSS and settings of the lock-in amplifiers ........ 293

I.3 Optical scheme of the PSWSS ........ 294

I.4 Calibration of the polarizers and quarter-wave plates ........ 297

I.4.1 Calibration of the linear polarizers (LPs) ........ 297

I.4.2 Calibration of the quarter-wave plates (QWPs) ........ 298

**References** ........ **301**

**Vita** ........ **323**

# LIST OF TABLES

Table 2.1. Model used for each fundamental process of thermal radiation in the far- and near-field regimes. 20

Table 6.1. Summary of theoretical and numerical modeling of nano-TPV power generation devices. 147

Table 7.1. Optimal configuration for the estimation of a given parameter. 206

Table 8.1. Optimal set of orientation angles for the LPs and QWPs used in the PSWSS. 212

Table 8.2. Recovered Mueller matrix elements of a LP oriented at $\xi = 0°$. 218

Table 8.3. Mueller matrix elements of a LP ($\xi = 0°$) recovered numerically by adding stochastic noise on the intensities (see section I.1 of appendix I for details of the procedure). 219

Table 8.4. Scattering angles of SPPs excited by a grating as a function of the diffraction order ($\theta_i = 38°$) 221

# LIST OF FIGURES

Figure 1.1. (a) Evanescent wave at an interface. (b) Scattering of an evanescent wave by a particle. (c) Tunneling of an evanescent wave by a surface. ........ 2

Figure 2.1. Schematic representation of an evanescent wave generated at the interface of two dielectrics via total internal reflection. ........ 25

Figure 2.2. Schematic representation of a surface polariton at the interface delimiting a material supporting surface polariton with a dielectric function $\varepsilon_{r1}(\omega)$ and a vacuum with $\varepsilon_{r2} = 1$ ........ 28

Figure 2.3. (a) SPhP dispersion relation at a SiC-vacuum interface. (b) Real part of the dielectric function of SiC. ........ 32

Figure 3.1. Schematic representation of the one-dimensional layered medium, where $N - 1$ layers of finite thicknesses are sandwiched between two half-spaces. ........ 38

Figure 3.2. Field patterns in each layer due to a point source $z'$ located in layer $s$ emitting in the $z$-positive and $z$-negative directions; $z_c$ in layer $l$ is the point where the radiative heat flux is calculated. ........ 40

Figure 3.3. (a) Schematic representation of two bulks of *c*BN separated by a vacuum gap of thickness $d_c$. (b) Schematic representation of a *c*BN film of thickness $t$ and a bulk *c*BN separated by a distance $d_c$. ........ 57

Figure 3.4. (a) Monochromatic evanescent component of the radiative heat flux per unit $k_\rho$ between two *c*BN bulks ($T$ = 300 K and 0 K) separated by a 100 nm thick vacuum gap. (b) Real part of the dielectric function of *c*BN as a function of $\omega$. ........ 58

Figure 3.5. (a) Propagating and evanescent components of the monochromatic radiative heat flux between two bulks of *c*BN ($T$ = 300 K and 0 K) separated by a vacuum gap $d_c$ = 100 nm. (b) Monochromatic radiative heat flux between two bulks of *c*BN ($T$ = 300 K and 0 K) separated by vacuum of $d_c$ = 50 nm, 100 nm, 500 nm, 1 μm, and 500 μm; the values are compared with the predictions for two blackbodies. ........ 60

Figure 3.6. Monochromatic radiative heat flux between a *c*BN film emitter (at 300 K) of variable thickness $t$ and a bulk of *c*BN (at 0 K) separated by a 100 nm thick vacuum gap; comparisons are shown for $t$ = 1 nm, 10 nm, 100 nm, 1 μm, 100 μm, and a bulk. ........ 62

Figure 3.7. Schematic representation of two emitting films of *c*BN of equal thicknesses $t$ separated by a vacuum gap Δ; the top-most emitting film (medium 3) is located at a distance $d_c$ of a bulk *c*BN. ........ 63

Figure 3.8. Monochromatic radiative heat flux between a 10 nm thick *c*BN film (at 300 K) and a bulk of *c*BN (at 0 K) separated by a 100 nm vacuum gap. The influence of the presence of a film of *c*BN behind the emitter (medium 1) is analyzed for separation distances between the films Δ of

1 nm, 10 nm, 100 nm, and 1 μm; results are compared with the case that no film is behind the emitter. 64

Figure 3.9. Near-field radiative heat transfer between two SiC bulk regions separated by a vacuum gap of thickness $d_c$: (a) $d_c$ = 10 nm, 100 nm, and 1 μm; results are compared with the fluxes in the far-field regime and between blackbodies. (b) evanescent TE and TM contributions for $d_c$ = 10 nm; results are compared with the flux between blackbodies. 69

Figure 3.10. Radiative heat transfer coefficient $h_r$ between two bulks of SiC as a function of $d_c$ for $T$ = 300 K; the $d_c^{-2}$ asymptote is also plotted in the figure. 72

Figure 4.1. Schematic representation of the geometry considered: the LDOS is calculated at a distance Δ above the emitting film 1 within the gap of thickness $d_c$. 76

Figure 4.2. Dispersion relations of SPhPs for $t_1$ and $t_3$ thick SiC films submerged in vacuum and separated by a gap $d_c$: (a) $t_1 = t_3$ = 10 nm, and $d_c$ = 10 nm and 100 nm. (b) $t_1$ = 100 nm, $t_3$ = 10 nm, and $d_c$ = 10 nm and 100 nm. Results are compared with the dispersion relations of single SiC films in vacuum and a single SiC-vacuum interface. 82

Figure 4.3. Results of Δ-independent integrand of the TM evanescent component of the monochromatic LDOS (in log-scale) are presented for: (a) $t_1$ = 10 nm. (b) $t_1$ = 100 nm. The dashed lines correspond to the dispersion relation of a single film, while the full line is the dispersion relation of a single interface. 85

Figure 4.4. Penetration depth of evanescent waves in vacuum (in log-scale), and SPhP dispersion relation for a 100 nm thick SiC film: (a) evanescent waves with $\delta_2$ greater or equal than 50 nm are in color. (b) evanescent waves with $\delta_2$ greater or equal than 500 nm are in color. 87

Figure 4.5. TM evanescent component of the monochromatic LDOS for Δ = 1 nm, 10 nm, 50 nm, 100 nm, and 500 nm. Results are provided for two different SiC film thicknesses: (a) $t_1$ = 10 nm. (b) $t_1$ = 100 nm. 90

Figure 4.6. Approximate prediction of anti-symmetric and symmetric SPhP resonant frequencies, calculated via Eq. (4.8), as a function of $t_1/\Delta$ for SiC and *c*BN films submerged in vacuum; the frequency is normalized as $\Omega = (\omega - \omega_{TO})/(\omega_{LO} - \omega_{TO})$. 92

Figure 4.7. TM evanescent component of the monochromatic LDOS in the gap at $\Delta = d_c$ = 10 nm, 100 nm, 200 nm, and 500 nm: (a) $t_1 = t_3$ = 10 nm. (b) $t_1$ = 100 nm and $t_3$ = 10 nm. Results are compared with a single emitting film. 95

Figure 4.8. TM evanescent component of the monochromatic LDOS in the gap for $t_1 = t_3$ = 10 nm, $d_c$ = 100 nm, and Δ = 10 nm, 50 nm, and 100 nm; results are compared with a single 10 nm thick emitting film. 96

Figure 4.9. TM evanescent component of the monochromatic LDOS in the gap for $t_1$ = 100 nm, $t_3$ = 10 nm, Δ = 50 nm, and $d_c$ = 50 nm, 70 nm, 100 nm, and 500 nm; results are compared with a single 100 nm thick emitting film. 98

Figure 4.10. TM evanescent component of the monochromatic LDOS per unit $k_\rho$ (in log-scale) in the gap for $t_1$ = 100 nm, $t_3$ = 10 nm, and $\Delta$ = 50 nm: (a) $d_c$ = 50 nm. (b) $d_c$ = 100 nm. ................. 99

Figure 4.11. TM evanescent component of the monochromatic LDOS in the gap for $t_1$ = 10 nm, $\Delta = d_c$ = 100 nm, and $t_3$ = 10 nm, 50 nm, 100 nm, and 500 nm; results are compared with a single 10 nm thick emitting film. ........................................................................................................ 100

Figure 5.1. Schematic representation of the geometry considered: the radiative heat flux is calculated between two SiC films (media 1 and 3) submerged in vacuum and separated by a gap $d_c$. ........................................................................................................................ 104

Figure 5.2. Spectral distribution of radiative heat flux absorbed by layer 3 ($T_3$ = 0 K) due to an emitting film 1 ($T_1$ = 300 K): $t_1 = t_3$ = 10 nm, $d_c$ = 1 nm, 10 nm, 50 nm, 100 nm and 500 nm. .. 111

Figure 5.3. Spectral distribution of TM evanescent radiative heat flux per unit $k_\rho$ (in log-scale) absorbed by medium 3 ($T_3$ = 0 K) due to an emitting film 1 ($T_1$ = 300 K): (a) $t_1 = t_3 = d_c$ = 10 nm. (b) $t_1 = t_3$ = 10 nm and $d_c$ = 100 nm. SPhP dispersion relations for two films (full lines), a single film (dashed lines), and a single interface (dashed line) are shown for comparison. ................. 113

Figure 5.4. Spectral distribution of radiative heat flux absorbed by layer 3 ($T_3$ = 0 K) due to an emitting film 1 ($T_1$ = 300 K): $t_1$ =10 nm, $d_c$ = 100 nm, $t_3$ = 10 nm, 50 nm, 100 nm and 500 nm. 115

Figure 5.5. Spectral distribution of TM evanescent radiative heat flux per unit $k_\rho$ (in log-scale) absorbed by medium 3 ($T_3$ = 0 K) due to an emitting film 1 ($T_1$ = 300 K): (a) $t_1$ = 10 nm, $t_3$ = 50 nm, and $d_c$ = 100 nm. (b) $t_1$ = 10 nm, $t_3$ = 500 nm, and $d_c$ = 100 nm. SPhP dispersion relations for two films (full lines), single films (dashed lines), and a single interface (dashed line) are shown for comparison. ........................................................................................................ 117

Figure 5.6. Approximate predictions of SPhP resonant frequencies for a system of two SiC films submerged in vacuum: (a) variation of $t_1/d_c = t_3/d_c$. (b) $t_1/d_c$ is fixed at 0.1, while $t_3/d_c$ varies. Predictions are made by assuming $\delta_2 \approx \ln(10)\left|k_{z2}\right|^{-1}$ (full lines) and $\delta_2 \approx \left|k_{z2}\right|^{-1}$ (dashed lines). 119

Figure 5.7. (a) Radiative heat transfer coefficient $h_r$ as a function of $d_c$ for $t_1$ = 1 nm, 5 nm, 10 nm, and 50 nm and $t_3 \to \infty$ (bulk); the results are compared with $h_r$ between two bulks. (b) Identification of the $d_c^{-2}$ and $d_c^{-3}$ regimes for $t_1$ = 10 nm. .......................................................... 123

Figure 5.8. (a) Radiative heat transfer coefficient $h_r$ as a function of $d_c$ for $t_1 = t_3$ = 1 nm, $t_1$ = 1 nm and $t_3$ = 10 nm, $t_1 = t_3$ = 10 nm, and $t_1$ = 50 nm and $t_3$ = 10 nm; the results are compared with $h_r$ between two bulks. (b) Identification of the $d_c^{-2}$ and $d_c^{-3}$ regimes for $t_1$ = 10 nm and $t_3$ = 50 nm. (c) Identification of the $d_c^{-2}$ and $d_c^{-3}$ regimes for $t_1$ = 1 nm and $t_3$ = 10 nm. ..................................... 126

Figure 6.1. Schematic representation of a p-n junction (similar to Fig. 5-11 from [141]). .......... 139

Figure 6.2. Schematic representation of the *J-V* characteristic of a p-n junction. ....................... 141

Figure 6.3. Schematic representation of the nano-TPV power generation system under study. ....... 142

Figure 6.4. Dielectric function of $In_{0.18}Ga_{0.82}Sb$ at 300 K (GaSb is p-doped): (a) real part of the dielectric function. (b) imaginary part of the dielectric function. 158

Figure 6.5. Interband absorption coefficient of $In_{0.18}Ga_{0.82}Sb$: (a) $T$ = 300 K. Note that the exponential tail shown is not obtained from the model, but has been drawn in an approximate manner for the purpose of discussion. (b) $T$ = 300 K, 350 K, 400 K, 500 K and 600 K. 160

Figure 6.6. Performances of nano-TPV devices as a function of $d_c$ for $T_{cell}$ = 300 K: (a) radiation absorbed by the cell and electrical power output. (b) photocurrent generated. (c) conversion efficiency. 168

Figure 6.7. (a) Quantum efficiency of the nano-TPV device as a function of $d_c$ for $T_{cell}$ = 300 K. (b) Monochromatic radiative heat flux at $z = Z_2$ as a function of $d_c$. 169

Figure 6.8. Performances of nano-TPV devices as a function of $T_{cell}$ (300 K to 500 K) for of $d_c$ = 20 nm, 50 nm and 100 nm: (a) radiation absorbed by the cell and electrical power output. (b) total photocurrent generated. (c) conversion efficiency. 172

Figure 6.9. (a) $J$-$V$ characteristic of a nano-TPV device with $d_c$ = 20 nm for $T_{cell}$ = 300 K, 350 K, 400 K, 450 K and 500 K. (b) Dark current $J_0$ as a function of the forward bias $V_f$ for $T_{cell}$ = 300 K, 350 K, 400 K, 450 K and 500 K. 174

Figure 6.10. Averaged temperature of the cell as a function of $h_\infty$ ($T_\infty$ = 293 K) for $d_c$ = 5 μm, 100 nm, 50 nm and 20 nm. 177

Figure 6.11. Spatial distributions of the different contributions to the local heat generation term $Q(z)$ for $T_\infty$ = 293 K and $h_\infty = 10^4$ $Wm^{-2}K^{-1}$: (a) $d_c$ = 5 μm. (b) $d_c$ = 20 nm. 179

Figure 6.12. Performances of nano-TPV energy conversion as a function of $d_c$ and $h_\infty$ ($T_\infty$ = 293 K): (a) electrical power output $P_m$. (b) Conversion efficiency $\eta_c$. 181

Figure 7.1. Schematic representation of a: (a) linearly polarized wave. (b) right-circularly polarized wave. 187

Figure 7.2. Schematic representation of an elliptically polarized wave. 188

Figure 7.3. Schematic of the characterization concept where the nanoparticles are illuminated via a surface wave (evanescent wave or SPP) generated by total internal reflection of an external radiation beam. 192

Figure 7.4. Averaged normalized sensitivity coefficient to $d_m$. (a) Uniform distribution of particles with $d_m$ from 10 to 15 nm. (b) Uniform distribution of particles with $d_m$ from 45 to 50 nm. 199

Figure 7.5. Normalized scattering matrix elements as a function of $\theta_s$ for different $p$ values and $d_m$ = 40 nm. (a) $M_{11}$. (b) $M_{12}$. (c) $M_{33}$. (d) $M_{34}$. 200

Figure 7.6. Averaged normalized sensitivity coefficient to $p$ ($d_m$ = 40 nm). (a) Sensitivity of $M_{12}$. (b) Sensitivity of $M_{33}$. (c) Sensitivity of $M_{34}$. 202

Figure 7.7. Normalized scattering matrix elements as a function of $\theta_s$ for different $p$ values. Non-uniform distribution of particles and agglomerates with $d_m$ from 38 nm to 42 nm. (a) $M_{11}$. (b) $M_{12}$. (c) $M_{33}$. (d) $M_{34}$ .......... 204

Figure 7.8. Averaged normalized sensitivity coefficient to $d_m$. Non-uniform distribution of particles and agglomerates with $d_m$ from 38 nm to 42 nm. (a) Sensitivity of $M_{12}$. (b) Sensitivity of $M_{33}$. (c) Sensitivity of $M_{34}$. .......... 206

Figure 8.1. Diagram showing the necessary steps for the establishment of the characterization procedure. .......... 209

Figure 8.2. Schematic representation of the PSWSS. .......... 214

Figure 8.3. Picture of the PSWSS. .......... 216

Figure 8.4. Schematic representation of the prism-sample system. .......... 217

Figure 8.5. Schematic representation of the diffraction grating used to calibrate the far-field angular measurements of the PSWSS. .......... 219

Figure 8.6. Normalized intensity due to SPP coupling with the diffraction grating shown in Fig. 8.5 ($\theta_i = 38^{\circ}$) .......... 221

Figure 8.7. Direct measurement of scattered intensity ($M_{11}$); experiments 1 and 2 were performed on the exact same location on the sample. .......... 223

Figure 8.8. Direct measurement of scattered intensity ($M_{11}$); comparison between the results of Fig. 8.7 and those obtained after repositioning the sample on the prism. .......... 224

Figure 8.9. Scattering profiles measured via the four intensity method: (a) $M_{11}$; the results are compared with the scattered intensity measured directly. (b) $M_{12}$, $M_{21}$ and $M_{22}$. .......... 225

Figure 8.10. Scattering profiles measured via the four intensity method: (a) $M_{11}$; the results are compared with the scattered intensity measured directly. (b) $M_{12}$, $M_{21}$ and $M_{22}$. The measurements were performed on a different location on the sample than in Fig. 8.9. .......... 226

Figure 8.11. Scattering profiles measured via the six intensity method: (a) $M_{11}$; the results are compared with the scattered intensity measured directly. (b) $M_{12}$, $M_{22}$, $M_{33}$, $M_{34}$ and $M_{44}$. .......... 228

Figure 8.12. Scattering profiles measured via the four intensity and the six intensity method: (a) $M_{11}$; the results are compared with the scattered intensity measured directly. (b) $M_{12}$ and $M_{21}$. (c) $M_{22}$. (d) $M_{33}$, $M_{34}$ and $M_{44}$ .......... 231

Figure 8.13. Scattering profiles measured via the four intensity method; results are compared with numerical predictions for $p$ values of 0 % and 100 %: (a) $M_{11}$. (b) $M_{12}$. .......... 233

# NOMENCLATURE

| | |
|---|---|
| $a$, $b$, $c$, $d$ | coefficients of discretization equation |
| $A$, $B$, $C$, $D$ | field amplitude coefficients |
| $\mathbf{A}$ | magnetic vector potential [Wb m$^{-3}$] |
| $\mathbf{B}$ | magnetic induction [Wb m$^{-2}$] |
| $c_v$ | speed of light in vacuum (= 2.998×10$^{8}$ m s$^{-1}$) |
| $C_{ij}$ | coefficient matrix elements |
| $C_N$ | condition number of the coefficient matrix |
| $d_m$ | diameter of a spherical particle [m] |
| $D_{(e,h)}$ | diffusion coefficient of electron / hole [m$^{2}$ s$^{-1}$] |
| $\mathbf{D}$ | electric displacement [C m$^{-2}$] |
| $e$ | electron charge (= 1.6022×10$^{-19}$ J eV$^{-1}$) |
| $E$ | wave energy (= $\hbar\,\omega/e$) [eV] |
| $E_g$ | bandgap [eV] |
| $\mathbf{E}$ | electric field vector [V m$^{-1}$] |
| $FF$ | fill factor |
| $g$ | generation rate of electron-hole pairs [m$^{-3}$ s$^{-1}$] |
| $\overline{\overline{\mathbf{g}}}^{E}, \overline{\overline{\mathbf{g}}}^{H}$ | electric / magnetic Weyl component of the dyadic Green's function [m] |
| $G_0$ | scalar Green's function [m$^{-1}$] |
| $\overline{\overline{\mathbf{G}}}^{E}, \overline{\overline{\mathbf{G}}}^{H}$ | electric / magnetic dyadic Green's function [m$^{-1}$] |
| $h_r$ | radiative heat transfer coefficient [W m$^{-2}$ K$^{-1}$] |
| $h_\infty$ | convective heat transfer coefficient [W m$^{-2}$ K$^{-1}$] |
| $\hbar$ | circular Planck's constant (= 1.0546×10$^{-34}$ J s) |
| $\mathbf{H}$ | magnetic field vector [A m$^{-1}$] |
| $i$ | complex constant (= (-1)$^{1/2}$) |
| $I$, $Q$, $U$, $V$ | Stokes parameters |
| $I_b$ | blackbody intensity [W m$^{-2}$ sr$^{-1}$] |
| $\mathbf{I}$ | Stokes vector |
| $\overline{\overline{\mathbf{I}}}$ | unit dyad |
| Im | imaginary part |
| $J$ | effective photocurrent [A m$^{-2}$] |
| $J_0$ | dark current [A m$^{-2}$] |
| $J_m$ | photocurrent associated with a maximum power output [A m$^{-2}$] |
| $J_{ph}$ | photocurrent generated [A m$^{-2}$] |
| $J_{sc}$ | short-circuit photocurrent [A m$^{-2}$] |
| $\mathbf{J}$ | current density vector [A m$^{-2}$] |
| $\mathbf{J}^{r}$ | stochastic current density vector [A m$^{-2}$] |
| $k$ | wavevector (= $k' + ik''$) [rad m$^{-1}$] |
| $k_b$ | Boltzmann constant (= 1.3807×10$^{-23}$ J K$^{-1}$) |
| $k_{cond}$ | thermal conductivity [W m$^{-1}$ K$^{-1}$] |
| $\mathbf{K}$ | intensity vector |
| $L_{dp}$ | thickness of depletion region [m] |
| $m_0$ | electron rest mass (= 9.109×10$^{-31}$ kg) |

| | |
|---|---|
| $m^*_{(e,h)}$ | effective electron / hole mass [kg] |
| $M_{ij}$ | normalized scattering (Mueller) matrix elements |
| $n$ | index of refraction ($= n' + in''$) |
| $n_i$ | intrinsic carrier concentration [m$^{-3}$] |
| $n_{(e,h)}$ | electron / hole concentration [m$^{-3}$] |
| $n_{(e,h)0}$ | electron / hole equilibrium concentration [m$^{-3}$] |
| $\hat{\mathbf{n}}$ | unit vector normal to a surface |
| $N_a$ | acceptor concentration [m$^{-3}$] |
| $N_c$ | effective density of states in the conduction band [m$^{-3}$] |
| $N_d$ | donor concentration [m$^{-3}$] |
| $N_n$ | number of spatial nodes in n-doped region |
| $N_p$ | number of spatial nodes in p-doped region |
| $N_v$ | effective density of states in the valence band [m$^{-3}$] |
| $p$ | percentage of single nanoparticles in an agglomerate [%] |
| $\hat{\mathbf{p}}$ | TM-polarized unit vector |
| $P_j$ | propagation matrix of layer $j$ |
| $P_m$ | maximum electrical power output [W m$^{-2}$] |
| $q$ | radiative heat flux [W m$^{-2}$] |
| $Q$ | heat source [W m$^{-3}$] |
| $Q_{NRR}$ | heat source due to non-radiative recombination of electron-hole pairs [W m$^{-3}$] |
| $Q_{RR}$ | heat source due to radiative recombination of electron-hole pairs [W m$^{-3}$] |
| $Q_T$ | heat source due to thermalization [W m$^{-3}$] |
| $r_{ij}$ | Fresnel's reflection coefficients at interface $i-j$ |
| $\mathbf{r}$ | position vector [m] |
| $R_j$ | reflection coefficient of layer $j$ |
| Re | real part |
| $\hat{\mathbf{s}}$ | TE-polarized unit vector |
| $S_i$ | amplitude scattering matrix elements |
| $S_{ij}$ | scattering (Mueller) matrix elements |
| $S_r$ | radiative heat source [W m$^{-3}$] |
| $S_{(e,h)}$ | surface recombination velocity of electron / hole [m s$^{-1}$] |
| $S(i,j)$ | scattering matrix between layers $i$ and $j$ |
| $S^{+,-}$ | amplitude of source propagating in forward / backward direction |
| $\mathbf{S}$ | Poynting vector [W m$^{-2}$] |
| $t$ | time [s] |
| $t_j$ | thickness of layer $j$ [m] |
| $t_{ij}$ | Fresnel's transmission coefficients at interface $i-j$ |
| $T$ | temperature [K] |
| $T_j$ | transmission coefficient of layer $j$ |
| $T_\infty$ | temperature of thermal management system [K] |
| $u_\omega$ | monochromatic energy density [J m$^{-3}$ (rad/s)$^{-1}$] |
| $V$ | volume [m$^3$] |
| $V_0$ | equilibrium potential in depletion region [V] |
| $V_f$ | forward bias [V] |
| $V_{ij}$ | transmission matrix at interface $i-j$ |

| | |
|---|---|
| $V_m$ | voltage associated with a maximum power output [V] |
| $V_{oc}$ | open-circuit voltage [V] |
| $w_k$ | weighting factor associated to a distribution function |
| $X$ | sensitivity coefficient |
| $\mathbf{Z}$ | vector containing six scattering matrix elements |

**Greek symbols**

| | |
|---|---|
| $\alpha$ | angle of the vibration ellipse [rad] |
| $\beta$ | orientation angle of the fast axis of a quarter-wave plate [rad] |
| $\delta$ | penetration depth of an evanescent wave [m] |
| $\Delta z$ | control volume [m] |
| $\varepsilon$ | electric permittivity [$C^2$ $N^{-1}$ m] |
| $\varepsilon_r$ | dielectric function (=$\varepsilon_r' + i\varepsilon_r''$) |
| $\varepsilon_s$ | static relative permittivity [F $m^{-1}$] |
| $\varepsilon_v$ | absolute permittivity [F $m^{-1}$] |
| $\varepsilon_\infty$ | high frequency dielectric constant |
| $\hat{\varepsilon}_j$ | emissivity of surface $j$ |
| $\Phi_e$ | electric scalar potential [V] |
| $\Phi_{PR}$ | photon recycling factor |
| $\gamma$ | damping factor [$s^{-1}$] |
| $\Gamma$ | damping factor [$s^{-1}$] |
| $\eta$ | known parameter of a system |
| $\eta_c$ | internal conversion efficiency |
| $\eta_{q,\omega}$ | quantum efficiency |
| $\kappa$ | absorption coefficient [$m^{-1}$] |
| $\lambda$ | wavelength [m] |
| $\lambda_w$ | Wien's wavelength (= 2897.8/$T$ μm) |
| $\Lambda$ | period of a grating [m] |
| $\mu$ | magnetic permeability [N $A^{-2}$] |
| $\mu_{(e,h)}$ | electron / hole mobility [$m^2$ $V^{-1}$ $s^{-1}$] |
| $\theta$, $\phi$ | polar / azimuthal angle (chapters 7 and 8) [rad] |
| $\theta_{cr}$ | critical angle for total internal reflection [rad] |
| $\theta_d$ | angle of diffraction [rad] |
| $\Theta$ | mean energy of a Planck oscillator [J] |
| $\rho$, $\theta$, $z$ | polar coordinate system (chapters 2 to 6) |
| $\rho_e$ | electric charge density [C $m^{-3}$] |
| $\rho_\omega$ | monochromatic density of electromagnetic states [$m^{-3}$ $(rad/s)^{-1}$] |
| $\hat{\rho}_{ij}$ | reflectivity at interface $i$ - $j$ |
| $\sigma$ | electrical conductivity [$C^2$ $N^{-1}$ $m^{-1}$ $s^{-1}$] |
| $\tau_{(e,h)}$ | electron / hole lifetime [s] |
| $\omega$ | angular frequency [rad $s^{-1}$] |
| $\omega_{LO}$ | longitudinal optical phonon frequency [rad $s^{-1}$] |
| $\omega_p$ | plasma frequency [rad $s^{-1}$] |

|  |  |
|---|---|
| $\omega_{res}$ | resonant frequency of a single interface [rad $s^{-1}$] |
| $\omega_{TO}$ | transverse optical phonon frequency [rad $s^{-1}$] |
| $\xi$ | orientation angle of the transmission axis of a linear polarizer [rad] |
| $\psi$ | parameter to be estimated |

**Subscripts and superscripts**

|  |  |
|---|---|
| +, - | resonant modes of a film |
| * | complex conjugate |
| $'$, $''$ | source point |
| 1, 2, 3, 4 | resonant modes of two film configuration |
| *abs* | absorbed |
| *avg* | averaged |
| *Auger* | Auger recombination |
| *dp* | depletion |
| *e* | electron |
| *emi* | emitted |
| *evan* | evanescent |
| *fc* | free carriers |
| *h* | hole |
| *i* | incident |
| *ib* | interband |
| *latt* | lattice |
| max | resonance of the near-field thermal radiation spectrum |
| *n* | n-doped |
| *norm* | normalized |
| *NRR* | non-radiative recombination |
| *p* | p-doped |
| *prop* | propagating |
| *rad* | radiative recombination |
| *s* | scattered |
| *SRH* | Shockley-Read-Hall recombination |
| *tot* | total |
| *TE* | transverse electric |
| *TM* | transverse magnetic |
| *v* | vacuum |
| $\omega$, $E$, $\lambda$ | monochromatic |

# Chapter 1

# Introduction

### 1.1 Definition of near-field radiative transfer

Generally speaking, radiative transfer can be defined as a mode of energy transfer via electromagnetic waves. A typical example of energy transfer via electromagnetic waves well-known from mechanical engineers arises in radiation heat exchanges between blackbodies. In that case, thermal generation of propagating electromagnetic waves, carrying energy away from a surface, are transferred from one body to another, thus resulting in a net heat transfer. There exists however another type of waves, called evanescent waves or surface waves, through which energy transfer can arise. Conversely to propagating waves, evanescent waves are propagating only along the interface of two media, and are exponentially decaying over a distance of about a wavelength $\lambda$ normal to that interface, as schematically depicted in Fig. 1.1(a). In the absence of a structure interacting with the evanescent wave field, as in Fig. 1.1(a), it can be shown that no net energy is radiated away from the interface [1-3].

On the other hand, the interaction of a structure with an evanescent wave leads to a multitude of intriguing physical phenomena that can be used for engineering applications. For example, in Fig. 1.1(b), the evanescent wave excites the charges within the particle, which in turn radiates the energy away from the surface. In Fig. 1.1(c), a surface is brought within the evanescent field associated with medium 1, and a net energy transfer thus occurs between the bodies due to tunneling of the evanescent wave. In these cases, the evanescent wave becomes propagating due to the interaction with a structure, and thus actively contributes to radiative energy transfer.

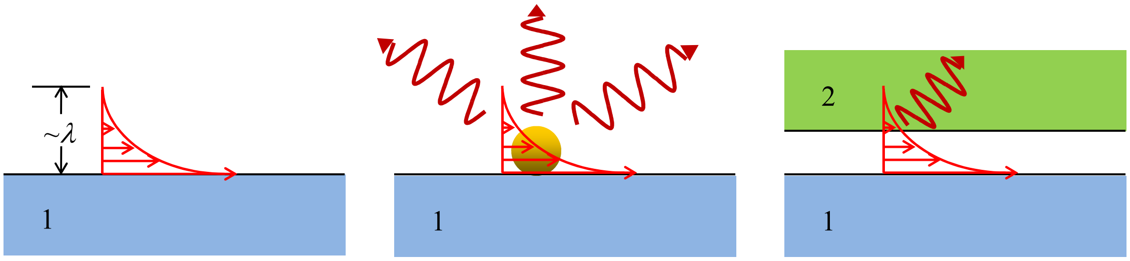

(a) (b) (c)

Figure 1.1. (a) Evanescent wave at an interface. (b) Scattering of an evanescent wave by a particle. (c) Tunneling of an evanescent wave by a surface.

The definition of radiative transfer can therefore be refined. Based on the distinction between propagating and evanescent waves, it is possible to define two regimes of radiative transfer. The far-field regime of radiative transfer arises when energy is exchanged through propagating electromagnetic waves only. Bodies exchanging radiative energy that are separated by distances greater than the wavelength of radiation are in the far-field regime, since evanescent waves decay exponentially over a distance of about a wavelength. Conversely, the near-field regime arises when energy, or a part of the energy, is transferred through evanescent waves. Following the above discussion, this happens when bodies are separated by sub-wavelength distances since a structure needs to be interacting with the evanescent field in order to excite these modes away from a surface. In this latter regime, energy can also be transferred via propagating waves; however, at sub-wavelength distances, coherence effects may become important.

In this dissertation, we are interested by electromagnetic waves in the ultraviolet, visible and infrared ranges. As a consequence, near-field radiative transfer can alternatively be referred to as “near-field optics” and “nano-optics.” Indeed, for the range of wavelengths considered, the near-field effects of radiative transfer are dominant when the bodies are separated by few tens to few hundreds of nanometers, such that the term “nano-optics” is appropriate.

Engineering applications of near-field radiative transfer are numerous, such as in energy conversion technologies [4,5], in tailoring materials with new optical properties [6], in designing surfaces selectively emitting thermal radiation [7], in developing optical techniques overcoming the diffraction limit [1,8], in bottom-up nano-patterning [9,10], and in waveguiding [11-13] to name only a few. In this dissertation, we investigate more specifically thermal radiation in the near-field, nanoscale-gap thermophotovoltaic power generation and optical characterization of nanoparticles.

## 1.2 Near-field radiative transfer applied to thermal radiation, thermophotovoltaic power generation and optical characterization

The classical theory of thermal radiation, pioneered by Max Planck, is based on the blackbody concept [14-17]. Planck's blackbody distribution is however restricted to a fundamental assumption: the distances between the bodies exchanging thermal radiation are greater than the dominant wavelength of emission [14], such that thermal energy is transferred through propagating waves only. In the near-field, radiative heat transfer can exceed by few orders of magnitude the values predicted between blackbodies due to the presence of evanescent waves. The first correct modeling of near-field radiative heat transfer, based on Rytov's electromagnetic description of thermal emission [18,19], was provided by Polder and Van Hove [20]. Since then, numerical modeling of near-field thermal radiation has been limited to relatively simple problems [21-29]. The first objective of this dissertation is therefore to develop a numerical model to solve near-field thermal radiation problems in one-dimensional layered media without limitation on the number of layers. Such a model is of high practical importance, since the one-dimensional analysis does sufficiently describe the physics of many practical systems, as in most cases the separation distance between the bodies exchanging thermal radiation is much smaller than the other dimensions of the system.

Mulet et al. [30] were the first to point out the importance of surface phonon-polaritons (SPhPs) in near-field thermal radiation as these waves, having high degrees of spatial and temporal coherence, can lead to quasi-monochromatic radiant energy exchanges. Greffet et al. [7] demonstrated that the high degree of spatial coherence of SPhPs can be used to design structures selectively emitting thermal radiation in the far-field. While it was shown in the past that it is possible to use the near-field effects to tune far-field thermal emission, no discussion on tuning near-field thermal emission has been proposed so far in the literature. In this dissertation, the possibilities of tuning near-field thermal emission and radiative transfer via coupling of SPhPs in thin films are explored. Such an analysis is fundamental is many fields of engineering, such as in energy conversion technologies.

The fundamental analysis of near-field thermal radiation is afterwards applied to thermophotovoltaic (TPV) power generation. TPV power generation is similar to solar photovoltaic energy conversion, except that a radiator is employed as a source of thermal radiation instead of the sun [31]. Current TPV technologies however suffer from low conversion efficiency and power output [32]. Whale and Cravalho [33,34] proposed to separate the radiator and the cells, converting thermal radiation into electricity, by a sub-wavelength distance in order to increase the power output via tunneling of evanescent waves. So far, research efforts on these nanoscale-gap TPV, or nano-TPV, devices have shown that it is indeed possible to increase the electrical power output via evanescent waves [33-37]. The objective of this part of the dissertation is twofold. First, we aim to provide an accurate modeling of nano-TPV energy conversion systems through the solution of the coupled near-field thermal radiation, charge and heat transport problem, which has not been done so far in the literature. The second objective is to analyze the impacts of the thermal effects on the performances of nano-TPV devices, which is fundamental for the development of a viable energy conversion technology.

The last subject of this dissertation is relatively different from what has been discussed so far, but is of course still related to near-field radiative transfer. Nanoparticles are of primary importance in multiple applications, and their uses may allow to obtain unique optical, electrical and structural properties [38]. The synthesis of nanoparticles is however still considered art, and without measurement of their properties in real-time, it may be difficult to achieve the desired configurations. Mengüç's group addressed this problem by proposing a non-intrusive, and potentially on-line, tool for characterizing nanoparticles from 5 nm to 100 nm in size [39-42]. To circumvent the diffraction limit [1], the nanoparticles to be characterized are illuminated by an evanescent wave or a surface plasmon-polariton generated by total internal reflection of an external radiation beam having a wavelength in the visible spectrum. The far-field scattered surface waves can thus be used, through the measurement of the Mueller matrix elements, to infer the properties of the particles via an inverse algorithm. The objective of this last part of the dissertation is to develop an experimental procedure for measuring the far-field intensity and state of polarization of scattered surface waves. Although the characterization framework can be applied to scatterers of any shape, we restrict the analysis in this dissertation to metallic spherical nanoparticles.

### 1.3 Organization of the dissertation

Near-field thermal radiation is a new and emerging field of heat transfer engineering. Since this subject is relatively unknown, the fundamentals of near-field radiative heat transfer are given in chapter 2. The modeling of such a problem via the Maxwell equations and the fluctuational electrodynamics formalism is described in details, and a discussion about evanescent waves and surface polaritons is also provided. The solution of the stochastic Maxwell equations via the method of potentials is presented in appendix A.

The numerical procedure to solve near-field thermal radiation problems in one-dimensional layered media is treated in chapter 3. The algorithm is tested for different cases involving cubic boron nitride. The physics of near-field radiative heat transfer is explained through the solution of a problem involving two bulks of silicon carbide (SiC), supporting SPhPs in the infrared region, separated by a vacuum gap. The dielectric function models employed to perform the simulations are provided in appendix B, while the unit vectors used in deriving the equations are explained in appendix C. The procedure developed in chapter 3 is also validated against results from the literature, and these comparisons are shown in appendix D. The length scales of transition from the near- to the far-field regime of radiative heat transfer for the specific case of two dielectric bulks are finally explored in appendix E.

The possibility of tuning near-field radiative heat transfer is investigated in chapters 4 and 5. This is accomplished in chapter 4 by calculating the local density of electromagnetic states (LDOS) within the nanometric gap formed between two films of

SiC. The influence of the layer thicknesses, their distance of separation and the location where the LDOS is calculated on the near-field thermal spectrum emitted are analyzed in details using SPhP dispersion relations for a system of two thin films.

The study of chapter 4 is extended in chapter 5 via the analysis of the near-field radiative heat flux between two films of SiC. For this purpose, an analytical expression for the flux is derived, and the critical steps of this derivation are outlined in appendix F. The flux profiles are studied as a function of the layer thicknesses and their distance of separation, and an approximate approach is proposed to predict the resonances of the flux as a function of these parameters. The coexistence of two regimes of near-field thermal radiation between two SiC films is finally investigated via an asymptotic analysis of the radiative heat transfer coefficient.

Nano-TPV power generation is treated in chapter 6. The mathematical details for modeling the coupled near-field thermal radiation, charge and heat transport within the nano-TPV device are provided along with the optical, electrical and thermophysical properties required for the solution of this problem. The performances of nano-TPV power generators are investigated as a function of the temperature of the cell and by accounting for the thermal effects via the solution of the energy equation. The numerical details and the validation of the nano-TPV model are discussed in appendix G.

The general concept of characterizing nanoparticles via scattering of surface waves is described in chapter 7. The possibility of characterizing nanoparticles via the intensity and the polarization state of scattered surface waves is explored through a sensitivity analysis. Details about the modeling of agglomerates of particles and the generation of a database of scattering profiles are given in appendix H.

The experimental system developed to characterize nanoparticles, called the polarized-surface-wave-scattering system (PSWSS), is the subject of chapter 8. Two experimental procedures employed to measure the scattering matrix elements are overviewed, and the PSWSS is described in details. The PSWSS is tested by measuring: the Mueller matrix elements of a linear polarizer (calibration), the scattered light by a diffraction grating, and the scattering matrix elements of 200 nm and 50 nm gold spherical particles. Technical details of the PSWSS (components, settings of the lock-in amplifiers, optical scheme and calibration of the polarizers and quarter-wave plates) are provided in appendix I.

The main results of this dissertation, and some recommendations for future research efforts, are summarized in chapter 9.

# Chapter 2

# Fundamentals of Near-Field Thermal Radiation

The classical theory of thermal radiation is based on the blackbody concept. A blackbody is defined as an ideal body that absorbs all radiation at all angles of incidence and at all wavelengths [15]. A blackbody is the perfect absorber of thermal radiation, and consequently the perfect emitter of radiant heat energy [14-17]. The definition of such an ideal body is useful as it serves as a reference for real materials. For example, the ratio of the radiation emitted by a real material at temperature $T$ at a given angle and a given wavelength, over the emissive power of a blackbody at temperature $T$, gives the spectral-directional emissivity of the real material at temperature $T$.

The spectrum emitted by a blackbody is given by the Planck distribution, and the dominant wavelength emitted at temperature $T$ can be determined using the Wien law. Based on the Planck blackbody concept, it is possible to calculate radiant energy exchanges between surfaces using the view factor theory, and via the radiative transfer equation (RTE) when the media separating the surfaces are participating (i.e., emitting, absorbing, and scattering) [15-17]. In both cases, transport of radiant energy is considered as incoherent (i.e., the wave nature of thermal radiation is neglected), and the concepts of geometric optics can therefore be used for modeling such a transport mechanism.

The blackbody concept is based on an important assumption given in chapter 1 of Max Planck's book *The Theory of Heat Radiation* (*Theorie der Wärmestrahlung*) [14]: "Throughout the following discussion it will be assumed that the linear dimensions of all parts of space considered, […], are large compared with the wavelengths of the rays considered.” Therefore, the blackbody concept is valid when the typical dimensions of space, which include the size of the bodies and their distances of separation, are large compared to the wavelengths emitted. In this dissertation, this classical theory of thermal radiation is alternatively referred as the far-field regime of radiative heat transfer, where thermal radiation can be conceptualized as a particle (photon) and where the transport process is assumed to be incoherent. This last assumption is acceptable in the far-field regime since the coherence length of a blackbody is of the same order of magnitude than the dominant wavelength of thermal emission as predicted by Wien’s law [3].

As the typical size between structures exchanging thermal radiation decreases to a size comparable or below the dominant emitted wavelength, the classical theory of radiative transfer ceases to be valid, as the wave nature needs to be considered in the calculations. At such short distances, or, in the near-field regime, radiative heat transfer is correctly described by the Maxwell equations combined with the fluctuational electrodynamics formalism used to model thermal emission [18,19]. Since the typical wavelengths involved in thermal radiation are a few microns, near-field effects become dominant when bodies are separated by a few hundreds of nanometers. For this reason, near-field thermal radiation is also referred in the literature as “nanoscale thermal radiation.” The electromagnetic description of thermal radiation emission was pioneered by Rytov [18,19]. In Rytov’s description, thermal radiation emission is conceptualized as the field generated via chaotic motion of charges within a material, behaving like small radiant dipoles with random amplitudes [43]. From this electrodynamics point of view, oscillating dipoles emit waves that carry the radiative energy away from the surface of an emitting body, namely the propagating waves, accounted for in the far-field regime of thermal radiation. They also emit evanescent waves that are confined very near the surface of the body [33,44], which do not carry any importance in the far-field calculations. These evanescent waves exist and propagate along the interface between two materials, while exponentially decaying over a distance of about a wavelength normal to that interface.

The concept of an evanescent wave field is usually discussed in the literature in the context of total internal reflection, where an external light beam propagating through a medium with a large refractive index is reflected at the interface of a medium of lower refractive index [1,45]. If the angle of incidence of the beam at the interface between the high and low refractive index media is larger than the critical angle as calculated from Snell's law, the light is totally reflected back into the high refractive index medium. Still, an evanescent wave forms and propagates at the interface delimiting the high and low refractive index media, while being confined normal to that interface with the field exponentially decaying in the low refractive index medium. From the electromagnetic description of thermal radiation, evanescent waves are generated by chaotic motions of charges and are present at the surface of any material that has a finite temperature ($T > 0$ K). Even though evanescent waves do not propagate to the far-field, energy transfer through these modes can occur if a second body is brought within the evanescent wave field of the emitting material. It is observed from the mathematical treatment of the problem that even though there is no normal component of the Poynting vector at the first interface, there is a non-zero component at the second one, indicating that net energy exchange can occur. Physically, the evanescent wave supported by medium 1 affects the motion of the charges within the second body, and the resulting electronic motion thus dissipates the energy of the evanescent wave field and generates Joule heat [33]. This mode of radiant energy transfer is usually referred as radiation tunneling, and causes radiative heat transfer in the near-field to exceed the values predicted by the Planck blackbody distribution.

A thermal radiation source is an example of an incoherent radiative source. The temporal, or spectral, coherence of a radiative source manifests itself through emission within a narrow spectral band, while emission in a narrow angular band is a manifestation of spatial coherence [2,46-48]. In the far-field regime, thermal radiation emission can be treated as a broadband phenomenon with quasi-isotropic angular distribution. The opposite of this example is a laser source which has a high degree of both spatial and temporal coherence as the radiation is emitted around one wavelength with a narrow angular distribution. In the near-field, thermal sources can also exhibit high spatial and temporal coherences due to the presence of surface polaritons, also referred as surface modes or resonant surface electromagnetic waves.

Surface polaritons are hybrid modes that arise from the coupling of an electromagnetic field and a mechanical oscillation of energy carriers within a material. The hybrid mode of the collective motion of free electrons and electromagnetic radiation is called a surface plasmon-polariton (SPP), arising in metals and doped semiconductors. Similarly, the hybrid mode of lattice vibrations (transverse optical phonons) and an electromagnetic field is a surface phonon-polariton (SPhP), which is supported by polar crystals [49]. Similar to evanescent waves, surface polaritons propagate along an interface between two materials, but with an evanescent field decaying in both media [11,50]. Surface polaritons greatly modify the coherence properties in the near-field of a thermal source [47]. Indeed, radiative heat transfer between closely spaced bodies supporting surface polaritons not only exceeds the Planck distribution, but becomes quasi-monochromatic due to the high degree of spectral coherence of these waves [46]. It is also possible to achieve highly directional thermal sources in the far-field by exciting surface waves having high degree of spatial coherence via for example a grating [7].

With the recent advances in nanotechnology and nanopatterning procedures, near-field radiation heat transfer is no longer a pure conceptual phenomenon. Near-field thermal radiation problems are becoming increasingly important in thermal management of MEMS (micro-electro-mechanical systems) and NEMS (nano-electro-mechanical systems), in nanoscale-gap thermophotovoltaic power generation [5,33-37], in tuning far-field thermal radiation emission [7,51-64], in near-field thermal microscopy [8], and in advanced nanofabrication techniques [9,10] to name only a few.

The objective of this chapter is to provide the fundamentals of near-field thermal radiation. Chapter 2 is structured as follows. In the next section, the differences between the far- and near-field regimes of thermal radiation are overviewed. Then, the modeling of near-field thermal radiation is discussed in section 2.2, and the expressions needed to compute the radiative flux and local density of electromagnetic states are provided in sections 2.3 and 2.4, respectively. Brief discussions about the concepts of spatial and temporal coherence and the experimental evidences of the near-field thermal radiation enhancement are afterwards given, and a detailed review of evanescent waves and surface polaritons is finally provided.

A part of chapter 2 was published in the *Journal of Quantitative Spectroscopy and Radiative Transfer* in 2008 [65], while most of this chapter will be published in 2010 in the upcoming fifth edition of *Thermal Radiation Heat Transfer* (see Ref. [15] for the fourth edition),

## 2.1 Fundamental processes in radiative heat transfer: Near-field versus far-field treatment

Radiative heat transfer can be categorized in terms of four fundamental processes: emission, absorption, scattering, and propagation of radiative energy. In general terms, emission refers to how the radiative energy emanates from an object, where its internal energy is converted to electromagnetic waves. Absorption is when these waves interact with a body and the energy is converted back into the internal energy of the object. Scattering is defined as the re-direction of radiant energy, and involves the phenomena of refraction, reflection, transmission, and diffraction.

In the most strict sense, emission of thermal radiation from a body at finite temperature can be explained by quantum mechanics. A body loses energy due to emission, which is as a result of transitions of the elementary energy carriers (electrons, molecules, phonons, etc.) from a higher energy level to a lower energy level [66]. This emitted energy is associated with the concept of photons, which has been questioned for some time (see Kidd [67] and Mischenko [68] and references there in). As shown in [68,69], the electromagnetic wave approach is physically more conducive to represent the propagation of radiative energy. Absorption, which needs to be explained by quantum mechanics, occurs when the wave incident on an atom or molecule has sufficient and necessary energy to raise the atomic energy to a higher level. The scattering processes are also fundamentally due to quantum effects. For example, if the energy of radiation incident on an atom is too small to cause a transition to a higher energy level, there is no atomic transition. Nevertheless, the cloud of electrons bounding the atom starts vibrating at the frequency of the incident light. This system constitutes an oscillating dipole (with respect to the positive nucleus) and instantaneously begins to radiate at the same frequency. The resulting scattered radiation consists of a radiation propagating in some random direction. If the scattered radiation carries the same amount of energy as the incident radiation, then scattering is considered as elastic [45]. Yet, sometimes scattering by an atom or molecule occurs at a frequency different than the original frequency. This is called inelastic scattering. In a general manner, the processes of diffraction, transmission, reflection and refraction are macroscopic manifestations of scattering that fundamentally occur on an atomic level [45]. These quantum mechanics descriptions however cannot be readily used in solving radiative heat transfer problems in most practical applications. Instead, simplified models are preferred to describe the emission, absorption, and scattering processes.

In the far-field regime of thermal radiation, where the size between objects exchanging radiant energy is much larger than the dominant wavelength emitted, radiative energy propagation is modeled using ray tracing or geometric optics approximations. This approach implies that the energies of two rays incident at a given point are simply added without any consideration of their respective phases. The RTE describes the conservation of intensity along a line of sight at a given wavelength, and is used to calculate radiation transfer involving participating media [15-17]. The emission of thermal radiation is included in the RTE via the Planck blackbody intensity. Derivation of the Planck blackbody radiation formulation, which is based on the statistical mechanics approach of Boltzmann, is widely credited for opening the path towards quantum mechanics. In the classical sense, attenuation (absorption and out-scattering) along the line-of-sight are linearly related to the radiative intensity, where the proportionality constants are called the absorption coefficient ($m^{-1}$) and the scattering coefficient ($m^{-1}$), respectively. For the in-scattering term, the probability that a ray coming from any direction being scattered in the direction for which the RTE is solved is given by the scattering phase function. These proportionality constants can be derived from quantum mechanical information, but also by following the wave theory [69]. For example, when dealing with particulate media, it is necessary to use the electromagnetic wave approach to calculate the scattering and absorption cross-sections and coefficients, as well as the scattering phase function. Radiative properties of ideal surfaces can also be theoretically predicted using the electromagnetic wave approach, provided the fundamental properties (i.e., spectral electric permittivity and magnetic permeability) are available.

Radiative heat transfer is in the near-field regime when bodies exchanging thermal radiation are spaced by a distance of the same order of magnitude, or less, than the dominant wavelength emitted. The demarcation of far- and near-fields can be achieved by using a critical length scale, which is traditionally determined from the Wien law corresponding to the wavelength of peak emission according to the Planck blackbody distribution: $\lambda_w T = 2897.8$ μmK. This length scale is however an approximation and more precise values have been proposed for some specific cases [65]. Since incoherent transport can no longer be assumed in the near-field, the electromagnetic description of thermal radiation based on the macroscopic Maxwell equations needs to be used [18,19].

The Maxwell equations describe the inter-relationship between the fields, the sources, and the material properties [6]. Radiation absorption by the medium is included in this set of equations via the imaginary part of the dielectric function, or equivalently, via the imaginary part of the complex refractive index. Scattering of electromagnetic waves is also calculated directly via the Maxwell equations by assuming for example that the total field is the superposition of incident and scattered fields. However, thermal radiation emission is not included in the Maxwell equations. The fluctuational electrodynamics theory of Rytov [18,19], discussed in the next section, provides this bridge between the classical Maxwell equations and thermal radiation emission.

## 2.2 Electromagnetic description of thermal radiation: Fluctuational electrodynamics and the stochastic Maxwell equations

Inclusion of a thermal radiation emission term in the Maxwell equations is not straightforward. To be able to link this phenomenon with electromagnetic waves, we need to consider thermal radiation emission from an electrodynamics point of view [19,30,33].

Using the electrodynamics viewpoint, propagating and evanescent waves are emitted via the out-of-phase oscillations of charges of opposite signs. A couple of charges of opposite signs is called a dipole [44,45]. At any finite temperature ($T > 0$ K), thermal agitation causes a chaotic motion of charged particles inside the body, which induces oscillating dipoles. The random fluctuations of the charges generate in turn a fluctuating electromagnetic field, called the thermal radiation field, as it originates from random thermal motion [19,30]. On a macroscopic level, the field fluctuations are due to thermal fluctuations of the volume densities of charges and currents. In other words, the electromagnetic field generated thermally is not the sum of the fields of the individual charges, but is a field produced by sources that are also macroscopic (volume densities of charges and currents). The fluctuational electrodynamics (FE) formalism is built on this simplified macroscopic description. Since it is based on fluctuations around an equilibrium temperature $T$, the theory is thus applicable to media of any form that is in local thermodynamic equilibrium, where an equilibrium temperature can be defined at any given location inside the body at any instant. The FE approach is also said to be applicable to non-equilibrium conditions, in cases where the transport phenomena required to maintain steady-state conditions are negligible when compared to the energy emitted by the body [19]. The FE is the key for solving near-field radiation heat transfer problems, since it allows calculation of thermal emission starting from the Maxwell equations, which otherwise allow to describe only the absorption, scattering, and propagation of electromagnetic waves.

In this dissertation, we are dealing with frequency-dependent quantities, such that it is convenient to use the Maxwell equations in the frequency-domain. By assuming that the time-harmonic fields have the form $\exp(-i\omega t)$, the Maxwell equations for nonmagnetic materials (which are considered throughout this work) can be written as [44,70]:

$$\nabla \times \mathbf{E}(\mathbf{r},\omega) = i\omega \mathbf{B}(\mathbf{r},\omega) = i\omega\mu_v \mathbf{H}(\mathbf{r},\omega) \text{ (Faraday's law)} \tag{2.1a}$$

$$\begin{aligned}\nabla \times \mathbf{H}(\mathbf{r},\omega) &= -i\omega \mathbf{D}(\mathbf{r},\omega) + \mathbf{J}(\mathbf{r},\omega) = -i\omega\hat{\varepsilon}\mathbf{E}(\mathbf{r},\omega) + \sigma\mathbf{E}(\mathbf{r},\omega) = -i\omega(\hat{\varepsilon} + i\sigma/\omega)\mathbf{E}(\mathbf{r},\omega) \\ &= -i\omega\varepsilon\mathbf{E}(\mathbf{r},\omega) \text{ (Ampère's law)}\end{aligned} \tag{2.1b}$$

$$\nabla \cdot \mathbf{D}(\mathbf{r},\omega) = \nabla \cdot (\hat{\varepsilon}\mathbf{E}(\mathbf{r},\omega)) = \rho_e \text{ (Gauss's law)} \tag{2.1c}$$

$$\nabla \cdot \mathbf{B}(\mathbf{r},\omega) = \nabla \cdot (\mu_v \mathbf{H}(\mathbf{r},\omega)) = 0 \text{ (Gauss's law)} \tag{2.1d}$$

with the continuity equation:

$$\nabla \cdot \mathbf{J}(\mathbf{r},\omega) = i\omega\rho_e \tag{2.1e}$$

where the subscript $v$ refers to vacuum. In Ampère's law, $\hat{\varepsilon}$ is the electric permittivity of the material (real number). The combination of the electric permittivity and electric conductivity ($\hat{\varepsilon} + i\sigma/\omega$) leads to a frequency-dependent complex electric permittivity, denoted by $\varepsilon$. The dielectric constant $\varepsilon_r$ of the material is then defined as the ratio of the complex electric permittivity $\varepsilon$ and the electric permittivity of the vacuum $\varepsilon_v$. It is important to note that since the time-harmonic fields have been expressed as exp($-i\omega t$), complex quantities such as the refractive index and dielectric function are given by $a = a' + ia''$, where $a'$ and $a''$ refer respectively to the real and imaginary components of the variable $a$. If the time-harmonic fields were expressed as exp($i\omega t$), the complex quantities would be given by $a = a' - ia''$. Both formulations are of course equally valid, as long as we are consistent throughout the calculations. Also, from here on, we assume that there is no free charge density (i.e., $\rho_e = 0$).

To account for the discontinuity of the material properties at the interface of two media, the boundary conditions of the Maxwell equations must be applied. The boundary conditions at an interface free of surface current density and free of surface charge density delimiting media 1 and 2 can be written as [1,71]:

$$\hat{\mathbf{n}} \times (\mathbf{E}_2 - \mathbf{E}_1) = 0 \tag{2.2a}$$

$$\hat{\mathbf{n}} \times (\mathbf{H}_2 - \mathbf{H}_1) = 0 \tag{2.2b}$$

$$\hat{\mathbf{n}} \cdot (\mathbf{D}_2 - \mathbf{D}_1) = 0 \tag{2.2c}$$

$$\hat{\mathbf{n}} \cdot (\mathbf{B}_2 - \mathbf{B}_1) = 0 \tag{2.2d}$$

where $\hat{\mathbf{n}}$ is a unit vector normal to the interface 1-2. The first two conditions (Eqs. (2.2a) and (2.2b)) ensure that the tangential components of the electric and magnetic fields are continuous across the interface 1-2, while the two last conditions (Eqs. (2.2c) and (2.2d)) enforce the continuity of the normal components of the electric displacement and magnetic induction at the boundary 1-2. These boundary conditions are not independent from each other, and it can be shown that the conditions for the normal components of the fields are automatically satisfied if the continuity of the tangential fields across an interface is enforced [1].

From the qualitative description of radiative emission given earlier, thermal fluctuations of a body around an equilibrium temperature $T$ imply random fluctuations of current, which constitutes the source term of thermal radiation. In Ampère's law (Eq. (2.1b)), the current density **J** is combined (using Ohm's law: $\mathbf{J} = \sigma\mathbf{E}$) with the electric permittivity $\hat{\varepsilon}$, leading to a complex electric permittivity $\varepsilon$. For electrical insulators, the current density **J** → 0, and then $\varepsilon \to \hat{\varepsilon}$. Therefore, to account for the random thermal fluctuations of current in the Maxwell equations which are present regardless of the nature of the materials, an extraneous current density term should be added in Ampère's law [19]:

$$\nabla \times \mathbf{H}(\mathbf{r},\omega) = -i\omega\varepsilon\mathbf{E}(\mathbf{r},\omega) + \mathbf{J}^r(\mathbf{r},\omega) \tag{2.3}$$

The current density $\mathbf{J}^r$ plays the role of a random external source causing thermal fluctuations of the field [19]. The mean value of this random current density, $\langle \mathbf{J}^r \rangle$, is zero implying that the mean radiated field is also zero. On the other hand, quantities such as the Poynting vector (i.e., radiative flux) and energy density are functions of the spatial correlation function of the fluctuating currents which is a non-zero quantity. By using Ampère's law as given by Eq. (2.3), instead of Eq. (2.1b), the Maxwell equations become stochastic due to the fact that $\mathbf{J}^r$ is a random variable, and are sometimes referred in the literature as the "stochastic Maxwell equations." This is the basis of FE.

To calculate quantities that are useful for heat transfer analyses, the stochastic Maxwell equations need to be solved. Different approaches can be used. The most common technique adopted in near-field thermal radiation calculations is to express the fields in terms of dyadic Green's functions (DGFs). Using the method of potentials [65,70], the electric and magnetic fields can be expressed as [65,72]:

$$\mathbf{E}(\mathbf{r},\omega) = i\omega\mu_v \int_V dV' \overline{\overline{\mathbf{G}}}^E(\mathbf{r},\mathbf{r}',\omega) \cdot \mathbf{J}^r(\mathbf{r}',\omega) \tag{2.4a}$$

$$\mathbf{H}(\mathbf{r},\omega) = \int_V dV' \overline{\overline{\mathbf{G}}}^H(\mathbf{r},\mathbf{r}',\omega) \cdot \mathbf{J}^r(\mathbf{r}',\omega) \tag{2.4b}$$

where $\overline{\overline{\mathbf{G}}}^E(\mathbf{r},\mathbf{r}',\omega)$ and $\overline{\overline{\mathbf{G}}}^H(\mathbf{r},\mathbf{r}',\omega)$ are the electric and magnetic DGFs, and $\mathbf{r}$ and $\mathbf{r}'$ denote field and source point, respectively [73]. Note that the derivation of Eqs. (2.4a) and (2.4b) starting from the Maxwell equations and using the method of potentials is provided in appendix A. The DGF is a 3×3 matrix and is alternatively referred to as the Green tensor. The electric DGF can be written as [1]:

$$\overline{\overline{\mathbf{G}}}^E(\mathbf{r},\mathbf{r}',\omega) = \left[\overline{\overline{\mathbf{I}}} + \frac{1}{k^2}\nabla\nabla\right] G_0(\mathbf{r},\mathbf{r}',\omega) \tag{2.5}$$

where $G_0$ is the scalar Green's function, which can be determined by solving the scalar Helmholtz equation for a single point source located at $\mathbf{r}' = \mathbf{r}$. The dyadic $\overline{\overline{\mathbf{I}}}$ is called an idem factor, which is a 3×3 identity matrix. Physically, the DGF can be seen as a spatial transfer function relating the field observed at location $\mathbf{r}$ with a frequency $\omega$ due to a vector source located at $\mathbf{r}'$. The magnetic DGF is calculated from the electric DGF as: $\overline{\overline{\mathbf{G}}}^H(\mathbf{r},\mathbf{r}',\omega) = \nabla \times \overline{\overline{\mathbf{G}}}^E(\mathbf{r},\mathbf{r}',\omega)$. The physical interpretation of Eqs. (2.4a) and (2.4b) is quite straightforward, as they imply that the fields observed, or calculated, at location $\mathbf{r}$ are proportional to the sum of currents $\mathbf{J}^r$ distributed at different $\mathbf{r}'$ locations within an emitting body of volume $V$. Also, as mentioned before, the averaged radiated fields, $\langle \mathbf{E} \rangle$ and $\langle \mathbf{H} \rangle$, are zero since $\langle \mathbf{J}^r \rangle = 0$.

To be able to calculate the radiative heat flux or the energy density, we need to determine the link between the local temperature of an emitting body and the stochastic current density $\mathbf{J}^r$. This link is provided by the fluctuation-dissipation theorem (FDT), which makes the bridge between the ensemble average of the spatial correlation function of $\mathbf{J}^r$ and the temperature $T$ [19]. In other words, the FDT establishes the relationship between the electromagnetic description of thermal radiation and the usual theory of heat transfer [43].

A simple and intuitive derivation of the FDT is provided in references [65,72]; more formal derivations can be found in references [1,19,74]. In the framework of this dissertation, the derivation of the FDT is restricted by the following assumptions: (i) the bodies are assumed in local thermodynamic equilibrium at an equilibrium temperature $T$; (ii) all the media considered are isotropic; (iii) the media are nonmagnetic and are defined by a frequency-dependent dielectric function $\varepsilon_r(\omega)$; (iv) the dielectric function is local in space (i.e., the polarization at a given point in a medium is directly proportional to the electric field at that point, and does not directly depend on the fields from other points [73]), and consequently the fluctuations are uncorrelated between neighboring volume elements [73,75]. While the last three assumptions can be relaxed [76,77], the condition of local thermodynamic equilibrium where a temperature can be defined must be satisfied when applying the FDT.

The FDT is not limited to electrodynamics, and was applied to thermal radiation by Rytov [18,19]. Following the assumptions stated above, the FDT can be written as follows:

$$\left\langle J_\alpha^r(\mathbf{r}',\omega)J_\beta^{r*}(\mathbf{r}'',\omega')\right\rangle = \frac{\omega\varepsilon_v\varepsilon_r''(\omega)}{\pi}\Theta(\omega,T)\delta(\mathbf{r}'-\mathbf{r}'')\delta(\omega-\omega')\delta_{\alpha\beta} \tag{2.6}$$

where the subscripts $\alpha$ and $\beta$ refer to orthogonal components indicating the state of polarization of the source, while $\langle\ \rangle$ denotes an ensemble average. The term $\Theta(\omega,T)$ is the mean energy of a Planck oscillator in thermal equilibrium at frequency $\omega$ and temperature $T$ given by:

$$\Theta(\omega,T) = \frac{\hbar\omega}{\exp(\hbar\omega/k_bT)-1} \tag{2.7}$$

In Eq. (2.6), the Dirac function $\delta(\mathbf{r}'-\mathbf{r}'')$ mathematically translates the assumption of locality for the dielectric constant (i.e., the fluctuations at two different points are correlated in the limit $\mathbf{r}'' \to \mathbf{r}'$). The Dirac function $\delta(\omega-\omega')$ represents the fact that the fluctuating currents are stationary (i.e., the spectral components with different frequencies are totally uncorrelated), and $\delta_{\alpha\beta}$ accounts for the assumption of isotropic media.

At this point, all the necessary tools to solve near-field radiative heat transfer problems have been provided. A summary of the models used to describe each fundamental process of thermal radiation for both the far- and near-field regimes is provided in Table 2.1.

Table 2.1. Model used for each fundamental process of thermal radiation in the far- and near-field regimes.

| | Far-field regime | Near-field regime |
|---|---|---|
| Emission | Blackbody radiative intensity | Fluctuational electrodynamics (fluctuation-dissipation theorem) |
| Absorption | Absorption coefficient (empirical, or from solution of the Maxwell equations) | Related to electric permittivity and magnetic permeability; obtained directly by solving the Maxwell equations |
| Scattering | Scattering coefficient and scattering phase function (empirical, or from solution of the Maxwell equations) | Related to electric permittivity and magnetic permeability; obtained directly by solving the Maxwell equations |
| Propagation | Incoherent transport | Coherent transport |

### 2.3 Near-field radiative heat flux

In heat transfer analyses, one is mostly interested by the radiative heat flux given by the time-averaged Poynting vector, which is the quantity measureable by a detector [3]:

$$\langle \mathbf{S}(\mathbf{r},\omega) \rangle = 4 \times \frac{1}{2} \mathrm{Re}\left\{ \langle \mathbf{E}(\mathbf{r},\omega) \times \mathbf{H}^*(\mathbf{r},\omega) \rangle \right\} \tag{2.8}$$

This expression of the Poynting vector is four times larger than its customary definition, since only the positive frequencies are considered in the Fourier decomposition of the time-dependent fields into frequency-dependent quantities [2,75]. Substitution of the electric and magnetic field expressions (Eqs. (2.4a) and (2.4b)) into Eq. (2.8) gives:

$$\langle \mathbf{S}(\mathbf{r},\omega) \rangle = 2\omega\mu_v \, \mathrm{Re}\left\{ i \int_V dV' \int_V dV'' G^E_{m\alpha}(\mathbf{r},\mathbf{r}',\omega) G^{H*}_{n\beta}(\mathbf{r},\mathbf{r}'',\omega') \left\langle J^r_\alpha(\mathbf{r}',\omega) J^{r*}_\beta(\mathbf{r}'',\omega') \right\rangle \right\} \tag{2.9}$$

where the subscripts *m* and *n* refer to orthogonal components. For example, if the quantity $\langle E_x H_y^* \rangle$ is calculated, then $m = x$ and $n = y$. To apply the FDT to Eq. (2.9), we use the ergodic hypothesis, where it is assumed that averaging over time can be replaced by an ensemble average [69,78,79]. Then, application of the FDT (Eq. (2.6)) to Eq. (2.9) leads to the following general expression for the radiative heat flux:

$$\langle \mathbf{S}(\mathbf{r},\omega) \rangle = \frac{2k_v^2 \Theta(\omega,T)}{\pi} \mathrm{Re}\left\{ i\varepsilon_r''(\omega) \int_V dV' G_{m\alpha}^{E}(\mathbf{r},\mathbf{r}',\omega) G_{n\alpha}^{H*}(\mathbf{r},\mathbf{r}',\omega) \right\} \tag{2.10}$$

where $k_v$ is the magnitude of the wavevector in vacuum. The subscripts *m* and *n* represent the state of polarization of the fields observed at $\mathbf{r}$, while $\alpha$ represents the state of polarization of the source at $\mathbf{r}'$. The set of indices $m\alpha$ implies that a summation is performed over all components (i.e., $xx + xy + \ldots + zz$).

At this point, the radiative heat flux can be calculated given that the DGFs for the system under study are known. The solution for the near-field radiative heat flux in a one-dimensional layered geometry is discussed in details in chapter 3.

### 2.4 Density of electromagnetic states

The concept of density of electromagnetic states (DOS) is important to understand the underlying physics of near-field thermal radiation. Using the principles of energy quantization and statistical thermodynamics [2,3], the density of energy of a system at a given frequency $\omega$ is obtained as the product of the DOS and the mean energy of a state at frequency $\omega$ and temperature $T$ [80]. The mean energy of a state, or mean energy of a Planck oscillator, at $\omega$ and $T$ is given by Eq. (2.7). Therefore, the DOS can be seen as the number of states, or modes, per unit frequency and per unit volume [2]. In vacuum, the DOS is given by [3,80]:

$$\rho_\omega = \frac{\omega^2}{\pi^2 c_v^3} \tag{2.11}$$

The product of the DOS given by Eq. (2.11) and the mean energy of a Planck oscillator leads to:

$$u_\omega(T) = \frac{\hbar\omega^3}{\pi^2 c_v^3[\exp(\hbar\omega/k_b T) - 1]} \tag{2.12}$$

which is the energy density of a blackbody at temperature $T$. Starting from Eq. (2.12), it is possible to derive the Planck blackbody intensity and the blackbody emissive power [3].

In the near-field of a thermal source, an increase of the DOS is expected due to the presence of evanescent waves and surface polaritons. As these waves depend strongly on the distance from the thermal source, the local density of electromagnetic states (LDOS) at a given location **r** in space is calculated [80]. Assuming that a body a temperature $T$ is emitting in free space, the energy density in vacuum is calculated as the sum of the electric and magnetic energies [2,80]:

$$\langle u_\omega(\mathbf{r},T)\rangle = 4\times\frac{1}{4}\left[\varepsilon_v\left\langle|\mathbf{E}(\mathbf{r},\omega)|^2\right\rangle + \mu_v\left\langle|\mathbf{H}(\mathbf{r},\omega)|^2\right\rangle\right] \tag{2.13}$$

where again an extraneous factor four is included for the same reason as for the Poynting vector. An explicit expression for the energy density, similar to Eq. (2.10) for the Poynting vector, can be derived by substituting the electric and magnetic field expressions into Eq. (2.13) and by applying the FDT. The resulting equation is given by:

$$\langle u_\omega(\mathbf{r},T)\rangle = \frac{\omega\varepsilon_r''(\omega)}{\pi c_v^2}\Theta(\omega,T)\left[k_v\int_V dV'\left|G_{m\alpha}^E(\mathbf{r},\mathbf{r}',\omega)\right|^2 + \int_V dV'\left|G_{m\alpha}^H(\mathbf{r},\mathbf{r}',\omega)\right|^2\right] \tag{2.14}$$

The energy density given by Eq. (2.14) is relative to the vacuum energy density, as the vacuum fluctuations are neglected in the mean energy of a Planck oscillator since they do not affect radiative heat flux calculations [2]. The LDOS $\rho_\omega(\mathbf{r})$ in the near-field is calculated by dividing Eq. (2.14) by $\Theta(\omega,T)$.

## 2.5 Spatial and temporal coherence of thermal radiation

The coherence properties of an emitted thermal field are directly related to the wave nature of radiation. Spatial and temporal coherence of an electromagnetic field can be quantified by calculating the correlation function $\langle \mathbf{E}(\mathbf{r}_1,t_1)\mathbf{E}(\mathbf{r}_2,t_2)\rangle$, where **r** denotes a spatial location and $t$ represents the time. The fields are perfectly correlated if the field $\mathbf{E}(\mathbf{r}_2,t_2)$ follows the same evolution as $\mathbf{E}(\mathbf{r}_1,t_1)$ [54]. Temporal coherence, or spectral coherence, is the measure of the correlation of the fields at times $t_1$ and $t_2$. A temporally coherent radiative source emits in a narrow spectral band for any given direction [2]. The spatial coherence is a measure of the correlation of the fields at locations $\mathbf{r}_1$ and $\mathbf{r}_2$ [46]. A radiative source that is spatially coherent emits radiation in a narrow angular band [2].

The thermal radiation field observed in the far-field is broadband and generally quasi-isotropic. In fact, the coherence length of blackbody radiation is about $\lambda/2$, such that coherence properties of thermal radiation are not observed in the far-field [46]. However, by nano-structuring surfaces, it is possible to transmit the near-field coherence of thermal radiation to the far-field. In that way, quasi-monochromatic and directional thermal radiative sources can be achieved. This is especially true when the emitting materials support surface polaritons which show a high degree of temporal and spatial coherence in the near-field.

## 2.6 Experimental evidences of radiative heat transfer enhancement in the near-field

A number of experimental investigations regarding radiative heat transfer enhancement in the near-field were performed between parallel surfaces from 1968 to 1994 [81-86]. Whale [33] analyzed in a single figure these aforementioned experimental data and concluded that the results reported in the literature up to 1994 were inconsistent, suspect to invalidity, divergent from theoretical predictions, and insufficient to infer a general trend and length scale for near-field thermal radiation.

Recently, there are renewed interests in measuring near-field radiative heat transfer due to the lack of experimental evidences combined with the advances in nanotechnologies. Kittel et al. [87] measured the radiative heat flux between the tip of a scanning thermal microscope (STM) and a planar surface of gold and gallium nitride. They reported a good agreement between the experimental and the theoretical results for tip-surface distances down to 10 nm, while they found that the near-field radiative heat flux diverged significantly from theoretical predictions for distances less than 10 nm. Hu et al. [88] measured near-field radiative heat transfer between two glass plates separated by nanoparticles, and reported an enhancement of the flux above the blackbody predictions for a separation gap of 1.6 μm. Shen et al. [89] measured the near-field radiative heat flux between a micron-size sphere and a surface down to a gap of 30 nm. The authors reported that the radiative heat transfer in the near-field can exceed by three orders of magnitude the Planck blackbody distribution. Details about the set-up can be found in reference [90], and a summary of the near-field thermal radiation experiments performed by Gang Chen's group is provided in [91]. Recent experimental evidences of near-field radiative heat transfer have been provided by Rousseau et al. [92], where the fluxes were measured between a micron-size sphere (sodalime glass) and a plate (borosilicate glass) separated by gaps of 2.5 μm down to 30 nm. Excellent agreement between the experimental results and theoretical predictions were found.

Clearly, near-field enhancement of the radiative heat flux beyond the blackbody predictions has been shown experimentally. There is still however a need to perform these measurements in more practical configurations, such as between parallel surfaces separated by nanometric distances, which can find applications in thermophotovoltaic power generation.

## 2.7 Evanescent waves and surface polaritons

### *2.7.1 Evanescent waves and total internal reflection*

Evanescent waves are discussed hereafter through the concept of total internal reflection (TIR). For this purpose, the interface 1-2 between two lossless dielectric half-spaces with index of refraction $n_1 > n_2$, as shown in Fig. 2.1, is considered.

A wave propagating in medium 1 at an angle $\theta_i$ is incident at the interface 1-2. This wave is partially reflected back in medium 1 at an angle $\theta_r = \theta_i$, while another part of the wave is transmitted in medium 2 at an angle $\theta_t$. The angle $\theta_t$ can be predicted via the Snell law [45]:

$$n_1 \sin\theta_i = n_2 \sin\theta_t \tag{2.15}$$

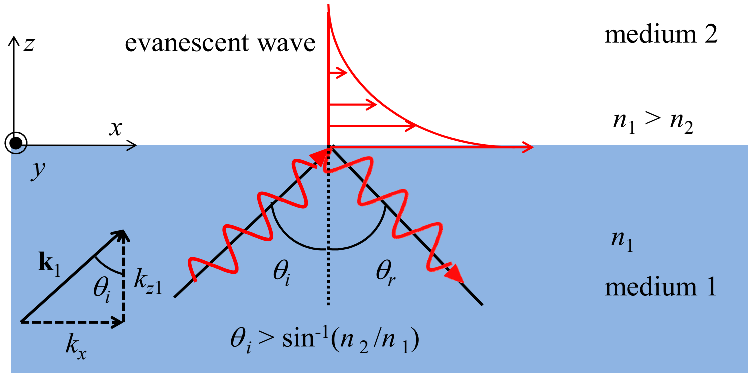

Figure 2.1. Schematic representation of an evanescent wave generated at the interface of two dielectrics via total internal reflection.

Since the index of refraction of medium 1 is greater than the index of refraction of medium 2, there is an angle of incidence for which no wave is transmitted in medium 2, such that all the energy is reflected back in medium 1. This phenomenon is called TIR. The critical incident angle for TIR can easily be predicted via the Snell law. Indeed, the angle $\theta_t$ of the wave transmitted in medium 2 cannot exceed 90º. Imposing this condition in Eq. (2.15), we find that the critical angle for TIR is given by $\theta_{cr} = \sin^{-1}(n_2/n_1)$. However, when TIR occurs, an evanescent wave is generated at the interface 1-2 with an exponentially decaying field in medium 2, as depicted in Fig. 2.1 [1,45].

The presence of the evanescent wave at the interface 1-2 can be better understood by working with wavevectors instead of angles. It is assumed that the wave incident in medium 1 is described with an electric field $\mathbf{E}_1 \exp[i(\mathbf{k}_1 \cdot \mathbf{r} - \omega t)]$ which can be either TE- or TM-polarized. The term TE polarization means that the electric field is perpendicular to the plane of incidence, defined here as the *x-z* plane. Conversely, a TM-polarized wave means that the magnetic field is oscillating normal to the plane of incidence *x-z*. Without loss of generality, we can assume that waves are propagating in the *x-z* plane only. The magnitude of the wavevector $k_1 = |\mathbf{k}_1|$ is given by $n_1 k_v$. The *z*-component of the wavevector in medium 1 can thus be written as:

$$k_{z1} = \sqrt{n_1^2 k_v^2 - k_x^2} \tag{2.16}$$

It is also possible to express the *x*-component of the wavevector in term of the angle of incidence as follows:

$$k_x = n_1 k_v \sin\theta_i \tag{2.17}$$

If the angle of incidence is equal to the critical angle for TIR, the *x*-component of the wavevector is:

$$k_x = n_2 k_v \tag{2.18}$$

Equation (2.18) provides the smallest value of $k_x$ for TIR. Also, note that the *x*-component of the wavevector is conserved from medium 1 to 2 due to the assumption that the media are infinite along that direction. Similarly, we can write the *z*-component of the wavevector in medium 2 as follows:

$$k_{z2} = \sqrt{n_2^2 k_v^2 - k_x^2} \tag{2.19}$$

Inspection of Eqs. (2.18) and (2.19) reveals that when $\theta_i > \theta_c$, then $k_x > n_2 k_v$, and $k_{z2}$ becomes a pure imaginary number. Assuming that the field in medium 2 has the form $\mathbf{E}_2 \exp[i(\mathbf{k}_2 \cdot \mathbf{r} - \omega t)]$, substitution of a pure imaginary $k_{z2}$ in this last expression leads to $\mathbf{E}_2 \exp[i(k_x x - \omega t)]\exp(-k_{z2} z)$. This equation shows clearly that the wave is propagating along the *x*-direction, while being evanescently confined at the interface 1-2 in the *z*-direction. While a field is present above the interface 1-2 in medium 2, it can be shown that the time-averaged Poynting vector of the evanescent wave field is zero, such that there is no net energy flow in medium 2 [3]. The penetration depth of an evanescent wave, $\delta$, is defined as the distance from the interface where the field amplitude has decayed by $e^{-1}$ of its original value; therefore, the penetration depth of an evanescent wave in medium *j* is given by $\delta_j \approx |k_{zj}|^{-1}$.

The presence of evanescent waves at the surface of a body a temperature *T* can be conceptualized via an analogy with TIR [21], as done in the late sixties by Tien's group [93,94]. Referring to Fig. 2.1, where we assume from now on that medium 2 is a vacuum, we can imagine that electromagnetic propagating radiation is emitted throughout the volume of medium 1. Waves with $k_x < k_v$ are transmitted through the interface 1-2, while waves with $k_x > k_v$ experience TIR. The largest $k_x$ value for an evanescent wave is $n_1 k_v$, since the maximum angle of incidence $\theta_i$ is 90º (see Eq. (2.17)).

If a medium 3 with index of refraction $n_3 = n_1$ is brought at a distance $d_c$ much larger than the dominant wavelength emitted from the interface 1-2, only waves with $k_x < k_v$ participate in radiative energy transfer. In that case, we are in the far-field regime. If the separation distance $d_c$ is less than the dominant wavelength emitted, the evanescent wave field of medium 1 excites the charges within medium 3 and dissipates its energy through Joule heating [30]; this mode of energy transfer is referred as radiation tunneling, or frustrated TIR, as the Poynting vector in medium 3 from the evanescent wave is no longer zero [2].

For the case of lossless dielectric materials with refractive indices $n_1$, the maximum radiative heat transfer occurs at the limit $d_c \rightarrow 0$, and its achievable value is $n_1^2$ times the values predicted between blackbodies; this limit comes from the fact that the blackbody intensity in a lossless material is proportional to $n_1^2$ [15,16,66,72]. This simple picture for describing near-field radiative heat transfer is however inadequate when dealing with materials supporting surface polaritons, such as metals, doped semiconductors, and polar crystals. As discussed previously in this chapter, thermal radiation emission should be seen from the electrodynamics point of view where oscillating dipoles generate propagating and evanescent waves [30]. Indeed, when materials can support surface polaritons, the largest contributing wave vector $k_x$ can greatly exceed the limit $n_1 k_v$ established via the analogy with TIR [2,21,30].

### *2.7.2 Surface polaritons*

Surface polaritons are the hybrid modes of a mechanical oscillation and an electromagnetic field. In a metal or a doped semiconductor, the out-of-phase longitudinal oscillations of free electrons (i.e., plasma oscillations), relative to the positive ion cores, creates dipoles generating an electromagnetic field [11,49,50,75]. The evanescent component of the spectrum emitted is called a surface plasmon-polariton (SPP).

Similarly, the out-of-phase oscillations of transverse optical phonons in polar crystals, such as silicon carbide (SiC), generate an electromagnetic field, and its evanescent component is called a surface phonon-polariton (SPhP) [30,49,75]. Surface polaritons propagate along the interface between two media with evanescent fields decaying in both materials [11,50].

To illustrate the physics of surface polaritons, we consider the plane interface depicted in Fig. 2.2, where both media 1 and 2 are infinite along the *x*- and *y*-directions.

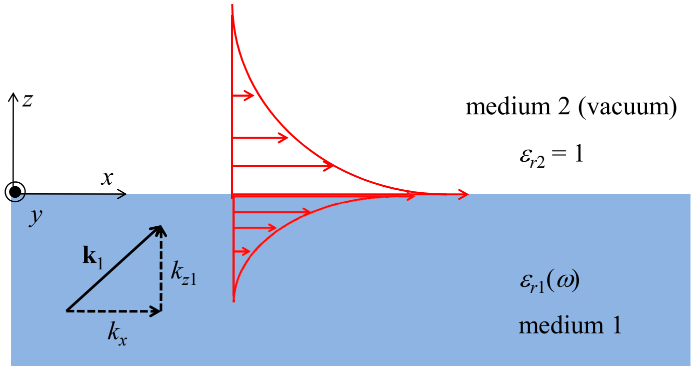

Figure 2.2. Schematic representation of a surface polariton at the interface delimiting a material supporting surface polariton with a dielectric function $\varepsilon_{r1}(\omega)$ and a vacuum with $\varepsilon_{r2} = 1$.

At $z < 0$, the frequency-dependent dielectric function of medium 1 is given by $\varepsilon_{r1}(\omega)$, while medium 2 at $z > 0$ is assumed to be a vacuum with $\varepsilon_{r2} = 1$. Without loss of generality, it is also assumed that surface polaritons are propagating along the *x*-direction only.

The impact of surface polaritons on near-field radiative heat transfer can be understood by analyzing the dispersion relation. The dispersion relation is the relationship between the periodicity of the wave in time (i.e., angular frequency $\omega$) and its periodicity in space (i.e., wavevector $k_x$ here). Such a dispersion relation can be determined by solving the Maxwell equations at the interface 1-2 separately for TE- and TM-polarized waves [11,25]. In TE polarization, the electric field, parallel to the *y*-axis, can be written as follows in media 1 and 2:

$$\mathbf{E}_1(\mathbf{r},\omega) = \hat{\mathbf{y}} E_{y1} \exp[i(k_x x - k_{z1} z - \omega t)] \tag{2.20a}$$

$$\mathbf{E}_2(\mathbf{r},\omega) = \hat{\mathbf{y}}E_{y2}\exp[i(k_x x + k_{z2}z - \omega t)] \tag{2.20b}$$

The magnetic field oscillates in the *x*-*z* plane, and the components $H_x$ and $H_z$ can be determined from Eqs. (2.20a) and (2.20b) and by using Ampère's law (Eq. (2.1b)). The resulting magnetic field vector in media 1 and 2 is thus given by:

$$\mathbf{H}_1(\mathbf{r},\omega) = -\omega\mu_v E_{y1}(\hat{\mathbf{x}}k_{z1} + \hat{\mathbf{z}}k_x)\exp[i(k_x x - k_{z1}z - \omega t)] \tag{2.21a}$$

$$\mathbf{H}_2(\mathbf{r},\omega) = \omega\mu_v E_{y2}(\hat{\mathbf{x}}k_{z2} - \hat{\mathbf{z}}k_x)\exp[i(k_x x + k_{z2}z - \omega t)] \tag{2.21b}$$

The boundary conditions of Maxwell's equations ensure the continuity of the tangential components of the electric and magnetic fields at the interface 1-2 (Eqs. (2.2a) and (2.2b)). The application of these boundary conditions at the interface 1-2 ($z = 0$) yields the following relationships:

$$E_{y1} = E_{y2} \tag{2.22a}$$

$$k_{z1}E_{y1} = -k_{z2}E_{y2} \tag{2.22b}$$

The above system of equations has a non-trivial solution if and only if $k_{z1} + k_{z2} = 0$. We are interested by the dispersion relation of surface polaritons, with an exponentially decaying field in both media 1 and 2 along the *z*-direction. Therefore, we deal with surface polaritons only and only if both $k_{z1}$ and $k_{z2}$ are pure imaginary numbers. Following the convention used in this chapter, the imaginary part of the *z*-component of the wavevector is always positive, such that no surface polariton exists in TE polarization. It can however be shown that surface polaritons can exist in TE polarization if the materials are magnetic [25].

An alternative approach to determine the above condition, and thus surface polariton dispersion relation, is to find the poles of the Fresnel reflection and transmission coefficients at the interface 1-2 [25]. The poles of the Fresnel reflection and transmission coefficients correspond to the conditions for which these coefficients tend infinity [25].

The Fresnel reflection and transmission coefficients in TE and TM polarizations in terms of wavevectors are given by [1,71]:

$$r_{12}^{TE} = \frac{k_{z1} - k_{z2}}{k_{z1} + k_{z2}} \tag{2.23a}$$

$$r_{12}^{TM} = \frac{\varepsilon_{r2}(\omega)k_{z1} - \varepsilon_{r1}(\omega)k_{z2}}{\varepsilon_{r2}(\omega)k_{z1} + \varepsilon_{r1}(\omega)k_{z2}} \tag{2.23b}$$

$$t_{12}^{TE} = \frac{2k_{z1}}{k_{z1} + k_{z2}} \tag{2.23c}$$

$$t_{12}^{TM} = \frac{2n_1(\omega)n_2(\omega)k_{z1}}{\varepsilon_{r2}(\omega)k_{z1} + \varepsilon_{r1}(\omega)k_{z2}} \tag{2.23d}$$

These relations can be determined by considering a plane wave incident on the interface 1-2, and by applying the boundary conditions of the Maxwell equations [1]. It can be seen from Eqs. (2.23a) and (2.23c) that the Fresnel reflection and transmission coefficients in TE polarization diverge if $k_{z1} + k_{z2} = 0$, which is consistent with the result obtained above.

The same procedure obviously applies in TM polarization, such that we can proceed directly with the Fresnel coefficients. In TM polarization, the Fresnel reflection and transmission coefficients tend to infinity if $\varepsilon_{r2}(\omega)k_{z1} + \varepsilon_{r1}(\omega)k_{z2}$ = 0. Assuming that medium 2 is a vacuum with $\varepsilon_{r2}$ = 1 as in Fig. 2.2, and since the real part of the dielectric function of medium 1 can take negative values, surface polaritons can therefore exist in TM polarization. Using $k_{zj} = \sqrt{\varepsilon_{rj}k_v^2 - k_x^2}$, the above condition can be written as:

$$k_x = k_v\sqrt{\frac{\varepsilon_{r1}(\omega)}{\varepsilon_{r1}(\omega) + 1}} \tag{2.24}$$

Equation (2.24) is the dispersion relation at the interface 1-2, and poses two conditions for the existence of surface polaritons. First, since surface polaritons are propagating along the interface 1-2, the wavevector $k_x$ must be a real number. Moreover, since surface polaritons are evanescent waves along the $z$-direction, $k_x$ must be greater than the wavevector in vacuum $k_v$. By combining these two conditions, surface polaritons exist when the term within the square root in Eq. (2.24) is greater than unity, which can happen when $\varepsilon_{r1}(\omega) < -1$ [25].

To illustrate the dispersion relation of surface polaritons, we assume that medium 1 is SiC, which is a polar crystal supporting SPhPs in the infrared. The dielectric function of SiC is given in appendix B. To plot SPhP dispersion relation, the losses in the dielectric function of SiC are neglected (i.e., $\Gamma = 0$). The dispersion relation at the interface 1-2 for a single SiC-vacuum interface is shown in Fig. 2.3(a), where the light line in vacuum $k_x = k_v$, and the frequencies of transverse and longitudinal optical phonons, respectively given as $\omega_{TO}$ and $\omega_{LO}$, are identified; the real part of the dielectric function of SiC is plotted in Fig. 2.3(b).

To better understand the dispersion relation shown in Fig. 2.3(a), it is necessary to identify the zones where the waves are either propagating or evanescent in vacuum. The $z$-component of the wavevector in vacuum is given by $k_{z2} = \sqrt{k_v^2 - k_x^2}$. When $k_x \leq k_v$, the $z$-component of the wavevector is a pure real number, and therefore the wave is propagating. As a consequence, the part that is on the left-hand side of the light line in vacuum in Fig. 2.3(a) corresponds to propagating waves. On the other hand, when $k_x > k_v$, $k_{z2}$ becomes a pure imaginary number, and therefore the wave is evanescent, such that the part of the dispersion relation on the right-hand side of the light line in vacuum in Fig. 2.3(a) corresponds to evanescent waves.

To show this more clearly, we plotted a part of the dispersion relation that does not correspond to a SPhP (left of light line in vacuum). This curve is obtained by solving Eq. (2.24), but does not satisfy the requirement that the term under the square root be greater than unity. This can be seen by examining the real part of the dielectric function of SiC shown in Fig. 2.3(b); indeed, for frequencies greater than $\omega_{LO}$, the real part of the dielectric function of SiC is greater than -1. The same observation is true for a part of the lower branch of the dispersion relation for frequencies less than $\omega_{TO}$, where the real part of the dielectric function of SiC is greater than -1.

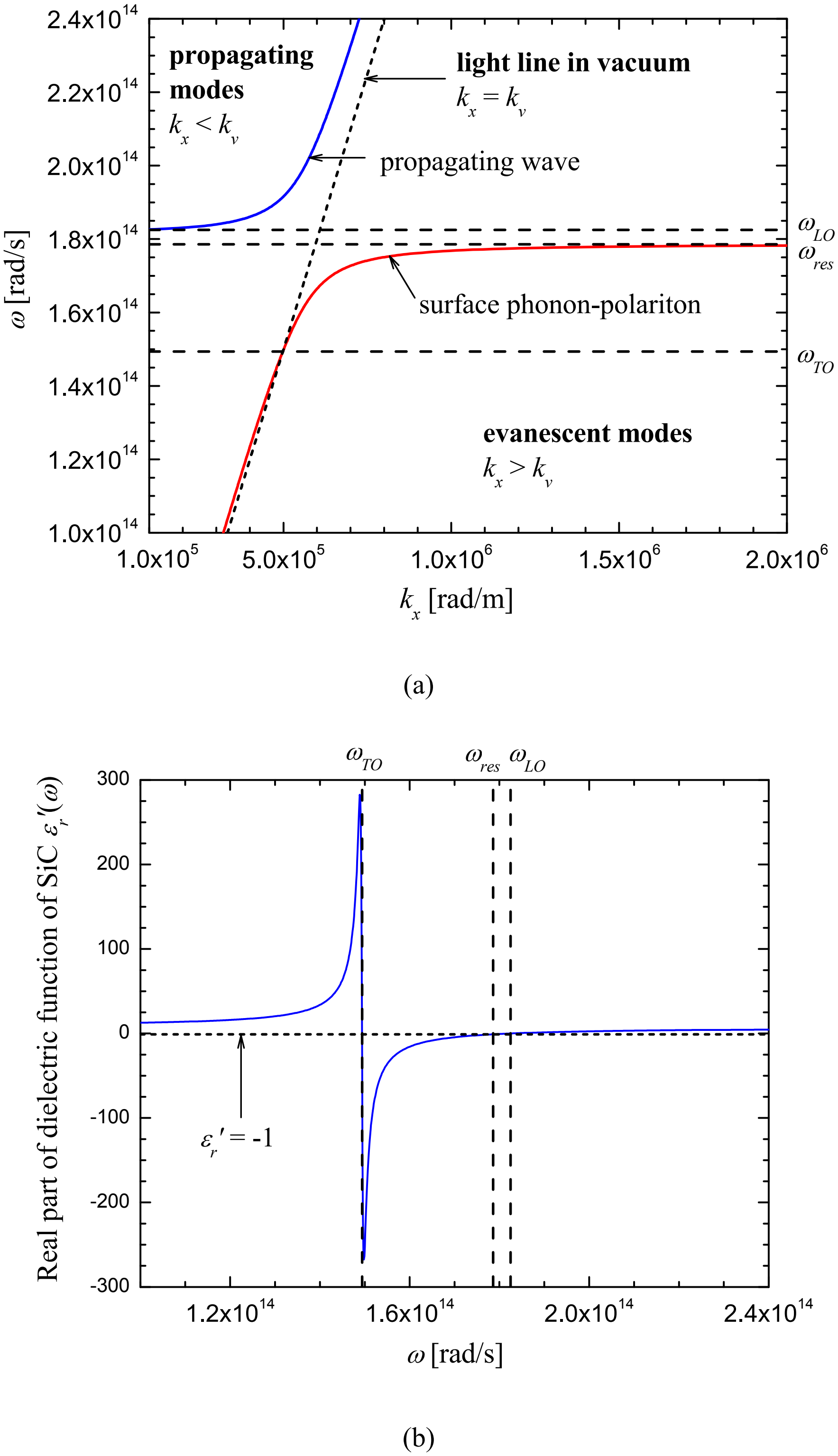

Figure 2.3. (a) SPhP dispersion relation at a SiC-vacuum interface. (b) Real part of the dielectric function of SiC.

On the other hand, the part of the lower branch included in the region between $\omega_{LO}$ and $\omega_{TO}$ is a SPhP, where $k_x > k_v$. By inspecting Fig. 2.3(b), it is seen that the real part of the dielectric function of SiC in the spectral region between $\omega_{LO}$ and $\omega_{TO}$ is less than -1. When the real part of the dielectric function of SiC equals -1, SPhP dispersion relation reaches an asymptote referred hereafter as $\omega_{res}$, which is defined as the resonant frequency of surface polariton at a single interface. Indeed, when the real part of the dielectric function of SiC is exactly -1, the denominator of Eq. (2.24) becomes zero, and then $k_x \rightarrow \infty$. Using the condition $\varepsilon'_{r1}(\omega) = -1$, we find that the resonant frequency is $\omega_{res} = \sqrt{(\varepsilon_\infty \omega_{LO}^2 + \omega_{TO}^2)/(1+\varepsilon_\infty)}$ ; for the SiC-vacuum interface, $\omega_{res} = 1.786\times10^{14}$ rad/s, corresponding to a wavelength of 10.55 μm.

We defined earlier in this chapter the DOS, or LDOS, as the number of electromagnetic modes per unit frequency and per unit volume; as a consequence, the LDOS is directly proportional to $|dk_x/d\omega|$. At resonance, $|dk_x/d\omega| \rightarrow \infty$, such that the LDOS and the energy density become very large. We therefore expect radiative heat exchange between materials supporting surface polaritons to be much greater than the values predicted by the Planck distribution. Also, the fact that an important enhancement takes place around a given frequency $\omega_{res}$ imply temporal, or spectral, coherence in the near-field [1,47]. The spatial coherence in the near-field of a thermal source is also greatly modified due to the presence of surface polaritons [46,47]. Indeed, the high degree of spatial coherence very close to an emitting material supporting surface polaritons can be physically understood by the fact that the mechanical oscillations within the material (plasma oscillations or lattice vibrations) transmit their spatial coherency to the emitted electromagnetic field [46]. Excitation in the far-field of surface polaritons leads to thermal emission in a narrow spectral band and narrow angular lobe [7].

Surface polaritons are usually discussed in the framework of near-field optics. In these applications, surface polaritons are excited via an external radiation beam that experience TIR. Different techniques exist in order to excite surface polaritons via an external radiation beam, such as the Krestchmann and Otto configurations [1,11,50]. In thermal radiation, the situation is different as surface polaritons are excited via the random fluctuations of charges within the emitting material. For typical temperatures involved in thermal radiation applications, SPhPs in SiC can easily be excited as $\Theta(\omega,T)$ reach its peak value around 10 μm at 300 K, as predicted from Wien's law.

If we consider that medium 1 in Fig. 2.2 is a bulk region of gold, then the SPP resonant frequency is around $9.69\times10^{15}$ rad/s, which corresponds to a wavelength of about 0.194 μm. These calculations can be done easily using a Drude model for the dielectric function of gold (see appendix B). For typical thermal radiation temperatures between 300 to 2000 K, $\Theta(\omega,T)$ is very small at this frequency such that the energy density at resonance is also small. Therefore, SPhPs with resonance in the infrared spectrum are usually more interesting from a thermal radiation point of view than SPPs [30]. However, materials such as doped silicon support SPPs in the infrared, and can thus behave like polar crystals supporting SPhPs [26,95-97].

### 2.8 Concluding remarks

The fundamentals of near-field thermal radiation and its mathematical description via the Maxwell equations combined with the FE formalism have been discussed throughout this chapter. It should be understood that the electromagnetic description of thermal radiation can theoretically be used unilaterally at all length scales. However, from a practical point of view, such calculations are unrealistic as the computational requirements are usually prohibitive once the computational domain reaches to a span of a few wavelengths. Then, the view factor theory and the RTE are used to overcome this difficulty and to bring a clear understanding to practical problems.

In the next chapter, a numerical procedure is provided to solve near-field radiative heat transfer problems in one-dimensional layered media.

# Chapter 3

# Numerical Solution of Near-Field Thermal Radiation in One-Dimensional Layered Media

In chapter 2, the electromagnetic description of thermal radiation has been presented. Using this background, it is now possible to discuss the typical problems encountered by a heat transfer engineer, which almost always require calculation of the radiative heat flux.

Despite the fact that near-field thermal radiation seems to be a relatively new subject, the problem of near-field radiative heat flux calculations were addressed in the late sixties by Tien's group [93,94]. Their work provided near-field thermal radiation calculation results between two bulk materials separated by a vacuum gap. They used the analogy with total internal reflection discussed in section 2.7.1 to define the source of thermal radiation, which did not account for all evanescent modes. Polder and Van Hove [20] reported the first correct radiative heat flux calculations between two bulk materials using fluctuational electrodynamics (FE) and the fluctuation-dissipation theorem (FDT). Mulet et al. [30] have shown that quasi-monochromatic radiative heat transfer can be achieved between two bulks when the materials support surface phonon-polaritons (SPhPs), as discussed in section 2.7.2.

Near-field radiative heat transfer between two bulk materials has been investigated in many publications [21,22,25,26,35,65,72,76,96-102]. Also, numerical predictions of radiative flux in the near-field have been investigated for a film emitter [103-110], between a dipole and a surface [23], between two dipoles [22,24,28], in a cylindrical cavity [27], between two large spheres [29], and between a dipole and a structured surface [111]. In all these cases, the combined Maxwell's equations and FE are solved using dyadic Green's functions (DGFs). Solution of near-field thermal radiation problems beyond the aforementioned relatively simple geometries still remains an open research area.

Accurate predictions of near-field radiant energy exchanges in one-dimensional layered structures are of high practical importance, since these predictions can guide the applications involving far-field emission from one-dimensional thermal photonic crystals, nanoscale-gap thermophotovoltaic power generators, and thermal management problems of micro/nanoscale devices. The one-dimensional analysis does sufficiently describe the physics of many practical systems, as in most cases the separation distance between the bodies exchanging thermal radiation is much smaller than the other dimensions of the system. Indeed, Lee et al. [112,113] have developed a method to visualize the pathway of the Poynting vector due to evanescent waves. They have shown that two silicon carbide (SiC) plates exchanging thermal radiation can be considered as semi-infinite (i.e., one-dimensional approximation) when the lateral dimension of the surfaces are about two hundred times larger than the gap separating them [113]. This means that surfaces with lateral dimensional of about 2 μm can be considered as semi-infinite when the separation gap is around 10 nm. This criterion demonstrates that the one-dimensional approximation in near-field thermal radiation is realistic and can arise for a variety of practical cases.

The objective of this chapter is to provide a stable and complete solution methodology for application to near-field thermal radiation problems in one-dimensional layered media. Most of the available papers on one-dimensional layered media have focused on two half-spaces separated by a vacuum gap, and they report only the final equation of the radiative heat flux for a specific configuration. Narayanaswamy and Chen [72] have provided a more general formulation for near-field thermal radiation in one-dimensional layered structures, but with an emphasis on the theoretical aspects rather than on the solution procedure. In this chapter, we provide the general formulation of the problem and a discussion of the equations required to solve near-field thermal radiation transfer in one-dimensional geometry. We also propose a stable general algorithm based on the scattering matrix method to calculate radiative heat flux profiles. Note that although the emphasize of the chapter is on the calculation of the radiative heat flux, the procedure described hereafter is equally applicable for computing the energy density, and consequently the local density of electromagnetic states.

This chapter is constructed as follows. The problem under consideration is presented first. Expressions for the DGFs in one-dimensional layered media are then given in section 3.2. Subsequently, the scattering matrix method allowing the calculation of the amplitudes of the fields in each layer is described. In section 3.4, numerical details and a general algorithm of solution are proposed. Finally, consistency and stability of the procedure are then tested for problems involving bulk and film emitters.

The content of this chapter was published in the *Journal of Quantitative Spectroscopy and Radiative Transfer* in 2009 [114].

### 3.1 Description of the problem

The physical system considered for the calculation of the near-field radiative heat flux in one-dimensional layered medium is depicted in Fig. 3.1, where both Cartesian ($x$, $y$, $z$) and polar ($\rho$, $\theta$, $z$) coordinate systems are shown. $N - 1$ layers with finite thicknesses are sandwiched between two half-spaces denoted medium 0 ($z < z_1$) and medium $N$ ($z > z_N$). Referring to the Cartesian coordinate system, the one-dimensional layered structure is infinite along the $x$- and $y$-directions, and therefore only variations along the $z$-axis need to be considered. The assumptions stated in section 2.2 are applicable here: it is assumed that a given layer $l$ is in local thermodynamic equilibrium at a prescribed temperature $T_l$, homogeneous, isotropic, nonmagnetic, and described by a frequency-dependent dielectric function local in space denoted by $\varepsilon_{rl}(\omega)$. The surfaces of the layers are assumed to be perfectly smooth and parallels.

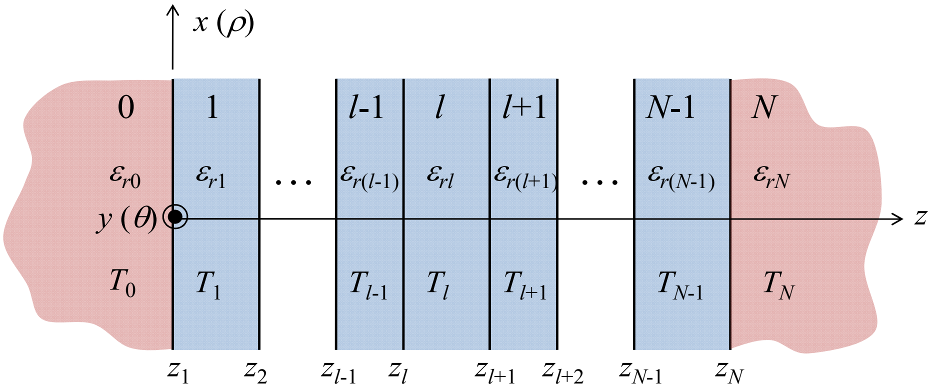
$x\ (\rho)$
0
1
$l$-1
$l$
$l$+1
$N$-1
$N$
$\varepsilon_{r0}$
$\varepsilon_{r1}$
. . .
$\varepsilon_{r(l\text{-}1)}$
$\varepsilon_{rl}$
$\varepsilon_{r(l+1)}$
. . .
$\varepsilon_{r(N\text{-}1)}$
$\varepsilon_{rN}$
$y\ (\theta)$
$z$
$T_0$
$T_1$
$T_{l\text{-}1}$
$T_l$
$T_{l+1}$
$T_{N\text{-}1}$
$T_N$
$z_1$
$z_2$
$z_{l\text{-}1}$
$z_l$
$z_{l+1}$
$z_{l+2}$
$z_{N\text{-}1}$
$z_N$

Figure 3.1. Schematic representation of the one-dimensional layered medium, where $N - 1$ layers of finite thicknesses are sandwiched between two half-spaces.

In section 2.3, the following general expression for the Poynting vector has been derived:

$$\langle \mathbf{S}(\mathbf{r},\omega)\rangle = \frac{2k_v^2\Theta(\omega,T)}{\pi}\mathrm{Re}\left\{ i\varepsilon_r''(\omega)\int_V dV' G^E_{m\alpha}(\mathbf{r},\mathbf{r}',\omega)G^{H*}_{n\alpha}(\mathbf{r},\mathbf{r}',\omega)\right\} \tag{3.1}$$

The monochromatic radiative heat flux at location $\mathbf{r}$ along the $z$-direction in layer $l$ due to an emitting layer $s$ is found by considering the $z$-component of the Poynting vector:

$$\begin{aligned} q_{\omega,sl}(z_c) &= \frac{2k_v^2\Theta(\omega,T_s)}{\pi} \\ &\times \mathrm{Re}\left\{ i\varepsilon_{rs}''(\omega)\int_V dV'\left[G^E_{slx\alpha}(\mathbf{r},\mathbf{r}',\omega)G^{H*}_{sly\alpha}(\mathbf{r},\mathbf{r}',\omega) - G^E_{sly\alpha}(\mathbf{r},\mathbf{r}',\omega)G^{H*}_{slx\alpha}(\mathbf{r},\mathbf{r}',\omega)\right]\right\} \end{aligned} \tag{3.2}$$

where the subscript $\alpha$ involves a summation over the three orthogonal components (state of polarization of the source), and $T_s$, $V$, and $\varepsilon_r''$ are respectively the temperature, volume, and imaginary part of the dielectric function of the emitting layer. The first two subscripts of the DGF terms show explicitly that they are calculated between layers $s$ and $l$. The only unknowns in Eq. (3.2) are the components of the electric and magnetic DGFs, which are discussed next.

### 3.2 Dyadic Green's functions for one-dimensional layered media

It is convenient to use a plane wave representation of the DGF in a one-dimensional geometry. Such a representation is found by applying a two-dimensional spatial Fourier transform as follows [73,75]:

$$\overline{\overline{\mathbf{G}}}_{sl}(\mathbf{r},\mathbf{r}',\omega)=\int_{-\infty}^{\infty}\frac{d\mathbf{k}_{\rho}}{(2\pi)^{2}}\overline{\overline{\mathbf{g}}}_{sl}(\mathbf{k}_{\rho},z_{c},z',\omega)e^{i\mathbf{k}_{\rho}\cdot(\mathbf{R}-\mathbf{R}')} \tag{3.3}$$

where $\mathbf{k}_{\rho}=k_{x}\hat{\mathbf{x}}+k_{y}\hat{\mathbf{y}}$, $d\mathbf{k}_{\rho}=dk_{x}dk_{y}$, $\mathbf{R}=x\hat{\mathbf{x}}+y\hat{\mathbf{y}}$, $z'$ is the location of the source, and $\overline{\overline{\mathbf{g}}}$ is the Weyl component of the DGF. As shown in Eq. (3.2), calculation of the radiative heat flux involves computation of terms $\int_{V}dV'G^{E}_{sli\alpha}G^{H*}_{slj\alpha}$, where *i* and *j* refer to *x* and *y* ($i\neq j$). Substitution of the Weyl development of the DGF in the above term leads to [75]:

$$\int_{V}dV'G^{E}_{sli\alpha}(\mathbf{r},\mathbf{r}',\omega)G^{H*}_{slj\alpha}(\mathbf{r},\mathbf{r}',\omega)=\int_{-\infty}^{\infty}\frac{d\mathbf{k}_{\rho}}{(2\pi)^{2}}\int_{z}dz'g^{E}_{sli\alpha}(\mathbf{k}_{\rho},z_{c},z',\omega)g^{H*}_{slj\alpha}(\mathbf{k}_{\rho},z_{c},z',\omega) \tag{3.4}$$

From now, due to the azimuthal symmetry of the problem, a polar coordinate system ($\rho$, $\theta$, $z$) is adopted. For this, the following transformation is performed on $d\mathbf{k}_{\rho}$:

$$\int_{-\infty}^{\infty}d\mathbf{k}_{\rho}=\int_{-\infty}^{\infty}\int_{-\infty}^{\infty}dk_{x}dk_{y}=\int_{k_{\rho}=0}^{\infty}\int_{\theta=0}^{2\pi}k_{\rho}dk_{\rho}d\theta=2\pi\int_{0}^{\infty}k_{\rho}dk_{\rho} \tag{3.5}$$

where $k_{\rho}$ stands for any wavevector parallel to the surfaces of the layers. Substitution of Eqs. (3.4) and (3.5) into Eq. (3.2) in polar coordinates gives the monochromatic radiative heat flux at $z_c$ along the *z*-direction in terms of the Weyl components of the DGF:

$$\begin{aligned}q_{\omega,sl}(z_{c})=&\frac{k_{v}^{2}\Theta(\omega,T_{s})}{\pi^{2}}\\&\times\mathrm{Re}\left\{i\varepsilon''_{rs}(\omega)\int_{0}^{\infty}k_{\rho}dk_{\rho}\int_{z}dz'\begin{pmatrix}g^{E}_{sl\rho\alpha}(k_{\rho},z_{c},z',\omega)g^{H*}_{sl\theta\alpha}(k_{\rho},z_{c},z',\omega)\\-g^{E}_{sl\theta\alpha}(k_{\rho},z_{c},z',\omega)g^{H*}_{sl\rho\alpha}(k_{\rho},z_{c},z',\omega)\end{pmatrix}\right\}\end{aligned} \tag{3.6}$$

The formalism introduced by Sipe [115] is used hereafter to express the Weyl components of the DGF. To do this, TE- and TM-polarized unit vectors are respectively defined as follows:

$$\hat{\mathbf{s}} = -\hat{\boldsymbol{\theta}} \tag{3.7a}$$

$$\hat{\mathbf{p}}_i^{\pm} = \frac{1}{k_i}(k_\rho \hat{\mathbf{z}} \mp k_{zi} \hat{\boldsymbol{\rho}}) \tag{3.7b}$$

Note that the derivation and physical explanations of Sipe's unit vectors are given in appendix C.

The most general case of a layer $s$ of finite thickness $z_{s+1} - z_s$ emitting thermal radiation, as shown in Fig. 3.2, is considered.

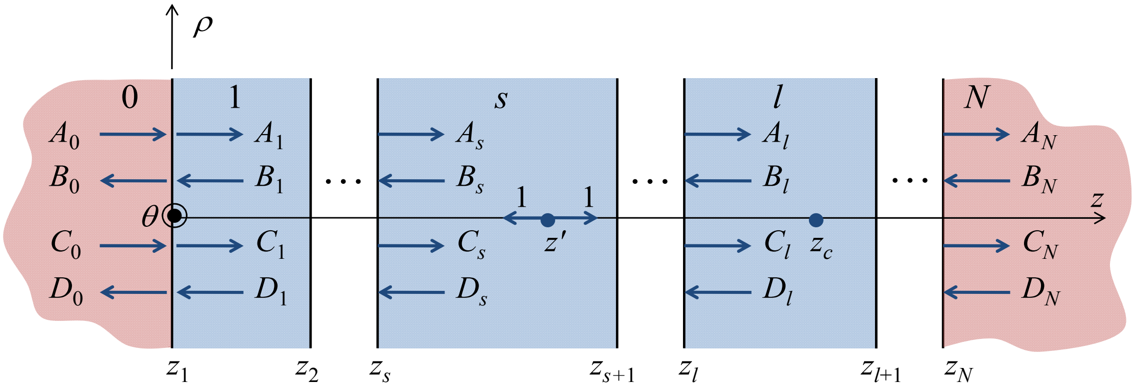

Figure 3.2. Field patterns in each layer due to a point source $z'$ located in layer $s$ emitting in the $z$-positive and $z$-negative directions; $z_c$ in layer $l$ is the point where the radiative heat flux is calculated.

Let us consider that waves of unit amplitudes are emitted both in the forward ($z$-positive) and backward ($z$-negative) directions from the source point $z'$. The emitting layer $s$ consists of multiple source points $z'$ distributed along $z$ in the volume $z_{s+1} - z_s$. The radiative heat flux calculated at $z_c$ in layer $l$ is therefore proportional to the integration of these source points over the volume of layer $s$. Note that layer $l$ could have been located on the left of the source layer $s$.

The field in each layer, resulting from multiple reflections within the structure, is divided into four patterns. The coefficients *A* and *B* denote the amplitudes of forward and backward traveling waves, respectively, arising from a source emitting in the forward direction. Similarly, the coefficients *C* and *D* represent respectively the amplitudes of forward and backward traveling waves generated this time by a source emitting in the backward direction. For the layers $j = 1$ to $N - 1$, these coefficients are calculated on the left boundary of the film at $z = z_j^+$. For the two half-spaces 0 and *N*, the coefficients are calculated respectively at $z = z_1^-$ and $z = z_N^+$.

Sipe's unit vectors (Eqs. (3.7a) and (3.7b)) are used to write the Weyl components of the DGF in terms of dyads $\hat{\mathbf{a}}\hat{\mathbf{b}}$, where $\hat{\mathbf{b}}$ represents the polarization of the wave at the source, and $\hat{\mathbf{a}}$ the polarization of the wave at the point $z_c$ where the field is calculated. The electric Weyl representation of the DGF can be written as:

$$\begin{aligned}&\overset{=E}{\mathbf{g}}_{sl}(k_\rho, z_c, z', \omega)\\ &= \frac{i}{2k_{zs}}\left[\begin{matrix}\left(A_l^{TE}\hat{\mathbf{s}}\hat{\mathbf{s}} + A_l^{TM}\hat{\mathbf{p}}_l^+\hat{\mathbf{p}}_s^+\right)e^{i[k_{zl}(z_c - z_l) - k_{zs}z']} + \left(B_l^{TE}\hat{\mathbf{s}}\hat{\mathbf{s}} + B_l^{TM}\hat{\mathbf{p}}_l^-\hat{\mathbf{p}}_s^+\right)e^{i[-k_{zl}(z_c - z_l) - k_{zs}z']}\\ + \left(C_l^{TE}\hat{\mathbf{s}}\hat{\mathbf{s}} + C_l^{TM}\hat{\mathbf{p}}_l^+\hat{\mathbf{p}}_s^-\right)e^{i[k_{zl}(z_c - z_l) + k_{zs}z']} + \left(D_l^{TE}\hat{\mathbf{s}}\hat{\mathbf{s}} + D_l^{TM}\hat{\mathbf{p}}_l^-\hat{\mathbf{p}}_s^-\right)e^{i[-k_{zl}(z_c - z_l) + k_{zs}z']}\end{matrix}\right]\end{aligned} \tag{3.8}$$

In Eq. (3.8), the term $A_l^{TM}\hat{\mathbf{p}}_l^+\hat{\mathbf{p}}_s^+$ means that a forward traveling wave with polarization $\hat{\mathbf{p}}_l^+$ and amplitude $A_l^{TM}$ is observed in layer *l* due to a forward traveling wave emitted in layer *s* with polarization $\hat{\mathbf{p}}_s^+$; the physical interpretation of the other terms is similar.

The magnetic Weyl representation of the DGF is found using $\overset{=H}{\mathbf{g}} = \nabla \times \overset{=E}{\mathbf{g}}$, and is written as follows:

$$\begin{aligned}&\overset{=H}{\mathbf{g}}_{sl}(k_\rho, z_c, z', \omega)\\ &= \frac{k_l}{2k_{zs}}\left[\begin{matrix}\left(A_l^{TE}\hat{\mathbf{p}}_l^+\hat{\mathbf{s}} - A_l^{TM}\hat{\mathbf{s}}\hat{\mathbf{p}}_s^+\right)e^{i[k_{zl}(z_c - z_l) - k_{zs}z']} + \left(B_l^{TE}\hat{\mathbf{p}}_l^-\hat{\mathbf{s}} - B_l^{TM}\hat{\mathbf{s}}\hat{\mathbf{p}}_s^+\right)e^{i[-k_{zl}(z_c - z_l) - k_{zs}z']}\\ + \left(C_l^{TE}\hat{\mathbf{p}}_l^+\hat{\mathbf{s}} - C_l^{TM}\hat{\mathbf{s}}\hat{\mathbf{p}}_s^-\right)e^{i[k_{zl}(z_c - z_l) + k_{zs}z']} + \left(D_l^{TE}\hat{\mathbf{p}}_l^-\hat{\mathbf{s}} - D_l^{TM}\hat{\mathbf{s}}\hat{\mathbf{p}}_s^-\right)e^{i[-k_{zl}(z_c - z_l) + k_{zs}z']}\end{matrix}\right]\end{aligned} \tag{3.9}$$

Equations (3.8) and (3.9) are valid if the point $z_c$ is located in a layer other than the one where the source is located (i.e., if $l \neq s$). Indeed, the coefficients *A*, *B*, *C*, and *D* can be seen as the amplitudes of the waves after multiple reflections within the one-dimensional structure. If the point $z_c$ is located in layer $s$ (i.e., $l = s$), the DGFs have also to account for the primary wave propagation in unbounded medium (i.e., the part of the wave reaching the point $z_c$ without being scattered by the boundaries), which can be written as follows for the electric component [72,73]:

$$\overline{\overline{\mathbf{g}}}_{ss}^{E,P}(k_\rho, z_c, z', \omega) = \frac{i}{2k_{zs}} \begin{cases} \left(\hat{\mathbf{s}}\hat{\mathbf{s}} + \hat{\mathbf{p}}_s^+\hat{\mathbf{p}}_s^+\right) e^{ik_{zs}(z_c - z')}, & z_c > z' \\ \left(\hat{\mathbf{s}}\hat{\mathbf{s}} + \hat{\mathbf{p}}_s^-\hat{\mathbf{p}}_s^-\right) e^{-ik_{zs}(z_c - z')}, & z_c < z' \end{cases} \tag{3.10}$$

where the superscript $P$ refers to primary wave. A similar term exists for the magnetic DGF. Therefore, if $l = s$, the electric DGF becomes the superposition of the response of the layered medium, given by Eq. (3.8), and the primary wave propagating in unbounded medium, given by Eq. (3.10). For more clarity, we will omit the primary wave term in the expressions of the DGFs, keeping in mind that it should be accounted for when $l = s$.

In the expression of the monochromatic radiative heat flux (Eq. (3.6)), the Weyl components of the DGF are written as a function of $\rho$, $\theta$, $z$. We therefore need to convert the dyads $\hat{\mathbf{a}}\hat{\mathbf{b}}$ of Eqs. (3.8) and (3.9) in terms of these coordinates. For example, using Eq. (3.7a), we find that the dyad $\hat{\mathbf{s}}\hat{\mathbf{s}}$ is given by $\hat{\boldsymbol{\theta}}\hat{\boldsymbol{\theta}}$. By regrouping the terms of Eq. (3.8) as a function of $\hat{\boldsymbol{\rho}}\hat{\boldsymbol{\rho}}$, $\hat{\boldsymbol{\rho}}\hat{\boldsymbol{\theta}}$, … $\hat{\mathbf{z}}\hat{\mathbf{z}}$, the Weyl representation of the electric DGF can be written in tensor form as:

$$\overline{\overline{\mathbf{g}}}_{sl}^{E}(k_\rho, z_c, z', \omega) = \begin{bmatrix} g_{sl\rho\rho}^{E} & 0 & g_{sl\rho z}^{E} \\ 0 & g_{sl\theta\theta}^{E} & 0 \\ g_{slz\rho}^{E} & 0 & g_{slzz}^{E} \end{bmatrix} \tag{3.11a}$$

with components:

$$g_{sl\rho\rho}^{E}(k_\rho, z_c, z', \omega) = \frac{ik_{zl}}{2k_s k_l} \begin{pmatrix} A_l^{TM} e^{i[k_{zl}(z_c - z_l) - k_{zs}z']} - B_l^{TM} e^{i[-k_{zl}(z_c - z_l) - k_{zs}z']} \\ - C_l^{TM} e^{i[k_{zl}(z_c - z_l) + k_{zs}z']} + D_l^{TM} e^{i[-k_{zl}(z_c - z_l) + k_{zs}z']} \end{pmatrix} \tag{3.11b}$$

$$g_{sl\rho z}^{E}(k_\rho, z_c, z', \omega) = \frac{ik_{zl}k_\rho}{2k_{zs}k_s k_l} \begin{pmatrix} - A_l^{TM} e^{i[k_{zl}(z_c - z_l) - k_{zs}z']} + B_l^{TM} e^{i[-k_{zl}(z_c - z_l) - k_{zs}z']} \\ - C_l^{TM} e^{i[k_{zl}(z_c - z_l) + k_{zs}z']} + D_l^{TM} e^{i[-k_{zl}(z_c - z_l) + k_{zs}z']} \end{pmatrix} \tag{3.11c}$$

$$g_{sl\theta\theta}^{E}(k_\rho, z_c, z', \omega) = \frac{i}{2k_{zs}} \begin{pmatrix} A_l^{TE} e^{i[k_{zl}(z_c - z_l) - k_{zs}z']} + B_l^{TE} e^{i[-k_{zl}(z_c - z_l) - k_{zs}z']} \\ + C_l^{TE} e^{i[k_{zl}(z_c - z_l) + k_{zs}z']} + D_l^{TE} e^{i[-k_{zl}(z_c - z_l) + k_{zs}z']} \end{pmatrix} \tag{3.11d}$$

$$g_{slz\rho}^{E}(k_\rho, z_c, z', \omega) = \frac{ik_\rho}{2k_s k_l} \begin{pmatrix} - A_l^{TM} e^{i[k_{zl}(z_c - z_l) - k_{zs}z']} - B_l^{TM} e^{i[-k_{zl}(z_c - z_l) - k_{zs}z']} \\ + C_l^{TM} e^{i[k_{zl}(z_c - z_l) + k_{zs}z']} + D_l^{TM} e^{i[-k_{zl}(z_c - z_l) + k_{zs}z']} \end{pmatrix} \tag{3.11e}$$

$$g_{slzz}^{E}(k_\rho, z_c, z', \omega) = \frac{ik_\rho^2}{2k_{zs} k_s k_l} \begin{pmatrix} A_l^{TM} e^{i[k_{zl}(z_c - z_l) - k_{zs}z']} + B_l^{TM} e^{i[-k_{zl}(z_c - z_l) - k_{zs}z']} \\ + C_l^{TM} e^{i[k_{zl}(z_c - z_l) + k_{zs}z']} + D_l^{TM} e^{i[-k_{zl}(z_c - z_l) + k_{zs}z']} \end{pmatrix} \tag{3.11f}$$

In the same manner, the Weyl representation of the magnetic DGF is given in tensor form as follows:

$$\overline{\overline{\mathbf{g}}}_{sl}^{H}(k_x, z_c, z', \omega) = \begin{bmatrix} 0 & g_{sl\rho\theta}^{H} & 0 \\ g_{sl\theta\rho}^{H} & 0 & g_{sl\theta z}^{H} \\ 0 & g_{slz\theta}^{H} & 0 \end{bmatrix} \tag{3.12a}$$

with components:

$$g_{sl\rho\theta}^{H}(k_\rho, z_c, z', \omega) = \frac{k_{zl}}{2k_{zs}} \begin{pmatrix} A_l^{TE} e^{i[k_{zl}(z_c - z_l) - k_{zs}z']} - B_l^{TE} e^{i[-k_{zl}(z_c - z_l) - k_{zs}z']} \\ + C_l^{TE} e^{i[k_{zl}(z_c - z_l) + k_{zs}z']} - D_l^{TE} e^{i[-k_{zl}(z_c - z_l) + k_{zs}z']} \end{pmatrix} \tag{3.12b}$$

$$g_{sl\theta\rho}^{H}(k_\rho, z_c, z', \omega) = \frac{k_l}{2k_s} \begin{pmatrix} - A_l^{TM} e^{i[k_{zl}(z_c - z_l) - k_{zs}z']} - B_l^{TM} e^{i[-k_{zl}(z_c - z_l) - k_{zs}z']} \\ + C_l^{TM} e^{i[k_{zl}(z_c - z_l) + k_{zs}z']} + D_l^{TM} e^{i[-k_{zl}(z_c - z_l) + k_{zs}z']} \end{pmatrix} \tag{3.12c}$$

$$g_{sl\theta z}^{H}(k_\rho, z_c, z', \omega) = \frac{k_l k_\rho}{2k_s k_{zs}} \begin{pmatrix} A_l^{TM} e^{i[k_{zl}(z_c - z_l) - k_{zs}z']} + B_l^{TM} e^{i[-k_{zl}(z_c - z_l) - k_{zs}z']} \\ + C_l^{TM} e^{i[k_{zl}(z_c - z_l) + k_{zs}z']} + D_l^{TM} e^{i[-k_{zl}(z_c - z_l) + k_{zs}z']} \end{pmatrix} \tag{3.12d}$$

$$g_{slz\theta}^{H}(k_\rho, z_c, z', \omega) = \frac{k_\rho}{2k_{zs}} \begin{pmatrix} - A_l^{TE} e^{i[k_{zl}(z_c - z_l) - k_{zs}z']} - B_l^{TE} e^{i[-k_{zl}(z_c - z_l) - k_{zs}z']} \\ - C_l^{TE} e^{i[k_{zl}(z_c - z_l) + k_{zs}z']} - D_l^{TE} e^{i[-k_{zl}(z_c - z_l) + k_{zs}z']} \end{pmatrix} \tag{3.12e}$$

The monochromatic radiative heat flux at location $z = z_c$ in layer $l$ along the $z$-direction, due to a source layer $s$ of volume $z_{s+1} - z_s$, can therefore be written as:

$$q_{\omega,sl}(z_c) = \frac{k_v^2 \Theta(\omega,T_s)}{\pi^2} \times \mathrm{Re}\left\{ i\varepsilon''_{rs}(\omega) \int_0^\infty k_\rho dk_\rho \int_{z_s}^{z_{s+1}} dz' \begin{bmatrix} g^E_{sl\rho\rho}(k_\rho,z_c,z',\omega) g^{H*}_{sl\theta\rho}(k_\rho,z_c,z',\omega) \\ + g^E_{sl\rho z}(k_\rho,z_c,z',\omega) g^{H*}_{sl\theta z}(k_\rho,z_c,z',\omega) \\ - g^E_{sl\theta\theta}(k_\rho,z_c,z',\omega) g^{H*}_{sl\rho\theta}(k_\rho,z_c,z',\omega) \end{bmatrix} \right\} \tag{3.13}$$

where $g^E_{sl\rho\rho} g^{H*}_{sl\theta\rho} + g^E_{sl\rho z} g^{H*}_{sl\theta z}$ can be seen as a spatial transfer function from $z'$ to $z_c$ for TM-polarized waves, and $g^E_{sl\theta\theta} g^{H*}_{sl\rho\theta}$ for TE-polarized waves. The only remaining step for the calculation of the radiative heat flux is to set-up a procedure to compute the coefficients $A_l$, $B_l$, $C_l$, and $D_l$ for $l = 0$ to $N$; this is discussed in the next section.

## 3.3 Solution for the field amplitudes via the scattering matrix approach

### *3.3.1 Scattering matrix method*

For one-dimensional media consisting of multiple layers, an efficient way to determine the coefficients $A_l$, $B_l$, $C_l$, $D_l$ is to use a transfer matrix (T-matrix) approach [71]. Even if there are four coefficients to be determined in each layer, it is possible to solve separately for the forward emitting sources ($A_l$ and $B_l$) and backward emitting sources ($C_l$ and $D_l$). We therefore only consider the coefficients $A_l$ and $B_l$ hereafter, keeping in mind that the procedure is the same for $C_l$ and $D_l$. It is also worth noting that the four coefficients need to be solved for each polarization state (i.e., TE and TM).

Using the T-matrix approach, the coefficients in half-spaces 0 and $N$ are related as follows (see Fig. 3.2) [71]:

$$\begin{bmatrix} A_0 \\ B_0 \end{bmatrix} = \left( \prod_{l=0}^{N-2} V_{l,l+1} P_{l+1} \right) V_{N-1,N} \begin{bmatrix} A_N \\ B_N \end{bmatrix} \tag{3.14}$$

where $V_{l,l+1}$ is the transmission matrix linking the amplitudes of the waves at the interface $l - l+1$, and $P_l$ is the propagation matrix in layer $l$. The transmission matrix $V_{l,\, l+1}$ is found by applying the boundary conditions of Maxwell's equations in each polarization state at the interface $l - l+1$ and is given by [71]:

$$V_{l,l+1} = \frac{1}{t_{l,l+1}} \begin{bmatrix} 1 & r_{l,l+1} \\ r_{l,l+1} & 1 \end{bmatrix} \tag{3.15}$$

where $t_{l,l+1}$ and $r_{l,l+1}$ are respectively Fresnel's transmission and reflection coefficients at the interface $l$ – $l$+1 defined in section 2.7.2; the coefficients $A_l$ and $B_l$ can therefore be calculated in TE (TM) polarization using the definition of Fresnel's coefficients in TE (TM) polarization. The propagation matrix $P_l$, describing wave propagation in layer $l$, is written as follows [71]:

$$P_l = \begin{bmatrix} e^{-ik_{zl}(z_{l+1}-z_l)} & 0 \\ 0 & e^{ik_{zl}(z_{l+1}-z_l)} \end{bmatrix} \tag{3.16}$$

Numerical instabilities in the T-matrix approach given above are likely to arise when solving near-field thermal radiation problems, since it involves simultaneous computations of $e^{\pm ik_{zl}(z_{l+1}-z_l)}$. Following the convention used in this work, the $z$-component of the wavevector in layer $l$ is given by $k_{zl} = k'_{zl} + ik''_{zl}$. Therefore, the terms $e^{ik_{zl}(z_{l+1}-z_l)}$ and $e^{-ik_{zl}(z_{l+1}-z_l)}$ can become respectively very small and very large if $k''_{zl}$ is large, which arise if there are evanescent waves. Indeed, the $z$-component of the wavevector can also be written as $k_{zl} = \sqrt{k_l^2 - k_\rho^2}$, where $k_\rho$ is a pure real number. If we assume that $k_l$ is a pure real number (if medium $l$ is vacuum for example), waves are evanescent when $k_\rho > k_l$, and $k''_{zl}$ becomes very large when $k_\rho >> k_l$. Consequently, to ensure the stability of the algorithm, we need to modify the T-matrix in such a way that only $e^{ik_{zl}(z_{l+1}-z_l)}$ terms, converging to zero when $k''_{zl} \to \infty$, are calculated.

A modified version of the T-matrix approach, called the scattering matrix (S-matrix) method, was proposed by Auslender and Hava [116] and recently applied to near-field thermal radiation by Drevillon [54]. The idea with this approach is to calculate separately the outgoing and incoming wave amplitudes in each layer in such a way that only $e^{ik_{zl}(z_{l+1}-z_l)}$ terms are computed. From the scattering theory, it is possible to assume a linear relationship between $A_l$ and $B_l$ [116]. Then, the relationship between incoming and outgoing waves in layers 0 and $l$ can be written as:

$$\begin{bmatrix} A_l \\ B_0 \end{bmatrix} = S(0,l)\begin{bmatrix} A_0 \\ B_l \end{bmatrix} \tag{3.17}$$

where $S(0,l)$ is the S-matrix between layers 0 and $l$. The above equation gives the following linear relationship between incoming and outgoing wave amplitudes:

$$A_l = S_{11}(0,l)A_0 + S_{12}(0,l)B_l \tag{3.18a}$$

$$B_0 = S_{21}(0,l)A_0 + S_{22}(0,l)B_l \tag{3.18b}$$

To determine the coefficients in each layer $l$, the relationship between the matrix $S(0,l)$ and $S(0,l+1)$ needs to be determined. The relation between the coefficients $A$ and $B$ in layers $l$ and $l+1$ can be found using the following T-matrix relation:

$$\begin{bmatrix} A_l \\ B_l \end{bmatrix} = \frac{1}{t_{l,l+1}}\begin{bmatrix} e^{-ik_{zl}(z_{l+1}-z_l)} & r_{l,l+1}e^{-ik_{zl}(z_{l+1}-z_l)} \\ r_{l,l+1}e^{ik_{zl}(z_{l+1}-z_l)} & e^{ik_{zl}(z_{l+1}-z_l)} \end{bmatrix}\begin{bmatrix} A_{l+1} \\ B_{l+1} \end{bmatrix} = \begin{bmatrix} u_{11} & u_{12} \\ u_{21} & u_{22} \end{bmatrix}\begin{bmatrix} A_{l+1} \\ B_{l+1} \end{bmatrix} \tag{3.19}$$

The coefficients $A_l$ and $B_l$, written in terms of $A_{l+1}$ and $B_{l+1}$, from the T-matrix relation given by Eq. (3.19), are then substituted into Eqs. (3.18a) and (3.18b). This gives the following S-matrix relation between the coefficients in layers 0 and $l+1$:

$$\begin{aligned} \begin{bmatrix} A_{l+1} \\ B_0 \end{bmatrix} &= \begin{bmatrix} u_{11} - S_{12}(0,l)u_{21} & 0 \\ -S_{22}(0,l)u_{21} & 1 \end{bmatrix}^{-1}\begin{bmatrix} S_{11}(0,l) & S_{12}(0,l)u_{22} - u_{12} \\ S_{21}(0,l) & S_{22}(0,l)u_{22} \end{bmatrix}\begin{bmatrix} A_0 \\ B_{l+1} \end{bmatrix} \\ &= \begin{bmatrix} S_{11}(0,l+1) & S_{12}(0,l+1) \\ S_{21}(0,l+1) & S_{22}(0,l+1) \end{bmatrix}\begin{bmatrix} A_0 \\ B_{l+1} \end{bmatrix} \end{aligned} \tag{3.20}$$

Equation (3.20) gives the necessary relationship to calculate the S-matrix at $l+1$ from the S-matrix at $l$. The S-matrix components at $l+1$ in terms of the S-matrix components at $l$ are given by:

$$S_{11}(0,l+1) = \frac{S_{11}(0,l)t_{l,l+1}e^{ik_{zl}(z_{l+1}-z_l)}}{1 - S_{12}(0,l)r_{l,l+1}e^{2ik_{zl}(z_{l+1}-z_l)}} \tag{3.21a}$$

$$S_{12}(0,l+1) = \frac{S_{12}(0,l)e^{2ik_{zl}(z_{l+1}-z_l)} - r_{l,l+1}}{1 - S_{12}(0,l)r_{l,l+1}e^{2ik_{zl}(z_{l+1}-z_l)}} \tag{3.21b}$$

$$S_{21}(0,l+1)=\frac{S_{11}(0,l+1)S_{22}(0,l)r_{l,l+1}e^{ik_{zl}(z_{l+1}-z_l)}}{t_{l,l+1}}+S_{21}(0,l) \tag{3.21c}$$

$$S_{22}(0,l+1)=\frac{S_{22}(0,l)\left[r_{l,l+1}S_{12}(0,l+1)+1\right]e^{ik_{zl}(z_{l+1}-z_l)}}{t_{l,l+1}} \tag{3.21d}$$

Equations (3.21a) to (3.21d) do not involve calculations of $e^{-ik_{zl}(z_{l+1}-z_l)}$ such that the S-matrix algorithm is stable regardless of the value of $k''_{zl}$. The elements of the S-matrix are calculated using Eqs. (3.21a) to (3.21d) and the following initialization:

$$\begin{bmatrix} S_{11}(0,0) & S_{12}(0,0) \\ S_{21}(0,0) & S_{22}(0,0) \end{bmatrix}=\begin{bmatrix} 1 & 0 \\ 0 & 1 \end{bmatrix} \tag{3.22}$$

The S-matrix coefficients can also be calculated relative to any arbitrary layer *k* (i.e., not necessary layer 0). Similarly, the S-matrix relative to itself (i.e., *S*(*k*, *k*)) is initialized by a 2 by 2 identity matrix, and the calculations of *S*(*k*, *l*), for *l* = *k*+1 to *N* are carried out using Eqs. (3.21a) to (3.21d). Again, the coefficients in each polarization state are calculated independently using the appropriate definitions of Fresnel's transmission and reflection coefficients in TE and TM polarizations.

### *3.3.2 Determination of coefficients*

The unknown coefficients in each layer are calculated via the S-matrix method starting with information known *a priori*. As depicted in Fig. 3.2, the coefficients $A_0$, $C_0$, $B_N$, and $D_N$ correspond to amplitudes of waves coming from outside of the structure. For near-field thermal radiation calculations, there is no external source of energy incident on the one-dimensional layered media since wave emission is originating from the layers themselves. As a consequence, we can always set that $A_0 = C_0 = B_N = D_N = 0$.

The case of a layer of finite thickness (film) emitting thermal radiation, and the case of an emitting half-space are treated in details in the next two sub-sections.

*3.3.2.1 Case of an emitting film*

As depicted in Fig. 3.2, the source point $z'$ in layer $s$ is emitting waves of unit amplitude in both the forward and backward directions. The S-matrix procedure is first set-up for the source emitting in the forward direction (i.e., solution for $A_l$ and $B_l$). As pointed out earlier, the fact that no field is incident on the structure implies that $A_0 = B_N = 0$. Therefore, if we consider layers 0, $s$, and $N$, we are left with four unknowns ($B_0$, $A_s$, $B_s$, $A_N$), that can be determined via the S-matrix method; two equations are provided by the S-matrix relation between layers 0 and $s$, and two other equations via the S-matrix relating layers $s$ and $N$.

The relationship between layers 0 and $s$ is given as follows in terms of S-matrix components:

$$A_s = S_{12}(0,s)B_s \tag{3.23a}$$

$$B_0 = S_{22}(0,s)B_s \tag{3.23b}$$

The relationship between layers $s$ and $N$ is given by:

$$\begin{bmatrix} A_N \\ B_s \end{bmatrix} = \begin{bmatrix} S_{11}(s,N) & S_{12}(s,N) \\ S_{21}(s,N) & S_{22}(s,N) \end{bmatrix} \begin{bmatrix} A_s + S^+ \\ 0 \end{bmatrix} \tag{3.24}$$

Here, since the coefficients in layer $N$ are located at $z$ greater than $z'$, the presence of the source in layer $s$ has to be accounted for. The amplitude of the source at the boundary $z_s$ in layer $s$ is denoted by $S^+$ and is given by:

$$S^+ = e^{ik_{zs}(z_s - z')} \tag{3.25}$$

Equation (3.25) means that the field in layer $s$ is decomposed in two categories when $z > z'$. The coefficients $A_s$ and $B_s$ are the wave amplitudes resulting from multiple reflection within the one-dimensional layered medium; in other words, this is the response of the layered medium due to an excitation in the forward direction originating from $z'$. The second type of wave is the emitted wave traveling in layer $s$ in the forward direction only.

From the matrix relation given by Eq. (3.24), the following two relations can be written:

$$A_N = S_{11}(s,N)(A_s + S^+) \tag{3.26a}$$

$$B_s = S_{21}(s,N)(A_s + S^+) \tag{3.26b}$$

Substitution of Eq. (3.23a) into (3.26b) leads to:

$$B_s = \frac{S_{21}(s,N)S^+}{1 - S_{21}(s,N)S_{12}(0,s)} \tag{3.27}$$

The coefficients $B_0$, $A_s$, and $A_N$ can afterwards be calculated starting with Eq. (3.27).

The coefficients in each layer can be found using a recursive scheme based on S-matrix relations. Starting at layer 0 where $A_0$ and $B_0$ are known, $A_1$ and $B_1$ can be calculated using the two equations provided by the S-matrix between layers 0 and 1. For $z < z'$, the coefficients in layer $l = 1, s\text{-}1$ are given by:

$$B_l = \frac{B_0}{S_{22}(0,l)} \tag{3.28a}$$

$$A_l = S_{12}(0,l)B_l \tag{3.28b}$$

For $z > z'$, the S-matrix between layers $s$ and $l$ ($l = s+1, N-1$) provide the necessary equations to calculate the coefficients in each layer; they are given by:

$$B_l = \frac{B_s - S_{21}(s,l)(A_s + S^+)}{S_{22}(s,l)} \tag{3.29a}$$

$$A_l = S_{11}(s,l)(A_s + S^+) + S_{12}(s,l)B_l \tag{3.29b}$$

The case of the source emitting in the backward direction is now under consideration (i.e., solution for $C_l$ and $D_l$). As pointed out in the beginning of section 3.3.2, the fact that no wave is coming from outside the structure implies that $C_0 = D_N = 0$. Similarly to the case of a forward emitted wave, there are four unknowns in layers 0, $s$, and $N$ ($D_0$, $C_s$, $D_s$, $C_N$) that can be found using the four equations provided by the S-matrix relations between layers 0 and $s$, and layers $s$ and $N$.

The relationship between layers 0 and $s$ is given by:

$$\begin{bmatrix} C_s \\ D_0 \end{bmatrix} = \begin{bmatrix} S_{11}(0,s) & S_{12}(0,s) \\ S_{21}(0,s) & S_{22}(0,s) \end{bmatrix} \begin{bmatrix} 0 \\ D_s + S^- \end{bmatrix} \tag{3.30}$$

Since the coefficients in layer 0 are located at $z < z'$, the presence of the source in layer $s$ has to be accounted for. The amplitude of the source at the boundary $z_s$ in layer $s$, denoted by $S^-$, is given by:

$$S^- = e^{ik_{zs}(z'-z_s)} \tag{3.31}$$

In the same way as for a wave emitted in the forward direction, the field in layer $s$ when $z < z'$ is due to multiple reflections within the layered medium (described by the coefficients $C_s$ and $D_s$) and the emitted wave traveling in the backward direction.

The following two relations can be written from Eq. (3.30):

$$C_s = S_{12}(0,s)(D_s + S^-) \tag{3.32a}$$

$$D_0 = S_{22}(0,s)(D_s + S^-) \tag{3.32b}$$

The other two equations are provided by the S-matrix relation between layers $s$ and $N$:

$$C_N = S_{11}(s,N)C_s \tag{3.33a}$$

$$D_s = S_{21}(s,N)C_s \tag{3.33b}$$

Insertion of Eq. (3.33b) into Eq. (3.32a) leads to:

$$C_s = \frac{S_{12}(0,s)S^-}{1 - S_{12}(0,s)S_{21}(s,N)} \tag{3.34}$$

The coefficients $D_0$, $D_s$, and $C_N$ can then be easily found starting with Eq. (3.34). The coefficients in layers $l = 1$ to $s - 1$ for $z < z'$ can be calculated using the S-matrix relation between layers 0 and $l$:

$$D_l = \frac{D_0}{S_{22}(0,l)} \tag{3.35a}$$

$$C_l = S_{12}(0,l)D_l \tag{3.35b}$$

Similarly, the coefficients in layers $l = s + 1$ to $N - 1$ for $z > z'$ are determined from the S-matrix between layers $s$ and $l$:

$$D_l = \frac{D_s - S_{21}(s,l)C_s}{S_{22}(s,l)} \tag{3.36a}$$

$$C_l = S_{11}(s,l)C_s + S_{12}(s,l)D_l \tag{3.36b}$$

### *3.3.2.2 Case of an emitting half-space*

The problem is simplified if the source is in one of the half-spaces. If we assume that half-space 0 is emitting, all $C_l$ and $D_l$ coefficients for $l = 0$ to $N$ are zero since there is no wave emitted in the backward direction that can propagate in the one-dimensional layered medium. Similarly, if half-space $N$ is emitting, all $A_l$ and $B_l$ coefficients for $l = 0$ to $N$ are zero since there is no wave emitted in the forward direction that can propagate in the structure. Below, we provide the solution only for the emitting half-space 0, since the procedure is exactly the same for the emitting half-space $N$.

Again, the fact that no field is coming from an external source implies that $A_0 = B_N = 0$. The two unknown coefficients $B_0$ and $A_N$ can therefore be determined using the two equations provided by the S-matrix relation between layers 0 and $N$:

$$\begin{bmatrix} A_N \\ B_0 \end{bmatrix} = \begin{bmatrix} S_{11}(0,N) & S_{12}(0,N) \\ S_{21}(0,N) & S_{22}(0,N) \end{bmatrix} \begin{bmatrix} S^+ \\ 0 \end{bmatrix} \tag{3.37}$$

where the amplitude of the source $S^+$ is unity. As shown in Eq. (3.37), the field in layer 0 is composed of the response from the layered structure after multiple reflections ($B_0$) and the wave of unit amplitude emitted in the forward direction ($S^+$). From the matrix relation given by Eq. (3.37), we find:

$$A_N = S_{11}(0,N) \tag{3.38a}$$

$$B_0 = S_{21}(0,N) \tag{3.38b}$$

The coefficients $A_l$ and $B_l$ for layers $l = 1$ to $N - 1$ are found from the S-matrix relating layer 0 to layer $l$:

$$B_l = \frac{B_0 - S_{21}(0,l)}{S_{22}(0,l)} \tag{3.39a}$$

$$A_l = S_{11}(0,l) + S_{12}(0,l)B_l \tag{3.39b}$$

The S-matrix method described in this section provides the necessary tool to compute the Weyl components of the DGF needed for the calculation of the near-field radiative heat flux. In the next section, the general algorithm to solve a one-dimensional near-field thermal radiation problem with an arbitrary number of layers is given.

### 3.4 Algorithm for solution of one-dimensional near-field thermal radiation problems

Equation (3.13) gives the monochromatic radiative heat flux at location $z_c$ in layer $l$ due to a layer $s$ of volume $z_{s+1} - z_s$ at temperature $T_s$ emitting thermal radiation; the total radiative heat flux can be found by integrating Eq. (3.13) over all angular frequencies (i.e., $q_{sl}^{tot}(z_c) = \int_{\omega=0}^{\infty} q_{\omega,sl}(z_c)d\omega$).

Equation (3.13) involves the computation of different integral terms, discussed hereafter. The integration over the parallel wavevector, $k_\rho$, needs to be performed from 0 to infinity. It is usually more efficient to brake down the integration in few parts to allow a variable discretization of $k_\rho$, since the integrand behaves quite differently from one $k_\rho$ interval to another. For example, if layers $s$ and $l$ are spaced by a vacuum gap, the radiative heat flux from $k_\rho$ = 0 to $k_v$ (=$\omega/c_v$) corresponds to the contribution from propagating waves, while $k_\rho$ > $k_v$ is the contribution from evanescent modes. As a consequence, for that case, the radiative flux can be solved separately for propagating and evanescent waves.

As pointed out by Fu and Zhang [26], the function to be integrated over $k_\rho$ can become highly oscillatory for propagating waves when the separation distances between the bodies exchanging thermal radiation is large (i.e., few tens of microns at room temperature). Therefore, numerical integration using Simpson's method is recommended due to its efficiency when dealing with oscillatory integrands; note that in this work, all integral terms are solved numerically via a composite Simpson's rule.

When performing the integration over $k_\rho$ for evanescent waves, a cut-off value for the upper limit of integration must be determined. For example, if two bulks exchanging thermal radiation are separated by a vacuum gap of thickness $d_c$, it can be shown that the penetration depth of evanescent waves in vacuum $\delta_v$ decreases as $k_\rho$ increases [104,105,117]. Evanescent waves with $\delta_v \geq d_c$ can contribute to the radiative heat flux by radiation tunneling, and, using this criterion, it can be shown that the largest contributing parallel wavevector is $k_\rho \approx d_c^{-1}$ [104,105]. Note that the physics behind this approximation is detailed in section 3.5.2. However, in the simulations, to ensure the accuracy of the results, the integration over $k_\rho$ is performed until the relative variation between successive calculations of the integrand is less than a convergence criterion.

The integration over the volume can be simplified when the emitter is a bulk (modeled as a half-space). For example, if medium 0 is emitting, by inspecting Eqs. (3.11) and (3.12), it can be seen that the $z'$-dependence of the Weyl components of the DGF can be written as:

$$g^{E}_{sli\alpha}(k_\rho, z_c, z', \omega) g^{H*}_{slj\alpha}(k_\rho, z_c, z', \omega) = g^{E}_{sli\alpha}(k_\rho, z_c, \omega) g^{H*}_{slj\alpha}(k_\rho, z_c, \omega) e^{2k''_{zs}z'} \tag{3.40}$$

The integration over $z'$ can therefore be performed analytically from $z_s = -\infty$ to $z_{s+1} = 0$ (see Fig. 3.2); the monochromatic radiative heat flux due to an emitting bulk (medium 0) is therefore given by:

$$q_{\omega,0l}(z_c) = \frac{k_v^2 \Theta(\omega, T_0)}{2\pi^2} \mathrm{Re}\left\{ i\varepsilon''_{r0}(\omega) \int_0^\infty \frac{k_\rho dk_\rho}{k''_{z0}} \left[ \begin{matrix} g^{E}_{0l\rho\rho}(k_\rho, z_c, \omega) g^{H*}_{0l\theta\rho}(k_\rho, z_c, \omega) \\ + g^{E}_{0l\rho z}(k_\rho, z_c, \omega) g^{H*}_{0l\theta z}(k_\rho, z_c, \omega) \\ - g^{E}_{0l\theta\theta}(k_\rho, z_c, \omega) g^{H*}_{0l\rho\theta}(k_\rho, z_c, \omega) \end{matrix} \right] \right\} \tag{3.41}$$

In the general case that $A_l$, $B_l$, $C_l$, $D_l \neq 0$, which arises when both the emitter and irradiated medium are layers of finite thicknesses, it is also possible to perform analytically the integration over $z'$. The process is straightforward, albeit cumbersome; therefore, the mathematical details are not presented here.

Equations (3.11) and (3.12) are substituted in the expression for the radiative heat flux, given by Eq. (3.13), and four types of $z'$-dependent terms arise from this operation: $e^{\pm i(k_{zs}-k_{zs}^*)z'}$ and $e^{\pm i(k_{zs}+k_{zs}^*)z'}$. Using $k_{zs} = k'_{zs} + ik''_{zs}$ and $k_{zs}^* = k'_{zs} - ik''_{zs}$, the above terms reduce to $e^{\pm 2k''_{zs}z'}$ and $e^{\pm 2ik''_{zs}z'}$, which can then be easily integrated over $z'$ from $z_s$ to $z_{s+1}$.

This procedure can however lead to numerical instabilities when the emitter is thick, due to the term $e^{\pm 2k''_{zs}z'}$. This can be better understood by first assuming that $z_s = 0$ and $z_{s+1} = t$. The integration of $e^{\pm 2k''_{zs}z'}$ over $z'$ from 0 to $t$ gives the following two terms: $(2k''_{zs})^{-1}(e^{2k''_{zs}t} - 1)$ and $(2k''_{zs})^{-1}(1 - e^{-2k''_{zs}t})$. It can be seen that for waves with large $k''_{zs}$ (i.e., evanescent waves), the exponential term $e^{2k''_{zs}t}$ can become very large if the emitter is thick. An efficient way to circumvent this problem is to artificially divide the emitter of thickness $t$ into thinner sub-layers. Then, the radiative heat flux at $z_c$ becomes the summation of contributions from all sub-layers constituting the emitter. Also, to ensure numerical stability, when the calculations are performed for a given emitting sub-layer, its left boundary should always be set at a coordinate $z = 0$. Of course, for a sufficiently thick emitting layer, thermal radiation emitted is equivalent to the one from a bulk, and consequently the radiative heat flux can be calculated using Eq. (3.41). Finally, it is worth noting that the spatial integration can be performed numerically, so that the numerical instabilities discussed above do not arise at all; however, this procedure has the drawback of increasing the required computation time.

In far-field thermal radiation, the lower and upper spectral limits for calculation of the total radiative flux can easily be found using the fraction of blackbody emission $F_{0\rightarrow\lambda T}$ tabulated as a function of the product of the wavelength and temperature $\lambda T$ [15,16]. Due to the contribution from evanescent waves in the near-field, these limits do not hold anymore, and the spectral integration should be performed on a broader range. Since radiation tunneling depends strongly on both the emitting and irradiated materials, it is difficult to define a universal law in order to find these spectral limits. An efficient way to determine these thresholds for a given problem is to plot the monochromatic radiative flux as a function of the angular frequency or wavelength, and determine the spectral band where more than 99% of the radiant energy exchanges arise.

Based on the above discussion, the following algorithm is proposed to solve near-field radiative heat transfer problems in one-dimensional layered media:

1. Provide the number of layers in the one-dimensional structure; for each layer, specify the layer thickness, the dielectric constant, and the temperature.

2. Designate the emitting layer(s) $s$.

3. Determine the location $z_c$ and layer $l$ where the radiative heat flux is to be calculated.

4. Enter the limiting values of angular frequencies $\omega$.

5. Enter the discretization for the integration over $k_\rho$ and $\omega$.

6. Provide a convergence criterion for the integration over $k_\rho$.

7. For a given emitting layer $s$, apply the following procedure:

   (a) For a given $k_\rho$ and $\omega$, calculate the field amplitude coefficients $A_l$, $B_l$, $C_l$, and $D_l$ in each layer ($l = 0, N$) and in each polarization state (TE and TM) using the S-matrix method.

   (b) Calculate the Weyl components of the DGF using Eqs. (3.11) and (3.12).

   (c) Integrate over $k_\rho$ by repeating steps (a) and (b) for all $k_\rho$ until convergence.

   (d) Calculate the monochromatic radiative heat flux using Eq. (3.13) (if emitter is a film) or Eq. (3.41) (if emitter is a bulk).

   (e) Repeat steps (a) to (d) for all $\omega$ determined in step 4 and integrate over $\omega$ if the total radiative heat flux is needed.

8. Repeat the procedure described in 7 for all emitting layers specified in step 2.

9. Calculate the radiative heat flux at $z_c$ by summing the contributions from all emitting layers.

Note that if the emitter is a thick film that requires to be divided into sub-layers, this should be specified in step 1 of the algorithm.

## 3.5 Numerical solution of the near-field radiative heat flux

### *3.5.1 Near-field radiative heat transfer involving cubic boron nitride*

Two cases solved hereafter are depicted in Fig. 3.3. In Fig. 3.3(a), two bulks of cubic boron nitride (*c*BN) are separated by a vacuum gap of thickness $d_c$. It is assumed that medium 0 is maintained at 300 K, while medium 2 is a heat sink (0 K). The radiative heat flux absorbed by medium 2 is calculated just after the boundary $z = z_2$ (i.e., $z = z_2^+$), since all energy crossing the interface 1-2 is absorbed by medium 2. A similar case is depicted in Fig. 3.3(b), except that the emitter (medium 1 at 300 K) is a film of thickness $t$ surrounded by vacuum. Again, the objective here is to compute the radiative flux absorbed by the bulk *c*BN, labeled medium 3, which is a heat sink.

*c*BN is a material supporting SPhPs in the infrared region around 7.94 $\mu$m ($2.373\times10^{14}$ rad/s), and its dielectric constant is given in appendix B. For the case of Fig. 3.3(a), the integration over $k_\rho$ is first split in two parts (propagating and evanescent modes). Moreover, depending on the problem to be solved, the integration over $k_\rho$ for evanescent waves can also be split in few parts, thus allowing different $k_\rho$-discretizations in different $k_\rho$-intervals. The behavior of the function to be integrated is strongly dependent on the materials exchanging thermal radiation. To visualize the variations of the integrand for the problem considered in Fig. 3.3(a), Eq. (3.41) is calculated, without integrating over $k_\rho$, and reported in Fig. 3.4(a) as a function of $\omega$ and $K = k_\rho/k_v$ for a vacuum gap of 100 nm; the real part of the dielectric constant of *c*BN, as a function of $\omega$, is shown in Fig. 3.4(b).

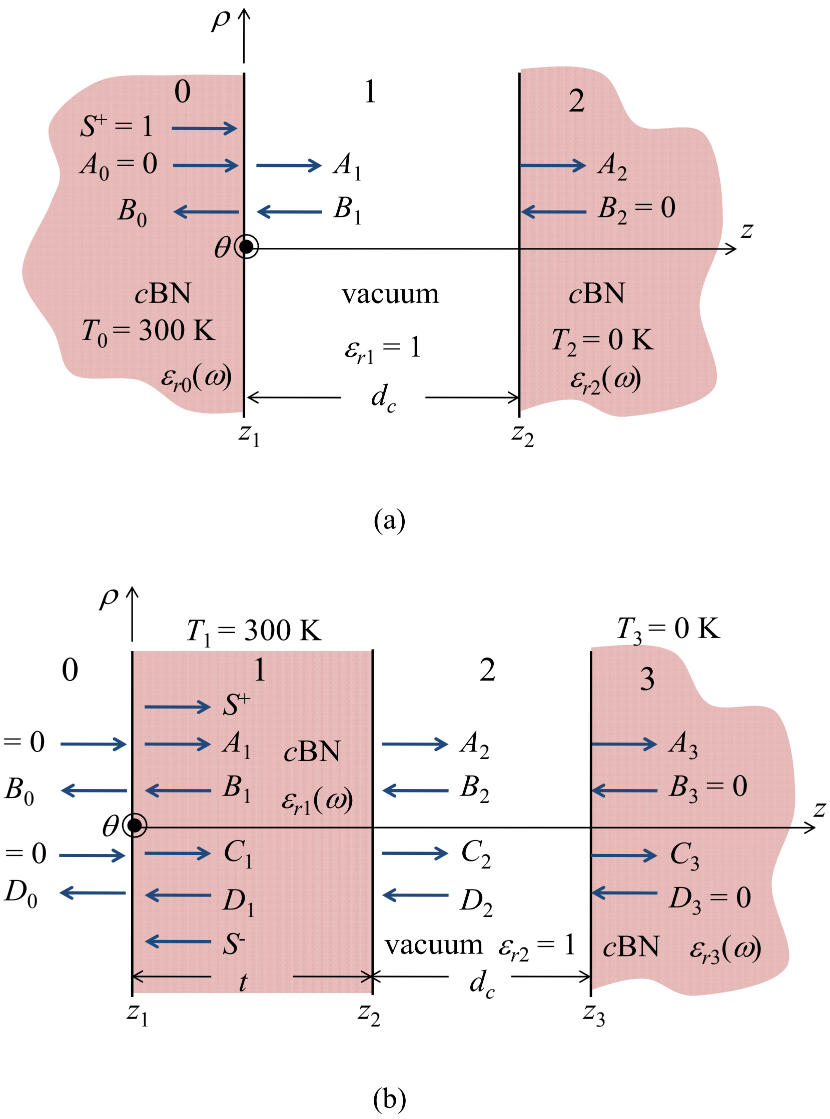
ρ
0
1
2
S+ = 1
A0 = 0
A1
A2
B0
B1
B2 = 0
θ
z
cBN
T0 = 300 K
εr0(ω)
vacuum
εr1 = 1
cBN
T2 = 0 K
εr2(ω)
dc
z1
z2
(a)
ρ
T1 = 300 K
T3 = 0 K
0
1
2
3
S+
A0 = 0
A1
cBN
A2
A3
B0
B1
εr1(ω)
B2
B3 = 0
θ
z
C0 = 0
C1
C2
C3
D0
D1
D2
D3 = 0
S-
vacuum
εr2 = 1
cBN
εr3(ω)
t
dc
z1
z2
z3
(b)

Figure 3.3. (a) Schematic representation of two bulks of *c*BN separated by a vacuum gap of thickness $d_c$. (b) Schematic representation of a *c*BN film of thickness $t$ and a bulk *c*BN separated by a distance $d_c$.

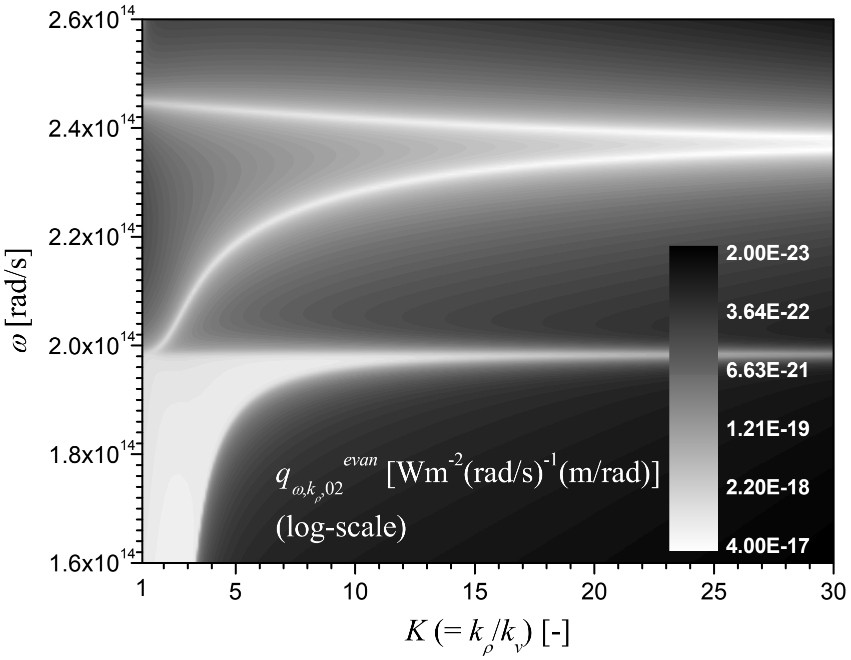

(a)

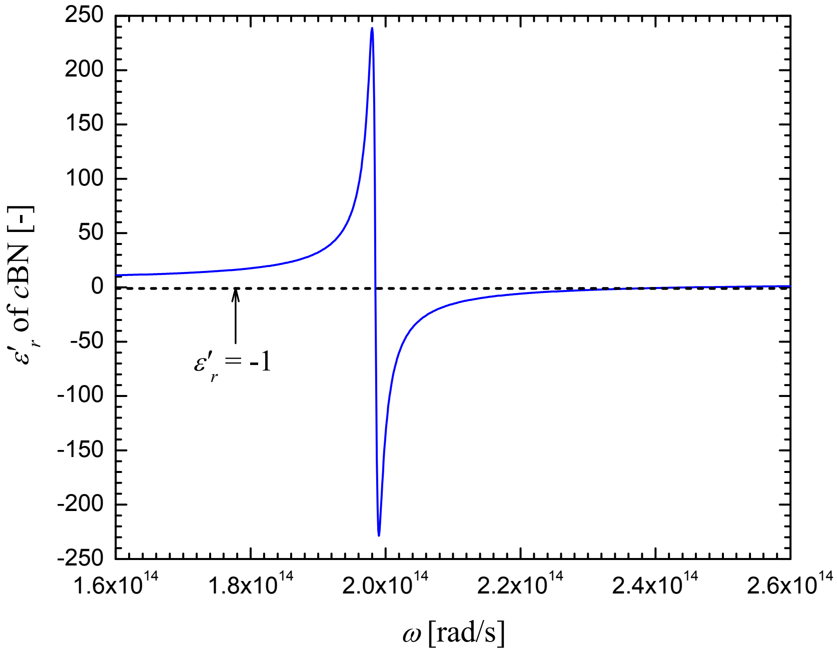

(b)

Figure 3.4. (a) Monochromatic evanescent component of the radiative heat flux per unit $k_\rho$ between two *c*BN bulks ($T$ = 300 K and 0 K) separated by a 100 nm thick vacuum gap. (b) Real part of the dielectric function of *c*BN as a function of $\omega$.

The large values of $q^{evan}_{\omega,k_\rho,02}$ around 1.980×10$^{14}$ rad/s are due to the fact that the real part of the dielectric constant of *c*BN, $\varepsilon'_r$, is large in that spectral region, as shown in Fig. 3.4(b). Indeed, below $\omega$ = 1.985×10$^{14}$ rad/s, there is no SPhPs, and therefore the maximum near-field radiative heat flux for that case is proportional to $\varepsilon'_r$ times blackbody radiation [72]. The two branches of high $q^{evan}_{\omega,k_\rho,02}$ above 1.985×10$^{14}$ rad/s corresponds to SPhPs.

Since $q^{evan}_{\omega,k_\rho,02}$ varies sharply with $k_\rho$ for low values of *K*, the integration over $k_\rho$ for evanescent waves is also split in two parts; a first integration from $k_v$ to $6k_v$ with a fine $k_\rho$ -discretization, and a second one from $6k_v$ to infinity with a coarser $k_\rho$-discretization. Note that the $k_\rho$-discretization dictates the number of sub-intervals used when applying Simpson's rule. For example, if $\Delta k_\rho$ = $0.1k_v$, this means that the Simpson rule is first applied to the interval [0, 0.1 $k_v$], and so forth until convergence of the integration over $k_\rho$.

The monochromatic radiative heat flux between two bulks of *c*BN separated by a vacuum gap $d_c$ of 100 nm is plotted in Fig. 3.5(a) as a function of $\omega$. The radiative flux profiles for $d_c$ = 50 nm, 100 nm, 500 nm, 1 μm, and 500 μm are also reported in Fig. 3.5(b) and compared with the predictions for two blackbodies (i.e., far-field regime).

In Fig. 3.5(a), for the propagating component of the radiative flux, the integration over $k_\rho$ is done by steps of $1\times10^{-3}k_v$; for the first ($k_v$ to $6k_v$) and second ($6k_v$ to infinity) parts of the evanescent waves, the integration is respectively done by steps of $1\times10^{-3}k_v$ and $1\times10^{-2}k_v$. For the upper limit of integration over $k_\rho$, a convergence criterion of $10^{-6}$ has been found to be optimal. The upper limit of integration over $k_\rho$ has been found to be of the order of few tens of $k_v$, which is also in good agreement with the approximation that the largest contributing $k_\rho$ is proportional to $d_c^{-1}$; indeed, using this last criterion, the limiting $k_\rho$ for 1.60×10$^{14}$ rad/s is $19k_v$, while it is $12k_v$ at 2.60×10$^{14}$ rad/s. It is also important to note that even for calculating spectral variations of the monochromatic radiative flux, the spectral discretization should be fine enough to be able to represent

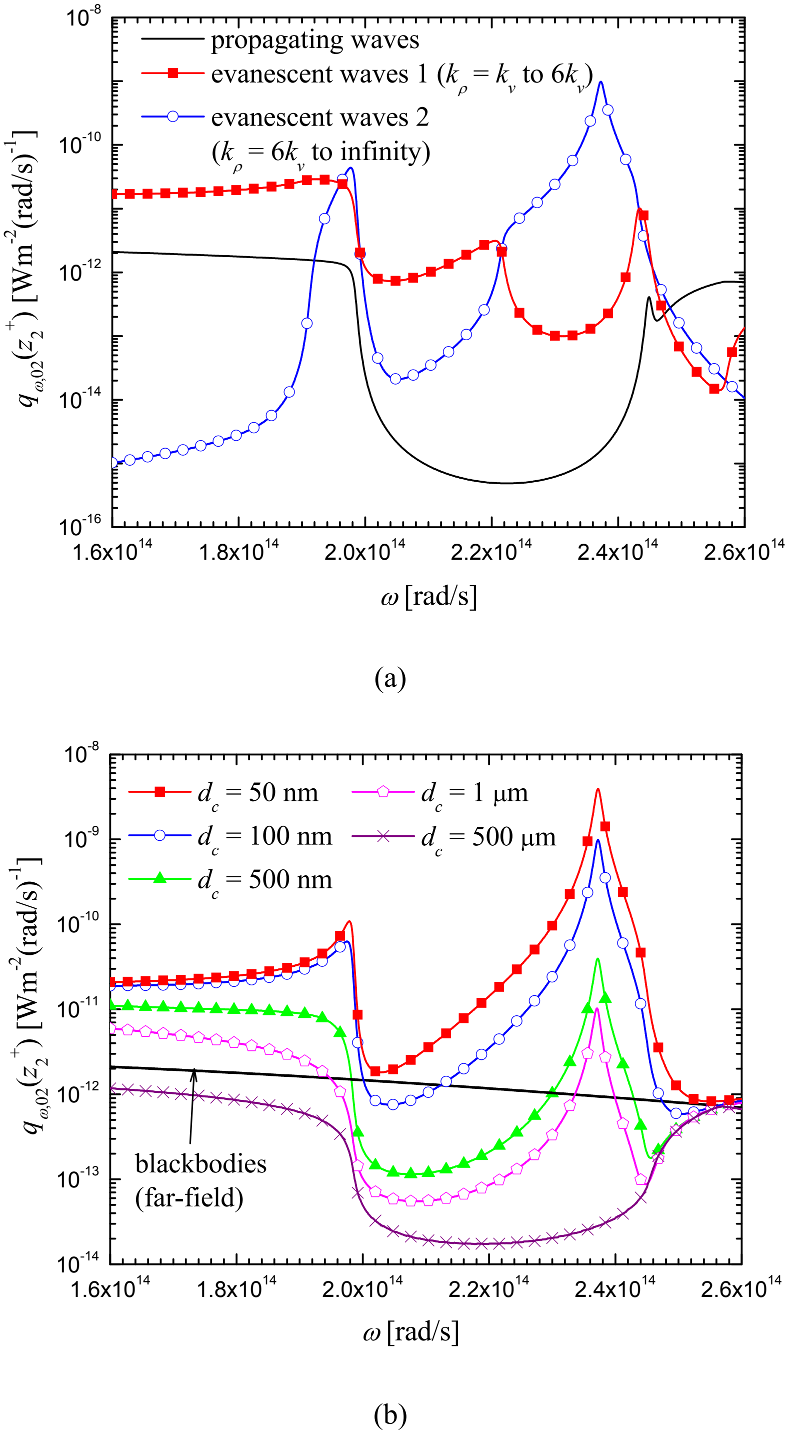

Figure 3.5. (a) Propagating and evanescent components of the monochromatic radiative heat flux between two bulks of *c*BN ($T$ = 300 K and 0 K) separated by a vacuum gap $d_c$ = 100 nm. (b) Monochromatic radiative heat flux between two bulks of *c*BN ($T$ = 300 K and 0 K) separated by vacuum of $d_c$ = 50 nm, 100 nm, 500 nm, 1 μm, and 500 μm; the values are compared with the predictions for two blackbodies.

correctly the peaks due to regular evanescent waves where $\varepsilon_r'$ of *c*BN is large, and SPhP resonance. In the simulations presented here, the radiative heat flux is calculated by steps of $0.001\times10^{14}$ rad/s. For these simulations, calculation of the monochromatic radiative flux for a given emitting layer takes between 30 to 50 minutes on a personal computer with 3.16 GHz Intel Core 2 Duo processor.

As expected, it can be seen in Fig. 3.5(a) that SPhP resonance is visible on the radiative heat flux for the part corresponding to the integration over $k_\rho$ from $6k_v$ to infinity. Indeed, as shown in Fig. 3.4(a), a high density of electromagnetic states, which is proportional to $\left|dk_\rho/d\omega\right|$, arises below $2.400\times10^{14}$ rad/s for $k_\rho$ much larger than $6k_v$. Also, the results depicted in Fig. 3.5(b) show clearly that for small vacuum gaps, the radiative heat flux is a few orders of magnitude higher than the predictions for blackbodies; for a 500 μm gap, the far-field regime is reached, and the flux is obviously below the values for blackbodies.

The consistency of the algorithm is further tested by comparing the radiative flux from a bulk *c*BN with the values predicted for a *c*BN emitting film (see Fig. 3.3(b)). The vacuum gap $d_c$ is 100 nm, and film thicknesses $t$ of 1 nm, 10 nm, 100 nm, 1 μm, and 100 μm are considered; results of monochromatic radiative heat flux are shown in Fig. 3.6.

A 100 μm thick film emitter leads to numerical instabilities when the spatial integration is performed analytically, as discussed in section 3.4. Consequently, results for that case have been obtained by dividing the *c*BN film into three layers of 50 μm, 40 μm, and 10 μm. The radiative flux at $z = z_3^+$ is the sum of contributions from these aforementioned three sub-layers.

It can be seen in Fig. 3.6 that the radiative flux from a bulk in the spectral band from $1.600\times10^{14}$ to $2.600\times10^{14}$ rad/s is fully recovered when the *c*BN film is 100 μm thick. On the other hand, most of the radiative energy is transferred in the spectral region from $1.980\times10^{14}$ to about $2.500\times10^{14}$ rad/s; in this band, values predicted for a 1 μm thick *c*BN film match those from a bulk emitter. It is also worth noting that at SPhP resonance ($2.373\times10^{14}$ rad/s), the radiative heat flux predicted for a 100 nm thick film is higher than the values for a bulk emitter; this arises due to SPhP coupling in the *c*BN emitting film [108]. As the film thickness decreases to 10 nm and to 1 nm, the radiative flux predicted at SPhP resonance does not increase, but rather splits into two peaks, again due to coupling of SPhPs within the film. The physical interpretation of these spectral distributions of fluxes with a thin emitting layer is discussed in details in chapters 4 and 5. Results of Fig. 3.6 show the consistency and stability of the algorithm, since the bulk values are retrieved with a sufficiently thick film emitter.

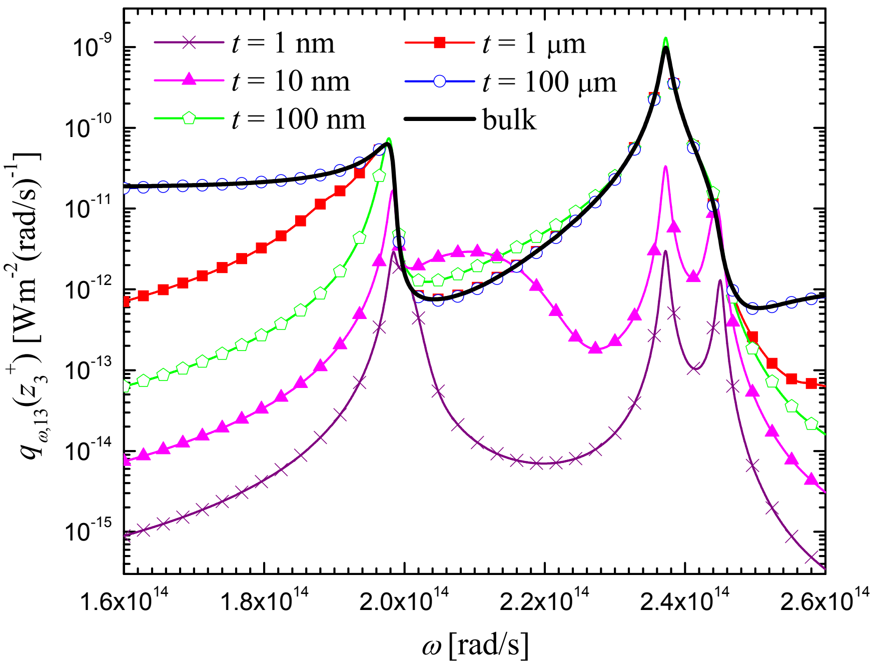

Figure 3.6. Monochromatic radiative heat flux between a *c*BN film emitter (at 300 K) of variable thickness *t* and a bulk of *c*BN (at 0 K) separated by a 100 nm thick vacuum gap; comparisons are shown for *t* = 1 nm, 10 nm, 100 nm, 1 μm, 100 μm, and a bulk.

Control of far-field thermal radiation emission via one-dimensional layered media and photonic crystals has been discussed in the past years. Yet, control of the emitted near-field radiation spectrum has been tackled only very recently in the literature [54,103-105]. In the following, we show that the algorithm proposed in this dissertation can be used to perform such study. The case under consideration is depicted in Fig. 3.7.

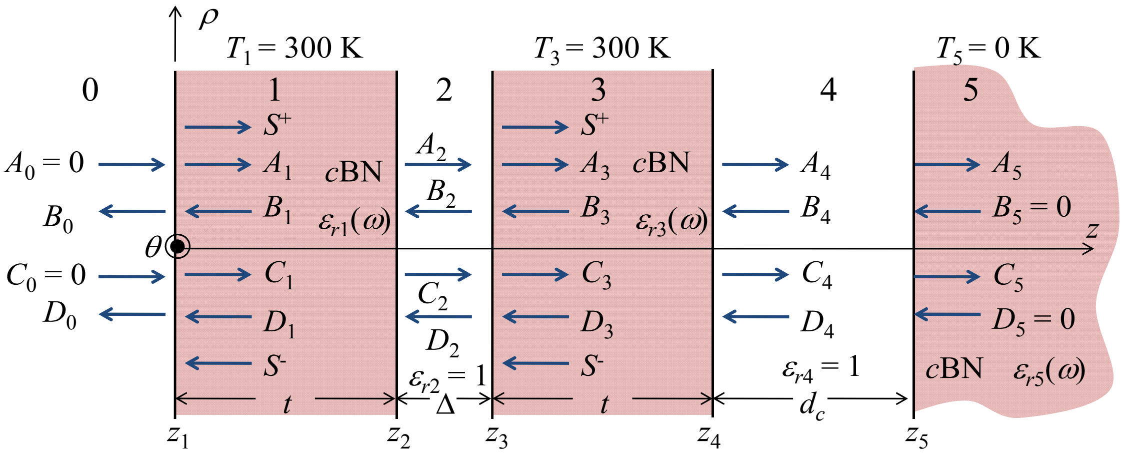
$\rho$
$T_1 = 300$ K
$T_3 = 300$ K
$T_5 = 0$ K
0
1
2
3
4
5
$S^+$
$A_0 = 0$
$A_1$
cBN
$A_2$
$B_2$
$A_3$
cBN
$A_4$
$A_5$
$B_0$
$B_1$
$\varepsilon_{r1}(\omega)$
$B_3$
$\varepsilon_{r3}(\omega)$
$B_4$
$B_5 = 0$
$\theta$
$z$
$C_0 = 0$
$C_1$
$C_2$
$C_3$
$C_4$
$C_5$
$D_0$
$D_1$
$D_2$
$D_3$
$D_4$
$D_5 = 0$
$S^-$
$\varepsilon_{r2} = 1$
$\varepsilon_{r4} = 1$
cBN $\varepsilon_{r5}(\omega)$
$t$
$\Delta$
$t$
$d_c$
$z_1$
$z_2$
$z_3$
$z_4$
$z_5$

Figure 3.7. Schematic representation of two emitting films of *c*BN of equal thicknesses $t$ separated by a vacuum gap $\Delta$; the top-most emitting film (medium 3) is located at a distance $d_c$ of a bulk *c*BN.

As shown in Fig. 3.7, two films of equal thicknesses $t$ and separated by a distance $\Delta$ are emitting thermal radiation toward a bulk *c*BN (heat sink). The distance $d_c$ between film 3 and the bulk is set at 100 nm, and both films have thicknesses of 10 nm. The idea is to analyze the influence of the presence of medium 1 on the radiative heat flux emitted by medium 3 and absorbed by medium 5. The monochromatic radiative heat flux between media 3 and 5 is presented in Fig. 3.8 for $\Delta$ = 1 nm, 10 nm, 100 nm, and 1 μm; these results are compared with the predictions obtained when there is no film behind the emitter (i.e., corresponds to Fig. 3.3(b)).

It is interesting to note in Fig. 3.8 that spectral distribution of radiative flux transferred from medium 3 to medium 5 is affected by the presence of a film behind the emitter (medium 1), due to a perturbation of the dispersion relation of SPhPs. The distribution of radiative flux is modified between the two peaks located approximately at $1.980\times10^{14}$ and $2.370\times10^{14}$ rad/s for distances $\Delta$ of 1 nm, 10 nm, and 100 nm; for $\Delta$ = 1 nm and 10 nm, the peak located around $2.440\times10^{14}$ rad/s is also slightly affected by the presence of medium 1. It can also be observed that at $\Delta$ = 1 μm, the presence of medium 1 does not affect anymore the near-field radiative heat flux between media 3 and 5. These results show that it is possible to affect the near-field thermal radiation spectrum solely via the presence of another body in close proximity.

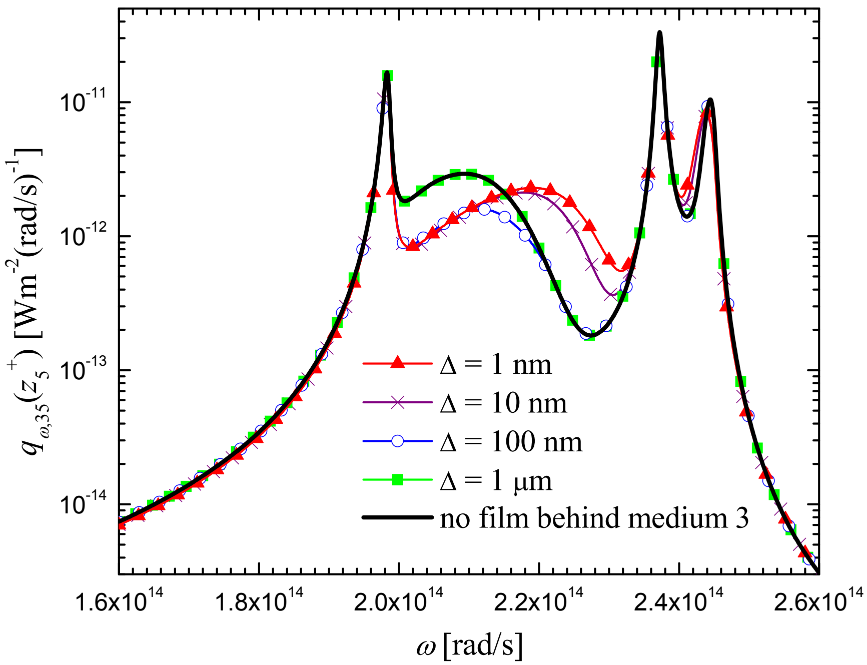

Figure 3.8. Monochromatic radiative heat flux between a 10 nm thick *c*BN film (at 300 K) and a bulk of *c*BN (at 0 K) separated by a 100 nm vacuum gap. The influence of the presence of a film of *c*BN behind the emitter (medium 1) is analyzed for separation distances between the films Δ of 1 nm, 10 nm, 100 nm, and 1 μm; results are compared with the case that no film is behind the emitter.

Based on these observations, we study in more details near-field thermal emission by a single thin film and within the gap between two thin layers in chapter 4, while we analyze the near-field radiative heat flux between two thin films in chapter 5. Before going through these details, we discuss in section 3.5.2 the physical details underlying near-field thermal radiation between two bulks separated by a vacuum gap.

Note that the algorithm presented in this chapter has also been verified against results published in the literature; these validations tests are presented in appendix D.

### *3.5.2 Physical details of near-field radiative heat transfer between two bulks separated by a vacuum gap*

The different physical phenomena involved in radiation heat transfer in the near-field are discussed in this section with the analysis of a simple problem involving two bulks of SiC, material that has been discussed in section 2.7.2. The problem is the same as the one depicted in Fig. 3.3(a), except that the two layers of *c*BN are replaced by SiC; note that the temperatures of media 0 and 2 are the same as in Fig. 3.3(a).

Before discussing the physical details of the problem, we show hereafter the consistency of the mathematical procedure described in this chapter by reducing the general expression given by Eq. (3.41) to the near-field radiative heat flux between two bulks reported in the literature [26,30,48,65].

The only emitting layer here is assumed to be the medium 0. Since medium 0 is a bulk, the monochromatic radiative heat flux is given by Eq. (3.41) with $l = 2$ and $z_c = z_2^+$. As explained in section 3.3.2, the fact that there is no external source of energy incident on the one-dimensional layered structure implies that $A_0 = B_2 = 0$. Therefore, the calculation of the Weyl components of the DGF at $z = z_2^+$ only requires the value of $A_2$ in both polarization states. Using Eqs. (3.21a), (3.21b), (3.22), and (3.38a), we find that:

$$A_2 = \frac{t_{01}t_{12}e^{ik_{z1}d_c}}{1 + r_{01}r_{12}e^{2ik_{z1}d_c}} \tag{3.42}$$

Note that $A_2$ in TE (TM) polarization is calculated using the Fresnel transmission and reflection coefficients in TE (TM) polarization. The expression of $A_2$ determined via the S-matrix method can be interpreted as a field transmission coefficient through a layer of finite thickness $d_c$ commonly reported in thin film optics. Due to the simplicity of the geometry, Eq. (3.42) could have been derived by summing the amplitudes of successive reflections and refractions (Airy's formulas) [71].

Substitution of the appropriate Weyl components of the DGF (Eqs. (3.11) and (3.12)) into the monochromatic radiative flux (Eq. (3.41)) yields:

$$q_{\omega,02}(z_2^+) = \frac{\Theta(\omega,T_0)}{4\pi^2}\int_0^\infty \frac{k_\rho dk_\rho}{|k_{z0}|^2}\left[\frac{\mathrm{Re}(\varepsilon_{r0}k_{z0}^*)\,\mathrm{Re}(\varepsilon_{r2}k_{z2}^*)}{|n_0|^2|n_2|^2}\left|A_2^{TM}\right|^2 + k'_{z0}k'_{z2}\left|A_2^{TE}\right|^2\right] \tag{3.43}$$

where the identities $k_v^2\varepsilon''_{ri} = 2k'_{zi}k''_{zi}$ and $k'_{zi}\left(|k_{zi}|^2 + k_\rho^2\right) = k_v^2\,\mathrm{Re}(\varepsilon_{ri}k_{zi}^*)$ have been used [75]. The square of the magnitude of $A_2$, needed in Eq. (3.43), is given by:

$$|A_2|^2 = \frac{|t_{01}|^2|t_{21}|^2}{\left|1 - r_{10}r_{12}e^{2ik_{z1}d_c}\right|^2}\frac{|k_{z1}|^2}{|k_{z2}|^2} \tag{3.44}$$

where the identities $r_{ij} = -r_{ji}$ and $t_{ij} = (k_{zi}/k_{zj})t_{ji}$ have been used. The following relations are also employed in order to express the radiative flux strictly in terms of the Fresnel reflection coefficients [75]:

$$\frac{k'_{zi}}{|k_{zi}|^2}\left|t_{ij}^{TE}\right|^2 = \frac{1}{|k_{zj}|^2}\left[k'_{zj}\left(1 - \left|r_{ij}^{TE}\right|^2\right) - 2k''_{zj}\,\mathrm{Im}(r_{ij}^{TE})\right] \tag{3.45a}$$

$$\frac{\mathrm{Re}(\varepsilon_{ri}k_{zi}^*)}{|n_i|^2|k_{zi}|^2}\left|t_{ij}^{TM}\right|^2 = \frac{1}{|k_{zj}|^2}\left[k'_{zj}\left(1 - \left|r_{ij}^{TM}\right|^2\right) - 2k''_{zj}\,\mathrm{Im}(r_{ij}^{TM})\right] \tag{3.45b}$$

The $z$-component of the wavevector in vacuum, $k_{z1}$, is a pure real number (i.e., $k_{z1} = k'_{z1}$) for propagating waves with $k_\rho \le k_v$, while it is a pure imaginary number (i.e., $k_{z1} = i\,k''_{z1}$) for evanescent waves with $k_\rho > k_v$. By splitting the integration over $k_\rho$ as a function of propagating and evanescent waves, and by using this distinction when evaluating the identities given by Eqs. (3.45a) and (3.45b), we find the following expressions for the radiative heat fluxes:

$$q_{\omega,02}^{prop}(z_2^+) = \frac{\Theta(\omega,T_0)}{4\pi^2}\int_0^{k_v} k_\rho dk_\rho\left[\frac{\left(1 - \left|r_{10}^{TE}\right|^2\right)\left(1 - \left|r_{12}^{TE}\right|^2\right)}{\left|1 - r_{10}^{TE}r_{12}^{TE}e^{2ik'_{z1}d_c}\right|^2} + \frac{\left(1 - \left|r_{10}^{TM}\right|^2\right)\left(1 - \left|r_{12}^{TM}\right|^2\right)}{\left|1 - r_{10}^{TM}r_{12}^{TM}e^{2ik'_{z1}d_c}\right|^2}\right] \tag{3.46a}$$

$$q_{\omega,02}^{evan}(z_2^+) = \frac{\Theta(\omega,T_0)}{\pi^2}\int_{k_v}^{\infty} k_\rho dk_\rho e^{-2k''_{z1}d_c}\left[\frac{\mathrm{Im}(r_{10}^{TE})\,\mathrm{Im}(r_{12}^{TE})}{\left|1 - r_{10}^{TE}r_{12}^{TE}e^{-2k''_{z1}d_c}\right|^2} + \frac{\mathrm{Im}(r_{10}^{TM})\,\mathrm{Im}(r_{12}^{TM})}{\left|1 - r_{10}^{TM}r_{12}^{TM}e^{-2k''_{z1}d_c}\right|^2}\right] \tag{3.46b}$$

where again the identity $r_{ij}$ = $-r_{ji}$ has been used. The propagating and evanescent contributions to the radiative heat flux between two bulks given by Eqs. (3.46a) and (3.46b) are the same (or equivalent) to those reported in [26,30,48,65]; this shows the consistency of the general formulation presented in this chapter based on the S-matrix approach.

It can be seen that the integration over $k_\rho$ for the evanescent waves is performed from $k_v$ to infinity. From a numerical point of view, however, a cut-off value of $k_\rho$ is needed in order to obtain the evanescent component of the radiative heat flux. The physics behind this cut-off $k_\rho$ value can be explained as follows. The decay length of an evanescent wave in medium $j$ can be approximated as $\delta_j \approx \left|k_{zj}\right|^{-1}$. For the problem treated here, only evanescent waves emitted by medium 0 with penetration depths in vacuum $\delta_1$ equal or greater than the vacuum gap $d_c$ can be tunneled in medium 2, and thus contribute to radiant energy transfer. For evanescent waves with $k_\rho$ much larger than $k_v$, the $z$-component of the wave vector in medium $j$, given by $k_{zj} = \sqrt{\varepsilon_{rj} k_v^2 - k_\rho^2}$, can be approximated by $k_{zj} \approx ik_\rho$. This is quite acceptable, even for moderate values of $k_\rho$. For example, in vacuum, if $k_\rho = 2k_v$, then $k_{z2} = i1.732k_v$; similarly, if $k_\rho = 5k_v$, then $k_{z2} = i4.90k_v$. By substituting this approximation within the definition of penetration depth of evanescent waves in vacuum, we find that $k_\rho \approx \delta_1^{-1}$. Using the limiting condition $\delta_1 = d_c$, we find that the largest contributing wavevector to the evanescent radiative heat flux is approximately given by $k_\rho \approx d_c^{-1}$. This relation shows that as the gap decreases between the two bulk regions, the limiting $k_\rho$ increases, and therefore more energy is transferred via radiation tunneling.

The denominator in Eqs. (3.46a) and (3.46b) accounts for multiple wave reflection and interference within the vacuum gap. The terms $\left(1-\left|r_{1j}^{TE,TM}\right|^2\right)$ in the numerator of Eq. (3.46a) represents the spectral absorptance of medium $j$ and also play the role of spectral emittance of medium $j$. The interpretation of $\mathrm{Im}(r_{1j}^{TE,TM})$ in the numerator of Eq. (3.46b) is similar: this term can be seen as a spectral emittance / absorptance of medium $j$ for evanescent waves [30]. The evanescent nature of these modes is also explicitly shown in Eq. (3.46b) via the exponentially decaying term $e^{-2k''_{z1}d_c}$.

In the far-field limit, the radiative heat flux between the two bulk materials is independent of the gap thickness $d_c$. Indeed, as $d_c \to \infty$, $e^{-2k''_{z1}d_c} \to 0$ such that $q^{evan}_{\omega,02}(z_2^+) \to 0$. Also, in the far-field limit, radiation heat transfer becomes incoherent, such that the denominator of Eq. (3.46a) can be written as [26]:

$$\frac{1}{\left|1-r_{10}^{TE,TM}r_{12}^{TE,TM}e^{2ik'_{z1}d_c}\right|^2} \to \frac{1}{1-\hat{\rho}_{r,12}^{TE,TM}\hat{\rho}_{r,12}^{TE,TM}} \tag{3.47}$$

where $\hat{\rho}_{r,ij}^{TE,TM}$ is the reflectivity of the interface *i-j*, calculated from the Fresnel reflection coefficient as $\hat{\rho}_{r,ij}^{TE,TM} = \left|r_{ij}^{TE,TM}\right|^2$. We can also recast the integration over $k_\rho$ as an integration over the polar angle $\phi_i$ by letting $k_\rho = k_v \sin\phi_i$. By using the emissivity of medium $j$ ($\hat{\varepsilon}_j^{TE/TM} = 1-\hat{\rho}_{r,ij}^{TE,TM}$ for a bulk material), and the Planck blackbody intensity ($I_{b,\omega}(T) = \Theta(\omega,T)\omega^2/4\pi^3c_v^2$), the radiative heat flux in the far-field limit is:

$$q^{prop}_{\omega,02}(z_2^+) = 2\pi I_{b,\omega}(T_0)\int_{\phi_i=0}^{\pi/2}\frac{\hat{\varepsilon}_0\hat{\varepsilon}_2}{1-\hat{\rho}_{r,10}\hat{\rho}_{r,12}}\cos\phi_i\sin\phi_i d\phi_i \tag{3.48}$$

where it has been assumed that TE and TM polarized waves have equal contributions to the radiative heat flux. Equation (3.48) is the same as the expression obtained from a ray tracing approach, showing clearly that the classical theory of thermal radiation is a particular case of the electromagnetic description of near-field radiative heat transfer.

Spectral distributions of radiative heat flux between two SiC bulks are shown in Fig. 3.9(a) for vacuum gaps $d_c$ of 10 nm, 100 nm, and 1 μm. These results are compared with the flux calculated in the far-field regime (Eq. (3.48)) and the values obtained for blackbodies. In Fig. 3.9(b), the TE and TM evanescent contributions to the radiative heat flux are shown for $d_c$ = 10 nm, and compared with the radiative flux between blackbodies.

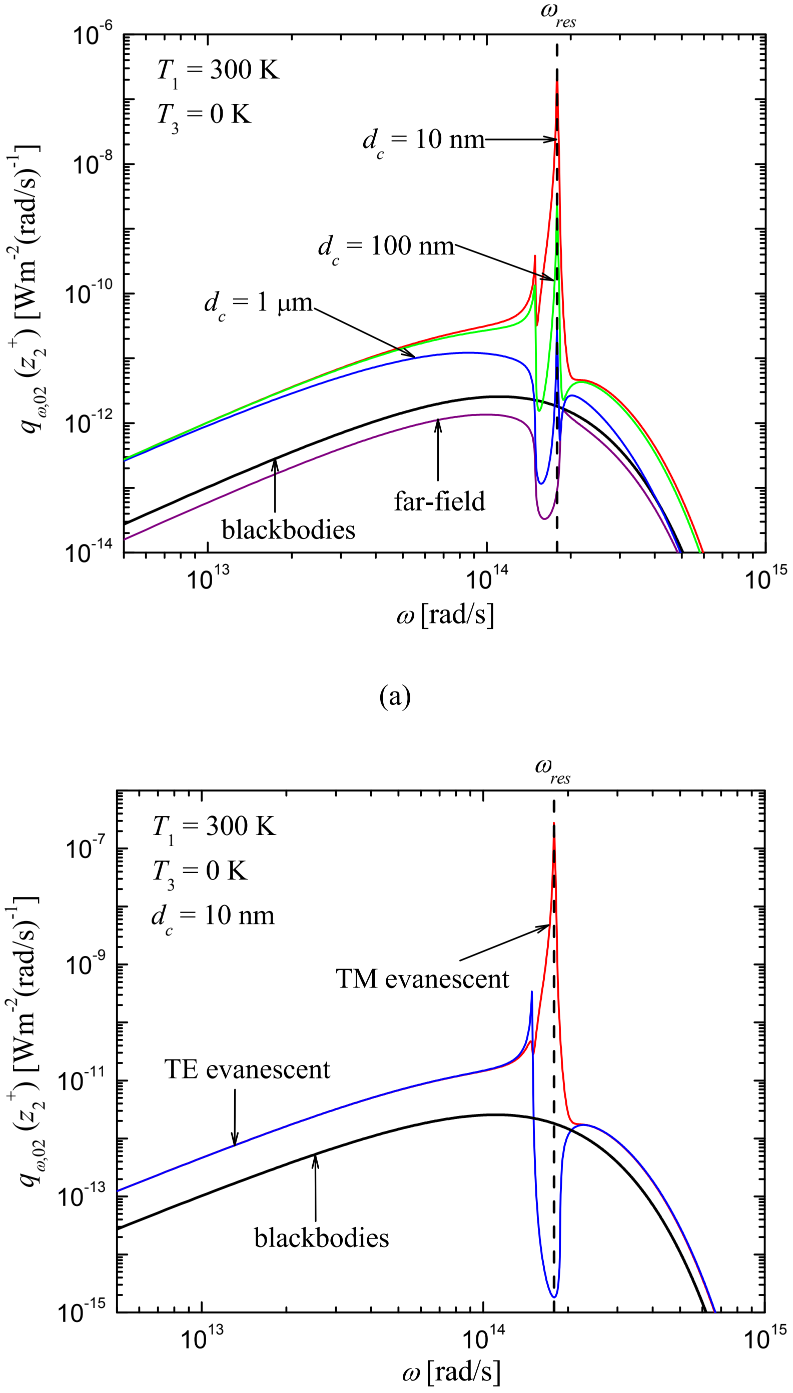

(a)

(b)

Figure 3.9. Near-field radiative heat transfer between two SiC bulk regions separated by a vacuum gap of thickness $d_c$: (a) $d_c$ = 10 nm, 100 nm, and 1 μm; results are compared with the fluxes in the far-field regime and between blackbodies. (b) evanescent TE and TM contributions for $d_c$ = 10 nm; results are compared with the flux between blackbodies.

Figure 3.9(a) shows that the radiative heat flux in the near-field exceeds by several orders of magnitude the values predicted for two blackbodies. For small gap thicknesses, the radiative heat flux is quasi-monochromatic due to excitation of SPhPs. Note that this does not mean that the broadband radiation emission is suppressed. Since in a very narrow frequency range there is significant increase in emission, the spectral nature of emission shows this quasi-monochromatic behavior. Resonance of the flux arises at $1.786\times10^{14}$ rad/s, where the density of electromagnetic states is very large, as discussed in section 2.7.2. For a frequency smaller than the resonant frequency of SPhPs, there is also a small peak of radiative heat flux due to tunneling of evanescent waves. The radiative heat flux due to regular evanescent waves is directly proportional to the real part of the dielectric function of the emitting material, and the smaller peak corresponds to a frequency where $\varepsilon'_{r0}$ takes a very large value (see Fig. 2.3(b)). Figure 3.9(b) shows clearly that the TM evanescent component of the radiative heat flux dominates the energy exchanges, as SPhPs can only be excited in TM polarization for nonmagnetic materials.

It is interesting to look at the dependence of the radiative heat transfer versus the gap thickness $d_c$. To perform this analysis, the radiative heat transfer coefficient $h_r$ is calculated. The problem shown in Fig. 3.3(a) is considered, with $d_c \ll \lambda_w$, where $\lambda_w$ is the dominant wavelength emitted as predicted by Wien's law. It is also assumed that medium 0 is at temperature $T$ while layer 2 is at temperature $T + \delta T$, such that $h_r$, defined as the net radiative flux divided by $\delta T$ as $\delta T \to 0$, is calculated [2]. Using Eqs. (3.46a) and (3.46b), $h_r$ can be written as follows:

$$\begin{aligned} h_r &= \frac{1}{\pi^2}\int_0^\infty d\omega \frac{\partial\Theta(\omega,T)}{\partial T} \\ &\times \sum_{\gamma=TE,TM}\left[\int_0^{k_v} k_\rho dk_\rho \frac{\left(1-\left|r_{10}^\gamma\right|^2\right)\left(1-\left|r_{12}^\gamma\right|^2\right)}{4\left|1-r_{10}^\gamma r_{12}^\gamma e^{2ik'_{z1}d_c}\right|^2} + \int_{k_v}^\infty k_\rho dk_\rho e^{-2k''_{z1}d_c}\frac{\mathrm{Im}(r_{10}^\gamma)\,\mathrm{Im}(r_{12}^\gamma)}{\left|1-r_{10}^\gamma r_{12}^\gamma e^{-2k''_{z1}d_c}\right|^2}\right] \end{aligned} \tag{3.49}$$

where $\partial\Theta(\omega,T)/\partial T$ is the derivative of the mean energy of an electromagnetic state with respect to the temperature, and is given by $\hbar^2\omega^2 e^{\hbar\omega/k_bT}\big/k_bT^2(e^{\hbar\omega/k_bT}-1)^2$.

For SiC, as $d_c \rightarrow 0$, radiative heat transfer is dominated by SPhPs, existing only in TM polarization for nonmagnetic materials, with $k_\rho >> k_v$ where there is a large number of electromagnetic states in a very narrow spectral band. In the electrostatic limit where $k_\rho >> k_v$, the $z$-component of the wavevector in medium $j$ can be approximated as $k_{zj} \approx ik_\rho$, and the Fresnel reflection coefficients $r_{1j}^{TM}$ in Eq. (3.49) thus become independent of $k_\rho$, and can therefore be approximated as:

$$r_{1j}^{TM} \approx \frac{\varepsilon_{rj} - 1}{\varepsilon_{rj} + 1} \tag{3.50}$$

Using the dimensionless variable $\eta = k_\rho d_c$ [106], the near-field radiative heat transfer coefficient between two bulks is approximated as follows:

$$h_r \approx \frac{1}{\pi^2 d_c^2} \int_0^\infty d\omega \frac{\partial \Theta(\omega, T)}{\partial T} \left[ \mathrm{Im}(r_{01}^{TM}) \right]^2 \int_0^\infty \eta e^{-2\eta} d\eta \frac{1}{\left| 1 - (r_{01}^{TM})^2 e^{-2\eta} \right|^2} \tag{3.51}$$

where the lower limit of integration over $\eta$ has been approximated by 0 in the limit $d_c \rightarrow 0$ [106], and where the fact that $r_{12}^{TM} = r_{10}^{TM}$ has been used. The integration over $\eta$ in Eq. (3.51) converges to unity [2], such that the near-field radiative heat transfer coefficient can be approximated as follows:

$$h_r \approx \frac{1}{\pi^2 d_c^2} \int_0^\infty d\omega \frac{\partial \Theta(\omega, T)}{\partial T} \left[ \mathrm{Im}(r_{01}^{TM}) \right]^2 \tag{3.52}$$

Equation (3.52) shows clearly that in the limit that $d_c << \lambda_w$, $h_r$ varies as $d_c^{-2}$. The $d_c^{-2}$ behavior is also shown in Fig. 3.10 where the radiative heat transfer coefficient $h_r$ is calculated using Eq. (3.49) for vacuum gaps $d_c$ of 1 nm to 100 nm.

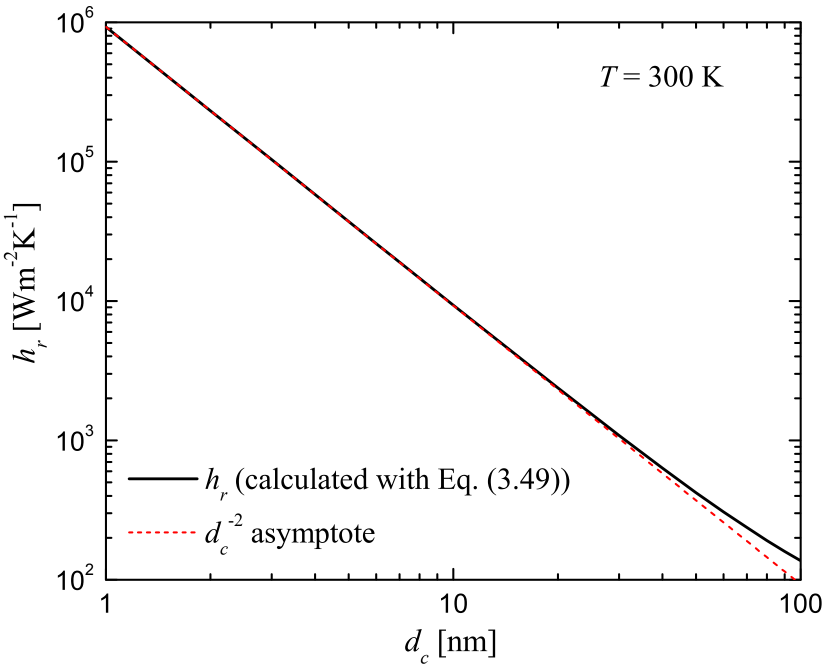

Figure 3.10. Radiative heat transfer coefficient $h_r$ between two bulks of SiC as a function of $d_c$ for $T$ = 300 K; the $d_c^{-2}$ asymptote is also plotted in the figure.

Using similar arguments, it can be shown that the energy density, and therefore the local density of electromagnetic states, increases proportionally to $d_c^{-3}$ close to an emitting material.

Note finally that the length scale of demarcation between the near- and far-field regimes based on the Wien wavelength law is an approximation. More precise values have been determined for cases involving lossless dielectric materials; these results are provided in appendix E.

### 3.6 Concluding remarks

In this chapter, a general algorithm for the solution of near-field thermal radiation problems in one-dimensional layered media without any limitation on the number of layers has been provided. The emphasis was on the accurate and efficient computation of the radiative heat flux; yet this procedure is also applicable for calculations of the near-field energy density and the local density of electromagnetic states. The procedure given in this chapter will be used to predict the performances of nanoscale-gap thermophotovoltaic power generation devices (chapter 6).

It has been shown in section 3.5.1 that the presence of a body in close proximity to an emitter can modify the near-field spectrum emitted. Without giving detailed physical explanations, we mentioned that the perturbation of the near-field radiative flux profiles were due to SPhP coupling between the layers. In chapters 4 and 5, we analyze more closely near-field thermal emission and radiative transfer by and between thin SiC films supporting SPhPs.

# Chapter 4

# Local Density of Electromagnetic States within a Nanometric Gap formed Between Two Thin Films supporting Surface Phonon-Polaritons

Control of far-field thermal emission via a single film [51,52], one-dimensional multi-layered structures [53,54], and one-dimensional photonic crystals [55-64], has been an active subject of research these past years. It is well known that coherent thermal radiation sources are of primary importance in energy conversion technologies where high radiative fluxes concentrated in a limited spectral band are required. On the other hand, the possibility of tuning the near-field thermal radiation spectrum has not been systematically explored so far, except for some preliminary works [54,103]. Polar materials supporting surface phonon-polaritons (SPhPs) in the infrared region, such as silicon carbide (SiC) and cubic boron nitride (*c*BN), exhibit near-field energy density spectra concentrated around SPhP resonance, as discussed in chapters 2 and 3. When the emitter of thermal radiation is a thin film, SPhPs associated with each interface couple within the layer and split the single resonance into anti-symmetric and symmetric modes, a phenomenon that was investigated in the past for both SPhPs and surface plasmon-polaritons (SPPs) [11,12,118-123]. This splitting of the resonance in a thin layer can thus be used to tune the near-field thermal radiation emission and absorption spectrum. Such a control over the emitted near-field spectrum can potentially find important applications in nanoscale-gap thermophotovoltaic power generation, a subject that will be discussed in chapter 6.

Biehs et al. [106,107] studied emission from thin metallic films and materials coated with metal films, and reported that the single SPP resonance at a bulk metal-vacuum interface is split into two frequencies due to the coupling of SPPs inside the layer, thus affecting the local density of electromagnetic states (LDOS) above the film in vacuum. Similar observations were made by Joulain and Henkel [124] who discussed the spatial correlation spectrum of near-field thermal radiation above a thin metallic film. Drevillon [54] provided a preliminary study of the near-field spectrum emitted by single and multiple thin films made of polar crystals and metals. He reported that surface polariton coupling influences the spectral distribution of energy density and LDOS without giving detailed physical explanations. This work was extended by Ben-Abdallah et al. [103], who analyzed the possibility of tailoring near-field LDOS spectra above one-dimensional metallo-dielectric media made of aluminium (Al) and lossless dielectric layers. A target LDOS was prescribed and a genetic algorithm was used to find the best structure, operating in the near ultraviolet, leading to that LDOS profile. While this work showed that it is possible to tune the near-field thermal radiation spectra via multi-layered structures, little information is provided about the physical details and on how the inter-film coupling of surface waves affects the LDOS profiles calculated.

From the above discussion, it is clear that there is a need to study the physics of near-field thermal emission involving thin layers supporting surface polaritons. The objective of this chapter is therefore to analyze thoroughly the physics of near-field thermal emission by a thin film supporting surface polaritons in the presence of a non-emitting body, also supporting surface polaritons, in close proximity. This task is accomplished by calculating the LDOS within the gap formed by two SiC films supporting SPhPs. The discussion and conclusions of this chapter are also applicable to materials supporting SPPs in the infrared, such as doped silicon.

The chapter is structured as follows. An analytical expression for the LDOS within the gap separating the thin layers is first derived. Then, the cross-coupled resonant modes for the two film system are investigated via calculation of the dispersion relation. In section

4.3, the near-field thermal spectrum emitted above a single thin film is analyzed. Finally, the impact of inter-film coupling on emitted near-field thermal radiation spectra is outlined via computation of the LDOS within the gap formed between two layers for various inter-film separation gaps, distances where the fields are observed, and layer thicknesses.

The content of this chapter was published in the proceedings of the *Eurotherm 83: Computational Thermal Radiation in Participating Media III* in 2009 [125], and the *Journal of Applied Physics* in 2010 [104].

## 4.1 Analytical expression of the LDOS in the gap formed between two thin films

The geometry considered is schematically depicted in Fig. 4.1, where a polar ($\rho$, $\theta$, $z$) coordinate system is shown.

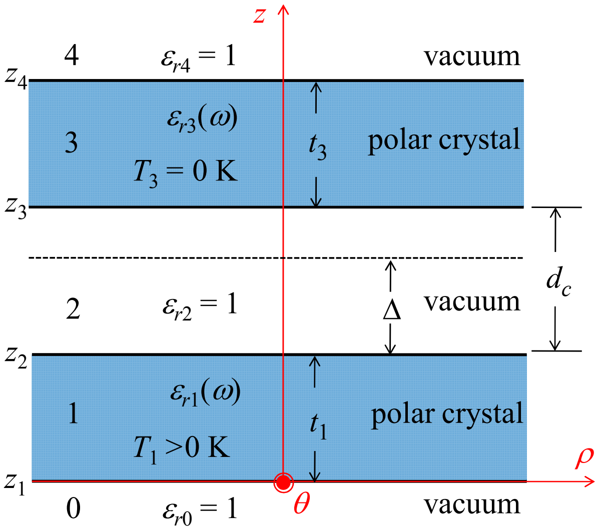

$z$
4
$\varepsilon_{r4} = 1$
vacuum
$z_4$
$\varepsilon_{r3}(\omega)$
3
$T_3 = 0$ K
$t_3$
polar crystal
$z_3$
$d_c$
2
$\varepsilon_{r2} = 1$
$\Delta$
vacuum
$z_2$
$\varepsilon_{r1}(\omega)$
1
$T_1 > 0$ K
$t_1$
polar crystal
$\rho$
$z_1$
0
$\varepsilon_{r0} = 1$
$\theta$
vacuum

Figure 4.1. Schematic representation of the geometry considered: the LDOS is calculated at a distance Δ above the emitting film 1 within the gap of thickness $d_c$.

The media are infinite along the $\rho$-direction and invariant over $\theta$ (i.e., azimuthal symmetry), such that only variations along the $z$-axis need to be considered. The assumptions stated in section 3.1 are applicable here. The two polar crystal films, labeled media 1 and 3 with thicknesses $t_1$ and $t_3$, respectively, are submerged in vacuum and separated by a gap of length $d_c$. Layer 1, at prescribed temperature $T_1$, is emitting thermal radiation while medium 3 is assumed to be non-emitting. The thermal radiation field is calculated in the gap at a distance Δ above the interface 1-2. The assumption of a non-emitting film is justified by the fact that when calculating radiation transfer between two layers, the energy emitted by one of the media absorbed by the other layer is calculated, and vice-versa. The difference between these two values gives the net radiant energy exchanged; therefore, understanding the physics of thermal radiation emission from one film with $T > 0$ K, while the other one is non-emitting, allows the interpretation of the realistic case of near-field radiative heat transfer between two emitting films.

The emitted near-field thermal radiation spectrum is analyzed via the calculation of the LDOS, which is determined by normalizing the electromagnetic energy density at location Δ by the mean energy of a state $\Theta(\omega,T_1)$. The LDOS in the near-field is calculated starting from the general expression for the energy density given in section 2.4:

$$\langle u_\omega(\mathbf{r},T_1)\rangle = \frac{\omega\varepsilon''_{r1}(\omega)}{\pi c_v^2}\Theta(\omega,T_1)\left[k_v\int_V dV'\left|G^E_{m\alpha}(\mathbf{r},\mathbf{r}',\omega)\right|^2 + \int_V dV'\left|G^H_{m\alpha}(\mathbf{r},\mathbf{r}',\omega)\right|^2\right] \tag{4.1}$$

As done in section 3.2 for the Poynting vector, the energy density given by Eq. (4.1) can be expressed in terms of the Weyl components of the dyadic Green's function (DGF). After some algebraic manipulations, and after normalization of the energy density by $\Theta(\omega,T_1)$, the monochromatic LDOS at location Δ above film 1 in medium 2 can be written as follows:

$$\rho_{\omega,12}(\Delta) = \frac{\omega\varepsilon''_{r1}(\omega)}{2\pi^2 c_v^2}\int_0^\infty k_\rho dk_\rho \int_{z_1}^{z_2} dz'\left(k_v^2\left|g^E_{12m\alpha}(k_\rho,\Delta,z',\omega)\right|^2 + \left|g^H_{12m\alpha}(k_\rho,\Delta,z',\omega)\right|^2\right) \tag{4.2}$$

where the subscripts $m$ and $\alpha$ involve summation over the components $\rho$, $\theta$, and $z$. The terms $g^E_{12m\alpha}$ and $g^H_{12m\alpha}$ are the Weyl components of the electric and magnetic DGFs, discussed in section 3.2, relating the fields observed at Δ in medium 2 with frequency $\omega$ and wavevector $k_\rho$ to a source $z'$ located in layer 1.

Since the field is computed in medium 2, the coefficients $A_2^\gamma$, $B_2^\gamma$, $C_2^\gamma$ ,and $D_2^\gamma$ need to be calculated, where $\gamma$ = TE or TM (see sections 3.2 and 3.3 for a discussion about the coefficients). Again, it is important to remember that $A_2^\gamma$ and $B_2^\gamma$ represent amplitudes of forward (*z*-positive) and backward (*z*-negative) traveling waves, respectively, in layer 2 and polarization state $\gamma$, arising from a source emitting in the forward direction. Similar explanations hold for $C_2^\gamma$ and $D_2^\gamma$, except that these coefficients arise from a source emitting in the backward direction. Using a transfer matrix approach as described in section 3.3, the coefficients in medium 2 are given by:

$$A_2^\gamma = \frac{e^{ik_{z1}t_1} t_{12}^\gamma}{(1 + r_{01}^\gamma r_{12}^\gamma e^{2ik_{z1}t_1})(1 - R_1^\gamma R_3^\gamma e^{2ik_{z2}d_c})} \tag{4.3a}$$

$$B_2^\gamma = R_3^\gamma e^{2ik_{z2}d_c} A_2^\gamma \tag{4.3b}$$

$$C_2^\gamma = r_{34}^\gamma A_2^\gamma \tag{4.3c}$$

$$D_2^\gamma = r_{34}^\gamma R_3^\gamma e^{2ik_{z2}d_c} A_2^\gamma \tag{4.3d}$$

where $r_{j,j+1}^\gamma$ and $t_{j,j+1}^\gamma$ are respectively the Fresnel reflection and transmission coefficients at the interface delimiting media *j* and *j* + 1 in polarization state $\gamma$ defined in section 2.7.2, while $R_j^\gamma$ is the reflection coefficient of layer *j* in polarization state $\gamma$ given by [71]:

$$R_j^\gamma = \frac{r_{j-1,j}^\gamma + r_{j,j+1}^\gamma e^{2ik_{zj}t_j}}{1 + r_{j-1,j}^\gamma r_{j,j+1}^\gamma e^{2ik_{zj}t_j}} \tag{4.4}$$

The coefficients given by Eqs. (4.3a) to (4.3d) are then included in the electric and magnetic Weyl components of the DGF, which are in turn substituted in Eq. (4.2). The detailed mathematical manipulations are not provided here, as they are given in appendix F when deriving the near-field radiative heat flux between two thin films (chapter 5). The procedure employed in appendix F is exactly the same as the one used to derive the LDOS in the gap formed between the two thin layers.

Since SPhPs exist only in TM polarization for nonmagnetic media [11,50], we consider strictly the TM evanescent component of the LDOS. After plenty of algebraic manipulations, the following compact expression for the TM evanescent component of the monochromatic LDOS is obtained:

$$\rho_{\omega,12}^{evan,TM}(\Delta) = \frac{1}{2\pi^2\omega}\int_{k_v}^{\infty}\frac{k_\rho^3 dk_\rho}{|k_{z2}|}\frac{\mathrm{Im}(R_1^{TM})e^{-2k''_{z2}\Delta}}{\left|1-R_1^{TM}R_3^{TM}e^{2ik_{z2}d_c}\right|^2} \times\left[\left|1+R_3^{TM}e^{-2k''_{z2}(d_c-\Delta)}\right|^2 - 2\frac{|k_{z2}|^2}{k_\rho^2}\mathrm{Re}(R_3^{TM})e^{-2k''_{z2}(d_c-\Delta)}\right] \tag{4.5}$$

Such an analytical expression for the LDOS within the gap between two films has never been reported in the literature, and it is therefore important to analyze its physical meaning. The denominator $\left|1-R_1^{TM}R_3^{TM}e^{2ik_{z2}d_c}\right|^2$ accounts for multiple reflection and wave interference between the two films, while the term in the numerator, $\mathrm{Im}(R_1^{TM})$, can be seen as the spectral near-field emittance of film 1. The evanescent nature of these modes is also explicitly shown via the exponentially decaying term $e^{-2k''_{z2}\Delta}$. The last term in square bracket on the right-hand side of Eq. (4.5) accounts for the increase of the emittance of film 1 due to the presence of layer 3. It can be seen via the exponential term $e^{-2k''_{z2}(d_c-\Delta)}$ that the influence of film 3 on the near-field thermal radiation spectrum emitted is maximal when $\Delta = d_c$ and minimal when $\Delta \rightarrow 0$.

In the limiting case that $d_c \rightarrow \infty$, $e^{-2k''_{z2}d_c} \rightarrow 0$ such that both the denominator and the term in square bracket in Eq. (4.5) tend to 1. The TM evanescent component of the monochromatic LDOS above a single emitting film is then retrieved:

$$\rho_{\omega,12}^{evan,TM}(\Delta) = \frac{1}{2\pi^2\omega}\int_{k_v}^{\infty}\frac{k_\rho^3 dk_\rho}{|k_{z2}|}\mathrm{Im}(R_1^{TM})e^{-2k''_{z2}\Delta} \tag{4.6}$$

Moreover, if medium 1 is thick (i.e., bulk), then $t_1 \rightarrow \infty$, $e^{ik_{z1}t_1} \rightarrow 0$, and $R_1^{TM} \rightarrow r_{21}^{TM}$. Substitution of $\mathrm{Im}(r_{21}^{TM})$ in Eq. (4.6), instead of $\mathrm{Im}(R_1^{TM})$, provide the LDOS at distance $\Delta$ above an emitting bulk as reported by Joulain [48].

It is important to note that the numerical approach described in chapter 3 could have been used to compute the LDOS between the films. Indeed, the LDOS profiles obtained using the method of chapter 3 and those obtained by solving Eq. (4.5) lead to the exact same results, as it should be. In this chapter, since we are interested by analyzing the physics of the problem, it is better to derive an analytical expression for the LDOS. Also, no results were available in the literature for the LDOS between two films, such that the comparisons between the results obtained from Eq. (4.5) and those from the method of chapter 3 have served as a tool of validation. These comparisons are not shown here, since the results obtained from both approaches were exactly the same. Finally, it is important to point out that the numerical integration in Eq. (4.5), or in any other analytical expressions, is performed following the procedure provided in section 3.4.

## 4.2 Dispersion relation of cross-coupled surface phonon-polaritons

Since medium 1 is at a finite temperature ($T_1 \neq 0$ K), thermal excitation of transverse optical phonons generate SPhPs at each polar crystal-vacuum interfaces 0-1 and 1-2 with evanescent fields decaying in both media. SPhPs are also excited at interfaces 2-3 and 3-4 of medium 3, but via different mechanisms. SPhPs at the interface 2-3 are excited via tunneling of evanescent waves generated by the emitting layer, which is analog to the Otto configuration used to excite SPPs, where a prism and a metallic film are spaced by an air gap [11,50]. In such a configuration, the prism is used to generate evanescent waves via total internal reflection, and tunneling of these waves into the metal layer thus excite SPPs. In the case treated in this work, the emitting layer (film 1) can be seen as the prism, where evanescent waves are generated by thermal agitation of charges rather than total internal reflection of an external radiation beam. At the interface 3-4, excitation of SPhPs is done via tunneling of evanescent waves of the interface 2-3 through the film 3, similar to the Kretschmann configuration, used to excite SPPs, where a metallic film is coated on a prism [11,50]. Evanescent waves are generated at the prism-metal interface via total internal reflection of an external radiation source; tunneling of these evanescent waves through the metallic film thus excites SPPs at the metal-air interface. In our case, evanescent waves are present at the interface 2-3 due to radiation tunneling from layer 1 to layer 3. When both $T_1$ and $T_3$ are greater than 0 K, SPhP excitation for each layer is due to thermal excitation of charges, as well as excitation via Otto and Kretschmann configurations.

SPhP dispersion relation can be determined by analyzing the resonance condition of the two film system. Resonance arises when $\rho_{\omega,12}^{evan,TM} \rightarrow \infty$. Inspection of Eq. (4.5) shows that divergence of the TM evanescent component of the monochromatic LDOS can only happen when the following condition is fulfilled:

$$1 - R_1^{TM} R_3^{TM} \exp(2ik_{z2}d_c) = 0 \tag{4.7}$$

If medium 3 is removed, the TM evanescent component of the LDOS is given by Eq. (4.6), and $\rho_{\omega,12}^{evan,TM} \rightarrow \infty$ is satisfied when $1 - (r_{21}^{TM})^2 \exp(2ik_{z1}t_1) = 0$. Solution of this last expression provides the resonant modes of a single film submerged in a given medium. Moreover, if the emitting layer 1 is thick (i.e., bulk), the single resonance condition is given by $r_{21}^{TM} \rightarrow \infty$. Using the definition of the Fresnel reflection coefficient in TM polarization, this condition is fulfilled when $\varepsilon_{r1}k_{z2} + \varepsilon_{r2}k_{z1} = 0$, which corresponds to the resonant mode of a single interface delimiting media 1 and 2, as discussed in section 2.7.2.

SPhP dispersion relation for the two film system leads to four branches, and is determined by solving Eq. (4.7) using the secant method. For the simulations, the dielectric constant of polar crystals is approximated by a damped harmonic oscillator model, as given in appendix B. Note that the losses are neglected when calculating the dispersion relation (i.e., $\Gamma = 0$); the full damped harmonic oscillator is however used when computing the LDOS.

In Fig. 4.2(a), dispersion relations for two 10 nm thick SiC films spaced by a variable $d_c$ of 10 nm and 100 nm are shown, while SPhP dispersion relations for $t_1 = 100$ nm, $t_3 = 10$ nm, and $d_c = 10$ nm and 100 nm are presented in Fig. 4.2(b). The four branches are identified as a function of their frequencies; the lowest frequency branch is referred as $\omega_1$, while the highest one is called $\omega_4$. For clarity, this nomenclature is shown in Figs. 4.2(a)

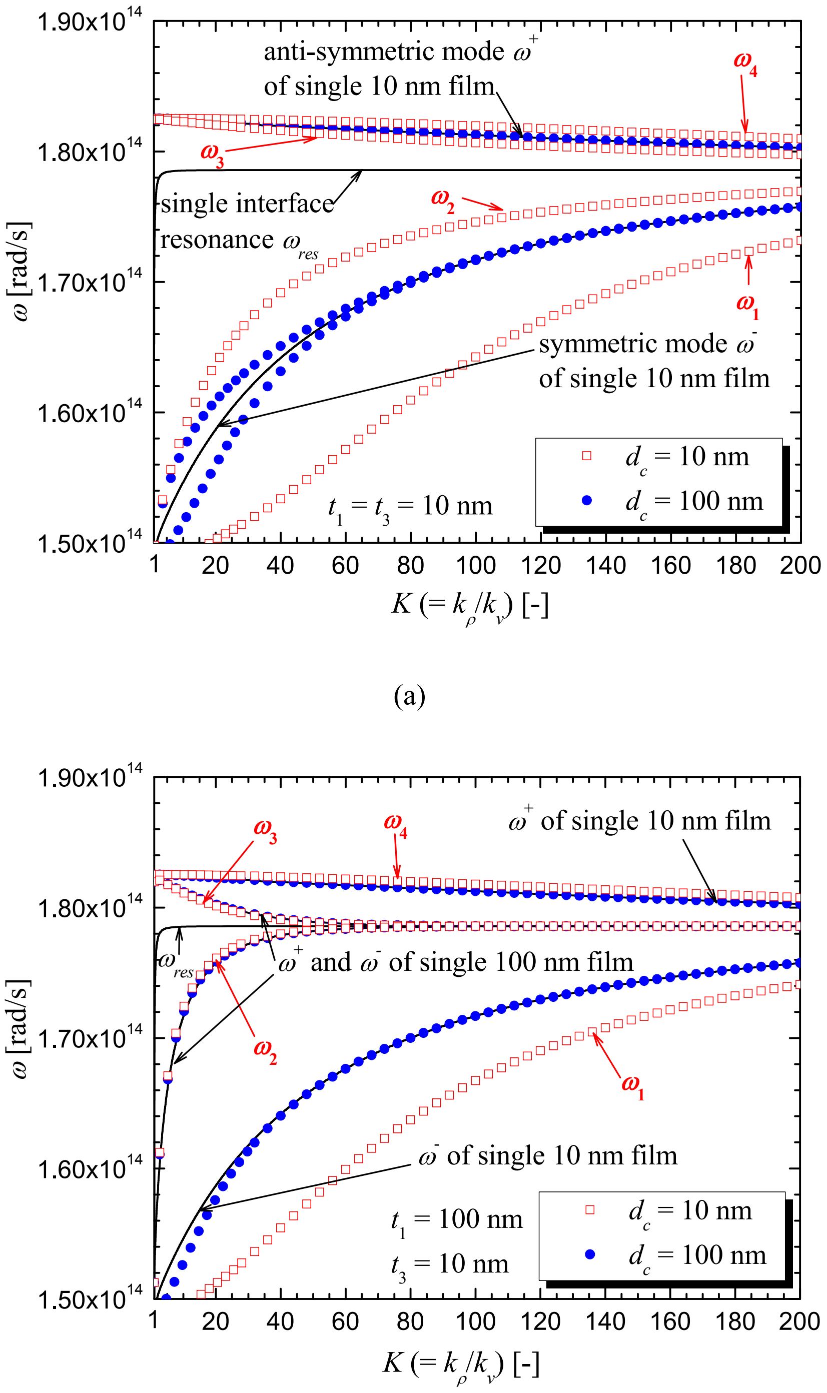

(a)

(b)

Figure 4.2. Dispersion relations of SPhPs for $t_1$ and $t_3$ thick SiC films submerged in vacuum and separated by a gap $d_c$: (a) $t_1 = t_3 = 10$ nm, and $d_c = 10$ nm and 100 nm. (b) $t_1 = 100$ nm, $t_3 = 10$ nm, and $d_c = 10$ nm and 100 nm. Results are compared with the dispersion relations of single SiC films in vacuum and a single SiC-vacuum interface.

and 4.2(b) only for $d_c$ = 10 nm. In both figures, results are compared with the dispersion relations of single SiC films in vacuum and a single SiC-vacuum interface.

In a thin film, the evanescent field of SPhPs associated with each interface can interact with each other, thus leading to a splitting of the SPhP dispersion relation into anti-symmetric $\omega^+$ (high frequency) and symmetric $\omega^-$ (low frequency) modes [11,12,118-123]. The symmetric mode corresponds to the case where the tangential electric field $E_\rho$ has a symmetric distribution with respect to the middle plane of the layer (magnetic fields $H_\theta$ at each interface are in phase), and vice-versa for the anti-symmetric resonance [12]. Comparison of the dispersion relations for 10 nm and 100 nm thick single SiC films in vacuum shows that the splitting of the resonance becomes more pronounced as the thickness of the film decreases. For large $K$ (= $k_\rho/k_v$) values, the dispersion relations of both modes approach asymptotically the dispersion curve of a single SiC-vacuum interface. Indeed, the penetration depth of SPhPs in the film is small for large $K$ values. As a consequence, when $K$ is large, the anti-symmetric and symmetric branches become degenerate as SPhPs do not couple inside the films, and therefore the SPhPs at each interface behave independently from each other [121].

When two films supporting SPhPs are placed in close proximity, further coupling takes place, and the dispersion relation splits into four branches showing anti-symmetric and symmetric resonances for each film and for the entire structure [126,127]. This fact is illustrated by analyzing the case $d_c$ = 10 nm in Fig. 4.2(a), where both films are 10 nm thick. The modes $\omega_1$ and $\omega_2$ come from the symmetric resonance of each film. The interaction of these symmetric modes in the vacuum gap leads to anti-symmetric ($\omega_2$) and symmetric resonances ($\omega_1$) for the whole structure. The anti-symmetric resonance $\omega_2$ arises when $H_\theta$ oscillations, in phase at the two interfaces of a given layer, are out-of-phase from one film relative to the other one. Similarly, the symmetric resonance $\omega_1$ due to inter-film coupling arises when $H_\theta$ at the four interfaces are in phase. It can be seen in Fig. 4.2(a) that as $d_c$ increases, $\omega_1$ and $\omega_2$ get closer to the symmetric branch of a single 10 nm thick film submerged in vacuum, since when $d_c$ is large enough, SPhPs on each film behave independently. Similar explanations are applicable to $\omega_3$ and $\omega_4$, which are generated by the coupling of the anti-symmetric modes of each film. For the $d_c$ values considered in Fig. 4.2(a), $\omega_3$ and $\omega_4$ are very close to each other; the proximity effect between the films is more visible for the modes $\omega_1$ and $\omega_2$. For films of different thicknesses (Fig. 4.2(b)), $\omega_4$ is located above $\omega^+$ of the thinner film (10 nm), and $\omega_3$ is below $\omega^+$ of the thicker film (100 nm). Similar observations can be made for $\omega_1$ and $\omega_2$, which are respectively located below and above $\omega^-$ of 10 nm and 100 nm thick films. Note that due to the symmetry of the problem, SPhP dispersion relation for $t_1$ = 10 nm and $t_3$ = 100 nm is the same as the one presented in Fig. 4.2(b). For sufficiently large $K$ values where SPhP coupling is impossible in each layers and between the films, all four branches converge toward the resonant frequency $\omega_{res}$ of a single SiC-vacuum interface.

## 4.3 LDOS profiles above a single thin film

In order to demonstrate that near-field thermal emission by a thin film supporting SPhPs is dominated by the anti-symmetric and symmetric resonant modes, the integrand of the TM evanescent component of the monochromatic LDOS in Eq. (4.6) is plotted in Figs. 4.3(a) and 4.3(b) for 10 nm and 100 nm thick SiC films surrounded by vacuum, respectively; here, the Δ-dependence is omitted and the results are compared against the dispersion relation for a film and the dispersion relation for a single SiC-vacuum interface.

Comparison of the integrand of the TM evanescent component of the monochromatic LDOS against the dispersion relations in Figs. 4.3(a) and 4.3(b) shows clearly that the anti-symmetric and symmetric modes dominate the near-field thermal radiation spectrum emitted. On the other hand, even for a layer sufficiently thin to allow coupling of SPhPs (i.e., $t_j << \lambda_w$, where $\lambda_w$ is the dominant wavelength emitted), the TM evanescent component of the monochromatic LDOS calculated at Δ above the film does not necessarily exhibit the splitting of the resonance into two distinct frequencies. Indeed, manifestation of the resonance splitting on the near-field thermal radiation spectrum emitted by a thin film is not only function of its thickness $t_1$, but also the distance Δ where the fields are calculated [107,125].

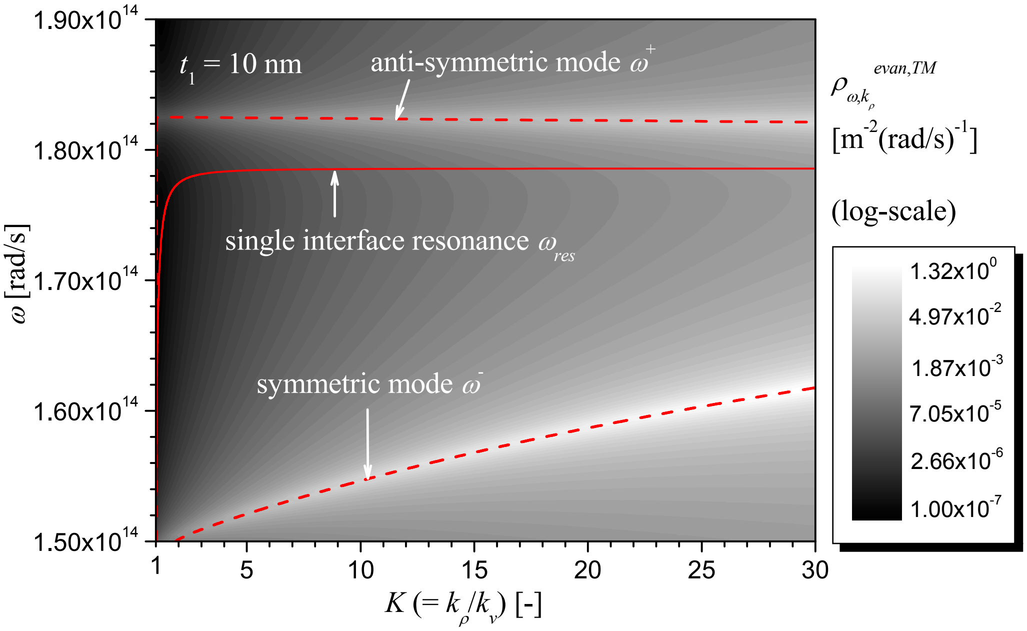

(a)

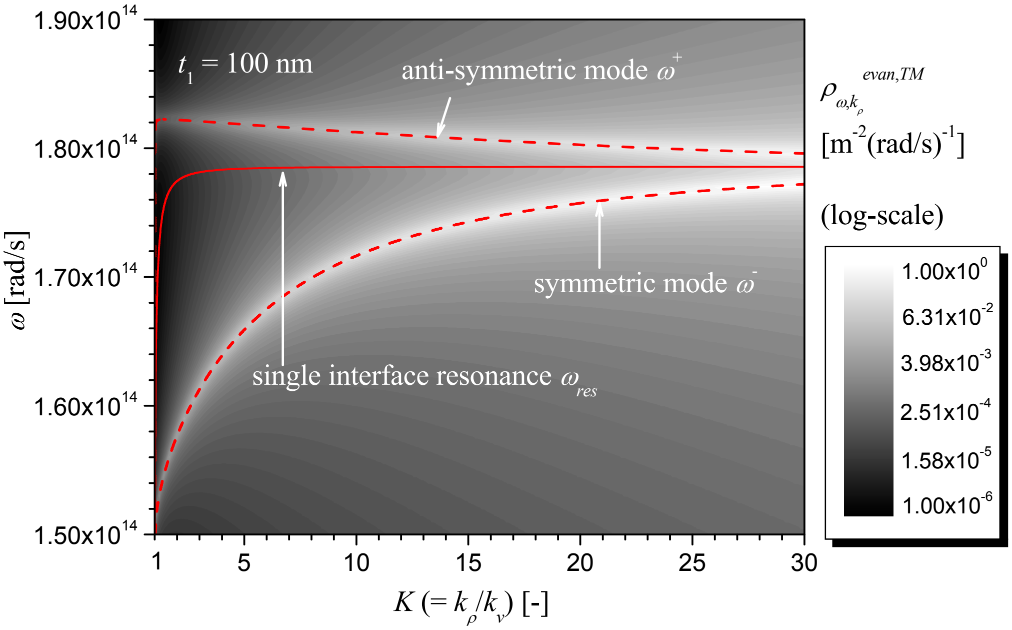

(b)

Figure 4.3. Results of Δ-independent integrand of the TM evanescent component of the monochromatic LDOS (in log-scale) are presented for: (a) $t_1$ = 10 nm. (b) $t_1$ = 100 nm. The dashed lines correspond to the dispersion relation of a single film, while the full line is the dispersion relation of a single interface.

The interdependence between the film thickness and distance where the LDOS is calculated on the emitted near-field spectrum can be physically explained by analyzing the penetration depth of evanescent waves in vacuum, calculated as $\delta_2 \approx |k_{z2}|^{-1}$. For the sake of the explanations, we consider a 100 nm thick SiC film and Δ values of 50 nm and 500 nm. Figures 4.4(a) and 4.4(b) show $\delta_2$, in nanometers, as a function of $\omega$ and $K$; note that $\delta_2$ is independent of $t_1$. The interdependence between the LDOS and $t_1$ is visualized by plotting the dispersion relation of SPhPs for the 100 nm thick film, as done in Figs. 4.4(a) and 4.4(b). In order to analyze the influence of Δ, evanescent waves with $\delta_2$ greater or equal than 50 nm are in color in Fig. 4.4(a), while evanescent waves with $\delta_2$ greater or equal than 500 nm are in color in Fig. 4.4(b); evanescent waves with $\delta_2$ below these thresholds are left in white. Therefore, the colored zones in Figs. 4.4(a) and 4.4(b) correspond to evanescent waves contributing to the LDOS at Δ = 50 nm and 500 nm, respectively.

Before interpreting Figs. 4(a) and 4(b), it is important to make the distinction between the resonant modes of the single film configuration and the "resonance of the LDOS" (or, equivalently, the "resonance of the near-field spectrum"). As discussed in section 4.2, the resonance of the single film occurs at all frequencies along the two branches of SPhP dispersion relation. On the other hand, we refer to the resonance of the LDOS as the frequencies maximizing the near-field spectrum emitted. Such resonance of the LDOS can be estimated from SPhP dispersion relation using the following arguments. The LDOS provides a measure of the number of states, or modes, per unit volume and per unit frequency at a given spatial location, and is therefore direction proportional to $|dk_\rho / d\omega|$. As $k_\rho$ increases, the branches of SPhP dispersion relation flatten, thus implying a large $|dk_\rho / d\omega|$ value. We consequently expect the near-field spectrum emitted at Δ to be maximal at the frequencies corresponding to the largest contributing parallel wavevector, $k_{\rho,\max}$, where $|dk_\rho / d\omega|$ is the highest. By estimating the value of $k_{\rho,\max}$ as a function of Δ, it is then possible to evaluate the resonance of the LDOS using SPhP

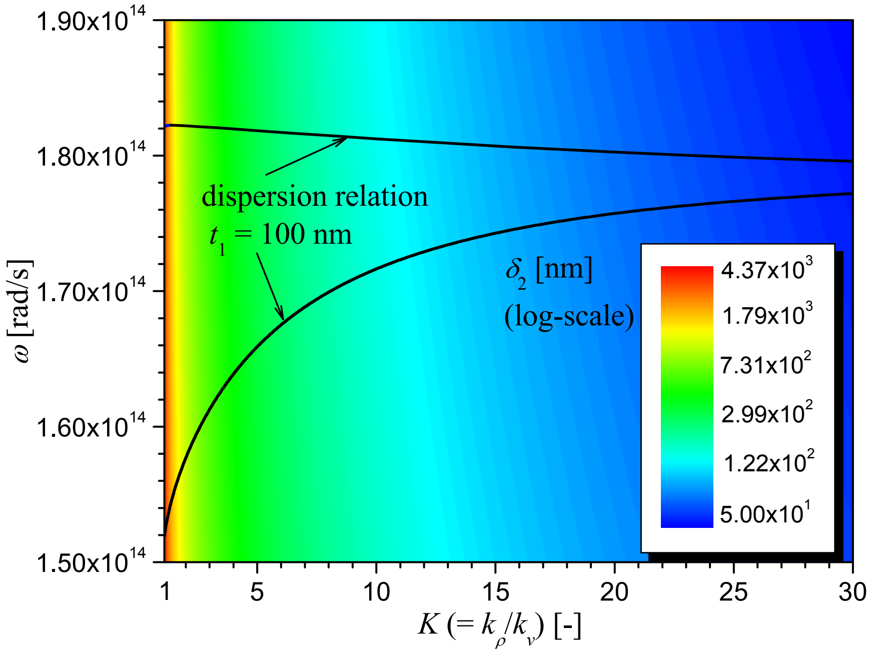

(a)

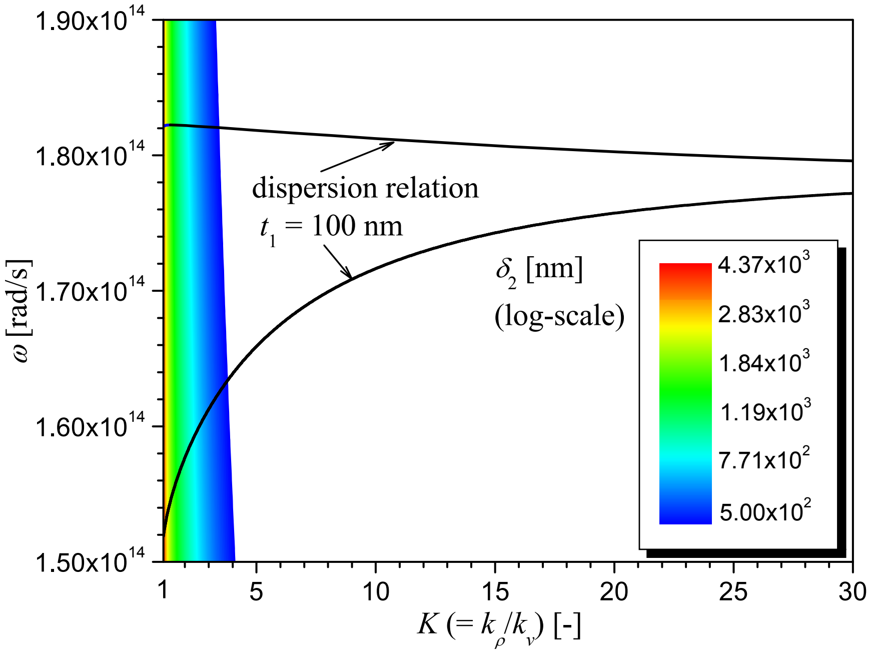

(b)

Figure 4.4. Penetration depth of evanescent waves in vacuum (in log-scale), and SPhP dispersion relation for a 100 nm thick SiC film: (a) evanescent waves with $\delta_2$ greater or equal than 50 nm are in color. (b) evanescent waves with $\delta_2$ greater or equal than 500 nm are in color.

dispersion relation. Given that, Figs. 4.4(a) and 4.4(b) illustrate in a graphical manner this relationship between $k_{\rho,\max}$ and Δ.

It is clear that for Δ = 50 nm, all evanescent waves will contribute to the LDOS for the range of $\omega$ and $K$ considered in Fig. 4.4(a). Note that a $\delta_2$ of 50 nm is reached for a $K$ value around 40, where both anti-symmetric and symmetric modes converge toward the resonance of a single SiC-vacuum interface. As a consequence, we expect to see one peak, corresponding to the resonance of a single SiC-vacuum interface, on the spectral distribution of LDOS. The LDOS is also expected to be spread out over a larger spectral band, as compared to the LDOS of a single SiC-vacuum interface, due to splitting of the dispersion relation. On the other hand, Fig. 4.4(b) shows clearly that convergence of anti-symmetric and symmetric modes into a single resonant frequency cannot be observed at Δ = 500 nm, since the associated evanescent field penetrating in vacuum is less than Δ. Instead, we expect to observe two peaks of resonance on the LDOS profiles. Moreover, the symmetric mode should be wider in a spectral sense than the anti-symmetric one, since it spreads out over multiple frequencies.

The limiting frequencies of LDOS resonance can be determined by performing an asymptotic analysis of SPhP dispersion relation for a single film; these limits are also applicable for the two film configuration. We assume that only evanescent waves with penetration depth in vacuum $\delta_2 \geq \Delta$ contribute to the LDOS calculated at Δ. For a large $k_\rho$ value (i.e., $k_\rho >> k_v$), the $z$-component of the wavevector in medium $j$ can be approximated by $k_{zj} \approx ik_\rho$ (see section 3.5.2). Using the definition of penetration depth of evanescent wave, $\delta_2 \approx \left|k_{z2}\right|^{-1}$, we can write that the largest contributing parallel wavevector to the LDOS is $k_{\rho,\max} \approx \Delta^{-1}$. Substitution of this approximation into the dispersion relation of a single film (given below Eq. (4.7)) leads to:

$$\omega_{\max}^{\pm} \approx \left[ \frac{\varepsilon_\infty \omega_{LO}^2 + \omega_{TO}^2 \mp e^{-t_1/\Delta}(\omega_{TO}^2 - \varepsilon_\infty \omega_{LO}^2)}{\varepsilon_\infty + 1 \mp e^{-t_1/\Delta}(1 - \varepsilon_\infty)} \right]^{1/2} \tag{4.8}$$

where losses have been neglected in the dielectric function of polar crystals. Equation (4.8) provides an approximation of the anti-symmetric and symmetric resonances of the fields above a single polar crystal film submerged in vacuum as a function of $t_1$ and Δ. In the limiting case that $t_1 >> \Delta$, both modes $\omega_{\max}^{+}$ and $\omega_{\max}^{-}$ maximizing the LDOS converge toward $\omega_{res} \approx \left[(\varepsilon_{\infty}\omega_{LO}^{2} + \omega_{TO}^{2})/(\varepsilon_{\infty}+1)\right]^{1/2}$, which is the resonant frequency of a single polar crystal-vacuum interface [108]. The other extreme case arises when $t_1 << \Delta$ leading to $\omega_{\max}^{+} \approx \omega_{LO}$, and $\omega_{\max}^{-} \approx \omega_{TO}$, limits that prevails regardless of the media surrounding the film. These observations for a film supporting SPhPs are in line with what was reported by Biehs for the case of metallic films [107]: for $t_1 >> \Delta$, $\omega_{res} = \omega_{\max}^{+} = \omega_{\max}^{-} \approx \omega_{p}/\sqrt{2}$, which is the resonance of a single metal-vacuum interface, and for $t_1 << \Delta$, $\omega_{\max}^{+} \approx \omega_{p}$ and $\omega_{\max}^{-} \approx 0$, where $\omega_p$ represents the plasma frequency defined in appendix B.

Next, the TM evanescent component of the monochromatic LDOS is calculated for 10 nm and 100 nm thick SiC films and shown in Figs. 4.5(a) and 4.5(b), respectively, for Δ = 1 nm, 10 nm, 50 nm, 100 nm, and 500 nm. For comparison, Eq. (4.8) is used to predict the resonant modes, and these predictions are included in Figs. 4.5(a) and 4.5(b); the limiting frequencies $\omega_{LO}$, $\omega_{TO}$, and $\omega_{res}$ are also identified.

It is interesting to note that LDOS profiles reported in Fig. 4.5(b) for $t_1$= 100 nm and Δ = 50 nm and 500 nm corroborate the predictions made earlier solely by inspecting Figs. 4.4(a) and 4.4(b). Moreover, predictions of anti-symmetric and symmetric resonant frequencies via Eq. (4.8) are in qualitative agreement with the TM evanescent component of the monochromatic LDOS. However, as discussed in chapter 5, the accuracy of these predictions can be improved by modifying the definition of penetration depth of evanescent waves.

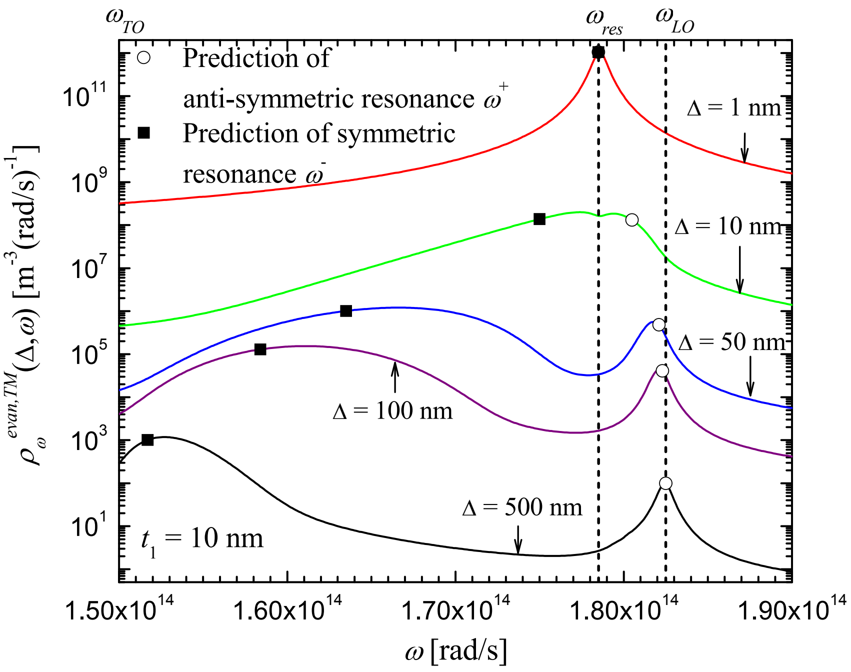

(a)

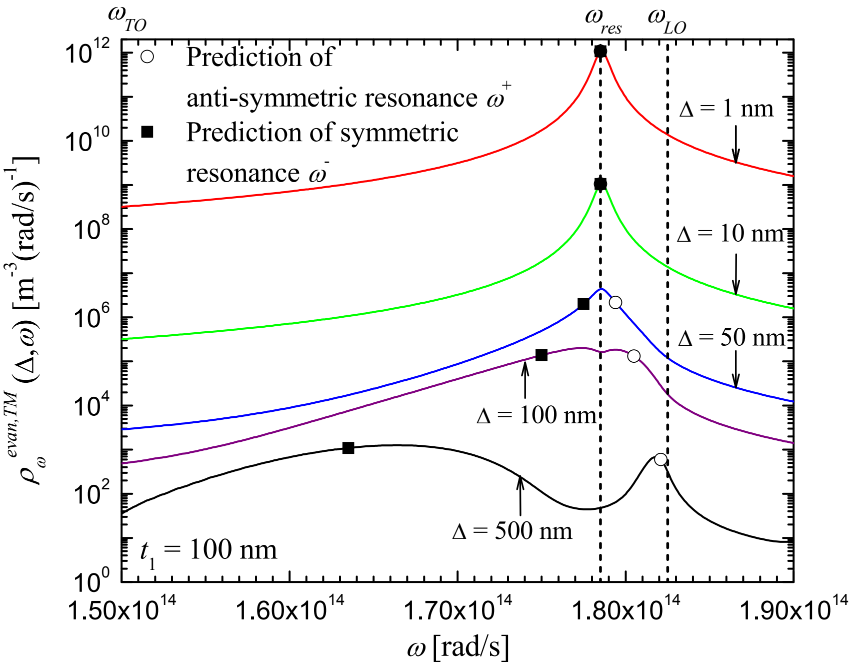

(b)

Figure 4.5. TM evanescent component of the monochromatic LDOS for Δ = 1 nm, 10 nm, 50 nm, 100 nm, and 500 nm. Results are provided for two different SiC film thicknesses: (a) $t_1$ = 10 nm. (b) $t_1$ = 100 nm.

From the numerical simulations shown in Fig. 4.5(a) and 4.5(b), the splitting of the resonance is visible on the spectral distribution of LDOS when the ratio $t_1/\Delta$ is equal or less than unity. As the ratio $t_1/\Delta$ decreases below unity, the frequencies maximizing the LDOS clearly converge toward $\omega_{LO}$ and $\omega_{TO}$. The $t_1/\Delta$ dependence on the emitted near-field spectrum can be easily interpreted by solely inspecting SPhP dispersion relations. For example, when $\Delta = 10$ nm in Fig. 4.5(a), using $k_{\rho,\max} \approx \Delta^{-1}$, the largest contributing $K$ ($K_{\max} = k_{\rho,\max}/k_v$) value to the LDOS is estimated to be 200. Inspection of the dispersion relation around this approximate limit for a single 10 nm thick film (Fig. 4.2(a)) reveals that both anti-symmetric and symmetric modes have almost reached a plateau where $\left|dk_\rho / d\omega\right|$ is very large. As a consequence, even if the portion of dispersion relation below $K$ values of 200 contributes to the LDOS at $\Delta = 10$ nm, only the region near $K_{\max}$ can be seen in Fig. 4.5(a) where $\left|dk_\rho / d\omega\right|$ is the highest. As $\Delta$ increase, the value of $K_{\max}$ decreases, the gap between $\omega^+$ and $\omega^-$ increases, and the near-field thermal radiation spectrum emitted clearly exhibits two distinct resonances. Also, inspection of Figs. 4.5(a) and 4.5(b) for small $t_1/\Delta$ ratios shows that the LDOS resonance between $\omega_{res}$ and $\omega_{LO}$ (corresponding to $\omega^+_{\max}$) has a higher degree of spectral coherence than the LDOS resonance between $\omega_{TO}$ and $\omega_{res}$ (corresponding to $\omega^-_{\max}$), due to greater losses of the symmetric mode [124].

Physically, the $t_1/\Delta$ dependence is quite straightforward to interpret given the above discussion. The near-field spectrum emitted is dominated by SPhPs having penetration depths of about $\Delta$. Therefore, if $\Delta < t_1$, SPhPs dominating thermal emission cannot couple within the film, and only one resonance is observed on the LDOS profile. Conversely, if $\Delta \approx t_1$ or $\Delta > t_1$, SPhPs dominating thermal emission can couple within the thin layer, thus resulting in a splitting of the resonance of the LDOS.

Results presented here are interesting from the point of view of designing customized nanostructures. These discussions reveal that for the case of a polar crystal film submerged in a given medium, it is possible to tune the resonance of the near-field thermal emission spectrum between $\omega_{TO}$ and $\omega_{LO}$ by varying the value of $t_1/\Delta$. Therefore, based on Eq. (4.8), we propose a mapping of the splitting of the resonance as a function of $t_1/\Delta$ and a given material. A dimensionless frequency $\Omega = (\omega - \omega_{TO})/(\omega_{LO} - \omega_{TO})$ is used to allow the visualization of the resonance splitting for different materials in a single figure. The dimensionless resonant frequencies of anti-symmetric $\Omega^+$ and symmetric $\Omega^-$ modes are in that way restricted to the interval $[\Omega_{TO},\Omega_{LO}] = [0,1]$. The variations of $\Omega^+$ and $\Omega^-$ as a function of $t_1/\Delta$ are presented in Fig. 4.6 for SiC and *c*BN. For reference, the curves corresponding to resonance of singles SiC-vacuum and *c*BN-vacuum interfaces are also shown.

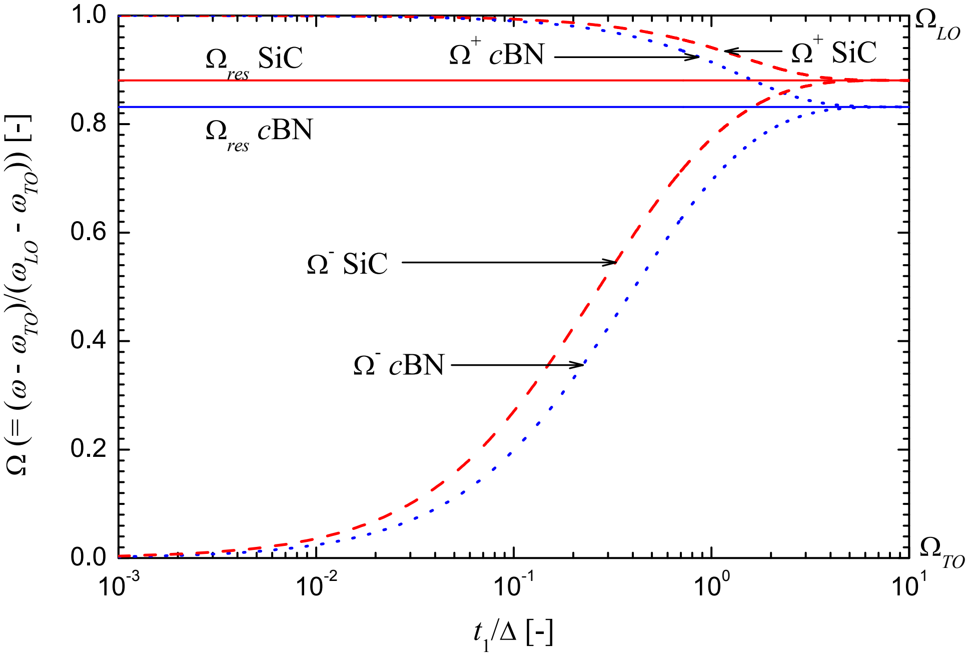

Figure 4.6. Approximate prediction of anti-symmetric and symmetric SPhP resonant frequencies, calculated via Eq. (4.8), as a function of $t_1/\Delta$ for SiC and *c*BN films submerged in vacuum; the frequency is normalized as $\Omega = (\omega - \omega_{TO})/(\omega_{LO} - \omega_{TO})$.

It can be seen in Fig. 4.6 that the splitting of the resonance arises for both SiC and *c*BN below a $t_1/\Delta$ value of about 4; however, the resonance splitting becomes distinguishable on LDOS profiles when $t_1/\Delta$ is equal or less than unity. For both SiC and *c*BN, the anti-symmetric mode converges toward $\Omega_{LO}$ for $t_1/\Delta$ values larger than for the symmetric mode toward $\Omega_{TO}$. Figure 4.6 constitutes a useful guide in designing near-field thermal radiation spectrum from thin emitting films.

Before closing this section, it is important to note that Eq. (4.8) and Fig. 4.6 are valid if the film is thin enough to allow SPhP coupling and if $\Delta$ is within the evanescent field extent of SPhPs in vacuum (i.e., $t_1$ and $\Delta < \lambda_w$). The limiting $\Delta$ values are determined by analyzing penetration depths of SPhPs in vacuum, and values of about 14 μm and 10 μm have been found for SiC and *c*BN, respectively. Similarly, the limiting film thicknesses are determined via the analysis of SPhP penetration depths within the medium; limiting $t_1$ values of about 1.7 μm and 1.3 μm have been calculated for SiC and *c*BN, respectively. This corroborate the approximate threshold $t_1$ and $\Delta < \lambda_w$, since $\lambda_w$ is of the order of few microns for typical thermal radiation temperatures.

## 4.4 LDOS profiles within the gap formed between the two films

The near-field thermal radiation spectrum emitted by film 1 within the gap formed between two films is analyzed in this section by calculating the TM evanescent component of the monochromatic LDOS given by Eq. (4.5). These LDOS profiles are calculated in the vacuum gap at distance $\Delta$ above layer 1, such that when $\Delta = d_c$, this implies that the LDOS is computed just before crossing the interface 2-3 (i.e., at $z = z_3^-$). Following the discussion of sections 4.2 and 4.3, the near-field thermal radiation spectrum emitted is expected to be strongly dependent on the parameters $t_1$, $t_3$, $d_c$, and $\Delta$.

As for the case of a single emitting film, a distinction is made hereafter between the resonant modes of the two film configuration and the "resonance of the LDOS." The four branches of SPhP dispersion relations presented in section 4.2 spreading out over multiple frequencies correspond to the resonance of the two film configuration, while the resonance of the LDOS refers to the frequencies maximizing the near-field thermal spectrum emitted.

The perturbation of the near-field thermal radiation spectrum emitted by film 1 due to layer 3 is analyzed as a function of three parameters: the inter-film separation gap $d_c$, the distance where the fields are calculated $\Delta$, and the thickness of film 3 $t_3$. The limiting frequencies $\omega_{TO}$, $\omega_{LO}$, and $\omega_{res}$ are identified in all figures.

*4.4.1 Impact of inter-film distance*

LDOS profiles for $d_c = \Delta = 10$ nm, 100 nm, 200 nm, and 500 nm are shown in Fig. 4.7(a) for $t_1 = t_3 = 10$ nm and Fig. 4.7(b) for $t_1 = 100$ nm and $t_3 = 10$ nm. In both cases, for each $\Delta$ considered, results are compared with the case $d_c \rightarrow \infty$ (i.e., when there is no medium 3).

Figures 4.7(a) and 4.7(b) show that the presence of film 3 can enhance significantly emission by layer 1, and perturb slightly the spectral location of the resonance of the LDOS. The enhancement of the LDOS is particularly important for $\Delta = d_c = 10$ nm (more than an order of magnitude), in both Figs. 4.7(a) and 4.7(b), as strong inter-film SPhP coupling increases the number of electromagnetic modes. For a 10 nm thick emitter and $\Delta = d_c = 10$ nm (Fig. 4.7(a)), the LDOS resonance converges to $\omega_{res}$ when medium 3 is present. Figure 4.2(a) shows that due to SPhP coupling, $\omega_2$ and $\omega_3$ are pushed respectively above $\omega^-$ and below $\omega^+$, thus resulting in a maximum LDOS closer to $\omega_{res}$ than for a single film. For the 100 nm thick emitter, the resonance of the near-field spectrum emitted is at $\omega_{res}$ even for $d_c \rightarrow \infty$; the presence of medium 3 at $\Delta = d_c = 10$ nm spreads out the resonance over a broader spectral band (i.e., small loss of spectral coherence) as SPhP coupling pushes $\omega_1$ and $\omega_4$ respectively below $\omega^-$ and above $\omega^+$ of a single 10 nm film (see Fig. 4.2(b)).

As $d_c$ increases, SPhP coupling between the films decreases, and the enhancement of the near-field thermal radiation spectrum emitted by layer 1 consequently decreases. In Fig. 4.7(a) for $\Delta = d_c = 100$ nm, 200 nm, and 500 nm, the presence of film 3 does not alter much the strength and spectral coherence of the LDOS resonance between $\omega_{res}$ and $\omega_{LO}$ as the anti-symmetric mode is not significantly altered by SPhP coupling (see Fig. 4.2(a) for $d_c = 100$ nm). Medium 3 mostly affects the resonance between $\omega_{TO}$ and $\omega_{res}$ in terms of LDOS enhancement, spectral location and broadening. Indeed, for a given $d_c$ value, $\left|dk_\rho / d\omega\right|$ is usually larger for $\omega_2$ than $\omega_1$. Since $\omega_2$ is at higher frequencies than $\omega^-$, the resonance between $\omega_{TO}$ and $\omega_{res}$ therefore occurs at a slightly higher frequency when film 3 is present. Similar explanations hold when the emitter is 100 nm thick.

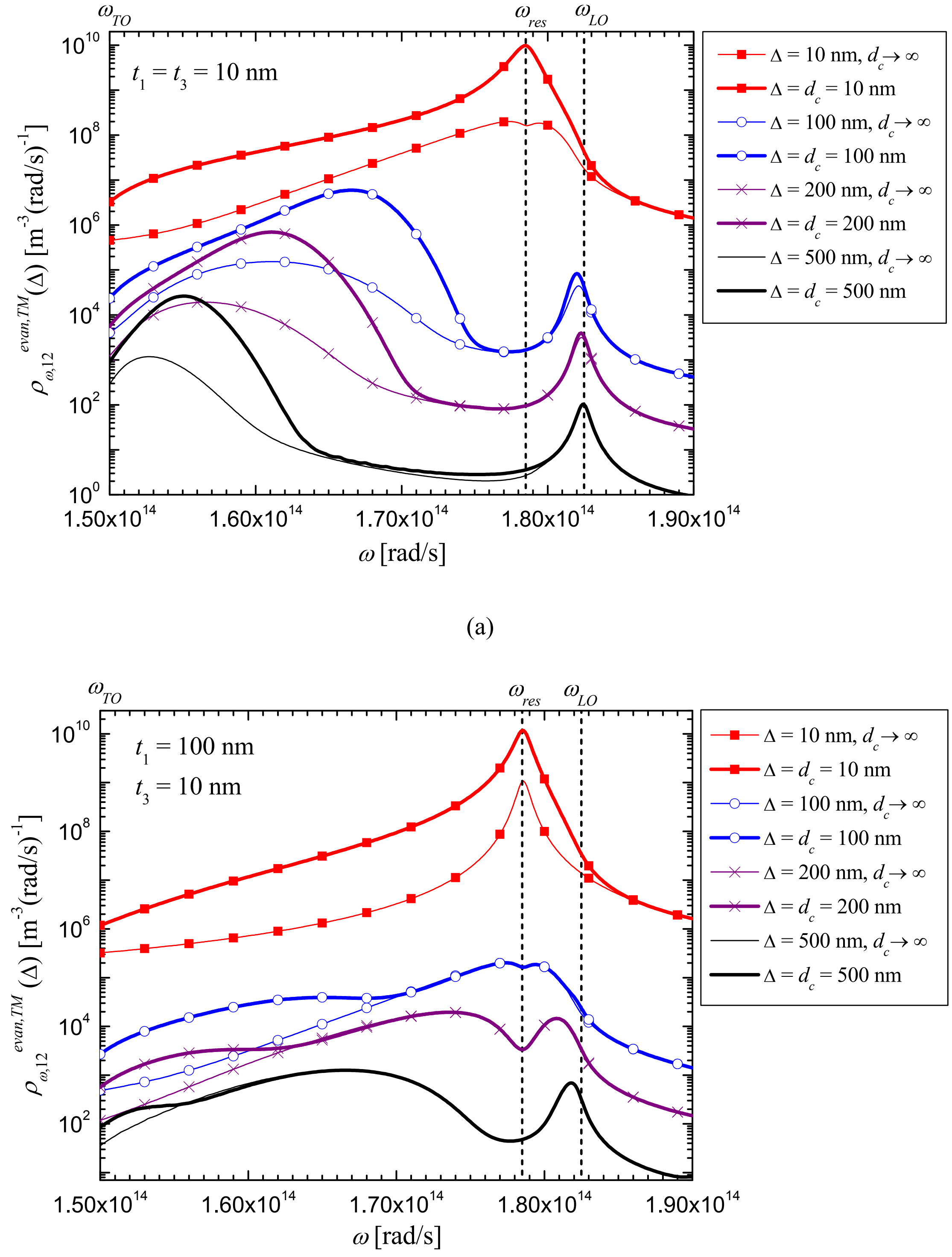

(a)

(b)

Figure 4.7. TM evanescent component of the monochromatic LDOS in the gap at $\Delta = d_c = 10$ nm, 100 nm, 200 nm, and 500 nm: (a) $t_1 = t_3 = 10$ nm. (b) $t_1 = 100$ nm and $t_3 = 10$ nm. Results are compared with a single emitting film.

The near-field thermal radiation spectrum emitted by film 1 calculated at $\Delta = d_c$ is always perturbed by the presence of medium 3. Indeed, if the LDOS is greater than zero at $\Delta = d_c$, then SPhPs emitted by film 1 necessarily couple with layer 3 thus affecting the thermal radiation field at $\Delta$.

### *4.4.2 Impact of distance where the LDOS is calculated*

To analyze the influence of $\Delta$ on the LDOS profiles, we first study the case $t_1 = t_3 = 10$ nm and $d_c = 100$ nm already presented in Fig. 4.7(a) for $\Delta = 100$ nm, and calculate the LDOS at two other locations $\Delta$ of 10 nm and 50 nm. In all cases, spectral distributions of TM evanescent component of the LDOS are compared with those without medium 3; results are presented in Fig. 4.8.

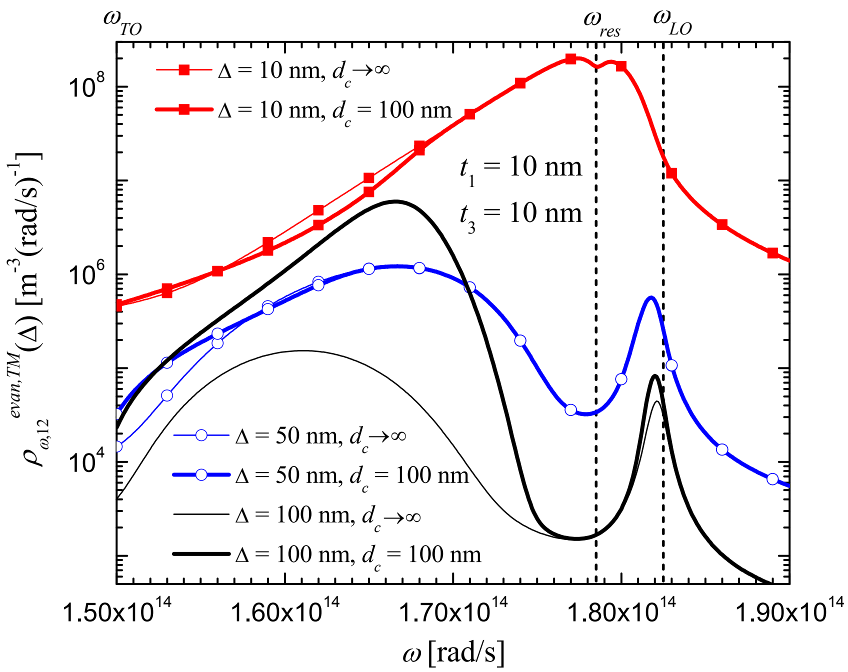

Figure 4.8. TM evanescent component of the monochromatic LDOS in the gap for $t_1 = t_3 = 10$ nm, $d_c = 100$ nm, and $\Delta$ = 10 nm, 50 nm, and 100 nm; results are compared with a single 10 nm thick emitting film.

Clearly, for $\Delta$ values of 10 nm and 50 nm, the near-field spectrum emitted is only slightly affected by film 3 located at $d_c = 100$ nm above film 1. As pointed out earlier, the perturbation of the near-field spectrum emitted by film 1 is mathematically described by the term in square brackets on the right-hand side of Eq. (4.5), which has a decreasing influence as $\Delta$ decreases. Physically, the $\Delta$-dependence can be explained by inspecting SPhP dispersion relation shown in Fig. 4.2(a). Using $k_{\rho,\max} \approx \Delta^{-1}$, the largest contributing $K$ values to the LDOS (i.e., $K_{\max}$) are estimated to be around 20, 40, and 200 for $\Delta$ values of 100 nm, 50 nm, and 10 nm, respectively. As $K_{\max}$ increases from 20 to 40, and from 40 to 200, the cross-coupled SPhP modes for the two layer system converge toward $\omega^{+}$ and $\omega^{-}$ of a single 10 nm thick layer. For large $K$, the branches of the dispersion relation become flattened, and $\left|dk_{\rho}/d\omega\right|$ takes very large values. Therefore, even if inter-film SPhP coupling arises for lower $K$ values, it does not have a significant influence on the near-field thermal radiation spectrum emitted by film 1 at $\Delta << d_c$ as the LDOS is dominated by SPhPs, with small penetration depths, that do not couple with the modes of the non-emitting film.

LDOS profiles are reported in Fig. 4.9 for $t_1$ and $t_3$ fixed respectively at 100 nm and 10 nm, $\Delta$ = 50 nm, and inter-film distances $d_c$ of 50 nm, 70 nm, 100 nm, and 500 nm; results are compared with the case of a single emitting film. Moreover, the TM evanescent component of the monochromatic LDOS per unit wavevector $k_{\rho}$ is reported for the aforementioned configuration with $d_c$ = 50 nm in Fig. 4.10(a), and for $d_c$ = 100 nm in Fig. 4.10(b); SPhP dispersion relations are also plotted in these figures.

In Fig. 4.9, regardless of the value of $d_c$, the maximum LDOS is always located at $\omega_{res}$ since for $\Delta$ = 50 nm, $K_{\max}$ is estimated around 40 where the modes $\omega_2$ and $\omega_3$ have almost reached a plateau. As $d_c$ decreases from 100 nm to 50 nm, LDOS resonance between $\omega_{TO}$ and $\omega_{res}$ shift toward higher frequencies. Indeed, as $d_c$ decreases, coupling between the films becomes stronger and arises for SPhPs with lower penetration depths (i.e., larger $K$ values), such that the resonance shifts toward higher frequencies where $\left|dk_{\rho}/d\omega\right|$ is large.

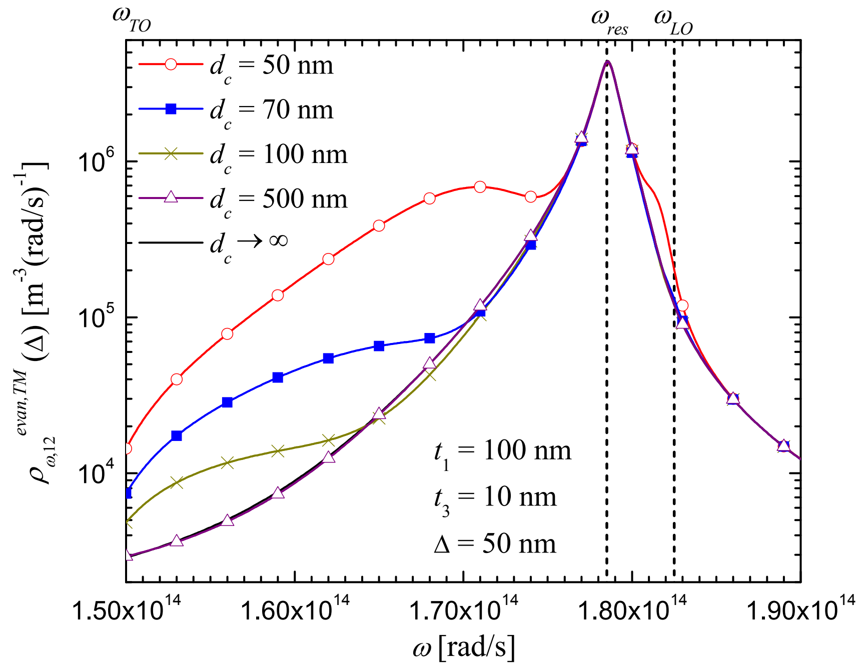

Figure 4.9. TM evanescent component of the monochromatic LDOS in the gap for $t_1$ = 100 nm, $t_3$ = 10 nm, Δ = 50 nm, and $d_c$ = 50 nm, 70 nm, 100 nm, and 500 nm; results are compared with a single 100 nm thick emitting film.

Figure 4.10(a) for $d_c = \Delta$ = 50 nm shows clearly that film 3 enhances near-field radiation emission around the four branches of the dispersion relation. Emission is however much stronger around $\omega_{res}$, where the density of electromagnetic modes is large (i.e., where $\left|dk_\rho / d\omega\right|$ is flat). When $d_c$ increases to 100 nm (Fig. 4.10(b)), the resonance at $\omega_{res}$ is still present, while the enhancement of the LDOS due inter-film coupling has significantly decreased. It is worth noting that $K_{\max}$ estimated using $k_{\rho,\max} \approx \Delta^{-1}$ is smaller than what is shown in Figs. 4.10(a) and 4.10(b). To derive this approximation, we have used the definition of penetration depth of evanescent waves as $\delta_j \approx \left|k_{zj}\right|^{-1}$, which corresponds to the distance from the interface where the field amplitude has decayed by $e^{-1}$ of its value. Therefore, while $k_{\rho,\max} \approx \Delta^{-1}$ combined with SPhP dispersion relations can be used to explain the LDOS profiles, this procedure cannot predict with great accuracy the spectral locations of the resonant modes maximizing the near-field spectrum emitted. This subject is discussed in chapter 5.

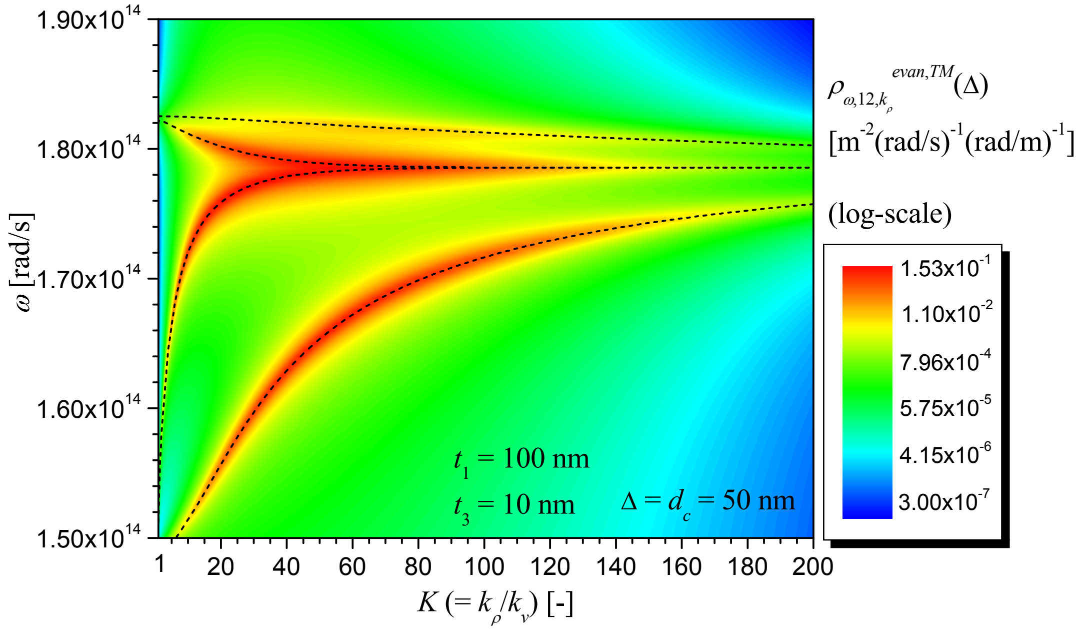

(a)

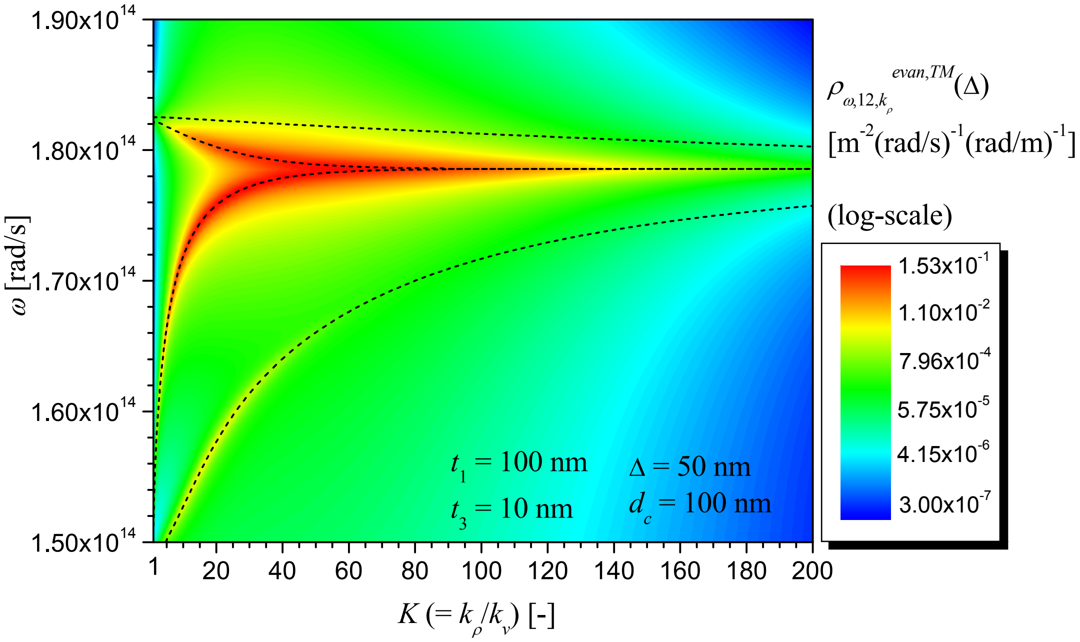

(b)

Figure 4.10. TM evanescent component of the monochromatic LDOS per unit $k_\rho$ (in log-scale) in the gap for $t_1$ = 100 nm, $t_3$ = 10 nm, and Δ = 50 nm: (a) $d_c$ = 50 nm. (b) $d_c$ = 100 nm.

### *4.4.3 Impact of thickness of film 3*

The TM evanescent component of the monochromatic LDOS is shown in Fig. 4.11 for $t_1$ = 10 nm, $\Delta = d_c$ = 100 nm, and varying $t_3$ values of 10 nm, 50 nm, 100 nm, and 500 nm; results are compared with the case when there is no film 3.

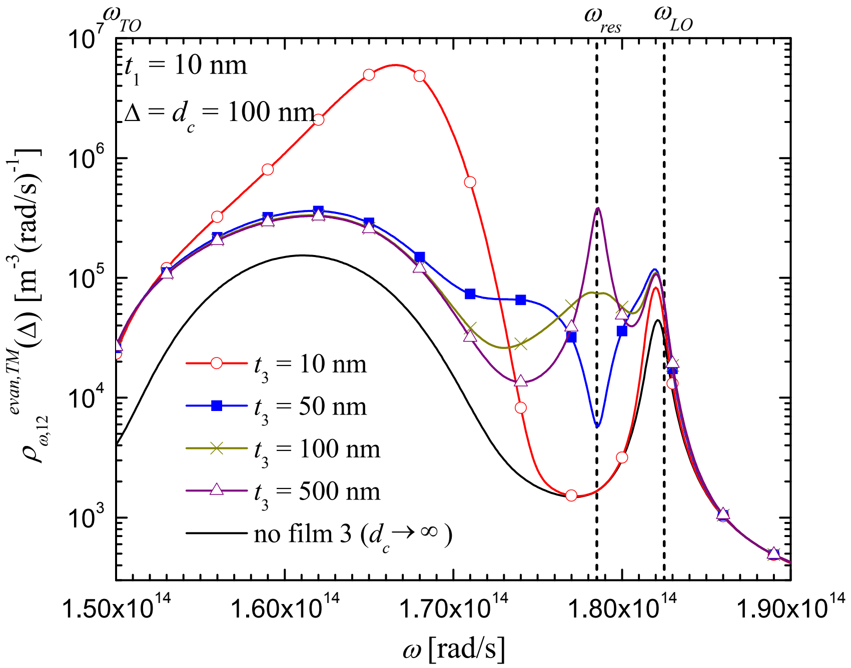

Figure 4.11. TM evanescent component of the monochromatic LDOS in the gap for $t_1$ = 10 nm, $\Delta = d_c$ = 100 nm, and $t_3$ = 10 nm, 50 nm, 100 nm, and 500 nm; results are compared with a single 10 nm thick emitting film.

Regardless of the value of $t_3$, near-field thermal radiation emission is enhanced when film 3 is present compared to the case $d_c \to \infty$. As $t_3$ increases, the spectral distributions of LDOS in TM polarization vary significantly. Indeed, when the thickness of medium 3 increases, the modes $\omega_2$ and $\omega_3$ converge toward $\omega_{res}$ for lower $K$ values, while $\omega_1$ and $\omega_4$ are only slightly affected; this can be seen by comparing SPhP dispersion relations of Figs. 4.2(a) and 4.2(b) for $d_c$ = 100 nm. Therefore, it can be seen in Fig. 4.11 that as $t_3$ increases, the LDOS also increases around $\omega_{res}$. When $t_3$ = 500 nm, a resonant peak clearly emerges at $\omega_{res}$ as the modes $\omega_2$ and $\omega_3$ converge to $\omega_{res}$ for very small $K$ values, since SPhP coupling in a 500 nm thick medium is weak.

### 4.5 Concluding remarks

The physics of near-field thermal radiation emission involving thin films supporting SPhPs has been analyzed in this chapter via computation of the TM evanescent component of the LDOS. It has been shown that the LDOS profiles are significantly affected by the structure of the system, due to SPhP coupling within and between the layers.

Two important conclusions emerge from this analysis. First, it has been shown that near-field thermal radiation emission depends not only on the emitter, but also on the absorber or receiver of thermal radiation. This observation is quite crucial when designing nanoscale-gap thermophotovoltaic devices for example.

Also, the results have suggested that it is possible to tune near-field thermal radiation emission by simply varying the structure of the emitter and the absorber. In this work, the structure is limited to thin films, but the outcome of this chapter suggests that better control over the near-field thermal spectrum emitted could be achieved using complex nanostructures that would suppress / enhance the near-field at selected frequencies.

# Chapter 5

# Near-Field Radiative Heat Transfer between Two Thin Films supporting Surface Phonon-Polaritons

In this chapter, we extend the analysis of chapter 4 by studying the near-field radiative heat flux between two thin films supporting surface phonon-polaritons (SPhPs). The literature regarding near-field radiative heat transfer between thin films supporting surface polaritons is extremely scarce, and is summarized below.

Fu and Tan [110] addressed the problem of radiative heat transfer between two bulks with one of the material coated with a film supporting SPhPs; however, the focus of their study was mainly on the spectrally integrated fluxes, and no discussion of the physics behind this problem was given. In parallel with the work presented in this chapter, Ben-Abdallah et al. [109] investigated near-field radiative heat transfer between two silicon carbide (SiC) films. They showed that the total radiative heat transfer coefficient $h_r$ varies as $d_c^{-2}$, where $d_c$ is the separation gap between the films, when the layers are of the same thicknesses. For films of different thicknesses, the authors reported that $h_r$ varies as $d_c^{-3}$. On the other hand, little information is provided regarding the cross-coupling of SPhPs within and between the films, and on how this complex interaction affects radiant energy exchanges in the near-field.

When tuning near-field thermal emission, the ultimate objective is to deliver the highest possible radiative flux at selected frequencies while reducing the energy transfer at other parts of the spectrum. With this idea in mind, in this chapter, we study the possibility of fine tuning of the spectral distribution of the radiative flux exchanged between two SiC films separated by nanometric distances. We also aim to provide a relatively simple approximate approach to predict the resonant frequencies at which the flux is maximized.

This chapter is structured as follows. A simple and compact analytical expression for the near-field radiative heat flux between two films is presented in terms of film reflection and transmission coefficients, and the consistency of this equation is verified against several simpler cases treated in the literature. Then, an approximate relation is derived to predict resonance of the two film system based on an asymptotic analysis of SPhP dispersion relation. Near-field radiative heat transfer between two SiC films is subsequently studied, and the resonant frequencies at which the flux is maximal are mapped. Finally, the variations of $h_r$ as a function of $d_c$ for two thin films are studied, and the conclusions stated by Ben-Abdallah et al. [109] are revisited.

A part of this chapter was published in the *Journal of Physics D: Applied Physics* in 2010 [105], while preliminary studies were published in *Applied Physics Letters* in 2008 [108].

### 5.1 Analytical expression of the near-field radiative heat flux between two thin films

Near-field radiative heat transfer between two thin films is considered for the geometry, as shown in Fig. 5.1. Again, the assumptions stated in section 3.1 are applicable here. The system is infinite along the $\rho$-direction and azimuthally symmetric, such that only variations of the radiative flux along the $z$-direction need to be accounted for in the analysis. The films of thicknesses $t_1$ and $t_3$, maintained at temperatures $T_1$ and $T_3$, are separated by a gap of length $d_c$.

The monochromatic radiative heat flux at location $z_c$ in layer $l$ due to the emitting film 1 is given by (see section 3.2):

$$q_{\omega,1l}^{tot}(z_c) = \frac{k_v^2 \Theta(\omega,T_1)}{\pi^2} \times \mathrm{Re}\left\{ i\varepsilon''_{r1}(\omega) \int_0^{\infty} k_\rho dk_\rho \int_{z_1}^{z_2} dz' \begin{pmatrix} g_{1l\rho\alpha}^{E}(k_\rho, z_c, z', \omega) g_{1l\theta\alpha}^{H*}(k_\rho, z_c, z', \omega) \\ - g_{1l\theta\alpha}^{E}(k_\rho, z_c, z', \omega) g_{1l\rho\alpha}^{H*}(k_\rho, z_c, z', \omega) \end{pmatrix} \right\} \tag{5.1}$$

where $\alpha$ involves a summation over the three orthogonal components and the superscript *tot* means that contributions from both propagating and evanescent waves are accounted for.

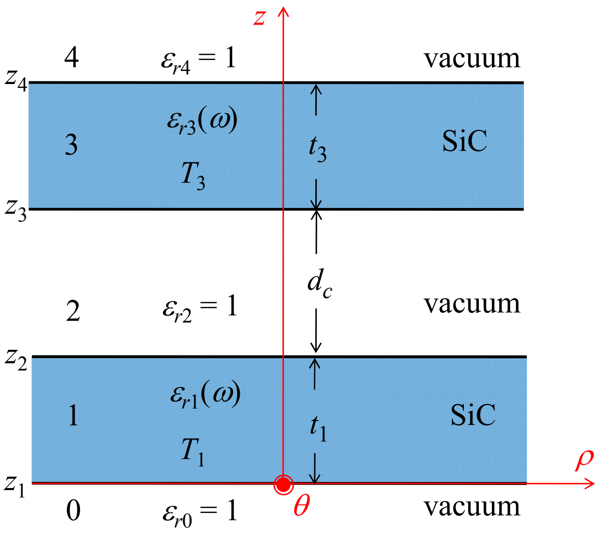
$z$
4
$\varepsilon_{r4} = 1$
vacuum
$z_4$
3
$\varepsilon_{r3}(\omega)$
$T_3$
$t_3$
SiC
$z_3$
$d_c$
2
$\varepsilon_{r2} = 1$
vacuum
$z_2$
1
$\varepsilon_{r1}(\omega)$
$T_1$
$t_1$
SiC
$\rho$
$z_1$
0
$\varepsilon_{r0} = 1$
$\theta$
vacuum

Figure 5.1. Schematic representation of the geometry considered: the radiative heat flux is calculated between two SiC films (media 1 and 3) submerged in vacuum and separated by a gap $d_c$.

The radiative heat flux absorbed by medium 3 is calculated by computing the difference between the flux crossing the interface 2-3 (i.e., $l$ = 3 and $z = z_3^+$), and the flux crossing the interface 3-4 (i.e., $l$ = 4 and $z = z_4^+$). Note that for evanescent waves, the flux in medium 4 is nil since there is no dissipative medium above film 3. An explicit expression for the radiative heat flux between two films can be derived starting with Eq. (5.1) and by using the appropriate Weyl components of the DGF. We report only the final result in this chapter, but the main steps are summarized in appendix F. The propagating and evanescent contributions to the monochromatic radiative heat flux absorbed by layer 3 due to the emitting film 1 at temperature $T_1$ are given by:

$$q_{\omega,abs}^{prop} = \frac{\Theta(\omega,T_1)}{4\pi^2}\int_0^{k_v} k_\rho dk_\rho \sum_{\gamma=TE,TM} \frac{\left(1-\left|R_1^\gamma\right|^2-\left|T_1^\gamma\right|^2\right)\left(1-\left|R_3^\gamma\right|^2-\left|T_3^\gamma\right|^2\right)}{\left|1-R_1^\gamma R_3^\gamma e^{2ik_{z2}d_c}\right|^2} \tag{5.2a}$$

$$q_{\omega,abs}^{evan} = \frac{\Theta(\omega,T_1)}{\pi^2}\int_{k_v}^{\infty} k_\rho dk_\rho e^{-2k''_{z2}d_c} \sum_{\gamma=TE,TM} \frac{\mathrm{Im}(R_1^\gamma)\mathrm{Im}(R_3^\gamma)}{\left|1-R_1^\gamma R_3^\gamma e^{2ik_{z2}d_c}\right|^2} \tag{5.2b}$$

where the superscripts *prop* and *evan* refer to propagating and evanescent waves, respectively, while the subscript *abs* means that the flux absorbed by layer 3 is calculated. The radiative heat flux emitted by medium 3 and absorbed by layer 1 is exactly the same as Eqs. (5.2a) and (5.2b), except that the mean energy of an electromagnetic state, Θ, is calculated at temperature $T_3$. For simplicity, we assume throughout this paper that medium 3 is non-emitting. In Eqs. (5.2a) and (5.2b), $R_j^\gamma$ and $T_j^\gamma$ (resp. $\left|R_j^\gamma\right|^2$ and $\left|T_j^\gamma\right|^2$) represent the reflection and transmission coefficients (resp. reflectance and transmittance) of layer *j* in polarization state *γ*. Their expressions are given by [71]:

$$R_j^\gamma = \frac{r_{j-1,j}^\gamma + r_{j,j+1}^\gamma e^{2ik_{zj}t_j}}{1 + r_{j-1,j}^\gamma r_{j,j+1}^\gamma e^{2ik_{zj}t_j}} \tag{5.3a}$$

$$T_j^\gamma = \frac{t_{j-1,j}^\gamma t_{j,j+1}^\gamma e^{ik_{zj}t_j}}{1 + r_{j-1,j}^\gamma r_{j,j+1}^\gamma e^{2ik_{zj}t_j}} \tag{5.3b}$$

Due to the compact forms of the radiative flux equations, their physical interpretation is quite straightforward. For propagating waves, the term $\left(1-\left|R_j^\gamma\right|^2-\left|T_j^\gamma\right|^2\right)$ in the numerator of Eq. (5.2a) represents the spectral absorptance of film *j*. Since spectral emittance is the same as spectral absorptance, this term can then be seen as the spectral emittance for film 1 and spectral absorptance for layer 3. Similarly, for evanescent waves (Eq. (5.2b)), $\mathrm{Im}(R_j^\gamma)$ can be seen as a spectral near-field emittance / absorptance of film *j*. The evanescent nature of these modes is also explicit via the exponentially decaying term $e^{-2k''_{z2}d_c}$. Finally, both radiative heat flux expressions share the same denominator that accounts for the multiple reflections and wave interference within the two film system.

As for the local density of electromagnetic states (LDOS) discussed in chapter 4, the near-field radiative heat flux between two thin films could have been calculated using the procedure described in chapter 3; the analytical expressions are on the other hand very useful for interpreting the physics of the problem. Note that the radiative heat fluxes obtained by solving Eqs. (5.2a) and (5.2b) are exactly the same as those obtained from the algorithm described in chapter 3, as it should be.

## 5.2 Convergence of radiative flux for different near-field thermal radiation regimes

The correctness of the radiative heat flux expressions between two thin films derived in this chapter is verified hereafter by analyzing different near-field thermal radiation regimes previously addressed in the literature. They are discussed below for different cases.

### *5.2.1 Near-field radiative transfer between a bulk and a film*

We first consider the case of a thick emitter (i.e., bulk), such that $t_1 \to \infty$. For purpose of comparison with the literature, only the radiative flux at $z = z_3^+$ is calculated, which implies that $\left|T_3^\gamma\right|^2$ in Eq. (5.2a) can be removed (see Eq. (F.11) in appendix F). For the particular case of a bulk emitter, both exponential terms contained in $T_1^\gamma$ and $R_1^\gamma$, namely $e^{ik_{z1}t_1}$ (= $e^{ik'_{z1}t_1}e^{-k''_{z1}t_1}$) and $e^{2ik_{z1}t_1}$ (= $e^{2ik'_{z1}t_1}e^{-2k''_{z1}t_1}$), tend to zero as $t_1 \to \infty$. Therefore, $T_1^\gamma \to 0$, while the reflection coefficient can be written as $R_1^\gamma \to r_{21}^\gamma$; note that we used the fact that $r_{01}^\gamma = r_{21}^\gamma$ in this last expression. By substituting these terms into Eqs. (5.2a) and (5.2b), the following expressions for the monochromatic radiative heat flux between a bulk emitter (medium 1) and a film (medium 3) are determined:

$$q_{\omega,13}^{prop}(z_3^+) = \frac{\Theta(\omega,T_1)}{4\pi^2}\int_0^{k_v} k_\rho dk_\rho \sum_{\gamma=TE,TM} \frac{\left(1-\left|r_{21}^\gamma\right|^2\right)\left(1-\left|R_3^\gamma\right|^2\right)}{\left|1-r_{21}^\gamma R_3^\gamma e^{2ik_{z2}d_c}\right|^2} \tag{5.4a}$$

$$q_{\omega,13}^{evan}(z_3^+) = \frac{\Theta(\omega,T_1)}{\pi^2}\int_{k_v}^{\infty} k_\rho dk_\rho e^{-2k''_{z2}d_c} \sum_{\gamma=TE,TM} \frac{\mathrm{Im}(r_{21}^\gamma)\,\mathrm{Im}(R_3^\gamma)}{\left|1-r_{21}^\gamma R_3^\gamma e^{2ik_{z2}d_c}\right|^2} \tag{5.4b}$$

The above equations are the same as those reported previously by Biehs [107] for calculating the radiative heat flux between a bulk and a material coated with a thin film.

### *5.2.2 Near-field radiative transfer between two bulks*

Consistency of Eqs. (5.2a) and (5.2b) is next verified against the well known result of near-field radiative heat flux between two bulks. The analysis presented in section 5.2.1 is still applicable to film 1, and we now have to account for the fact that $t_3 \to \infty$, such that $T_3^\gamma \to 0$ and $R_3^\gamma \to r_{23}^\gamma$ . Then, Eqs. (5.2a) and (5.2b) reduce to:

$$q_{\omega,abs}^{prop} = q_{\omega,13}^{prop}(z_3^+) = \frac{\Theta(\omega,T_1)}{4\pi^2}\int_0^{k_v} k_\rho dk_\rho \sum_{\gamma=TE,TM} \frac{\left(1-\left|r_{21}^\gamma\right|^2\right)\left(1-\left|r_{23}^\gamma\right|^2\right)}{\left|1-r_{21}^\gamma r_{23}^\gamma e^{2ik_{z2}d_c}\right|^2} \tag{5.5a}$$

$$q_{\omega,abs}^{evan} = q_{\omega,13}^{evan}(z_3^+) = \frac{\Theta(\omega,T_1)}{\pi^2}\int_{k_v}^{\infty} k_\rho dk_\rho e^{-2k''_{z2}d_c} \sum_{\gamma=TE,TM} \frac{\mathrm{Im}(r_{21}^\gamma)\,\mathrm{Im}(r_{23}^\gamma)}{\left|1-r_{21}^\gamma r_{23}^\gamma e^{2ik_{z2}d_c}\right|^2} \tag{5.5b}$$

which is in perfect agreement with the expressions reported in section 3.5.2 (see Eqs. (3.46a) and (3.46b)).

### *5.2.3 Thermal radiation emission by a single film*

We can calculate the radiative heat flux from a single film (medium 1) by assuming that there is no film 3. Then, Eq. (5.2a) is modified as:

$$\begin{aligned} q_{\omega,12}^{prop}(z_2^+) &= \frac{\Theta(\omega,T_1)}{4\pi^2}\int_0^{k_v} k_\rho dk_\rho \sum_{\gamma=TE,TM}\left(1-\left|R_1^\gamma\right|^2-\left|T_1^\gamma\right|^2\right) \\ &= \frac{\Theta(\omega,T_1)}{4\pi^2}\int_0^{k_v} k_\rho dk_\rho \sum_{\gamma=TE,TM} \frac{\left(1-\left|r_{21}^\gamma\right|^2\right)a^\gamma - 4\,\mathrm{Im}(r_{21}^\gamma)b^\gamma}{\left|1-(r_{21}^\gamma)^2 e^{2ik_{z1}t_1}\right|^2} \end{aligned} \tag{5.6}$$

where the last term on the right-hand side of the above expression has been obtained according to Eq. (F.7a). The terms $a^\gamma$ and $b^\gamma$ are given respectively by Eqs. (F.6a) and (F.6b) in appendix F. Equation (5.6) for the radiative heat flux of a thin film submerged in vacuum is exactly the same as the expression reported by Biehs et al. [106]. Note that Biehs et al. give an expression for the evanescent component of the radiative heat flux; however, inspection of this equation (Eq. (47) in [106]) shows that the flux is equal to zero, as it should be, since the real part of the *z*-component of the wavevector in vacuum is zero for evanescent modes.

### 5.3 Asymptotic analysis of surface phonon-polariton dispersion relation

SiC supports SPhPs in the infrared region, such that these resonant electromagnetic surface modes can be easily thermally excited. As a consequence, the near-field radiative heat flux between two SiC bulks separated by a vacuum gap is quasi-monochromatic around the resonant frequency of a SiC-vacuum interface ($1.786 \times 10^{14}$ rad/s), referred hereafter as $\omega_{res}$. The situation is quite different for emitting thin films, as discussed in chapter 4. Since the evanescent wave fields of the surface polaritons decay both in the vacuum and the material, SPhPs associated with each interface can couple within the layer, thus leading to a splitting of the single resonance into anti-symmetric $\omega^{+}$ and symmetric $\omega^{-}$ modes. Similar to $\omega_{res}$, the mode $\omega^{+}$ exhibits a high degree of spectral coherence, which implies that a large number of electromagnetic states are concentrated in a narrow spectral band. Conversely, the mode $\omega^{-}$ induces a loss of spectral coherence, when compared to $\omega_{res}$, due to higher losses in SiC [124].

In this chapter, we are dealing with two SiC films that are separated by a sub-wavelength distance. In that case, further SPhP coupling takes place between the layers, and four resonant modes develop, as explained in section 4.2. In the previous chapter, we studied the effect of the presence of a non-emitting film in close proximity of an emitting thin layer by calculating the LDOS within the vacuum gap separating the two media. We found that the presence of the non-emitting film enhances near-field thermal radiation emission at selected frequencies, perturbs the spectral coherence of the modes, and slightly shifts the resonant peaks. These effects are strongly correlated to the parameters $t_1$, $t_3$, and $d_c$. The objective here is to provide an approximate correlation between these aforementioned parameters and the resonant frequencies maximizing the radiative flux between two films.

SPhPs exist only in TM polarization for nonmagnetic media [11,50]. Inspection of Eq. (5.2b) shows that the radiative heat flux diverges when the following condition is fulfilled:

$$1 - R_1^{TM} R_3^{TM} \exp(2ik_{z2}d_c) = 0 \tag{5.7}$$

Note that the above condition is, as expected, exactly the same as the one for the resonance of the LDOS between two films (see Eq. (4.7)). Dispersion relations of the cross-coupled SPhP modes for two SiC films, determined by solving Eq. (5.7), were discussed in great details in section 4.2. For evanescent waves with $k_\rho >> k_v$, the $z$-component of the wavevector in medium $j$ can be approximated by $k_{zj} \approx ik_\rho$. This approximation can then be substituted, along with the dielectric function of polar crystal given in appendix B, into Eq. (5.7). Solving for the frequency, the following relation is obtained:

$$\omega_{\psi^\pm}^{\pm} \approx \left[ \frac{\varepsilon_\infty \omega_{LO}^2 + \omega_{TO}^2 \mp (1/\psi^\pm)(\omega_{TO}^2 - \varepsilon_\infty \omega_{LO}^2)}{\varepsilon_\infty + 1 \mp (1/\psi^\pm)(1 - \varepsilon_\infty)} \right]^{1/2} \tag{5.8}$$

where $\psi^\pm = \sqrt{(-h_2 \pm \sqrt{h_2{}^2 - 4h_1h_3})/2h_1}$ and

$$h_1 = e^{k_\rho(d_c - t_1 - t_3)} \tag{5.9a}$$

$$h_2 = e^{k_\rho(-d_c - t_1 + t_3)} + e^{k_\rho(-d_c + t_1 - t_3)} - e^{k_\rho(d_c - t_1 + t_3)} - e^{k_\rho(d_c + t_1 - t_3)} - e^{k_\rho(-d_c - t_1 - t_3)} - e^{k_\rho(-d_c + t_1 + t_3)} \tag{5.9b}$$

$$h_3 = e^{k_\rho(d_c + t_1 + t_3)} \tag{5.9c}$$

where the losses are neglected in the dielectric function. Equation (5.8) provides an approximation of the four resonant modes of the two film system as a function of $t_1$, $t_3$, $d_c$ and $k_\rho$. Hereafter, the frequencies $\omega_{\psi^-}^-$, $\omega_{\psi^+}^-$, $\omega_{\psi^+}^+$, and $\omega_{\psi^-}^+$ are referred respectively as $\omega_1$, $\omega_2$, $\omega_3$, and $\omega_4$, where $\omega_1$ correspond to the lowest frequency polariton mode, while $\omega_4$ is the highest frequency mode (see Figs. 4.2(a) and 4.2(b)).

The idea with Eq. (5.8) is to determine, in an approximate manner, the resonant frequencies at which the radiative heat flux between two films is maximal. Such approximation can be performed by calculating Eq. (5.8) at the largest contributing parallel wavevector to the radiative flux, $k_{\rho,\max}$. The rationale behind this assumption was explained in section 4.3. As for the case of the LDOS, a distinction is made between the resonant modes for the two film system and the "resonance of the flux" (i.e., spectral zones where the flux is maximal). The resonance of the two film system occurs at all frequencies along the branches of SPhP dispersion relation, while for simplicity the "resonance of the flux" designation will refer here to resonant frequencies corresponding to $k_{\rho,\max}$ where $\left|dk_\rho / d\omega\right|$ is the highest.

The task is now to determine this limiting $k_{\rho,\max}$, which will be discussed in greater details in section 5.5. Meanwhile, as a first order approximation, the definition of penetration depth of evanescent waves in vacuum ($\delta_2 \approx \left|k_{z2}\right|^{-1}$) can be used to argue that only evanescent waves with $\delta_2 \geq d_c$ can contribute to the radiative heat exchanges between layers 1 and 3. Combining $\delta_2 \approx \left|k_{z2}\right|^{-1}$ with $k_{z2} \approx ik_\rho$, as done before, the largest contributing wavevector to the radiative heat flux can be approximated as $k_{\rho,\max} \approx d_c^{-1}$.

In the case that film 3 is removed, Eq. (5.8) is still valid if $\psi^{\pm}$ is replaced by $e^{k_\rho t_1}$, thus giving an approximation of the anti-symmetric $\omega^+$ and symmetric $\omega^-$ resonances of the fields calculated above a film of thickness $t_1$ (same as Eq. (4.8)), showing clearly the consistency of Eq. (5.8)

## 5.4 Spectral distribution of radiative heat flux near surface phonon-polariton resonance

Spectral distributions of radiative heat flux, including contributions from TM- and TE-polarized waves as well as propagating and evanescent modes (i.e., sum of Eqs. (5.2a) and (5.2b)), are reported. Only layer 1, with $T_1$ = 300 K, is emitting. It is worth noting that the spectral distributions of radiative heat flux reported in this section are also applicable if the temperature of film 3 is greater than 0 K. As mentioned in section 5.1, the radiative heat flux absorbed by layer 1 due to the emitting medium 3 is also given by Eqs. (5.2a) and (5.2b), except that the mean energy of a state $\Theta$ is calculated at $T_3$ instead of $T_1$. The flux profiles are reported hereafter in the spectral band from $1.5\times10^{14}$ rad/s to $1.9\times10^{14}$ rad/s where SPhPs dominate near-field radiant energy exchanges. Therefore, the spectral shapes of the flux are dominated by the high LDOS introduced by the SPhPs, and consequently, the spectral distribution of $\Theta$ does not affect in a perceptible manner the flux profiles.

Radiative flux profiles are shown in Fig. 5.2 for two SiC films of equal thicknesses (10 nm) separated by distances $d_c$ of 1 nm, 10 nm, 50 nm, 100 nm and 500 nm.

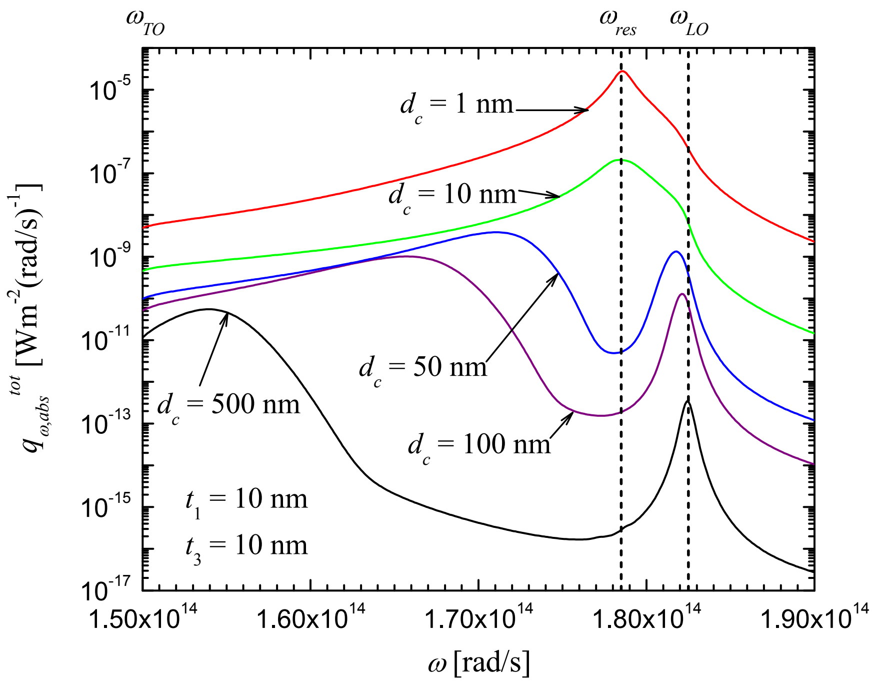

Figure 5.2. Spectral distribution of radiative heat flux absorbed by layer 3 ($T_3$ = 0 K) due to an emitting film 1 ($T_1$ = 300 K): $t_1 = t_3$ = 10 nm, $d_c$ = 1 nm, 10 nm, 50 nm, 100 nm and 500 nm.

As expected, the spectral distribution of radiative flux, dominated by the TM evanescent component, is highly dependent on the thickness of the vacuum gap $d_c$. As discussed in section 5.1, the term $\mathrm{Im}(R_1^{TM})$ can be seen as the near-field spectral emittance of film 1 in TM polarization. By considering solely the emitting film 1, when the ratio $t_1/d_c$ is equal or less than unity, the near-field spectrum is expected to split into two resonant modes, as discussed in section 4.3. Similarly, $\mathrm{Im}(R_3^{\gamma})$ has been interpreted as the spectral absortance of film 3. Since spectral absorption is equivalent to spectral emission, then, the splitting of the resonant frequencies maximizing radiation absorption can also be analyzed via the ratio $t_3/d_c$. In Fig. 5.2, both films are of same thicknesses, such that the spectral bands of high radiation emission match those of high absorption ($\mathrm{Im}(R_1^{\gamma})$ =

$\text{Im}(R_3^\gamma)$). It can be seen in Fig. 5.2 that for $t_1/d_c$ (= $t_3/d_c$) < 1, the maximum flux at $\omega_{res}$ split into two modes approaching $\omega_{LO}$ and $\omega_{TO}$ as $t_1/d_c$ (= $t_3/d_c$) decreases. However, for $t_1/d_c$ (= $t_3/d_c$) = 1, the flux is still concentrated around $\omega_{res}$, while for a single emitting film, the splitting of the resonance occurs. Indeed, assuming that the frequencies leading to maximum emission and absorption are exactly the same is not correct, as SPhPs couple between the films, thus disrupting this otherwise perfect symmetry. The perturbation of resonances of absorption and emission is mathematically described in Eq. (5.2b) by the term $\left|1 - R_1^\gamma R_3^\gamma e^{2ik_{z2}d_c}\right|^2$. The effect of SPhP coupling between the films can be better understood by analyzing the TM evanescent component of the monochromatic radiative heat flux per unit $k_\rho$, as presented in Fig. 5.3(a) for $d_c$ = 10 nm, and in Fig. 5.3(b) for $d_c$ = 100 nm. In both cases, SPhP dispersion relations for the two film configuration, for a single 10 nm thick SiC film, and a single SiC-vacuum interface are shown.

First, it can be seen in Figs. 5.3(a) and 5.3(b) that inter-film coupling mostly affect the symmetric resonance $\omega^-$, while the anti-symmetric one $\omega^+$ is still concentrated in a narrow spectral band. This leads to spectrally larger resonances for the radiative flux when compared to the near-field spectrum emitted by a single film. For $d_c$ = 10 nm, the largest contributing $K_{\max}$ (= $k_{\rho,\max}/k_v$) value to the flux is estimated to be 200 using $k_{\rho,\max} \approx d_c^{-1}$. At such large $K$ values, $\omega_2$ and $\omega_3$ have almost reached a plateau (near $\omega_{res}$) where $\left|dk_\rho/d\omega\right|$ is large. Consequently, even if the modes below $K_{\max} \approx 200$ contribute to radiant energy transfer, the flux is the highest around $\omega_{res}$ where a large number of electromagnetic states are available in a narrow spectral band. In that sense, Fig. 5.2 shows that for a smaller vacuum gap $d_c$ of 1 nm, the flux at $\omega_{res}$ is sharper than for $d_c$ = 10 nm, due to the fact that as $d_c$ decreases, the value of the largest contributing $K_{\max}$ increases where $\omega_1$, $\omega_2$, $\omega_3$, and $\omega_4$ are closer to $\omega_{res}$ than for $d_c$ = 10 nm despite stronger SPhP inter-film coupling. Moreover, due to inter-film coupling, $\omega_2$ and $\omega_3$ for $d_c$ = 10 nm are closer to $\omega_{res}$ than $\omega^-$ and $\omega^+$, which can explain why the splitting of the resonance can be seen when $t_1/d_c$ = 1 for a single emitting film, and not on the flux profile when $t_1/d_c$ = $t_3/d_c$ = 1. This discussion is in line with the remark made in section 5.3. Although the entire four branches of SPhP dispersion relation are the resonant modes for the two film

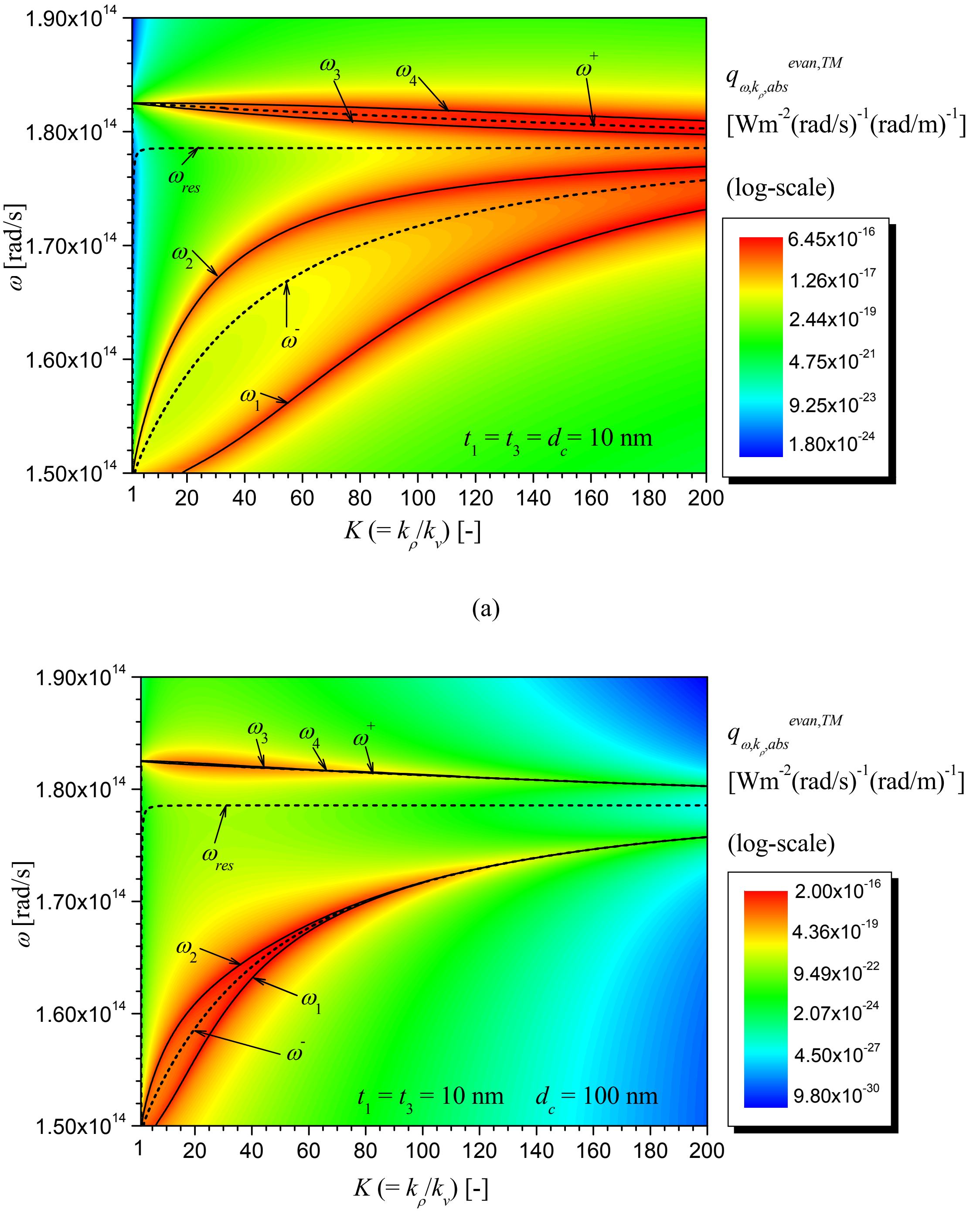

(a)

(b)

Figure 5.3. Spectral distribution of TM evanescent radiative heat flux per unit $k_\rho$ (in log-scale) absorbed by medium 3 ($T_3$ = 0 K) due to an emitting film 1 ($T_1$ = 300 K): (a) $t_1 = t_3 = d_c$ = 10 nm. (b) $t_1 = t_3$ = 10 nm and $d_c$ = 100 nm. SPhP dispersion relations for two films (full lines), a single film (dashed lines), and a single interface (dashed line) are shown for comparison.

system, the maximal radiative heat flux (called here resonance of the flux) occurs at the frequencies of the SPhP dispersion relation where $\left|dk_\rho / d\omega\right|$ is the highest, which is generally at $k_{\rho,\max}$.

For $d_c$ = 100 nm (Fig. 5.3(b)), $\omega^+$ is almost not affected by inter-film coupling, such that the resonance of the flux close to $\omega_{LO}$ occurs in a small spectral band, which becomes narrower as $d_c$ increases, since inter-film coupling has a decreasing influence on SPhP dispersion relation. Using $k_{\rho,\max} \approx d_c^{-1}$, the value of $K_{\max}$ is estimated to be around 20. Inspection of SPhP dispersion relation in Fig. 5.3(b) shows clearly for such a low value, the modes have not converge at $\omega_{res}$, thus explaining why two resonances are observed on the flux profile shown in Fig. 5.2. It is important to note that modes with larger $K$ than $K_{\max}$ determined via $k_{\rho,\max} \approx d_c^{-1}$ contribute to the flux. This will be discussed in section 5.5.

In Fig. 5.2, for $d_c$ values of 50 nm, 100 nm, and 500 nm, while the radiative heat flux is quite large between $\omega_{TO}$ and $\omega_{res}$, it does not result in a clear peak as $\omega_1$ and $\omega_2$ spread out over a large spectral band without reaching a plateau. Despite this, it is interesting to note that for the aforementioned gap thicknesses, the strength of the flux is always higher between $\omega_{TO}$ and $\omega_{res}$ than between $\omega_{res}$ and $\omega_{LO}$; for $d_c$ = 500 nm, the resonance near $\omega_{TO}$ is about two orders of magnitude larger than the mode at $\omega_{LO}$. This can be explained by the fact that in the spectral band between $\omega_{TO}$ and $\omega_{res}$, the imaginary part of the dielectric function of SiC takes high values, especially near $\omega_{TO}$. This, therefore, implies that both emission by film 1 and absorption by layer 3 is large in that spectral range, resulting in a higher radiative heat flux, which is apparent only on the flux profiles when $t_1/d_c$ (= $t_3/d_c$) is small enough such that $\omega_1$ to $\omega_4$ have not merged into $\omega_{res}$.

Next, we study the effect of varying the thickness of one film relative to another for a fixed $d_c$. Due to the equivalence between spectral emission and absorption, variation of $t_1$ relative to $t_3$ or $t_3$ relative to $t_1$ leads to the same radiative heat flux profiles. Therefore, spectral distributions of radiative flux for an emitter of fixed thickness $t_1$ = 10 nm are shown in Fig. 5.4 for $d_c$ = 100 nm and $t_3$ = 10 nm, 50 nm, 100 nm and 500 nm.

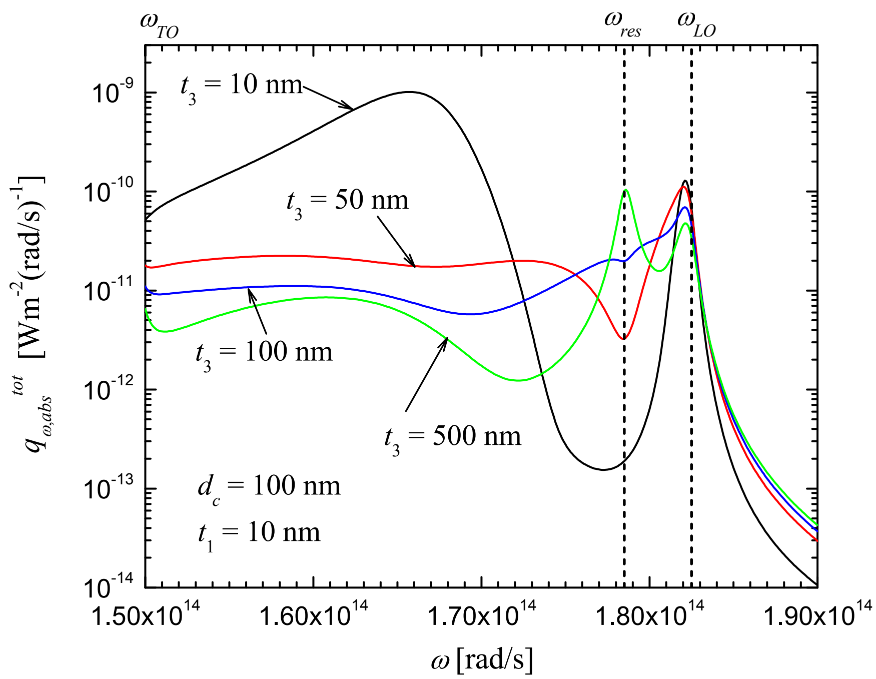

Figure 5.4. Spectral distribution of radiative heat flux absorbed by layer 3 ($T_3$ = 0 K) due to an emitting film 1 ($T_1$ = 300 K): $t_1$ =10 nm, $d_c$ = 100 nm, $t_3$ = 10 nm, 50 nm, 100 nm and 500 nm.

Spectral distributions of radiative heat flux shown in Fig. 5.4 are highly dependent on the thickness of medium 3. For a single 10 nm thick film emitting in vacuum, the resonance of the near-field spectrum emitted is split into two distinct frequencies (lower and higher than $\omega_{res}$) since $t_1/d_c < 1$. When considering the full system, the resonant frequencies maximizing emission and absorption are close to each other when $t_3$ = 10 nm. As $t_3$ increases, SPhP coupling within medium 3 decreases such that the resonant frequencies of high radiation absorption converge toward $\omega_{res}$. Therefore, by increasing $t_3$ relative to $t_1$, the original small mismatch between the resonant frequencies of maximum radiation emission and absorption for $t_1 = t_3$, solely due to inter-film coupling, becomes more pronounced thus altering significantly the radiant energy exchanged between the two films. This behavior can be better observed by analyzing the TM evanescent component of the flux per unit $k_\rho$, as shown in Fig. 5.5(a) for $t_3$ = 50 nm and Fig. 5.5(b) for $t_3$ = 500 nm. Again, SPhP dispersion relations for the two film system, as well as dispersion relations for single films in vacuum and a SiC-vacuum interface are shown.

When medium 3 is 50 nm thick (Fig. 5.5(a)), the modes $\omega_1$ and $\omega_2$ are relatively far from each other, thus resulting in a spectral distribution of radiative flux that is almost flat between $\omega_{TO}$ and $\omega_{res}$. The loss of spectral coherence near $\omega_{LO}$ observed in Fig. 5.4 for $t_3$ = 50 nm can also be seen in Fig. 5.5(a) where $\omega_3$ and $\omega_4$ clearly decouple as compared to the case $t_3$ = 10 nm (see Fig. 5.3(b)). As $t_3$ increases relative to $t_1$, the modes $\omega_1$ and $\omega_4$ are only slightly affected solely due to perturbations of SPhP inter-film coupling. When medium 3 is 500 nm thick, $\omega_2$ and $\omega_3$ merge into $\omega_{res}$ for very low $K$ values, such that high radiation absorption occurs at this frequency, resulting in a clear resonance of the flux around $\omega_{res}$. At the same time, two other maxima are observed, near $\omega_1$ and $\omega_4$, as near-field thermal radiation emission by film 1 is high around these modes. However, the highest radiative heat flux is at $\omega_{res}$, where the density of electromagnetic states is the largest.

The spectral distributions of radiative heat flux shown in Figs. 5.2 and 5.4 share similarities with the LDOS profiles calculated just below the interface 2-3, as reported in section 4.4. In the former case, the perturbation of the near-field spectrum emitted by layer 1 was attributed to SPhP coupling between the films, and was mathematically translated by an extraneous term accounting for the modification of thermal emission by film 1. In an equivalent way, the flux results are interpreted here by defining resonant frequencies maximizing absorption. Therefore, the presence of film 3 above film 1 introduce new resonances on the radiative heat flux profiles that cannot be observed for a single emitting film, as layer 3 introduces zones of high radiation absorption.

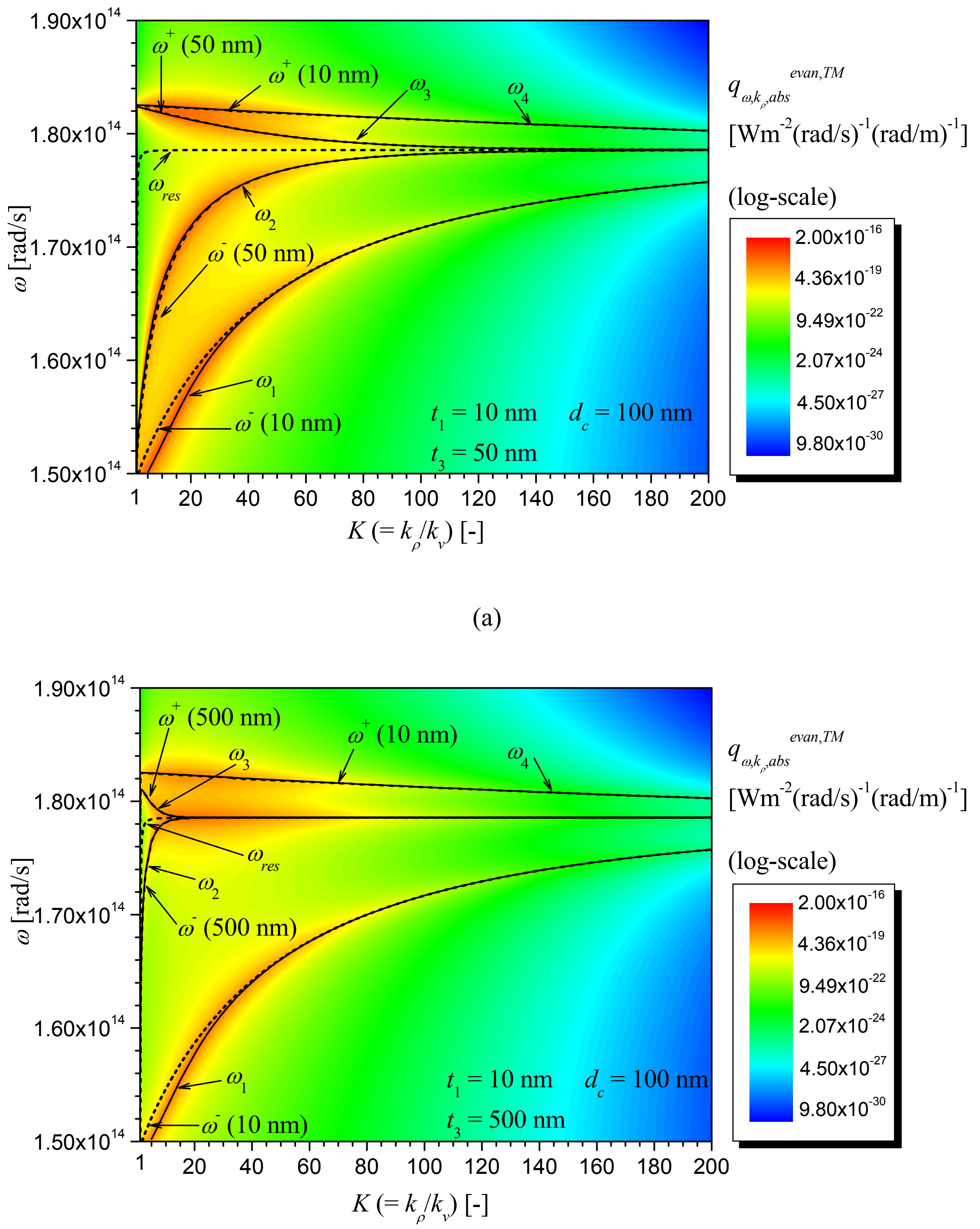

(a)

(b)

Figure 5.5. Spectral distribution of TM evanescent radiative heat flux per unit $k_\rho$ (in log-scale) absorbed by medium 3 ($T_3$ = 0 K) due to an emitting film 1 ($T_1$ = 300 K): (a) $t_1$ = 10 nm, $t_3$ = 50 nm, and $d_c$ = 100 nm. (b) $t_1$ = 10 nm, $t_3$ = 500 nm, and $d_c$ = 100 nm. SPhP dispersion relations for two films (full lines), single films (dashed lines), and a single interface (dashed line) are shown for comparison.

## 5.5 Approximate predictions of resonant frequencies maximizing the radiative heat flux

It is possible, using Eq. (5.8), to map the resonant frequencies $\omega_{1,\max}$, $\omega_{2,\max}$, $\omega_{3,\max}$, and $\omega_{4,\max}$ maximizing the radiative flux as a function of $t_1/d_c$ and $t_3/d_c$. Such mapping is thus applicable to any $t_1$, $t_3$, and $d_c$ values. We used earlier the approximation $k_{\rho,\max} \approx d_c^{-1}$ to determine the value of the largest contributing parallel wavevector to the flux. In section 5.4, for $d_c$ = 100 nm, we estimated $K_{\max}$ to be around 20, while Fig 5.3(b) showed clearly that modes with much larger $K$ contribute to the flux. When deriving this approximation, we used $\delta_j \approx |k_{zj}|^{-1}$ to describe the spatial extent of an evanescent wave, which corresponds to the distance from the interface where the field amplitude has decayed by $e^{-1}$ of its value, since the evanescent field in medium $j$ is proportional to $e^{|k_{zj}|z}$.

In order to perform a better estimation of $k_{\rho,\max}$, determination of the spatial extent of the evanescent wave along $z$ needs to be revisited. This has been done by defining $\delta_j$ values corresponding to the distance from the interface where the field amplitude has decayed by 80%, 90%, 95%, and 99% of its original value. By comparing $\omega_{1,\max}$, $\omega_{2,\max}$, $\omega_{3,\max}$, and $\omega_{4,\max}$ predictions calculated via Eq. (5.8) with the flux profiles of Figs. 5.2 and 5.4, we found that the best match occurs when the 90% criterion is used, such that the penetration depth of evanescent wave in vacuum is estimated as $\delta_2 \approx \ln(10)|k_{z2}|^{-1}$.

To verify the accuracy of this approximate approach, the evolution of the resonant frequencies maximizing the flux, $\omega_{1,\max}$, $\omega_{2,\max}$, $\omega_{3,\max}$, and $\omega_{4,\max}$, predicted via Eq. (5.8) is shown in Fig. 5.6(a) as a function of $t_1/d_c = t_3/d_c$ (it corresponds to the case of Fig. 5.2), while Fig. 5.6(b) shows these frequencies as a function of $t_3/d_c$ for a fixed $t_1/d_c = 0.1$ (it corresponds to the case of Fig. 5.4). In both figures, predictions using $\delta_2 \approx \ln(10)|k_{z2}|^{-1}$ (full lines) are compared with those using $\delta_2 \approx |k_{z2}|^{-1}$ (dashed lines).

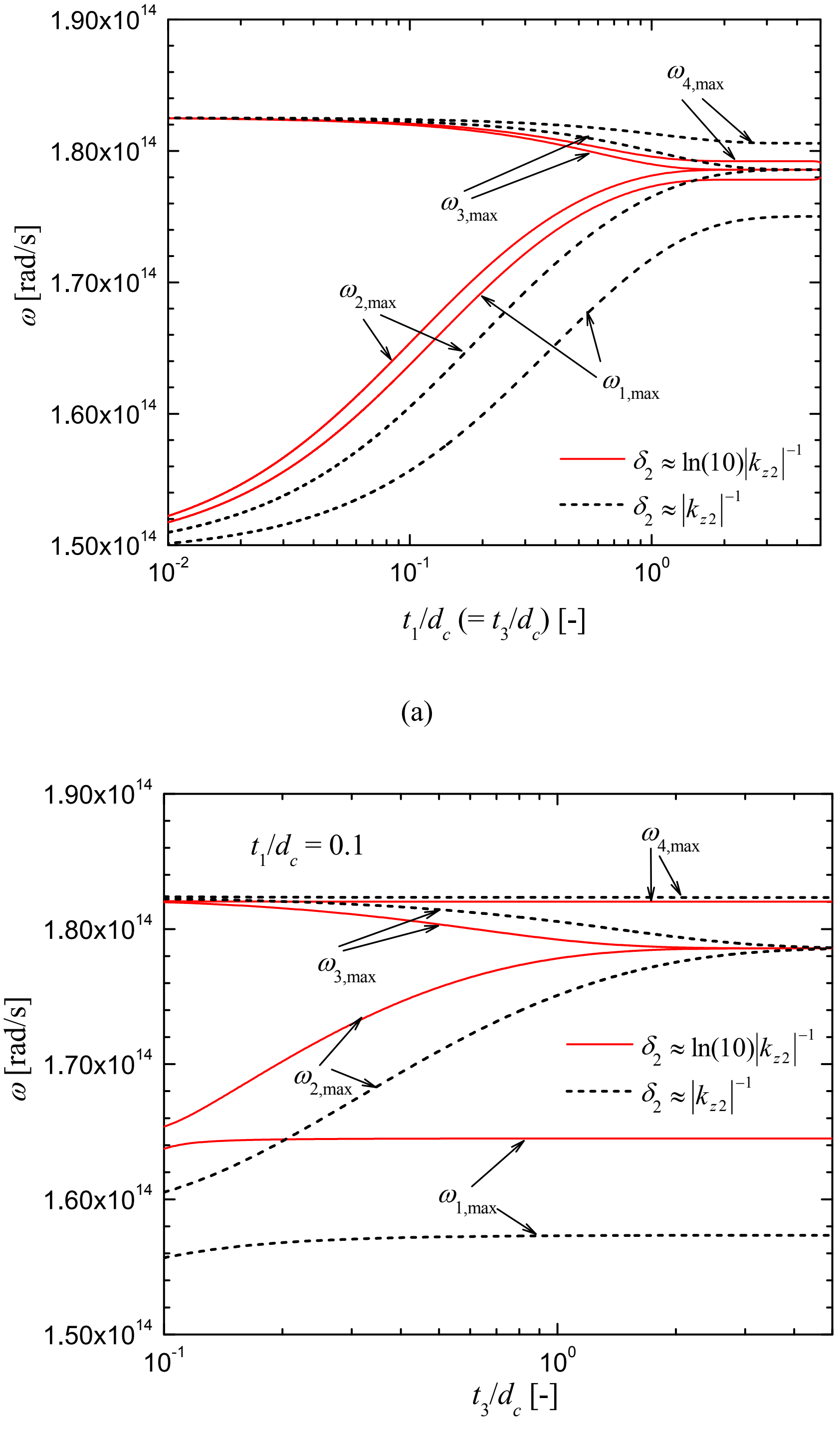

(a)

(b)

Figure 5.6. Approximate predictions of SPhP resonant frequencies for a system of two SiC films submerged in vacuum: (a) variation of $t_1/d_c = t_3/d_c$. (b) $t_1/d_c$ is fixed at 0.1, while $t_3/d_c$ varies. Predictions are made by assuming $\delta_2 \approx \ln(10)\left|k_{z2}\right|^{-1}$ (full lines) and $\delta_2 \approx \left|k_{z2}\right|^{-1}$ (dashed lines).

We consider the case $t_1 = t_3 = d_c = 10$ nm in Fig. 5.2. In Fig. 5.6(a), when $\delta_2 \approx \ln(10)|k_{z2}|^{-1}$, the four modes are split, but very close to $\omega_{res}$. This is in good agreement with the flux profile shown in Fig. 5.2, where the resonance concentrated around $\omega_{res}$ is not as sharp as for $d_c = 1$ nm. When $\delta_2 \approx |k_{z2}|^{-1}$ is used, the resonant modes are too far from $\omega_{res}$, especially $\omega_{1,\max}$ and $\omega_{4,\max}$, such that the criterion $\delta_2 \approx \ln(10)|k_{z2}|^{-1}$ definitely provides a better approximation. In a general manner, the resonant frequencies at which the flux is maximal are correctly predicted for the case of Fig. 5.2 when comparing the spectral distribution of radiative heat with the curves shown in Fig. 5.6(a).

In Fig. 5.6(b), only the ratio $t_3/d_c$ varies (with fixed $t_1/d_c = 0.1$), such that the modes $\omega_{1,\max}$ and $\omega_{4,\max}$, always associated to the thinner film, are nearly constant; the slight variations of $\omega_{1,\max}$ and $\omega_{4,\max}$ are only due to perturbations of inter-film coupling as $t_3$ increases. Comparison of Figs. 5.4 and 5.6(b) reveal that although resonance of the flux is predicted for a $\omega_{1,\max}$ value around $1.645 \times 10^{14}$ rad/s for $t_3 = 50$ nm, 100 nm, and 500 nm, the flux is almost flat. This shows that care must be taken when making predictions with Eq. (5.8), especially between $\omega_{TO}$ and $\omega_{res}$. Indeed, since the low frequency modes spread out over multiple frequencies, it is difficult to define a specific frequency region where resonance of the flux is the largest since the branches of SPhP dispersion relation never reach a plateau (see Figs. 5.5(a) and 5.5(b)). However, as $t_3/d_c$ increases, the proximity of $\omega_{2,\max}$ and $\omega_{3,\max}$ allows one to guess that the radiative heat flux increases around $\omega_{res}$, and eventually becomes a strong resonance for a sufficiently large $t_3/d_c$ value.

Therefore, Eq. (5.8) should be used with some *a priori* knowledge of the system under study, such as surface polariton dispersion relation on a single interface. It is also worth noting that as $d_c$ increases, $k_{\rho,\max}$ decreases and the approximation $k_{zj} \approx ik_\rho$ becomes less accurate. This is especially true near $\omega_{TO}$ where the magnitude of the real part of the dielectric function of SiC takes very large values. Nevertheless, despite the aforementioned limitations, the approximate method for predicting the resonant frequencies at which the flux is maximal can be useful when designing near-field thermal radiation spectra, and could also be extended to systems involving multiple thin films.

Based on Figs. 5.2 and 5.6(a), for two films of equal thicknesses, the splitting of the resonance can be seen on the radiative heat flux profile when $t_1/d_c$ (= $t_3/d_c$) is less than unity. When splitting occurs, two distinct modes develop; these modes are less coherent than the fields emitted by a single emitting layer, as SPhP inter-film coupling splits the dispersion relation into four branches. The mode between $\omega_{TO}$ and $\omega_{res}$ is mostly affected by inter-film coupling, while the mode between $\omega_{res}$ and $\omega_{LO}$ retrieves its spectral coherence for $t_1/d_c$ (= $t_3/d_c$) values less than about 0.1.

When the films have different thicknesses, the situation is different. If the thickness of one film varies relative to the other, the modes associated with the layer of constant thickness are almost unaffected. The resonance of the flux observed between $\omega_{TO}$ and $\omega_{res}$, when $t_1/d_c$ (= $t_3/d_c$) < 1, is also significantly damped as $\omega_1$ and $\omega_2$ are far from each other; despite this, the flux is still high in that spectral region, but it becomes difficult to refer to this peak as a resonant mode since the flux does not exhibit any spectral coherence. When the thickness of one film is sufficiently large such that SPhP coupling within the layer becomes weak, the maximum radiative flux is around $\omega_{res}$ where there is a large number of electromagnetic states located in a very narrow spectral band.

## 5.6 Coexistence of two near-field thermal radiation regimes between two thin SiC films

Near-field radiative heat transfer between two SiC bulks supporting SPhPs varies as $d_c^{-2}$ when $d_c \ll \lambda_w$, where $\lambda_w$ is the dominant wavelength emitted, as outlined in section 3.5.2. We mentioned in the introduction of this chapter that Ben-Abdallah et al. [109] reported that the radiative heat transfer coefficient $h_r$ between two SiC films varied as $d_c^{-2}$ when both layers were of equal thicknesses, while they observed a $d_c^{-3}$ regime when the symmetry between the film thicknesses was broken. In this section, we demonstrate that these conclusions are not totally correct. More specifically, we show that the emergence of the $d_c^{-2}$ and $d_c^{-3}$ regimes is not only function of film thicknesses $t_1$ and $t_3$, but depends on the ratios $t_1/d_c$ and $t_3/d_c$. This behavior is demonstrated via the calculation of the total net radiative heat transfer coefficient $h_r$, and also via an asymptotic analysis of the analytical expression for $h_r$.

We consider the problem shown in Fig. 5.1, where $t_1$, $t_3$, and $d_c$ are much thinner than the dominant wavelength emitted $\lambda_w$. The total net radiative heat flux exchanged by the thin films is calculated as follows:

$$q_{net}^{tot} = \left[q_{13}^{tot}(z_3^+) - q_{14}^{tot}(z_4^+)\right] - \left[q_{31}^{tot}(z_2^-) - q_{30}^{tot}(z_1^-)\right] \tag{5.10}$$

where the first term in square brackets represents the flux absorbed by layer 3 due to the emitting film 1, and vice-versa for the second term. As done in section 3.5.2, it is assumed that medium 1 is at temperature $T$ while layer 3 is at temperature $T + \delta T$, such that the radiative heat transfer coefficient $h_r$, defined as the net radiative flux divided by $\delta T$ as $\delta T \to 0$, is calculated. The resulting expression is given by:

$$\begin{aligned} h_r = {} & \frac{1}{\pi^2}\int_0^\infty d\omega \frac{\partial\Theta(\omega,T)}{\partial T} \\ & \times \sum_{\gamma=TE,TM} \left[ \begin{aligned} & \int_0^{k_v} k_\rho dk_\rho \frac{\left(1-\left|R_1^\gamma\right|^2-\left|T_1^\gamma\right|^2\right)\left(1-\left|R_3^\gamma\right|^2-\left|T_3^\gamma\right|^2\right)}{4\left|1-R_1^\gamma R_3^\gamma e^{2ik_{z2}d_c}\right|^2} \\ & + \int_{k_v}^\infty k_\rho dk_\rho e^{-2\,\mathrm{Im}(k_{z2})d_c} \frac{\mathrm{Im}(R_1^\gamma)\,\mathrm{Im}(R_3^\gamma)}{\left|1-R_1^\gamma R_3^\gamma e^{2ik_{z2}d_c}\right|^2} \end{aligned} \right] \end{aligned} \tag{5.11}$$

where the derivative of the mean energy of an electromagnetic state with respect to the temperature, $\partial\Theta(\omega,T)/\partial T$, is given by $\hbar^2\omega^2 e^{\hbar\omega/k_bT} / k_bT^2(e^{\hbar\omega/k_bT}-1)^2$.

First, $h_r$ values are reported for SiC as a function of $d_c$ (from 1 nm to 100 nm) for $T = 300$ K and by assuming that medium 3 is a bulk (i.e., $t_3 \to \infty$), while $t_1$ = 1 nm, 5 nm, 10 nm, and 50 nm. The results of Fig. 5.7(a) suggest that both $d_c^{-2}$ and $d_c^{-3}$ regimes can coexist between a film and a bulk, an observation that is clearly depicted in Fig. 5.7(b) for $t_1$ = 10 nm. Using the dimensionless ratio $D_j = t_j/d_c$, it can be seen that when $D_1 << 1$ and $D_3 \to \infty$, $h_r$ varies as $d_c^{-2}$, while for $D_1 >> 1$ and $D_3 \to \infty$, $h_r$ varies as $d_c^{-3}$. When $D_1 \approx 1$, there is a region of transition between the $d_c^{-2}$ and $d_c^{-3}$ regimes where $h_r$ can slightly exceed the values predicted for two bulks [108].

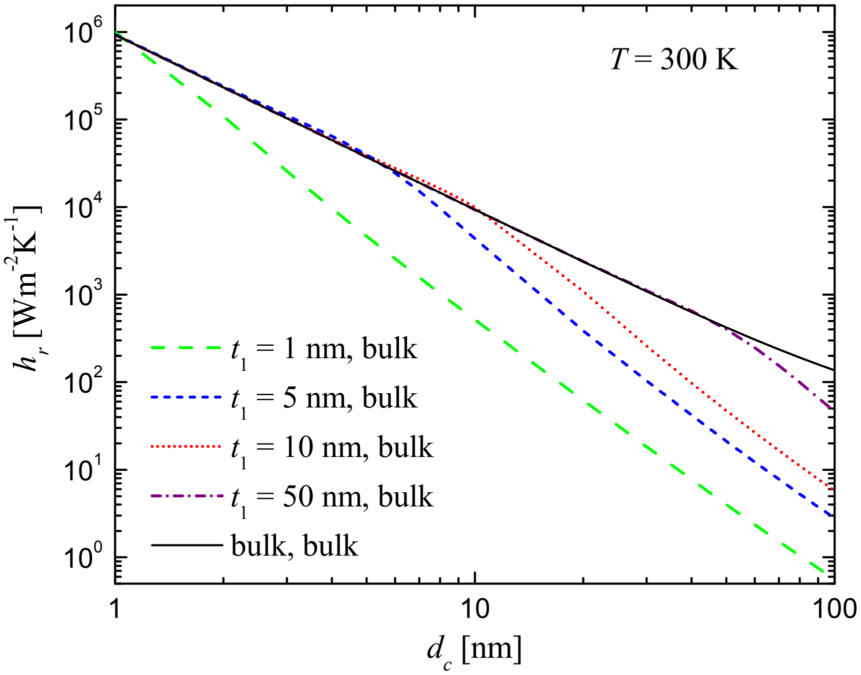

(a)

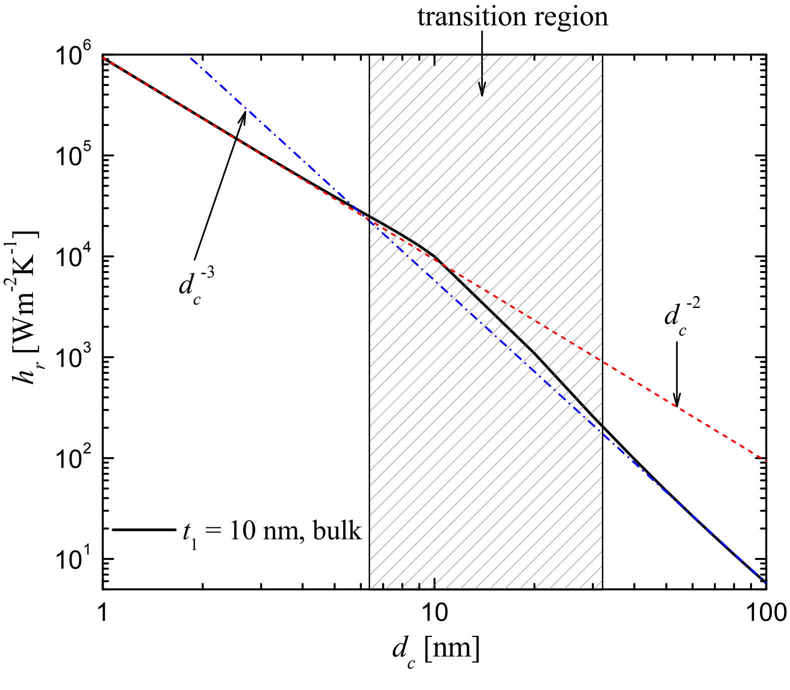

(b)

Figure 5.7. (a) Radiative heat transfer coefficient $h_r$ as a function of $d_c$ for $t_1$ = 1 nm, 5 nm, 10 nm, and 50 nm and $t_3 \rightarrow \infty$ (bulk); the results are compared with $h_r$ between two bulks. (b) Identification of the $d_c^{-2}$ and $d_c^{-3}$ regimes for $t_1$ = 10 nm.

Figure 5.8(a) shows $h_r$ values as a function of $d_c$, but this time both media 1 and 3 are of finite thicknesses; the results are compared with $h_r$ values for two bulk materials. In Figs. 5.8(b) and 5.8 (c), the cases where $t_1$ = 50 nm and $t_3$ = 10 nm, and $t_1$ = 1 nm and $t_3$ = 10 nm are analyzed more closely.

When $D_1 = D_3$, $h_r$ varies as $d_c^{-2}$ for all $d_c$ values. When both layers are 1 nm thick, it can be seen that starting at $d_c \approx 50$ nm, $h_r$ values diverge from the $d_c^{-2}$ asymptote, but do not obey the $d_c^{-3}$ regime. The behavior reported here for films of equal thicknesses is in good agreement with the observations made in reference [109]

On the other hand, Ben-Abdallah et al. [109] concluded that $h_r$ varies as $d_c^{-3}$ when the films have different thicknesses. Clearly, by inspecting Figs. 5.7 and 5.8, this is not the case, as both $d_c^{-2}$ and $d_c^{-3}$ regimes coexist. In Fig. 5.8(b), when $d_c << 10$ nm, $D_1$ and $D_3 >> 1$, and the $d_c^{-2}$ regimes is retrieved up to a $d_c$ value of about 6 nm. Between $d_c$ values of about 10 nm up to 30 nm, $h_r$ varies as $d_c^{-3}$, where $D_1 << 1$ and $D_3 >> 1$. Then, starting at $d_c \approx 70$ nm, where both $D_1 << 1$ and $D_3 << 1$, $h_r$ varies as $d_c^{-2}$. Similar observations can be made by inspecting Fig. 5.8(c), where $t_1$ = 1 nm and $t_3$ = 10 nm. However, for this latter case, the transition region between the $d_c^{-2}$ and $d_c^{-3}$ regimes spread out over a larger range of $d_c$ values.

Based on the observations made by analyzing Figs. 5.7 and 5.8, the $d_c^{-2}$ regime is retrieved when $D_1 <<$ and $D_3 << 1$ or $D_1 >> 1$ and $D_3 >> 1$. On the other, the $d_c^{-3}$ behavior can be observed when $D_1 << 1$ and $D_3 >> 1$, and vice-versa. Hereafter, we analyze more closely the coexistence of the $d_c^{-2}$ and $d_c^{-3}$ regimes between two thin films from a mathematical point of view.

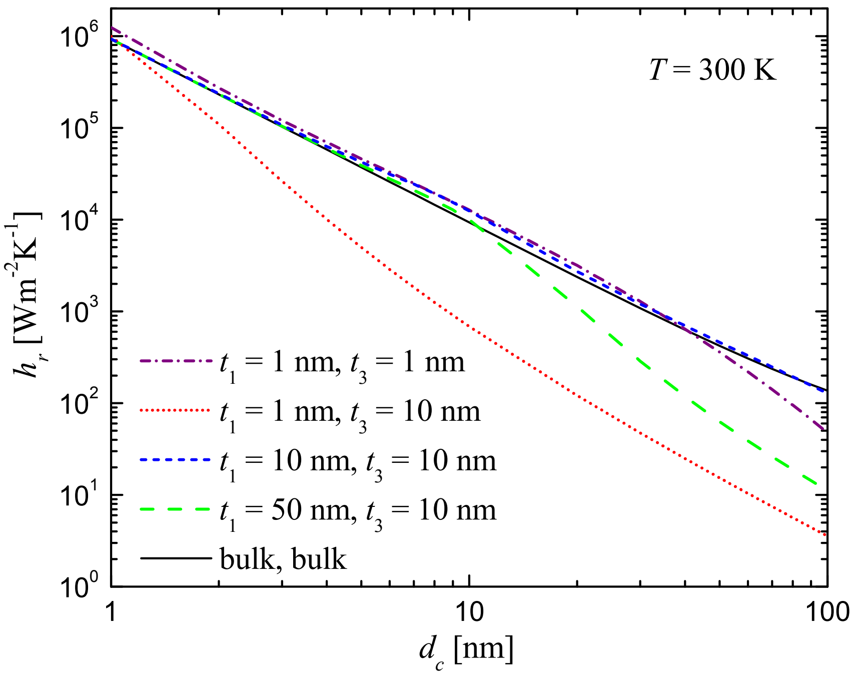

$T = 300$ K
$t_1 = 1$ nm, $t_3 = 1$ nm
$t_1 = 1$ nm, $t_3 = 10$ nm
$t_1 = 10$ nm, $t_3 = 10$ nm
$t_1 = 50$ nm, $t_3 = 10$ nm
bulk, bulk
$h_r$ [Wm$^{-2}$K$^{-1}$]
$d_c$ [nm]
$10^0$
$10^1$
$10^2$
$10^3$
$10^4$
$10^5$
$10^6$
1
10
100

(a)

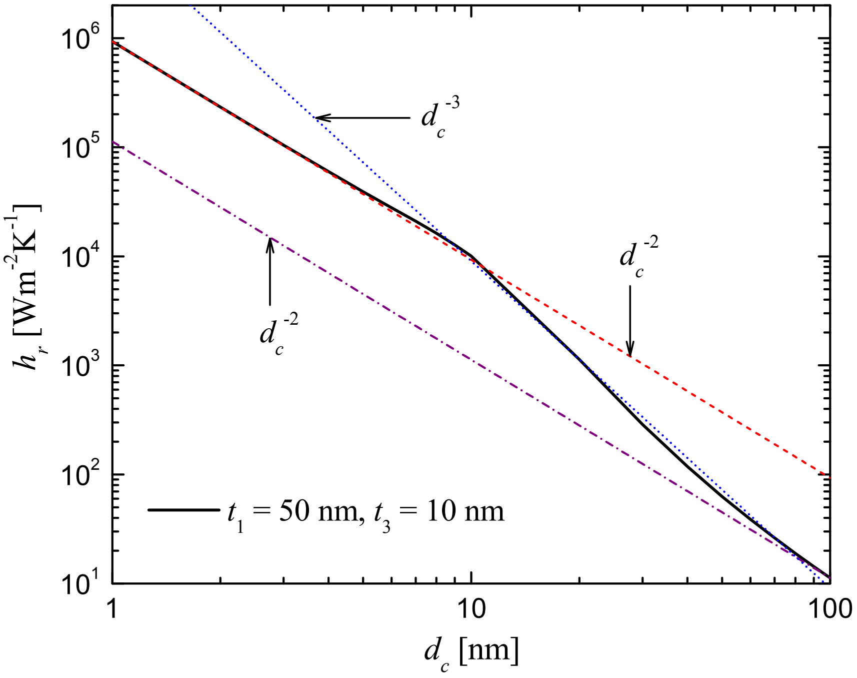

$d_c^{-3}$
$d_c^{-2}$
$d_c^{-2}$
$t_1 = 50$ nm, $t_3 = 10$ nm
$h_r$ [Wm$^{-2}$K$^{-1}$]
$d_c$ [nm]
$10^1$
$10^2$
$10^3$
$10^4$
$10^5$
$10^6$
1
10
100

(b)

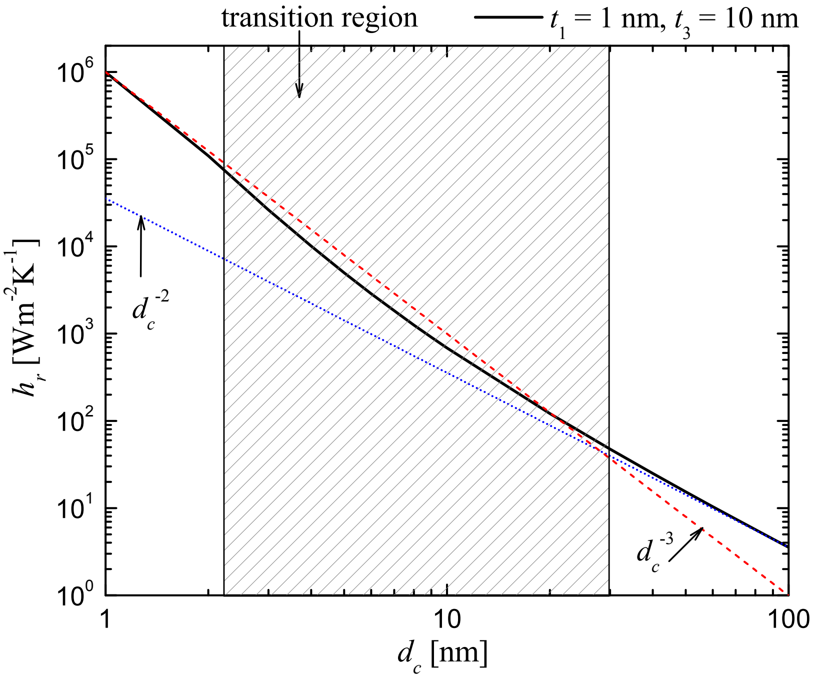

(c)

Figure 5.8. (a) Radiative heat transfer coefficient $h_r$ as a function of $d_c$ for $t_1 = t_3 = 1$ nm, $t_1 = 1$ nm and $t_3 = 10$ nm, $t_1 = t_3 = 10$ nm, and $t_1 = 50$ nm and $t_3 = 10$ nm; the results are compared with $h_r$ between two bulks. (b) Identification of the $d_c^{-2}$ and $d_c^{-3}$ regimes for $t_1 = 10$ nm and $t_3 = 50$ nm. (c) Identification of the $d_c^{-2}$ and $d_c^{-3}$ regimes for $t_1 = 1$ nm and $t_3 = 10$ nm.

The near-field thermal radiation regimes between two SiC films supporting SPhPs are analyzed via an asymptotic analysis of Eq. (5.11). As $d_c \rightarrow 0$, radiative heat transfer is dominated by SPhPs, existing only in TM polarization for nonmagnetic materials, with $k_\rho >> k_v$ where there is a large number of electromagnetic states in a very narrow spectral band. In the electrostatic limit where $k_\rho >> k_v$, the $z$-component of the wavevector in medium $j$ can be approximated as $k_{zj} \approx ik_\rho$, and the Fresnel reflection coefficients thus become independent of $k_\rho$ ($r_{ij}^{TM} \approx (\varepsilon_{rj} - \varepsilon_{ri})/(\varepsilon_{rj} + \varepsilon_{ri})$). Using the dimensionless variable $\eta = k_\rho d_c$ [106], the near-field radiative heat transfer coefficient between two films can be approximated as follows:

$$h_r \approx \frac{1}{\pi^2 d_c^2}\int_0^\infty d\omega \frac{\partial \Theta(\omega,T)}{\partial T}\int_0^\infty \eta e^{-2\eta} d\eta \frac{\mathrm{Im}(R_1^{TM})\,\mathrm{Im}(R_3^{TM})}{\left|1 - R_1^{TM} R_3^{TM} e^{-2\eta}\right|^2} \tag{5.12}$$

where the lower limit of integration over $\eta$ has been approximated by 0 in the limit $d_c \rightarrow 0$ [106]. This approximation is justified as follows. The lower limit of integration for evanescent waves is $k_\rho = k_v$, which is, in terms of the dimensionless variable $\eta$, given by $\eta_v = k_v d_c$. For example, the magnitude of the wavevector in vacuum $k_v$ (= $\omega/c_v$) at the frequency $\omega_{res} = 1.786\times10^{14}$ rad/s is $5.957\times10^5$ rad/m. Assuming that the vacuum gap $d_c$ is 10 nm thick, the dimensionless lower limit of integration over $\eta$ becomes $\eta_v = 5.957\times10^{-3}$. It is therefore justified to approximate the lower limit at 0.

The film reflection coefficient in medium $j$, where $j$ = 1 and 3, can then be written as $R_j^{TM} = r_{01}^{TM}(1-e^{-2\eta D_j})/(1-(r_{01}^{TM})^2 e^{-2\eta D_j})$, where the fact that $r_{01}^{TM} = -\, r_{12}^{TM} = r_{23}^{TM} = -\, r_{34}^{TM}$ has been used. As suggested by Figs. 5.7 and 5.8, the variations of $h_r$ as a function of $d_c$ are function of the dimensionless variables $D_1$ and $D_3$. When both $t_1$ and $t_3 >> d_c$, $D_1$ and $D_3 >> 1$, $R_j^{TM} \rightarrow r_{01}^{TM}$ for $j$ = 1 and 3, and Eq. (5.12) can be simplified as follows:

$$\begin{aligned} h_r &\approx \frac{1}{\pi^2 d_c^2}\int_0^\infty d\omega \frac{\partial\Theta(\omega,T)}{\partial T}\left[\mathrm{Im}(r_{01}^{TM})\right]^2 \int_0^\infty \eta e^{-2\eta} d\eta \frac{1}{\left|1-(r_{01}^{TM})^2 e^{-2\eta}\right|^2} \\ &\approx \frac{1}{\pi^2 d_c^2}\int_0^\infty d\omega \frac{\partial\Theta(\omega,T)}{\partial T}\left[\mathrm{Im}(r_{01}^{TM})\right]^2 \end{aligned} \tag{5.13}$$

where the integration over $\eta$ converges to unity [2]. Equation (5.13) is the same as the expression obtained between two bulks (Eq. (3.52) in section 3.5.2), clearly showing that when both $t_1$ and $t_3 >> d_c$, but still with $t_1$ and $t_3 << \lambda_w$, the films behave as bulks, with a $h_r$ varying as $d_c^{-2}$. Physically, this result can be explained by analyzing the radiation penetration depth. In the electrostatic limit, the penetration depth of an evanescent wave in medium $j$, strictly defined as $\delta_j = \left|k_{zj}\right|^{-1}$, can be approximated by $\delta_j \approx k_\rho^{-1}$. Also, near-field radiative transfer between materials supporting SPhPs is dominated by evanescent waves with large parallel wavevector $k_{\rho,\max} \approx d_c^{-1}$, and therefore penetration depth $\delta_{\max} \approx d_c$, having a very large number of electromagnetic states in a narrow spectral band. Since the radiation penetration depth is much smaller than the film thicknesses, SPhPs dominating radiant energy exchanges are fully absorbed by the thin layers, thus leading to $h_r$ values similar to those obtained between two bulks. This conclusion is in line with the discussion provided recently by Basu and Zhang [117]. For thin layers with $t_1$ and $t_3 <<$ $\lambda_w$, SPhP coupling within and between the films occur. However, when both $D_1$ and $D_3$ $>> 1$, SPhPs dominating near-field radiative heat transfer do not couple within the films since $\delta_{\max} << t_1$ and $t_3$, such that the resonance of $h_r$ still occur at $\omega_{res}$.

Figures 5.7 and 5.8 suggested that $h_r$ varies as $d_c^{-3}$ when $D_1 << 1$ and $D_3 >> 1$, and vice-versa. For the purpose of discussion, we set $t_1 << d_c$ and $t_3 >> d_c$, such that $D_1 << 1$ and $D_3 >> 1$, keeping in mind that the inverse case will lead to the exact same results due to the symmetry of the geometry. For this limiting case, Eq. (5.12) reduces to:

$$h_r \approx \frac{1}{\pi^2 d_c^2}\int_0^\infty d\omega \frac{\partial\Theta(\omega,T)}{\partial T}\operatorname{Im}(r_{01}^{TM}) \times \int_0^\infty \eta^2 e^{-2\eta} d\eta \operatorname{Im}\left(\frac{r_{01}^{TM}(1-e^{-2\eta D_1})}{1-(r_{01}^{TM})^2 e^{-2\eta D_1}}\right)\frac{1}{\left|1-\dfrac{(r_{01}^{TM})^2(1-e^{-2\eta D_1})e^{-2\eta}}{1-(r_{01}^{TM})^2 e^{-2\eta D_1}}\right|^2} \tag{5.14}$$

When $D_1 << 1$, the term $\exp(-a\eta D_1)$, where $a$ is an arbitrary constant, can be approximated as $\exp(-a\eta D_1) \approx 1 - a\eta D_1$ using a first order Maclaurin series expansion, such that Eq. (5.14) can be written as follows:

$$h_r \approx \frac{1}{\pi^2 d_c^2}\int_0^\infty d\omega \frac{\partial\Theta(\omega,T)}{\partial T}\int_0^\infty \eta^2 e^{-2\eta} d\eta \frac{2\eta D_1 \operatorname{Im}(r_{01}^{TM})\operatorname{Im}[r_{01}^{TM}(1-(r_{01}^{TM})^2(1-2\eta D_1))^*]}{\left|1-(r_{01}^{TM})^2\left[1-2\eta D_1(1-e^{-2\eta})\right]\right|^2} \tag{5.15}$$

where the superscript * denotes a complex conjugate. As mentioned above, the near-field radiative transfer is dominated by SPhPs with $k_{\rho,\max} \approx d_c^{-1}$, which implies that $h_r$ is dominated by waves with $\eta_{\max} \approx 1$. At such a value of $\eta$, the term $(1-e^{-2\eta})$ has an order of magnitude of unity, and the term $1 - 2\eta D_1$ can be approximated as 1 since $D_1 << 1$. Consequently, Eq. (5.15) can be re-arranged as follows:

$$
\begin{aligned}
h_r &\approx \frac{2t_1}{\pi^2 d_c^3}\int_0^\infty d\omega \frac{\partial\Theta(\omega,T)}{\partial T}\frac{\left[\mathrm{Im}(r_{01}^{TM})\right]^2(1+\left|r_{01}^{TM}\right|^2)}{\left|1-(r_{01}^{TM})^2\right|^2}\int_0^\infty \eta^3 e^{-2\eta}d\eta \\
&\approx \frac{t_1}{2\pi^2 d_c^3}\int_0^\infty d\omega \frac{\partial\Theta(\omega,T)}{\partial T}\frac{\left[\mathrm{Im}(r_{01}^{TM})\right]^2(1-\left|r_{01}^{TM}\right|^2)}{\left|1-(r_{01}^{TM})^2\right|^2}
\end{aligned}
\tag{5.16}
$$

where the integration over $\eta$ gives 1/4. The $d_c^{-3}$ behavior obtained in Eq. (5.16), confirming the results shown in Figs. 5.7 and 5.8, can potentially be interpreted on the basis of SPhP coupling within the layers. The near-field spectrum emitted by film 1 at location $z_3$ is split into two distinct modes (anti-symmetric and symmetric) since $D_1 << 1$. Indeed, the evanescent waves dominating the field at $z_3$ have a penetration depth $\delta_{\max}$ ($\approx d_c$) $>> t_1$, such that SPhP coupling within layer 1 can be seen on the near-field spectrum emitted at $z_3$. Conversely, the field emitted by layer 3 and observed at $z_2$ is dominated by SPhPs that do not couple within film 3, resulting in a maximum near-field thermal emission at $\omega_{res}$. As discussed in section 5.4, the near-field spectral emittance / absorptance of film $j$ in TM polarization is given by $\mathrm{Im}(R_j^{TM})$, such that near-field spectral emission is equivalent to spectral absorption. Consequently, for $D_1 << 1$ and $D_3 >> 1$, the spectral bands of high near-field thermal radiation emission / absorption of layer 1 do not match the bands of high near-field thermal radiation emission / absorption of layer 3, thus leading to a $d_c^{-3}$ regime.

The last case arises when the films are thinner than the gap $d_c$, such that both $D_1$ and $D_3 << 1$. The near-field radiative heat transfer coefficient given by Eq. (5.12) can thus approximated as follows:

$$
\begin{aligned}
h_r \approx \frac{1}{\pi^2 d_c^2}\int_0^\infty d\omega \frac{\partial\Theta(\omega,T)}{\partial T} \\
\times \int_0^\infty \eta e^{-2\eta} d\eta\, \mathrm{Im}\left(\frac{r_{01}^{TM}}{1-(r_{01}^{TM})^2(1-2\eta D_1)}\right)\mathrm{Im}\left(\frac{r_{01}^{TM}}{1-(r_{01}^{TM})^2(1-2\eta D_3)}\right) \\
\times 4\eta^2 D_1 D_3 \frac{1}{\left|1-\dfrac{4\eta^2 D_1 D_3 (r_{01}^{TM})^2 e^{-2\eta}}{[1-(r_{01}^{TM})^2(1-2\eta D_1)][1-(r_{01}^{TM})^2(1-2\eta D_3)]}\right|^2}
\end{aligned}
\tag{5.17}
$$

Due to the fact that $D_1$ and $D_3 << 1$, the resonances of near-field thermal emission and absorption for both films 1 and 3 are split into two distinct modes located around $\omega_{res}$, where the denominators $1-(r_{01}^{TM})^2(1-2\eta D_j)$ in Eq. (5.17) can take very small values [106]. Indeed, the resonant modes of emission and absorption eventually converge to $\omega_{TO}$ and $\omega_{LO}$ for $D_1$ and $D_3 << 1$. Using the oscillator model for polar crystals given in appendix B, the real and imaginary parts of the dielectric function of SiC can be written as follows at $\omega = \omega_{TO}$:

$$\varepsilon'_{r1}(\omega) = \varepsilon_\infty \tag{5.18a}$$

$$\varepsilon''_{r1}(\omega) = \frac{\varepsilon_\infty(\omega_{LO}^2 - \omega_{TO}^2)}{\Gamma\omega_{TO}} \tag{5.18b}$$

Inserting Eqs. (5.18a) and (5.18b) into the square of the Fresnel reflection coefficient in TM polarization in the electrostatic limit leads to:

$$(r_{01}^{TM})^2 \approx \frac{(\varepsilon_\infty - 1)^2 - \varepsilon_\infty^2(\omega_{LO}^2 - \omega_{TO}^2)^2 / \Gamma^2\omega_{TO}^2 + i2(\varepsilon_\infty - 1)\varepsilon_\infty(\omega_{LO}^2 - \omega_{TO}^2)^2 / \Gamma^2\omega_{TO}^2}{(\varepsilon_\infty + 1)^2 - \varepsilon_\infty^2(\omega_{LO}^2 - \omega_{TO}^2)^2 / \Gamma^2\omega_{TO}^2 + i2(\varepsilon_\infty + 1)\varepsilon_\infty(\omega_{LO}^2 - \omega_{TO}^2)^2 / \Gamma^2\omega_{TO}^2} \tag{5.19}$$

For SiC, $\varepsilon_\infty = 6.7$, such that it is possible to pose the following approximation: $(\varepsilon_\infty - 1) \approx (\varepsilon_\infty + 1) \approx \varepsilon_\infty$. By combining this approximation with Eq. (5.19), we find that $\mathrm{Re}((r_{01}^{TM})^2) \approx 1$ while $\mathrm{Im}((r_{01}^{TM})^2) << 1$.

At $\omega = \omega_{LO}$, the real and imaginary parts of the dielectric function can be written as follows:

$$\varepsilon'_{r1}(\omega) = \varepsilon_\infty\left[1 - \frac{(\omega_{LO}^2 - \omega_{TO}^2)^2}{(\omega_{LO}^2 - \omega_{TO}^2)^2 + \Gamma^2\omega_{LO}^2}\right] \tag{5.20a}$$

$$\varepsilon''_{r1}(\omega) = \frac{\varepsilon_\infty\Gamma\omega_{LO}(\omega_{LO}^2 - \omega_{TO}^2)}{(\omega_{LO}^2 - \omega_{TO}^2)^2 + \Gamma^2\omega_{LO}^2} \tag{5.20b}$$

Inserting the numerical values for $\varepsilon_\infty$, $\omega_{TO}$, $\omega_{LO}$ and $\Gamma$ into Eq. (5.20a), it can be seen that the second term in the square brackets converges to unity, such that $\varepsilon'_{r1}(\omega) \rightarrow 0$.

Similarly, substitution of the numerical values for SiC in Eq. (5.20b) leads to $\varepsilon''_{r1}(\omega)$ << 1. Therefore, we have $(r_{01}^{TM})^2$ → 1, such that $\mathrm{Re}((r_{01}^{TM})^2)$ ≈ 1 while $\mathrm{Im}((r_{01}^{TM})^2)$ << 1. These values of $\mathrm{Re}((r_{01}^{TM})^2)$ and $\mathrm{Im}((r_{01}^{TM})^2)$ at $\omega_{TO}$ and $\omega_{LO}$ can lead to integrand in Eq. (5.17) with very small denominators.

To circumvent this problem, the term $(r_{01}^{TM})^2$ is expanded into its real and imaginary components as follows [106]:

$$1-(r_{01}^{TM})^2(1-2\eta D_j) \approx 2\eta D_j - i\,\mathrm{Im}((r_{01}^{TM})^2)\left[1-2\eta D_j\right] \approx 2\eta D_j - i\,\mathrm{Im}((r_{01}^{TM})^2) \qquad (5.21)$$

where the fact that $\mathrm{Re}((r_{01}^{TM})^2) \approx 1$ has been used. By assuming that $2\eta D_j$ >> $\mathrm{Im}((r_{01}^{TM})^2)$ [106], it is possible to write that:

$$\mathrm{Im}\left(\frac{r_{01}^{TM}}{1-(r_{01}^{TM})^2(1-2\eta D_1)}\right)\mathrm{Im}\left(\frac{r_{01}^{TM}}{1-(r_{01}^{TM})^2(1-2\eta D_3)}\right) \approx \frac{[\mathrm{Im}(r_{01}^{TM})]^2}{4\eta^2 D_1 D_3} \qquad (5.22)$$

and

$$\frac{1}{\left|1-\dfrac{4\eta^2 D_1 D_3 (r_{01}^{TM})^2 e^{-2\eta}}{[1-(r_{01}^{TM})^2(1-2\eta D_1)][1-(r_{01}^{TM})^2(1-2\eta D_3)]}\right|^2} \approx \frac{1}{\left|1-(r_{01}^{TM})^2 e^{-2\eta}\right|^2} \qquad (5.23)$$

Substitutions of Eqs. (5.22) and (5.23) into Eq. (5.17) leads to the following approximation for the near-field radiative heat transfer coefficient when both $D_1$ and $D_3$ << 1:

$$\begin{aligned} h_r &\approx \frac{1}{\pi^2 d_c^2}\int_0^\infty d\omega \frac{\partial\Theta(\omega,T)}{\partial T}[\mathrm{Im}(r_{01}^{TM})]^2 \int_0^\infty \eta e^{-2\eta} d\eta \frac{1}{\left|1-(r_{01}^{TM})^2 e^{-2\eta}\right|^2} \\ &\approx \frac{1}{\pi^2 d_c^2}\int_0^\infty d\omega \frac{\partial\Theta(\omega,T)}{\partial T}\left[\mathrm{Im}(r_{01}^{TM})\right]^2 \end{aligned} \qquad (5.24)$$

Equation (5.24) is the same as Eq. (5.13) for $D_1$ and $D_3$ >> 1 where $h_r$ varies as $d_c^{-2}$, thus confirming the trend observed in Figs. 5.8. Note that for the cases discussed previously, near-field radiative transfer was dominated by SPhPs with frequencies around $\omega_{res}$, where the aforementioned conditions on the Fresnel reflection coefficients were not applicable. This is why the extraneous operation of splitting $(r_{01}^{TM})^2$ into its real and imaginary components is done strictly for the case $D_1$ and $D_3 << 1$. The physical significance of this last result is not obvious. The emergence of the $d_c^{-2}$ regime might be due to the fact that the resonant modes maximizing near-field thermal emission / absorption of film 1 match more or less the resonant modes of layer 3.

At $\omega = \omega_{TO}$, $\mathrm{Im}((r_{01}^{TM})^2) = \mathrm{O}(10^{-3})$, while $\mathrm{Im}((r_{01}^{TM})^2) = \mathrm{O}(10^{-1})$ at $\omega = \omega_{LO}$. The approximation $2\eta D_j >> \mathrm{Im}((r_{01}^{TM})^2)$ used to derived Eqs. (5.22) and (5.23) is therefore questionable around $\omega = \omega_{LO}$, and is not applicable when $D_j$ is very small, as the near-field is dominated with SPhPs having $\eta_{max} \approx 1$. This might explain the result of Fig. 5.8(a) where $h_r$ for two 1 nm thick films diverge from the $d_c^{-2}$ asymptote for $d_c$ values greater than about 50 nm.

It is also interesting to note that the asymptotic expansion of $h_r$ given by Eq. (5.24) contains no information about the film thicknesses, even though SPhP coupling arises. This might confirm the hypothesis stated above. When the resonances of near-field thermal emission / absorption of film 1 match those of layer 3, the $d_c^{-2}$ regime is retrieved, and the asymptotic expansion of $h_r$ contains no information about the layer thicknesses. On the other hand, when there is an important mismatch between the resonances of near-field thermal emission / absorption between films 1 and 3, the $d_c^{-3}$ regime is retrieved, and the asymptotic expansion of $h_r$ contains information about the thinner film only (see Eq. (5.16)).

The dual $d_c^{-2}$ and $d_c^{-3}$ regimes were not observed in reference [109] since $h_r$ was calculated for the following cases only: $t_1 = t_3 = 5$ μm, $t_1 = t_3 = 1$ nm, and $t_1 = 5$ μm and $t_3 = 1$ nm for $d_c$ values from 1 nm to 100 nm. When $t_1 = t_3 = 5$ μm, the $d_c^{-2}$ regime is retrieved, as for the case $t_1 = t_3 = 1$ nm. When $t_1 = 5$ μm and $t_3 = 1$ nm, $D_1 >> 1$ and $D_3 << 1$ for all $d_c$ values considered, thus leading to the $d_c^{-3}$ regime only. This is why Ben-Abdallah et al. [109] concluded that the emergence of the $d_c^{-2}$ and $d_c^{-3}$ regimes was function of $t_1$ and $t_3$.

The results presented in this section are quite interesting, as they show clearly the coexistence of two near-field thermal radiation regimes between two thin SiC films. At this point, it is however difficult to generalize the conclusions to all materials supporting surface polaritons that can be thermally excited, as Eq. (5.24) has been derived for the specific case of SiC. As a future research effort, it would be interesting to perform the analysis with other materials such as *c*BN or doped silicon in order to verify if the conclusions stated in this section are applicable to any thin films supporting surface polaritons.

## 5.7 Concluding remarks

The physical analysis presented in chapters 4 and 5 provides in a quantitative and systematic manner how thermal emission and radiative heat flux at nanoscale is affected by the structure of the system. The approximate formulation used to predict resonance of the radiative heat flux could potentially be extended to systems involving multiple films, as an alternative to formal optimization procedures, for tuning near-field radiant energy exchanges, which can be important for nanoscale-gap thermophotovoltaic power generation.

Before closing the discussions of chapters 4 and 5, it is worth noting that for thin films, spatial dispersion of the dielectric function of the materials might be important, and consequently non-local effects should be investigated in a future research effort. Moreover, when applying the fluctuational electrodynamics formalism, the media are assumed to be in local thermodynamic equilibrium. For films with thicknesses of the order of few nanometers, this assumption might be questionable. On the other hand, this theory, built on macroscopic electrodynamics, is currently the only tool available to treat near-field thermal radiation emission. Validation of the application of fluctuational electrodynamics to very thin layers should come from experiments.

# Chapter 6

# Nanoscale-Gap Thermophotovoltaic Power Generation

In the previous chapters, we discussed the fundamentals of near-field thermal radiation, provided a numerical procedure to solve such problems in one-dimensional layered media, and explored the possibility of tuning near-field radiant energy exchanges using thin films supporting surface phonon-polaritons (SPhPs). In this chapter, the near-field effects of thermal radiation are applied to clean and renewable energy conversion. More specifically, we investigate nanoscale-gap thermophotovoltaic power generation devices.

The current world energy consumption is about 14 TW, among which less than 1% is coming from clean and renewable sources [128]. By 2050, it is expected that this global demand will double to about 25-30 TW. In order to minimize the environmental impacts of this energy consumption, experts estimated that about 20 TW should come from carbon-free renewable energy resources [128]. In an opinion paper recently published, Baxter et al. [128] pointed out the importance of nanoengineering to develop low-cost and high-efficiency renewable energy technologies, and discussed, among other technologies, solar thermophotovoltaic (TPV) power generators that could greatly benefit from nanoscale design. In such TPV devices, solar irradiation is absorbed by a radiator, which in turns re-emits selectively thermal radiation toward a cell generating electricity. The use of an intermediate medium can allow to design customized thermal radiation spectra optimizing the conversion efficiency of the device.

TPV power generators are not restricted to solar applications, as any kind of heat source can be used to heat up the radiator. Beyond their potential versatility, TPV systems are expected to be quiet, low-maintenance, modular, relatively safe and pollution-free [129]. Standardized performance data of TPV devives are somehow difficult to define, as the thermal radiation spectrum emitted strongly depends on the material and structure of the radiator. Mauk [129] reported that the typical electrical power output of a TPV system is about $10^4$ $Wm^{-2}$ with an internal conversion efficiency of about 20 % to 30 %.

Silicon-based photovoltaic (PV) cells, with a bandgap of about 1.1 electron volts (eV) at room temperature, are usually used for direct solar energy conversion. For TPV applications, the radiator is typically maintained between 1000 K to 2000 K, such that cells with bandgaps lower than 1.1 eV are required. For this reason, the distinction is usually made between TPV and PV cells. So far, research on TPV cells has mainly focused on III-V binary compounds, such as GaSb and GaAs, and their ternary and quaternary III-V alloys [129,130].

In order to potentially improve the power output and conversion efficiency of TPV systems, Whale and Cravalho [33,34] proposed to separate the radiator and TPV cells by a sub-wavelength vacuum gap. At sub-wavelength distances, radiation heat transfer is in the near-field regime, such that the energy exchanges can exceed the values predicted for blackbodies due to radiation tunneling. For typical temperatures involved in thermal radiation, the near-field effects become dominant when the bodies are separated by few tens to few hundreds of nanometers. Therefore, a TPV system using the near-field effects of thermal radiation is referred hereafter as a nanoscale-gap TPV device, or more simply, a nano-TPV device.

While the literature has shown that radiation tunneling can substantially improve the electrical power output of nano-TPV systems [33-37,131,132], some important questions about the feasibility of nano-TPV energy conversion are still unanswered. Among these interrogations, three major issues are identified: (1) What is the cost, in terms of energy, for maintaining the TPV cells at room temperature? (2) How is it possible to fabricate nano-TPV devices with a radiator and TPV cells separated by few tens to few hundreds of nanometers? (3) Is it possible to maintain the temperature gradient usually discussed in the literature (1000-2000 K for the radiator and 300 K for the TPV cells)? In this chapter, we aim to answer the first question by analyzing the thermal effects in nano-TPV devices. For purpose of comparison with the literature, we study systems based on indium gallium antimonide ($In_{0.18}Ga_{0.82}Sb$) cells. To date, the most sophisticated mathematical modeling of nano-TPV devices was provided by Park et al. [37], where minority carrier diffusion equations within the TPV cell were solved. In this chapter, we go a step further by also considering the thermal effects within the cell.

Chapter 6 is structured as follows. A brief historical overview and main components of typical TPV power generators are first provided. Then, the photovoltaic effect, which is the basis of TPV energy conversion, is discussed. Nano-TPV devices are overviewed in greater details in section 6.3, and an extensive review of the current literature on this subject is also given. The modeling of the coupled near-field thermal radiation, minority carrier and heat transport problem within a nano-TPV power generator is then explained. Section 6.5 is devoted to the modeling of the optical, electrical and thermophysical properties needed to solve the coupled problem. Finally, the impacts of the thermal effects on the performances of nano-TPV devices are analyzed. It is important to note that TPV devices refer to systems where the gap between the radiator and the cell is large (i.e., larger than the dominant wavelength emitted), while nano-TPV power generators refer to devices where the radiator and cell are separated by a sub-wavelength gap.

### 6.1 Historical overview and main components of TPV power generators

The invention of TPV devices, between 1955 and 1960, is unclear. According to Nelson [133], the first TPV device was built at the Massachussets Institute of Technology (MIT) by Henry H. Kolm [134]. This first TPV system used a lantern as a radiator to illuminate silicon PV cells. However, the literature usually attributes the invention of TPV systems to Pierre Aigrain following a series of lectures given at MIT in 1960 and 1961 [133,135]. Important research efforts were deployed after Aigrain lectures, mainly driven by the US army who were interested by low noise and portable power sources. The first TPV prototype documented in the scientific literature was built by Werth in 1963 using a propane-fuelled emitter maintained at 1700 K and germanium PV cells [136,137]. Some industrials were also attracted by TPV power generation, and General Motors were the most active in the development of such systems.

TPV development slowed down significantly in the seventies since thermoelectric technologies were preferred as portable power sources over TPV devices by the US army. During that period, General Motors also discontinued their TPV project [133]. In the eighties, some scattered efforts by uncorrelated groups were carried out on TPV power generation using silicon cells. Due to the use of silicon having a high bandgap, there was a need to maintain the radiator at very high temperature to ensure optimal performances of the TPV device [133]. The idea of increasing the efficiency of TPV systems via selective emitters and reflectors (filters) was proposed and discussed in that decade [135]. Strong interests in TPV power generation came in the nineties due to the developments of low bandgap TPV cells (GaSb-related alloys) and selective thermal emitters [135].

Potential applications for TPV systems are power sources for MEMS devices, energy source in transportation, stand-alone gas furnaces, power systems for navigation of sailing boats, silent power supplies on recreational vehicles, co-generation of electricity and heat, remote electricity generators, electric-grid independent appliances, aerospace and military power supplies, to name only a few [5,32,34]. TPV systems are particularly attractive for energy recuperation purposes, since wasted heat can be converted into useful electricity. Also, in many devices such as PV cells, laptop or cells phone, heat generated is not only wasted energy, but also decreases the performances of these systems. TPV systems could be simultaneously employed in these applications as a passive cooling device and a power generator.

The main components of a TPV system are: (i) the source of heat, (ii) the radiator, (iii) the TPV cells, (iv) a recirculation system for radiation with energy that does not match the bandgap of TPV cells (optional), (v) a cooling device to maintain the TPV cells at room temperature (optional), and (vi) a power conditioning system [32].

Performances of TPV systems can be improved, or optimized, by maximizing the conversion efficiency as well as the power output [5,36,37,138]. The internal conversion efficiency, or simply the conversion efficiency, is defined as the ratio of the electrical power output of the TPV device over the total (i.e., integrated over all frequencies) radiation absorbed by the TPV cell. Since thermal radiation is a broadband phenomenon, selective filters with high transmittance around the bandgap of the TPV cell and high reflectance for other frequencies can be placed between the radiator and the cell, in order to increase the conversion efficiency of the system [32]. Another way to potentially improve the conversion efficiency is to use radiators emitting at selected frequencies. Periodic structures, such as photonic crystals, can lead to high emissivity of the radiator for a given frequency (around the bandgap of the cell) and low emissivity for other frequencies [55,60,62,139]. Other structures such as gratings can be employed for selective emission of thermal radiation, where surface polaritons are excited via the periodicity of the surface, leading to thermal emission in narrow spectral bands [140].

All the techniques mentioned above have positive impacts on the conversion efficiency. On the other hand, none of these techniques can increase the power output of TPV devices. One way to achieve this goal, while maintaining the temperature of the radiator in the same range, is to transfer energy via evanescent waves by spacing the radiator and the TPV cells by a sub-wavelength distance. Before discussing these nano-TPV devices, a brief overview of the photovoltaic effect and the working principles of a p-n junction is provided next.

### 6.2 Basics of a p-n junction and photovoltaic effect

In this work, the TPV cell is assumed to be a single p-n junction, where a p on n configuration has been chosen for purpose of comparison with the literature [37].

A material is positively doped (p-doped) by the addition of group III impurities accepting electrons from the valence band of the semiconductor, thus creating an excess of holes. Assuming full ionization, concentration of holes in the p-doped region is given by $n_h \approx N_a$, where $N_a$ is the concentration of group III impurities (i.e., acceptor density). Conversely, electrons are in excess in the negatively doped (n-doped) region by the addition of group V impurities; concentration of electrons is given by $n_e \approx N_d$, where $N_d$ is the concentration of group V impurities (i.e., donor density).

When the p- and n-doped semiconductors are brought into contact, as shown in Fig. 6.1, holes in excess in the p-doped material flow toward the region where they are in low concentration (n-doped region), and vice-versa for electrons in excess in the n-doped material. This charge diffusion leaves uncompensated ionized acceptors (p-region) and ionized donors (n-region) near the p-n junction, thus generating an electric field $E$ opposing the diffusion of electrons and holes. At equilibrium, no net current flow through the p-n junction since the drift current exactly cancels the diffusion current. The diffusion current is, as its name says, due to diffusion of holes from the p- to the n-region, and vice-versa for the electrons. The drift is the motion of charged particles due to an applied electric field, such that the drift current, opposing the diffusion current, is generated by the electric field $E$ at the junction. The region near the junction where the electric field appears is called the depletion region; the thickness of this zone is denoted $L_{dp}$. Due to the electric field, there is an equilibrium potential difference $V_0$ across the depletion region [141].

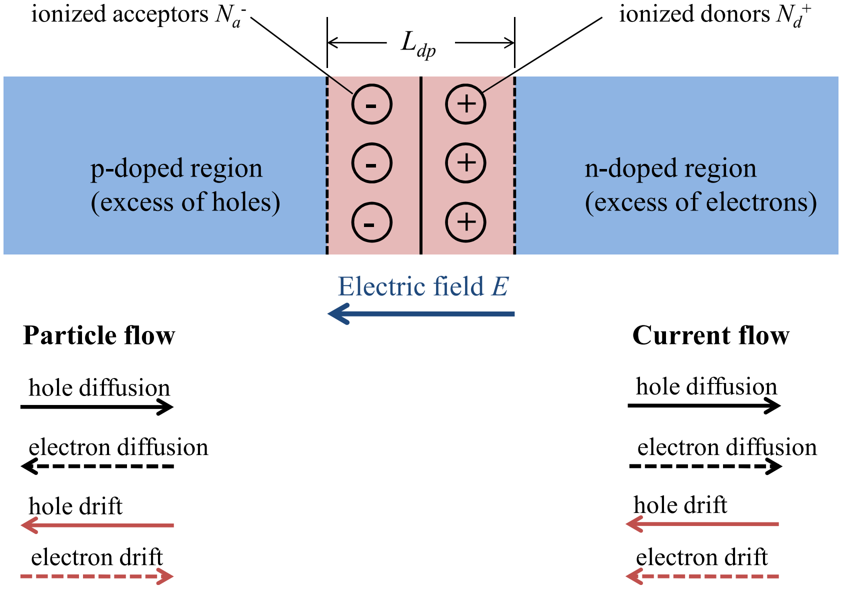
ionized acceptors $N_a^-$
ionized donors $N_d^+$
$L_{dp}$
-
-
-
+
+
+
p-doped region
(excess of holes)
n-doped region
(excess of electrons)
Electric field $E$
Particle flow
hole diffusion
electron diffusion
hole drift
electron drift
Current flow
hole diffusion
electron diffusion
hole drift
electron drift

Figure 6.1. Schematic representation of a p-n junction (similar to Fig. 5-11 from [141]).

When the p-n junction is illuminated, the absorption of a wave with an energy equal or larger than the bandgap $E_g$ of the semiconductor generates mobile charges by electron-hole pairs (EHPs). Note that the energy of a wave in eV is related to its angular frequency by the relation $E = \hbar\omega/e$, where $e$ is the electron charge. The bandgap $E_g$ of a semiconductor can be defined as the minimal energy required to excite an electron from the valence band to the conduction band. EHPs created by radiation absorption within the depletion region of the TPV cell are separated by the electric field at the junction, such that electrons are collected in the n-doped side, and vice-versa for holes [141]. If the junction is connected to an electrical load under a forward bias (i.e., positive voltage from p relative to n, as explained in the next paragraph), the drift of EHPs in the depletion region generates a photocurrent [142]. On the other hand, when EHPs are generated outside the depletion region, the minority carriers diffuse toward the region where they are majority carriers (the minority carriers in the p-doped region are electrons, and vice-versa for the n-doped region). To better understand this, let us assume that an EHP is generated within the p-region. In that case, the hole in the p-region is the majority carrier, while the electron is the minority carrier. Since holes are in excess in the p-region, the EHP (with hole as a majority carrier) diffuses from the p-side toward the n-region, such that the minority carrier in the p-region (electron) diffuses toward the region where he is majority carrier. The EHP may reach the edge of the depletion region or may recombine before. In the event that the EHP reaches the edge of the depletion region, the minority carrier electron is swept by the electric field at the junction toward the n-region, and a photocurrent is thus generated [142,143]. As depicted in Fig. 6.1, the electric field at the junction induces an electron drift from p to n, which is in the same direction as the diffusion of minority electrons from the p- to the n-region. The same logic can be applied to EHPs generated in the n-side, where electrons are majority carriers and holes minority carriers.

Power generation by a p-n junction via radiation absorption can be understood by inspecting the $J$-$V$ characteristic which provides the relation between the effective photocurrent generated by the device $J$ and the bias $V$. As shown in Fig. 6.2, when the p-n junction is not illuminated (i.e., dark conditions), there is a current due to the applied voltage at the junction, called the dark current $J_0$. When the junction absorbs radiation, there is generation of a photocurrent $J_{ph}$ flowing opposite to the dark current $J_0$. In Fig. 6.2, it can be seen that $J$-$V$ characteristic in illuminated condition is lowered by an amount $J_{ph}$ relative to the dark $J$-$V$ curve. Depending on the applied voltage at the junction, the device can be operated either in the third or fourth quadrant. For power generation applications, power is to be extracted from the junction, such that we need to work in the fourth quadrant; the electrical load connected at the junction should consequently be positive from p relative to n (forward bias) [141].

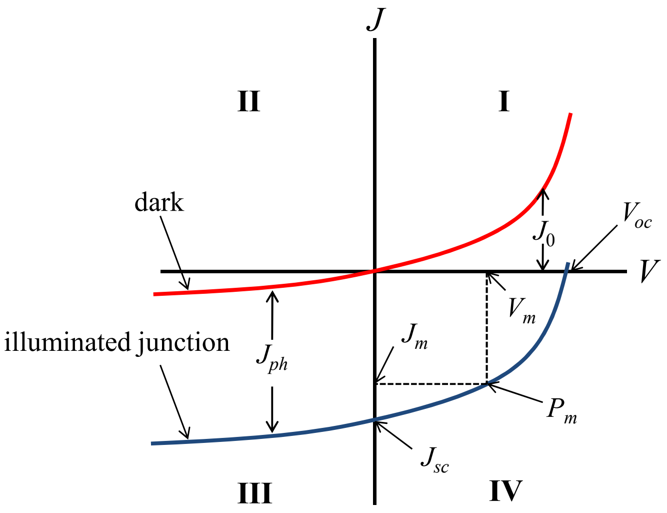

Figure 6.2. Schematic representation of the *J*-*V* characteristic of a p-n junction.

The effective photocurrent generated by the p-n junction $J$ is calculated as: $J(V) = J_{ph} - J_0(V)$, where $J$ is taken as positive, even if strictly speaking $J$ is negative on the *J*-*V* characteristic; this is however the usual practice to consider positive values of $J$ for simplicity. The parameter identified as $J_{sc}$ in Fig. 6.2 is the short-circuit current, corresponding to the current when $V = 0$. The open-circuit voltage, denoted $V_{oc}$, corresponds to the voltage when the current is nil. The point $P_m$ corresponds to the maximum power output of the junction; as shown in Fig. 6.2, $P_m$ is simply the area of the rectangle delimited by $V_m$ and $J_m$. Based on these definitions, it is possible to define the fill factor $FF$ as follows: $FF = J_mV_m/J_{sc}V_{oc}$. The fill factor is a measure of how "square" the *J*-*V* characteristic is [142]. To ensure optimal performances of the device, $J_0$ needs to be as small as possible to ensure a maximum value of $V_{oc}$ [142]. Indeed, the effective current $J$ will reach the plane $V = 0$ at a much lower value of voltage if $J_0$ is large than if $J_0$ is small. This will result in a small value of $V_{oc}$. A small value of $V_{oc}$, for a fixed value of $J_{ph}$, implies a decrease in the power output of the p-n junction (i.e., the area of the rectangle shown in Fig. 6.2 would decrease). This subject will be discussed in greater details in section 6.6.2 when analyzing the performances of nano-TPV devices as a function of the temperature of the p-n junction.

## 6.3 Nano-TPV power generators

### *6.3.1 Description of a nano-TPV energy conversion device*

The geometry of the nano-TPV device under consideration is shown in Fig. 6.3, where all the layers are assumed to be parallel and perfectly smooth. The system is azimuthally symmetric and infinite along the $\rho$-direction, such that only variations along the $z$-axis need to be considered.

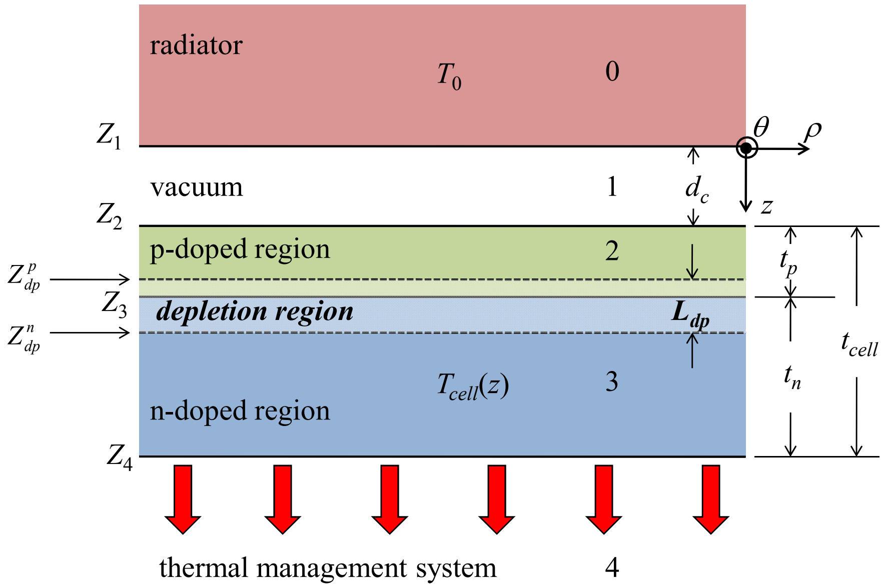
radiator
$T_0$
0
$Z_1$
$\theta$
$\rho$
vacuum
1
$d_c$
$z$
$Z_2$
p-doped region
2
$t_p$
$Z_{dp}^p$
$Z_3$
depletion region
$L_{dp}$
$Z_{dp}^n$
$t_{cell}$
$T_{cell}(z)$
3
$t_n$
n-doped region
$Z_4$
thermal management system
4

Figure 6.3. Schematic representation of the nano-TPV power generation system under study.

A bulk radiator (modeled as a half-space) and a TPV cell of thickness $t_{cell}$ are separated by a sub-wavelength vacuum gap of length $d_c$. The radiator is maintained at constant and uniform temperature $T_0$ via an external heat input, while the cell temperature is given by $T_{cell}(z)$. The TPV cell consists of a single p-n junction (p on n configuration), where the thicknesses of the p-doped and n-doped regions are given respectively by $t_p$ and $t_n$. As the TPV cell is likely to heat up from various sources, a thermal management system is used to maintain the p-n junction around room temperature.

The potential advantage of such a nano-TPV device over a “macroscale-gap” TPV device is straightforward to understand. By transferring more radiant energy from the radiator toward the cell via tunneling of evanescent waves, the nano-TPV system is likely to generate more electricity than a conventional TPV energy conversion device.

The idea of using the near-field effects of thermal radiation to improve the performances of TPV systems is a relatively new idea. More than a decade after the first publication on this subject, very few works have been devoted to nano-TPV power generation. In the next section, a literature review on nano-TPV devices is provided.

### *6.3.2 State-of-the-art on nano-TPV power generation*

#### *6.3.2.1 Literature on numerical modeling of nano-TPV power generation*

The idea of nano-TPV power generation was proposed by Whale and Cravalho [33,34]. The authors considered two bulk materials separated by a vacuum gap $d_c$, where the TPV cells were maintained at a constant and uniform temperature of 300 K. A fictitious low conductivity material was used for the radiator with a dielectric function described by a Drude model. Indium gallium arsenide ($In_{1-x}Ga_xAs$) with a bandgap varying from 0.36 to 1.4 eV, depending on the relative proportion of indium and gallium, was considered for the cells. The conversion efficiency for a relatively large vacuum gap of 5 μm was first calculated as a function of the radiator temperature and cell bandgap. A maximum conversion efficiency was found for a radiator at 2000 K and cells with a bandgap around 0.6 eV. For sub-wavelength $d_c$ values, the results showed a substantial increase of the electrical power output combined with a slight decrease of the conversion efficiency. The authors pointed out that for vacuum gaps $d_c$ between 300 nm and 10 nm, the conversion efficiency increased as $d_c$ decreased, while for $d_c$ less than 10 nm, the conversion efficiency decreased as $d_c$ decreased. The authors concluded that nano-TPV devices provided a significant enhancement of the electrical power output, with marginal gains in conversion efficiency.

Whale [144] extended his work, using the parameters given above, to study wave interference and multi-junctions on the performances of nano-TPV devices. Numerical predictions for $d_c$ values of 800 nm, 1 μm, 1.5 μm and 3 μm revealed that interference of propagating waves in the gap can be used to increase the conversion efficiency of nano-

TPV devices by tuning the peak of the thermal radiation spectrum at the bandgap of the cells. A maximum gain of about 10 % of conversion efficiency was obtained by using wave interference. Whale pointed out that another potential way to increase the conversion efficiency of nano-TPV devices is to use multiple junctions. For a single p-n junction, radiation with energy greater than the bandgap creates EHPs. However, when the p-n junction absorbs radiation with energy greater than the bandgap, the electron is elevated to an energy level greater than the conduction band, and the electron thus releases its excess of energy into heat (thermalization). Whale suggested that this problem could be circumvented by designing a layered TPV cell with different bandgaps (i.e., multi-junction). Whale calculated the near-field radiative heat flux between two bulks, and the radiative flux absorbed at the surface of the cell was then used to calculate the absorption within the TPV cell using Beer's law [15,16]. A 10 μm thick TPV cell was considered, with a 0.5 μm thick top layer of $In_{0.8}Ga_{0.2}As$ (bandgap of 0.47 eV) and a bottom layer of $In_{0.95}Ga_{0.05}As$ (bandgap of 0.37 eV). Whale calculated the conversion efficiency (temperatures of radiator and TPV cells respectively of 2000 K and 300 K) for the multi-junction, and compared the results with single junctions made of $In_{0.8}Ga_{0.2}As$ and $In_{0.95}Ga_{0.05}As$. Results showed that for gaps $d_c$ varying from 2 μm to 10 μm, the conversion efficiency was always about 5 % higher for the multi-junction compared to the single junction case.

Pan et al. [145] provided near-field radiative heat transfer calculations between two lossless dielectric bulks for nano-TPV applications. For the radiative heat flux calculations, the authors used the analogy with total internal reflection to define the source of thermal radiation, as discussed in section 2.7.1. While the methodology is correct for dielectric materials, it cannot be applied to metals, doped semiconductors, or polar crystals since surface polaritons are not accounted for. Near-field radiative heat transfer results presented in the paper are therefore of low interest, and no performance analysis of nano-TPV system was presented.

Narayanaswamy and Chen [35] proposed to use a radiator supporting SPhPs in order to increase the power output and conversion efficiency of nano-TPV devices. They considered a bulk radiator made of cubic boron nitride (*c*BN) maintained at a constant and uniform temperature of 1000 K (the resonance of SPhPs for a *c*BN-vacuum interface is around 0.157 eV). They modeled the TPV cell as 100 nm thick layer submerged into vacuum maintained at a constant and uniform temperature of 300 K. A fictitious dielectric function for the TPV cell was used to approximate the behavior of a direct bandgap semiconductor ($E_g$ = 0.13 eV). The results showed that for a 20 nm gap, the power absorbed by the cell was about three orders of magnitude higher than absorption of solar irradiation. The authors also provided results of photon overexcitation efficiency, defined as the fraction of the energy absorbed by the cell which can be used for energy conversion. In the near-field regime, when SPhPs are excited, a photon overexcitation efficiency of 0.86, as opposed to 0.445 for a blackbody source, was calculated. This increase was due to the quasi-monochromatic near-field radiative heat flux.

Laroche et al. [36,131] studied a nano-TPV system consisting of two bulks separated by a vacuum gap $d_c$. The TPV cells, maintained at a constant and uniform temperature of 300 K, were made of GaSb with a bandgap of 0.7 eV. It was assumed that all radiation with energy higher than the bandgap of the TPV cell contributed to the photocurrent generation (i.e., 100 % of quantum efficiency). Two types of radiator (maintained at 2000 K) were considered in the simulations: a tungsten (W) emitter and a fictitious quasi-monochromatic source described by a Drude model having a resonance matching the bandgap of the TPV cell. For the W radiator, numerical simulations showed that the photocurrent generation increased by more than one order of magnitude for $d_c$ values varying from 10 μm to 5 nm. For the Drude source, the photocurrent increased by a factor 400 from $d_c$ = 10 μm to $d_c$ = 5 nm. The authors also provided theoretical calculations showing that the near-field thermal spectrum emitted by the radiator does not affects the lifetime, or recombination rate, of EHPs. For the W radiator, calculations of the electrical power output showed an enhancement by a factor 50 for vacuum gaps varying from of 10 μm to 5 nm; for the fictitious Drude radiator, an enhancement by a factor 3000 was found between the far-field ($d_c$ = 10 μm) and the near-field ($d_c$ = 5 nm) regimes. The authors however mentioned that this last result was misleading since the far-field emissivity of the fictitious Drude model was very low. A more appropriate comparison with a blackbody at 2000 K in the far-field showed an enhancement of about

35 for a vacuum gap of 5 nm. Finally, the authors reported conversion efficiencies varying non-monotonically from 21 % to 27 % for $d_c$ values from 10 μm to 5 nm when the W radiator was considered; efficiencies varying from 10 % to 35 % for the fictitious Drude radiator were calculated.

The most recent modeling effort of nano-TPV power generation was done by Park et al. [37,132], where the objectives were to study the spatial distribution of radiation absorbed by the cell and to account for the fact that EHPs generated do not necessarily produce a photocurrent (i.e., quantum efficiency less than 100 %). This analysis was performed by solving for the first time the coupled near-field thermal radiation and charge transport problem within the TPV cell. The radiator was modeled as a bulk of W maintained at 2000 K, while $In_{0.18}Ga_{0.82}Sb$ TPV cells (p on n configuration), with a bandgap of 0.56 eV at 300 K, were considered. The TPV cells were assumed to be maintained at a constant and uniform temperature of 300 K. The conversion efficiency of the nano-TPV system, when the quantum efficiency was 100 %, increased as $d_c$ decreased; for $d_c$ values between 2 nm and 10 μm, the conversion efficiency varied from 35 % to approximately 23 %. When quantum efficiencies lower than 100 % were considered via the solution of the charge transport problem, the conversion efficiency was lowered by 5 % to 10 %. For vacuum gaps $d_c$ between 2 nm and 10 μm, the conversion efficiency varied non-monotonically between 17 % and 23 %. An interesting observation was made for $d_c$ values below 10 nm, where the conversion efficiency decreased as $d_c$ decreased. The authors explained this behavior by the combination of the decreasing quantum efficiency and increasing absorption of thermal radiation. For a vacuum gap of 10 nm, the authors estimated that about 1 $MWm^{-2}$ of electrical power was generated, such that a device having a cross-sectional area of 25 $cm^2$ could produce 2.5 kW.

Table 6.1 provides a summary of the aforementioned modeling efforts on nano-TPV power generation devices.

Table 6.1. Summary of theoretical and numerical modeling of nano-TPV power generation devices.

| Reference | Geometry (1D for all cases) | Near-field radiative transfer model | Material for the radiator | Material for the TPV cell | Main assumptions | Original features | Main results |
|---|---|---|---|---|---|---|---|
| Whale and Cravalho [33,34] | Two bulks separated by a vacuum gap | Fluctuational electrodynamics | Drude model | $In_{1-x}Ga_xAs$ (bandgaps from 0.36 to 1.4 eV). | - 100% quantum efficiency<br>- No thermal effects in TPV cells | First modeling work on nano-TPV devices | Near-field effects increase significantly the electrical power output, with marginal gain of conversion efficiency. |
| Whale [144] | Two bulks separated by a vacuum gap | Fluctuational electrodynamics | Drude model | $In_{1-x}Ga_xAs$ (single and multi-junctions). | - 100% quantum efficiency<br>- No thermal effects in TPV cells<br>- radiation propagation in TPV cells modeled via Beer's law | Consideration of multi-junction for TPV cells | Increase of conversion efficiency of about 5% when using TPV cells with two junctions. |
| Pan et al. [145] | Two bulks separated by a vacuum gap | Analogy with total internal reflection | Lossless dielectric | Lossless dielectric | No performance analysis of nano-TPV device | N/A | N/A |
| Narayanaswamy and Chen [35] | Bulk radiator and thin film TPV cell separated by a vacuum gap | Fluctuational electrodynamics | Cubic boron nitride | Fictitious direct bandgap semiconductor (bandgap of 0.13 eV). | - 100% quantum efficiency<br>- No thermal effects in TPV cells<br>- No performance analysis | Proposed to use surface polaritons for spectral control | - Surface phonon-polaritons increase photon overexcitation efficiency by a factor 2 compared to a blackbody source. |
| Laroche et al. [36,131] | Two bulks separated by a vacuum gap | Fluctuational electrodynamics | Tungsten and Drude model | GaSb (bandgap of 0.7 eV) | - 100% quantum efficiency<br>- No thermal effects in TPV cells | Studied the possibilities that the near-field might affect the lifetime of EHPs | - The near-field does not affect the lifetime of EHPs<br>- Conversion efficiencies between 10% and 35% with Drude radiator. |
| Park et al. [37,132] | Two bulks separated by a vacuum gap | Fluctuational electrodynamics | Tungsten | $In_{0.18}Ga_{0.82}Sb$ (bandgap of 0.56 eV). | - No thermal effects in TPV cells | - The TPV cell is discretized into control volumes<br>- Calculation of radiation penetration depth within the TPV cell<br>- Solution of the coupled near-field thermal radiation and charge transport problem. | - Conversion efficiency from 17% to 23% for vacuum gaps between 2 nm and 10 $\mu$m.<br>- Generation of $1 MWm^{-2}$ of electrical power for a 10 nm thick vacuum gap. |

### *6.3.2.2 Literature on nano-TPV experimental works*

The first experimental investigation on nano-TPV power generators was published in 2001 by DiMatteo et al. [146]. The system was made of a silicon radiator (thickness of 500 μm) and InAS cells. The gap between the radiator and the cells was maintained via $SiO_2$ spacers, and a capacitor plate was used to measure this gap. The cells were mounted on a brass block placed on a thermoelectric cooler which was in turn mounted on a liquid cooling block. The entire system was placed under vacuum conditions (40 mTorr range). The gap between the radiator and TPV cells was varied using a piezoactuator flexing the heater chip by fraction of microns. By decreasing the gap for initial radiator temperatures of 348 K, 378 K and 408 K, it was observed that the short-circuit current increased by a factor 5. A dynamic test was also performed, where the piezoactuator was oscillating between frequencies of 200 Hz and 1000 Hz, thus causing the vacuum gap to oscillate. Results showed that variations of the short-circuit current followed in-phase the gap oscillation frequency, meaning that the increase of the current was due to the sub-wavelength spacing between the radiator and TPV cells. While this work demonstrated qualitatively the potential benefits of radiation tunneling on nano-TPV devices, no quantitative data were provided.

The experimental device described above was refined by DiMatteo et al. [147]. The new generation of the system used InGaAs TPV cells. Measurements of the electrical power output for a vacuum gap of about 200 nm showed an enhancement as the temperature of the radiator increased from 550°C to 850°C. Results also revealed that the enhancement in radiation absorption by the TPV cells was proportional to the enhancement of the electrical power output. Tubular spacers were used to reduce heat conduction from the radiator toward the cell; the authors evaluated that parasitic heat conduction through the spacers was less than 3 % of the total heat transfer by radiation. The tubular spacers were compressible, such that the gap between the radiator and TPV could vary by applying an external force to the emitter. Again, this work did not provide any quantitative data about the performances of the nano-TPV device.

More recently, an experimental study of nano-TPV systems was performed by Hanamura and Mori [148]. The radiator and TPV cells were respectively made of W and GaSb, and measurements were done in a vacuum chamber. The TPV cells were mounted on a water-cooled copper block, while a $CO_2$ laser was used to heat up the W radiator with a constant energy input of 20 W. Measurement of the *J-V* characteristic for a radiator temperature of 1000 K showed an increase of the current density as the vacuum decreased. For gaps less than 10 μm (down to 1 μm), the temperature of the radiator greatly decreased, which was explained by the increasing radiative heat flux from the radiator toward the TPV cells (due to radiation tunneling). Similarly to the aforementioned experimental efforts, this work did not provide any quantitative data about the performances of the nano-TPV device. Moreover, relatively large vacuum gaps were considered.

It is worth noting that a company called MTPV (Micron-gap Thermal PhotoVoltaics) claims that they have reached experimentally conversion efficiencies of 10 % to 15 % by spacing the radiator and TPV cells by a micon-size gap [149]. Rob DiMatteo, cited above, is the founder, CEO and Chairman of MTPV. However, no data is available regarding the TPV devices commercialized by MTPV beyond the experimental investigations cited in the above paragraphs.

## 6.4 Modeling of coupled near-field thermal radiation, charge and heat transport in the TPV cell

Nano-TPV system performances are evaluated via the numerical solution of the coupled near-field thermal radiation, charge and heat transport problem. This is done by discretizing the TPV cell into $N$ control volumes $\Delta z_j^{(p,n)}$. The spatial discretizations of the p-doped and n-doped regions are different, since $t_p$ is typically much smaller than $t_n$ [143]. Details about the discretization are provided in section G.1 of appendix G.

### *6.4.1 Near-field thermal radiation modeling*

Near-field radiant energy exchanges between the radiator and the TPV cell are calculated using the fluctuational electrodynamics formalism discussed in chapter 2. The near-field radiative heat flux absorbed by a control volume $\Delta z_j^{(p,n)}$ within the TPV cell, delimited by the boundaries $z_{j+1}^{(p,n)}$ and $z_j^{(p,n)}$, is found by calculating the difference between the flux crossing the boundary $z_j^{(p,n)}$ (i.e., at $z_j^{(p,n),+}$) and the flux crossing the boundary $z_{j+1}^{(p,n)}$ (i.e., $z_{j+1}^{(p,n),+}$). The monochromatic near-field radiative heat flux absorbed by the control volume $\Delta z_j^{(p,n)}$ due to the emitting radiator maintained at temperature $T_0$ is determined from Eq. (3.41):

$$q^{abs}_{\omega,\Delta z_j^{(p,n)}} = \frac{k_v^2 \Theta(\omega,T_0)}{2\pi^2} \mathrm{Re}\left\{ i\varepsilon''_{r0} \int_0^\infty \frac{k_\rho dk_\rho}{k''_{z0}} \left[ \begin{pmatrix} g^E_{0l\rho\alpha}(k_\rho, z_j^{(p,n)},\omega) g^{H*}_{0l\theta\alpha}(k_\rho, z_j^{(p,n)},\omega) \\ - g^E_{0l\theta\alpha}(k_\rho, z_j^{(p,n)},\omega) g^{H*}_{0l\rho\alpha}(k_\rho, z_j^{(p,n)},\omega) \end{pmatrix} - \begin{pmatrix} g^E_{0l\rho\alpha}(k_\rho, z_{j+1}^{(p,n)},\omega) g^{H*}_{0l\theta\alpha}(k_\rho, z_{j+1}^{(p,n)},\omega) \\ - g^E_{0l\theta\alpha}(k_\rho, z_{j+1}^{(p,n)},\omega) g^{H*}_{0l\rho\alpha}(k_\rho, z_{j+1}^{(p,n)},\omega) \end{pmatrix} \right] \right\} \quad (6.1)$$

where the subscript $l$ refers to the layer where $\Delta z_j^{(p,n)}$ is located ($l$ = 2 for the p-doped layer and $l$ = 3 for the n-doped layer). Equation (6.1) is solved using the numerical procedure described in chapter 3, and the assumptions stated in section 3.1 are applicable.

Thermal radiation emitted by the TPV cell toward the radiator has also to be accounted for. The near-field radiative heat flux absorbed by a control volume $\Delta z_j^{(p,n)}$ due to the emitting radiator at temperature $T_0$ is the same as the radiative heat flux absorbed by the radiator due to an emitting control volume $\Delta z_j^{(p,n)}$ at temperature $T_0$. Therefore, Eq. (6.1) normalized by the mean energy of a state Θ depends solely on the geometry of the system and the material properties. Given that, the near-field radiative heat flux emitted by a control volume $\Delta z_j^{(p,n)}$ at temperature $T_{cell,j}$ and absorbed by the radiator, $q_{\omega,\Delta z_j^{(p,n)}}^{emi}$, is calculated by dividing Eq. (6.1) by $\Theta(\omega,T_0)$ and then by multiplying the resulting transfer function by the mean energy of an electromagnetic state at temperature $T_{cell,j}$, $\Theta(\omega, T_{cell,j})$.

Note that medium 4 below the TPV cell is the thermal management system (see Fig. 6.3). For purpose of near-field thermal radiation modeling, the dielectric function of medium 4 is assumed equal to unity.

### *6.4.2 Minority carrier transport modeling*

Minority carrier transport within the TPV cell is modeled via the steady-state continuity equations written as [142,143]:

$$D_{(e,h)}\frac{d^2\Delta n_{(e,h),\omega}(z)}{dz^2}-\frac{\Delta n_{(e,h),\omega}(z)}{\tau_{(e,h)}}+g_\omega(z)=0 \tag{6.2}$$

The term $\Delta n_{(e,h),\omega}(z)$ is the local excess of minority carrier above the equilibrium concentration $n_{(e,h)0}$ generated by absorption of radiation with frequency $\omega$ (i.e., $\Delta n_{(e,h),\omega}(z) = n_{(e,h),\omega} - n_{(e,h)0}$, where $n_{(e,h),\omega}$ is the local carrier concentration). The equilibrium concentrations of minority carriers in the p-doped and n-doped regions are given respectively as $n_{e0}=n_i^2/N_a$ and $n_{h0}=n_i^2/N_d$, where $n_i$ is the intrinsic carrier concentration. In Eq. (6.2), $D_{(e,h)}$ is the diffusion coefficient, while $\tau_{(e,h)}$ is the minority carrier lifetime that accounts for radiative recombination as well as non-radiative Auger and Shockley-Read-Hall (SRH) recombination processes. Radiative recombination refers to radiation emission by an electron falling from the conduction to the valence band of a semiconductor. Radiation thus emitted by the TPV cell can either be re-absorbed within the cell, or be transmitted outside the semiconductor. Since radiation emitted by radiative recombination has $E \geq E_g$, the re-absorption of such waves generates another EHP within the TPV cell; this phenomenon is referred in the literature as "photon recycling" [150]. Photon recycling is accounted for in this work using an approximate method, where a radiative lifetime multiplication factor $\Phi_{PR}$ is introduced. Using this approach, an effective radiative lifetime $\Phi_{PR}\,\tau_{(e,h),rad}$ is defined, which accounts strictly for radiation emitted by radiative recombination that is transmitted outside the TPV cell. The total minority carrier lifetime is calculated as $\tau_{(e,h)} = (1/\tau_{(e,h),Auger} + 1/\tau_{(e,h)SRH} + 1/\Phi_{PR}\tau_{(e,h),rad})^{-1}$.

The minority carrier diffusion equations are coupled with the near-field thermal radiation problem via the local generation rate of EHPs calculated as follows at location $\Delta z_j^{(p,n)}$:

$$g_{j,\omega} = \frac{1}{\hbar\omega}\kappa_{j,\omega}^{ib}\left(\frac{q^{abs}_{\omega,\Delta z_j^{(p,n)}}}{\Delta z_j^{(p,n)}\kappa_{j,\omega}}\right) \tag{6.3}$$

where $\kappa_{j,\omega}$ is the local monochromatic absorption coefficient that accounts for absorption by the lattice and the free carriers, as well as the interband absorption process, while $\kappa_{j,\omega}^{ib}$ is the local monochromatic interband absorption coefficient, which is non-zero for $E \geq E_g$. Strictly speaking, the generation rate of EHPs is given by the incident radiation power multiplied by the interband absorption coefficient [143]. The term in parentheses in Eq. (6.3) corresponds to the incident radiation power, which is then multiplied by $\kappa_{j,\omega}^{ib}$. If absorption by the lattice and the free carriers is negligible above $E_g$, Eq. (6.3) is simplified as $g_{j,\omega} = q^{abs}_{\omega,\Delta z_j^{(p,n)}}/(\hbar\,\omega\Delta z_j^{(p,n)})$ for $E \geq E_g$.

The solution of the minority carrier diffusion equations requires boundary conditions at $z = Z_2$ and $z = Z_4$ (see Fig. 6.3) where there is recombination of EHPs [143]:

$$D_{(e,h)}\frac{d\Delta n_{(e,h),\omega}(Z_{(2,4)})}{dz} = S_{(e,h)}\Delta n_{(e,h),\omega}(Z_{(2,4)}) \tag{6.4}$$

where $S_{(e,h)}$ is the surface recombination velocity. At the edges of the depletion region (i.e., at $Z_{dp}^{p}$ and $Z_{dp}^{n}$), all minority carriers are assumed to be swept by the electric field, such that $\Delta n_{(e,h),\omega}(Z_{dp}^{(p,n)}) = 0$ [143].

### 6.4.3 Modeling of heat transport in the TPV cell

Typical TPV cells are few micrometers thick, such that it is possible to apply Fourier's law. The one-dimensional steady-state energy equation with heat generation applied to the TPV cell is given by:

$$k_{cond}\frac{d^2T_{cell}(z)}{dz^2} + Q(z) = 0 \tag{6.5}$$

where $Q(z)$ is the local heat generation term given by $Q(z) = -S_r(z) + Q_T(z) + Q_{NRR}(z) - Q_{RR}(z)$. Each of these terms is explained hereafter.

$S_r(z)$ is the local radiative heat source representing the balance between thermal radiation emission and absorption by the lattice and free carriers. This term is computed using the solution of the near-field thermal radiation problem as follows:

$$S_{r,j} = \int_0^\infty (\kappa_{j,\omega}^{fc} + \kappa_{j,\omega}^{latt}) \left[ \frac{q_{\omega,\Delta z_j^{(p,n)}}^{emi} - q_{\omega,\Delta z_j^{(p,n)}}^{abs}}{\Delta z_j^{(p,n)} \kappa_{j,\omega}} \right] d\omega \tag{6.6}$$

where the term within the square brackets can be seen as the net radiation power, which is multiplied by the sum of the absorption coefficients due to the lattice $\kappa_{j,\omega}^{latt}$ and the free carriers $\kappa_{j,\omega}^{fc}$ [143]. It is important to note that net radiation power, as calculated in Eq. (6.6), does not account for the redistribution of energy inside the TPV cell due to radiative exchanges between the control volumes. Indeed, this contribution is negligibly small compared to heat conduction within the layer. Moreover, for the temperatures involved in the simulations presented in section 6.6, near-field thermal radiation emitted by the radiator and absorbed by a control volume dominates the value of the heat generation term, such that radiative transfer between the control volumes does not affect in a perceptible manner the net radiation power.

If the absorption by the lattice and free carriers is negligible for $E \geq E_g$, Eq. (6.6) is simplified as:

$$S_{r,j} \approx \int_0^{\omega_g} \left[ \frac{q^{emi}_{\omega,\Delta z_j^{(p,n)}} - q^{abs}_{\omega,\Delta z_j^{(p,n)}}}{\Delta z_j^{(p,n)}} \right] d\omega \tag{6.7}$$

where $\omega_g$ ($= E_g e/\hbar$ ) is the frequency corresponding to the bandgap $E_g$ of the TPV cell.

Radiation absorbed by the cell with $E > E_g$ releases its excess of energy into heat. This contribution to the local heat generation term, $Q_T(z)$, is called thermalization and is also calculated from the solution of the near-field thermal radiation problem as follows [143]:

$$Q_{T,j} = \int_{\omega_g}^{\infty} \kappa^{ib}_{j,\omega} \left[ \frac{q^{abs}_{\omega,\Delta z_j^{(p,n)}}}{\Delta z_j^{(p,n)} \kappa_{j,\omega}} \right] \left( 1 - \frac{E_g}{(\hbar\omega)/e} \right) d\omega \tag{6.8}$$

The term within the square brackets is the incident radiation power, while the expression in parentheses corresponds to the fraction of energy in excess above the bandgap of the cell. If the absorption by the lattice and the free carriers is negligible for $E \geq E_g$, the absorption coefficients on the right-hand side of Eq. (6.8) cancel out.

Minority carriers that recombine before reaching the depletion region, through non-radiative Auger and SRH processes, contribute to raise the temperature of the TPV cell. The contribution of these non-radiative recombination, $Q_{NRR}(z)$, to the local heat generation term is calculated from the solution of the minority carrier diffusion equations as follows [143]:

$$Q_{NRR,j} = \int_{\omega_g}^{\infty} \frac{eE_g}{\tau_{(e,h),NRR}} \Delta n_{(e,h),j,\omega} d\omega \tag{6.9}$$

where $\tau_{(e,h),NRR}$ is the minority carrier lifetime due to non-radiative recombinations, calculated as $\tau_{(e,h),NRR} = (1/\tau_{(e,h),Auger} + 1/\tau_{(e,h),SRH})^{-1}$.

Radiative recombination $Q_{RR}(z)$ contributing to the local heat generation term is calculated in the same way as Eq. (6.9), except that $\tau_{(e,h),NRR}$ is replaced by $\Phi_{PR}\tau_{(e,h),rad}$. Note that by using Eq. (6.9) to calculate $Q_{RR}(z)$, it is implicitly assumed that all radiative energy generated by radiative recombination leaving the p-n junction is not reflected back toward the cell.

At the boundaries of the cell, the internal heat conduction and surface recombination are balanced with an external heat flux. At $z < Z_2$, there is a vacuum, such that the external heat flux is equal to zero (i.e., insulated boundary); this boundary condition can therefore be written as:

$$-k_{cond}\frac{dT_{cell}(Z_2)}{dz}+S_e eE_g\int_{\omega_g}^{\infty}\Delta n_{e,\omega}(Z_2)d\omega=0 \tag{6.10}$$

At the boundary $z = Z_4$, there is an external heat flux due to the thermal management system (modeled as a convective boundary condition). Moreover, surface recombination at $z = Z_4$ can be neglected due to the relatively large thickness of the p-n junction [37,151]. The boundary condition at $z = Z_4$ is consequently written as:

$$-k_{cond}\frac{dT_{cell}(Z_4)}{dz}=h_\infty[T_{cell}(Z_4)-T_\infty] \tag{6.11}$$

where $h_\infty$ and $T_\infty$ are respectively the heat transfer coefficient and temperature of the cooling fluid at $z > Z_4$.

### *6.4.4 Evaluation of nano-TPV device performances*

The photocurrent generated by the cell has to be calculated in order to evaluate the performances of the nano-TPV device. It is assumed that all EHPs generated in the depletion region contribute to generate a photocurrent:

$$J_{dp,\omega}=e\int_{Z_{dp}^{p}}^{Z_{dp}^{n}}g_{j,\omega}dz \tag{6.12}$$

The photocurrents due to EHPs generated outside the depletion region, proportional to the gradient of minority carrier concentration at the edges of the depletion region, are given by [143]:

$$J_{e,\omega} = eD_e \frac{d\Delta n_{e,\omega}(Z_{dp}^{p})}{dz} \tag{6.13a}$$

$$J_{h,\omega} = -eD_h \frac{d\Delta n_{h,\omega}(Z_{dp}^{n})}{dz} \tag{6.13b}$$

The monochromatic photocurrent generated by the TPV cell is therefore given by: $J_{ph,\omega} = J_{e,\omega} + J_{h,\omega} + J_{dp,\omega}$. The total photocurrent $J_{ph}$ is then calculated by integrating $J_{ph,\omega}$ over $\omega$ from $\omega_g$ to infinity.

A forward bias $V_f$ has to be applied at the junction in order to extract power from the TPV cell (see section 6.2) [141]. This applied voltage perturbs the equilibrium at the p-n junction, and consequently induces a current (called dark current $J_0$) opposite to $J_{ph}$. The dark current $J_0$ is calculated by solving the minority carrier diffusion equations in dark conditions (i.e., $g_\omega(z) = 0$) [143]. The boundary conditions at $z = Z_2$ and $z = Z_4$ are the same as Eq. (6.4) in illuminated conditions, except that there is no frequency dependence. The boundary conditions at the edges of the depletion region are on the other hand modified to account for the forward bias $V_f$ [142,143]:

$$\Delta n_{(e,h),\omega}(Z_{dp}^{(p,n)}) = n_{(e,h)0} \exp\left(\frac{eV_f}{k_b T_{cell}}\right) \tag{6.14}$$

Once the minority carrier diffusion equations are solved in dark conditions, $J_0$ can be calculated as a function of the forward bias $V_f$. The dark current is the sum of currents due to minority carriers at the edges of the depletion region, and is consequently calculated using Eqs. (6.13a) and (6.13b) (without the spectral dependence). The effective photocurrent generated by the nano-TPV device is then given by the difference between the total photocurrent and the dark current, $J(V_f) = J_{ph} - J_0(V_f)$, as discussed in section 6.2. By calculating $J_0$ for a series of $V_f$ (starting with $V_f = 0$), the $J$-$V$ characteristic of the TPV cell can be computed.

In this work, both the quantum efficiency and the conversion efficiency of the TPV cell are analyzed. The quantum efficiency is defined as the photocurrent generated at frequency $\omega$

over the radiative energy absorbed by the cell at the same frequency; this efficiency is calculated as [37]:

$$\eta_{q,\omega} = \frac{\hbar\omega J_{ph,\omega}}{e[q_\omega(Z_2^+) - q_\omega(Z_4^+)]} \tag{6.15}$$

The conversion efficiency, which is the ratio of the maximum power output of the nano-TPV device over the total radiative heat flux absorbed by the cell, is calculated as [37]:

$$\eta_c = \frac{P_m}{q_{cell}^{abs}} \tag{6.16}$$

The maximum power output $P_m$ is easily determined using the $J$-$V$ characteristic of the TPV cell (see section 6.2), while the flux absorbed by the cell is calculated as the difference between the total flux crossing the boundary $z = Z_2$ and the boundary $z = Z_4$.

### 6.5 Modeling of optical, electrical and thermophysical properties

In this work, nano-TPV devices with a tungsten (W) radiator and indium gallium antimonide ($In_{0.18}Ga_{0.82}Sb$) cells are considered. The p-doped region is assumed to be 0.4 μm thick with a doping level $N_a$ of $10^{19}$ cm$^{-3}$, while the n-doped material is 10 μm thick with $N_d = 10^{17}$cm$^{-3}$. These parameters are the same as those used by Park et al. [37]; this will allow to perform a direct comparison between the results reported in this dissertation and those from reference [37]. The modeling of the relevant properties needed to perform nano-TPV simulations are explained hereafter.

#### *6.5.1 Dielectric functions of the radiator and TPV cells*

The dielectric function of W has been modeled by curve-fitting the data reported in reference [152]. For direct bandgap semiconductors such as GaSb and InSb, radiation absorption above $E_g$ is dominated by the interband process. For energy slightly lower than $E_g$, there is a spectral band of transparency where the absorption coefficient is very low. As the energy decreases below the transparency region, the absorption coefficient increases due to contributions from the lattice and the free carriers [33,153].

For $E \geq E_g$, the interband dielectric function of the TPV cell is modeled using the semi-empirical model proposed by Adachi [154]. It accounts for the various energy transitions within the semiconductor, and fitting parameters are required to calculate these contributions. The temperature-dependence of the fitting parameters, provided for both GaSb and InSb, is accounted for using Varshni's equation: $E(T_{cell}) = E(0) - \delta T_{cell}^2/(T_{cell} + \beta)$, where $E(0)$ corresponds to an energy level, such as the fundamental bandgap $E_g$, at 0 K. The variables $\delta$ (eV/K) and $\beta$ (K) are fitting constants provided in reference [130]. The dielectric function of the ternary alloy of GaSb and InSb, which can be formulated as $In_{1-x}Ga_xSb$, is calculated using the parameters for GaSb and InSb combined with Vegard's law: $P_{alloy}(x) = xP_{GaSb} + (1 - x)P_{InSb} - x(1 - x)C_B$, where $P$ refers to a given parameter, while $C_B$ is the so-called bowing constant that accounts for deviations from the linear interpolation due to lattice disorders [130]. Note that due to a lack of data in the literature, the doping-dependence of the interband dielectric function is not accounted for in the current version of the model.

The lattice and free carrier contributions to the dielectric function of the TPV cell is accounted for via a Lorentz-Drude model. The parameters for GaSb have been found in [155], while the parameters for InSb have been determined using reference [153]. To calculate the dielectric function due to the lattice and free carriers for $In_{0.18}Ga_{0.82}Sb$ from the parameters for GaSb and InSb, Vegard's law is used with $x = 0.82$ and $C_B = 0$. It is important to note that the temperature-dependence of the dielectric function due to the lattice and free carriers is not accounted for; the doping-dependence is taken into account only for GaSb; the values do not directly depend on the doping level, but on whether if the semiconductor is p- or n-doped.

The real and imaginary parts of the dielectric function of the TPV cell are shown in Figs. 6.4(a) and 6.4(b), respectively. In each figure, the data for $In_{0.18}Ga_{0.82}Sb$ are given at 300 K and by assuming that GaSb is p-doped.

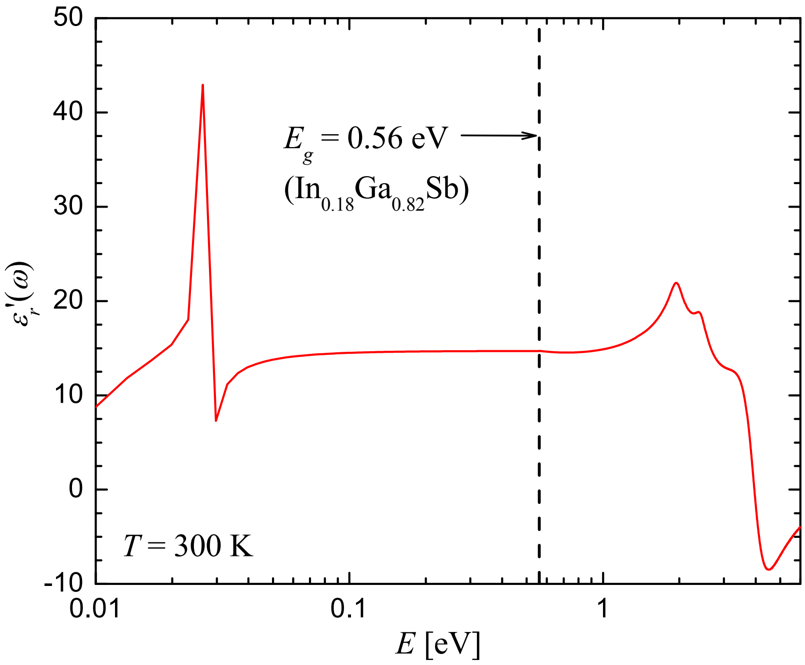

(a)

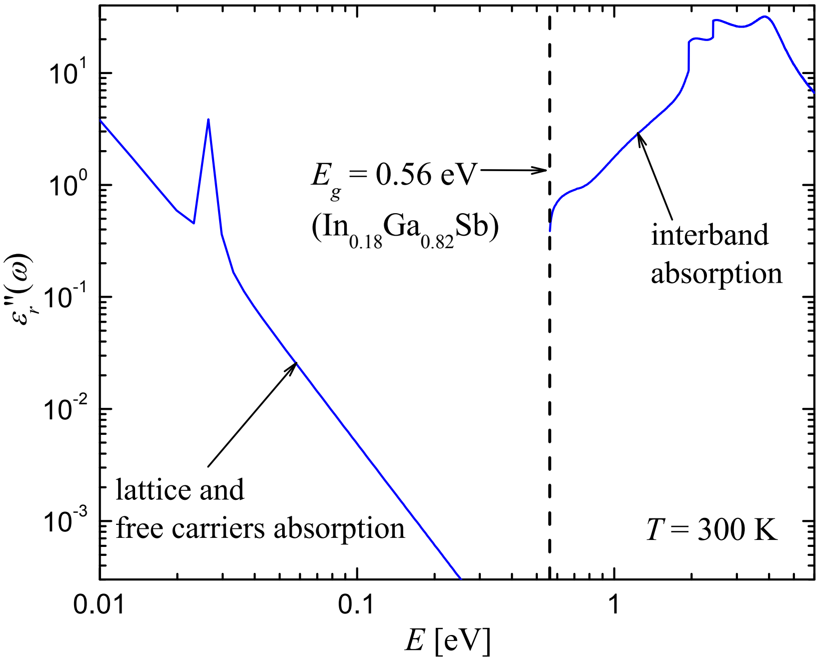

(b)

Figure 6.4. Dielectric function of In$_{0.18}$Ga$_{0.82}$Sb at 300 K (GaSb is p-doped): (a) real part of the dielectric function. (b) imaginary part of the dielectric function.

It is clear by inspecting Fig. 6.4(b) that the imaginary part of the dielectric function is very low below $E_g$, resulting in the so-called "transparency" spectral band. At $E_g$, the imaginary part of the interband dielectric function is much higher than for the lattice and the free carriers. Therefore, it is possible to assume that the contributions from the free carriers and the lattice for energies $E \geq E_g$ is negligible. Note that at 300 K, the bandgap of GaSb is 0.72 eV, while it is 0.18 eV for InSb. For the ternary alloy $In_{0.18}Ga_{0.82}Sb$, $E_g = 0.56$ eV, which corresponds to an angular frequency of $8.51\times10^{14}$ rad/s and a wavelength in vacuum of 2.21 μm.

It is also instructive to analyze the absorption coefficient of $In_{0.18}Ga_{0.82}Sb$. The absorption coefficient is calculated from the dielectric function as follows [156]:

$$\kappa_\omega = \frac{2\omega}{c_v}\left[\frac{\sqrt{(\varepsilon_r'(\omega))^2 + (\varepsilon_r''(\omega))^2} - \varepsilon_r'(\omega)}{2}\right]^{1/2} \tag{6.17}$$

The interband absorption coefficient of $In_{0.18}Ga_{0.82}Sb$, in $m^{-1}$, is shown in Fig. 6.5(a) at $T$ = 300 K and in Fig. 6.5(b) at various temperatures.

The curve in blue in Fig. 6.5(a) (i.e., curve at $E \geq E_g$) corresponds to the actual interband absorption coefficient that drops sharply at the bandgap. For direct bandgap semiconductor such as indium gallium antimonide, the absorption coefficient drops more abruptly than for indirect bandgap semiconductors such as silicon.

Using the model proposed by Adachi [154] to calculate the dielectric function of the TPV cell, interband absorption arises starting at $E \geq E_g$. However, in reality, low interband absorption can be observed at energies slightly less than the bandgap threshold, especially in heavily doped materials [129]. The interband absorption at $E < E_g$ is called the "exponential tail" (represented in red in Fig. 6.5(a)). Note that the exponential tail cannot be predicted with Adachi's model; the red curve shown in Fig. 6.5(a) has been drawn in an approximate manner for purpose of discussion. Since the exponential tail cannot be represented with the current model, we should expect quantities such as the spectral radiative heat flux and the quantum efficiency to drop sharply at $E = E_g$. Experimental data are required to accurately represent the exponential tail. Despite the

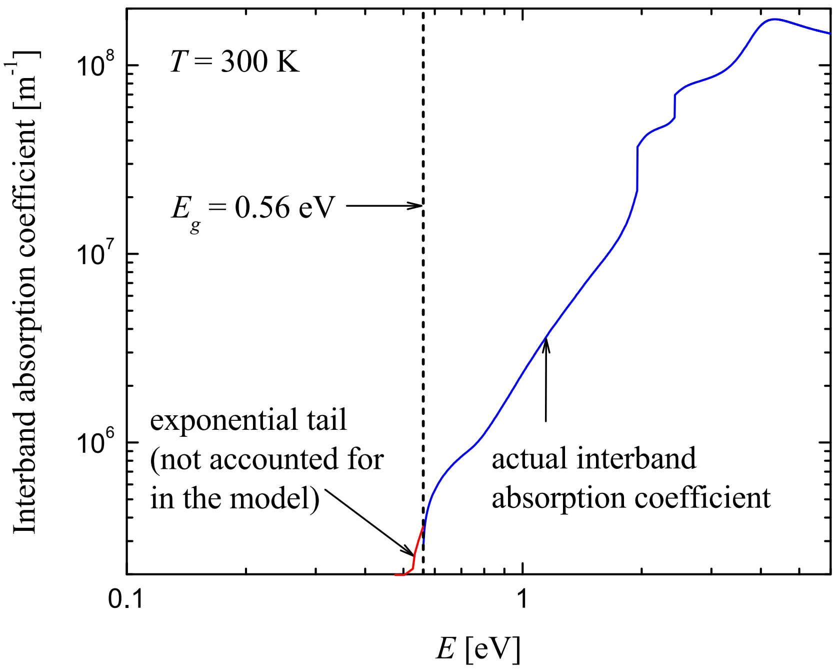

(a)

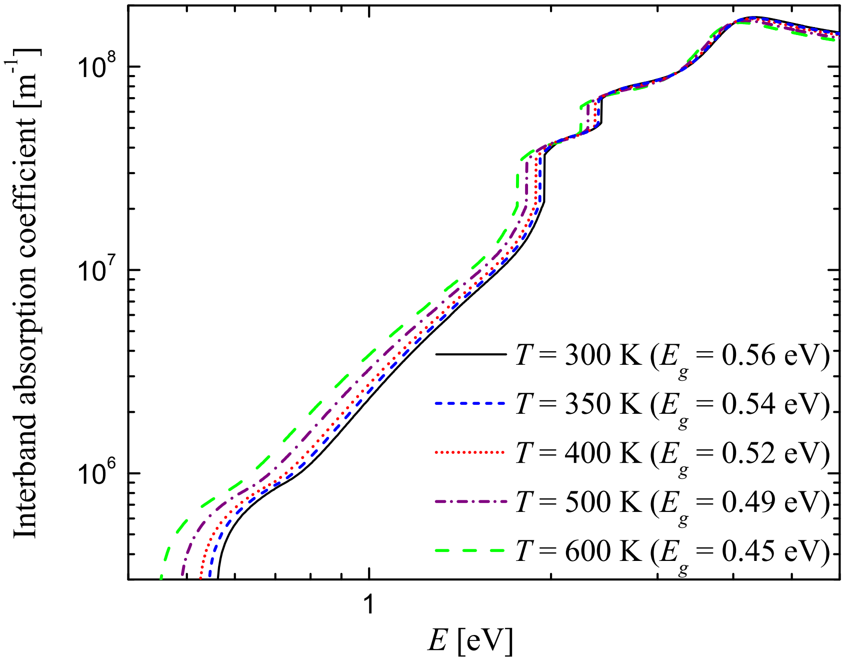

(b)

Figure 6.5. Interband absorption coefficient of $In_{0.18}Ga_{0.82}Sb$: (a) $T$ = 300 K. Note that the exponential tail shown is not obtained from the model, but has been drawn in an approximate manner for the purpose of discussion. (b) $T$ = 300 K, 350 K, 400 K, 500 K and 600 K.

fact that Adachi's model will induce some very low imprecision near the bandgap $E_g$, this will not affect at all the predictions of the performances of the nano-TPV device.

Figure 6.5(b) shows clearly that $E_g$ decreases as $T$ increases. Indeed, the bandgap $E_g$ drops from 0.56 eV at 300 K to a value to 0.45 eV at 600 K. Between $E = E_g$ and 2 eV, the interband absorption coefficient for a given $E$ increases as the temperature increases. For $E > 4$ eV, this trend is inverted.

### *6.5.2 Thermal conductivity*

The temperature-dependent thermal conductivities of GaSb and InSb are calculated as $k_{cond}(T_{cell}) = AT_{cell}^n$ [157]. For GaSb, $A$ and $n$ are given respectively by $7\times10^4$ $\mathrm{Wm^{-1}K^{-1}}$ and -1.35; these values are valid for temperatures from 50 K up to 920 K [157]. For InSb, $A$ and $n$ are respectively given by 5729.7 $\mathrm{Wm^{-1}K^{-1}}$ and -1.028, values that are valid for temperatures equal or larger than 300 K [158]. Note that the doping-dependence on the thermal conductivities of GaSb and InSb is not accounted for. The thermal conductivity of the ternary compound $\mathrm{In_{0.18}Ga_{0.82}Sb}$ is calculated via Vergard's law with $P = k_{cond}$, $x = 0.82$, and $C_B = 0$. At 300 K, the thermal conductivity of $\mathrm{In_{0.18}Ga_{0.82}Sb}$ is 28.9 $\mathrm{Wm^{-1}K^{-1}}$.

### *6.5.3 Intrinsic carrier concentration*

Calculation of the intrinsic carrier concentration $n_i$ requires the knowledge of the effective density of states in the conduction and valence band, which in turn depends on the effective electron and hole masses. The effective electron and hole masses for $\mathrm{In_{1-x}Ga_xSb}$ are calculated respectively as $m_e^* = (0.015 + 0.01x + 0.025x^2)m_0$ and $m_h^* = (0.43 - 0.03x)m_0$, where $m_0$ is the electron rest mass ($9.109\times10^{-31}$ kg) [151]. Once the effective masses are determined, the effective density of states in the conduction and valence band are calculated respectively as $N_c = 2(m_e^* k_b T_{cell}/2\pi\hbar)^{3/2}$ and $N_v = 2(m_h^* k_b T_{cell}/2\pi\hbar)^{3/2}$. Finally, using $N_c$ and $N_v$, the intrinsic carrier concentration is calculated as $n_i = (N_c N_v)^{1/2}\exp(-E_g/2k_b T_{cell})$ [142]. At 300 K, the intrinsic carrier concentration of $\mathrm{In_{0.18}Ga_{0.82}Sb}$ is $2.22\times10^{13}$ $\mathrm{cm^{-3}}$.

### *6.5.4 Thickness of the depletion region*

The thickness of the depletion region is calculated as follows [141,142]:

$$L_{dp} = \left[ \frac{2\varepsilon_s}{e} V_0 \left( \frac{1}{N_a} + \frac{1}{N_d} \right) \right]^{1/2} \tag{6.18}$$

where $V_0$ is the equilibrium voltage at the p-n junction given by $V_0 = (k_b T_{cell}/e)\ln(N_a N_d/n_i^2)$. The term $\varepsilon_s$ is the static relative permittivity calculated as $\varepsilon_s = (16.8 - 1.1x)\varepsilon_v$ for $\mathrm{In}_{1-x}\mathrm{Ga}_x\mathrm{Sb}$, where $\varepsilon_v$ is the absolute permittivity ($8.85\times10^{-12}$ $\mathrm{Fm}^{-1}$) [151]. At 300 K and for the doping levels given in the beginning of section 6.5, the thickness of the depletion region for $\mathrm{In}_{0.18}\mathrm{Ga}_{0.82}\mathrm{Sb}$ is estimated to be 99 nm.

Note that under a forward bias $V_f$, the thickness of the depletion region should be calculated as follows [142]:

$$L_{dp} = \left[ \frac{2\varepsilon_s}{e} (V_0 - V_f) \left( \frac{1}{N_a} + \frac{1}{N_d} \right) \right]^{1/2} \tag{6.19}$$

The procedure used for the nano-TPV calculations follows the technique described by Vaillon et al. [143]. The problem is solved by assuming that the thickness of the depletion region is given by Eq. (6.18). Once the calculations have converged (convergence made on the TPV cell temperature), the dark current is calculated for a series of $V_f$, and the *J*-*V* characteristics of the nano-TPV system is thus generated. Alternatively, Eq. (6.19) could have been used to calculate the thickness of the depletion region under a forward bias, such that the effective photocurrent would have been obtained directly. This procedure is however currently unpractical, since the convergence would need to be performed for each $V_f$ value considered in order to generate the *J*-*V* characteristic. This would lead to excessive CPU requirements, and for this reason, the approach suggested by Vaillon et al. [143] is preferred.

The length of the depletion region in the p-doped zone ($L_{dp}^p$) and in the n-doped material ($L_{dp}^n$) can be calculated as follows [141]:

$$L_{dp}^{p} = \left[ \frac{2\varepsilon_s}{e} V_0 \left( \frac{N_d}{N_a (N_a + N_d)} \right) \right]^{1/2} \tag{6.20a}$$

$$L_{dp}^{n} = \left[ \frac{2\varepsilon_s}{e} V_0 \left( \frac{N_a}{N_d (N_a + N_d)} \right) \right]^{1/2} \tag{6.20b}$$

For the doping levels considered here, we calculated that more than 99% of the depletion region is located in the n-region regardless of the temperature of the cell. Consequently, it is assumed that the entire depletion region is located in the n-doped material.

### *6.5.5 Diffusion coefficients and surface recombination velocities*

The diffusion coefficients are calculated from the electron and hole mobility, $\mu_e$ and $\mu_h$, via the Einstein relation $D_{(e,h)} = \mu_{(e,h)}(k_b T_{cell}/e)$ [151]. The temperature- and doping-dependent electron and hole mobilities are computed using the relation reported in reference [159] and the parameters provided by Gonzalez-Cuevas et al. [151] for GaSb and InSb. The carrier mobility of the ternary alloy $In_{0.18}Ga_{0.82}Sb$ is calculated using Vergard's law with $P = \mu^{-1}$, $C_B = 0$, and $x = 0.82$. At 300 K, the electron and hole diffusion coefficients are given respectively by 35.2 $cm^2s^{-1}$ and 18.3 $cm^2s^{-1}$ for $In_{0.18}Ga_{0.82}Sb$.

Due to the relatively large thickness of the cell, surface recombination velocity of holes in the n-doped region is neglected ($S_h \approx 0$) [151]. For the p-doped region, it is difficult to determine a precise value for $S_e$, as the surface recombination velocity depends not only on the material, but also on the surface treatment of the cell. A precise $S_e$ value should come from experiments. Nevertheless, Martin and Algora [159] suggested that a $S_e$ of about $2\times10^4$ $m\cdot s^{-1}$ can be used for GaSb. Frank and Wherrett [160] suggested that $S_e$ for InSb should take values between 1 to $10^4$ $m\cdot s^{-1}$, depending on surface preparation. For purpose of simulations, we used $S_e = 2\times10^4$ $m\cdot s^{-1}$ for $In_{0.18}Ga_{0.82}Sb$.

### *6.5.6 Minority carrier lifetimes*

Minority carrier lifetime due to SRH non-radiative recombination is calculated as: $\tau_{(e,h),SRH} = (1/\sigma N_t)[m_{(e,h)}^*/(3k_b T_{cell})]^{1/2}$, where $N_t$ is the density of traps ($1.17\times10^{21}$ $m^{-3}$), and

$\sigma$ is the capture cross section of minority carriers ($1.5\times10^{-19}$ m$^2$) [151]. Temperature-dependent minority carrier lifetime due to non-radiative Auger recombination is calculated via the model presented in reference [151]. At 300 K, the total non-radiative minority carrier lifetimes of electrons and holes are 9.8 ns and 31.1 ns, respectively, for $\text{In}_{0.18}\text{Ga}_{0.82}\text{Sb}$.

The minority carrier radiative lifetime is calculated using the following simple model [129]: $\tau_{(e,h),rad} = (BN_{(a,d)})^{-1}$, where $B$ is the bimolecular recombination coefficient ($B_{GaSb} = 8.5\times10^{-11}$ cm$^3$s$^{-1}$ [159] and $B_{InSb} = 5\times10^{-11}$ cm$^3$s$^{-1}$ [158]). The minority carrier radiative lifetime of the ternary alloy $\text{In}_{0.18}\text{Ga}_{0.82}\text{Sb}$ is calculated using Vergard's law with $P = B$, $C_B = 0$, and $x = 0.82$. A photon recycling factor $\Phi_{PR}$ of 10 is used [159]. At 300 K, the effective minority carrier radiative lifetimes of electrons and holes are 13 ns and 1.27 μs, respectively, for $\text{In}_{0.18}\text{Ga}_{0.82}\text{Sb}$.

Finally, the total minority carrier lifetimes of electrons and holes at 300 K are respectively 5.5 ns and 30.3 ns for $\text{In}_{0.18}\text{Ga}_{0.82}\text{Sb}$.

## 6.6 Evaluation of nano-TPV system performances

### *6.6.1 Algorithm for solving the coupled near-field thermal radiation, charge and heat transport problem*

The coupled near-field thermal radiation, charge and heat transport problem is solved using a standard finite-volume discretization method [161]; the numerical details are provided in section G.1 of appendix G. The general algorithm used to predict the performances of nano-TPV device is:

1. Specify the initial temperature $T_{cell}(z)$ of the TPV cell.

2. Specify the heat transfer coefficient and the temperature at $z > Z_4$ (thermal management system).

3. Calculate the properties of the cell at temperature $T_{cell}(z)$.

4. Solve the near-field thermal radiation problem.

5. Calculate the local radiative heat source and thermalization term.

6. Calculate the local generation rate of EHPs.

7. Solve the minority carrier diffusion equations.

8. Calculate the photocurrent generated.

9. Calculate the non-radiative and radiative recombination source terms.

10. Solve the energy equation and obtain an updated temperature distribution of the cell.

11. Compare the temperature distribution obtained in step 10 with the temperature distribution from the previous iteration; if the difference is greater than a specified convergence criterion, go back to step 3. Otherwise, go to step 12.

12. Solve the minority carrier diffusion equations in dark conditions for a series of forward bias.

13. Calculate the effective current density generated by the nano-TPV system, and plot the *J*-*V* characteristic.

14. Determine the point on the *J*-*V* characteristic where the power generated by the device is maximal.

15. Evaluate the performances of the nano-TPV power generation system.

The nano-TPV model presented in this chapter has been validated against the results of Park et al. [37], where the thermal effects within the TPV cell were not accounted for. These validation results are presented in section G.2 of appendix G.

### *6.6.2 Performances of nano-TPV power generation as a function of the temperature of the cell*

The performances of the nano-TPV system are analyzed in this section as a function of the temperature of the cell. In other words, the coupled near-field thermal radiation and charge transport problem is solved for a fixed and uniform temperature of the cell $T_{cell}$.

As a reminder, a bulk of W maintained at uniform and constant temperature of 2000 K is considered for the radiator, while the TPV cells are made of $In_{0.18}Ga_{0.82}Sb$.

Figures 6.6(a) to 6.6(c) show the radiation absorbed by the p-n junction $q_{cell}^{abs}$, the electrical power output $P_m$, the photocurrents $J_{ph}$, $J_{dp}$, $J_h$ and $J_e$, and the conversion efficiency $\eta_c$ of the nano-TPV system for gaps $d_c$ from 1 nm to 10 μm at $T_{cell} = 300$ K.

As expected, the radiation absorbed by the cell, and therefore the electrical power output, increases as the gap separating the radiator and the p-n junction decreases (due to radiation tunneling). It is interesting to note that an increase of $q_{cell}^{abs}$ and $P_m$ is observable when $d_c$ increases from 800 nm to about 1 μm. This inverse trend is likely to be due to wave interference within the gap. Figure 6.6(b) shows that the photocurrent due to diffusion of minority electrons in the p-region increases as $d_c$ decreases, while the photocurrents due to diffusion of holes in the n-region and within the depletion zone saturate, and decrease slightly below $d_c$ values of about 10 nm. Similarly, the conversion efficiency of the nano-TPV device decreases significantly below a gap of 10 nm. The optimum $\eta_c$ values are found for gaps between 10 nm and 100 nm ($\eta_c \approx 24\%$). For a sufficiently large gap (i.e., starting at about $d_c \approx 5$ μm), all the parameters shown in Figs. 6.6(a) to 6.6(c) become independent of $d_c$ as the far-field regime of thermal radiation is reached. In the far-field limit, an electrical power output and a conversion efficiency of $2.40\times10^4$ Wm$^{-2}$ and 19.8 %, respectively, have been calculated. This is in good agreement with the typical performances of "macroscale-gap" TPV devices reported in the literature, as discussed in the beginning of chapter 6 ($P_m \approx 10^4$ Wm$^{-2}$ and $\eta_c \approx$ 20-30 %) [129]. For a gap of 1 nm, the electrical power output increases substantially to a value of $3.91\times10^7$ Wm$^{-2}$, which is three orders of magnitude higher than the $P_m$ obtained in the far-field. The conversion efficiency is on the other hand quite low at $d_c = 1$ nm ($\eta_c = 14.0$ %). A maximum conversion efficiency of 24.8 % has been predicted for a 20 nm thick gap, where the electrical power output is $5.83\times10^5$ Wm$^{-2}$.

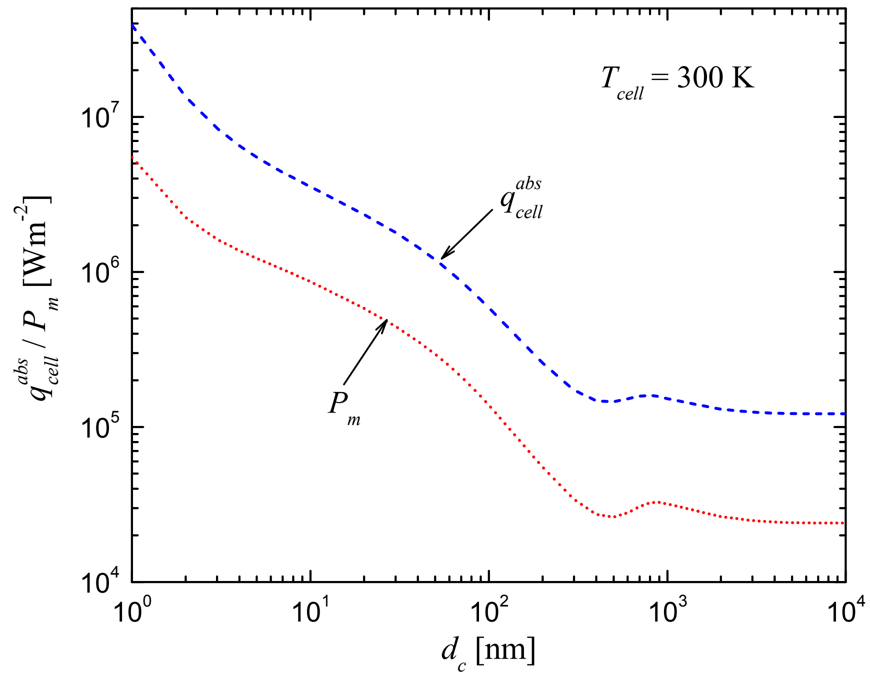

$T_{cell}$ = 300 K
$q^{abs}_{cell}$
$P_m$
$q^{abs}_{cell}$ / $P_m$ [Wm$^{-2}$]
$10^4$
$10^5$
$10^6$
$10^7$
$10^0$
$10^1$
$10^2$
$10^3$
$10^4$
$d_c$ [nm]

(a)

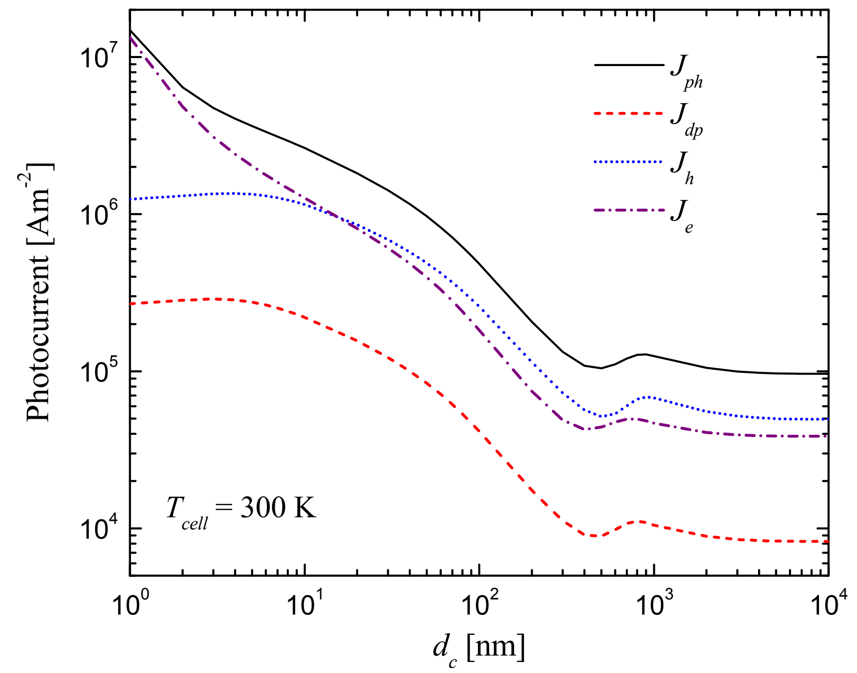

$J_{ph}$
$J_{dp}$
$J_h$
$J_e$
$T_{cell}$ = 300 K
Photocurrent [Am$^{-2}$]
$10^4$
$10^5$
$10^6$
$10^7$
$10^0$
$10^1$
$10^2$
$10^3$
$10^4$
$d_c$ [nm]

(b)

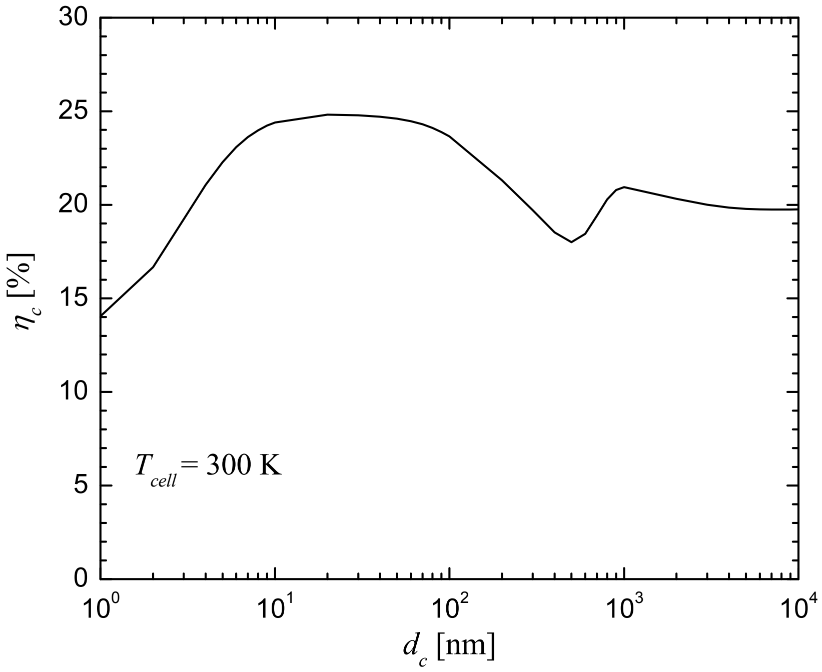

(c)

Figure 6.6. Performances of nano-TPV devices as a function of $d_c$ for $T_{cell}$ = 300 K: (a) radiation absorbed by the cell and electrical power output. (b) photocurrent generated. (c) conversion efficiency.

When considering a quantum efficiency of 100 %, as done by Laroche et al. [36], the conversion efficiency increases with decreasing the gap $d_c$. However, when the fact that the quantum efficiency is less than 100 % is taken into account as done here by solving the minority carrier diffusion equations, a decreasing conversion efficiency is observed for gaps $d_c$ below 10 nm. This behavior, explained by Park et al. [37], can be better understood by inspecting the quantum efficiency for various gap thicknesses, as depicted in Fig. 6.7(a). Note that in this chapter, spectral quantities are presented as a function of the energy of a wave in eV. The monochromatic radiative heat flux at $z = Z_2^+$ is presented in Fig. 6.7(b); note that the spectral flux in $\mathrm{Wm^{-2}eV^{-1}}$ is calculated from the flux in $\mathrm{Wm^{-2}(rad/s)^{-1}}$ as follows: $q_E = q_\omega e/\hbar$ .

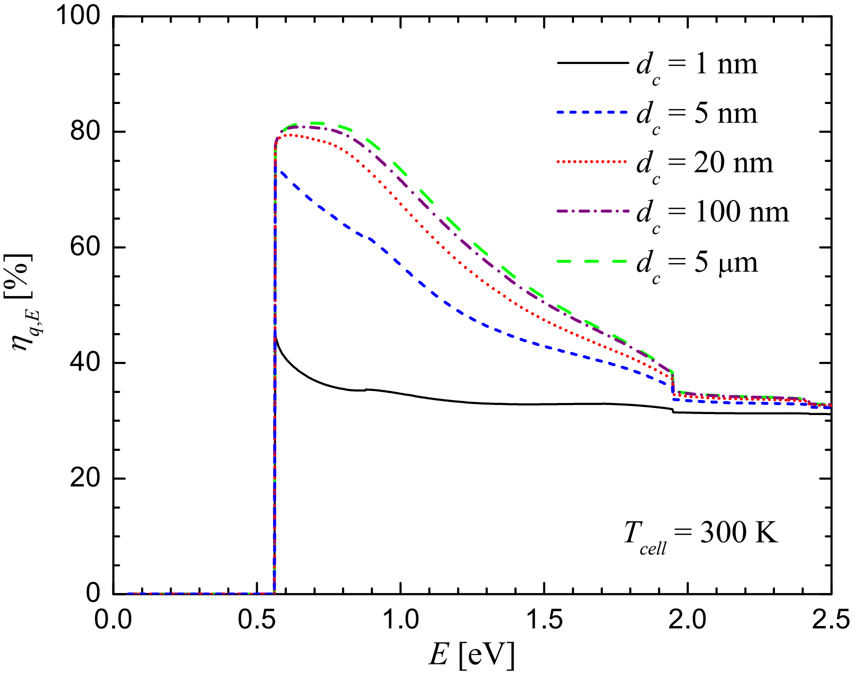

(a)

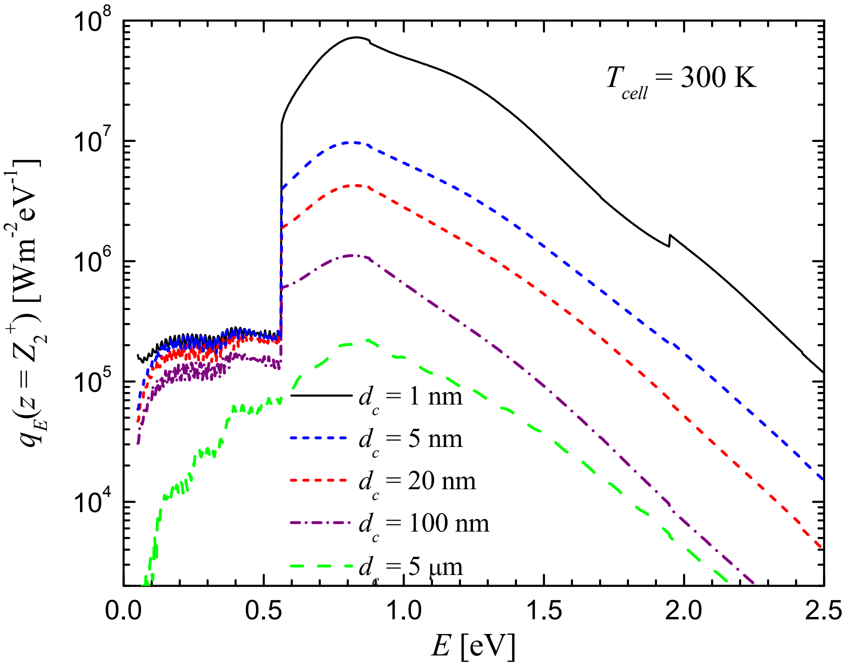

(b)

Figure 6.7. (a) Quantum efficiency of the nano-TPV device as a function of $d_c$ for $T_{cell}$ = 300 K. (b) Monochromatic radiative heat flux at $z = Z_2$ as a function of $d_c$.

Figure 6.7(b) shows that the radiative heat flux at the entrance of the p-n junction (i.e., at $z = Z_2^+$) increases as $d_c$ decreases due to tunneling of evanescent waves. Note that W supports surface plasmon-polaritons (SPPs), and the resonant frequency of a single W-vacuum interface is about $E_{res} \approx 0.92$ eV ($\approx 1.39 \times 10^{15}$ rad/s). Clearly, the maximum radiative heat flux occurs around $E_{res}$. However, the enhancement due to SPPs is not spectacular as for SPhPs, due to high losses in W around $E_g$. Note that below $E_g$, the radiative heat flux drops abruptly, and shows an oscillatory behavior. These oscillations are not associated to any numerical instability, but are rather due to the fact that this spectral band corresponds to the transparency region, as discussed in section 6.5.1. Therefore, a wave penetrating the p-n junction with $E < E_g$ experiences low absorption within the cell, and is therefore likely to reflect back and forth between the boundaries $z = Z_2$ and $z = Z_4$, thus resulting in the interference patterns shown in Fig. 6.7(b).

On the other hand, Fig. 6.7(a) shows that the quantum efficiency decreases as $d_c$ decreases. As discussed in chapters 4 and 5, as the gap $d_c$ decreases, near-field radiative heat transfer is dominated by evanescent waves with decreasing penetration depths in vacuum (and therefore in the TPV cell) of the order of $\delta_{\max} \approx d_c$. This implies that for small $d_c$ values, a large proportion of the radiative energy is absorbed near the boundary $z = Z_2$, and the EHPs thus generated are more likely to recombine before reaching the depletion region. As a consequence, the combination of increasing thermal radiation absorption by the cell and decreasing quantum efficiency as $d_c$ decreases result in low conversion efficiencies, as reported in Fig. 6.6(c) and by Park et al. [37]. This also explains the results of Fig. 6.6(b), where the photocurrents generated in the n-doped and depletion regions, $J_h$ and $J_{dp}$, decrease as $d_c$ decreases below 10 nm.

The performances of the nano-TPV system are investigated further as a function of the temperature of the cell. Figures 6.8(a) to 6.8(c) show the radiation absorbed by the p-n junction, the electrical power output, the total photocurrent generated, and the conversion efficiency for $T_{cell}$ varying from 300 K to 500 K and for gaps $d_c$ of 20 nm, 50 nm and 100 nm.

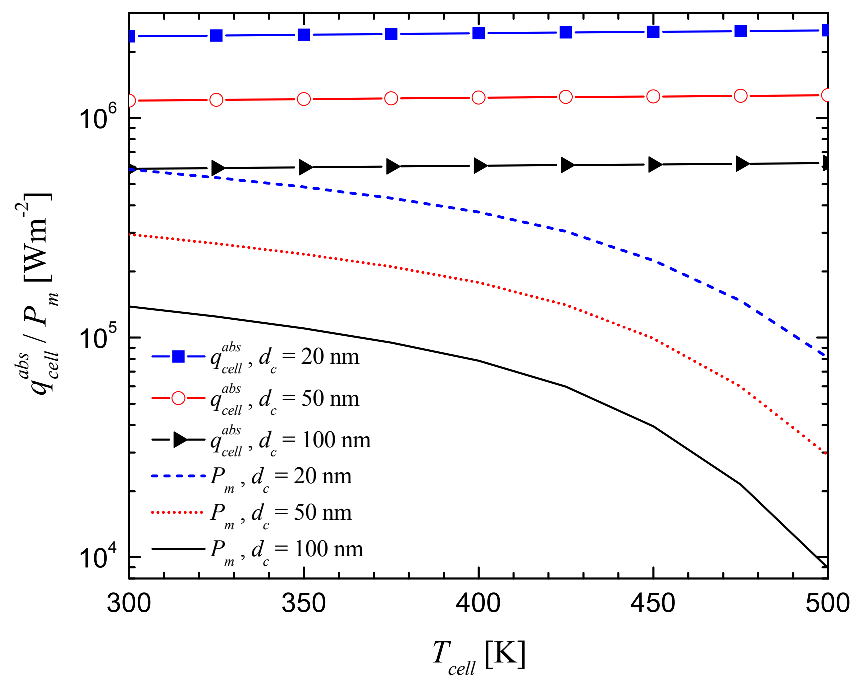

$q_{cell}^{abs}$ / $P_m$ [Wm$^{-2}$]
$10^6$
$10^5$
$10^4$
$q_{cell}^{abs}$, $d_c$ = 20 nm
$q_{cell}^{abs}$, $d_c$ = 50 nm
$q_{cell}^{abs}$, $d_c$ = 100 nm
$P_m$, $d_c$ = 20 nm
$P_m$, $d_c$ = 50 nm
$P_m$, $d_c$ = 100 nm
300
350
400
450
500
$T_{cell}$ [K]

(a)

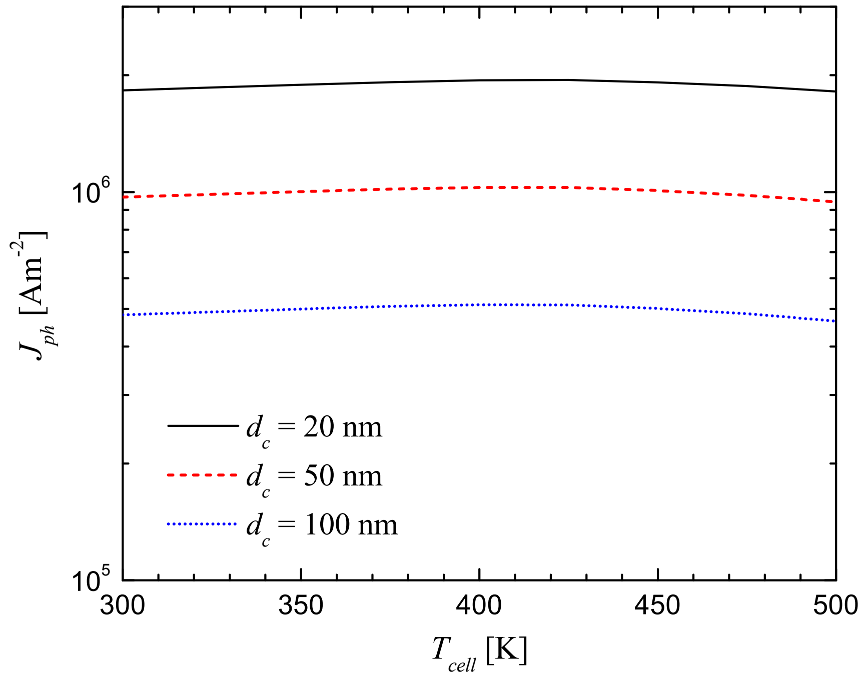

$J_{ph}$ [Am$^{-2}$]
$10^6$
$10^5$
$d_c$ = 20 nm
$d_c$ = 50 nm
$d_c$ = 100 nm
300
350
400
450
500
$T_{cell}$ [K]

(b)

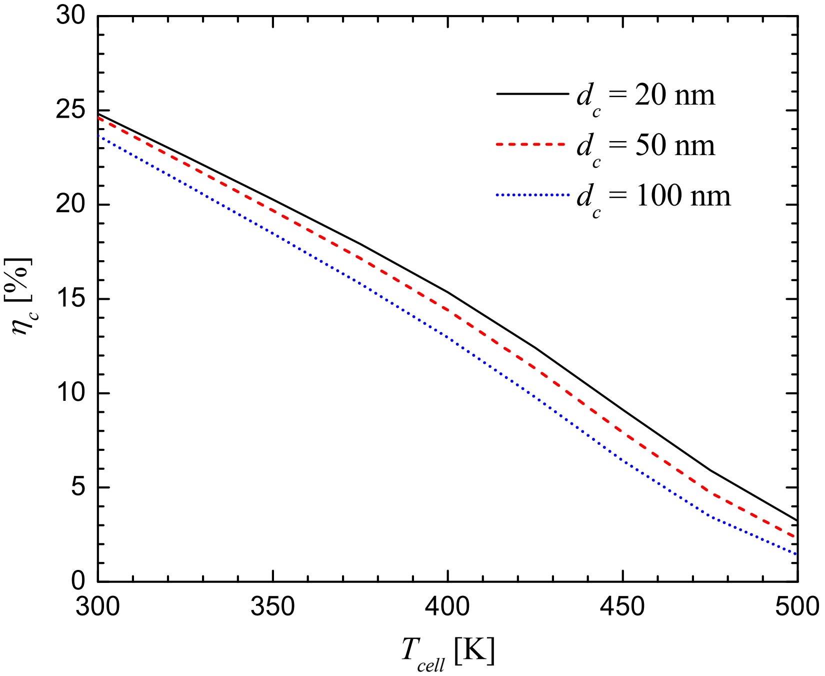

(c)

Figure 6.8. Performances of nano-TPV devices as a function of $T_{cell}$ (300 K to 500 K) for of $d_c$ = 20 nm, 50 nm and 100 nm: (a) radiation absorbed by the cell and electrical power output. (b) total photocurrent generated. (c) conversion efficiency.

It can be observed in Fig. 6.8(a) that thermal radiation absorption increases slightly as the temperature of the cell increases. For example, for a gap of 20 nm, the radiation absorbed at $T_{cell}$ = 300 K is $2.35\times10^6$ $\mathrm{Wm^{-2}}$, while it is $2.51\times10^6$ $\mathrm{Wm^{-2}}$ at $T_{cell}$ = 500 K. This small increase of $q_{cell}^{abs}$ is due to the slight increase in the interband absorption coefficient as $T_{cell}$ increases, and most importantly due to the fact that $E_g$ decreases with increasing the temperature (see Fig. 6.5(b)). On the other hand, the electrical power output $P_m$ of the TPV device decreases significantly when $T_{cell}$ increases, regardless of the gap $d_c$ separating the radiator and the p-n junction. For a $d_c$ value of 20 nm, the electrical power output is about $5.83\times10^5$ $\mathrm{Wm^{-2}}$ at $T_{cell}$ = 300 K, and drops significantly at $8.09\times10^4$ $\mathrm{Wm^{-2}}$ at $T_{cell}$ = 500 K. It is interesting to note that despite this significant drop in electrical power output when increasing $T_{cell}$, the photocurrent $J_{ph}$ is almost insensitive to the temperature of the cell, as shown in Fig. 6.8(b). Indeed, it can be seen that regardless of the gap $d_c$, $J_{ph}$ slightly increases when $T_{cell}$ increases from 300 K to about 425 K, and then slightly decreases for $T_{cell}$ > 425 K. As mentioned above and as depicted in Fig. 6.8(a), an increase of $T_{cell}$ leads to an increase of the absorbed thermal radiation by the cell. Therefore, when $q_{cell}^{abs}$ increases, more EHPs are generated, thus leading to an increase of $J_{ph}$. On the other hand, minority carrier lifetimes $\tau_e$ and $\tau_h$ decrease as $T_{cell}$ increases, thus leading to a larger recombination rate of EHPs. Figure 6.8(b) suggests that below a temperature of about 425 K, the increase in radiation absorption overcomes the increase in EHP recombination, thus leading to an increasing $J_{ph}$ with $T_{cell}$; above 425 K, recombination of EHPs overcomes the increasing thermal radiation absorption, thus leading to a decreasing $J_{ph}$ with increasing $T_{cell}$. However, from a practical point of view, $J_{ph}$ can be considered as nearly constant as a function of the temperature. Finally, as expected from the results depicted in Fig. 6.8(a), Fig. 6.8(c) shows a significant drop in conversion efficiency as the temperature of the cell decreases. For example, the conversion efficiency is 24.8 % when $d_c = 20$ nm and $T_{cell} = 300$ K, a value that drops at 3.23 % when $T_{cell} = 500$ K.

The results presented in Fig. 6.8(a) to 6.8(c) are quite interesting, as they demonstrate clearly that the p-n junction needs to be maintained around room temperature to ensure optimal performances of the nano-TPV device. The trends observed in these figures are independent of the thickness of the gap separating the radiator and the p-n junction. This phenomenon can be better understood by inspecting the $J$-$V$ characteristic of the nano-TPV power generation device. In Fig. 6.9(a), $J$-$V$ characteristics are shown for a nano-TPV device with $d_c = 20$ nm and for various temperatures $T_{cell}$. Note that the $J$-$V$ characteristics are presented in the first quadrant instead of the fourth quadrant (i.e., $J$ is taken as positive). In Fig. 6.9(b), the dark current $J_0$ as a function of the forward bias $V_f$ is shown for various $T_{cell}$ values.

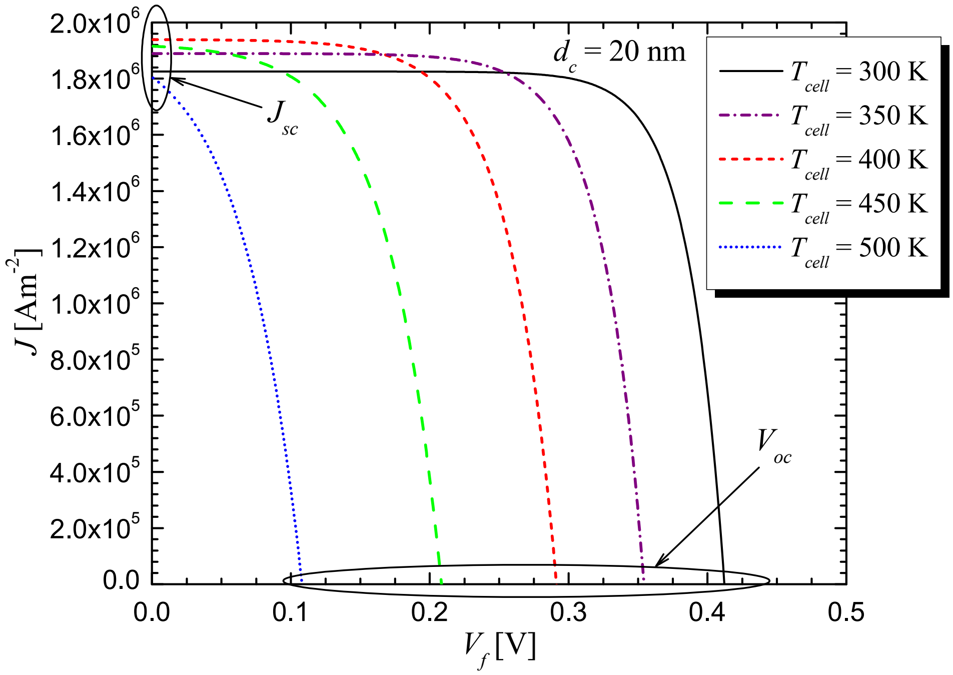

(a)

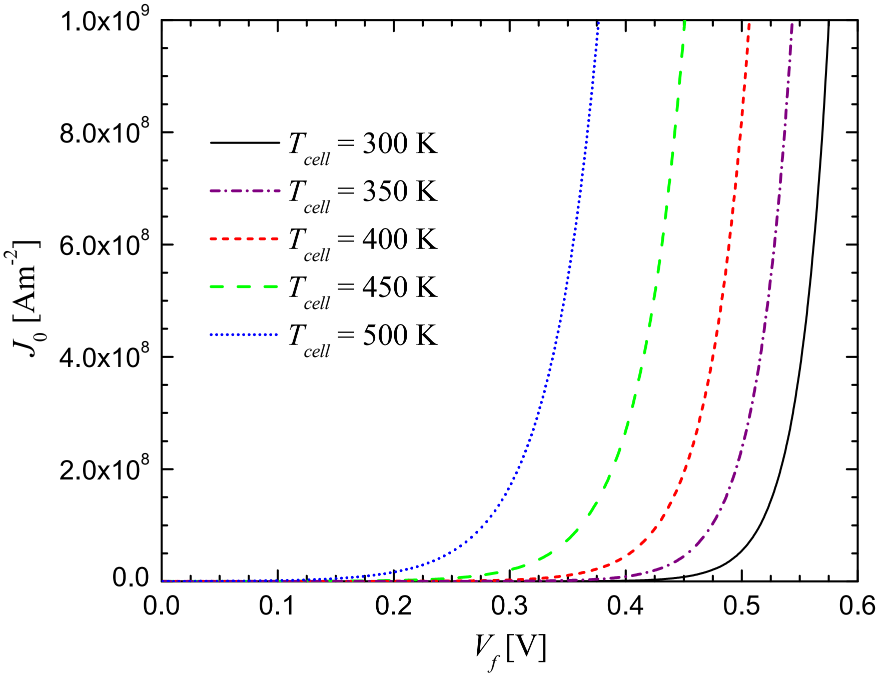

(b)

Figure 6.9. (a) $J$-$V$ characteristic of a nano-TPV device with $d_c$ = 20 nm for $T_{cell}$ = 300 K, 350 K, 400 K, 450 K and 500 K. (b) Dark current $J_0$ as a function of the forward bias $V_f$ for $T_{cell}$ = 300 K, 350 K, 400 K, 450 K and 500 K.

Figure 6.9(a) shows that the short-circuit current $J_{sc}$ slightly varies with $T_{cell}$, while the open-circuit voltage $V_{oc}$ significantly decreases with increasing $T_{cell}$. At $V_f = 0$, it is possible to assume that $J_{sc} \approx J \approx J_{ph}$, since $J_0$ is very small [142]. The variations of $J_{sc}$ as a function of $T_{cell}$ observed in Fig. 6.9(a) are mostly due to the fact that $E_g$ decreases when $T_{cell}$ increases, as explained when discussing the results of Fig. 6.8(b). On the other hand, $V_{oc}$ varies significantly as a function of $T_{cell}$, and these variations explain the low $P_m$ and $\eta_c$ values observed in Figs. 6.8(a) and 6.8(c). Indeed, as discussed in section 6.2, for a fixed $J_{ph}$ value ($J_{ph}$ is almost insensitive to the temperature), a decreasing value of $V_{oc}$ leads to a decreasing power output $P_m$, and thus a decreasing conversion efficiency $\eta_c$.

To ensure a maximal value of the open-circuit voltage $V_{oc}$, the dark current $J_0$ needs to be as small as possible. Figure 6.9(b) shows clearly that for a given $V_f$, the dark current $J_0$ increases when the temperature of the cell increases. Consequently, the decreasing power output and conversion efficiency of the nano-TPV device with increasing $T_{cell}$ are fundamentally due to an increasing dark current $J_0$. Indeed, as the temperature of the cell increases, the intrinsic carrier concentration $n_i$ increases. For example, $n_i = 2.22\times10^{13}$ cm$^{-3}$ and $3.66\times10^{15}$ cm$^{-3}$ for cell temperatures of 300 K and 500 K, respectively. Consequently, the equilibrium concentration of minority carriers, given by $n_{(e,h)0} = n_i^2/N_{(a,d)}$, also increases when increasing $T_{cell}$. The boundary conditions of the minority carrier diffusion equations at the edges of the depletion region in dark conditions (Eq. (6.14)) show that local excess of minority carriers above the equilibrium concentration is directly proportional to $n_{(e,h)0}$. The dark current is proportional to the local excess of minority carriers above the equilibrium concentration, which increases with increasing the temperature of the cell. Therefore, this results in an increase of the dark current $J_0$ with increasing $T_{cell}$, as shown in Fig. 6.9(b).

The observations made in this section are crucial, as they show that the cells need to be maintained around room temperature in order to design efficient nano-TPV power generation devices. To analyze more closely the thermal effects within the cell, the coupled near-field thermal radiation, charge and heat transport problem within the nano-TPV device is solved in the next section.

### *6.6.3 Predictions of nano-TPV power generation performances via the solution of the coupled near-field thermal radiation, charge and heat transport model*

As outlined in section 6.6.1, an iterative process is required to solve the coupled near-field thermal radiation, charge and heat transport problem, and the convergence is evaluated via the temperature of the cell. For each spatial node, the relative difference between the actual temperature and the temperature determined at a previous iteration is calculated. The maximum relative difference computed on the spatial domain is then compared with a predefined convergence criterion; the simulations have converged when this maximum relative difference is less than the convergence criterion. A convergence criterion of $10^{-4}$ (i.e., relative difference of 0.01 %) has been used, since the temperature distribution and the performances of the nano-TPV device were not affected when decreasing the value of this convergence criterion.

In all simulations, it is assumed that the temperature of medium 4 ($T_\infty$) is fixed at 293 K. Figure 6.10 shows averaged cell temperature $T_{cell,avg}$ as a function of the heat transfer coefficient $h_\infty$ for various gaps $d_c$ (5 μm, 100 nm, 50 nm and 20 nm). For all cases treated in this section, the temperature gradient within the cell was found to be very small. A maximum temperature gradient of 0.5 K was calculated for $d_c$ = 20 nm and $h_\infty = 5\times10^3$ $\mathrm{Wm^{-2}K^{-1}}$, such that it is justified to analyze the averaged cell temperature $T_{cell,avg}$ as done in Fig. 6.10.

As expected, for a fixed gap $d_c$, the temperature of the cell increases when the heat transfer coefficient $h_\infty$ decreases, while for a fixed $h_\infty$ value, the temperature of the cell increases as $d_c$ decreases. The melting temperature of GaSb is about 985 K [162], while it is 800 K for InSb [158]. Using Vegard's law with $C_B = 0$ and $P = T_{melt}$ (see section 6.5.1), the melting temperature of $In_{0.18}Ga_{0.82}Sb$ is estimated to be around 952 K. Due to the temperature-dependence of the interband dielectric function, the simulations do not converge when the TPV cell reaches a temperature higher than the melting point; indeed, at such high temperatures, the bandgap of $In_{0.18}Ga_{0.82}Sb$ calculated via Varshni's equation becomes negative, thus resulting in a non-convergence of the interband dielectric function [154]. For $d_c$ = 5 μm, 100 nm, 50 nm and 20 nm, the simulations did not converged for $h_\infty$ values equal or less than $2\times10^2$ Wm$^{-2}$K$^{-1}$, $10^3$ Wm$^{-2}$K$^{-1}$, $2\times10^3$ Wm$^{-2}$K$^{-1}$ and $4\times10^3$ Wm$^{-2}$K$^{-1}$, respectively.

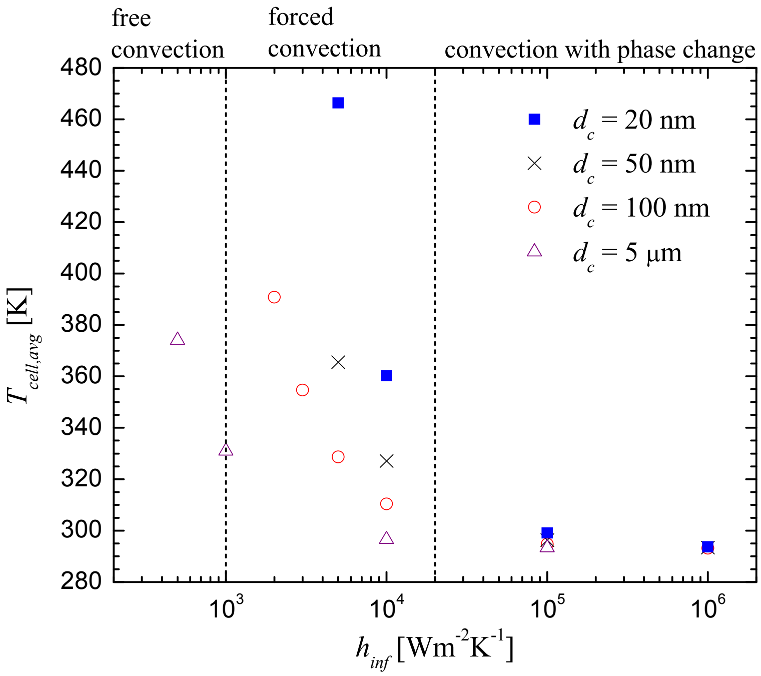

Figure 6.10. Averaged temperature of the cell as a function of $h_\infty$ ($T_\infty$ = 293 K) for $d_c$ = 5 μm, 100 nm, 50 nm and 20 nm.

The values of $h_\infty$ needed to maintain the TPV cell around 300 K are quite high. Indeed, for a gap $d_c$ of 5 μm, a $h_\infty$ value of $10^4$ Wm$^{-2}$K$^{-1}$ is required to maintain the p-n junction around room temperature, while a $h_\infty$ of $10^5$ Wm$^{-2}$K$^{-1}$ is needed for gaps $d_c$ of 100 nm, 50 nm and 20 nm. Generally speaking, heat transfer coefficients $h_\infty$ up to $10^3$ Wm$^{-2}$K$^{-1}$ can be achieved via free convection, while $h_\infty$ up to about $2\times10^4$ Wm$^{-2}$K$^{-1}$ can be reached by forced convection; heat transfer coefficients above this threshold is possible via convection involving phase change [163].

The results of Fig. 6.10 should not be surprising, even though such observations have not been reported so far in the literature. Indeed, radiation with energy $E$ below or above the bandgap $E_g$ largely contributes to heat generation in the p-n junction. On the other hand, the use of a bulk radiator in the near-field provides a broadband enhancement of the flux, which contributes simultaneously to increase the electrical power output and to increase heat generation within the p-n junction. Even when the gap $d_c$ between the radiator and the cell is relatively large (5 μm), the temperature of the junction becomes high (331 K and 374 K) for $h_\infty$ values corresponding to free convection. This is why it is necessary for "macroscale-gap" TPV devices to use radiators selectively emitting thermal radiation in the far-field or to employ filters between the radiator and the cell to reflect back unwanted radiation.

The spatial distributions of the different contributions to the local heat generation term are shown in Fig. 6.11(a) for $d_c$ = 5 μm and in Fig. 6.11(b) for $d_c$ = 20 nm; in both cases, results are given for a $h_\infty$ value of $10^4$ Wm$^{-2}$K$^{-1}$.

The heat source $Q(z)$ is maximum at $z = Z_2$, which corresponds to the irradiated boundary (see Fig. 6.3). Clearly, in both Figs. 6.11(a) and 6.11(b), $Q(z)$ is dominated by thermalization $Q_T(z)$, a conclusion that is applicable to all cases analyzed in this section. This is due to the fact that thermal radiation absorption is dominated by the interband process, where radiation with $E > E_g$ contributes to $Q(z)$ by thermalization. It can also be observed that $Q_T(z)$ decreases sharply as $z$ increases, and does not dominate anymore $Q(z)$ starting at a $z$ value of about 3 μm. Indeed, for $E >> E_g$, the absorption coefficient is quite high (see Fig. 6.5(a)), such that radiation mean free path is small. Therefore, radiation with $E >> E_g$ mostly releases its excess of energy near the boundary $z = Z_2$, since most of these waves are absorbed near the entrance of the cell.

For $d_c$ = 5 μm (Fig. 6.11(a)), after a depth $z$ of about 3.5 μm, the local heat generation term $Q(z)$ is dominated by non-radiative recombination. As pointed out in the previous paragraph, radiation with $E >> E_g$, contributing significantly to heat generation by thermalization, are mostly absorbed near the boundary $z = Z_2$. As the depth $z$ increases within the cell, the influence of $Q_T(z)$ decreases substantially. Since radiation absorption by the p-n junction is dominated by the interband process, heat generation due to non-radiative recombination of EHPs become dominant for large enough depth $z$ within the cell where the contribution from thermalization becomes small. Note that in both Figs. 6.11(a) and 6.11(b), the contributions due to non-radiative and radiative recombination become nil starting at $z = Z_{dp}^p$ (= 0.4 μm), up to a $z$ value corresponding to $z = Z_{dp}^n$, since EHP recombination is neglected in the depletion region.

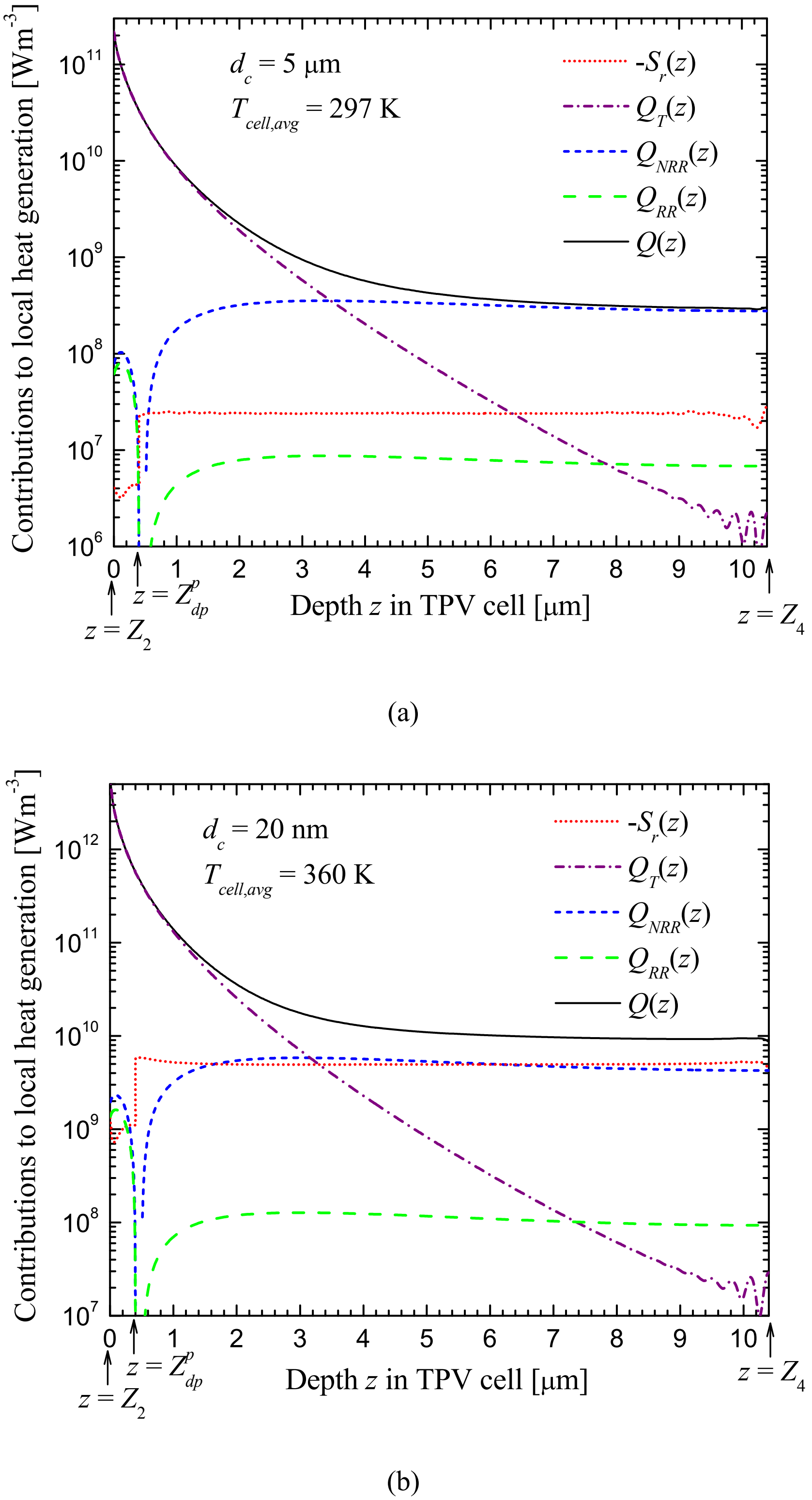

Figure 6.11. Spatial distributions of the different contributions to the local heat generation term $Q(z)$ for $T_\infty$ = 293 K and $h_\infty = 10^4$ Wm$^{-2}$K$^{-1}$: (a) $d_c$ = 5 μm. (b) $d_c$ = 20 nm.

For $d_c$ = 20 nm (Fig. 6.11(b)), $Q(z)$ is dominated by $Q_{NRR}(z)$ starting at $z \approx 3$ μm; however, the local radiative heat source $-S_r(z)$, due to radiation absorption and emission by the lattice and the free carriers, becomes slightly higher than $Q_{NRR}(z)$ starting at a $z$ value of about 7 μm. This behavior can be explained by inspecting Fig. 6.7(b) showing spectral distributions of fluxes at $z = Z_2$. For a $d_c$ value of 20 nm, the flux penetrating the cell with $E < E_g$ is substantially higher than for $d_c$ = 5 μm. Radiation absorbed by the lattice and the free carriers has relatively low energy ($E < E_g$), thus implying a large mean free path compared with waves having $E > E_g$ since the absorption by the lattice and the free carriers is significantly lower than the interband absorption (see Fig. 6.4(b)). This is why for large $z$ values the term $-S_r(z)$ becomes larger than $Q_{NRR}(z)$.

The electrical power output and the conversion efficiency of the nano-TPV devices investigated in Fig. 6.10 are presented respectively in Figs. 6.12(a) and 6.12(b) as a function of the heat transfer coefficient $h_\infty$.

As expected, the performances of the nano-TPV devices are significantly affected by the thermal boundary condition imposed at $z = Z_4$. For example, when $d_c$ = 20 nm, the conversion efficiency $\eta_c$ when $h_\infty = 10^6$ Wm$^{-2}$K$^{-1}$ ($T_{cell,avg}$ = 294 K) is 25.4 %, and this value drops at 6.9 % when $h_\infty = 5\times10^3$ Wm$^{-2}$K$^{-1}$ ($T_{cell,avg}$ = 466 K).

The power output and the conversion efficiency shown in Figs. 6.12(a) and 6.12(b) do not include the electrical power required for obtaining the desired heat transfer coefficient $h_\infty$. Taking into account this parameter, which will be done in a future research effort, is likely to lead to extremely low performances of the nano-TPV device discussed in this dissertation.

## 6.7 Concluding remarks

The results presented in section 6.6.3 suggest that the performances of the nano-TPV devices proposed so far in the literature are quite low. As discussed in this chapter, this is due to the fact that the near-field enhancement of the thermal radiation spectrum occurs at all frequencies, thus contributing not only in increasing the electrical power output, but also in increasing the heat source within the cell.

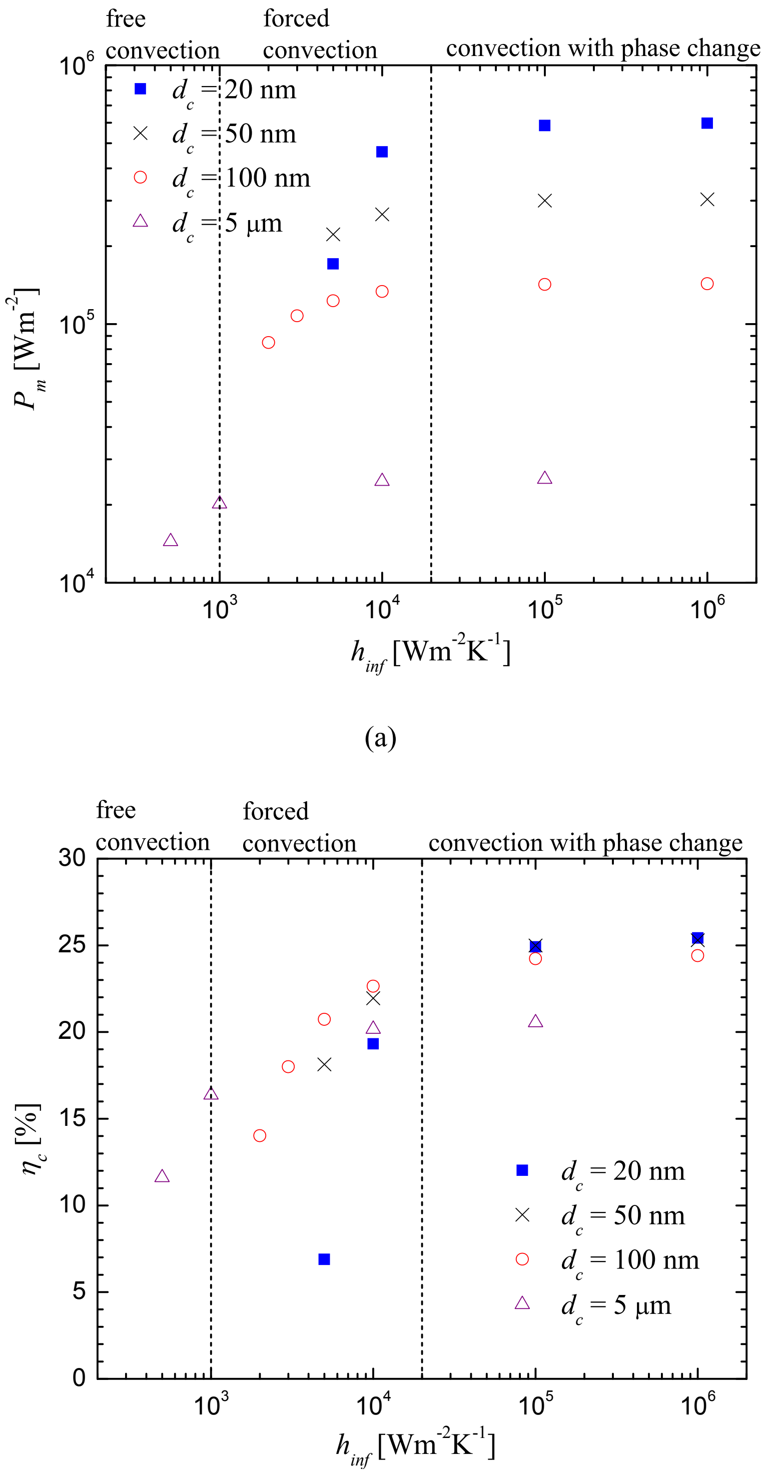

(a)

(b)

Figure 6.12. Performances of nano-TPV energy conversion as a function of $d_c$ and $h_\infty$ ($T_\infty$ = 293 K): (a) electrical power output $P_m$. (b) Conversion efficiency $\eta_c$.

The use of filters between the radiator and the junction to reflect back unwanted waves, as done in the “macroscale-gap” TPV community, is unpractical. Indeed, the presence of filters is likely to disrupt the near-field emitted from the radiator, and, from a practical point of view, it might be very difficult, or even impossible, to place filters between two materials separated by few tens of nanometers. A potential solution is to design nanostructures selectively emitting thermal radiation in the near-field, such that the analysis presented in chapters 4 and 5 could be applied for developing efficient nano-TPV devices.

The performances of the nano-TPV device discussed in this chapter could be analyzed further as a function of the doping levels, the configuration of the cell, the thicknesses of the p- and n-doped regions and the relative proportion of GaSb and InSb. It would also be interesting to quantify the electrical power $P_{cool}$ required to maintain the cell around room temperature in order to calculate the effective power output and the effective conversion efficiency of the device that would account for $P_{cool}$. Finally, the impacts of using radiators made of thin films of W, supporting SPPs, should be investigated in a future research effort.

# Chapter 7

# Characterization of Nanoparticles via Scattering of Surface Waves

In chapters 7 and 8, we explore the possibility of characterizing nanoparticles via scattered surfaces waves, where the term “surface waves” includes both regular evanescent waves and surface polaritons. These chapters, of course related to near-field radiative transfer, are quite different from chapters 2 to 6 both in the subject and the methodology. Near-field thermal radiation and thermophotovoltaic power generation were investigated from a theoretical and a numerical point of view, and significant efforts were deployed to analyze and interpret the physics underlying these problems. In chapters 7 and 8, a more engineering-oriented approach is adopted since the objective is to verify the feasibility of characterizing nanoparticles via scattered surface waves. In that sense, the efforts are mostly devoted to the practical aspects of the problem rather than the physical interpretation of the results. The feasibility of the characterization procedure is explored both from a theoretical / numerical (chapter 7) and an experimental (chapter 8) point of view.

Nanoparticles, defined roughly as particles sized between 1 nm and 100 nm, can have significant different properties from their bulk counterpart [38]. Their creative uses in engineering systems may allow to obtain unique optical, electrical, thermal and structural properties, and strong interests for biomedical and pharmaceutical applications also drive nanoparticle research [38,164-167]. However, synthesis of nanosize particles is still considered art, and without measurement of their properties in real-time, it may be difficult to achieve the desired configurations. To control the nanoscale syntheses or fabrication processes, composition, structure, shape and size distributions of such nanoparticles need to be known; there is consequently a need to develop real-time and non-intrusive characterization tools. Such a characterization technique of nanoparticles has the potential to significantly impact diverse fields of engineering. For example, carbon nanotubes (CNTs) are exploited in a variety of applications due to their extraordinary mechanical, chemical, electronic and thermal properties (see reference [168] and works cited therein). Their characteristics are strongly related to the synthesis method and growth environment, so that CNT growth has been, and is still, extensively studied [169]. Such studies are generally performed via *ex-situ* characterization, since *in-situ* techniques typically involve high equipment cost or low resolution at the early stage of CNT growth [169].

In this dissertation, since the objective is to show the feasibility of the characterization procedure, we restrict our attention to spherical metallic nanoparticles, which also have numerous applications. For example, various works have proposed using metallic nanoparticles to improve thin film photovoltaic (PV) cell efficiencies [4,170,171]. Excitation of metallic nanoparticles, deposited on PV cells, at their surface plasmon-polariton (SPP) resonance can significantly increase thermal radiation absorption. Parameters such as the particles' shapes and agglomeration levels must be controlled to achieve optimal light absorption enhancement, thus motivating the development of a characterization framework to visualize the agglomeration process of nanoparticles in real-time. This idea of using nanoparticles to improve PV cell efficiencies could also be applied to the thermophotovoltaic systems discussed in chapter 6.

The specific objective of this part of the dissertation is therefore to explore the possibility of characterizing spherical metallic nanoparticles, from 5 nm to 100 nm in size, in a non-intrusive manner and potentially in real-time. This is achieved by measuring the changes of intensity and polarization state of scattered surface waves in the far-field to infer properties such as the size, size distribution, shape and level of agglomeration of the nanoparticles. It is of course currently possible to visualize nanoparticles via for example electron microscopy (TEM, SEM) or atomic force microscopy (AFM). These techniques however provide only static measurements, are quite expensive, and can be intrusive in some cases. Note that we do not aim to compete with the well-established SEM or AFM, but we rather propose a framework that could be used in combinations with these tools for characterizing nanoparticles.

Chapter 7 is structured as follows. The concept of polarization state of light is explained in the next section, and the associated mathematical description is overviewed. Then, the characterization procedure investigated in this dissertation is explained in section 7.2. Finally, a sensitivity analysis is performed in order to verify if the quantities measurable in a laboratory are sensitive to the parameters to be estimated.

A part of this chapter was published in the *Journal of Quantitative Spectroscopy and Radiative Transfer* in 2007 [172].

## 7.1 Measurement of the state of polarization of light

The objective of this section is to describe briefly the basics of the polarization state of light, and to explain how this parameter can be measured and employed for characterization purpose. Further information on this subject can be found in references [69,156,173].

### *7.1.1 Polarization state of light*

An electromagnetic wave is fully described by its intensity, frequency, direction of propagation and state of polarization [156,174]. The polarization state of a wave is a measure of the temporal variations of the orientation of the electric field. Without loss of generality, we consider a plane electromagnetic wave propagating along the $x$-direction, such that its electric field is oscillating in the $y$-$z$ plane only. The electric field vector of this propagating wave can be written as follows:

$$\mathbf{E}(x,t) = \hat{\mathbf{y}}E_{0y}\cos(k_x x - \omega t) + \hat{\mathbf{z}}E_{0z}\cos(k_x x - \omega t - \varepsilon) \tag{7.1}$$

where $E_{0y}$ and $E_{0z}$ are the amplitudes of the $y$ ($E_y$) and $z$ ($E_z$) components of $\mathbf{E}$, while $\varepsilon$ is the relative phase difference between $E_y$ and $E_z$.

As shown in Fig. 7.1(a), if $\varepsilon = \pm 2\pi k$ ($k$ = 0, 1, 2, …), the components $E_y$ and $E_z$ are in phase, such that Eq. (7.1) can be written as:

$$\mathbf{E}(x,t) = (\hat{\mathbf{y}}E_{0y} + \hat{\mathbf{z}}E_{0z})\cos(k_x x - \omega t) \tag{7.2}$$

The resultant electric field has a magnitude $E$ ($=|\mathbf{E}(x,t)|$) varying cosinusoidally in time and a fixed orientation $(\hat{\mathbf{y}}E_{0y} + \hat{\mathbf{z}}E_{0z})$. As schematically depicted in Fig. 7.1(a), an observer facing the direction of propagation of the wave and looking back toward the source sees an electrical field that is oscillating along a single direction. In this case, the wave is said to be linearly polarized.

Similarly, if $\varepsilon = \pm\pi k$ ($k$ = 1, 2, 3, …), the electric field vector can be written as follows:

$$\mathbf{E}(x,t) = (\hat{\mathbf{y}}E_{0y} - \hat{\mathbf{z}}E_{0z})\cos(k_x x - \omega t) \tag{7.3}$$

where $E_y$ and $E_z$ are out-of-phase. Again, the wave is linearly polarized, but this time along the direction $(\hat{\mathbf{y}}E_{0y} - \hat{\mathbf{z}}E_{0z})$.

Another particular case arises when $E_y$ and $E_z$ are of same amplitudes (i.e., $E_{0y} = E_{0z} = E_0$) and when the relative phase difference between these two components is $\varepsilon = \pi/2 \pm 2\pi k$ ($k$ = 0, 1, 2, …,). The resulting electric field can thus be written as follows:

$$\mathbf{E}(x,t) = E_0[\hat{\mathbf{y}}\cos(k_x x - \omega t) + \hat{\mathbf{z}}\sin(k_x x - \omega t)] \tag{7.4}$$

In Eq. (7.4), the magnitude of the electric field is constant and is given by $E_0$. At the opposite of the previous cases, the direction of oscillation of **E**, described by the term in square brackets in Eq. (7.4), is not fixed, but rather varies with time. As shown in Fig. 7.1(b), an observer facing the direction of propagation of the wave and looking back at the source sees an electric field describing a circle of radius $E_0$ rotating clockwise. In that case, the wave is said to be right-circularly polarized. In a similar manner, if $\varepsilon = -\pi/2 \pm 2\pi k$ ($k$ = 0, 1, 2, …), the amplitude of **E** is unaffected, but the rotation of the electric field is now counterclockwise, such that the wave is said to be left-circularly polarized.

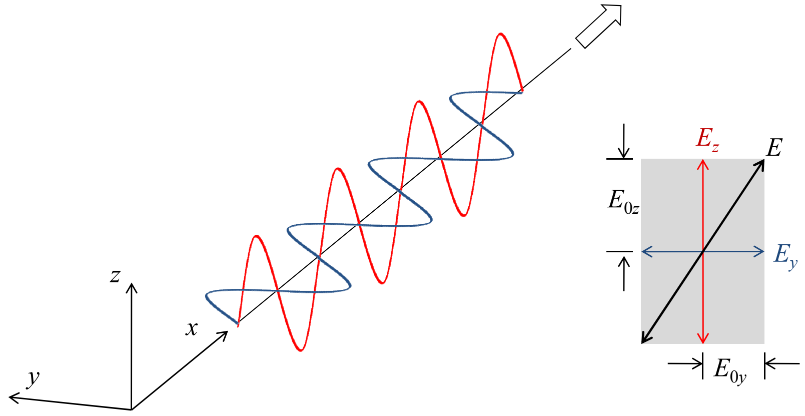

(a)

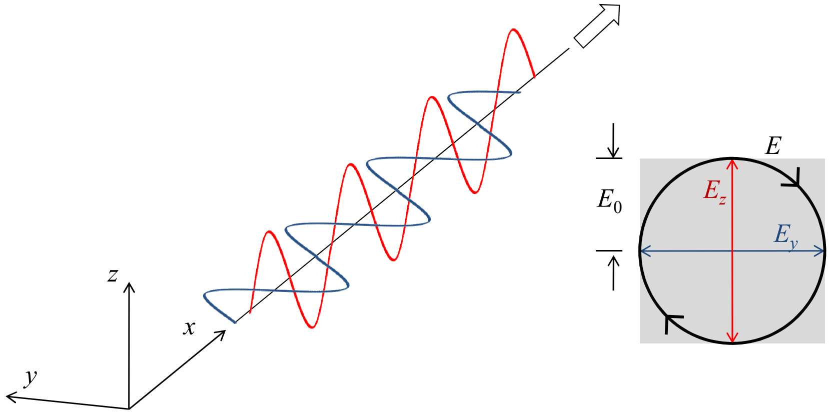

(b)

Figure 7.1. Schematic representation of a: (a) linearly polarized wave. (b) right-circularly polarized wave.

In general, both the magnitude and the orientation of the electric field vector can vary, such that the electric field describes an ellipse [45]. In that case, the wave is said to be elliptically polarized. Starting with Eq. (7.1), the following relation between $E_y$, $E_z$ and $\varepsilon$ can be established [45,174]:

$$\left(\frac{E_y}{E_{0y}}\right)^2 + \left(\frac{E_z}{E_{0z}}\right)^2 - 2\left(\frac{E_y}{E_{0y}}\right)\left(\frac{E_z}{E_{0z}}\right)\cos\varepsilon = \sin^2\varepsilon \tag{7.5}$$

where no initial assumption on the phase lag $\varepsilon$ has been used. The expression given by Eq. (7.5) is the equation of an ellipse, with a semimajor axis $a$ and a semiminor axis $b$, making an angle $\alpha$ with the $E_y$-$E_z$ coordinate system, as depicted in Fig. 7.2. The angle $\alpha$ is given by [45]:

$$\tan 2\alpha = \frac{2E_{0y}E_{0z}\cos\varepsilon}{E_{0y}^2 - E_{0z}^2} \tag{7.6}$$

By calculating the angle $\alpha$ for the specific values of the phase lag $\varepsilon$ discussed above (when deriving the linearly and circularly polarized waves), and by substituting the resulting $\alpha$ in Eq. (7.5), it can be shown that a linearly and a circularly polarized wave are particular cases of an elliptically polarized wave [45].

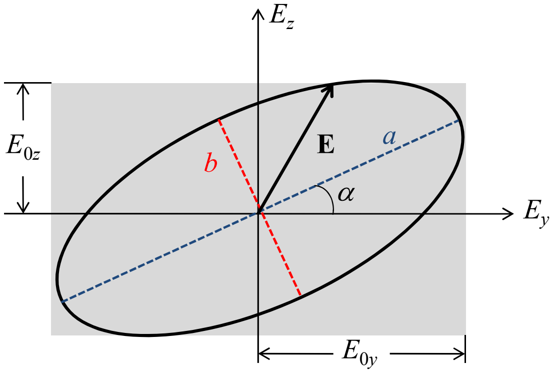

Figure 7.2. Schematic representation of an elliptically polarized wave.

The handedness (i.e., clockwise or counterclockwise rotation), the ellipticity (ratio $b/a$), the angle $\alpha$ and the monochromatic intensity fully describe the energy and polarization state of an electromagnetic wave; these parameters are called the ellipsometric parameters [156,174].

### *7.1.2 Stokes vector*

From a practical point of view, the ellipsometric parameters discussed in the previous section cannot be readily measured, except for the intensity. It is therefore necessary to describe the polarization state of light with quantities that are measurable experimentally. These alternative parameters, called the Stokes parameters, fully describe the energy and state of polarization of an electromagnetic wave, and are given by [45,156,174]:

$$\mathbf{I} = \begin{pmatrix} I \\ Q \\ U \\ V \end{pmatrix} = \begin{pmatrix} \left\langle E_y E_y^* + E_z E_z^* \right\rangle \\ \left\langle E_y E_y^* - E_z E_z^* \right\rangle \\ \left\langle E_y E_z^* + E_z E_y^* \right\rangle \\ i\left\langle E_y E_z^* - E_z E_y^* \right\rangle \end{pmatrix} \tag{7.7}$$

where $\langle\ \rangle$ denotes a temporal / statistical average, while the superscript * means complex conjugate. From an experimental point of view, the Stokes parameters can be measured as follows. The Stokes parameter $I = \left\langle E_y E_y^* + E_z E_z^* \right\rangle$ is simply the intensity of light, such that only a detector is needed to measure the light emerging from a source. The Stokes parameter $Q$ is obtained by performing two experiments, where a filter is placed between the light source and the detector. For the first experiment, the filter only transmits the $y$-component of the electric field, while being opaque for other orientations (i.e., linear polarizer with a transmission axis parallel to the $y$-axis); the intensity thus measured is $I_y = \left\langle E_y E_y^* \right\rangle$. In the second experiment, the transmission axis of the linear polarizer is oriented along the $z$-direction, such that the intensity measured at the detector is $I_z = \left\langle E_z E_z^* \right\rangle$. The parameter $Q$ is thus given by the difference between $I_y$ and $I_z$. Similarly, the Stokes parameter $U$ is measured via two experiments involving a linear polarizer. In the first experiment, the transmission axis of the polarizer is oriented at 45°, while the transmission axis is oriented at -45° for the second experiment. The parameter $Q$ is therefore given by $Q = I_{45^\circ} - I_{-45^\circ}$. The Stokes parameter $V$ is retrieved in a similar manner, except that the first experiment is performed by right-circularly polarizing the light, while the second one is done by left-circularly polarizing the wave. The difference of the intensities measured, $I_R - I_L$, provides the parameter $V$. The Stokes vector, containing the Stokes parameters $I$, $Q$, $U$ and $V$, provides all the information about the intensity and polarization state of light.

An electromagnetic wave is unpolarized when its components $E_y$ and $E_z$ are uncorrelated [174]. If the light is unpolarized, the intensity measured is independent of the orientation of a linear polarizer placed between the source and the detector, thus resulting in $Q = U = V = 0$. If the light is partially polarized, it can be shown that $I^2 \geq Q^2 + U^2 + V^2$ [156,174];

if the wave is fully polarized, the equally holds between the left- and right-hand side of the previous expression. It is then possible to define the degree of polarization of a wave as $P = (Q^2 + U^2 + V^2)^{1/2}/I$ [156]. In the limiting case that the light is unpolarized, $Q = U = V = 0$, such that $P = 0$; if the light is fully polarized, $I^2 = Q^2 + U^2 + V^2$, and therefore $P = 1$. For partially polarized radiation, $P$ takes values between 0 and 1. It is also worth noting that starting with the right-hand side of Eq. (7.7), the Stokes parameters can easily be written as a function of the ellipsometric parameters discussed in section 7.1.1 [156].

### *7.1.3 Mueller (scattering) matrix*

When a radiation beam is interacting with matter, its intensity, polarization state and direction of propagation are modified. It is possible to write a general relationship between an incident Stokes vector $\mathbf{I}_i$ and a scattered Stokes $\mathbf{I}_s$ vector as follows: $\mathbf{I}_s = [S_{ij}]\mathbf{I}_i$ [156,174]. The term $[S_{ij}]$ is a 4×4 matrix called the Mueller, or scattering, matrix. A Mueller matrix can be associated to any media modifying the intensity and polarization state of light; if the light is interacting with multiple media, the equivalent Mueller matrix is given by the multiplication of individual Mueller matrices describing each medium [174].

The Mueller matrix can be derived by considering the relationship between the incident and scattered electric field (in the far-field) after interaction with a medium modifying the intensity, polarization state and direction of propagation of light [156,174]:

$$\begin{pmatrix} E_s^{TM} \\ E_s^{TE} \end{pmatrix} = \frac{e^{ikr}}{ikr}\begin{bmatrix} S_2 & S_3 \\ S_4 & S_1 \end{bmatrix}\begin{pmatrix} E_i^{TM} \\ E_i^{TE} \end{pmatrix} = \frac{e^{ikr}}{ikr}\left[S_i\right]\begin{pmatrix} E_i^{TM} \\ E_i^{TE} \end{pmatrix} \tag{7.8}$$

In Eq. (7.8), the TM and TE components of the electric field are relative to a scattering plane defined using the scattering direction ($\theta_s$,$\phi_s$) and the direction of propagation of the wave [156,174]. The matrix $[S_i]$ is called the amplitude scattering matrix, and is a function of the scattering angles $\theta_s$ and $\phi_s$ and the properties of the material interacting with the wave. The variable $k$, representing the magnitude of the wavevector of the scattered wave, is introduced in the denominator of the factor multiplying $[S_i]$ in order to obtain dimensionless matrix elements [174]; the variable $r$ represents the distance between the points where the wave is scattered and measured in the far-field.

Using the definition of the Stokes vector (Eq. (7.7)) and the relationship between the incident and the scattered electric field (Eq. (7.8)), it is possible to establish the following general relationship between the incident and scattered Stokes vectors:

$$\mathbf{I}_s = \frac{1}{k^2r^2}\begin{bmatrix} S_{11} & S_{12} & S_{13} & S_{14} \\ S_{21} & S_{22} & S_{23} & S_{24} \\ S_{31} & S_{32} & S_{33} & S_{34} \\ S_{41} & S_{42} & S_{43} & S_{44} \end{bmatrix}\mathbf{I}_i = \frac{1}{k^2r^2}\left[S_{ij}\right]\mathbf{I}_i \tag{7.9}$$

The Mueller matrix elements $S_{ij}$ are directly function of the amplitude scattering matrix elements $S_i$; these specific relationships can be found in reference [173].

The Mueller matrix, relating the incident and scattered Stokes vectors, is function of the angles $\theta_s$ and $\phi_s$ and the properties of the medium modifying the intensity and polarization state of light. Therefore, the measurement and analysis of the Mueller matrix $[S_{ij}]$ can allow the determination of the properties of the scattering medium.

## 7.2 Characterization of nanoparticles via elliptically polarized surface waves

Mengüç's group successfully developed a non-intrusive characterization technique based on the measurements of the scattering matrix elements $S_{ij}$ [175-190]. The idea is to illuminate the particles with a propagating radiation beam in the visible spectrum, and to measure the far-field scattered light at different angles. Optical components are used to polarize the beam before and after scattering in order to measure the desired $S_{ij}$ elements, a subject that is discussed in greater details in section 8.2.

This characterization framework is adopted in this work, as it fulfilled the requirement of being a non-intrusive technology that could potentially be done in real-time. On the other hand, the procedure has been successfully applied to characterize particles down to a size of about 100 nm, while our objective is to retrieve the properties of nanoparticles from 5 nm to 100 nm in size. Indeed, due to the diffraction limit, a propagating beam can be focused down to a diameter of about half of the wavelength [1]. The visible spectrum includes wavelengths from 400 nm to 700 nm, such that the minimal diameter at which the beam can be focused is much greater than the targeted size of the particles. A way to circumvent the diffraction limit, while keeping the idea of measuring the change of intensity and polarization state of light, is to illuminate the nanoparticles with a surface wave. This characterization concept is schematically depicted in Fig. 7.3.

As shown in Fig. 7.3, the nanoparticles to be characterized need to be deposited on a surface in order to illuminate them with a surface wave. The layered medium consists of medium 0, having an index of refraction $n_0$ higher than the refractive index of air (medium 2, $n_2 \approx 1$). Between media 0 and 2, there is a thin metallic film (medium 1), such as gold or silver, with a thickness $t_1$ of the order of few tens of nanometers. While it is necessary to have medium 0 with $n_0 > n_2$, the presence of the metallic film is not mandatory.

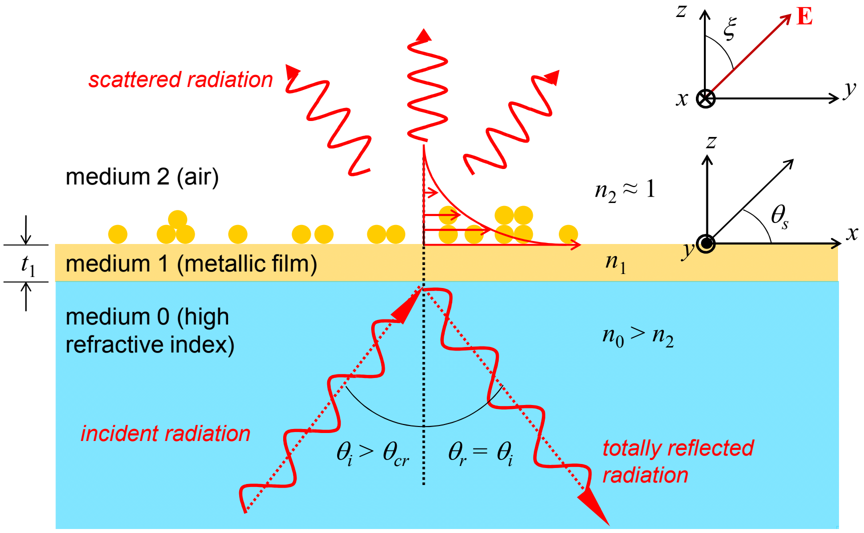
scattered radiation
medium 2 (air)
$n_2 \approx 1$
$t_1$
medium 1 (metallic film)
$n_1$
medium 0 (high refractive index)
$n_0 > n_2$
incident radiation
$\theta_i > \theta_{cr}$
$\theta_r = \theta_i$
totally reflected radiation
$z$
$\xi$
E
$x$
$y$
$z$
$\theta_s$
$x$
$y$

Figure 7.3. Schematic of the characterization concept where the nanoparticles are illuminated via a surface wave (evanescent wave or SPP) generated by total internal reflection of an external radiation beam.

In the absence of a metallic film, the particles are deposited directly on medium 0. An external radiation beam is incident at the interface 0-2 at an angle $\theta_i$ greater than the critical angle for total internal reflection (TIR) $\theta_{cr}$. As explained in section 2.7.1, an evanescent wave is thus generated in medium 2 and is used to illuminate the nanoparticles. If the metallic film is present, the external radiation beam is incident at the interface 0-1 with $\theta_i > \theta_{cr}$, thus generating an evanescent wave at this interface with an evanescent wave field decaying in medium 1. As pointed out in section 4.2, tunneling of this evanescent wave through the metallic film generates SPPs at the interface 1-2. The system used in Fig. 7.3 to generate SPPs is called the Kretschmann configuration, and more information on this subject can be found in references [11,50]. If there is a metallic film between media 0 and 2, the nanoparticles are illuminated via a SPP instead of a regular evanescent wave. The potential advantage of using SPPs, instead of evanescent waves, comes from the fact that the scattered far-field intensity will be higher, such that the resolution of the characterization tool might be optimized. On the other hand, the necessity of having a thin metallic film is somehow a supplementary restriction in the characterization procedure.

If there is no nanoparticle on the layered medium, the surface wave generated in medium 2 does not propagate in the far-field. Consequently, the detector located in the far-field does not measure any intensity, such that the system is in dark conditions. On the other hand, the interaction of an evanescent wave field with the nanoparticles excites the charges within these particles, which in turn radiates the surface wave in the far-field. In that case, the detector located in the far-field measures a scattered intensity.

The change of intensity and polarization state is measured by using optical components to polarize the light before and after scattering (discussed in section 8.2). The scattering matrix elements can thus be measured as a function of the angles $\theta_s$ and $\phi_s$. In this work, the detector located in the far-field can measure the scattered light for different polar angles $\theta_s$ at a fixed azimuthal angle $\phi_s = 0^{\circ}$. Following the convention shown in Fig. 7.3, the surface wave is propagating along the $x$-direction, and the plane of incidence is the $x$-$z$ plane. The polarization state of light is consequently defined in the $y$-$z$ plane. When the electric field vector $\mathbf{E}$ is linearly polarized perpendicular to the plane of incidence (TE polarization), the orientation of $\mathbf{E}$ is $\xi = 90^{\circ}$, while a linearly polarized wave parallel to the plane of incidence (TM polarization) has an electric field oscillating at an orientation $\xi = 0^{\circ}$. The experimental tool developed to perform these measurements is called the polarized-surface-wave-scattering system (PSWSS), and is the subject of chapter 8.

In the next section, the feasibility of the characterization procedure is investigated theoretically via a sensitivity analysis of selected Mueller (scattering) matrix elements.

### 7.3 Sensitivity analysis of the scattering matrix elements

Numerical prediction of surface wave scattering by spherical nanoparticles on a surface is a challenging problem. In this dissertation, the procedure and code developed by Venkata [41,42] is employed. The mathematical details of Venkata's model are not provided here, as they were given in references [41,42]. In a general manner, the numerical procedure is described as follows. The approach is based on a T-matrix method, which is an analytical solution of the scattering problem, where the incident and scattered fields are expanded in vector spherical harmonics (VSH) [156]. The expansion coefficients of the scattered and incident fields are then related through a T-matrix which depends on the properties of the scatterers. Since the expansion coefficients of the incident field and the T-matrix are known, the expansion coefficients of the scattered fields can thus be calculated [41]. The T-matrix method has been extensively applied to problems involving light scattering by particles over the years [191-194].

A difficulty arises when applying the T-matrix method to the problem of nanoparticles illuminated by surface waves due to the interaction between the scatterers and the surface. This problem is solved as follows. For a single spherical particle on a surface, Venkata's model is based on the formulation proposed by Videen et al. [39], where a supplementary field, due to the interaction between the particle and the surface, is accounted for. The interaction field is also expanded into VSH, and the determination of the expansion coefficients is the primary challenge of the approach. Since the particles are small compared with the wavelength, the interaction between the particle and the interface 0-1 is neglected (see Fig. 7.3), such that the interaction field is assumed to be solely due to the interaction between the sphere and the interface 1-2. The expansion coefficients of the interaction field are assumed to be approximately equal to the mirror image of the scattered field multiplied by the appropriate Fresnel's reflection coefficients at normal incidence; this is called the normal incidence approximation [195-199]. This approximation is acceptable for nanoparticles as the interaction field has a low influence on the far-field scattering [39]. For agglomerates of spherical particles, the T-matrix for the cluster of particles is first calculated, and the surface-cluster interaction is then included using the image theory and the normal incidence approximation discussed above. The T-matrix for the cluster of particles is computed using the approach proposed by Mackowski [200] and Mackowski and Mishchenko [201].

Once the expansion coefficients of the scattered field are calculated, the electric field scattered in the far-field can be calculated. Using Eq. (7.8), the elements of the amplitude scattering matrix $S_i$ are determined, and the Mueller matrix can finally be computed. Venkata's approach has been validated against the Lorenz-Mie theory [156] (scattering by a single spherical particle illuminated by a propagating wave) and against the results from Aslan et al. [40] (scattering by a single spherical particle on a surface illuminated by a surface wave); details of the validation are given in reference [42]. Finally, note that the T-matrix method applied scattering of surface waves by agglomerates of spherical nanoparticles on a surface has been recently improved by Mackowski, where an exact solution of the problem has been formulated [202,203].

Previous numerical simulations of surface waves scattering by spherical nanoparticles on a surface revealed that the angular variations of the $S_{ij}$ elements provided significant information about the size, shape, and orientation of particles and / or agglomerates [40,41]. These observations were performed in a qualitative manner, such that there is a need to quantify the sensitivity of the system, via a sensitivity analysis, to the parameters to be characterized. A sensitivity analysis is of primary importance in order to determine the conditions for which a particular parameter can be estimated. The objective here is therefore to perform a sensitivity analysis of systems composed of single and clusters of spherical nanoparticles in order to assess the feasibility of the characterization procedure, and to potentially find the optimal experimental configuration to estimate the desired parameters.

The sensitivity analysis is confined to four scattering matrix elements, namely $S_{11}$, $S_{12}$, $S_{33}$ and $S_{34}$, as prior research suggested that these elements were the most interesting for characterization purposes [176]. These four $S_{ij}$ elements are calculated from the amplitude scattering matrix elements $S_i$ as follows [173]:

$$S_{11} = \frac{1}{2}\left(|S_1|^2 + |S_2|^2 + |S_3|^2 + |S_4|^2\right) \tag{7.10a}$$

$$S_{12} = \frac{1}{2}\left(|S_2|^2 - |S_1|^2 + |S_4|^2 - |S_3|^2\right) \tag{7.10a}$$

$$S_{33} = \mathrm{Re}\left\{S_1 S_2^* + S_3 S_4^*\right\} \tag{7.10a}$$

$$S_{34} = \mathrm{Im}\left\{S_2 S_1^* + S_4 S_3^*\right\} \tag{7.10a}$$

where both the $S_i$ and $S_{ij}$ elements are function of the scattering angles $\theta_s$ and $\phi_s$. As mentioned in section 7.2, the $S_{ij}$ elements are reported and measured as a function of the polar angle $\theta_s$ in a fixed azimuthal plane ($\phi_s = 0°$), such that we can write that $S_{ij} = S_{ij}(\theta_s)$. Physically, $S_{11}$ is simply the scattered intensity, $S_{12}$ represents the depolarization of a linearly polarized beam (TM or TE, defined relative to the plane of incidence *x-z* as depicted in Fig. 7.3), $S_{33}$ provides the conversion of a beam initially linearly polarized at an angle $\xi = \pm 45°$ into a polarization state of the same type, while $M_{34}$ is an indicator of transformation of a beam initially polarized at $\xi = \pm 45°$ into circularly polarized light.

The sensitivity of the system is reported as a function of the normalized scattering matrix elements, $M_{ij}$, which are the quantities measurable in an experiment. These $M_{ij}$ elements are defined as follows: $M_{11}(\theta_s) = S_{11}(\theta_s)$, $M_{12}(\theta_s) = S_{12}(\theta_s)/S_{11}(\theta_s)$, $M_{33}(\theta_s) = S_{33}(\theta_s)/S_{11}(\theta_s)$, and $M_{34}(\theta_s) = S_{34}(\theta_s)/S_{11}(\theta_s)$.

The sensitivity of a measurement to the parameters to be estimated is given numerically by the sensitivity coefficients. In the frame of this study, the normalized sensitivity coefficients are used and can be written as follows [204]:

$$X_{\psi_k}^{norm}[M_{ij}](\eta,\psi) = \left|\frac{\partial M_{ij}(\eta,\psi)}{\partial \psi_k}\psi_k\right| \tag{7.11}$$

The normalized sensitivity coefficients defined by Eq. (7.11) provide the variation of the output / measurement (normalized scattering matrix elements, $M_{ij}$) associated to a relative variation of one parameter of the system ($\psi_k$), when all other parameters (known $\eta$ or to be estimated $\psi_{l,l\neq k}$) are fixed. In a general way, the estimation of a parameter is considered to be conceivable when the normalized sensitivity coefficients are greater than 0.1, difficult but feasible between 0.01 and 0.1, and very difficult or even impossible below the threshold 0.01 [204].

To calculate the global sensitivity of a given configuration / system to a parameter to be estimated, averaged normalized sensitivity coefficients are defined as follows:

$$X_{\psi_k}^{norm,avg}[M_{ij}](\eta,\psi) = \sum_{k=1}^{K} w_k \left| \frac{\partial M_{ij}(\eta,\psi)}{\partial \psi_k} \psi_k \right| \tag{7.12}$$

where $w_k$ is a weighting factor associated with the number of particles characterized by the parameter $\psi_k$ relative to the total number of particles (i.e., $w_k$ is given by a distribution function). By the same way, averaged $M_{ij}$ are defined following the distribution of particles, and are calculated as:

$$M_{ij}^{avg}(\eta,\psi) = \sum_{k=1}^{K} w_k M_{ij}(\eta,\psi) \tag{7.13}$$

The averaged normalized sensitivity coefficients (Eq. (7.12)) are calculated numerically via a centered finite-difference scheme.

For the simulations, gold spherical nanoparticles with diameters $d_m$ are located in medium 2 (air) on a 20 nm thick gold film (medium 1) coated on a sapphire substrate (medium 0). The wavelength of the incident radiation beam is taken as 514.5 nm (argon-ion laser); the corresponding real and imaginary parts of the complex refractive index of gold are 0.50 and 1.86, respectively, while the index of refraction of sapphire is 1.7730. The angle of incidence of the beam $\theta_i$ at the interface 0-1 is 23° (the critical angle for TIR, $\theta_{cr}$, is 17.1°).

First, we consider a case where there is a distribution of single spherical nanoparticles (no agglomerates) of varying diameters $d_m$. Sensitivities of $M_{ij}$ to the diameter are considered ($\psi_k = d_m$) for two size distributions of particles; the first involved a uniform distribution of single spherical particles having diameters from 10 to 15 nm, and the second a uniform distribution of diameters from 45 to 50 nm. The averaged scattering profiles $M_{ij}$

(available in Ref. [41]) and averaged normalized sensitivity coefficients (Figs. 7.4(a) and 7.4(b)) are calculated as a function of the polar angle $\theta_s$.

For both configurations, sensitivities of the normalized scattering matrix elements are found to be highly dependent on the angle $\theta_s$. For a uniform distribution of particles with $d_m$ from 10 to 15 nm (Fig. 7.4(a)), the sensitivity is generally low (sensitivity coefficients are below 0.1, a margin represented by a dashed line). On the other hand, averaged normalized sensitivity coefficients of $M_{12}$ are greater than 0.1 for angles from 0º to 10º, and from 145º to 180º. In the case of particles with $d_m$ from 45 to 50 nm (Fig. 7.4(b)), the sensitivity of all parameters is considerably increased; this can be explained by the fact that as the diameter increases, more energy is tunneled to the particle, which in turns increases the amount of scattered light. For this configuration, and for certain ranges of angle $\theta_s$, the sensitivity coefficient for $M_{12}$, $M_{33}$ and $M_{34}$ is higher than 0.1, suggesting that characterization is possible. It is interesting to note that for both cases, the sensitivity of $M_{11}$ is low regardless of $\theta_s$, which shows that a robust characterization framework of nanoparticles cannot be realized with only the measurement of the scattered intensity; it is therefore obvious that the use of the polarization information of the scattered radiation is quite important for our purposes.

This analysis shows that it is theoretically possible to characterize the diameter of single gold nanoparticles by using the polarization information of the scattered light and the appropriate windows of polar angles $\theta_s$. On the other hand, a real system to be characterized is made not only of single nanoparticles, but also of agglomerates of different shapes; therefore, a sensitivity analysis to such system needs to be analyzed. This is achieved by assuming that the system is composed of single nanoparticles as well as agglomerates. A given system is defined as a function of its composition in single spherical nanoparticles $p$. For example, if $p$ = 25 %, this implies that the remaining 75 % is composed of agglomerates. The composition of these agglomerates is provided in section H.1 of appendix H.

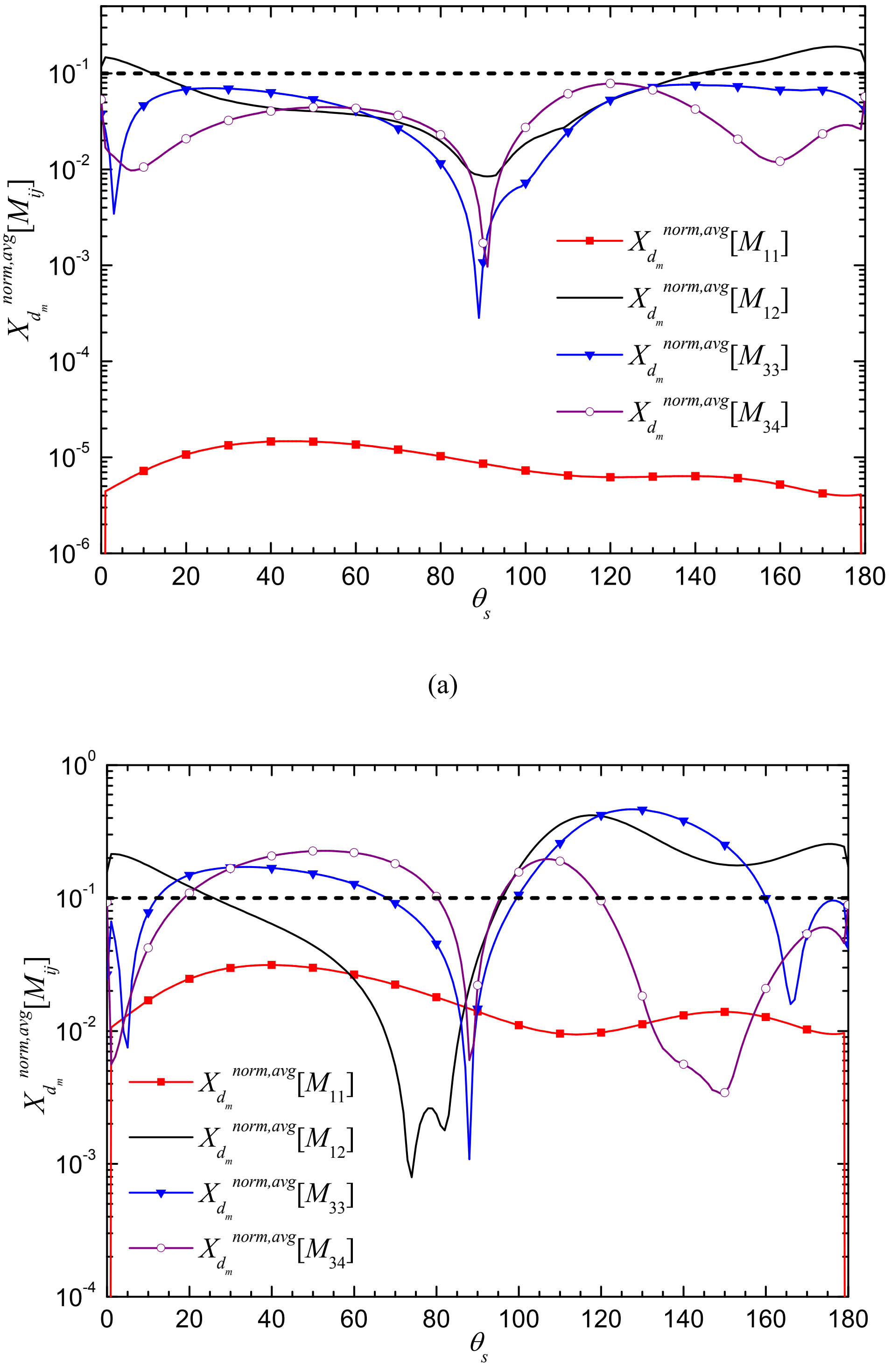

(a)

(b)

Figure 7.4. Averaged normalized sensitivity coefficient to $d_m$. (a) Uniform distribution of particles with $d_m$ from 10 to 15 nm. (b) Uniform distribution of particles with $d_m$ from 45 to 50 nm.

The purpose of the following analysis is to determine if it is theoretically possible to detect a small variation in the level of agglomeration of the system via the normalized scattering matrix elements. The sensitivity to the composition in single nanoparticles $p$ is first investigated and the results are outlined as a function of sensitivity parameter, $\psi_k$ (= $p$). For the test case, we assumed that all particles have a diameter $d_m$ of 40 nm. The normalized scattering matrix elements are shown in Figs. 7.5(a) to 7.5(d), while only the averaged normalized sensitivity coefficients for $M_{12}$, $M_{33}$ and $M_{34}$ are reported in Figs. 7.6(a) to 7.6(c).

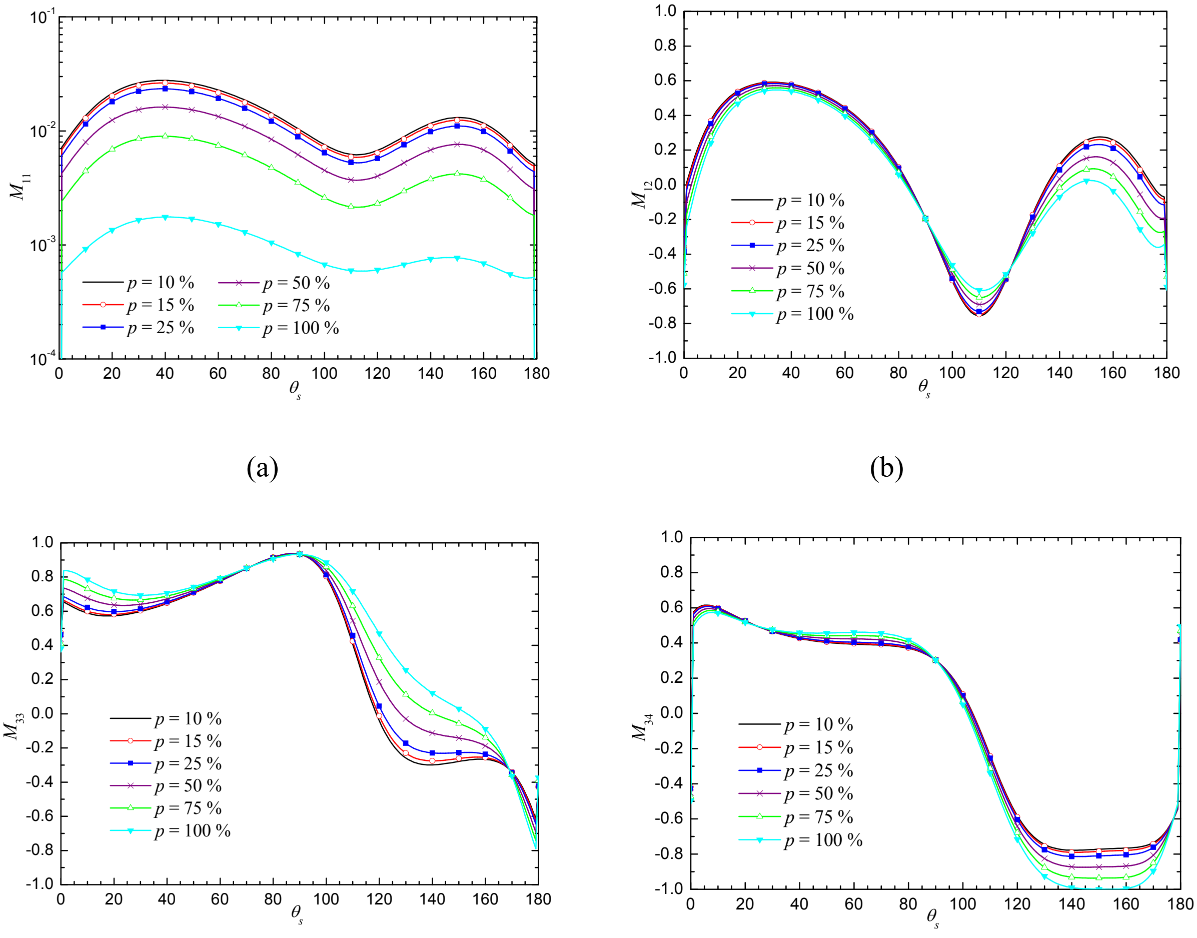

(a)

(b)

(c)

(d)

Figure 7.5. Normalized scattering matrix elements as a function of $\theta_s$ for different $p$ values and $d_m$ = 40 nm. (a) $M_{11}$. (b) $M_{12}$. (c) $M_{33}$. (d) $M_{34}$.

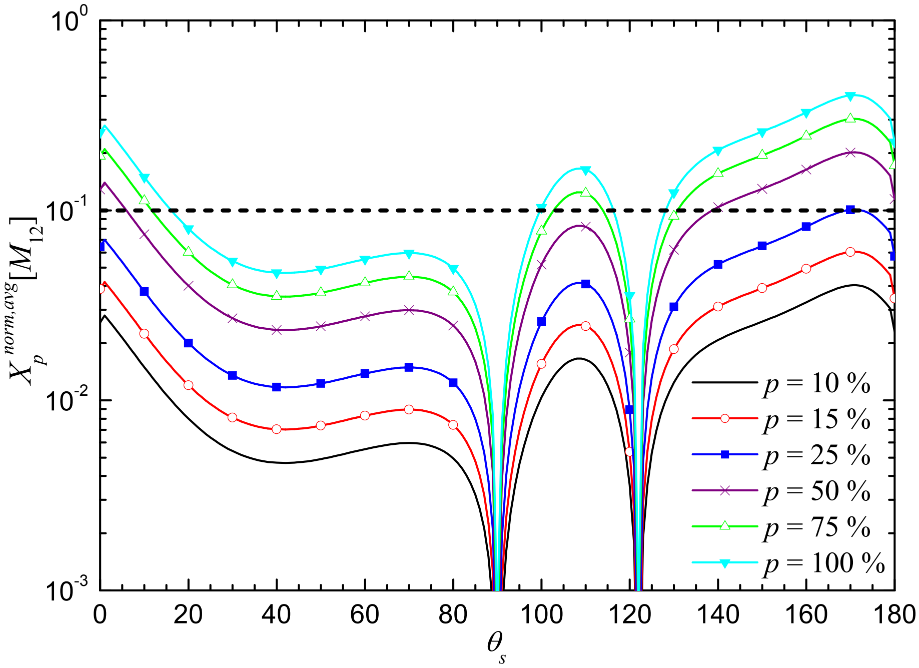
$10^0$
$10^{-1}$
$10^{-2}$
$10^{-3}$
$X_p^{norm,avg}[M_{12}]$
0
20
40
60
80
100
120
140
160
180
$\theta_s$
$p$ = 10 %
$p$ = 15 %
$p$ = 25 %
$p$ = 50 %
$p$ = 75 %
$p$ = 100 %

(a)

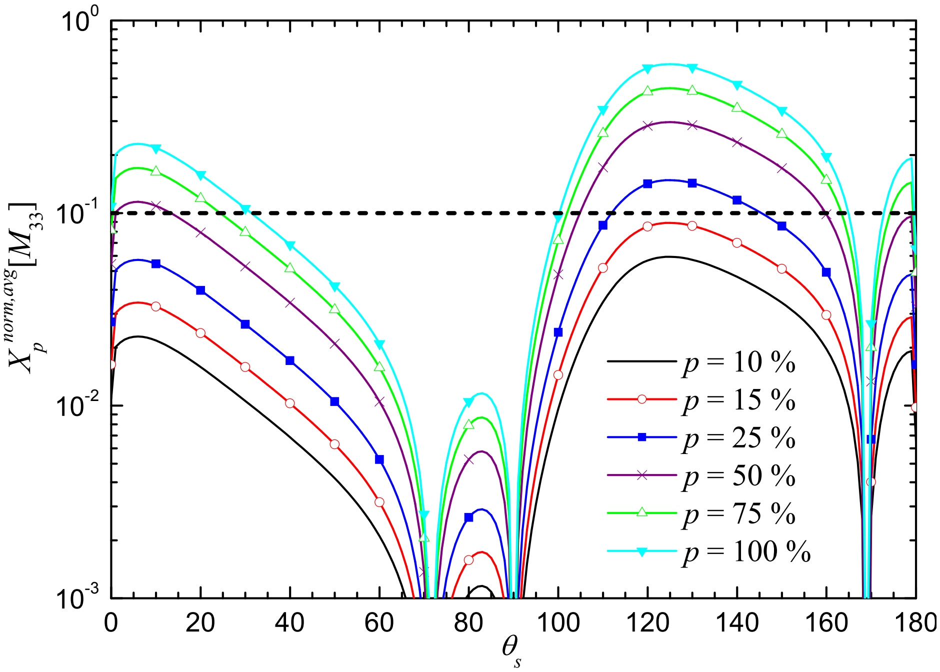
$10^0$
$10^{-1}$
$10^{-2}$
$10^{-3}$
$X_p^{norm,avg}[M_{33}]$
0
20
40
60
80
100
120
140
160
180
$\theta_s$
$p$ = 10 %
$p$ = 15 %
$p$ = 25 %
$p$ = 50 %
$p$ = 75 %
$p$ = 100 %

(b)

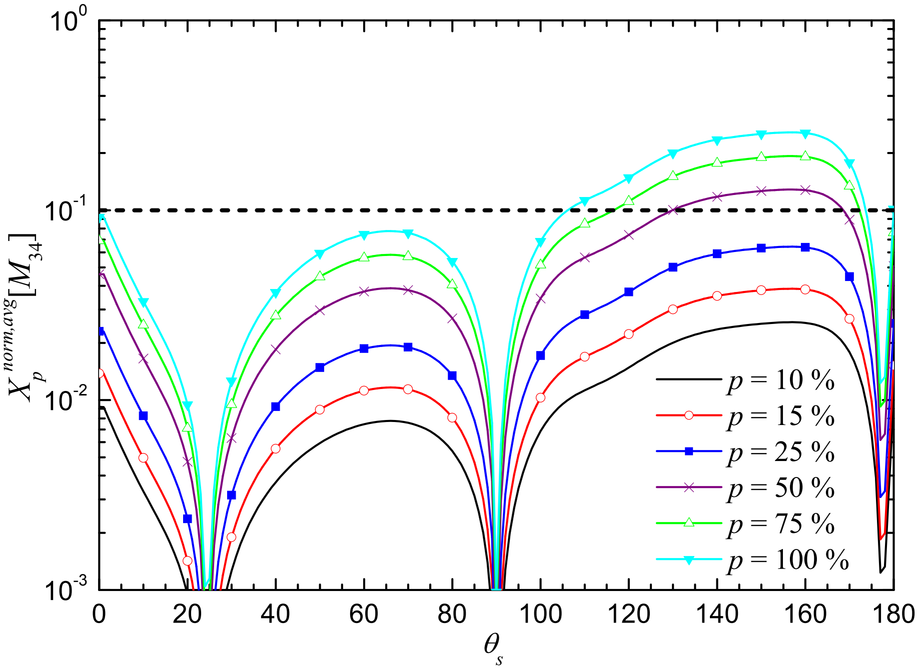

(c)

Figure 7.6. Averaged normalized sensitivity coefficient to $p$ ($d_m$ = 40 nm). (a) Sensitivity of $M_{12}$. (b) Sensitivity of $M_{33}$. (c) Sensitivity of $M_{34}$.

In general, for all normalized scattering matrix elements $M_{ij}$, the sensitivity increases as $p$ increases. This can be explained by the fact that when the system is composed of many agglomerates, the scattered light in the far-field is higher than the scattered light by a system composed strictly of single nanoparticles. Therefore, when the system is composed of many agglomerates, a perturbation of $p$ is more difficult to detect since the signal collected in the far-field is dominated by the scattering of the agglomerates. As the percentage of agglomerates is decreased, a perturbation of $p$ has more impact in the collected signal in the far-field; this behavior is confirmed by Figs. 7.6(a) to 7.6(c).

As in the case for single nanoparticles, the sensitivity of $M_{11}$ is very low (not shown). This can be explained by the fact that even if the $M_{11}$ profiles are quantitatively different (Fig. 7.5(a)), their shapes are very similar. From an experimental point of view, we are only interested by the shapes of the scattering profiles. Therefore, it is almost impossible to distinguish two different configurations in Fig. 7.5(a), since after normalization by their respective maximums, all the curves overlap. On the other hand, the scattering profiles for $M_{12}$, $M_{33}$, and $M_{34}$ differ in shape, for some angles $\theta_s$, as $p$ varies. We can then expect a higher sensitivity for these normalized scattering matrix elements. The sensitivity of $M_{34}$ is low but larger than 0.1 for $\theta_s$ between 130º and 170º and for higher $p$ values (50 %, 75 % and 100 %). It can also be seen that $M_{33}$ is the parameter that offers the highest sensitivity, for a wider range of observation angles $\theta_s$ and composition in single nanoparticles $p$ than $M_{12}$ and $M_{34}$. For $p$ values below 15%, the sensitivity of all $M_{ij}$ parameters is below the threshold 0.1, but the estimation remains feasible since the normalized sensitivity coefficients of $M_{33}$ are between 0.01 and 0.1 for $\theta_s$ between 100º and 165º (Fig. 7.6(b)).

The sensitivity of the normalized scattering matrix elements to the diameter is investigated next ($\psi_k = d_m$). It is assumed that there is a non-uniform distribution of diameters from 38 nm to 42 nm (10 % of 38 nm, 20 % of 39 nm, 40 % of 40 nm, 20 % of 41 nm and 10 % of 42 nm). The normalized scattering matrix elements are reported in Figs. 7.7(a) to 7.7(d) while the averaged normalized sensitivity coefficients of $M_{12}$, $M_{33}$ and $M_{34}$ are presented in Figs. 7.8(a) to 7.8(c).

In general, for all normalized scattering matrix elements $M_{ij}$, the sensitivity increases as $p$ decreases. This is explained by the fact that the signal is stronger (more scattered light) as the proportion of agglomerates is higher, and therefore a perturbation in the diameter result in a higher variation of $M_{ij}$ than for a system composed exclusively of single nanoparticles. As expected from the previous discussions, the sensitivity of $M_{11}$ is very low and below 0.1 (not shown). The estimation of the diameter is feasible for all $M_{12}$, $M_{33}$ and $M_{34}$ measurements, but the optimal sensitivity is found with $M_{12}$ in a zone of $\theta_s$ located approximately between 100º and 140º. In this range, the sensitivity of $M_{12}$ is higher than 0.1 regardless of the value of $p$.

Results presented in this section show that it is theoretically possible to estimate the diameter of the nanoparticles of a system made of single nanoparticles and agglomerates and to estimate its composition. Also, the sensitivity analysis shows that there is not a unique way to estimate a parameter; on the other hand, it is always possible to define an optimal solution for which the normalized sensitivity coefficients are the highest.

The optimal parameters found from the analyses performed in this section are summarized in table 7.1. It is important to note that a given parameter can be estimated in a different way than reported in table 7.1; only the configurations leading to the highest sensitivity (as given by the averaged normalized sensitivity coefficients) are reported in Table 7.1.

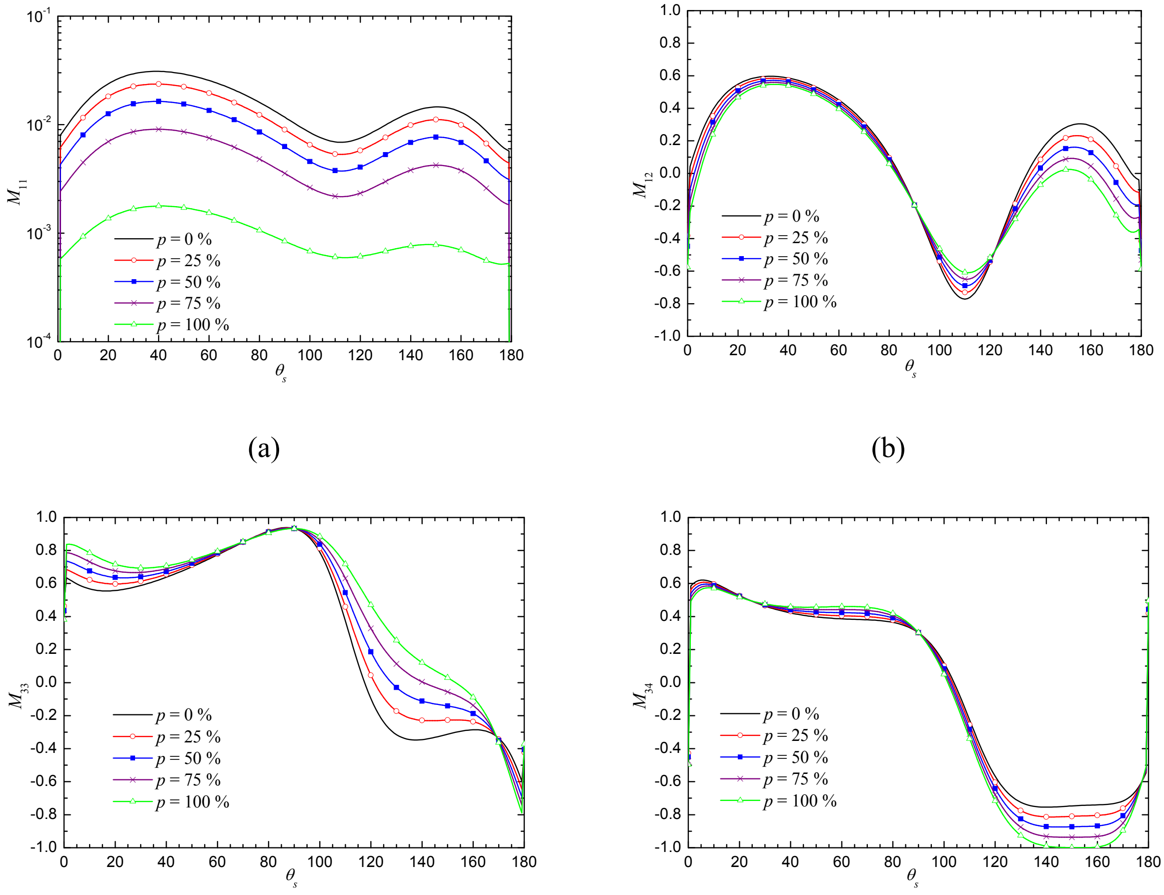

(a) (b)

(c) (d)

Figure 7.7. Normalized scattering matrix elements as a function of $\theta_s$ for different $p$ values. Non-uniform distribution of particles and agglomerates with $d_m$ from 38 nm to 42 nm. (a) $M_{11}$. (b) $M_{12}$. (c) $M_{33}$. (d) $M_{34}$.

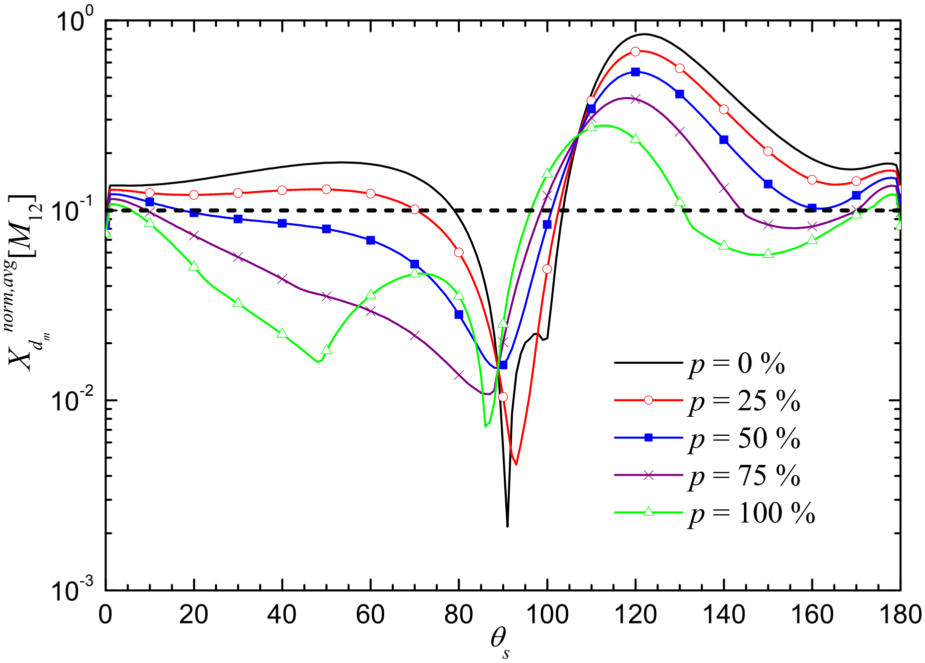
$10^0$
$10^{-1}$
$10^{-2}$
$10^{-3}$
$X_{d_m}^{norm,avg}[M_{12}]$
0
20
40
60
80
100
120
140
160
180
$\theta_s$
$p = 0$ %
$p = 25$ %
$p = 50$ %
$p = 75$ %
$p = 100$ %

(a)

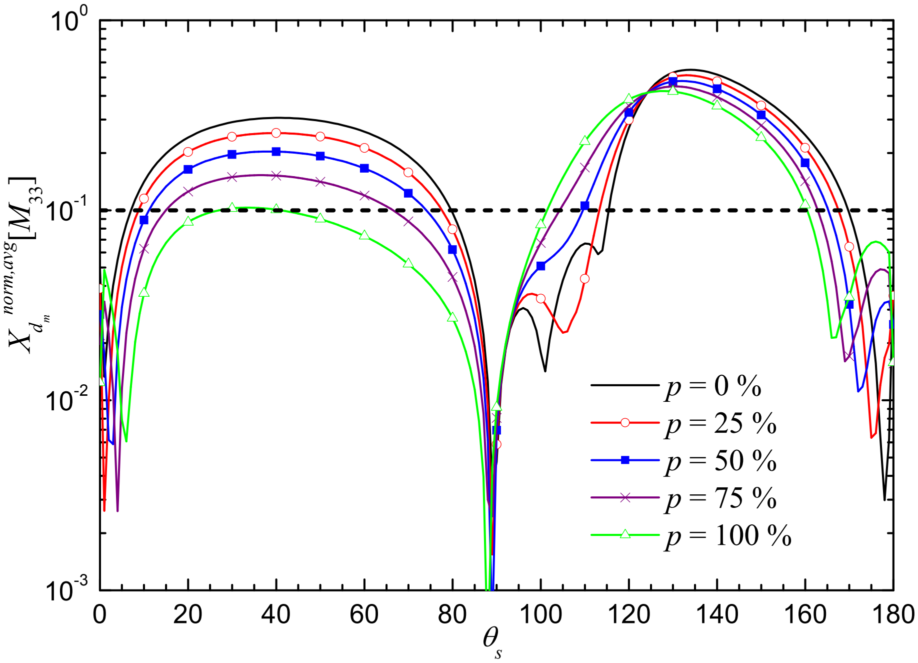
$10^0$
$10^{-1}$
$10^{-2}$
$10^{-3}$
$X_{d_m}^{norm,avg}[M_{33}]$
0
20
40
60
80
100
120
140
160
180
$\theta_s$
$p = 0$ %
$p = 25$ %
$p = 50$ %
$p = 75$ %
$p = 100$ %

(b)

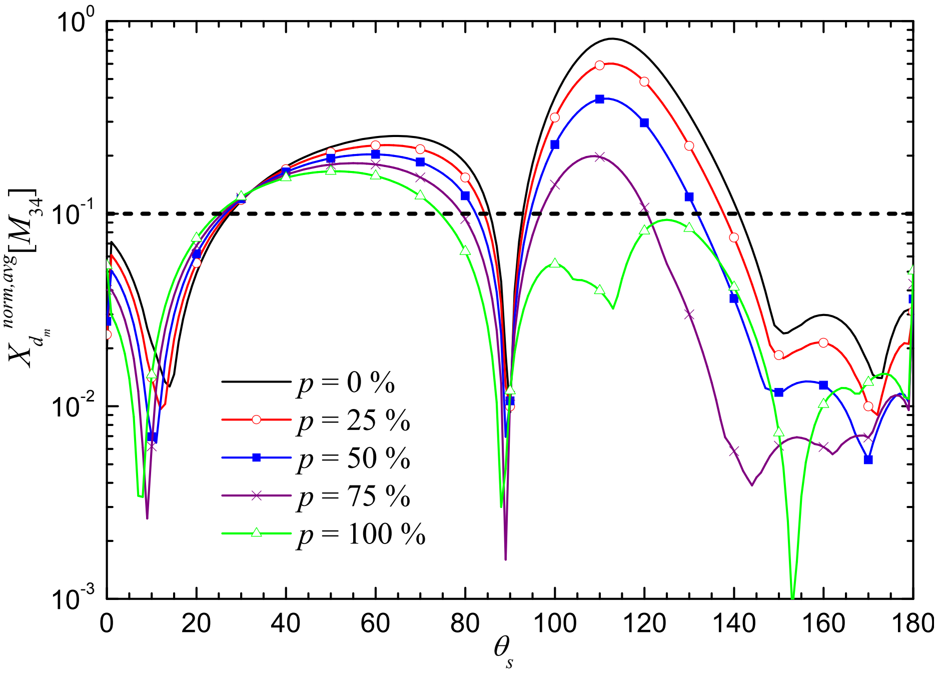

(c)

Figure 7.8. Averaged normalized sensitivity coefficient to $d_m$. Non-uniform distribution of particles and agglomerates with $d_m$ from 38 nm to 42 nm. (a) Sensitivity of $M_{12}$. (b) Sensitivity of $M_{33}$. (c) Sensitivity of $M_{34}$.

Table 7.1. Optimal configuration for the estimation of a given parameter.

| Composition of the sample | Parameter to be estimated | Optimal experimental configuration | |
|---|---|---|---|
| | | Optimal $M_{ij}$ | Optimal $\theta$ |
| 1- Single nanoparticles, $d_m$ = 10 to 15 nm (uniform distribution). | Diameter $d_m$ | $M_{12}$ | 145 to 180º |
| 2- Single nanoparticles, $d_m$ = 45 to 50 nm (uniform distribution). | Diameter $d_m$ | $M_{33}$ | 110 to 150º |
| 3- Single nanoparticles and agglomerates, $d_m$ = 40 nm. | Composition of single nanoparticles $p$ | $M_{33}$ | 110 to 150º |
| 4- Single nanoparticles and agglomerates, $d_m$ = 38 to 42 nm (non-uniform distribution). | Diameter $d_m$ | $M_{12}$ | 100 to 140º |

It is interesting to note that the maximum sensitivity is either obtained for $M_{12}$ or $M_{33}$ for angles $\theta_s$ above 100º.

## 7.4 Concluding remarks

The results presented in section 7.3 have clearly shown the necessity of measuring the change of polarization state of scattered surface waves in order to build a robust characterization procedure. The experimental apparatus used to measure the scattering matrix elements is the subject of the next chapter.

# Chapter 8

# The Polarized-Surface-Wave-Scattering System (PSWSS)

In chapter 7, the characterization framework of nanoparticles based on the measurements of the intensity and polarization state (scattering matrix elements) of scattered surface waves has been discussed. The objective of this chapter is to describe in details the characterization tool, called the polarized-surface-wave-scattering system (PSWSS), and to provide experimental measurements of surface wave scattering by metallic spherical nanoparticles. Chapter 8 is structured as follows. The critical steps necessary for developing the characterization procedure are first overviewed. Then, the experimental strategy for measuring the Mueller (scattering) matrix elements is provided in section 8.2. The PSWSS is afterward described in details, and experimental results are finally presented in section 8.4.

## 8.1 Steps for developing the characterization procedure

The framework for characterizing nanoparticles can be divided into four main steps, as schematically depicted in Fig. 8.1.

The characterization process works as follows. A database of scattering profiles (i.e., normalized scattering matrix elements $M_{ij}$) is built using a forward numerical model. The scattering profiles measured experimentally are then compared with the results from the database, and statistical tools are used to retrieve the theoretical configuration matching the best the experimental results. In that case, the properties of the scatterers can be retrieved as the inputs used to generate the database are known; this is called the inverse problem. The inversion procedure, developed by Prs. Charnigo and Srinivasan, is based on compound estimation; more information about this technique can be found in references [205,206].

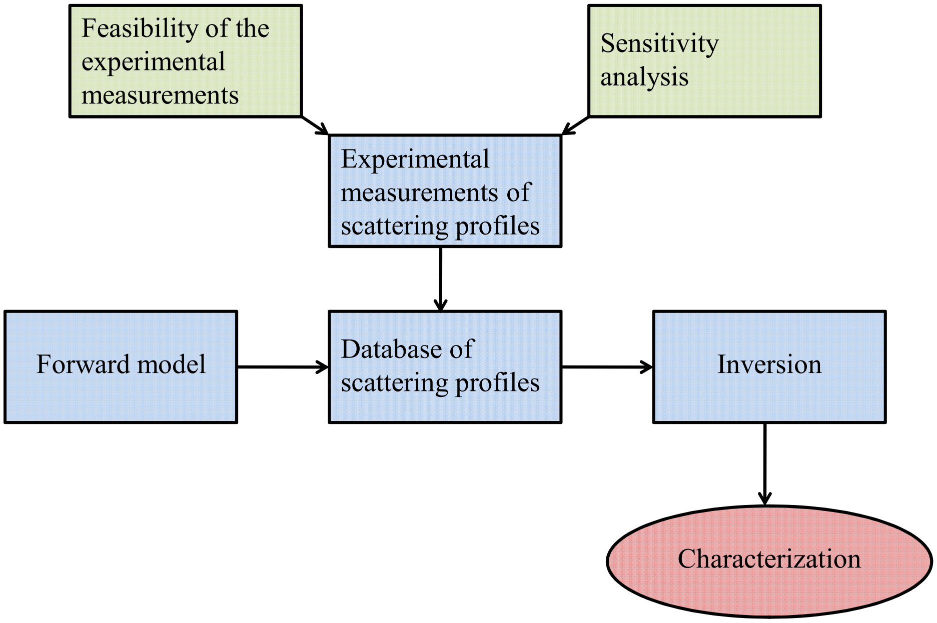
Feasibility of the experimental measurements
Sensitivity analysis
Experimental measurements of scattering profiles
Forward model
Database of scattering profiles
Inversion
Characterization

Figure 8.1. Diagram showing the necessary steps for the establishment of the characterization procedure.

A database of scattering profiles ($M_{11}$, $M_{12}$, $M_{33}$ and $M_{34}$) was developed in order to test the inversion procedure. The parameters used for generating the database are provided in section H.2 of appendix H. This collaborative work has led to a publication in the *Journal of the Optical Society of America A* in 2007 [207], and another manuscript is currently in review for *Inverse Problems* [208].

### 8.2 Experimental measurement of the scattering matrix elements

In the most general case, a linear polarizer (LP1) and a quarter-wave plate (QWP1) are located between the radiation source and the sample. Surface waves scattered by the particles are also polarized by placing first a quarter-wave plate (QWP2) and a linear polarizer (LP2) between the sample and the detector. A LP is an optical element polarizing the electric field of a wave in a specific direction $\xi$, while a QWP is an optical component introducing a relative phase lag $\varepsilon$ of $\pi/2$ between the $y$- and $z$-components of the electric field vector **E** (the surface wave is propagating along the $x$-direction) [45].

As discussed in section 7.1.3, a Mueller (scattering) matrix can be associated to any medium modifying the intensity and polarization state of a wave. For the general system described above, Mueller matrices are associated with the LPs, the QWPs and the scatterers of light. In an experiment, the scattering matrix of the sample is unknown, while the Mueller matrices of the LPs and QWPs are known. The Mueller matrix of an ideal LP is given by [156]:

$$[S_{ij}]_{LP} = \frac{1}{2}\begin{bmatrix} 1 & \cos 2\xi & \sin 2\xi & 0 \\ \cos 2\xi & \cos^2 2\xi & \cos 2\xi \sin 2\xi & 0 \\ \sin 2\xi & \sin 2\xi \cos 2\xi & \sin^2 2\xi & 0 \\ 0 & 0 & 0 & 0 \end{bmatrix} \tag{8.1}$$

while the Muller matrix of a QWP is [156]:

$$[S_{ij}]_{QWP} = \begin{bmatrix} 1 & 0 & 0 & 0 \\ 0 & \cos^2 2\beta & \cos 2\beta \sin 2\beta & -\sin 2\beta \\ 0 & 0 & \sin^2 2\beta & \cos 2\beta \\ 0 & \sin 2\beta & -\cos 2\beta & 0 \end{bmatrix} \tag{8.2}$$

In Eq. (8.1), $\xi$ is the orientation of the transmission axis of the LP, while $\beta$ in Eq. (8.2) is the orientation of the fast axis of the QWP. Both the transmission and fast axis are defined in the $y$-$z$ plane relative to the $z$-axis, as shown in Fig. 7.3. For example, if the transmission and fast axis are both collinear with the $z$-direction, then $\xi = \beta = 0^\circ$.

The optical scheme described in the beginning of this section consisting of two LPs and two QWPs was applied successfully by Mengüç's group for characterizing particles in suspension via propagating light [178]. This technique is based on the assumption that for a cloud of particles that have a plane of symmetry and are randomly oriented, the scattering matrix of the sample reduces to six independent and non-zero elements [156,178]:

$$[S_{ij}] = \begin{bmatrix} S_{11} & S_{12} & 0 & 0 \\ S_{12} & S_{22} & 0 & 0 \\ 0 & 0 & S_{33} & S_{34} \\ 0 & 0 & -S_{34} & S_{44} \end{bmatrix} \tag{8.3}$$

As discussed in section 7.1.3, the equivalent Mueller matrix of a system is given by the multiplication of individual Mueller matrices describing each medium / component perturbing the intensity and polarization state of light. Therefore, the following relationship between the incident and scattered Stokes vectors can be established:

$$\mathbf{I}_s = \{[S_{ij}]_{LP2} \cdot [S_{ij}]_{QWP2} \cdot [S_{ij}] \cdot [S_{ij}]_{QWP1} \cdot [S_{ij}]_{LP1}\}\mathbf{I}_i = [S_{ij}]_{system}\mathbf{I}_i \tag{8.4}$$

where $[S_{ij}]$ is the Mueller matrix of the sample, and $[S_{ij}]_{system}$ is the equivalent Mueller matrix that includes the LPs, the QWPs and the sample.

The detector can only measure the intensity of light (first Stokes parameter $I$). Assuming that the scattering matrix given by Eq. (8.3) is applicable to the case of spherical nanoparticles on a surface, it is necessary to perform six independent measurements of intensity in order to retrieve the six $S_{ij}$ elements. This system of six equations with six unknowns is constructed by orienting the LPs and QWPs at different angles. By considering only the first Stokes parameter $I$ in Eq. (8.4), the following system of equations can be established [178,209]:

$$\mathbf{K} = [C_{ij}]\mathbf{Z} \tag{8.5}$$

where $\mathbf{Z}$ is a vector containing the six scattering matrix elements of Eq. (8.3), $[C_{ij}]$ is a 6×6 matrix (coefficient matrix) consisting of coefficients multiplying the $S_{ij}$ elements obtained using different combinations of LP angles $\xi$ and QWP angles $\beta$, and $\mathbf{K}$ is a vector containing the six values of intensities obtained from the LP and QWP angle combinations. Therefore, six independent measurements of intensities, derived from six sets of LP and QWP angle combinations, are necessary to retrieve the $S_{ij}$ elements of Eq. (8.3). This procedure is referred hereafter as the six intensity method.

Equation (8.5) does not impose any restrictions on the orientations of the optical components. Govindan et al. [209] have shown that extreme care should be taken when choosing these angles, as the system of equations can become unstable when trying to retrieve the $S_{ij}$ elements. The coefficient matrix $[C_{ij}]$ has to be inverted for recovering the $S_{ij}$ elements. In order to obtain stable measurements of the $S_{ij}$ elements, we need to ensure that potential experimental errors in the measured intensities (vector **K**) are not amplified by the coefficient matrix. This can be achieved by minimizing the condition number $C_N$ of the coefficient matrix given by [209]:

$$C_N = \left\| [C_{ij}] \right\| \left\| [C_{ij}]^{-1} \right\| \tag{8.6}$$

where $\| \; \|$ is the norm. The condition number $C_N$ provides a measure of how a perturbation in **K** is reflected in the vector **Z** [178]. An optimal set of LP and QWP orientation angles, leading to a $C_N$ value of 17.2, was determined by Mengüç's group; this set of angles, provided in table 8.1, is used in the PSWSS. Note that the stability and feasibility of the six intensity approach is discussed in section I.1 of appendix I.

Table 8.1. Optimal set of orientation angles for the LPs and QWPs used in the PSWSS.

| Measurement | $\xi_1$ (LP1) | $\beta_1$ (QWP1) | $\beta_2$ (QWP2) | $\xi_2$ (LP2) |
|---|---|---|---|---|
| 1 | 45° | 60° | 5° | 15° |
| 2 | 45° | 25° | 25° | 65° |
| 3 | 45° | 80° | 0° | 60° |
| 4 | 45° | 30° | 65° | 80° |
| 5 | 45° | 70° | 25° | 10° |
| 6 | 45° | 30° | 40° | 25° |

The six intensity method is correct if the scattering matrix given by Eq. (8.3) is applicable. While this approach was successfully applied in the past by Mengüç's group, it is not clear at this point if the assumptions underlying the derivation of Eq. (8.3) are applicable for the case involving spherical nanoparticles on a surface. As a consequence, a supplementary measurement strategy is adopted hereafter, and will help to assess the validity of the six intensity approach.

The second measurement technique, called the four intensity method, is simpler, as it requires only a LP before and a LP after the sample. The incident and scattered Stokes vector are therefore related by the following relationship:

$$\mathbf{I}_s = \{[S_{ij}]_{LP2} \cdot [S_{ij}] \cdot [S_{ij}]_{LP1}\}\mathbf{I}_i = [S_{ij}]_{system}\mathbf{I}_i \tag{8.7}$$

In the first experiment, both LPs are oriented perpendicular to the plane of incidence, such that $\xi_1 = \xi_2 = 90°$ (TE-TE polarization). Substitution of $\xi = 90°$ in Eq. (8.1) leads to the following Mueller matrix for both LPs:

$$[S_{ij}]_{LP1} = [S_{ij}]_{LP2} = \frac{1}{2}\begin{bmatrix} 1 & -1 & 0 & 0 \\ -1 & 1 & 0 & 0 \\ 0 & 0 & 0 & 0 \\ 0 & 0 & 0 & 0 \end{bmatrix} \tag{8.8}$$

Using Eqs. (8.7) and (8.8), the following equivalent scattering matrix for the whole system is determined:

$$[S_{ij}]_{system} = \frac{1}{4}\begin{bmatrix} (S_{11} - S_{12} - S_{21} + S_{22}) & (-S_{11} + S_{12} + S_{21} - S_{22}) & 0 & 0 \\ (-S_{11} + S_{12} + S_{21} - S_{22}) & (S_{11} + S_{12} - S_{21} - S_{22}) & 0 & 0 \\ 0 & 0 & 0 & 0 \\ 0 & 0 & 0 & 0 \end{bmatrix} \tag{8.9}$$

Since the light emerging from the source is unpolarized, the incident Stokes vector can be written as $\mathbf{I}_i = (I_i,0,0,0)^T$. Using $\mathbf{I}_i$ along with Eqs. (8.7) and (8.9), the scattered light measured at the detector is given by: $I_{TE\text{-}TE}/I_i = (1/4)(S_{11} - S_{12} - S_{21} + S_{22})$.

For the second experiment, the incident electric field is still polarized perpendicular to the incident plane with $\xi_1 = 90°$ (TE polarization), while the second polarizer is oriented parallel to the plane of incidence with $\xi_2 = 0°$ (TM polarization). Using the aforementioned procedure, the light measured at the detector is given by: $I_{TE\text{-}TM}/I_i = (1/4)(S_{11} - S_{12} + S_{21} - S_{22})$. Similarly, the third experiment performed with $\xi_1 = \xi_2 = 0°$ gives: $I_{TM\text{-}TM}/I_i = (1/4)(S_{11} + S_{12} + S_{21} + S_{22})$. Finally, $I_{TM\text{-}TE}/I_i = (1/4)(S_{11} + S_{12} - S_{21} - S_{22})$ is obtained by letting $\xi_1 = 0°$ and $\xi_2 = 90°$.

This constitutes a system of four equations with four unknowns that can easily be solved. This four intensity technique will help to determine if Eq. (8.3) is applicable to spherical nanoparticles on a surface.

### 8.3 Description of the PSWSS

A schematic representation of the PSWSS is shown in Fig. 8.2.

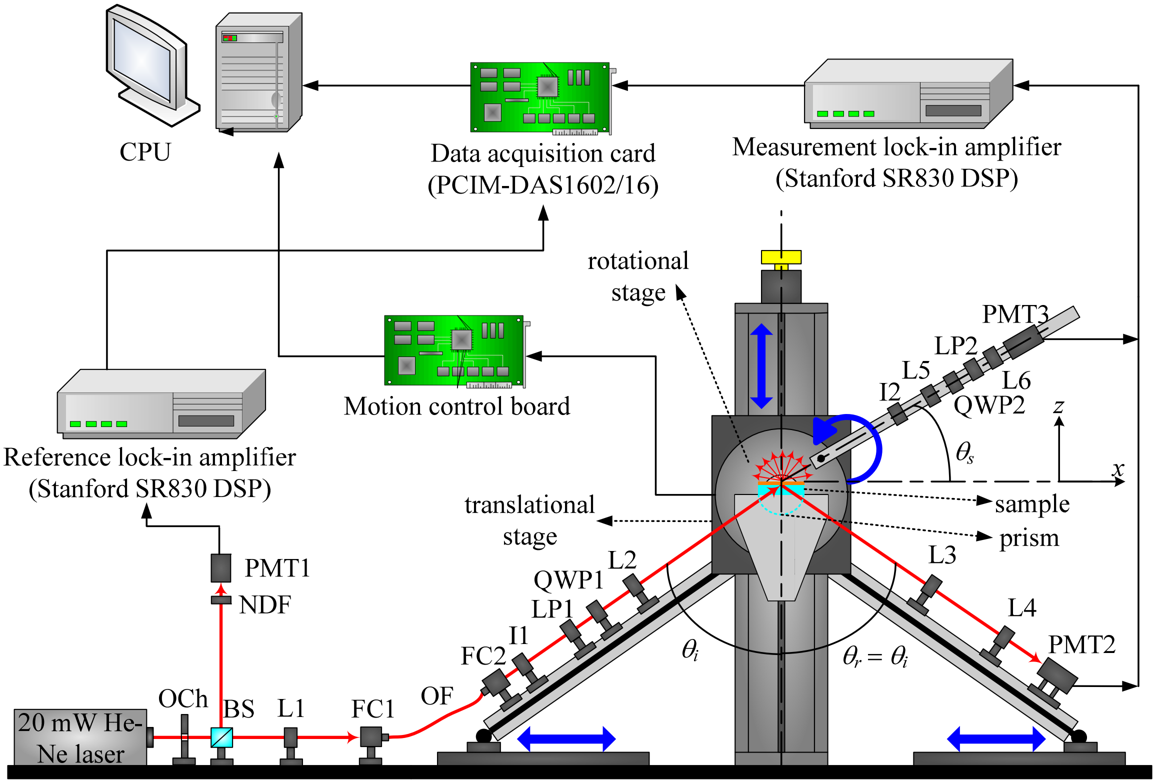
CPU
Data acquisition card
(PCIM-DAS1602/16)
Measurement lock-in amplifier
(Stanford SR830 DSP)
rotational
stage
PMT3
LP2
L5
L6
I2
QWP2
z
$\theta_s$
x
sample
prism
Motion control board
Reference lock-in amplifier
(Stanford SR830 DSP)
translational
stage
L3
L4
PMT2
L2
QWP1
LP1
I1
FC2
$\theta_i$
$\theta_r = \theta_i$
PMT1
NDF
OCh
BS
L1
FC1
OF
20 mW He-Ne laser

Figure 8.2. Schematic representation of the PSWSS.

The light source is a 20 mW helium-neon laser (wavelength of 632.8 nm). Note that an argon-ion laser (wavelength of 514.5 nm) was originally used in the PSWSS, but due to technical problems, it was replaced by a helium-neon laser. Light emerging from the laser passes through an optical chopper (OCh) in order to module the beam at a frequency $f_{OCh}$. The OCh is connected to both lock-in amplifiers (reference and measurement), such that only light modulated at $f_{OCh}$ is measured by the amplifiers.

Light emerging from the OCh passes through a beam splitter (BS), and part of the beam is deflected toward a detector that measure the intensity (photomultiplier tube, PMT1).

This is the reference measurement used to cancel out any potential temporal fluctuations of the laser. The signal is processed through the reference lock-in amplifier, and stored into a computer (Labview interface) via a data acquisition card. Before reaching the PMT1, a neutral density filter (NDF) is used to avoid saturation of the PMT1.

The remaining part of the beam passes through a first lens (L1) focusing the light toward a fiber collimator (FC1) bringing the beam on the left leg of the PSWSS via a fiber optics (OF) and a second fiber collimator (FC2). The beam emerging from FC2 makes an angle $\theta_i$ relative to the $z$-axis; the angle $\theta_i$ can be changed via a translational stage, controlled by a step motor, opening / closing the legs of the PSWSS. In the most general case, before reaching the prism, the incident beam passes though an iris (I1), a linear polarizer (LP1), a quarter-wave plate (QWP1) and a lens (L2).

The incident beam, with an angle $\theta_i$ greater than the critical angle for total internal reflection (TIR) $\theta_{cr}$, undergoes TIR at the sample-air interface (if there is no metallic film) or the substrate-metal interface. The reflected light at an angle $\theta_r = \theta_i$ can then be collected on the right leg of the PSWSS via a PMT2. Before reaching the PMT2, the beam passes through two lenses (L3 and L4). The light collected by the PMT2 is processed by the measurement lock-in amplifier, and is stored into a computer via a data acquisition card.

Surface waves generated by TIR are scattered in the far-field by the nanoparticles located on the sample, and the scattered radiation is measured at different angle $\theta_s$ via a PMT3 located on an arm attached to a rotational stage controlled via a stop motor. The light is again processed by the measurement lock-in amplifier and is stored in a computer via a data acquisition card. Before reaching the PMT3, in the most general case, the beam passes through an iris (I2), a lens (L5), a quarter-wave plate (QWP2), a linear polarizer (LP2) and another lens (L6).

Figure 8.3 shows a picture of the PSWSS, where it can be seen that the system is located in a black box in order to avoid any potential external light contamination.

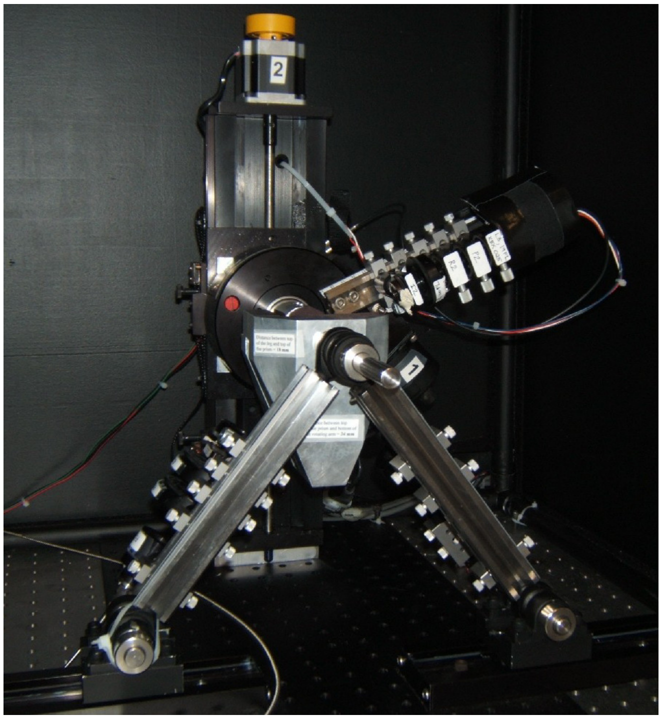

Figure 8.3. Picture of the PSWSS.

The details about the components of the PSWSS and the settings of the lock-in amplifiers used to perform the experimental measurements are provided in section I.2 of appendix I, while the optical scheme of the PSWSS is given in section I.3 of appendix I. Note also that all LPs and QWPs employed in the PSWSS were calibrated, and these calibration results are shown in section I.4 of appendix I.

A schematic representation of the prism-sample system is shown in Fig. 8.4. A semi-cylindrical sapphire prism is used as the high refractive index medium. The refractive index of sapphire at a wavelength of 632.8 nm is 1.7659. A sample on which a metallic film (optional) and nanoparticles are coated is deposited on the prism. A fluid matching the index of refraction of sapphire is used between the prism and the sample. Ideally, the substrate used for the sample should be made of sapphire, although it is not mandatory. If the substrate has a different refractive index than sapphire, a supplementary refraction occurs at the prism-substrate interface.

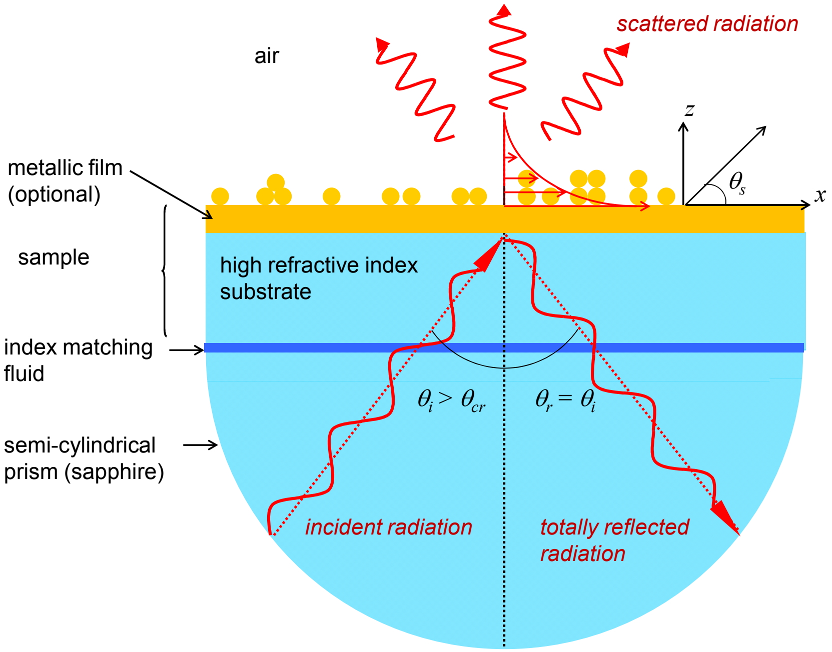
scattered radiation
air
metallic film
(optional)
$z$
$\theta_s$
$x$
sample
high refractive index
substrate
index matching
fluid
$\theta_i > \theta_{cr}$
$\theta_r = \theta_i$
semi-cylindrical
prism (sapphire)
incident radiation
totally reflected
radiation

Figure 8.4. Schematic representation of the prism-sample system.

## 8.4 Experimental results

Two calibration measurements on a LP and a diffraction grating are first discussed, and scattering matrix elements from 200 nm and 50 nm gold spherical particles are afterwards presented.

### *8.4.1 Mueller matrix of a linear polarizer*

An experiment is performed in order to measure the Mueller matrix of a LP with $\xi = 0^{\mathrm{o}}$. This LP should be seen as a sample for which the scattering matrix elements need to be recovered. Using Eq. (8.1), the Mueller matrix of the LP at $\xi = 0^{\mathrm{o}}$ is given by:

$$[S_{ij}]_{LP,\xi=0} = \frac{1}{2}\begin{bmatrix} 1 & 1 & 0 & 0 \\ 1 & 1 & 0 & 0 \\ 0 & 0 & 0 & 0 \\ 0 & 0 & 0 & 0 \end{bmatrix} \tag{8.10}$$

The idea is to use the six intensity approach to recover the Mueller matrix given by Eq. (8.10). This procedure assumes that the Mueller matrix of the sample is given by Eq.

(8.3). Therefore, by comparing Eqs. (8.3) with (8.10), we should retrieve $M_{11} = M_{12} = M_{22} = 1$ and $M_{33} = M_{34} = M_{44} = 0$. This experiment is performed by removing the prism in the PSWSS. Two sets of measurements were collected, and the results are provided in table 8.2 where the values are normalized by $S_{11}$ (i.e., $M_{ij} = S_{ij}/S_{11}$).

Table 8.2. Recovered Mueller matrix elements of a LP oriented at $\xi = 0°$.

| $M_{ij}$ | Theory | Set 1 | Set 2 |
|---|---|---|---|
| $M_{11}$ | 1 | 1.000 | 1.000 |
| $M_{12}$ | 1 | 1.037 | 1.032 |
| $M_{22}$ | 1 | 1.186 | 1.159 |
| $M_{33}$ | 0 | -0.235 | 0.100 |
| $M_{34}$ | 0 | 0.039 | -0.084 |
| $M_{44}$ | 0 | -0.022 | -0.028 |

It can be seen in table 8.2 that $M_{11}$, $M_{12}$, and $M_{22}$ are always close to 1, while $M_{33}$, $M_{34}$, and $M_{44}$ are not exactly equal to zero (but close to zero for $M_{34}$ and $M_{44}$). As suspected in section I.1 of appendix I, $M_{33}$ is the element diverging the most from its theoretical value.

The six intensity procedure is correct for characterizing particles (if Eq. (8.3) is applicable), but might be questionable to measure the Mueller matrix of a LP. Indeed, we are using elliptically polarized light to measure linear depolarization. By looking at the results obtained in table 8.2, the procedure used to recover the $S_{ij}$ elements might be unstable for characterizing a LP. Also, as discussed in section I.4.2 of appendix I, the quality and precision of the QWPs used in the PSWSS might affect the results.

The stability of the procedure for recovering the Mueller matrix of a LP can be evaluated in the same way as described in section I.1 of appendix I, and the results are shown in table 8.3.

The results of table 8.3 demonstrate that despite the fact that the condition number of the coefficient matrix is small, a perturbation of the $\mathbf{I}_i$ vector leads to some errors in the $M_{ij}$ elements, especially for $M_{33}$. Nevertheless, the elements $M_{11}$, $M_{12}$ and $M_{22}$ recovered experimentally are very close to the theoretical values.

Table 8.3. Mueller matrix elements of a LP ($\xi = 0°$) recovered numerically by adding stochastic noise on the intensities (see section I.1 of appendix I for details of the procedure).

| $M_{ij}$ | Recovered $M_{ij}$ with max stochastic noise of ±5% | Recovered $M_{ij}$ with max stochastic noise of ±10% | Recovered $M_{ij}$ with max stochastic noise of ±20% | Recovered $M_{ij}$ with max stochastic noise of ±30% |
|---|---|---|---|---|
| $M_{11}$ | 1.000 | 1.004 | 1.000 | 1.000 |
| $M_{12}$ | 0.999 | 0.995 | 0.988 | 0.986 |
| $M_{22}$ | 1.003 | 0.996 | 1.087 | 1.127 |
| $M_{33}$ | 0.003 | -0.017 | 0.067 | 0.116 |
| $M_{34}$ | 0.003 | -0.001 | 0.012 | 0.018 |
| $M_{44}$ | 0.004 | -0.006 | -0.031 | -0.041 |

### *8.4.2 Scattering by a diffraction grating*

In order to verify the accuracy of the angular measurements, scattering of surface plasmon-polaritons (SPPs) by a grating is investigated. Note that the objective here is not to measure the efficiency of the grating, but rather to determine if the PSWSS is able to measure accurately the angular distribution of scattered surface waves in the far-field. A schematic representation of the diffraction grating is shown in Fig. 8.5.

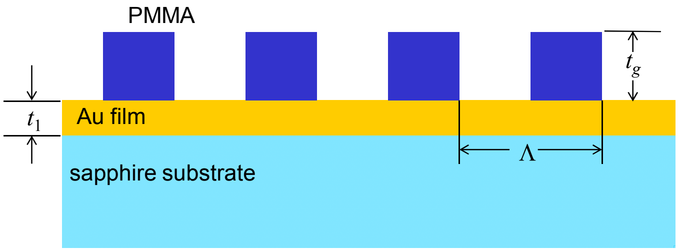

Figure 8.5. Schematic representation of the diffraction grating used to calibrate the far-field angular measurements of the PSWSS.

The sample is made of a gold thin film ($t_1$ = 60 nm) coated on a sapphire substrate by sputtering. A PMMA layer ($t_g$ = 780 nm) was deposited on the gold film by spin coating. The rectangular pattern was made by electron beam lithography; the period Λ of the grating is 2.4 μm. The sample of Fig. 8.5 is then placed on the prism using the index matching fluid, as indicated in Fig. 8.4.

A TM-polarized radiation beam is incident at the sapphire-gold interface with an angle $\theta_i$ of 38º such that SPPs are generated at the gold-air interface [11,50]. Referring to Fig. 7.3, the $x$-component of the wavevector $k_x$ is therefore given by $k_x = (n_0\omega/c_v)\sin\theta_i = (n_0 2\pi/\lambda_v)\sin\theta_i$, where $n_0$ is the refractive index of sapphire (1.7659 at 632.8 nm). Inserting the numerical values in this expression, we find a $k_x$ value of $1.079\times10^7$ rad/m. In air (medium 2), the $z$-component of the wavevector is given by $k_{z2} = (k_v - k_x)^{1/2}$, such that the wave is evanescent if $k_x > k_v$. The magnitude of the wavevector in air, $k_v = 2\pi/\lambda_v$, is $9.929\times10^6$ rad/s, such that $k_x > k_v$ (the $x$-component of the wavevector is conserved from one medium to another). Therefore, as expected, for $\theta_i = 38º$, where SPPs are excited, the PSWSS is in dark condition in the absence of a grating.

When the grating is present, SPPs couple with the grating and thus become propagating in air (i.e., SPPs radiate away from the metal-air interface). The angle at which the SPP is scattered in the far-field is given by [11,210,211]:

$$\theta_d = \sin^{-1}\left(\frac{(n_0\,2\pi/\lambda_v)\sin\theta_i - qK}{k_v}\right) \tag{8.11}$$

where $\theta_d$ is defined relative to the $z$-axis; in other words, $\theta_d = 0º$ when the wave is propagating along the $z$-axis. Following the convention used in chapters 7 and 8, the angle $\theta_s$ as defined in Fig. 7.3 is therefore given as: $\theta_s = 90º - \theta_d$. In Eq. (8.11), $q$ is the diffraction order ($q = 0, \pm1, \pm2, \ldots$) while $K$ ($= 2\pi/\Lambda$) is the grating vector. Equation (8.11) clearly shows that the grating reduces the $x$-component of the wavevector, such that when $k_x$ becomes less than $k_v$, SPPs become propagating.

Table 8.4 provides the scattering angles $\theta_s$ as a function of the diffraction order (up to the sixth diffraction order measured by the PSWSS). Figure 8.6 shows the intensity measured as a function of the scattering angle $\theta_s$. These measurements were performed via a continuous scan of the rotating arm. The experimental data are compared with the theoretical predictions of table 8.4.

Table 8.4. Scattering angles of SPPs excited by a grating as a function of the diffraction order ($\theta_i$ = 38º).

| Diffraction order | $\theta_d$ [º] | $\theta_s$ [º] |
|---|---|---|
| 1 | 55.44 | 34.56 |
| 2 | 34.05 | 55.95 |
| 3 | 17.23 | 72.77 |
| 4 | 1.864 | 88.14 |
| 5 | -13.36 | 103.36 |
| 6 | -29.66 | 119.66 |

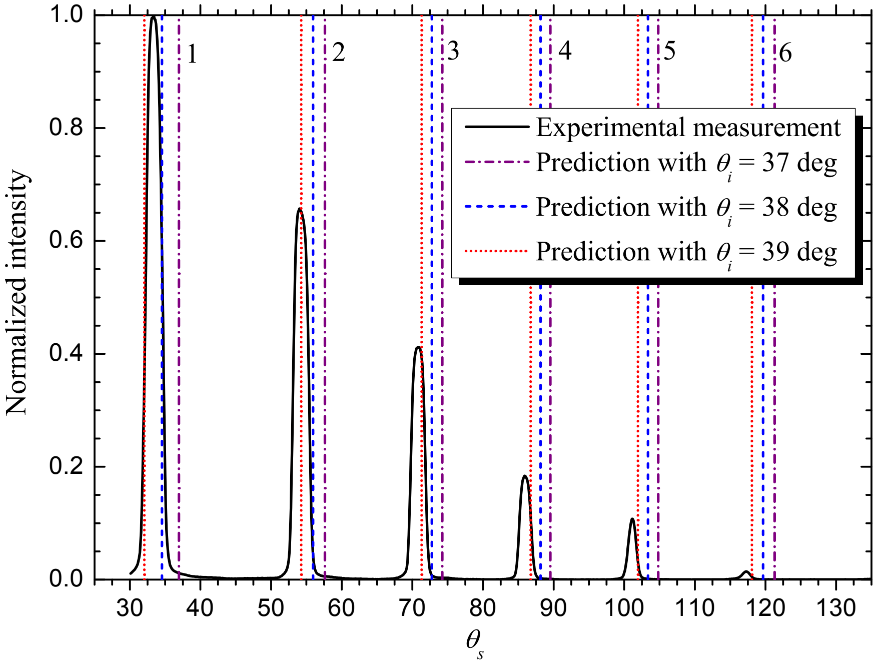

Figure 8.6. Normalized intensity due to SPP coupling with the diffraction grating shown in Fig. 8.5 ($\theta_i$ = 38º).

Figure 8.6 shows that the intensity is not nil only for angle $\theta_s$ corresponding to the diffraction orders presented in table 8.4. Also, the scattering angles theoretically predicted and those measured are generally in good agreement. The mismatch can be due to two main causes. The PSWSS does not have a system for accurate positioning of the sample, such that it is possible that the grating was not exactly at an azimuthal angle of $\phi$ = 0º. Also, while it is easy to measure the scattering angle $\theta_s$ in the PSWSS, it is very difficult to evaluate accurately the angle of incidence. The uncertainty in measuring $\theta_i$ is about ±1°. As shown in Fig. 8.6, the theoretical predictions are also given for $\theta_i$ values of 37° and 39°. It can be seen that the first three diffraction orders falls into the predictions for $\theta_i$ between 37° and 39°. For the last three diffraction orders, the angle $\theta_s$ measured is smaller than the predictions. Beyond the imprecision in measuring $\theta_i$ and the position of the sample on the prism, the grating period Λ might not be exactly 2.4 μm.

Finally, we estimated in section I.3 of appendix I that light is measured in the far-field within a solid angle of about ±0.8°. Results of Fig. 8.6 suggest that this range should be increased, and the uncertainty is closer to $\theta_s \pm 2°$.

### *8.4.3 Scattering by 200 nm gold spherical particles*

Scattered evanescent waves by 200 nm gold spherical particles coated directly on a sapphire substrate are measured for $\theta_i = 50°$. The scattering matrix elements are collected for $\theta_s$ values from 30° to 130° by increment of 10°. The normalized scattering matrix elements $M_{ij}$, as defined in section 7.3, are reported. Note that $M_{11}(\theta_s)$ is calculated as $S_{11}(\theta_s)/S_{11}(\theta_s = 30°)$.

A major limitation in the PSWSS comes from the fact that there is no system to position the sample accurately on the prism. Therefore, the repeatability of the results is quite impossible once the sample is moved. As a consequence, the measurements shown in this section and the next one have been obtained by performing two sets of measurements without moving the sample. At each angle $\theta_s$, the intensity is measured during 10 seconds at a rate of 10 points/seconds, such that 100 data are collected at each angle $\theta_s$ for a given experiment. Figure 8.7 shows two sets of measurements performed on the exact same location on the sample (i.e., the sample was not moved), where the scattered intensity ($M_{11}$) is measured directly without LPs and QWPs.

Figure 8.7 shows that the results are repeatable when measurements are made on the exact same location on the sample. It can also be observed that the measurements are stable (small error bars), which is due to the fact that the intensity scattered by 200 nm particles is quite large. In Fig. 8.7, the error bars for a given experiment were calculated using the 100 data collected at each angle $\theta_s$. For the results shown hereafter in this section and the next one, the overall error bars come from the combination of the error bars associated with the two sets of measurements performed on the same location on the sample.

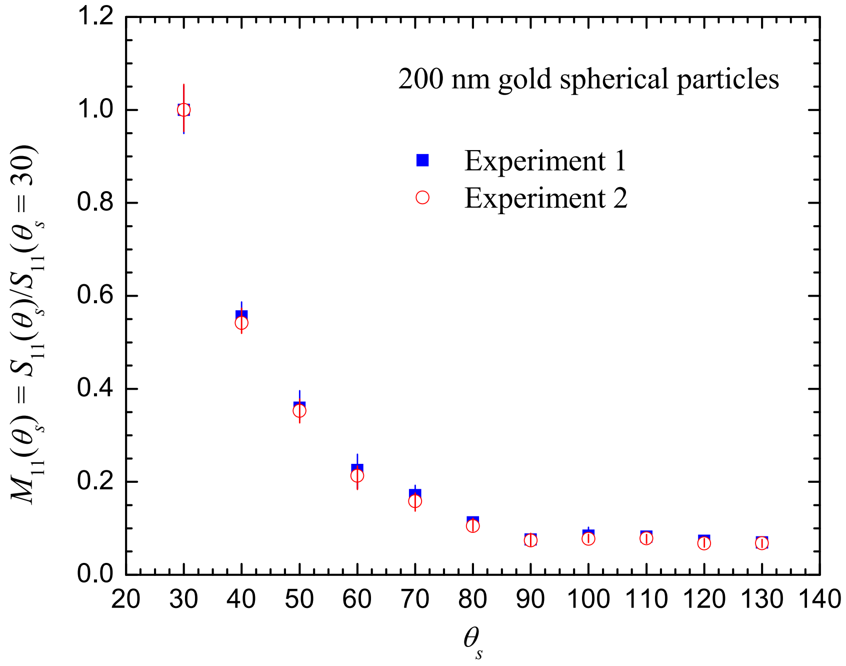

Figure 8.7. Direct measurement of scattered intensity ($M_{11}$); experiments 1 and 2 were performed on the exact same location on the sample.

The scattered intensity of Fig. 8.7 is compared in Fig. 8.8 with the data obtained after moving the sample and repositioning it at its original location. It can be seen in Fig. 8.8 that the scattered intensities are similar, but the match is not as good as in Fig. 8.7, which is likely to be due to the fact that the illuminated spot of particles is different from one experiment to another. Even when extreme care is taken to reposition the sample at its original location on the prism, results similar to those presented in Fig. 8.8 are obtained. To ensure the repeatability of the data collected by the PSWSS, it would be necessary to have a system allowing an accurate positioning of the sample on the prism.

On the other hand, the results of Fig. 8.8 are quite encouraging from a characterization point of view, as the scattering profiles are different when slightly different locations on the sample are illuminated. Since the shape, size and composition of the sample are known, the sensitivity of the $M_{11}$ profiles are likely to be due to a perturbation in the agglomeration level of the particles.

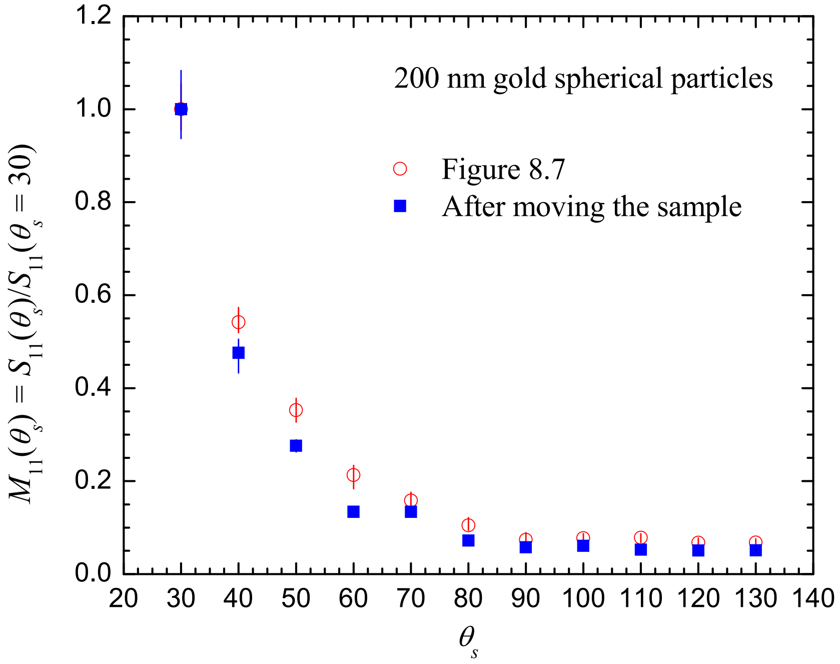

Figure 8.8. Direct measurement of scattered intensity ($M_{11}$); comparison between the results of Fig. 8.7 and those obtained after repositioning the sample on the prism.

Figures 8.9(a) presents $M_{11}$ derived from the four intensity technique described in section 8.2; the $M_{11}$ profile thus retrieved in an indirect manner is compared with $M_{11}$ measured directly without LPs and QWPs. The elements $M_{12}$, $M_{21}$ and $M_{22}$ obtained from the four intensity method are shown in Fig. 8.9(b).

The consistency of the four intensity method is confirmed by Fig. 8.9(a), where $M_{11}$ profiles measured indirectly and directly are very close to each other. The scattering profiles related to the polarization state of light vary quite smoothly (Fig. 8.9(b)) It is interesting to note that $M_{21}$ is not equal to $M_{12}$, as given by the Mueller matrix employed for the six intensity method (Eq. (8.3)). Therefore, results of Fig. 8.9(b) suggest that this technique might not be applicable to the case of spherical particles on a surface.

The measurements presented in Fig. 8.9(a) and 8.9(b) are repeated on a different location on the sample, and the results are shown in Figs. 8.10(a) and 8.10(b).

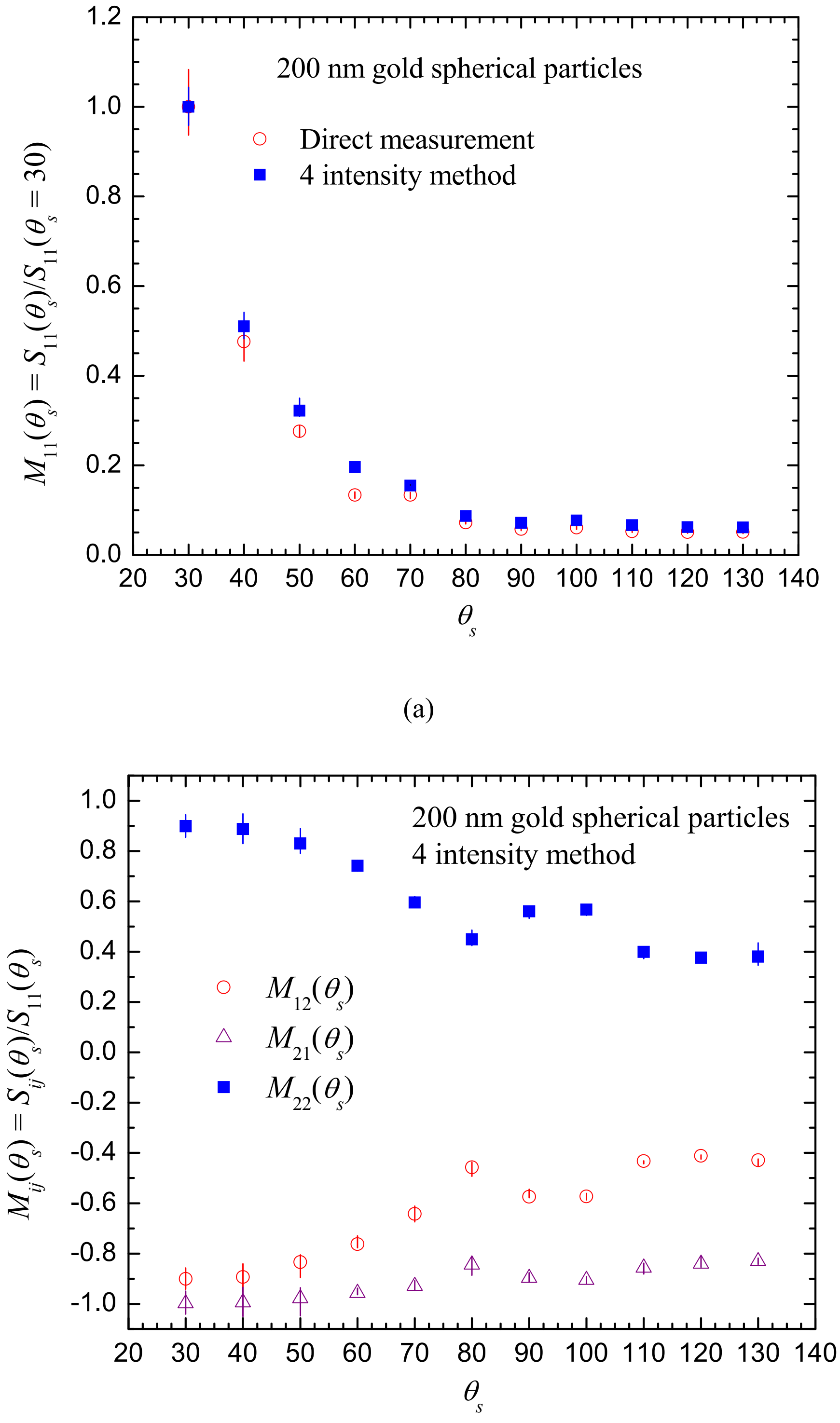

(a)

(b)

Figure 8.9. Scattering profiles measured via the four intensity method: (a) $M_{11}$; the results are compared with the scattered intensity measured directly. (b) $M_{12}$, $M_{21}$ and $M_{22}$.

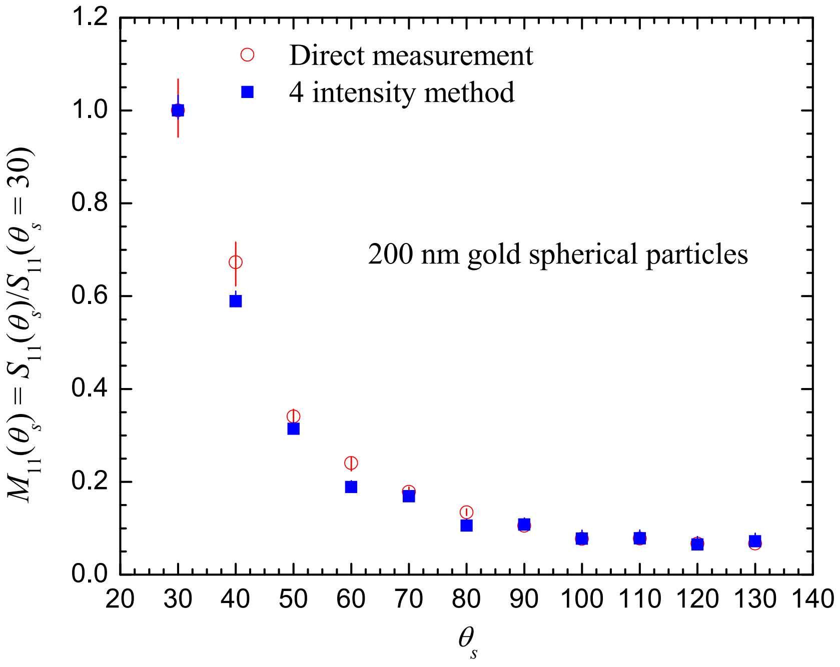

(a)

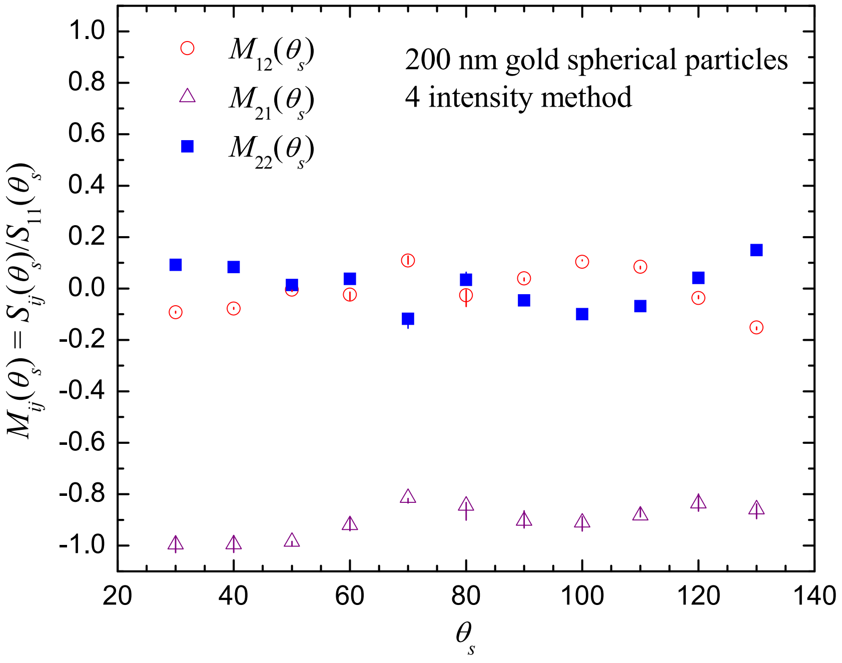

(b)

Figure 8.10. Scattering profiles measured via the four intensity method: (a) $M_{11}$; the results are compared with the scattered intensity measured directly. (b) $M_{12}$, $M_{21}$ and $M_{22}$. The measurements were performed on a different location on the sample than in Fig. 8.9.

Again, Fig. 8.10(a) shows clearly the consistency of the four intensity procedure where $M_{11}$ profiles from direct and indirect measurements are very close to each other. The elements $M_{12}$ and $M_{22}$ are different when comparing Fig. 8.9(b) with Fig. 8.10(b). This is quite encouraging, as it shows that these profiles are highly sensitive to the configuration of the sample. As mentioned earlier, the sensitive parameter is likely to be the level of agglomeration of the particles. Also, $M_{11}$ in Fig. 8.9(a) and 8.10(a) are not exactly the same, but are very similar. As a consequence, the observations made here are in good agreement with the sensitivity analysis of section 7.3. The element $M_{11}$ is not sensitive enough for characterization purpose, while $M_{12}$ is highly sensitive. It can also be observed that $M_{21}$ is almost the same in Figs. 8.9(b) and 8.10(b).

Figure 8.11(a) shows the scattered intensity ($M_{11}$) retrieved from the six intensity method, while $M_{12}$, $M_{22}$, $M_{33}$, $M_{34}$ and $M_{44}$ profiles are presented in Fig. 8.11(b). For comparison, $M_{11}$ measured directly without LPs and QWPs is given in Fig. 8.11(a). Note that these measurements were performed on a location different than in Figs. 8.9 and 8.10.

We suspected via the results of Figs. 8.9(b) and 8.10(b) that the six intensity procedure might not be applicable to the case of 200 nm spherical particles on a surface. Figures 8.11(a) and 8.11(b) confirm this hypothesis. Indeed, the intensity retrieved from the six intensity method is quite different than the intensity measured directly. Moreover, the polarization profiles presented in Fig. 8.11(b) do not make sense, as most of them take values beyond the boundaries ±1; indeed, following the normalization procedure of the $S_{ij}$ elements, $\left|M_{ij}\right| > 1$ ($\neq M_{11}$) would imply that more than 100 % of the light is depolarized in a given state. Therefore, it is very likely that the intensities of the **K** vector are the linear combinations of more than six scattering matrix elements. Note that the six intensity procedure was repeated on different locations on the sample, and results similar to those reported in Figs. 8.11(a) and 8.11(b) were found.

Results obtained for 200 nm gold spherical particles have shown the consistency of the four intensity method, while the six intensity procedure is clearly not appropriate.

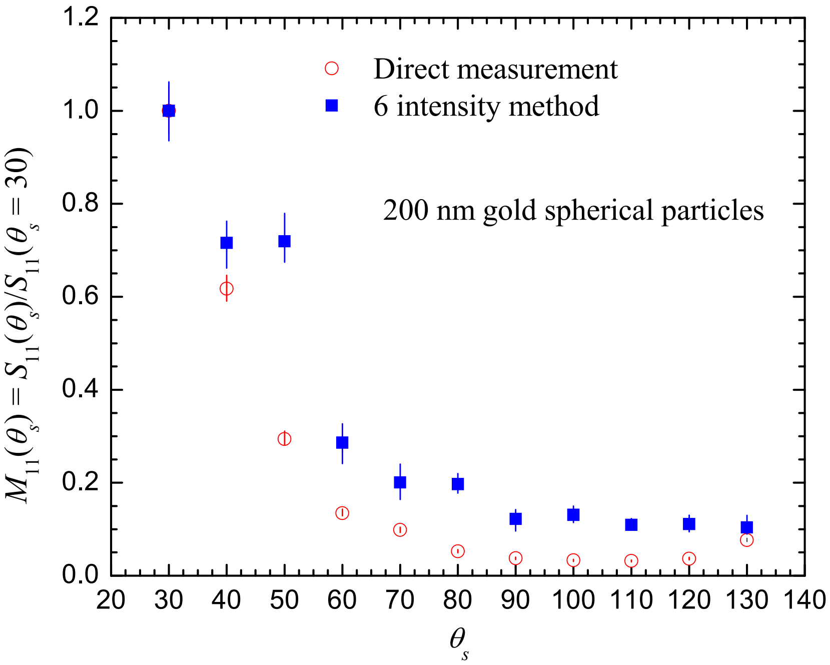

(a)

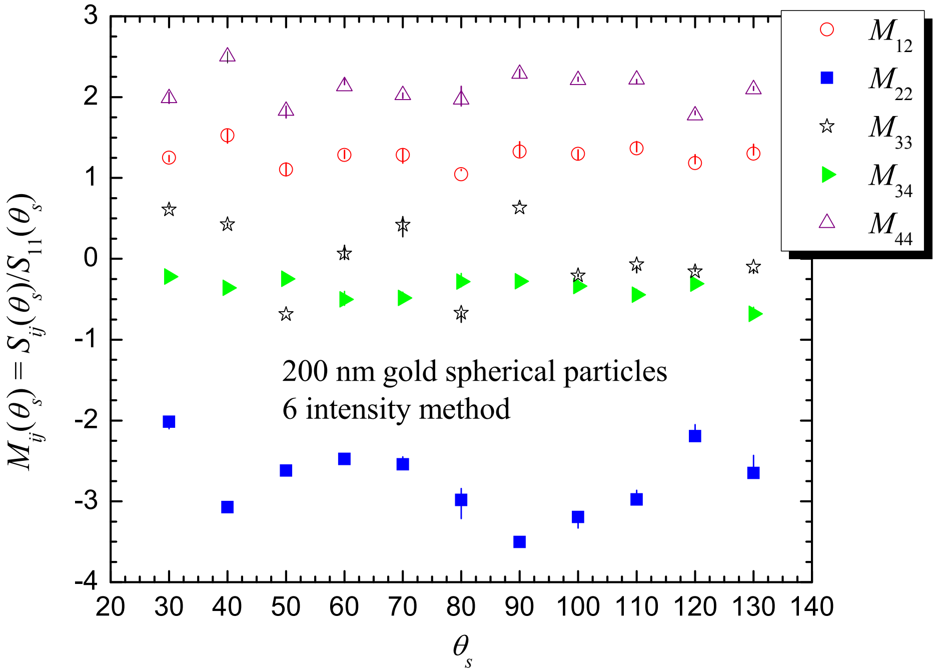

(b)

Figure 8.11. Scattering profiles measured via the six intensity method: (a) $M_{11}$; the results are compared with the scattered intensity measured directly. (b) $M_{12}$, $M_{22}$, $M_{33}$, $M_{34}$ and $M_{44}$.

### *8.4.4 Scattering by 50 nm gold spherical particles*

50 nm gold spherical nanoparticles are coated directly on a substrate having an index of refraction of 1.864 at a wavelength of 632.8 nm. This sample is placed on the prism, and the fluid matching the index of refraction of sapphire is used. Due to the mismatch of the refractive indices of the substrate and the prism, there is refraction at the prism-substrate interface. Light is propagating in the prism at an angle of 50º. After refraction in the sample, the angle of incidence $\theta_i$ at the sample-air interface is thus 46.5º; the critical angle for TIR $\theta_{cr}$ at the substrate-air interface is 32.4º.

As in the previous section, the normalized scattering matrix elements $M_{ij}$ are reported for $\theta_s$ values between 30º and 130º by increments of 10º. Figures 8.12(a) to 8.12(d) show $M_{ij}$ profiles measured in the same location on the sample using three techniques: the direct measurement of intensity ($M_{11}$), the four intensity method ($M_{11}$, $M_{12}$, $M_{21}$, $M_{22}$) and the six intensity procedure ($M_{11}$, $M_{12}$, $M_{22}$, $M_{33}$, $M_{34}$ and $M_{44}$).

First, it is interesting to note that the error bars are generally larger for the 50 nm particles than for the 200 nm particles, especially when performing the six intensity method. This is due to the fact that the scattered intensity by 50 nm particles is less than for 200 nm particles, thus resulting in experimental measurements that are less stable.

As for the case of 200 nm particles, Fig. 8.12(a) shows that $M_{11}$ recovered from the six intensity approach do not match the $M_{11}$ profiles from the two other experimental techniques. Therefore, as expected, $M_{12}$ and $M_{22}$ retrieved from the four and six intensity methods are not the same, as depicted in Figs. 8.12(b) and 8.12(c). Moreover, Fig. 8.12(b) demonstrates again that $M_{12}$ is not equal to $M_{21}$, thus implying that the scattering matrix given by Eq. (8.3), at the basis of the six intensity approach, is not applicable to the case of spherical nanoparticles on a surface. Therefore, the profiles $M_{33}$, $M_{34}$ and $M_{44}$ (Fig. 8.12(d)) are incorrect, as they have been recovered from the six intensity procedure.

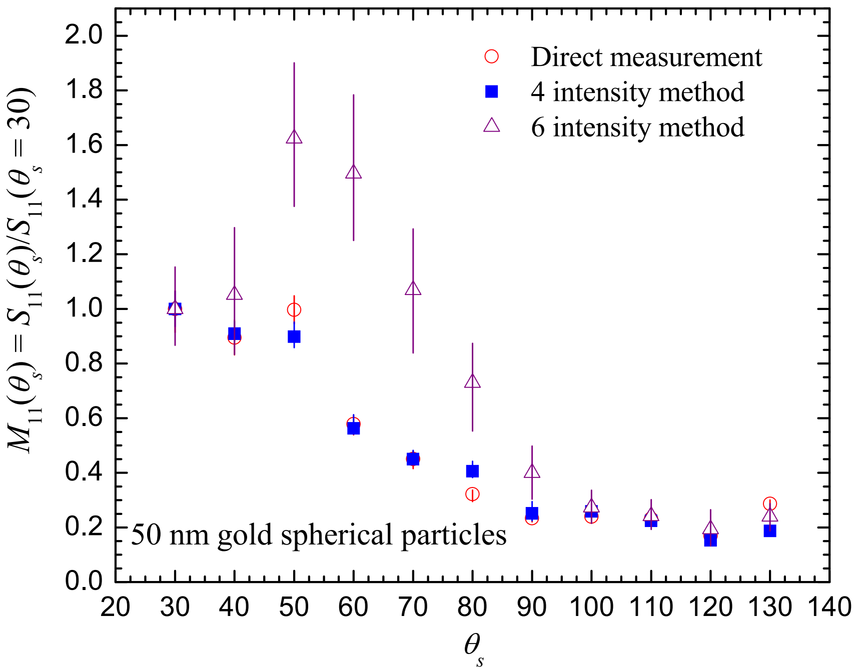

$M_{11}(\theta_s) = S_{11}(\theta_s)/S_{11}(\theta_s = 30)$
2.0
1.8
1.6
1.4
1.2
1.0
0.8
0.6
0.4
0.2
0.0
20
30
40
50
60
70
80
90
100
110
120
130
140
$\theta_s$
○ Direct measurement
■ 4 intensity method
△ 6 intensity method
50 nm gold spherical particles

(a)

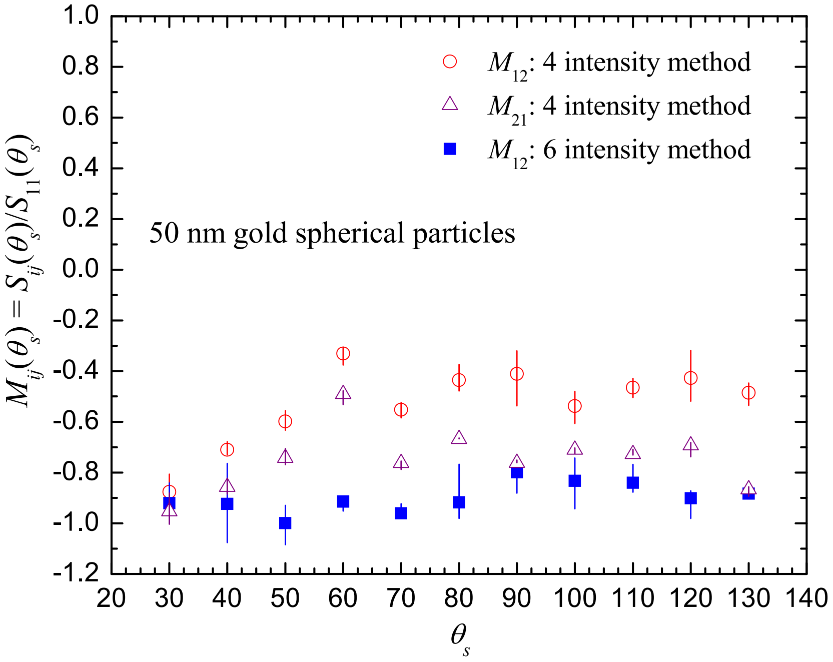

$M_{ij}(\theta_s) = S_{ij}(\theta_s)/S_{11}(\theta_s)$
1.0
0.8
0.6
0.4
0.2
0.0
-0.2
-0.4
-0.6
-0.8
-1.0
-1.2
20
30
40
50
60
70
80
90
100
110
120
130
140
$\theta_s$
○ $M_{12}$: 4 intensity method
△ $M_{21}$: 4 intensity method
■ $M_{12}$: 6 intensity method
50 nm gold spherical particles

(b)

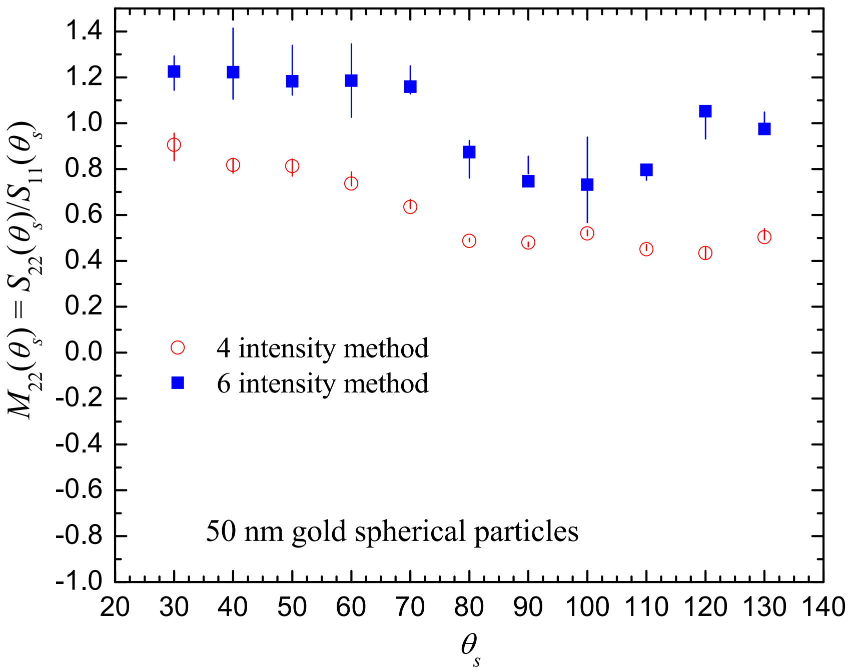

(c)

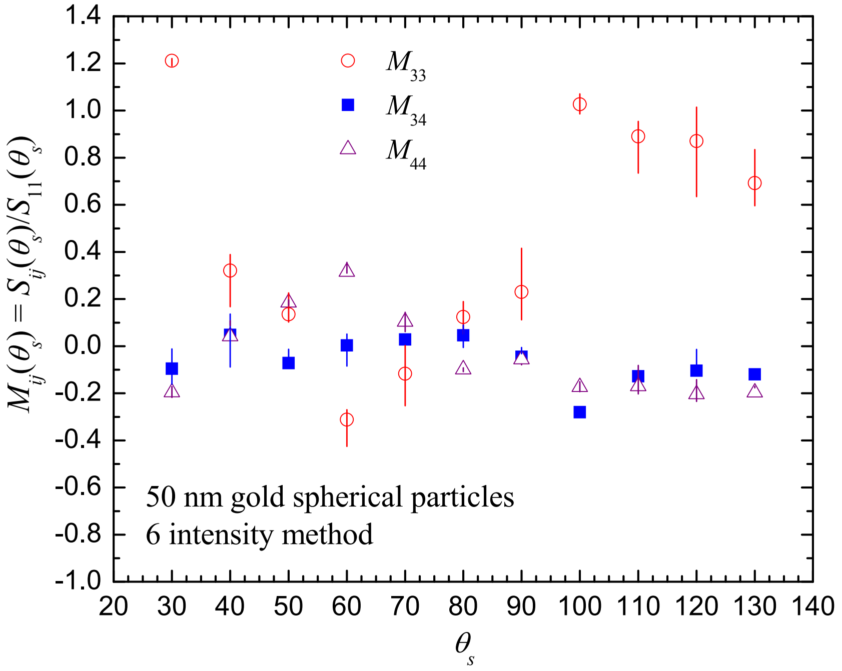

(d)

Figure 8.12. Scattering profiles measured via the four intensity and the six intensity method: (a) $M_{11}$; the results are compared with the scattered intensity measured directly. (b) $M_{12}$ and $M_{21}$. (c) $M_{22}$. (d) $M_{33}$, $M_{34}$ and $M_{44}$.

Finally, $M_{11}$ and $M_{12}$ profiles obtained from the four intensity method are compared with numerical simulations of 50 nm gold spherical particles for $p$ values of 0 % and 100 %, where $p$ represents the percentage of single nanoparticles. Note that the remaining $(100 - p)$ % of agglomerates were simulated according to the procedure described in section H.1 of appendix H.

Figure 8.13(a) shows that the experimental and numerical values of $M_{11}$ follow the same trend, but non-negligible discrepancies are observable. For the $M_{12}$ profiles, no qualitative agreement is found between the experiments and simulations. As discussed in section 7.3, the numerical model is subjected to various assumptions, which might lead to the discrepancies reported in Figs. 8.13(a) and 8.13(b). However, these differences are more likely to be due to the modeling of the agglomerates of particles. Indeed, these agglomerates take only very simple form, as described in section H.1, that are probably not representative of the real sample. Further efforts should be devoted to improving the numerical model.

### 8.5 Concluding remarks

The experimental results presented in this chapter have clearly demonstrated that the six intensity method used in the past by Mengüç’s group to characterize particles in suspension via a propagating radiation beam is not applicable for the case of spherical nanoparticles on a surface. On the other hand, the four intensity method was found to be quite stable and consistent for measuring four scattering profiles. With this approach, the element $M_{12}$ can be retrieved, which is highly sensitive to the parameters to be estimated, as discussed in section 7.3.

Scattering profiles have shown important variations depending on the location where the measurements were performed. This is quite encouraging, as it suggests that it might be possible to characterize nanoparticles via scattered surface waves. On the other hand, the repeatability of the results is difficult with the current version of the PSWSS, as no system can position accurately the sample on the prism.

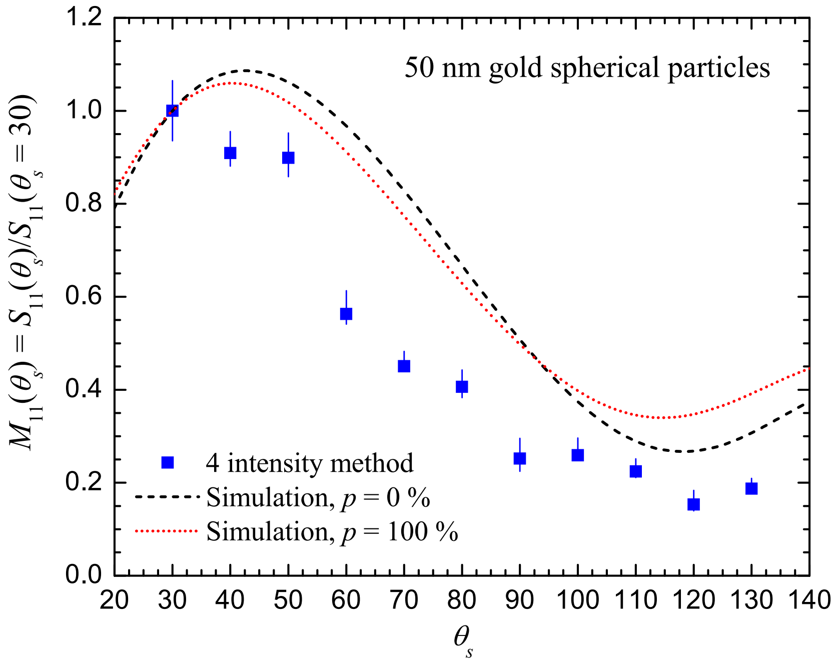

(a)

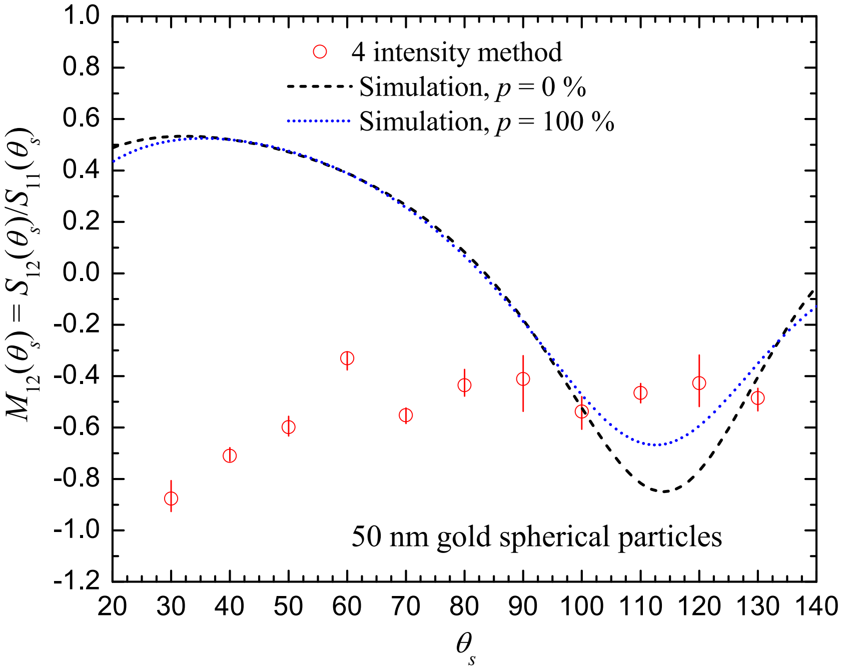

(b)

Figure 8.13. Scattering profiles measured via the four intensity method; results are compared with numerical predictions for $p$ values of 0 % and 100 %: (a) $M_{11}$. (b) $M_{12}$.

# Chapter 9

# Conclusions and Recommendations

Near-field thermal radiation, nanoscale-gap thermophotovoltaic power generation, and optical characterization of nanoparticles, all related to the broad discipline of near-field radiative transfer, have been discussed throughout this dissertation. In chapter 9, for each of these specific subjects, the main results obtained in this work are summarized, and numerous recommendations for future research efforts are provided.

## 9.1 Near-field thermal radiation

A general algorithm for the solution of near-field thermal radiation problems in one-dimensional layered media without any limitation on the number of layers has been presented in chapter 3. The emphasis has been on the accurate and efficient computation of the radiative heat flux; yet this procedure is also applicable for calculations of the near-field energy density and the local density of electromagnetic states (LDOS). The formulation is based on the solution of the dyadic Green's functions (DGFs) where the amplitudes of the fields in each layer of the structure are calculated via a scattering matrix approach in order to avoid instabilities, arising in a regular transfer matrix method, when dealing with evanescent waves. Complete recursive schemes for calculation of the amplitude of the fields in each layer have been described for the case of an emitting film and an emitting half-space. Consistency tests involving cubic boron nitride (*c*BN), supporting surface phonon-polaritons (SPhPs) in the infrared, have shown that predictions of near-field monochromatic radiative heat transfer for a bulk emitter are recovered for an emitting film of thickness above 1 μm. The accuracy and versatility of the procedure have been demonstrated via the solution of problems previously addressed in the literature involving far-field thermal emission from a single and multiple thin films, near-field radiative heat transfer between two bulks of *c*BN and silicon carbide (SiC), and near-field radiative heat transfer between two thin films of SiC. Further simulations involving multiple thin films of *c*BN have revealed that the presence of a body in close proximity to an emitter can modify the near-field spectrum emitted due to a perturbation of SPhP dispersion relation.

The possibility of fine tuning near-field thermal emission and radiative transfer via thin films of SiC, supporting SPhPs in the infrared, has been explored in chapters 4 and 5. This has been accomplished in chapter 4 by studying the physics of near-field thermal radiation emission by a thin layer of SiC, in the presence of a non-emitting film of SiC. The transverse magnetic (TM) evanescent component of the monochromatic LDOS within the gap formed between the two SiC films has been calculated for this purpose. An analytical expression for the LDOS in the gap between two films has been derived for the first time. The equation has shown that due to SPhP coupling within and between the layers, the dispersion relation splits into four resonant cross-coupled modes. The analysis of the equation has also revealed that thermal emission by a film increases due to the presence of a second non-emitting layer. The impact of inter-film separation $d_c$, the distance where the fields are calculated $\Delta$, and the thickness of the non-emitting film $t_3$ on the LDOS profiles have been analyzed in details. For $d_c \rightarrow \infty$ (i.e., thermal emission from a single film), the resonance of the LDOS profiles splits into two distinct modes when $t_1 \leq \Delta$ due to the fact that SPhPs dominating thermal emission, with penetration depths of the order of $\Delta$, couple within the thin emitting layer. When $\Delta$ and $d_c$ are of equal lengths, the results have shown that thermal emission can significantly increase solely due to the presence of a non-emitting layer supporting SPhPs (more than an order of magnitude for $d_c = 10$ nm). This perturbation is due to SPhP coupling between the films, which increase the number of available electromagnetic modes, while decreasing the spectral coherence of LDOS resonance. For a fixed configuration, it has been shown that as $\Delta$ decreases below $d_c$, the near-field spectrum is no longer affected by the presence of a second non-emitting film, since the LDOS is dominated by SPhPs with large parallel wavevectors (i.e., small penetration depths) that do not couple with the non-emitting medium. Finally, it has been shown that spectral distributions of LDOS are significantly altered as the thickness of the non-emitting film increases relative to the thickness of the emitter. This is due to the fact that as $t_3$ increases, a magnifying mismatch between the cross-coupled SPhP modes leading to a maximum LDOS develops, thus resulting in different spectra, which are highly dependent on the value of $t_3$.

The analysis of chapter 4 has been extended in chapter 5 via the computation and analysis of spectral distributions of radiative heat flux exchanged between the two SiC films. A compact analytical expression for the flux between two films has been derived for the first time in terms of film reflection and transmission coefficients, showing explicitly the resonant modes of thermal radiation emission, absorption and the cross-coupling of SPhP between the layers of finite thicknesses. The impact of varying the inter-film gap $d_c$ when both films are of the same thickness ($t_1 = t_3 = 10$ nm) has been considered first. The results suggest that splitting of the flux resonance into two modes happens when $t_1/d_c$ ($=t_3/d_c$) is less than unity. The splitting into two distinct frequencies is due to the fact that the resonant frequencies maximizing near-field emission and absorption are almost the same; the small discrepancies are due to inter-film coupling, leading to a loss of spectral coherence affecting mostly the low frequency mode. For fixed $d_c$ of 100 nm and $t_1$ of 10 nm, the results have revealed that spectral distributions of flux are significantly altered by increasing $t_3$ relative to $t_1$. In that case, the modes associated with the film of constant thickness are almost unaffected by the variation of $t_3$. The alteration of the near-field flux is mostly due to SPhP coupling with medium 3, which becomes weaker as $t_3$ increases. When $t_3$ is sufficiently thick, a clear peak of flux at the resonant frequency of a single SiC-vacuum interface is observed. An asymptotic analysis of the dispersion relation for the two film system has been performed for predictions of the resonant frequencies at which the flux is maximal as a function of $t_1$, $t_3$ and $d_c$. It has been shown that resonances of the flux are correctly predicted by modifying the definition of penetration depth of evanescent waves, as the distance from the interface where the field amplitude decays by 90 % of its original value.

The total (i.e., integrated over all angular frequencies) near-field radiative heat transfer coefficient $h_r$ between the two SiC films separated by a distance $d_c << \lambda_w$ has been analyzed, where $\lambda_w$ is the dominant wavelength emitted. It has been shown for the first time, via numerical simulations and an asymptotic analysis of $h_r$, that dual $d_c^{-2}$ and $d_c^{-3}$ near-field thermal radiation regimes coexist between two SiC thin films. When both $t_1$ and $t_3 >> d_c$, the $d_c^{-2}$ regime is retrieved since SPhPs dominating near-field radiant energy exchanges, with penetration depths of the order of $d_c$, do not couple within the films. For $t_1 << d_c$ and $t_3 >> d_c$ (and vice-versa), $h_r$ varies as $d_c^{-3}$ while the $d_c^{-2}$ regime is reached again when both $t_1$ and $t_3 << d_c$. The asymptotic expansion has also revealed that for the $d_c^{-2}$ regimes, the approximate expressions of $h_r$ contain no information about the film thicknesses, while $h_r$ is a function of the thickness of the thinner film in the $d_c^{-3}$ regime.

The physical analyses presented in chapters 4 and 5 are interesting from an engineering point of view, as they show clearly that near-field thermal emission and radiative transfer can be tuned by simply varying the structure of the system, the structure being the film thicknesses and their distance of separation. As mentioned in chapter 5, spatial dispersion of the dielectric function might have non-negligible effects when dealing with thin films, such that non-local effects should be investigated in the future [212]. Moreover, a direct extension of this work would be to consider the realistic case of thin films coated on substrates, which would require an in-depth analysis of how the presence of the substrates affects SPhP coupling within and between the layers. Physical investigations of systems involving multiple thin films should also be addressed in the future, such as one-dimensional thermal photonic crystals, which have been briefly discussed very recently [213].

Near-field thermal radiation is still an immature field, and considerable research efforts are required for further developments of engineering applications involving radiative heat transfer at nanoscale. One of the greatest limitations is related to the modeling of near-field thermal radiation problems in complex geometries due to the difficulty of solving the DGFs. A way to solve this problem would be to adapt pure numerical approaches, such as finite-difference time-domain (FDTD) or finite-difference frequency-domain (FDFD) formulations [214], to near-field thermal radiation. With such a powerful tool, it would be possible to investigate more realistic cases. For example, the analysis between two thin films presented in this dissertation assumes that the surfaces of the layers are perfectly smooth. In reality, there is always surface roughness, and this roughness could affect slightly or significantly near-field thermal emission and radiation heat transfer. Also, tuning near-field radiative transfer should not be limited to thin films, and a pure numerical approach would allow the investigation of more complex nanostructures. For example, near-field thermal emission by nanoparticles of SiC coated on a substrate might allow fine tuning of the emitted spectrum by varying the diameters and inter-particle distances.

As pointed out in section 5.7, the fluctuational electrodynamics formalism, where the local thermodynamic equilibrium is assumed, might be questionable when applied to nanometric structures. It is therefore necessary to address the problem of near-field thermal radiation emission by nanometric objects starting from fundamental statistical thermodynamics [215]. Also, when computing thermal emission via the fluctuation-dissipation theorem, it is assumed that the charges oscillate in a complete chaotic manner. However, when two emitting surfaces are brought in close proximity, the thermal near-field of one medium might polarize the charges of the other material in a preferential manner, and vice-versa. Such a phenomenon is likely to affect the randomness of charge oscillations, and might affect near-field thermal radiation emission.

Finally, experimental evidences of near-field thermal radiation have been done successfully between a large sphere and a substrate [89,92]. There is however a need to perform these experimentations in real systems, for example between surfaces separated by a gap of few tens of nanometers. It would also be interesting to validate the dual $d_c^{-2}$ and $d_c^{-3}$ regimes between SiC thin films. This could be done by coating the thin layers on substrates, and by using a system that would measure the near-field radiative heat flux at various gaps $d_c$.

### 9.2 Nanoscale-gap thermophotovoltaic power generation

The impacts of thermal effects on the performances of nanoscale-gap thermophotovoltaic (nano-TPV) power generation have been investigated for the first time in chapter 6. This has been accomplished by solving the coupled near-field thermal radiation, charge and heat transport problem within the nano-TPV device. A system consisting of a tungsten (W) radiator, maintained at a constant and uniform temperature of 2000 K, and TPV cells made of indium gallium antimonide ($In_{0.18}Ga_{0.82}Sb$) has been investigated. The temperature-dependent interband dielectric function of $In_{0.18}Ga_{0.82}Sb$ has been modeled via a semi-empirical model, while the dielectric function due to the free carriers and the lattice has been modeled via a Lorentz-Drude oscillator. The coupled near-field thermal radiation and charge transport model has been validated against results from the literature [37]. The discrepancies observed in the spectral distributions of radiative heat fluxes and quantum efficiencies have been attributed to potential differences in modeling the dielectric function of the $In_{0.18}Ga_{0.82}Sb$-based cell.

When the temperature of the cell is 300 K, an electrical power output and a conversion efficiency in the far-field regime (i.e., large gap $d_c$ between the radiator and the cell) of $2.40\times10^4$ $Wm^{-2}$ and 19.8 %, respectively, have been calculated. As the gap between the radiator and the cell decreases, a significant increase of the power output has been observed since more radiative energy is transferred due to tunneling of evanescent waves. For a gap of 1 nm, an electrical power output of $3.91\times10^7$ $Wm^{-2}$ has been calculated, while a low conversion efficiency of 14.0 % has been reported. This behavior, already pointed out in the past [37], is due to the fact that as the gap $d_c$ decreases, the near-field radiative heat flux is dominated by evanescent waves with small penetration depths of the order of $d_c$. These waves with low penetration depths are absorbed near the irradiated surface of the cell, and the electron-hole pairs (EHPs) generated are thus more likely to recombine before reaching the junction between the p- and n-doped regions. Optimal performances have been found for a gap of 20 nm, where the power output and conversion efficiency are respectively of $5.83\times10^5$ $Wm^{-2}$ and 24.8 %.

Investigation of the performances as a function of the temperature of the cell has revealed that both the conversion efficiency and the electrical power output significantly decrease as the temperature of the cell increases. For a gap of 20 nm, a power output and a conversion efficiency respectively of $8.09\times10^4$ $Wm^{-2}$ and 3.23 % have been calculated when the cell is maintained at 500 K. It has been shown that the radiation absorbed by the cell is almost insensitive to its temperature, while the open-circuit voltage decreases significantly with increasing the temperature of the p-n junction. These results have clearly demonstrated that optimal performances of nano-TPV power generators are found when the cells are maintained around room temperature.

The solution of the coupled near-field thermal radiation, charge and heat transport problem has shown that the nano-TPV devices proposed so far in the literature might be unpractical. The thermal management system has been modeled using a convective boundary with a fluid temperature fixed at 293 K. Even in the far-field regime, a considerably high value of $10^4$ $Wm^{-2}K^{-1}$ for the heat transfer coefficient is needed to maintain the cell around room temperature. For gaps of 20 nm, 50 nm and 100 nm, a heat transfer coefficient of $10^5$ $Wm^{-2}K^{-1}$ is required to maintain the cell at room temperature, a value that is extremely large. This behavior is due to the fact that the near-field radiative heat transfer enhancement from a W bulk is a broadband phenomenon, while only a certain part of the spectrum is useful for optimizing nano-TPV performances. For all cases investigated, the heat source within the TPV cell is dominated by thermalization. While the simulations have raised important interrogations about the feasibility of nano-TPV devices proposed in the literature by determining the heat transfer coefficient needed to maintain the cell at room temperature, it would be necessary in a future research effort to quantify the electrical power required by the cooling system.

The work performed in this dissertation on nano-TPV energy conversion should be seen as an introduction on this subject, and further theoretical and experimental research efforts are required to show the feasibility of these devices. As a direct extension of this work, it would be interesting to use the knowledge developed in chapters 4 and 5 to investigate the performances of nano-TPV power generators using a radiator made of thin films of W. From a practical point of view, nano-TPV devices discussed in chapter 6 involve a high temperature gradient (2000 K for the radiator and 300 K for the cell), which might not be realizable. Low-temperature nano-TPV devices might therefore be a nice alternative, where the radiator would be maintained between 350 K and 400 K. Such a system would be easier to operate and would be more versatile. This technology would however require the use of TPV cells with bandgaps much lower than the typical 0.50 eV to 0.70 eV employed for high-temperature TPV power generators. For example, the peak wavelength emitted at a temperature of 400 K is about 7.25 μm, which corresponds to an energy of 0.17 eV. Fortunately, current research efforts are devoted to developing low bandgap cells based on indium arsenide antimonide (InAsSb) and indium gallium antimonide nitride (InGaSbN) for applications to TPV devices operating at temperatures lower than 1000ºC [216].

For the nano-TPV system discussed in chapter 6, SiC or *c*BN cannot be used as the radiator. For example, SPhP resonance of a single SiC-vacuum interface is at $\omega_{res}$ = $1.786\times10^{14}$ rad/s, which corresponds to an energy of $E_{res}$ = 0.12 eV. Similarly, the resonant frequency of a *c*BN-vacuum interface is $E_{res}$ = 0.16 eV. On the other hand, these materials supporting SPhPs in the infrared could be used for low-temperature nano-TPV power generators involving low bandgap p-n junctions.

Low-temperature nano-TPV power generators could find numerous applications in recuperating energy for a multitude of small and portable electronic devices. For example, the heat generated by the processors of a computer is a major limiting performance factor. In typical personal computers, forced convection (fans) is used in order to maintain the electronic components at an acceptable temperature. This means that there is an energy cost for removing the heat generated by the processor. Nano-TPV device could be used as an alternative to fans. The nano-TPV device would serve simultaneously as a passive cooling system (i.e., no energy required to remove the heat generated), and as a power generator. This could improve drastically the energy consumption and battery lifetimes of small electronic devices. This concept could also be applied to photovoltaic cells [217].

Of course, one of the key issues in the viability of nano-TPV power generators is the design of a couple radiator-cell that would optimize the performances of the device. Before designing such a structure, it is crucial to know the spectrum optimizing nano-TPV efficiencies and power output. Another issue is to design cell that would be appropriate for nano-TPV technologies. Indeed, as discussed in section 6.6.2, most of the radiative energy at small vacuum gaps is absorbed near the entrance of the cell, such that it might be necessary to use thin TPV cells. Finally, although this subject has not been discussed in chapter 6, there are some important fabrication issues related to nano-TPV devices. For sure, it would extremely difficult to maintain gaps below 20 nm due to the surface roughness of both the radiator and the TPV cell. Further research efforts are needed regarding this issue.

### 9.3 Optical characterization of nanoparticles via scattered surface waves

The possibility of characterizing nanoparticles (5 nm to 100 nm in size) in a non-intrusive manner, and potentially in real-time, via far-field scattering of surface waves has been explored. This has been accomplished via the calculation and analysis of the scattering (Mueller) matrix elements in chapter 7, and the measurement of these aforementioned parameters (chapter 8) with the polarized-surface-wave-scattering system (PSWSS). The investigation has been restricted to metallic spherical nanoparticles.

A sensitivity analysis has been performed in chapter 7 in order to quantify the sensitivity of the scattering matrix elements to the parameters to be estimated. Averaged normalized sensitivity coefficients, which give the sensitivity of the normalized scattering matrix elements $M_{ij}$ to a parameter to be estimated, have been calculated. Sensitivities of $M_{ij}$ to the diameter of the particle have been reported for a system composed exclusively of single nanoparticles. In the same way, the sensitivity to the composition of single nanoparticles and diameter for a system composed of single nanoparticles and agglomerates has been analyzed. The averaged normalized sensitivity coefficients of $M_{11}$ (scattered intensity) are always very low, which imply that the characterization should be done by using the polarization information. For all cases considered, the scattering matrix elements $M_{12}$ and $M_{33}$ have been found to be the most sensitive elements.

Two approaches for measuring the $M_{ij}$ elements with the PSWSS have been discussed. The first one, called the six intensity method, is based on the assumption that the scattering matrix for a cloud of particles that have a plane of symmetry and are randomly oriented reduces to six independent and non-zero elements ($M_{11}$, $M_{12}$, $M_{22}$, $M_{33}$, $M_{34}$ and $M_{44}$). These elements are measured in an indirect manner by performing six experiments where six independent values of intensities are obtained. This is accomplished by using a linear polarizer (LP) and a quarter-wave plate (QWP) between the laser source and the sample, as well as between the sample and the detector measuring the scattered light. The second approach, called the four intensity method, is much simpler as it implies the measurement of four intensities using a LP before and after the sample. In that manner, four scattering matrix elements are retrieved ($M_{11}$, $M_{12}$, $M_{21}$ and $M_{22}$).

Measurements of the scattering matrix elements on 200 nm and 50 nm gold spherical particles have revealed that the six intensity method is not applicable to the case of spherical particles on a surface. When different locations on the same sample are illuminated, similar $M_{11}$ profiles have been obtained, while the profiles related to the polarization information have been found to be significantly different. These experimental observations are in good agreement with the conclusions of the sensitivity analysis, where it has been pointed out that a robust characterization framework cannot solely rely on the scattered intensity. On the other hand, the repeatability of the experimental results obtained with the PSWSS is very low. This is due to the fact that the PSWSS does not have a system to accurately position the sample on the prism.

Comparisons of the $M_{11}$ and $M_{12}$ profiles measured on 50 nm gold spherical particles against numerical predictions have shown some discrepancies. For $M_{11}$, the general trend between the experimental data and the theoretical predictions are the same, but it is not the case for $M_{12}$. Since the shape, composition, and size of the scatterers coated on the sample are known, the sensitivity of $M_{12}$ is likely to be due to different agglomeration levels and patterns. Numerical modeling of agglomerates of particles is limited to very simple geometries that are probably not representative of the real sample. This is likely to be the major cause of discrepancies between the experimental results and numerical predictions.

While the calibration of the PSWSS is still inconclusive, the results suggest that the characterization framework discussed in this dissertation might be possible to realize, due to a great sensitivity of the scattering matrix elements (other than $M_{11}$). However, further calibration tests are needed, which would require: (1) the development of a second generation of the PSWSS, and (2) the development of an accurate numerical model to solve the problem of surface wave scattering by nanoparticles (and complex agglomerates) on a surface.

One of the greatest challenges for calibrating the PSWSS is to obtain well-calibrated samples of spherical particles coated on a surface. Ideally, samples coated with single nanoparticles should be used, as the solution of the forward problem for this configuration is known. However, in practice, such a sample is very difficult to prepare.

As mentioned earlier, the repeatability of the results is a major issue that should be addressed in the future. Therefore, the next version of the PSWSS should have a system that would allow to position very accurately the sample on the prism, such that results could be reproduced quite easily.

Although the PSWSS is quite easy to operate, the alignment of the optics is challenging. The next version of the tool should make the alignment of the system much easier. In the same line, the orientation angles of the LPs and QWPs currently used in the PSWSS are changed manually, such that some experimental errors might come from imprecise alignments of the transmission and fast axis of these components. In the next version of the PSWSS, the orientation of the LPs and QWPs should be controlled by step motors.

We have measured scattered surface waves by 200 nm and 50 nm particles, and have shown that the quantities thus collected are quite stable. On the other hand, the resolution of the PSWSS should be investigated by measuring the scattering by smaller particles. Of course, such an investigation should be done once the system is well-calibrated for 50 nm particles or above. A challenge comes from the fact that for very small nanoparticles, say 5 nm, the surface roughness of the substrate might be of the same order of magnitude, or greater, than the particles themselves. Further experimental measurements on nanoparticles smaller than 50 nm should therefore be performed.

Measurements of the scattering matrix elements, as done in chapter 8, are performed in an indirect manner, such that instabilities can arise when recovering these elements from intensity measurements. Therefore, instead of using the scattering matrix elements, it would be possible to develop a characterization procedure by using directly the linear combinations of these elements (i.e., the intensities). By pursuing this avenue, it would be necessary to use orientation angles of the optical components that would optimize the sensitivity of the parameters to be determined.

To summarize, significant further research efforts are required to obtain a more consistent and definitive calibration of the PSWSS. Nevertheless, the results provided in this dissertation are encouraging, as they suggest that the non-intrusive characterization framework is viable.

# Appendix A

# Solution of the Stochastic Maxwell Equations via the Method of Potentials

Different approaches can be used to solve the stochastic Maxwell equations. In the current study, the method of potentials is adopted [70]. From Gauss's law (Eq. (2.1d)) and the vector identity $\nabla \cdot (\nabla \times \mathbf{A}) = 0$, the magnetic induction **B** can be written: $\mathbf{B}(\mathbf{r},\omega) = \nabla \times \mathbf{A}(\mathbf{r},\omega)$, where **A** is referred as the magnetic vector potential. This expression is then substituted in the right-hand side of Faraday's law (Eq. (2.1a)):

$$\nabla \times (\mathbf{E}(\mathbf{r},\omega) - i\omega \mathbf{A}(\mathbf{r},\omega)) = 0 \tag{A.1}$$

From the vector identity $\nabla \times (\nabla \Phi_e) = 0$ and Eq. (A.1), the electric field can be written as:

$$\mathbf{E}(\mathbf{r},\omega) = i\omega \mathbf{A}(\mathbf{r},\omega) - \nabla \Phi_e(\mathbf{r},\omega) \tag{A.2}$$

where $\Phi_e$ is referred as the electric scalar potential. Ampère's law (Eq. (2.3)) is then manipulated to express a relation between the magnetic vector potential and the electric scalar potential:

$$\nabla \times \nabla \times \mathbf{A}(\mathbf{r},\omega) = \mu_v \mathbf{J}^r(\mathbf{r},\omega) + i\omega\varepsilon\mu_v \nabla \Phi_e(\mathbf{r},\omega) + \omega^2 \varepsilon\mu_v \mathbf{A}(\mathbf{r},\omega) \tag{A.3}$$

The above equation can be manipulated using the vector identity $\nabla^2 \mathbf{A} = -\nabla \times \nabla \times \mathbf{A} + \nabla\nabla \cdot \mathbf{A}$, and the fact that $k^2 = \omega^2 \varepsilon\mu_v$:

$$(\nabla^2 + k^2)\mathbf{A}(\mathbf{r},\omega) = \nabla\nabla \cdot \mathbf{A}(\mathbf{r},\omega) - \mu_v \mathbf{J}^r(\mathbf{r},\omega) - i\omega\varepsilon\mu_v \nabla \Phi_e(\mathbf{r},\omega) \tag{A.4}$$

To close the problem, the Lorentz gauge is used to establish the relation between the magnetic vector potential and electric scalar potential [70]:

$$\nabla \cdot \mathbf{A}(\mathbf{r},\omega) = i\omega\varepsilon\mu_v \Phi_e(\mathbf{r},\omega) \tag{A.5}$$

The substitution of the Lorentz gauge in Eq. (A.4) leads to:

$$(\nabla^2 + k^2)\mathbf{A}(\mathbf{r},\omega) = -\mu_v \mathbf{J}^r(\mathbf{r},\omega) \tag{A.6}$$

which is the scalar Helmholtz equation. An expression for **A** is obtained by considering the impulse response of the system (i.e., the right-hand side of Eq. (A.6) is replaced by a single point source):

$$(\nabla^2 + k^2)G_0(\mathbf{r},\mathbf{r}',\omega) = -\delta(|\mathbf{r}\text{-}\mathbf{r}'|) \tag{A.7}$$

where $G_0$ is the scalar Green's function, and **r** and **r′** denote a field and a source point, respectively. Physically, the Green's function is the solution of the field for a point source (described by the Dirac function in Eq. (A.7)). By subtracting Eq. (A.7), multiplied by **A**, to Eq. (A.6), multiplied by $G_0$, and by applying Green's second identity [70], it can be shown that:

$$\mathbf{A}(\mathbf{r},\omega) = \mu_v \int_V \mathbf{J}^r(\mathbf{r}',\omega)G_0(\mathbf{r},\mathbf{r}',\omega)dV' \tag{A.8}$$

Physically, this equation means that the solution for the field due to a source $\mathbf{J}^r$ is the convolution of the Green's function with that source. The magnetic vector potential given by Eq. (A.8) and Lorentz gauge (Eq. (A.5)) are then substituted in Eq. (A.2) to give the following expression for the electric field observed at **r** due to a source located at **r′**:

$$\mathbf{E}(\mathbf{r},\omega) = i\omega\mu_v\left[1 + \frac{1}{k^2}\nabla\nabla\cdot\right]\int_V \mathbf{J}^r(\mathbf{r}',\omega)G_0(\mathbf{r},\mathbf{r}',\omega)dV' \tag{A.9}$$

Using the relation previously derived $\mathbf{B} = \nabla\times\mathbf{A}$, the magnetic field **H** follows directly from Eq. (A.8):

$$\mathbf{H}(\mathbf{r},\omega) = \int_V \nabla \times \mathbf{J}^r(\mathbf{r}',\omega) G_0(\mathbf{r},\mathbf{r}',\omega) dV' \tag{A.10}$$

The electric and magnetic fields given by Eqs. (A.9) and (A.10) are derived in terms of the Green's function for the scalar wave equation (Eq. (A.6)). This suggests that the Green's function of Eq. (A.7) is the solution of an infinitesimal electric dipole pointed in a given orthogonal direction [218]. Similar expressions for the electric and magnetic fields can be derived for sources pointed in the two other orthogonal directions. By juxtaposing the three solutions, the electric and magnetic fields can be written respectively as [70,73,218]:

$$\mathbf{E}(\mathbf{r},\omega) = i\omega\mu_v \int_V dV' G_0(\mathbf{r},\mathbf{r}',\omega) \left[ \overline{\overline{\mathbf{I}}} + \frac{1}{k^2} \nabla\nabla \cdot \right] \mathbf{J}^r(\mathbf{r}',\omega) \tag{A.11a}$$

$$\mathbf{H}(\mathbf{r},\omega) = \nabla \times \int_V dV' G_0(\mathbf{r},\mathbf{r}',\omega) \overline{\overline{\mathbf{I}}} \cdot \mathbf{J}^r(\mathbf{r}',\omega) \tag{A.11b}$$

where the dyadic $\overline{\overline{\mathbf{I}}}$ is called an idem factor [218], unit dyad, or unit tensor [1], and is nothing but a 3×3 identity matrix. In Eq. (A.11a), the following term is called the electric dyadic Green's function [70,73]:

$$\overline{\overline{\mathbf{G}}}^E(\mathbf{r},\mathbf{r}',\omega) = \left[ \overline{\overline{\mathbf{I}}} + \frac{1}{k^2} \nabla\nabla \right] G_0(\mathbf{r},\mathbf{r}',\omega) \tag{A.12}$$

Similarly, the magnetic dyadic Green's function is given by [70,73]:

$$\overline{\overline{\mathbf{G}}}^H(\mathbf{r},\mathbf{r}',\omega) = \nabla \times (G_0(\mathbf{r},\mathbf{r}',\omega) \overline{\overline{\mathbf{I}}}) \tag{A.13}$$

and the electric and magnetic dyadic Green's functions are related by the following relation:

$$\overline{\overline{\mathbf{G}}}^H(\mathbf{r},\mathbf{r}',\omega) = \nabla \times \overline{\overline{\mathbf{G}}}^E(\mathbf{r},\mathbf{r}',\omega) \tag{A.14}$$

Note that the dyadic Green's functions are 3×3 matrices, and are alternatively referred as Green's tensors. Finally, the electric and magnetic fields, written as a function of the dyadic Green's functions, are given by:

$$\mathbf{E}(\mathbf{r},\omega) = i\omega\mu_v \int_V dV' \overline{\overline{\mathbf{G}}}^E(\mathbf{r},\mathbf{r}',\omega) \cdot \mathbf{J}^r(\mathbf{r}',\omega) \tag{A.15a}$$

$$\mathbf{H}(\mathbf{r},\omega) = \int_V dV' \overline{\overline{\mathbf{G}}}^H(\mathbf{r},\mathbf{r}',\omega) \cdot \mathbf{J}^r(\mathbf{r}',\omega) \tag{A.15b}$$

Physically, the dyadic Green's function can be seen as a spatial transfer function between a current density vector $\mathbf{J}^r$ located at $\mathbf{r}'$ inside an emitting body to a point of observation $\mathbf{r}$ in an irradiated medium. Equations (A.15a) and (A.15b) mean that the electric and magnetic fields observed at $\mathbf{r}$ are the integration over the volume *V* of the emitting body of all point source $\mathbf{r}'$.

Equations (A.15a) and (A.15b) could have also been obtained more directly by first defining Green's functions for each component of the vector source $\mathbf{J}^r = J_x^r \hat{\mathbf{x}} + J_y^r \hat{\mathbf{y}} + J_z^r \hat{\mathbf{z}}$. Consequently, Eq. (A.7) can be generalized as follows when taking into account the three orthogonal directions [1]:

$$\nabla \times \nabla \times \overline{\overline{\mathbf{G}}}(\mathbf{r},\mathbf{r}',\omega) - k^2 \overline{\overline{\mathbf{G}}}(\mathbf{r},\mathbf{r}',\omega) = \overline{\overline{\mathbf{I}}}(|\mathbf{r}\text{-}\mathbf{r}'|) \tag{A.16}$$

It is clear from Eq. (A.16) that the dyadic Green's function $\overline{\overline{\mathbf{G}}}$ is a compact notation for the three Green's functions oriented in the orthogonal directions. The first column of the Green's tensor corresponds to the field produced by a point source in the *x*-direction, the second column to a field produced by a point source in the *y*-direction, and the third column to a field produced by a point source in the *z*-direction [1]. The point source oriented in a given orthogonal direction can produce a field in the three orthogonal directions. Therefore, the dyadic Green's function can be written as follows in tensor form:

$$\overline{\overline{\mathbf{G}}} = \begin{bmatrix} G_{xx} & G_{xy} & G_{xz} \\ G_{yx} & G_{yy} & G_{yz} \\ G_{zx} & G_{zx} & G_{zz} \end{bmatrix} \tag{A.17}$$

where the subscript $i$ in $G_{ij}$ refers to the state of polarization of the field produced by a source polarized in the $j$-direction.

# Appendix B

# Models for Dielectric Functions of Metals and Polar Crystals

The frequency-dependent dielectric function of polar crystals is modeled using a damped harmonic oscillator [75,152]:

$$\varepsilon_r(\omega) = \varepsilon_\infty \left( \frac{\omega^2 - \omega_{LO}^2 + i\Gamma\omega}{\omega^2 - \omega_{TO}^2 + i\Gamma\omega} \right) \tag{B.1}$$

where $\varepsilon_\infty$ is the high frequency dielectric constant, $\Gamma$ the damping factor, and $\omega_{LO}$ and $\omega_{TO}$ the frequencies of longitudinal and transverse optical phonons, respectively [152]. The parameters employed to model the dielectric functions of silicon carbide (SiC) and cubic boron nitride (*c*BN) are given in table B.1.

The frequency-dependent dielectric function of gold (Au) is modeled using a Drude model [75]:

$$\varepsilon_r(\omega) = 1 - \frac{\omega_p^2}{\omega(\omega + i\gamma)} \tag{B.2}$$

where $\omega_p$ is the plasma frequency and $\gamma$ is the damping factor. The parameters employed for Au are provided in table B.1.

Table B.1. Parameters used for modeling the dielectric function of various materials.

| Materials | $\varepsilon_\infty$ [-] | $\omega_{TO}$ [$10^{14}$ rad/s] | $\omega_{LO}$ [$10^{14}$ rad/s] | $\Gamma$ [$10^{11}$ s$^{-1}$] | $\omega_p$ [$10^{15}$ rad/s] | $\gamma$ [$10^{13}$ s$^{-1}$] |
|---|---|---|---|---|---|---|
| SiC [152] | 6.7 | 1.494 | 1.825 | 8.966 | - | - |
| *c*BN [35] | 4.46 | 1.985 | 2.451 | 9.934 | - | - |
| Au [75] | - | - | - | - | 13.71 | 4.05 |

# Appendix C

# Sipe's Unit Vectors

The unit vectors used to express the Weyl components of the dyadic Green's function follow the formalism introduced by Sipe [115]. As mentioned in section 3.2, the idea is to define TE- and TM-polarized unit vectors; their expressions are given by Eqs. (3.7a) and (3.7b). To better understand these equations, Sipe's unit vectors are schematically depicted in Fig. C.1.

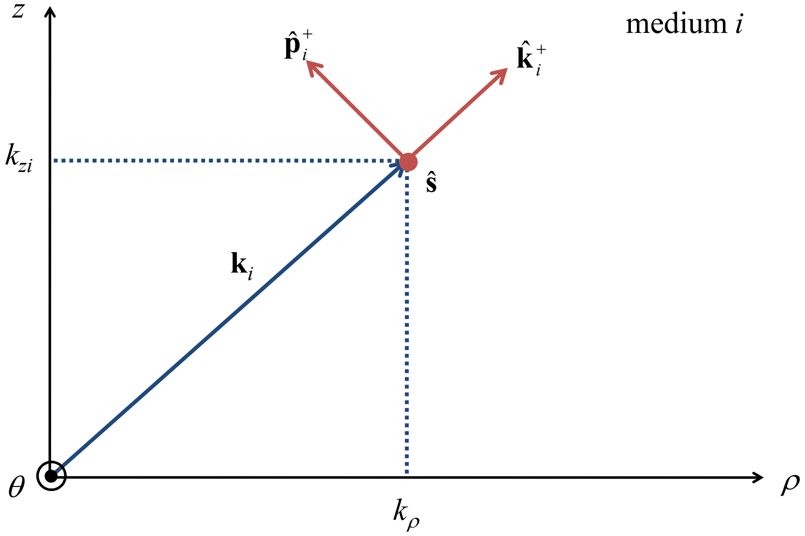

Figure C.1. Schematic representation of Sipe's unit vectors as defined in reference [115].

As pointed out in section 3.2, the system is azimuthally symmetric, such that it is assumed that the plane wave depicted in Fig. C.1 is propagating in the $\rho$-$z$ plane with a wavevector of magnitude $k_i$ (= $|\mathbf{k}_i|$), where $i$ denotes the medium where the wave is propagating. The $\rho$- and $z$-components of this wavevector are respectively denoted $k_\rho$ and

$k_{zi}$, where it is not specified that $k_\rho$ is in medium $i$, since its value does not change from one layer to another (one-dimensional approximation).

A TE-polarized unit vector, perpendicular to the plane $\rho$-$z$, can be written as: $\hat{\mathbf{s}} = -\hat{\boldsymbol{\theta}}$. The TE-polarized unit vector is simply a unit vector oriented along the $\theta$-direction, as shown in Fig. C.1.

The TM-polarized unit vector is perpendicular to the direction of propagation of the wave in the $\rho$-$z$ plane, and is therefore perpendicular to the wavevector $\mathbf{k}_i$. Since the wave depicted in Fig. C.1 is propagating in the $z$-positive direction, the TM-polarized unit vector is referred as $\hat{\mathbf{p}}_i^+$. A unit vector along the direction of propagation of the wave can be defined as follows:

$$\hat{\mathbf{k}}_i^+ = \frac{1}{k_i}(k_\rho \hat{\boldsymbol{\rho}} + k_{zi}\hat{\mathbf{z}}) \tag{C.1}$$

The TM-polarized unit vector is perpendicular to the unit vector along the direction of propagation of the wave, and is easily determined from Eq. (C.1)

$$\hat{\mathbf{p}}_i^+ = \frac{1}{k_i}(k_\rho \hat{\mathbf{z}} - k_{zi}\hat{\boldsymbol{\rho}}) \tag{C.2}$$

The dot product of Eqs. (C.1) and (C.2) is obviously zero, showing that $\hat{\mathbf{p}}_i^+$ is perpendicular to the direction of propagation of the wave. Similarly, if the wave is propagating in the $z$-negative direction, the unit vector oriented along the direction of propagation of the wave is given by:

$$\hat{\mathbf{k}}_i^- = \frac{1}{k_i}(k_\rho \hat{\boldsymbol{\rho}} - k_{zi}\hat{\mathbf{z}}) \tag{C.3}$$

thus resulting in the following TM-polarized unit vector:

$$\hat{\mathbf{p}}_i^- = \frac{1}{k_i}(k_\rho \hat{\mathbf{z}} + k_{zi}\hat{\boldsymbol{\rho}}) \tag{C.4}$$

Again, the dot product of Eqs. (C.3) and (C.4) is zero, as it should be. By combining the TM-polarized unit vectors in the *z*-positive direction (Eq. (C.2)) and in the *z*-negative direction (Eq. (C.4)), the following general expression for the TM-polarized unit vector is obtained:

$$\hat{\mathbf{p}}_i^{\pm} = \frac{1}{k_i}(k_\rho \hat{\mathbf{z}} \mp k_{zi} \hat{\boldsymbol{\rho}}) \tag{C.5}$$

Equation (C.5) is the same as Eq. (3.7b).

# Appendix D

# Validation of Near-Field Thermal Radiation Simulations

Near-field thermal radiation simulations based on the method described in chapter 3 are validated in this appendix against results previously published in the literature. The discretization scheme provided in section 3.5.1 has been employed to produce the results shown hereafter.

## D.1 Far-field thermal radiation emission from thin films

In this section, the far-field emissivity of silver (Ag) thin films is calculated. This problem has been solved by Nayaranaswamy and Chen [60]; the data from this reference have been extracted using *Plot Digitizer* [219].

In Fig. D.1, thermal radiation emission by a 10 nm thick Ag film and a bulk of Ag is compared. More specifically, the spectral hemispherical emissivity for wavelengths between 0.4 μm to 4 μm is calculated. The spectral hemispherical emissivity is computed in reference [60] as the propagating flux emerging from the film/bulk divided by $\pi I_b$, where $I_b$ is the blackbody intensity of a bulk. Results from the current method and those from reference [60] are compared in Fig. D.1. Note that the dielectric function of Ag is modeled as [60]: $5.17 + i - 9.013^2/(E(E + i0.018))$, where $E = \hbar\,\omega/e$.

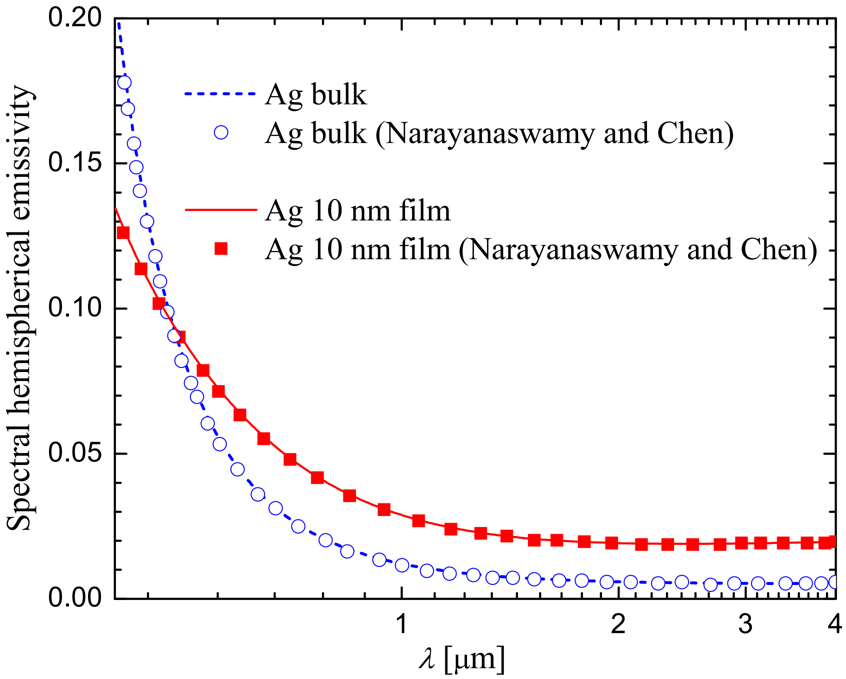

Figure D.1. Spectral hemispherical emissivity of a 10 nm thick Ag film and a bulk of Ag (this corresponds to Fig. 2 of reference [60]).

It can be seen in Fig. D.1 that the match between the results from the current method and those from Narayanaswamy and Chen [60] is perfect. Even if this problem is quite simple (i.e., there is no evanescent waves as only far-field thermal radiation emission is considered), the results show clearly that the methodology presented in chapter 3 is versatile, and can be used for far-field thermal radiation calculations.

In Fig. D.2, we considered eleven 10 nm thick films of Ag separated by vacuum gaps of 150 nm. As for the case depicted in Fig. D.1, the spectral hemispherical emissivity is computed. The idea of this problem is to calculate far-field thermal emission from only one film of the structure, while assuming that the ten other films are non-emitting. In reference [60], emissivities from the 6th layer alone and the 10th layer alone are presented.

The observations made for Fig. D.1 are applicable to the results shown in Fig. D.2. Here, the fact that a perfect agreement is found for a problem involving multiple thin films shows clearly that the algorithm is stable, regardless of the number of layers considered in the simulations.

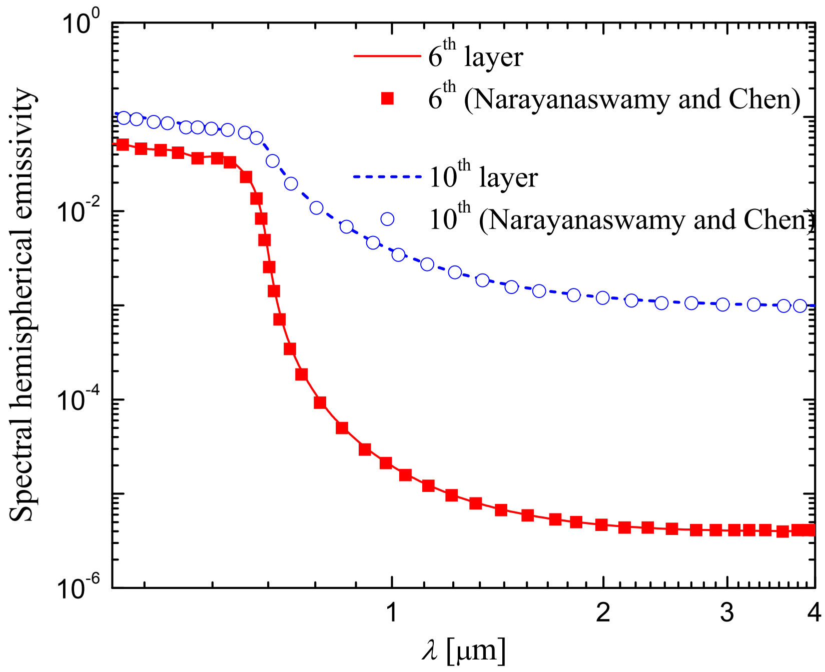

Figure D.2. Spectral hemispherical emissivity of layers 6 and 10 in a one-dimensional photonic crystals consisting of eleven 10 nm thick Ag films separated by 150 nm thick vacuum gaps (this corresponds to Fig. 3 of reference [60]).

## D.2 Near-field radiative heat transfer between two bulks of cubic boron nitride

Near-field thermal radiation between two bulks of cubic boron nitride (*c*BN), which has been solved in section 3.5.1, is compared hereafter against results published by Narayanaswamy and Chen [35].

Spectral distribution of radiative heat flux between the two *c*BN bulks, with $T_0$ = 1000 K and $T_2$ = 300 K (see Fig. 3.3(a)), are shown in Fig. D.3. The dielectric function of *c*BN used to perform the simulations is provided in appendix B.

Spectral distributions of near-field radiative heat flux calculated with the current approach is in perfect agreement with the results reported in reference [35]. This shows that the procedure described in chapter 3 is accurate for solution of thermal radiation problems both in the far-field and in the near-field.

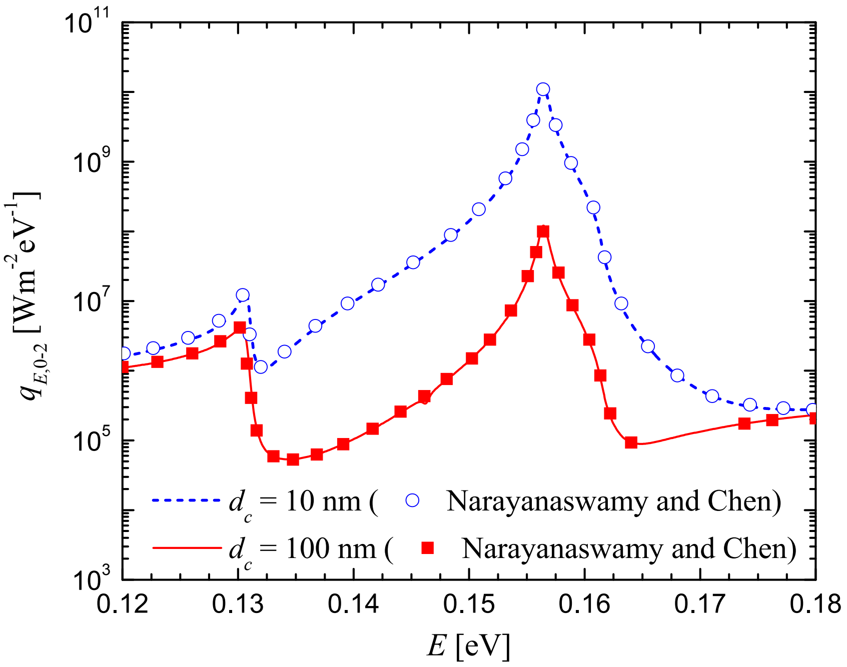

Figure D.3. Spectral distributions of near-field radiative heat flux between two bulks of *c*BN with $T_0$ = 1000 K and $T_2$ = 300 K for $d_c$ = 10 nm and 100 nm (corresponds to Fig. 1 of reference [35]).

### D.3 Near-field radiative heat transfer between two bulks of silicon carbide

Near-field radiative transfer between two bulks of silicon carbide (SiC) is validated against the results reported by Mulet et al. [30]. More specifically, the near-field radiative heat transfer coefficient $h_r$ is calculated as a function of $d_c$ at 300 K (Eq. (3.49)), and the results are shown in Fig. D.4.

Note that $h_r$ values below $d_c$ = 10 nm are not provided in reference [30]. Again, $h_r$ values obtained from the current method and those from Mulet et al. are in perfect agreement, thus validating the numerical procedure used to calculate total quantities (i.e., quantities integrated over all frequencies).

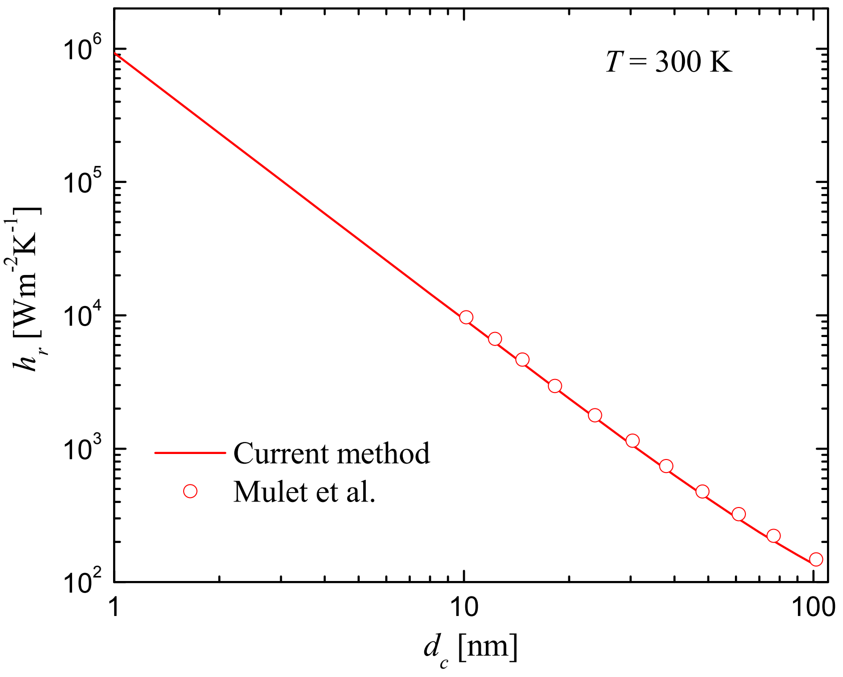

Figure D.4. Total near-field radiative heat transfer coefficient $h_r$ between two bulks of SiC at $T$ = 300 K as a function of $d_c$ (correspond to Fig. 3 of reference [30]).

### D.4 Near-field radiative heat transfer between two films of silicon carbide

To complete the validation of the procedure described in chapter 3, a near-field thermal radiation problem involving two thin films of SiC submerged in vacuum, as depicted in Fig. 5.1, is solved and compared against the results reported by Ben-Abdallah et al. [109]. The near-field radiative heat transfer coefficient $h_r$ is reported in Fig. D.5 between two 1 nm thick films of SiC as a function of the gap $d_c$.

As for the previous validation tests, results from the current approach are in perfect agreement with those from the literature [109]. Figure D.5 shows that near-field thermal radiation problems involving thin films can be solved correctly using the procedure described in chapter 3.

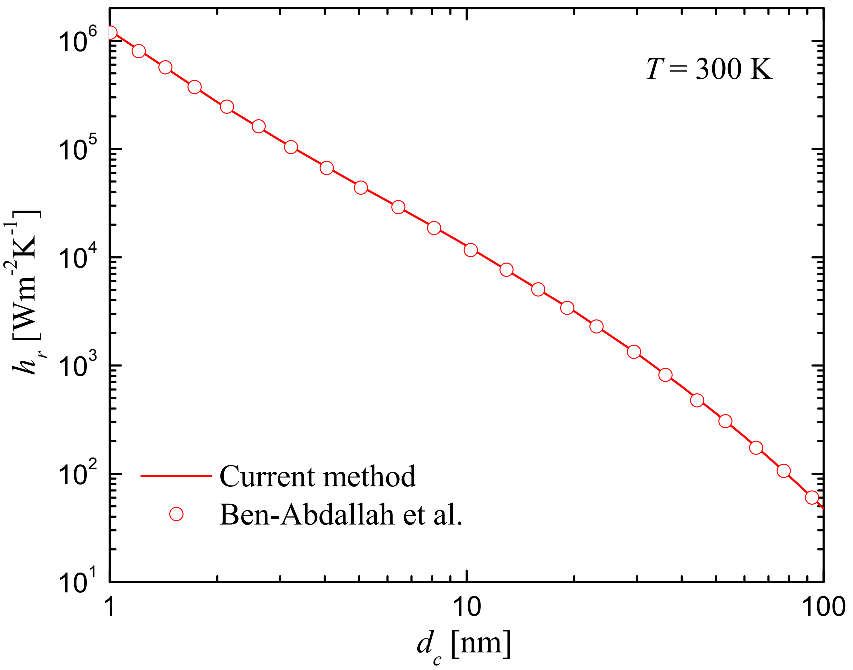

Figure D.5. Total near-field radiative heat transfer coefficient $h_r$ between two 1 nm thick films of SiC at $T$ = 300 K as a function of $d_c$ (correspond to Fig. 3 of reference [109]).

# Appendix E

# Length Scale of Transition from the Near- to the Far-Field Regime of Thermal Radiation between Two Dielectric Bulks

We investigate the length scale of transition from the near- to the far-field regime of thermal radiation between two dielectric bulks, separated by a vacuum gap $d_c$, described by a frequency-independent dielectric function. This analysis was published in the *Journal of Quantitative Spectroscopy and Radiative Transfer* in 2008 [65].

For the first set of simulations, both media are assumed to be dielectric materials (media 0 and 2), with the same frequency-independent dielectric constant of $\varepsilon_r = 20 + i0.0001$; their respective temperatures are taken as $T_0$ = 800 K and $T_2$ = 200 K. The dominant wavelengths of thermal radiation, as predicted by Wien's law, are approximately 3.6 μm and 14.5 μm for temperatures of 800 K and 200 K, respectively. We should consequently expect dominant near-field effects for gap thicknesses below these approximate thresholds. The net monochromatic radiative heat flux is reported in Fig. E.1(a), for different gap thicknesses $d_c$, as a function of the angular frequency $\omega$; the relative contributions of propagating and evanescent waves on the total (i.e., integrated over all angular frequencies) radiative flux are shown in Fig. E.1(b) as a function of $d_c$.

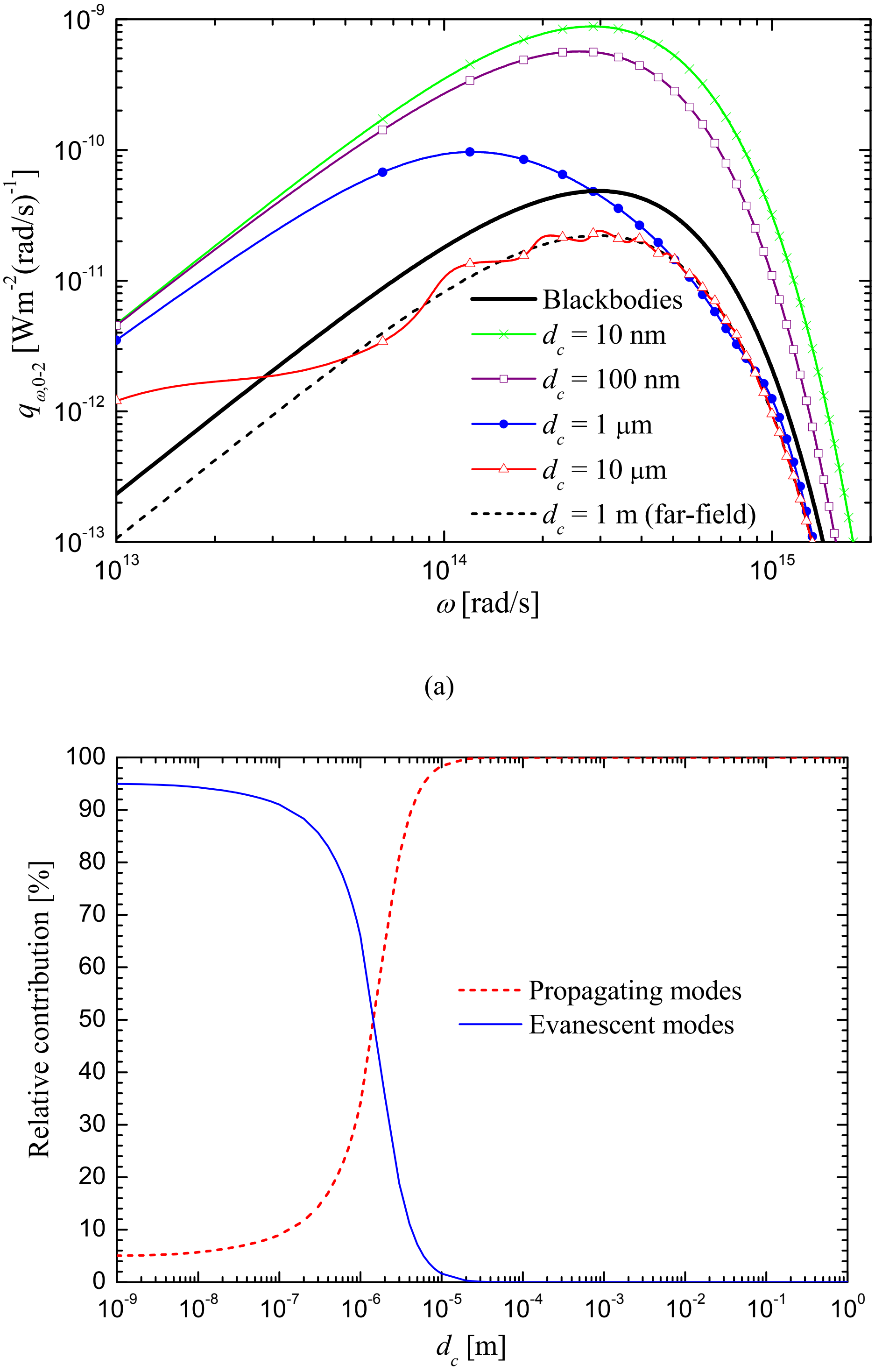

Figure E.1. Radiative heat transfer between two bulks, at $T_0$ = 800 K and $T_2$ = 200K, separated by a vacuum gap $d_c$. (a) Net monochromatic radiative heat flux. (b) Relative contribution from propagating and evanescent waves as a function of $d_c$.

As seen in Fig. E.1(a), the monochromatic radiative heat flux increases as $d_c$ decreases. The radiative heat flux between two blackbodies is also shown in Fig. E.1(a) to illustrate the fact that values obtained in the near-field can exceed the Planck distribution by few orders of magnitude. As discussed in section 2.7.1 for the case of lossless dielectric materials with refractive indices $n$, the maximum radiative heat transfer occurs at the limit $d_c \rightarrow 0$, and its achievable value is $n^2$ times the values predicted between blackbodies ($n^2 = \varepsilon_r$). Obviously, and as expected, in the far-field limit the radiative heat flux becomes independent of $d_c$. The large values of the radiative heat flux obtained at smaller gap distances, for 10 nm, 100 nm and 1 μm, are due to the tunneling of evanescent waves. As the gap thickness decreases, a more important proportion of evanescent waves are tunneled leading to an increase of the radiative heat flux. This is confirmed by Fig. E.1(b), where it is shown that for 10 nm, 100 nm and 1 μm, approximately 95%, 93%, and 65% of the radiative flux is due to evanescent waves, respectively. For 10 μm, the tunneling of evanescent waves is almost negligible (contribution of approximately 2%), while the interference phenomenon becomes dominant, which can be seen in Fig. E.1(a) by the oscillatory behavior of the radiative heat flux.

Despite all the research works on near-field radiative heat transfer between two bulk materials, there is still an important unanswered question: at what length scale near-field effects should be taken into account? The criterion based on Wien's law provides an approximate length scale. However, as research continues at the nanoscale, this question becomes less academic and carries more practical importance to define a strict length scale for which the near-field effects have to be taken into account. Below, an analysis is presented to answer this question in the particular case of two bulk dielectrics described by a frequency-independent dielectric function.

In the following simulations, medium 2 is modeled as a heat sink ($T_2 = 0$ K). Results are plotted, as a function of the product $T_0 d_c$, in terms of the normalized net total radiative heat flux, which is the sum of Eqs. (3.46a) and (3.46b) divided by the net total radiative flux in the far-field (Eq. (3.48)). The influence of $T_0$ (for a fixed $\varepsilon_r$) is shown in Fig. E.2(a), while the influence of the real part of the dielectric constant $\varepsilon_r'$ (for a fixed $T_0$) is presented in Fig. E.2(b).

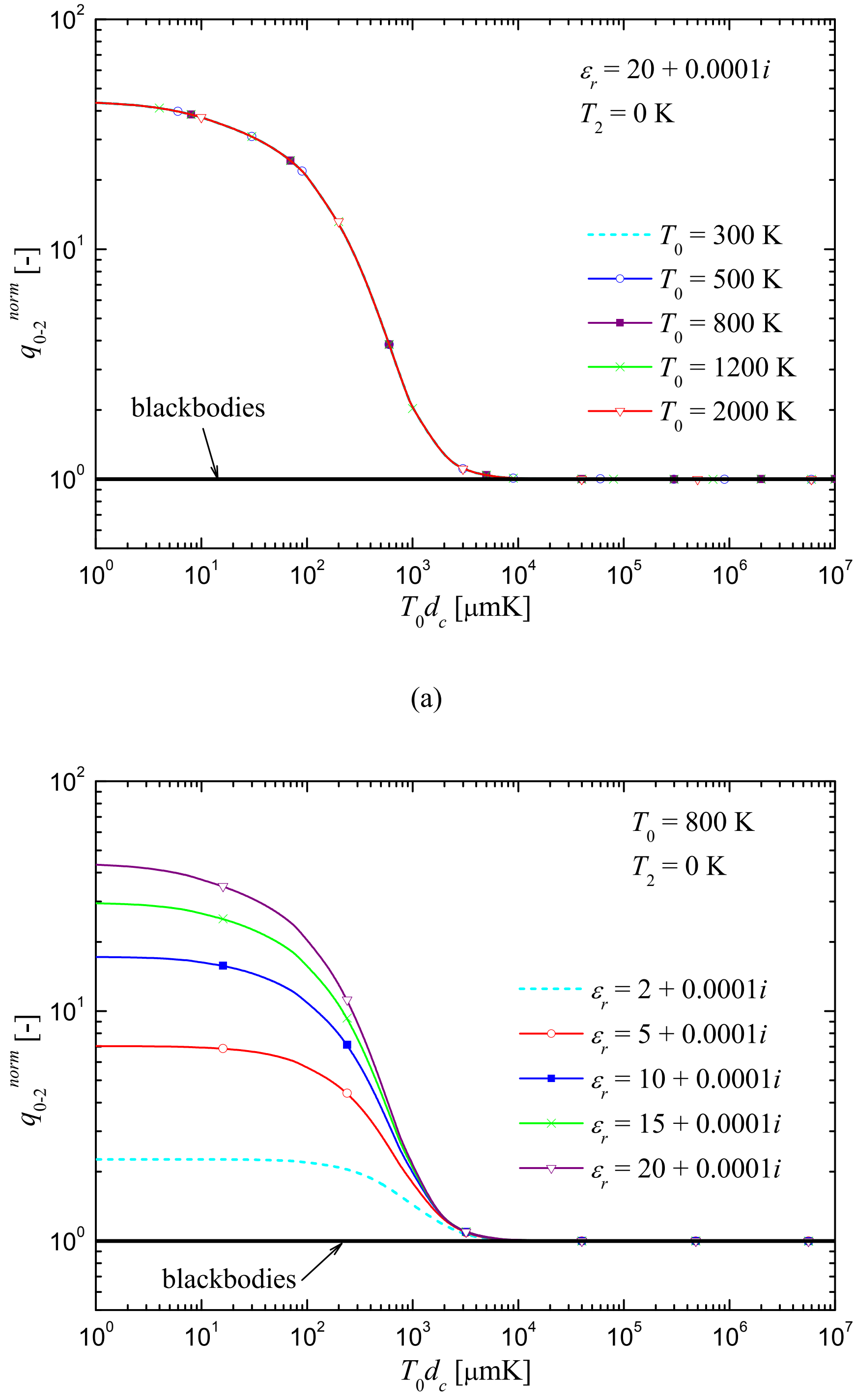

(a)

(b)

Figure E.2. Normalized net total radiative heat flux as a function of $T_0 d_c$. (a) Influence of the temperature $T_0$. (b) Influence of the real part of the dielectric constant.

It can be seen in Fig. E.2(a) that when the normalized radiative flux is plotted against the variable $T_0 d_c$, all curves overlap, regardless of $T_0$. The relative differences between the values of $q_{0-2}^{norm}$ (for the five different $T_0$ considered) for each $T_0 d_c$ vary from $7.7\times10^{-8}$ % to 0.64 %, which fall in the computational uncertainty range. Figure E.2(b) shows that the normalized radiative flux increases as $\varepsilon_r'$ increases (Fig. E.2(b)). On the other hand, the normalized fluxes seem to converge toward the same values of $T_0 d_c$ as $q_{0-2}^{norm} \to 1$.

The far-field regime is reached when the normalized radiative flux is 1. However, in the simulations, the normalized radiative flux never reaches the exact value of 1; starting from $T_0 d_c$ of approximately $6\times10^4$ μmK, the normalized flux oscillates around 1 (maximum of ± 0.25 %). This can be explained by the fact that for large values of $d_c$, the integrand of Eqs. (3.46a) is highly oscillatory. It becomes therefore impossible to predict the exact length scale for transition from the near- to the far-field regime using these numerical simulations. On the other hand, we can define approximate criteria for which 90%, 95%, and 99% of the radiative flux is due to the far-field regime (i.e., the criteria are based on the inverse of the normalized radiative fluxes). Moreover, results of Figs. E.2 suggest that these length scales are function of only two variables, namely $T_0 d_c$ and the dielectric constant $\varepsilon_r$.

From the data obtained to plot Fig. E.2(a), 90 %, 95 %, and 99 % of the radiative flux is due to the far-field regime for $T_0 d_c$ of 2977 μmK, 4443 μmK and 9056 μmK, respectively. These results show clearly that the transition from the near- to the far-field regime is above the length scale given by Wien's law (2898 μmK). If we consider a temperature $T_0$ of 800 K, the length scales based on the 90 %, 95 %, and 99 % are 3.72 μm, 5.55 μm and 11.32 μm, while the criterion based on Wien's law gives 3.62 μm. Therefore, the criterion based on Wien's law gives a good order of magnitude for the length scale, assuming that approximately 10 % of the radiative flux is due to near-field effects.

The same criteria are applied to the data of Fig. E.2(b). The length scales based on the 90 %, 95 % and 99% criteria are respectively: (i) 2513, 3645, and 7032 μmK (for $\varepsilon_r' = 2$); (ii) 2911, 4033, and 7827 μmK (for $\varepsilon_r' = 5$); (iii) 3014, 4306, and 8483 μmK (for $\varepsilon_r' =$

10); (iv) 3029, 4402, and 8832 μmK (for $\varepsilon_r'$ = 15); (v) 3030, 4437, and 9053 μmK (for $\varepsilon_r'$ = 20). These results suggest that as the real part of the dielectric constant increases, near-field effects have influence for larger values of $T_0d_c$. For example, the relative increase of $T_0d_c$ between the case $\varepsilon_r'$ = 2 and 20, for the criterion 90 %, is 18.7 %. Note also that $T_0d_c$ for $\varepsilon_r'$ = 20 found using the data from Fig. E.2(a) are not exactly the same than those obtained from the data of Fig. E.2(b). This is explained by the fact that the values of $T_0d_c$ have been found in Fig. E.2(a) using the average of the five temperatures, while the $T_0d_c$ have been calculated from Fig. E.2(b) using the data at 800 K. The maximum relative difference between these two set of calculations is 1.75%, which falls in the computational uncertainty range.

The results of this appendix suggest that the criterion for transition from near- to far-field radiative transfer based on Wien's law may be acceptable, with the disclaimer that approximately 10% of the radiative flux will still be due to near-field effects. On the other hand, it is important to note that the length scale at which $q_{0-2}^{norm} \to 1$ (based on the 99 % criterion) is about three times larger than Wien's law.

The analysis can be extended for lossy dielectric materials, systems involving two half-spaces of different dielectric constants, and to materials supporting surface polaritons, which will be left as a future research effort.

# Appendix F

# Derivation of the Near-Field Radiative Heat Flux between Two Films

An explicit expression for the near-field radiative heat flux between two thin films submerged in vacuum, as shown in Fig. 5.1, is derived here. The objective is to calculate the radiative flux absorbed by layer 3 due to the emitting layer 1 maintained at temperature $T_1$. In that case, the radiative flux needs to be calculated between layers 1 and 3, and layers 1 and 4; then, the difference between these two values provides the radiative heat flux absorbed by layer 3. We provide this derivation in detail, as it is not available in the literature.

The derivation starts with Eq. (5.1), where the radiative heat flux is written in terms of Weyl components of the DGF. The non-zero Weyl components of the DGF between layers 1 and $l$ at location $z_c$ are ($g^E_{1l\rho\rho}, g^E_{1l\rho z}, g^E_{1l\theta\theta}, g^E_{1lz\rho}, g^E_{1lzz}$) for the electric field, and ($g^H_{1l\rho\theta}, g^H_{1l\theta\rho}, g^H_{1l\theta z}, g^H_{1lz\theta}$) for the magnetic field; their explicit expressions are provided in section 3.2. Then, the summation over $\alpha$ can be performed in Eq. (5.1), and the following expression is obtained for the near-field radiative heat flux:

$$q^{tot}_{\omega,1l}(z_c) = \frac{k_v^2 \Theta(\omega,T_1)}{\pi^2} \times \mathrm{Re}\left\{ i\varepsilon''_{r1}(\omega) \int_0^\infty k_\rho dk_\rho \int_{z_1}^{z_2} dz' \begin{bmatrix} g^E_{1l\rho\rho}(k_\rho,z_c,z',\omega) g^{H*}_{1l\theta\rho}(k_\rho,z_c,z',\omega) \\ + g^E_{1l\rho z}(k_\rho,z_c,z',\omega) g^{H*}_{1l\theta z}(k_\rho,z_c,z',\omega) \\ - g^E_{1l\theta\theta}(k_\rho,z_c,z',\omega) g^{H*}_{1l\rho\theta}(k_\rho,z_c,z',\omega) \end{bmatrix} \right\} \tag{F.1}$$

Integration of the product of the Weyl components of the DGF over the volume of the emitter in Eq. (F.1) leads to the following terms in TM- and TE-polarization, respectively:

$$
\begin{aligned}
& g^{E}_{1l\rho\rho} g^{H*}_{1l\theta\rho}(k_\rho, z_c = z_l, \omega) + g^{E}_{1l\rho z} g^{H*}_{1l\theta z}(k_\rho, z_c = z_l, \omega) \\
& = \frac{ik_{zl}k_l^*}{8k'_{z1}k''_{z1}k_l\left|k_1\right|^2\left|k_{z1}\right|^2} \\
& \quad \times \left[ \begin{array}{l}
k'_{z1}(e^{2k''_{z1}t_1} - 1)\left(\left|k_{z1}\right|^2 + k_\rho^2\right)\left(-\left|A_l^{TM}\right|^2 - A_l^{TM}B_l^{TM*} + A_l^{TM*}B_l^{TM} + \left|B_l^{TM}\right|^2\right) \\
+ ik''_{z1}(e^{-2ik'_{z1}t_1} - 1)\left(\left|k_{z1}\right|^2 - k_\rho^2\right)\left(A_l^{TM}C_l^{TM*} + A_l^{TM}D_l^{TM*} - B_l^{TM}C_l^{TM*} - B_l^{TM}D_l^{TM*}\right) \\
+ ik''_{z1}(1 - e^{2ik'_{z1}t_1})\left(\left|k_{z1}\right|^2 - k_\rho^2\right)\left(A_l^{TM*}C_l^{TM} + B_l^{TM*}C_l^{TM} - A_l^{TM*}D_l^{TM} - B_l^{TM*}D_l^{TM}\right) \\
+ k'_{z1}(1 - e^{-2k''_{z1}t_1})\left(\left|k_{z1}\right|^2 + k_\rho^2\right)\left(-\left|C_l^{TM}\right|^2 - C_l^{TM}D_l^{TM*} + C_l^{TM*}D_l^{TM} + \left|D_l^{TM}\right|^2\right)
\end{array} \right]
\end{aligned}
\tag{F.2a}
$$

$$
\begin{aligned}
& g^{E}_{1l\theta\theta} g^{H*}_{1l\rho\theta}(k_\rho, z_c = z_l, \omega) \\
& = \frac{ik_{zl}^*}{8k'_{z1}k''_{z1}\left|k_{z1}\right|^2}
\left[ \begin{array}{l}
k'_{z1}(e^{2k''_{z1}t_1} - 1)\left(\left|A_l^{TE}\right|^2 - A_l^{TE}B_l^{TE*} + A_l^{TE*}B_l^{TE} - \left|B_l^{TE}\right|^2\right) \\
+ ik''_{z1}(e^{-2ik'_{z1}t_1} - 1)\left(A_l^{TE}C_l^{TE*} - A_l^{TE}D_l^{TE*} + B_l^{TE}C_l^{TE*} - B_l^{TE}D_l^{TE*}\right) \\
+ ik''_{z1}(1 - e^{2ik'_{z1}t_1})\left(A_l^{TE*}C_l^{TE} - B_l^{TE*}C_l^{TE} + A_l^{TE*}D_l^{TE} - B_l^{TE*}D_l^{TE}\right) \\
+ k'_{z1}(1 - e^{-2k''_{z1}t_1})\left(\left|C_l^{TE}\right|^2 - C_l^{TE}D_l^{TE*} + C_l^{TE*}D_l^{TE} - \left|D_l^{TE}\right|^2\right)
\end{array} \right]
\end{aligned}
\tag{F.2b}
$$

where the Weyl components of the DGF are calculated at $z_c = z_l$ since we are interested by radiative heat flux values at boundaries. The coefficients $A_l^\gamma$ and $B_l^\gamma$ represent amplitudes of forward ($z$-positive) and backward ($z$-negative) traveling waves, respectively, in layer $l$ and polarization state $\gamma$, arising from a source emitting in the forward direction. Similarly, the coefficients $C_l^\gamma$ and $D_l^\gamma$ are respectively amplitudes of forward and backward traveling waves in layer $l$ and polarization state $\gamma$ due to a source emitting in the backward direction.

The near-field radiative heat flux is first calculated between layers 1 and 3 at $z_3^+$, such that the field amplitude coefficients for $l = 3$ need to be calculated. In that case, all four coefficients $A_3^\gamma$, $B_3^\gamma$, $C_3^\gamma$, and $D_3^\gamma$ are non-zero, as explained in section 3.3.2. Using a transfer matrix approach [71], the coefficients in layer 3 needed to compute Eqs. (F.2a) and (F.2b) are given by:

$$A_3^\gamma = \frac{e^{ik_{z1}t_1} e^{ik_{z2}d_c} t_{23}^\gamma t_{34}^\gamma}{(1+r_{01}^\gamma r_{12}^\gamma e^{2ik_{z1}t_1})(1+r_{23}^\gamma r_{34}^\gamma e^{2ik_{z3}t_3})(1-R_1^\gamma R_3^\gamma e^{2ik_{z2}d_c})} \tag{F.3a}$$

$$B_3^\gamma = r_{34}^\gamma e^{2ik_{z3}t_3} A_3^\gamma \tag{F.3b}$$

$$C_3^\gamma = r_{34}^\gamma A_3^\gamma \tag{F.3c}$$

$$D_3^\gamma = (r_{34}^\gamma)^2 e^{2ik_{z3}t_3} A_3^\gamma \tag{F.3d}$$

The coefficients given by Eqs. (F.3a) to (F.3d) are then substituted in the product of the Weyl components of the DGF (Eqs. (F.2a) and (F.2b)), which are in turn substituted in the expression for the radiative heat flux. To perform the algebraic manipulations, we use the distinction between propagating and evanescent modes in vacuum. For $k_\rho \leq k_v$, the waves are propagating and the $z$-component of the wavevector in vacuum is a pure real number (i.e., $k_{zj} = k'_{zj}$), while for $k_\rho > k_v$, the waves are evanescent and the $z$-component of the wavevector in vacuum is a pure imaginary number (i.e., $k_{zj} = ik''_{zj}$). Also, the following useful relations are used [75]:

$$k_v^2 \varepsilon''_{ri} = 2k'_{zi}k''_{zi} \tag{F.4a}$$

$$k'_{zi}\left(|k_{zi}|^2 + k_\rho^2\right) = k_v^2 \,\mathrm{Re}(\varepsilon_{ri}k_{zi}^*) \tag{F.4b}$$

$$k''_{zi}\left(|k_{zi}|^2 - k_\rho^2\right) = k_v^2 \,\mathrm{Im}(\varepsilon_{ri}k_{zi}^*) \tag{F.4c}$$

$$\frac{k'_{zi}}{|k_{zi}|^2}\left|t_{ij}^{TE}\right|^2 = \frac{1}{|k_{zj}|^2}\left[k'_{zj}\left(1-\left|r_{ij}^{TE}\right|^2\right) - 2k''_{zj}\,\mathrm{Im}(r_{ij}^{TE})\right] \tag{F.4d}$$

$$\frac{\mathrm{Re}(\varepsilon_{ri}k_{zi}^*)}{|n_i|^2|k_{zi}|^2}\left|t_{ij}^{TM}\right|^2 = \frac{1}{|k_{zj}|^2}\left[k'_{zj}\left(1-\left|r_{ij}^{TM}\right|^2\right) - 2k''_{zj}\,\mathrm{Im}(r_{ij}^{TM})\right] \tag{F.4e}$$

$$\frac{k''_{zi}}{\left|k_{zi}\right|^2}\left|t_{ij}^{TE}\right|^2 = \frac{1}{\left|k_{zj}\right|^2}\left[k''_{zj}\left(1-\left|r_{ij}^{TE}\right|^2\right)+2k'_{zj}\,\mathrm{Im}(r_{ij}^{TE})\right] \tag{F.4f}$$

$$\frac{\mathrm{Im}(\varepsilon_{ri}k_{zi}^*)}{\left|n_i\right|^2\left|k_{zi}\right|^2}\left|t_{ij}^{TM}\right|^2 = \frac{-1}{\left|k_{zj}\right|^2}\left[k''_{zj}\left(1-\left|r_{ij}^{TM}\right|^2\right)+2k'_{zj}\,\mathrm{Im}(r_{ij}^{TM})\right] \tag{F.4g}$$

After lengthy, but straightforward, algebraic manipulations, the following equations are obtained for the propagating and evanescent contributions to the near-field radiative heat flux between layers 1 and 3:

$$\begin{aligned} q_{\omega,13}^{prop}(z_3^+) &= \frac{\Theta(\omega,T_1)}{4\pi^2}\int_0^{k_v} k_\rho dk_\rho \\ &\times \sum_{\gamma=TE,TM}\frac{\left[\left(1-\left|r_{12}^{\gamma}\right|^2\right)a^{\gamma}+4\,\mathrm{Im}(r_{12}^{\gamma})b^{\gamma}\right]\left[\left(1-\left|r_{34}^{\gamma}\right|^2\right)c^{\gamma}-4\,\mathrm{Im}(r_{34}^{\gamma})d^{\gamma}\right]}{\left|1+r_{01}^{\gamma}r_{12}^{\gamma}e^{2ik_{z1}t_1}\right|^2\left|1+r_{23}^{\gamma}r_{34}^{\gamma}e^{2ik_{z3}t_3}\right|^2\left|1-R_1^{\gamma}R_3^{\gamma}e^{2ik_{z2}d_c}\right|^2} \end{aligned} \tag{F.5a}$$

$$\begin{aligned} q_{\omega,13}^{evan}(z_3^+) &= \frac{\Theta(\omega,T_1)}{\pi^2}\int_{k_v}^{\infty} k_\rho dk_\rho e^{-2k''_{z2}d_c} \\ &\times \sum_{\gamma=TE,TM}\frac{\left[\left(1-\left|r_{12}^{\gamma}\right|^2\right)b^{\gamma}-\mathrm{Im}(r_{12}^{\gamma})a^{\gamma}\right]\left[-\left(1-\left|r_{34}^{\gamma}\right|^2\right)d^{\gamma}-\mathrm{Im}(r_{34}^{\gamma})c^{\gamma}\right]}{\left|1+r_{01}^{\gamma}r_{12}^{\gamma}e^{2ik_{z1}t_1}\right|^2\left|1+r_{23}^{\gamma}r_{34}^{\gamma}e^{2ik_{z3}t_3}\right|^2\left|1-R_1^{\gamma}R_3^{\gamma}e^{2ik_{z2}d_c}\right|^2} \end{aligned} \tag{F.5b}$$

where

$$a^{\gamma} = e^{-2k''_{z1}t_1}\left[\left|r_{01}^{\gamma}\right|^2(1-e^{-2k''_{z1}t_1})-(1-e^{2k''_{z1}t_1})\right] \tag{F.6a}$$

$$b^{\gamma} = e^{-2k''_{z1}t_1}\,\mathrm{Im}\left[r_{01}^{\gamma}(1-e^{2ik'_{z1}t_1})\right] \tag{F.6b}$$

$$c^{\gamma} = 1-\left|r_{23}^{\gamma}\right|^2 e^{-4k''_{z3}t_3} \tag{F.6c}$$

$$d^{\gamma} = \mathrm{Im}(r_{23}^{\gamma}e^{2ik_{z3}t_3}) \tag{F.6d}$$

Equations (F.5a) and (F.5b) can be written in compact forms using film reflection $R_j^\gamma$ and transmission $T_j^\gamma$ coefficients given by Eqs. (5.3a) and (5.3b), respectively. In that way, the following simplified terms are obtained:

$$\frac{\left(1-\left|r_{12}^\gamma\right|^2\right)a^\gamma + 4\,\mathrm{Im}(r_{12}^\gamma)b^\gamma}{\left|1+r_{01}^\gamma r_{12}^\gamma e^{2ik_{z1}t_1}\right|^2} = 1-\left|R_1^\gamma\right|^2-\left|T_1^\gamma\right|^2 \tag{F.7a}$$

$$\frac{\left(1-\left|r_{34}^\gamma\right|^2\right)c^\gamma - 4\,\mathrm{Im}(r_{34}^\gamma)d^\gamma}{\left|1+r_{23}^\gamma r_{34}^\gamma e^{2ik_{z3}t_3}\right|^2} = 1-\left|R_3^\gamma\right|^2 \tag{F.7b}$$

$$\frac{\left(1-\left|r_{12}^\gamma\right|^2\right)b^\gamma - \mathrm{Im}(r_{12}^\gamma)a^\gamma}{\left|1+r_{01}^\gamma r_{12}^\gamma e^{2ik_{z1}t_1}\right|^2} = \mathrm{Im}(R_1^\gamma) \tag{F.7c}$$

$$\frac{-\left(1-\left|r_{34}^\gamma\right|^2\right)d^\gamma - \mathrm{Im}(r_{34}^\gamma)c^\gamma}{\left|1+r_{23}^\gamma r_{34}^\gamma e^{2ik_{z3}t_3}\right|^2} = \mathrm{Im}(R_3^\gamma) \tag{F.7d}$$

Finally, by substituting Eqs. (F.7a) and (F.7b) into Eq. (F.5a) and Eqs. (F.7c) and (F.7d) within Eq. (F.5b), the propagating and evanescent contributions to the radiative heat flux are given by:

$$q_{\omega,13}^{prop}(z_3^+) = \frac{\Theta(\omega,T_1)}{4\pi^2}\int_0^{k_v} k_\rho dk_\rho \sum_{\gamma=TE,TM} \frac{\left(1-\left|R_1^\gamma\right|^2-\left|T_1^\gamma\right|^2\right)\left(1-\left|R_3^\gamma\right|^2\right)}{\left|1-R_1^\gamma R_3^\gamma e^{2ik_{z2}d_c}\right|^2} \tag{F.8a}$$

$$q_{\omega,13}^{evan}(z_3^+) = \frac{\Theta(\omega,T_1)}{\pi^2}\int_{k_v}^{\infty} k_\rho dk_\rho e^{-2k''_{z2}d_c} \sum_{\gamma=TE,TM} \frac{\mathrm{Im}(R_1^\gamma)\,\mathrm{Im}(R_3^\gamma)}{\left|1-R_1^\gamma R_3^\gamma e^{2ik_{z2}d_c}\right|^2} \tag{F.8b}$$

To calculate the flux absorbed by film 3, we also need to calculate the radiative flux between layers 1 and 4 at location $z_4^+$. For this case, only two field amplitude coefficients at $l = 4$ are non-zero, namely $A_4^\gamma$ and $C_4^\gamma$ (see section 3.3.2); they are given by:

$$A_4^\gamma = \frac{e^{ik_{z1}t_1} e^{ik_{z2}d_c} e^{ik_{z3}t_3} t_{12}^\gamma t_{23}^\gamma t_{34}^\gamma}{(1 + r_{01}^\gamma r_{12}^\gamma e^{2ik_{z1}t_1})(1 + r_{23}^\gamma r_{34}^\gamma e^{2ik_{z3}t_3})(1 - R_1^\gamma R_3^\gamma e^{2ik_{z2}d_c})} \tag{F.9a}$$

$$C_4^\gamma = r_{34}^\gamma A_4^\gamma \tag{F.9b}$$

Equations (F.9a) and (F.9b) are substituted in Eqs. (F.2a) and (F.2b), which are in turn substituted in the expression for the radiative heat flux. Using the distinction between propagating and evanescent waves, as well as the relations given by Eqs. (F.4a) to (F.4g), the radiative heat flux between layers 1 and 4 is given by:

$$\begin{aligned} q_{\omega,14}^{prop}(z_4^+) = {} & \frac{\Theta(\omega,T_1)}{4\pi^2} \int_0^{k_v} k_\rho dk_\rho \\ & \times \sum_{\gamma=TE,TM} \frac{\left|t_{23}^\gamma\right|^2 \left|t_{34}^\gamma\right|^2 \left|e^{ik_{z3}t_3}\right|^2 \left[\left(1-\left|r_{12}^\gamma\right|^2\right)a^\gamma + 4\,\mathrm{Im}(r_{12}^\gamma) b^\gamma\right]}{\left|1 + r_{01}^\gamma r_{12}^\gamma e^{2ik_{z1}t_1}\right|^2 \left|1 + r_{23}^\gamma r_{34}^\gamma e^{2ik_{z3}t_3}\right|^2 \left|1 - R_1^\gamma R_3^\gamma e^{2ik_{z2}d_c}\right|^2} \end{aligned} \tag{F.10}$$

Note that the radiative heat flux due to evanescent modes in that case is nil. Using the definition for the transmission coefficient of film 3 $T_3^\gamma$ and Eq. (F.7a), Eq. (F.10) can be written as follows:

$$q_{\omega,14}^{prop}(z_4^+) = \frac{\Theta(\omega,T_1)}{4\pi^2} \int_0^{k_v} k_\rho dk_\rho \sum_{\gamma=TE,TM} \frac{\left(1-\left|R_1^\gamma\right|^2 - \left|T_1^\gamma\right|^2\right)\left|T_3^\gamma\right|^2}{\left|1 - R_1^\gamma R_3^\gamma e^{2ik_{z2}d_c}\right|^2} \tag{F.11}$$

The propagating component of the radiative heat flux absorbed by film 3 is obtained by subtracting Eq. (F.11) to Eq. (F.8a); the final expression is given by Eq. (5.2a). The evanescent component of the radiative heat flux absorbed by film 3 is given by Eq. (F.8b), which is the same as Eq. (5.2b).

# Appendix G

# Numerical Solution and Validation of the Nanoscale-Gap Thermophotovoltaic Model

## G.1 Discretization equations

Figure G.1 illustrates the two spatial discretizations of the p-n junction.

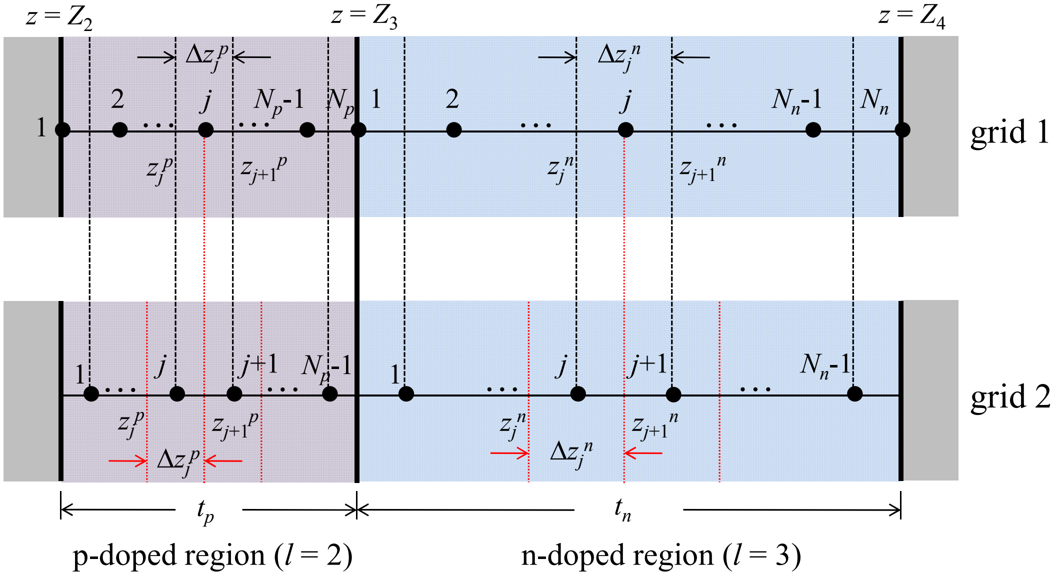

$z = Z_2$
$z = Z_3$
$z = Z_4$
$\Delta z_j^p$
$\Delta z_j^n$
1
2
$j$
$N_p$-1
$N_p$
1
2
$j$
$N_n$-1
$N_n$
$z_j^p$
$z_{j+1}^p$
$z_j^n$
$z_{j+1}^n$
grid 1
1
$j$
$j$+1
$N_p$-1
1
$j$
$j$+1
$N_n$-1
$z_j^p$
$z_{j+1}^p$
$\Delta z_j^p$
$z_j^n$
$\Delta z_j^n$
$z_{j+1}^n$
grid 2
$t_p$
$t_n$
p-doped region ($l$ = 2)
n-doped region ($l$ = 3)

Figure G.1. Spatial discretizations of the p-n junction.

The p-region is discretized in $N_p$ nodes in grid 1, while the n-region is discretized in $N_n$ node. There is a shared node at the junction, such that the total number of spatial nodes is given by: $N_{tot} = N_p + N_n - 1$. In the p-region (n-region), the thickness of a control volume for an internal node is given by: $\Delta z_j^{\,p} = t_p/(N_p - 1)$ ($\Delta z_j^n = t_n/(N_n - 1)$). The nodes at the boundary $j = 1$ and $N_p$ ($j = 1$ and $N_n$) are surrounded by a half-control volume $\Delta z_j^{\,p}/2$ ($\Delta z_j{}^n/2$).

The near-field radiative heat flux emitted from the radiator and observed at point $j$ in the TPV cell is calculated for $j = 1$ to $N_p - 1$ (p-side, $l = 2$) and for $j = 1$ to $N_n$ (n-side, $l = 3$). The radiative heat flux in medium 4 at $z = Z_4^+$ is also computed in order to calculate the amount of thermal radiation absorbed by the cell. Once the spatial distribution of flux is determined, it is necessary to compute the radiative energy absorbed by each control volume. This operation is done using the spatial grid 2 in Fig. G.1, where the p-region is divided into $N_p - 1$ nodes while the n-side is discretized into $N_n - 1$ nodes. As outlined in section 6.4.1, radiation absorbed by the control volume $\Delta z_j^{(p,n)}$ surrounding node $j$ is given by the difference of the flux calculated at $z_{j+1}^{(p,n)}$ and $z_j^{(p,n)}$ on grid 2. These fluxes on the spatial grid 2 correspond respectively to the fluxes at nodes $j$ and $j$ - 1 on the spatial grid 1. Also, as mentioned in section 6.4.1, the radiative heat flux emitted by the control volume $\Delta z_j^{(p,n)}$ toward the radiator is easily calculated using the flux absorbed. Once the radiative heat fluxes absorbed and emitted are computed, the local generation rate of electron-hole pairs (EHPs) (Eq. (6.3)), the local radiative heat source (Eq. (6.6)), and the local heat generation term due to thermalization (Eq. (6.8)) are calculated on the spatial grid 1. For example, at node $j$ on grid 1, the local radiative heat source is the average of the values computed at nodes $j$ and $j + 1$ on grid 2. The charge and heat transport equations are therefore solved on the spatial grid 1.

Using the spatial distribution of the local generation rate of EHPs, it is possible to calculate the photocurrent generated within the depletion region via Eq. (6.12). To perform such a calculation, it is necessary to identify the spatial nodes of grid 1 corresponding to the depletion region. As mentioned in section 6.5.4, it is assumed that the entire depletion region is located in the n-doped region. A difficulty arises when solving the coupled near-field thermal radiation, charge and heat transport problem due to the fact that the thickness of the depletion region $L_{dp}$ is temperature-dependent. The procedure adopted in this work is described as follows. There should be at least two spatial nodes included in $L_{dp}$ in order to delimit the depletion region, including $j = 1$ (n-side) since it is assumed that the depletion region emerges in the n-doped region. Therefore, the minimal length of the depletion region on grid 1 is $2(\Delta z_j^n/2)$, since the nodes limiting the boundaries of $L_{dp}$ are surrounded by half-control volumes. Then, the number of internal nodes $N_{\text{int}}$ in $L_{dp}$, surrounded by control volumes $\Delta z_j^n$, is estimated by dividing ($L_{dp}$ - $2(\Delta z_j^n/2)$) by $\Delta z_j^n$. The length of the depletion region on grid 1 is thus calculated as: $N_{\text{int}}\Delta z_j^n + 2(\Delta z_j^n/2)$. Note that this procedure introduces some errors in the thickness of the depletion region, which can be minimized by increasing the number of nodes $N_n$ in the n-side. The number of nodes $N_n$ is chosen to ensure an error less than 2 % in the thickness of the depletion region. If only the coupled near-field thermal radiation and charge transport problem is solved, this procedure is not necessary and the depletion region can be represented with its exact length $L_{dp}$ on the grid 1.

The photocurrents due to EHPs generated outside the depletion region are calculated by solving the minority carrier diffusion equations (Eq. (6.2)) separately in the p- and n-regions. This is done via a standard finite-volume approximation of Eq. (6.2). More specifically, the approach described in reference [161] is employed, where the general discretization equation is written as follows:

$$a_j\phi_j = b_j\phi_{j+1} + c_j\phi_{j-1} + d_j \tag{G.1}$$

In Eq. (G.1), $\phi_j$ is the dependent variable at node $j$, $a_j$, $b_j$ and $c_j$ are the coefficients multiplying this dependent variable at nodes $j$, $j$ +1 and $j$ – 1, respectively, while $d_j$ is a constant at node $j$. Using a piecewise-linear profile to interpolate the values of the dependent variable between neighboring nodes, the discretized minority carrier diffusion equation in the p-region can be written as follows for an internal node ($j$ = 2, $N_p$ – 1):

$$\Delta n_{e,\omega,j}\left[\frac{2D_e}{(\Delta z_j^p)^2} + \frac{1}{\tau_e}\right] = \Delta n_{e,\omega,j+1}\left[\frac{D_e}{(\Delta z_{j+1}^p)^2}\right] + \Delta n_{e,\omega,j-1}\left[\frac{D_e}{(\Delta z_{j-1}^p)^2}\right] + g_{\omega,j} \tag{G.2}$$

Therefore, from Eq. (G.2), the coefficients of Eq. (G.1) can be written as:

$$\phi_j = \Delta n_{e,\omega,j}\,,\; a_j = \frac{2D_e}{(\Delta z_j^p)^2} + \frac{1}{\tau_e}\,,\; b_j = \frac{D_e}{(\Delta z_{j+1}^p)^2}\,,\; c_j = \frac{D_e}{(\Delta z_{j-1}^p)^2} \text{ and } d_j = g_{\omega,j} \tag{G.3}$$

The coefficients in the n-doped region for the internal nodes (*j* = 2, $N_n$ - 1) are exactly the same, except that $\Delta n_{e,\omega,j}$, $D_e$, $\tau_e$ and $\Delta z_j^p$ are respectively substituted by $\Delta n_{h,\omega,j}$, $D_h$, $\tau_h$ and $\Delta z_j^n$.

To solve this system of equations, the boundary conditions are required. As mentioned in section 6.4.2, all minority carriers are assumed to be swept by the electric field at the edges of the depletion region. Therefore, the coefficients for the p- and n-doped regions can be written as:

$$a_{N_p}^p = a_{N_{\text{int}+2}}^n = 1 \text{ and } b_{N_p}^p = c_{N_p}^p = d_{N_p}^p = b_{N_{\text{int}+2}}^n = c_{N_{\text{int}+2}}^n = d_{N_{\text{int}+2}}^n = 0 \tag{G.4}$$

The boundary condition at $z = Z_2$ ($j = 1$) is given by:

$$a_1 = \frac{D_e}{(\Delta z_1^p)^2} + \frac{1}{2\tau_e} + \frac{S_e}{\Delta z_1^p},\ b_1 = \frac{D_e}{(\Delta z_2^p)^2},\ c_1 = 0 \text{ and } d_1 = \frac{g_{\omega,1}}{2} \tag{G.5}$$

and the boundary condition at $z = Z_4$ ($j = N_n$) is written as follows:

$$a_{N_n} = \frac{D_h}{(\Delta z_{N_n}^n)^2} + \frac{1}{2\tau_h} - \frac{S_h}{\Delta z_{N_n}^n},\ b_{N_n} = 0,\ c_{N_n} = \frac{D_h}{(\Delta z_{N_n}^n)^2} \text{ and } d_{N_n} = \frac{g_{\omega,N_n}}{2} \tag{G.6}$$

The system of linear equations is solved using the Thomas algorithm described in reference [161]. Once the minority carrier diffusion equations are solved, the photocurrents due to EHPs generated outside the depletion region are computed via Eqs. (6.13a) and (6.13b). The local heat generation term due to non-radiative and radiative recombination can also be calculated using Eq. (6.9).

At this point, it is possible to solve the energy equation within the TPV cell since the four contributions to the local heat generation term are known (radiative heat source, thermalization, non-radiative recombination and radiative recombination). The coefficients of the steady-state energy equation (Eq. (6.5)) for the internal nodes $j = 2, N_p$ (p-region) and $j = N_p, N_n - 1$ (n-region) are given by:

$$\phi_j = T_{cell,j},\ a_j = \frac{2k_{cond}}{(\Delta z_j^{(p,n)})^2},\ b_j = \frac{k_{cond}}{(\Delta z_{j+1}^{(p,n)})^2},\ c_j = \frac{k_{cond}}{(\Delta z_{j-1}^{(p,n)})^2} \text{ and } d_j = Q_j \tag{G.7}$$

where again a piecewise-linear profile has been used to interpolate the dependent variable between neighboring nodes. At $z = Z_2$, the discretized boundary condition given by Eq. (6.10) can be written as:

$$a_1 = \frac{k_{cond}}{(\Delta z_1^p)^2}\,,\; b_1 = \frac{k_{cond}}{(\Delta z_2^p)^2}\,,\; c_1 = 0 \text{ and } d_1 = \frac{Q_1}{2} + \frac{S_e e E_g \int_{\omega_g}^{\infty} \Delta n_{e,\omega,1} d\omega}{\Delta z_1^p} \tag{G.8}$$

while the boundary condition at $z = Z_4$ given by Eq. (6.11) is written as follows:

$$a_{N_n} = \frac{k_{cond}}{(\Delta z_{N_n}^n)^2} + \frac{h_\infty}{\Delta z_{N_n}^n}\,,\; b_{N_n} = 0\,,\; c_{N_n} = \frac{k_{cond}}{(\Delta z_{N_n-1}^n)^2} \text{ and } d_{N_n} = \frac{Q_{N_n}}{2} + \frac{h_\infty T_\infty}{\Delta z_{N_n}^n} \tag{G.9}$$

As for the minority carrier diffusion equations, the energy equation is solved using the Thomas algorithm [161].

When the calculations have converged, the *J-V* characteristic needs to be generated. Calculation of the *J-V* characteristic requires the computation of the dark current $J_0$, as explained in section 6.4.4. The dark current $J_0$ is calculated by solving the minority carrier diffusion equation in dark conditions. Therefore, Eqs. (G.3), (G.5) and (G.6) can be used by letting $g_\omega = 0$ and by dropping the frequency-dependence. At the edges of the depletion region, the discretized boundary conditions are written as:

$$a_{N_p}^p = a_{N_{\text{int}+2}}^n = 1,\; b_{N_p}^p = c_{N_p}^p = b_{N_{\text{int}+2}}^n = c_{N_{\text{int}+2}}^n = 0 \text{ and } d_{N_p}^p = d_{N_{\text{int}+2}}^n = \left( \frac{eV_f}{k_b T_{cell,(N_p,N_{\text{int}+2})}} \right) \tag{G.10}$$

For the near-field thermal radiation problem, the $k_\rho$-discretization discussed in section 3.5.1 is employed. The calculations are performed from $\omega = 7.7\times10^{13}$ rad/s to $\omega = 3.80\times10^{15}$ rad/s by increment $\Delta\omega$ of $0.5\times10^{13}$ rad/s. For the spatial discretization, values of $N_p = 401$ and $N_n = 801$ have been found to be optimal.

## G.2 Validation of the coupled near-field thermal radiation and charge transport model

The nano-TPV model is validated hereafter against the results provided by Park et al. [37]. Only the coupled near-field thermal radiation and charge transport part of the model can be validated, since no works have accounted for the thermal effects in nano-TPV power generation devices.

The problem solved in this appendix is the same as the one described in the beginning of section 6.5; the TPV cells are however assumed to be at a constant and uniform temperature of 300 K. The dielectric function of tungsten (W) in reference [37] has been modeled by curve-fitting the data of reference [152], as done in this work. For the dielectric function of the TPV cell, it is not clear which model Park et al. used in their simulations. Therefore, we use hereafter the dielectric function of $In_{0.18}Ga_{0.82}Sb$ described in section 6.5.1 at 300 K. Otherwise, when available, the properties used by Park et al. are employed in this appendix only (instead of the properties described in section 6.5). These properties are given in Table G.1.

Table G.1. Properties from reference [37] used in the nano-TPV simulations presented in appendix G.

| Property | p-doped region | n-doped region |
|---|---|---|
| Diffusion coefficient [cm$^2$s$^{-1}$] | 125 | 31.3 |
| Surface recombination velocity [m·s$^{-1}$] | $7.4\times10^4$ | 0 |
| Minority carrier lifetime [ns] | 9.75 | 30.8 |

The results provided in reference [37] have been extracted using *Plot Digitizer* [219].

Figure G.2 shows the monochromatic radiative heat flux for three specific wavelengths (1 μm, 1.5 μm and 2.5 μm) as a function of the depth in the TPV cell for a vacuum gap $d_c$ of 10 nm.

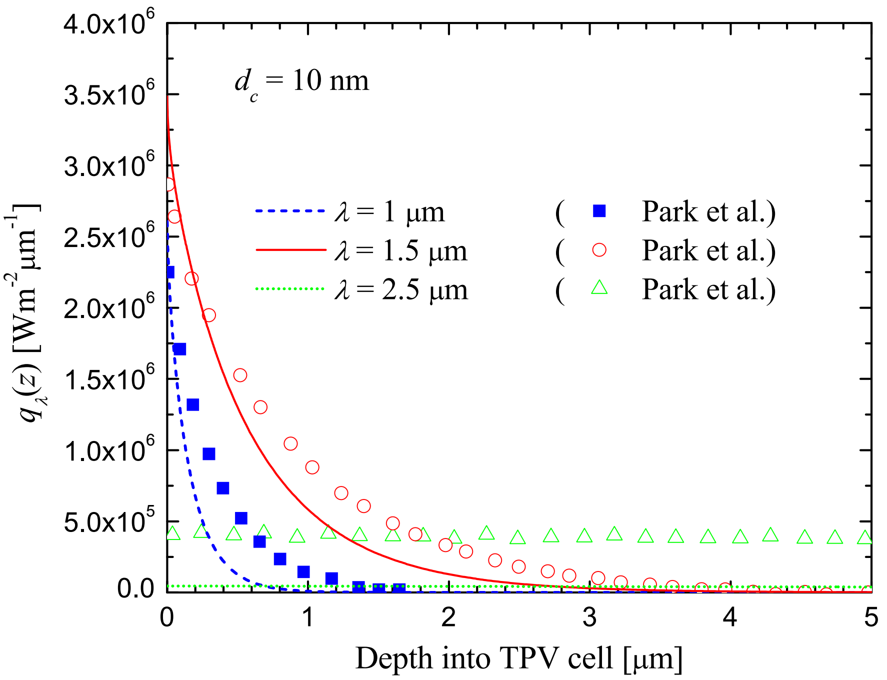

Figure G.2. Monochromatic radiative heat flux as a function of the depth in the TPV cell for $d_c$ = 10 nm and $\lambda$ = 1 μm, 1.5 μm and 2.5 μm (corresponds to Fig. 2(a) of reference [37]).

The bandgap of the TPV cell is 0.56 eV, which corresponds to a wavelength of 2.21 μm. Therefore, radiation with $\lambda \leq 2.21$ μm is absorbed through the interband process, while radiation with $\lambda > 2.21$ μm is due to absorption by the lattice and the free carriers.

The results from the current model and those from Park et al. are in qualitative agreement, certainly due to discrepancies in the dielectric function used for the TPV cell. At $\lambda$ = 2.5 μm (corresponds to an energy of 0.50 eV), the flux from our model is significantly lower than the flux from Park et al. This can potentially be explained as follows. Inspection of the imaginary part of the dielectric function of the cell (see Fig. 6.4(b)) shows that radiation absorption should be very low at 0.50 eV (transparency region). In reference [37], the authors do not discuss about the different absorption processes, such that it is unclear if the transparency region has been modeled. It is interesting to note that by extrapolating the interband dielectric function model for $\lambda >$ 2.21 μm (i.e., $E < E_g$), results similar to those from Park et al. have been obtained at $\lambda$ = 2.5 μm.

Figure G.3 shows the radiative heat flux at $\lambda = 1.5$ µm as a function of the depth in the TPV cell for vacuum gaps $d_c$ of 5 nm, 10 nm and 100 nm. Note that the radiative flux is normalized by its value at $z = Z_2^+$.

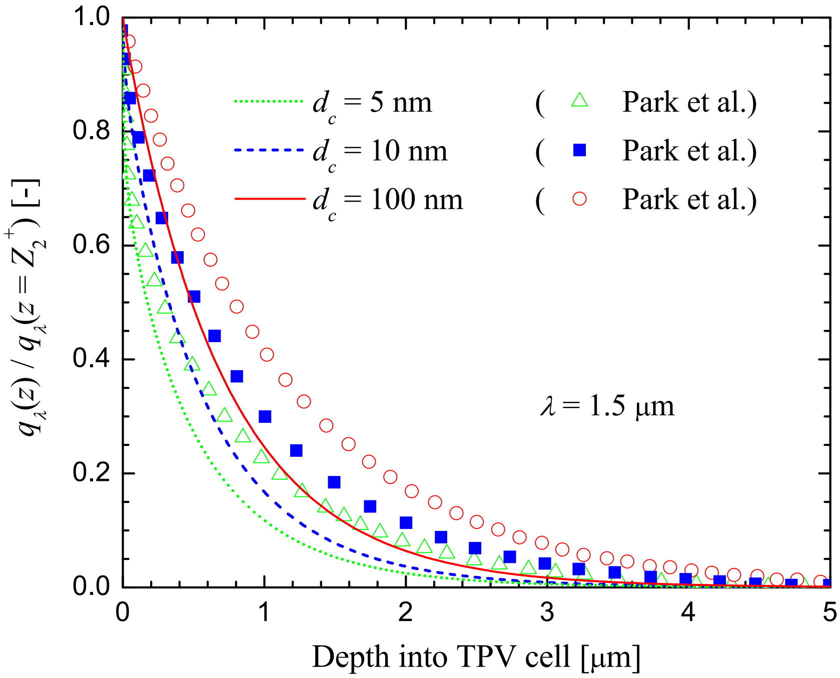

Figure G.3. Normalized monochromatic radiative heat flux as a function of the depth in the TPV cell for $d_c$ = 5 nm, 10 nm and 100 nm and $\lambda$ = 1.5 µm (corresponds to Fig. 3(b) of reference [37]).

The trends between the results from the current model and those form Park et al. are very similar. Figure G.3 shows that the interband absorption is higher in our model, as already observed in Fig. G.2. These results confirm the hypothesis that the dielectric function used for the TPV cell are different between this work and the model of Park et al. Indeed, Figs. G.2 and G.3 solely involve near-field thermal radiation calculations that have been extensively validated.

Figure G.4 shows the monochromatic radiative heat flux as a function of the wavelength at $z = Z_2^+$ for vacuum gaps $d_c$ of 5 nm, 10 nm, 100 nm, 1 µm and 10 µm.

Results of Fig. G.4 are quite interesting, and confirm in some way the imprecision of the dielectric function used by Park et al. for modeling the TPV cell. Indeed, even for $\lambda >$ 2.21 µm, the radiative heat flux from reference [37] is quite high, and the transition from

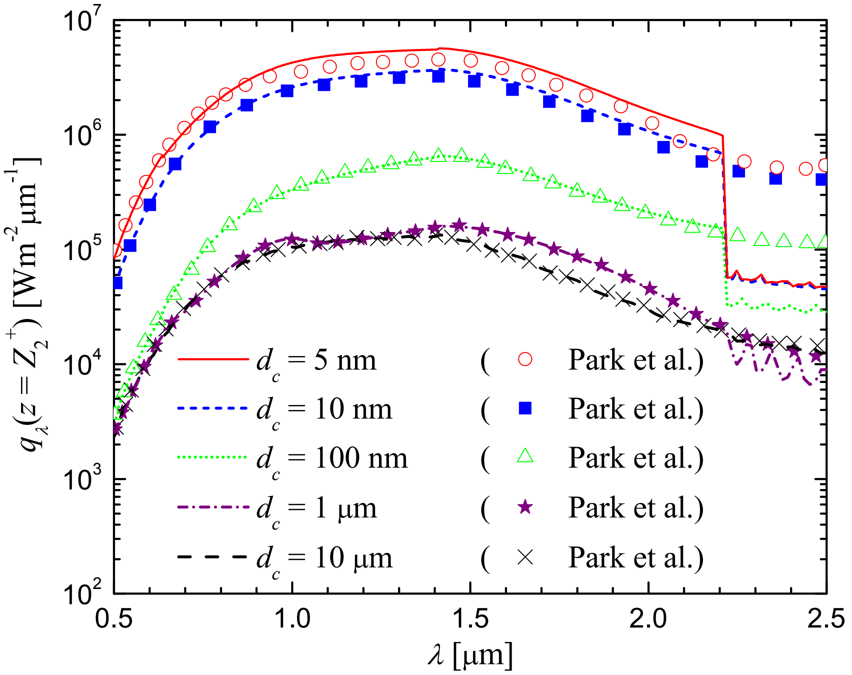

Figure G.4. Monochromatic radiative heat flux at $z = Z_2^+$ for $d_c$ = 5 nm, 10 nm, 100 nm, 1 μm and 10 μm (corresponds to Fig. 4(a) of reference [37]).

$\lambda \leq 2.21$ μm to $\lambda > 2.21$ μm is very smooth. By using only the interband dielectric function model for all wavelengths, results very similar to those from Park et al. have been obtained. In reality, a drop of radiative flux should occur at $\lambda > 2.21$ μm due to the transparency region. Note that the drop is quite abrupt in our case, as the exponential tail cannot be represented in the interband dielectric function (see Fig. 6.5(a) and the associated discussion). It is also important to note that the flux oscillates for $\lambda > 2.21$ μm. This behavior is not due to numerical instabilities, but can be explained by strong wave interference within the cell since the absorption is very low in that spectral region (i.e., waves are reflected back and forth between the boundaries $z = Z_2$ and $z = Z_4$).

Figure G.5 shows the monochromatic photocurrent generated by the nano-TPV device as a function of the wavelength for vacuum gaps $d_c$ of 5 nm, 10 nm, 100 nm, 1 μm and 10 μm.

It can be seen in Fig. G.5 that the monochromatic photocurrent calculated with the current method is in good agreement with the results from Park et al. Note that in our

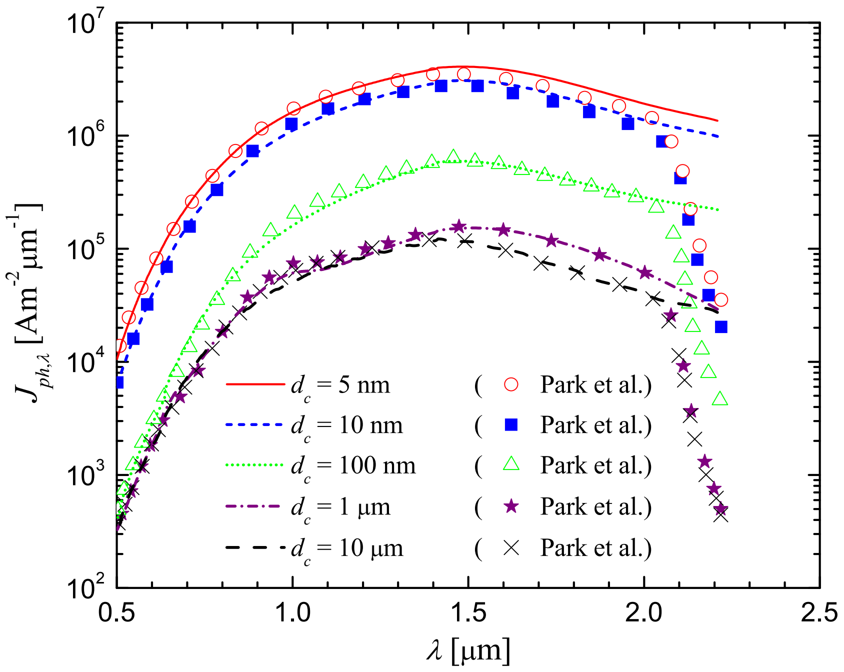

Figure G.5. Monochromatic photocurrent for $d_c$ = 5 nm, 10 nm, 100 nm, 1 µm and 10 µm (corresponds to Fig. 4(b) of reference [37]).

model, the photocurrent drops abruptly above a wavelength of 2.21 µm due to the fact that the interband dielectric function cannot represent the exponential tail. While the results of Park et al. vary more smoothly, something might be wrong. Indeed, the exponential tail observed experimentally should arise for wavelengths slightly higher than the bandgap wavelength of 2.21 µm. In reference [37], the drop occurs for wavelength slightly less than 2.21 µm.

Figure G.6 shows the quantum efficiency of the nano-TPV system as a function of the wavelength for vacuum gaps $d_c$ of 5 nm, 10 nm, 100 nm, 1 µm and 10 µm.

The discussion provided for Fig. G.5 is applicable to Fig. G.6. Also, the discrepancies in $\eta_{q,\lambda}$ are due to the fact that different interband absorptions are predicted between reference [37] and the current model.

Figure G.7 shows the spectral distribution of photocurrent generated in the n-, p-, and depletion regions as a function of the wavelength for a vacuum gap $d_c$ of 10 nm.

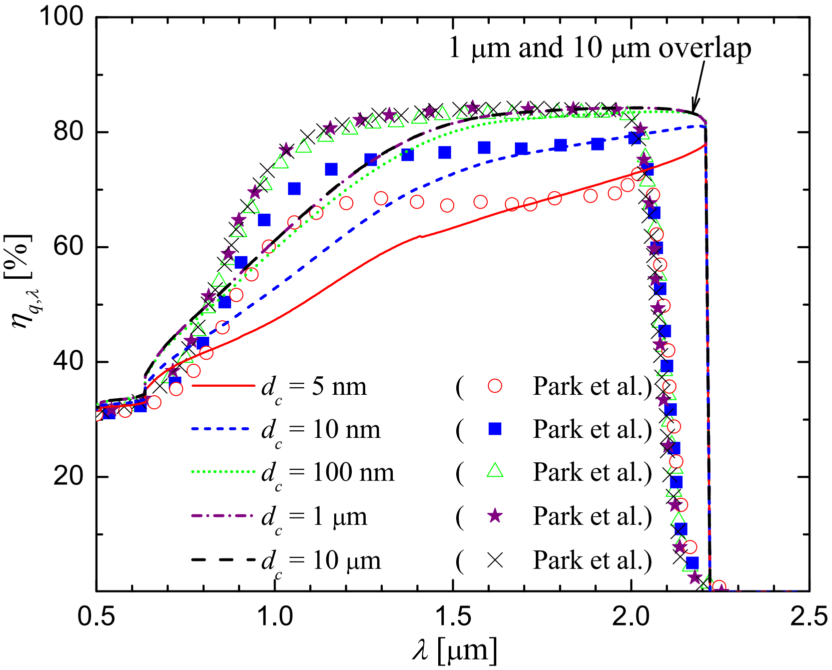

Figure G.6. Quantum efficiency for $d_c$ = 5 nm, 10 nm, 100 nm, 1 μm and 10 μm (corresponds to Fig. 4(c) of reference [37]).

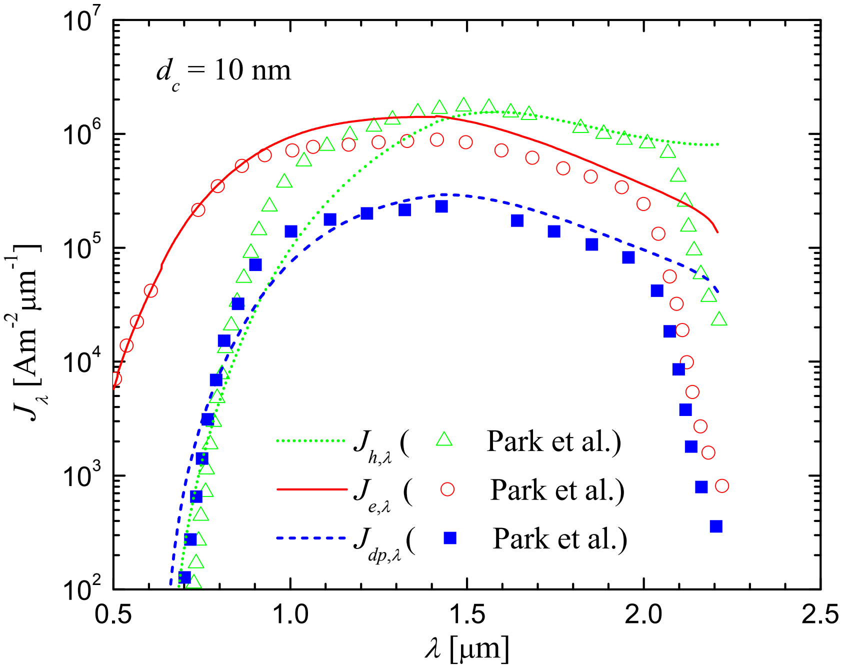

Figure G.7. Spectral photocurrents for $d_c$ = 10 nm (corresponds to Fig. 4(d) of reference [37]).

The discussions associated with Figs. G.5 and G.6 are applicable to Fig. G.7.

Figures G.8(a) to G.8(c) show the total (i.e., integrated over all wavelengths) photocurrent, the total radiative heat flux absorbed by the cell, the electrical power output and the conversion efficiency.

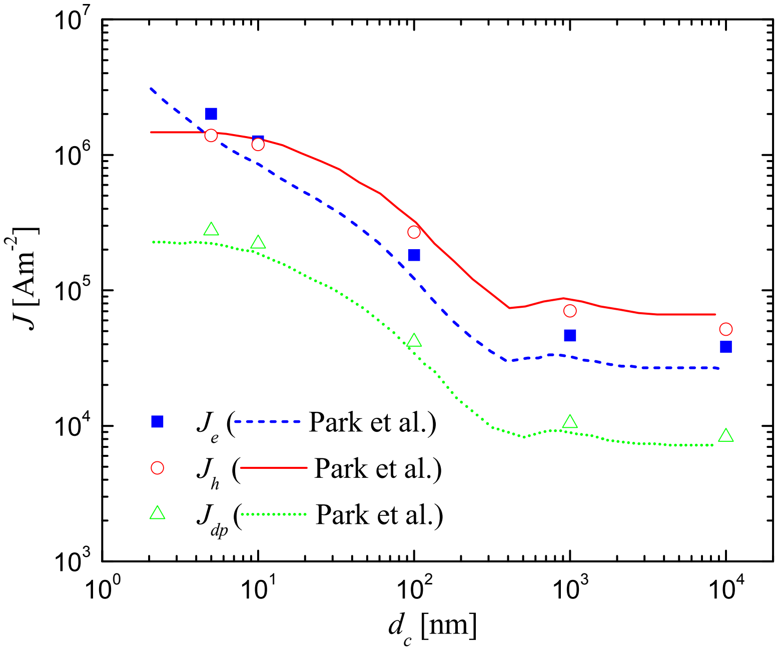

(a)

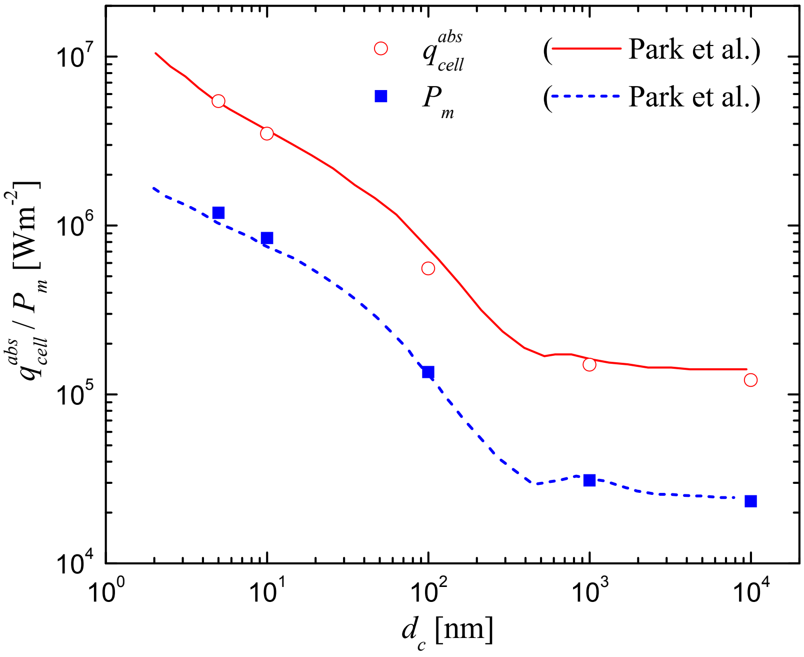

(b)

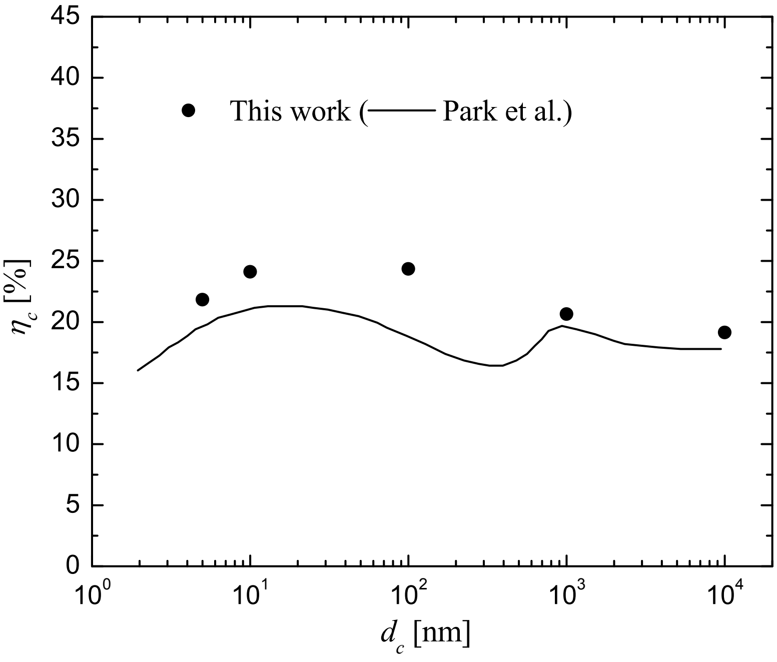

(c)

Figure G.8. (a) Total photocurrents as a function of $d_c$. (b) Total radiative heat flux absorbed by the cell and electrical power output as a function of $d_c$. (c) Conversion efficiency as a function of $d_c$. Results from the current method have been generated only for $d_c$ = 5 nm, 10 nm, 100 nm, 1 μm and 10 μm (corresponds to Figs. 5(a) to 5(c) of reference [37]).

The overall performances obtained by Park et al. and those calculated using the current method are generally in good agreement. The conversion efficiency obtained from our model is generally higher. This can potentially be explained as follows. We concluded earlier that the interband absorption is higher in the current model than in reference [37]. Also, stronger absorption is predicted by Park et al. at $\lambda$ > 2.21 μm, while our model predicts a transparency region. Therefore, these combined effects are likely to lead to lower $\eta_c$ values in the model of Park et al.

To conclude, the results from the current model are in acceptable agreement with those from Park et al. [37]. Indeed, the overall performances of the nano-TPV device obtained from the two models are very similar. The discrepancies are likely to be due to the dielectric function used for the TPV cell, which is not documented in reference [37].

# Appendix H

# Database of Scattering Matrix Elements

### H.1 Modeling of agglomerates of spherical nanoparticles

The four patterns shown in Fig. H.1 have been used to model agglomeration of particles in order to perform the sensitivity analysis (section 7.3) and to generate a database of scattering profiles for the inverse algorithm [207,208].

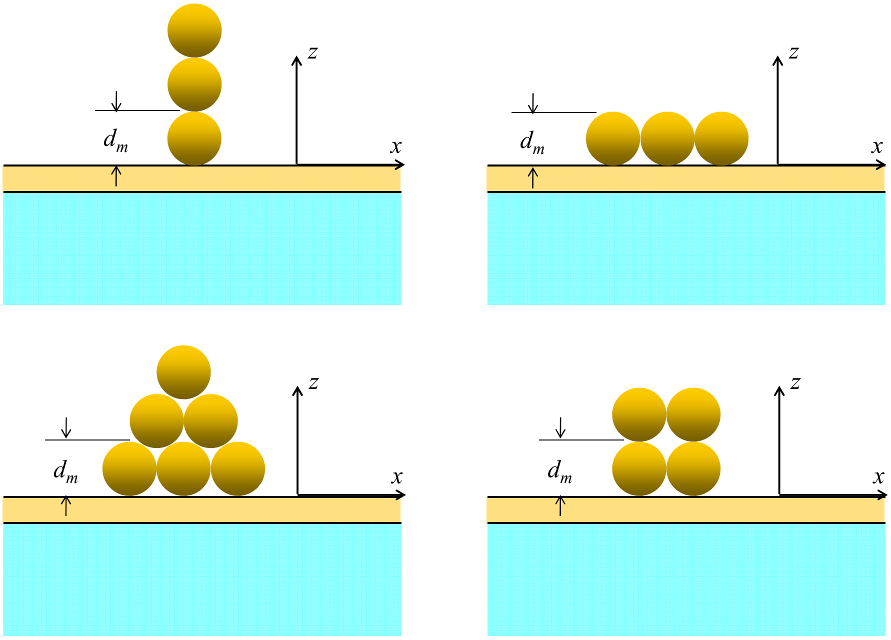

Figure H.1. Different patterns of agglomeration: vertical chain configuration, horizontal chain configuration, triangular configuration and square configuration.

For both cases, the agglomeration level of nanoparticles is defined using the parameter $p$, which represent the percentage of single nanoparticles. The remaining $(100 - p)$ % of agglomerated nanoparticles is composed as follows: 25 % of triangles (60 % three particles, 30 % six particles and 10 % 10 particles), 25 % of squares (60 % four particles, 30 % nine particles and 10 % sixteen particles), 25 % horizontal chains (60 % two particles, 30 % three particles and 10 % four particles), and 25 % of vertical chains (60 % two particles, 30 % three particles and 10 % four particles).

### H.2 Construction of a database of scattering profiles

A database of scattering profiles, used for the inverse algorithm [207,208], has been generated using the problem described in section 7.3. Two parameters were allowed to vary in the database, namely the diameter of the particle ($d_m$) and the level of agglomeration $p$. Normalized scattering profiles ($M_{11}$, $M_{12}$, $M_{33}$ and $M_{34}$) have been generated for $d_m$ values from 5 nm to 100 nm (increment of 5 nm) and for $p$ values from 0 % to 100 % (increment of 5 %).

For a given configuration ($d_m = d_{m,i}$, $p = p_i$), fifteen sets of scattering profiles have been generated. The first set corresponds to scattering profiles obtained in ideal conditions, while the fourteen other sets have been obtained by perturbing input parameters in order to model potential experimental errors in the measurement of the scattering matrix elements. The list of the conditions used to generate the fifteen sets of measurements is given in table H.1.

Table H.1. List of physical disturbances for mimicking potential experimental errors when measuring the scattering matrix elements.

| Set of scattering profiles | Disturbances of physical parameters |
|---|---|
| 1 | Ideal conditions (no disturbance) |
| 2 | Angle of incidence of 24º |
| 3 | Angle of incidence of 22º |
| 4 | Angle of incidence of 25º |
| 5 | Angle of incidence of 21º |
| 6 | +1º offset in measurement angle $\theta_s$ |
| 7 | -1º offset in measurement angle $\theta_s$ |
| 8 | Solid angle of 3º in far-field measurement |
| 9 | Angle of incidence of 21º, +1º offset in measurement angle $\theta_s$ |
| 10 | Angle of incidence of 25º, -1º offset in measurement angle $\theta_s$ |
| 11 | Incident beam spreading out over a solid angle (23º and 24º) |
| 12 | Incident beam spreading out over a solid angle (23º and 24º), solid angle of 3º in far-field measurement |
| 13 | Incident beam spreading out over a solid angle (22º, 23º and 24º), solid angle of 2º in far-field measurement |
| 14 | Incident beam spreading out over a solid angle (22º and 23º), +1º offset in measurement angle $\theta_s$ |
| 15 | Incident beam spreading out over a solid angle (22º and 23º), -1º offset in measurement angle $\theta_s$ |

# Appendix I

# Technical Details of the PSWSS

## I.1 Feasibility and stability of measuring the scattering matrix elements via the six intensity method

In order to test the stability of the six intensity method described in section 8.2, numerical results of surface wave scattering by a single 50 nm gold spherical particle are used (the input parameters given in section 7.3 are employed). Assuming that the Mueller matrix given by Eq. (8.3) is applicable, and using the orientation angles of the linear polarizers (LPs) and quarter-wave plates (QWPs) provided in table 8.1, the intensity vector **K** can be constructed. The six intensity profiles contained in **K** are shown in Fig. I.1.

The highest value of intensity is found for the sixth set of measurements given in table 8.1 (around a $\theta_s$ of about 40º). In the experiment, we do not measure the absolute value of the scattered light, but rather normalized profiles (i.e., normalized scattering matrix elements $M_{ij}$). Therefore, in a given experiment involving a certain number of measurements, the settings of the PSWSS should not vary (i.e., amplification of the signal and potential applied at the detectors). For the six intensity method, the settings of the PSWSS should be adjusted using the sixth set of measurements of table 8.1, as this set leads to the highest value of intensity. For example, if the settings of the PSWSS were adjusted using the first set of table 8.1, there would be a risk of overloading the amplifiers and detectors when performing the third and sixth sets. It is also worth noting that low surface wave scattering can arise without any particles on the substrate due to surface roughness. For the experiments performed in this dissertation, this contribution is negligibly small. An efficient way to cancel out this contribution is to adjust the amplifiers and detectors in such a way that a zero intensity reading is obtained when the sample is uncoated.

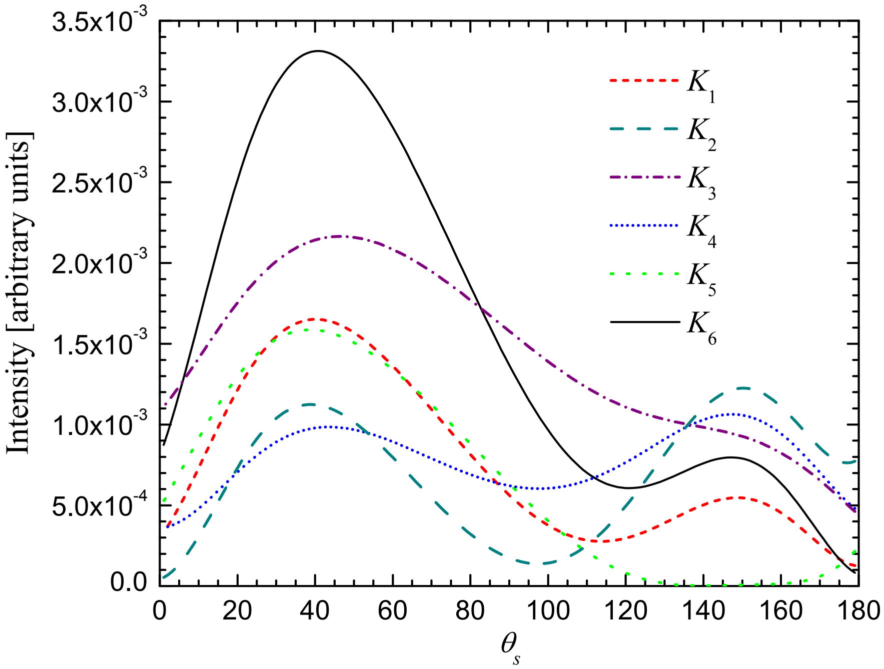

Figure I.1. **K** vector that would be measured experimentally by using the LP and QWP orientation angles given in table 8.1 (single 50 nm gold spherical particle).

Figure I.1 shows that the six intensity profiles are of the same order of magnitude. On the other hand, some of the $S_{ij}$ elements contained in the matrix given by Eq. (8.3) might be more difficult to recover. To verify the stability of the recovered $S_{ij}$ elements after inversion of the coefficient matrix [$C_{ij}$], the following analysis is performed. For a given physical configuration (here, single 50 nm gold spherical nanoparticle), the scattering profiles are computed. Using the orientation angles of the LPs and QWPs given in table 8.1, the coefficient matrix [$C_{ij}$] is calculated. The multiplication of the coefficient matrix with the scattering profiles (Eq. (8.5)) provides the **K** vector, as shown in Fig. I.1. Stochastic noise with a maximal amplitude of ±$x$ % is then added to the vector **K** in order to simulate potential experimental errors. The perturbed intensity vector is referred as $\mathbf{K}_p$. Using $\mathbf{K}_p$, the vector **Z** is calculated by inverting the coefficient matrix; the recovered vector is thus called $\mathbf{Z}_p$. This process is repeated 50 times using 50 sets of random numbers to generate stochastic noises in the **K** vector, such that 50 sets of $\mathbf{Z}_p$ are obtained. The average of these 50 sets of $\mathbf{Z}_p$ leads to the recovered scattering matrix elements, $\mathbf{Z}_p^{avg}$.

Using this procedure, the relative error between the actual vector **Z** and the recovered vector $\mathbf{Z}_p^{avg}$ can be calculated. Due to the fact that some $S_{ij}$ elements are nil for some angles $\theta_s$, the relative error for a given $S_{ij}$ element at a given angle $\theta_s$ is calculated as:

$$Er(S_{ij},\theta_s) = \frac{\left|S_{ij}(\theta_s) - S_{ij,p}^{avg}(\theta_s)\right|}{\max(S_{ij}(\theta_s))} \tag{I.1}$$

The maximum and average errors (averaged over all angles $\theta_s$) for the six scattering matrix elements are given in table I.1 for stochastic noises with amplitudes of ±10 %, ±20 % and ±30 %.

Table I.1. Maximum and average errors in recovering the $S_{ij}$ elements for different levels of stochastic noises.

| $S_{ij}$ element | Stochastic noise ±10 % | | Stochastic noise ±20 % | | Stochastic noise ±30 % | |
|---|---|---|---|---|---|---|
| | Average error [%] | Maximum error [%] | Average error [%] | Maximum error [%] | Average error [%] | Maximum error [%] |
| $S_{11}$ | 0.30 | 1.08 | 0.61 | 2.45 | 0.84 | 5.13 |
| $S_{12}$ | 0.93 | 4.62 | 1.82 | 8.05 | 2.77 | 14.73 |
| $S_{22}$ | 0.92 | 4.62 | 1.75 | 11.80 | 2.63 | 12.44 |
| $S_{33}$ | 1.19 | 5.46 | 2.38 | 13.80 | 3.87 | 19.55 |
| $S_{34}$ | 0.84 | 4.24 | 1.41 | 7.20 | 2.27 | 11.28 |
| $S_{44}$ | 0.58 | 2.53 | 1.20 | 5.49 | 1.87 | 10.46 |

Clearly, $S_{11}$ (scattered intensity) is the element that is the less affected by the stochastic noise. On the other hand, $S_{33}$ is the element that is the most affected by experimental errors in the **K** vector. Therefore, $S_{33}$ is likely to be the element that is the most difficult to recover experimentally.

## I.2 Components of the PSWSS and settings of the lock-in amplifiers

The main components of the PSWSS are listed in table I.2.

Table I.2. Components of the PSWSS.

| Component | Manufacturer | Model number | Comments |
|---|---|---|---|
| Helium-neon laser and power supply | Uniphase | 216-1 (power supply), 106-2 (laser) | Wavelength: 632.8 nm, power: 20 mW |
| Reference lock-in amplifier | Stanford Research Systems | SR510 | |
| Measurement lock-in amplifier | Stanford Research Systems | SR830 DSP | |
| Photomultiplier tubes (PMTs) | Hamamatsu | H6780-04 | Peak radiant sensitivity: 60 mA/W, min/max wavelengths: 185 nm-850 nm, output type: current |
| Power supplies for PMTs | Hamamatsu | C7169 | Output voltage: ±15 V, control voltage: 0 to +1.2 V. |
| Data acquisition card | Measurement Computing | PCIM-DAS1602/16 | |
| Optical chopper and power supply | Stanford Research Systems | SR540 | Chop frequency: 4 Hz to 3.7 kHz |
| Fiber collimators | OZ Optics | HPUC-23-400/700-P-16AC-11 | |
| Fiber optics | OZ Optics | SMJ-3S3S-633-4/125-3AS-2 | |
| Linear polarizer 1 (LP1) | Newport | 05LP-VIS-B | Precision linear polarizer, 12.7 mm diameter, 5.1 mm clear aperture, 430-670 nm |
| Linear polarizer 2 (LP2) | Newport | 10LP-VIS-B | Precision linear polarizer, 25.4 mm diameter, 17.8 mm clear aperture, 430-670 nm |
| Quarter-wave plate 1 (QWP1) | Newport | 05RP04-24 | Zero-order quartz wave plate, 12.7 mm diameter, 632.8 nm, $\lambda/4$ retardation |
| Quarter-wave plate 2 (QWP2) | Newport | 10RP04-24 | Zero-order quartz wave plate, 25.4 mm diameter, 632.8 nm, $\lambda/4$ retardation |

The settings of the reference and measurement lock-in amplifiers used to perform scattering measurement on nanoparticles are provided in table I.3.

Table I.3. Settings of the reference and measurement lock-in amplifiers for measuring surface wave scattering by nanoparticles.

| | Reference lock-in amplifier | Measurement lock-in amplifier |
|---|---|---|
| Signal input | Intensity $I$ | Intensity $I$ ($10^8$), AC, Ground |
| Sensitivity | 20 mV | 1 mV (1 nA) |
| Time constant | 100 ms | 300 ms, Slope/Oct: 24 dB |
| Dynamic reserve | Low | High reserve |
| Signal filters | Bandpass: out, line: out, line×2: out | Notch: 2×line |

## I.3 Optical scheme of the PSWSS

Figures I.2(a) to I.2(c) show the optical scheme of the PSWSS.

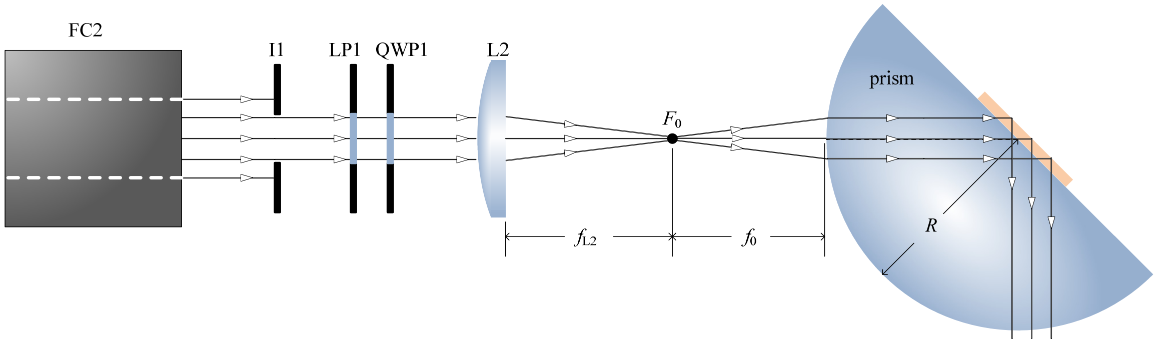
FC2
I1
LP1
QWP1
L2
$F_0$
prism
$f_{L2}$
$f_0$
R

(a)

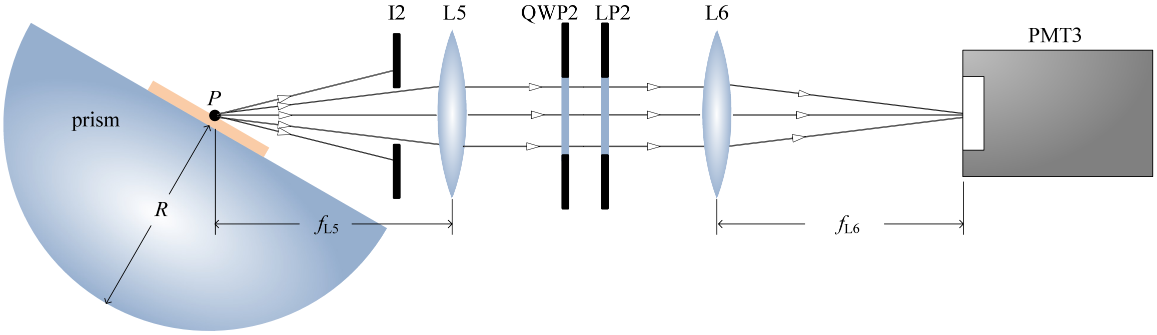
I2
L5
QWP2
LP2
L6
PMT3
P
prism
R
$f_{L5}$
$f_{L6}$

(b)

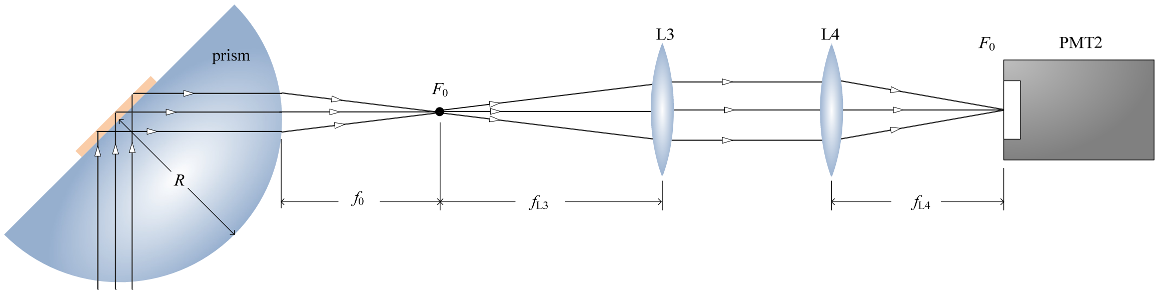

(c)

Figure I.2. Optical scheme of the PSWSS: (a) light path from the source to the prism (left leg of the PSWSS). (b) path of scattered light from the prism to the detector (rotating arm). (c) path of reflected light from the prism to the detector (right leg of the PSWSS).

Figure I.2(a) shows the light path from the source to the prism (left leg of the PSWSS). The beam emerging from the fiber collimator (FC2) passes through an iris (I1), with an aperture of 0.5 mm, before being polarized by a linear polarizer (LP1) and a quarter-wave plate (QWP1). The light is then focused at the point $F_0$ via a planar convex cylindrical lens (L2, Edmund Optics, NT46-016) having a focal length $f_{L2}$ = 47.20 mm. The beam is thus diverging after the point $F_0$, and the prism is therefore used as a lens. The relationship between the object distance $f_0$ and the image distance $f_i$ of a point $F_i$ within the prism (the distance $f_i$ is taken relative to the air-prism interface) is given by [45]:

$$\frac{n_1}{f_0}+\frac{n_2}{f_i}=\frac{n_1-n_2}{R} \tag{I.2}$$

where $n_1$ and $n_2$ are the refractive index of air (= 1) and sapphire (= 1.7659 at 632.8 nm), respectively, and $R$ (= 12.5 mm) is the radius of the semi-cylindrical prism. The idea here is to obtain a collimated beam in the prism, such that all rays are incident at the sample-air interface at the same angle. This can be done by imaging the point $F_0$ in Fig. I.2(a) at infinity ($f_i \rightarrow \infty$), such that Eq. (I.2) can be written as:

$$f_0=\frac{n_1}{n_1-n_2}R \tag{I.3}$$

After substitution of the numerical values in Eq. (I.3), the distance $f_0$ is found to be 16.32 mm.

The diameter of the spot illuminating the nanoparticles can easily be calculated from Fig. I.2(a). The deflection angle $\psi$ of the rays between L2 and $F_0$ is given by $\tan^{-1}(d_{\mathrm{I1}}/2f_{\mathrm{L2}})$, where $d_{\mathrm{I1}}$ is the aperture of the iris I1. Substitution of the appropriate numerical values in this last expression gives $\psi = 0.30^{\mathrm{o}}$. The diameter of the spot $d_s$ illuminating the nanoparticles is therefore given by $d_s = 2f_0\tan\psi$. After substituting the appropriate numerical values, the diameter of the spot illuminating the nanoaparticles is estimated to be about 170 μm.

Figure I.2(b) shows the path of the scattered light from the sample to the detector (rotating arm) where it is assumed that light is diverging from a point source $P$ located at the sample-air interface. The scattered radiation first passes through an iris (I2) having an aperture of 2 mm. The diverging beam is then collimated by a bi-convex lens (L5, Newport, KBX 064) with a focal length $f_{\mathrm{L5}}$ of 100 mm. The collimated beam is afterward polarized via a quarter-wave plate (QWP2) and a linear polarizer (LP2), before being focused by a bi-convex lens (L6, Newport, KBX 025), with a focal length $f_{\mathrm{L6}}$ of 19 mm, at the detector (PMT3).

The light measured by PMT3 is contained in a certain solid angle $\theta_s \pm \zeta$. The angle $\zeta$ can be calculated as $\zeta = \tan(d_{\mathrm{I2}}/L_{\mathrm{I2}})$, where $d_{\mathrm{I2}}$ is the aperture of the iris I2, while $L_{\mathrm{I2}}$ is the distance between the point $P$ and I2 (= 75 mm). By substituting the appropriate numerical values in this last expression, we find $\zeta = 0.8^{\mathrm{o}}$. Therefore, when the rotating arm is oriented at an angle $\theta_s$, light is measured within a solid angle $\theta_s \pm 0.8^{\mathrm{o}}$.

Figure I.2(c) shows the path of the reflected light from the prism to the detector (right leg of the PSWSS). The collimated beam emerging from the prism converges at the point $F_0$ at a distance $f_0 = 16.32$ mm from the prism-air interface according to Eq. (I.3). After the point $F_0$, the beam is diverging and is collimated with a bi-convex lens (L3, Newport, KBX 061) having a focal length $f_{\mathrm{L3}}$ of 88.30 mm. The collimated light is finally focused at the detector (PMT2) via a bi-convex lens (L4, Newport, KBX 052) having a focal length $f_{L4}$ of 50.20 mm.

## I.4 Calibration of the polarizers and quarter-wave plates

The idea here is to verify that the transmission axis (for the LPs) and the fast axis (for the QWPs) indicated by the manufacturer on the mountings of these optical components are correct.

### *I.4.1 Calibration of the linear polarizers (LPs)*

The location of the transmission axis of the LPs is verified against Malus's law [45]. This is accomplished by using two LPs (the prism is removed). The unpolarized beam emerging from the laser passes through a first LP to be calibrated, while the second LP, already calibrated, is referred as the analyzer. The transmission axis of the analyzer, $\xi_a$, is fixed at 0º, while the transmission axis of the LP varies from $\xi = 0º$ to 90º. We assume that the magnitude of the electric field incident on the LP is $E_0$, and we neglect the absorption along the transmission axis. When the LP is oriented at an angle $\xi$, only the component $E_0 \cos\xi$, parallel to the transmission axis of the analyzer, reaches the detector. The detector however measures the intensity, which is proportional to the square of the amplitude of the electric field. Given that, it can be shown that the intensity reaching the detector when the transmission axis of the LP is oriented at an angle $\xi$ is given by [45]:

$$I(\xi) = \frac{c_v \varepsilon_v}{2} E_0^2 \cos^2 \xi \tag{I.4}$$

The maximum intensity reaching the detector arises when $\xi = \xi_a = 0º$. This maximum intensity can be written as [45]:

$$I(0) = \frac{c_v \varepsilon_v}{2} E_0^2 \tag{I.5}$$

Substitution of Eq. (I.5) into (I.4) leads to the following relation:

$$\frac{I(\xi)}{I(0)} = \cos^2 \xi \tag{I.6}$$

The left-hand side of Eq. (I.6) can be measured experimentally, and the comparison of the profile thus obtained with the right-hand side of Eq. (I.6), computed theoretically, will allow us to determine if the transmission axis indicated on the mounting the LP is indeed correct. Figure I.3 shows $I(\xi)/I(0)$ versus $\xi$, from 0º to 90º by increment of 10º, for LP1 and LP2 used in the PSWSS; the results are compared with the theoretical curve given by $\cos^2\xi$.

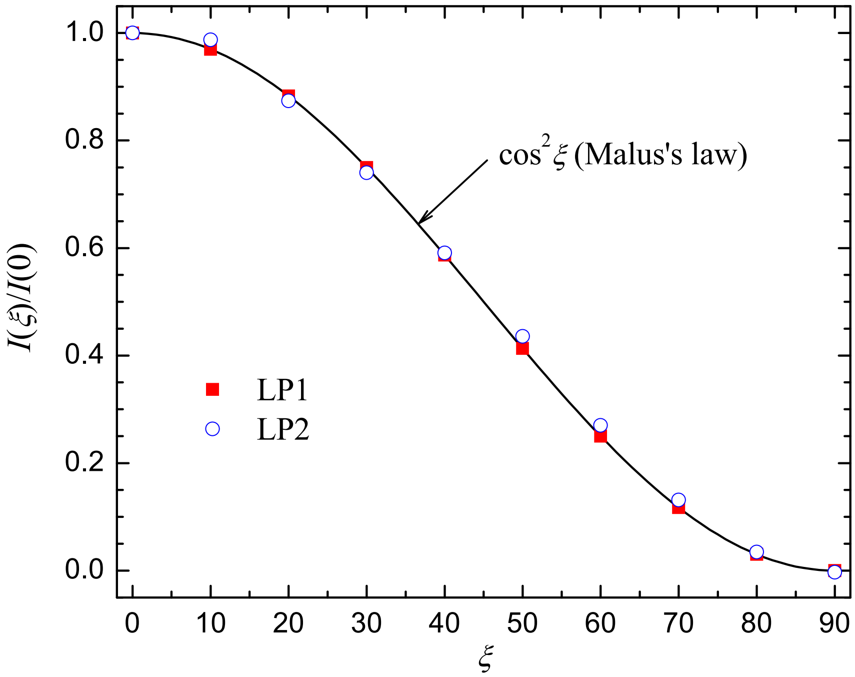

Figure I.3. Verification of Malus's law for the LPs used in the PSWSS (LP1 and LP2).

Figure I.3 clearly shows that the location of the transmission axis indicated on the mounting of both LPs is correct.

### *I.4.2 Calibration of the quarter-wave plates (QWPs)*

The QWPs are calibrated by right-circularly polarizing the light. This is done as follows. The unpolarized beam emerging from the laser first passes through a LP and then through a QWP. The difference in the orientation of the transmission axis (LP) and fast axis (QWP) should be 45º. Therefore, the polarizer is set at $\xi$ = 0º, while the QWP has an orientation $\beta$ = 45°. Assuming that there is no optical component after the QWP, the emerging Stokes vector can be written as:

$$\begin{pmatrix} I_s \\ Q_s \\ U_s \\ V_s \end{pmatrix} = [S_{ij}]_{QWP} \cdot [S_{ij}]_{LP} \begin{pmatrix} I_i \\ 0 \\ 0 \\ 0 \end{pmatrix} = \frac{1}{2} \begin{bmatrix} 1 & 0 & 0 & 0 \\ 0 & 0 & 0 & -1 \\ 0 & 0 & 1 & 0 \\ 0 & 1 & 0 & 0 \end{bmatrix} \begin{bmatrix} 1 & 1 & 0 & 0 \\ 1 & 1 & 0 & 0 \\ 0 & 0 & 0 & 0 \\ 0 & 0 & 0 & 0 \end{bmatrix} \begin{pmatrix} I_i \\ 0 \\ 0 \\ 0 \end{pmatrix} \qquad \text{(I.7)}$$

After normalization by $I_s$, the emerging Stokes vector is given by $(1,0,0,1)^T$, which corresponds to a wave that is right-circularly polarized [45].

The right-circularly polarized light then passes through an analyzer, which is a LP with a transmission axis oriented at $\xi_a$. As discussed in section 7.1.1, the magnitude of the electric field of a circularly polarized wave is constant. Therefore, the light reaching the detector, after passing though the analyzer, should be the same regardless of $\xi_a$.

When orienting the fast axis of the QWPs according to the indication provided on the mounting, the intensity measured at the detector varied with $\xi_a$. The best results have been obtained by letting $\beta_1$ = 49° for QWP1 (i.e., offset of +4°), and by letting $\beta_2$ = 47.5° for QWP2 (i.e., offset of +2.5°). These results are shown in Fig. I.4.

Results of Fig. I.4 show that the electric field emerging from the QWPs is not perfectly constant, and this might leads to experimental errors. A difficulty arises here due to the fact that the orientations of the QWPs are adjusted manually, and the graduation on the mountings is not very precise.

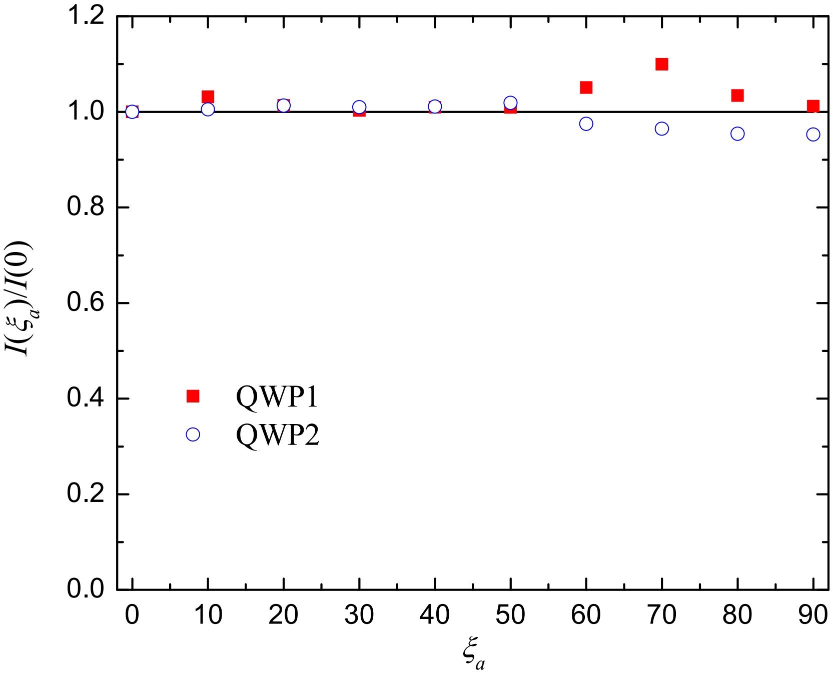

Figure I.4. Verification of the location of the fast axis on the QWPs used in the PSWSS (QWP1 and QWP2).

# References

[1] Novotny L. and Hecht B., *Principles of Nano-Optics*, Cambridge University Press, New York, 2006.

[2] Zhang Z.M., *Micro/Nanoscale Heat Transfer*, McGraw-Hill, New York, 2007.

[3] Chen G., *Nanoscale Energy Transport and Conversion*, Oxford University Press, New York, 2005.

[4] Catchpole K.R. and Polman A., Plasmonics solar cells, *Optics Express* **16**, 21793-21800, 2008.

[5] Basu S., Chen Y.-B. and Zhang Z.M., Microscale radiation in thermophotovoltaic devices: A review, *International Journal of Energy Research* **31**, 689-716, 2007.

[6] Cai W. and Shalaev V., *Optical Metamaterials*, Springer, New York, 2010.

[7] Greffet J.-J., Carminati R., Joulain K., Mulet J.-P., Mainguy S. and Chen Y., Coherent emission of light by thermal sources, *Nature* **416**, 61-64, 2002.

[8] De Wilde Y., Formanek F., Carminati R., Gralak B., Lemoine P.-A., Joulain K., Mulet J.-P., Chen Y. and Greffet J.-J., Thermal radiation scanning tunneling microscopy, *Nature* **444**, 740-743, 2006.

[9] Hawes E.A., Hastings J.T., Crofcheck C. and Mengüç M.P., Spectrally selective heating of nanosized particles by surface Plasmon resonance, *Journal of Quantitative Spectroscopy and Radiative Transfer* **104**, 199-207, 2007.

[10] Hawes E.A., Hastings J.T., Crofcheck C. and Mengüç M.P., Spatially selective melting and evaporation of nanosized gold particles, *Optics Letters* **33**, 1383-1385, 2008.

[11] Maier S.A., *Plasmonics*, Springer, New York, 2007.

[12] Dionne J., Sweatlock L.A., Atwater H.A. and Polman A., Planar metal Plasmon waveguides: frequency-dependent dispersion, propagation, localization, and loss beyond the free electron model, *Physical Review B* **72**, 075405, 2005.

[13] Dionne J., Sweatlock L.A., Polman A. and Atwater H.A., Plasmon slot waveguides: towards chip-scale propagation with subwavelength-scale localization, *Physical Review B* **73**, 035407, 2006.

[14] Planck M., *The Theory of Heat Radiation*, Dover Publications, New York, 1991.

[15] Siegel R. and Howell J., *Thermal Radiation Heat Transfer*, Taylor and Francis, 4th Edition, 2002.

[16] Modest M.F., Radiative Heat Transfer, Academic Press, 2nd Edition, San Diego, 2003.

[17] Viskanta R., *Radiative Transfer in Combustion Systems*, Begell House, New York, 2004.

[18] Rytov S.M., *Theory of Electric Fluctuations and Thermal Radiation*, Air Force Cambridge Research Center, Bedford, 1959.

[19] Rytov S.M., Kravtsov Y.A., Tatarskii V.I., *Principles of Statistical Radiophysics 3: Elements of Random Fields*, Springer, New York, 1989.

[20] Polder D. and Van Hove M., Theory of radiative heat transfer between closely spaced bodies, *Physical Review B* **4**(10), 3303-3314, 1971.

[21] Pendry J.B., Radiative exchange of heat between nanostructures, *Journal of Physics: Condensed Matter* **11**, 6621-6633, 1999.

[22] Volokitin A.I. and Persson B.N.J., Radiative heat transfer between nanostructures, *Physical Review B* **63**, 205404, 2001.

[23] Mulet J.-P., Joulain K., Carminati R. and Greffet J.-J., Nanoscale radiative heat transfer between a small particles and a plane surface, *Applied Physics Letters* **78**(19), 2931-2933, 2001.

[24] Domingues G., Volz S., Joulain K. and Greffet J-J., Heat transfer between two nanoparticles through near field interaction, *Physical Review Letters* **94**(8), 085901, 2005.

[25] Joulain K., Mulet J.-P., Marquier F., Carminati R. and Greffet J.-J., Surface electromagnetic waves thermally excited: Radiative heat transfer, coherence properties and Casimir forces revisited in the near field, *Surface Science Reports* **57**, 59-112, 2005.

[26] Fu C.J. and Zhang Z.M., Nanoscale radiation heat transfer for silicon at different doping levels, *International Journal of Heat and Mass Transfer* **49**, 1703-1718, 2006.

[27] Hammonds Jr. J.S., Thermal transport via surface phonon polaritons across a two-dimensional pore, *Applied Physics Letters* **88**, 041912, 2006.

[28] Chapuis P.-O., Laroche M., Volz S. and Greffet J-J., Radiative heat transfer between metallic nanoparticles, *Physical Review Letters* **92**, 201906, 2008.

[29] Narayanaswamy A. and Chen G., Thermal near-field radiative transfer between two spheres, *Physical Review B* **77**, 075125, 2008.

[30] Mulet J.-P., Joulain K., Carminati R. and Greffet J-J., Enhanced radiative heat transfer at nanometric distances, *Nanoscale and Microscale Thermophysical Engineering* **6**, 209-222, 2002.

[31] Chubb D.L., *Fundamentals of Thermophotovoltaic Energy Conversion*, Elsevier, The Netherlands, 2007.

[32] Coutts T.J., An overview of thermophovoltaic generation of electricity, *Solar Energy Materials and Solar Cells* **66**, 443-452, 2001.

[33] Whale M.D., A Fluctuational electrodynamics analysis of microscale radiative heat transfer and the design of microscale thermophotovoltaic devices, PhD Thesis, MIT, Cambridge, 1997.

[34] Whale M.D. and Cravalho E.G., Modeling and performance of microscale thermophotovoltaic energy conversion devices, *IEEE Transactions on Energy Conversion* **17**(1), 130-142, 2002.

[35] Narayanaswamy A. and Chen G., Surface modes for near field thermophotovoltaics, *Applied Physics Letters* **82**(20), 3544-3546, 2003.

[36] Laroche M., Carminati R. and Greffet J-J., Near-field thermophotovoltaic energy conversion, *Journal of Applied Physics* **100**, 063704, 2006.

[37] Park K., Basu S., King W.P. and Zhang ZM. Performance analysis of near-field thermophotovoltaic devices considering absorption distribution, *Journal of Quantitative Spectroscopy and Radiative Transfer* **109**, 305-316, 2008.

[38] Shipway A.N., Katz E. and Willner I., Nanoparticle arrays on surfaces for electronic, optical, and sensor applications, *ChemPhysChem* **1**, 18-52, 2000.

[39] Videen G., Aslan M.M. and Mengüç M.P., Characterization of metallic nano-particles via surface wave scattering: A. Theoretical framework and formulation, *Journal of Quantitative Spectroscopy and Radiative Transfer* **93**, 195-206, 2005.

[40] Aslan M.M., Mengüç M.P. and Videen G., Characterization of metallic nano-particles via surface wave scattering: B. Physical concept and numerical experiments, *Journal of Quantitative Spectroscopy and Radiative Transfer* **93**, 207-217, 2005.

[41] Venkata P.G., Aslan M.M., Mengüç M.P. and Videen G., Surface plasmon scattering patterns of gold nanoparticles and 2D agglomerates, *ASME Journal of Heat Transfer* **129**, 60-70, 2007.

[42] Venkata P.G., Surface wave scattering from metallic nano particles and agglomerates: theoretical framework and numerical analysis, Master Thesis, The University of Kentucky, Lexington, 2006.

[43] Greffet J.-J., Chapuis P.O., Carminati R., Laroche M., Marquier F., Volz S. and Henkel C., Thermal radiation revisited in the near-field, *Proceedings of the Fifth International Symposium on Radiative Transfer*, 2007.

[44] Jackson J.D., *Classical Electrodynamics*, John Wiley and Sons, 3rd Edition, 1999.

[45] Hecht E., *Optics*, Addison Wesley, 4th Edition, San Francisco, 2002.

[46] Carminati R. and Greffet J.-J., Near-field effects in spatial coherence of thermal sources, *Physical Review Letters* **82**(8), 1660-1663, 1999.

[47] Henkel C., Joulain K., Carminati R. and Greffet J.-J., Spatial coherence of thermal near fields, *Optics Communications* **186**, 57-67, 2000.

[48] Joulain K., Radiative transfer on short length scales, *Topics in Applied Physics: Microscale and Nanoscale Heat Transfer* **107**, Springer, Berlin/Heidelberg, 107-131, 2007.

[49] Kittel C., *Introduction to Solid State Physics*, John Wiley and Sons, 8th Edition, Hoboken, 2005.

[50] Raether H., *Surface Plasmons on Smooth and Rough Surfaces and on Gratings*, Springer Tracts in Modern Physics Vol. 111, Springer-Verlag, New York, 1988.

[51] Kollyukh O.G., Liptuga A.I., Morozhenko V. and Pipa V.I., Thermal radiation of plane-parallel semitransparent layers, *Optics Communications* **225**, 349-352, 2003.

[52] Ben-Abdallah P., Thermal antenna behavior for thin-film structures, *Journal of the Optical Society of America A* **21**(7), 1368-1371, 2004.

[53] Drevillon J. and Ben-Abdallah P., *Ab initio* design of coherent thermal sources, *Journal of Applied Physics* **102**, 114305, 2007.

[54] Drevillon J., Design ab-initio de matériaux micro et nanostructurés pour l'émission thermique cohérente en champ proche et en champ lointain, PhD Thesis (in french), Université de Nantes, Nantes, 2007.

[55] Lee B.J., Fu C.J. and Zhang Z.M., Coherent thermal emission from one-dimensional photonic crystals, *Applied Physics Letters* **87**, 071904, 2005.

[56] Lee B.J. and Zhang Z.M., Design and fabrication of planar multilayer structures with coherent thermal emission characteristics, *Journal of Applied Physics* **100**, 063529, 2006.

[57] Lee B.J. and Zhang Z.M., Coherent thermal emission from modified periodic multilayer structures, *ASME Journal of Heat Transfer* **129**, 17-26, 2007.

[58] Fu C.J., Zhang Z.M. and Tanner D.B., Planar heterogeneous structures for coherent emission of radiation, *Optics Letters* **30**(14), 1873-1875, 2005.

[59] Ben-Abdallah P. and Ni B., Single-defect Bragg stacks for high-power narrow-band thermal emission, *Journal of Applied Physics* **97**, 104910, 2005.

[60] Narayanaswamy A. and Chen G., Thermal emission control with one-dimensional metallodielectric photonic crystals, *Physical Review B* **70**, 125101, 2004.

[61] Narayanaswamy A. and Chen G., Thermal radiation in 1D photonic crystals, *Journal of Quantitative Spectroscopy and Radiative Transfer* **93**, 175-183, 2005.

[62] Luo C., Narayanaswamy A., Chen G. and Joannopoulos J.D., Thermal radiation from photonic crystals: A direct calculation, *Physical Review Letters* **93**, 213905, 2004.

[63] Celanovic I., Perreault D. and Kassakian J., Resonant-cavity enhanced thermal emission, *Physical Review B* **72**, 075127, 2004.

[64] Lee B.J., Fabrication and analysis of multilayer structures for coherent thermal emission, PhD Thesis, Georgia Institute of Technology, Atlanta, 2007.

[65] Francoeur M. and Mengüç M.P., Role of fluctuational electrodynamics in near-field radiative heat transfer, *Journal of Quantitative Spectroscopy and Radiative Transfer* **109**, 280-293, 2008.

[66] Carey V.P., Chen G., Grigoropoulos C., Kaviany M. and Majumdar A., A review of heat transfer physics, *Nanoscale and Microscale Thermophysical Engineering* **12**, 1-60, 2008.

[67] Kidd R., Ardini J. and Anton A., Evolution of the modern photon, *American Journal of Physics* **57**(1), 27-35, 1989.

[68] Mishchenko M.I., Maxwell's equations, radiative transfer, and coherent backscattering: A general perspective, *Journal of Quantitative Spectroscopy and Radiative Transfer* **101**, 540-555, 2006.

[69] Mishchenko M.I., Travis L.D. and Lacis A.A., *Multiple Scattering of Light by Particles: Radiative Transfer and Coherent Backscattering*, Cambridge University Press, Cambridge, 2006.

[70] Peterson A.F., Ray S.L. and Mittra R., *Computational Methods for Electromagnetics*, Oxford University Press, New York, 1998.

[71] Yeh P., *Optical Waves in Layered Media*, John Wiley and Sons, Hoboken, 2005.

[72] Narayanaswamy A. and Chen G., Direct computation of thermal emission from nanostructures, *Annual Reviews of Heat Transfer* **14**, 169-195, 2005.

[73] Tsang L., Kong J.A. and Ding K.H., *Scattering of Electromagnetic Waves*, Wiley, New York, 2000.

[74] Landau L.D. and Lifshitz E.M., *Electrodynamics of Continuous Media*, Addison-Wesley, Reading, 1960.

[75] Mulet J.-P., Modélisation du rayonnement thermique par une approche électromagnétique. Rôle des ondes de surfaces dans le transfert d'énergie aux courtes échelles et dans les forces de Casimir, PhD Thesis (in french), Université Paris-Sud 11, Paris, 2003.

[76] Chapuis P.-O., Volz S., Henkel C., Joulain K. and Greffet J.-J., Effects of spatial dispersion in near-field radiative heat transfer between two parallel metallic surfaces, *Physical Review B* **77**, 035431, 2008.

[77] Joulain K., Drevillon J. and Ben-Abdallah P., Noncontact heat transfer between two metamaterials, *Physical Review B* **81**, 165119, 2010.

[78] Mandel L. and Wolf E., *Optical Coherence and Quantum Optics*, Cambridge University Press, Cambridge, 1995.

[79] Goodman J.W., *Statistical Optics*, John Wiley and Sons, New York, 2000.

[80] Joulain K., Carminati R., Mulet J.-P. and Greffet J.-J., Definition and measurement of the local density of electromagnetic states close to an interface, *Physical Review B* **68**, 245405, 2003.

[81] Cravalho E.G., Domoto G.A. and Tien C.L., Measurement of thermal radiation of solids at liquid helium temperatures, *Progress in Aeronautics and Astronautics* **21**, 531-532, 1968.

[82] Domoto G.A., Boehm R.F. and Tien C.L., Experimental investigation of radiative transfer between metallic surfaces at cryogenic temperatures, *ASME Journal of Heat Transfer* **92**, 412-417, 1970.

[83] Hargreaves C.M., Radiative transfer between closely spaced bodies, *Philips Research Reports and Supplement*, Vol. 5, 1-80, 1973.

[84] Hargreaves C.M., Anomalous radiative transfer between closely spaced bodies, *Physics Letters A* **30**(9), 491-492, 1969.

[85] Kutateladze S.S., Rubtsov N.A. and Bal'tsevich Ya.A., Effect of magnitude of gap between metal plates on their thermal interactions at cryogenic temperatures, *Soviet Physics-Doklady* **8**, 577-578, 1979.

[86] Xu J.B., Läuger K., Möller R., Fransfield K. and Wilson I.H., Heat transfer between two metallic surfaces at small distances, *Journal of Applied Physics* **76**(11), 7209-7216, 1994.

[87] Kittel A., Müller-Hirsch W., Parisi J., Biehs S.-A., Reddig D. and M. Holthaus, Near-field radiative heat transfer in a scanning thermal microscope, *Physical Review Letters* **95**, 224301, 2005.

[88] Hu L., Narayanaswamy A., Chen X.Y. and Chen G., Near-field thermal radiation between two closely spaced glass plates exceeding Planck's blackbody radiation law, *Applied Physics Letters* **92**, 133106, 2008.

[89] Shen S., Narayanaswamy A. and Chen G., Surface phonon polaritons mediated energy transfer between nanoscale gaps, *Nano Letters* **9**(8), 2909-2913, 2009.

[90] Narayanaswamy A., Investigation of nanoscale thermal radiation: Theory and experiments, PhD Thesis, MIT, Cambridge, 2007.

[91] Narayanaswamy A., Chen S., Hu L., , Chen X.Y. and Chen G., Breakdown of the Planck blackbody radiation law at nanoscale gaps, *Applied Physics A: Materials Science and Processing* **96**(2), 357-362, 2009.

[92] Rousseau E., Siria A., Jourdan G., Volz S., Comin F., Chevrier J. and Greffet J.-J., Radiative heat transfer at the nanoscale, *Nature Photonics* **3**(9), 514-517, 2009.

[93] Cravalho E.G., Tien C.L. and Caren R.P., Effect of small spacing on radiative transfer between two dielectrics, *ASME Journal of Heat Transfer* **89C**, 351-358, 1967.

[94] Boehm R.F. and Tien C.L., Small spacing analysis of radiative transfer between parallel metallic surfaces, *ASME Journal of Heat Transfer* **92C**(3), 405-411, 1970.

[95] Basu S., Lee B.J. and Zhang Z.M., Infrared properties of heavily doped silicon at room temperature, *ASME Journal of Heat Transfer* **132**, 023301, 2010.

[96] Basu S., Lee B.J. and Zhang Z.M., Near-field radiation calculated with an improved dielectric function model for doped silicon, *ASME Journal of Heat Transfer* **132**, 023302, 2010.

[97] Rousseau E., Laroche M. and Greffet J.-J., Radiative heat transfer at nanoscale mediated by surface plasmons for highly doped silicon, *Applied Physics Letters* **95**, 231913, 2009.

[98] Basu S., Zhang Z.M. and Fu C.J., Review of near-field thermal radiation and its application to energy conversion, *International Journal of Energy Research* **33**(13), 1202-1232, 2009.

[99] Volokitin A.I. and Persson B.N.J., Resonant photon tunneling enhancement of the radiative heat transfer, *Physical Review B* **69**, 045417, 2004.

[100] Loomis J.J. and Maris H.J., Theory of heat transfer by evanescent electromagnetic waves, *Physical Review B* **50**(24), 18517-18524, 1994.

[101] Wang X.J., Basu S. and Zhang Z.M., Parametric optimization of dielectric functions for maximizing nanoscale radiative transfer, *Journal of Physics D: Applied Physics* **42**, 245403, 2009.

[102] Rousseau E., Laroche M. and Greffet J.-J., Radiative heat transfer at nanoscale: Closed-form expression for silicon at different doping levels, *Journal of Quantitative Spectroscopy and Radiative Transfer* **111**, 1005-1014, 2010.

[103] Ben-Abdallah P., Joulain K., Drevillon J. and Domingues G., Tailoring the local density of states of nonradiative field at the surface of nanolayered materials, *Applied Physics Letters* **94**, 153117, 2009.

[104] Francoeur M., Mengüç M.P. and Vaillon R., Local density of electromagnetic states within a nanometric gap formed between two thin films supporting surface phonon polaritons, *Journal of Applied Physics* **107**, 034313, 2010.

[105] Francoeur M., Mengüç M.P. and Vaillon R., Spectral tuning of near-field radiative heat flux between two thin silicon carbide films, *Journal of Physics D: Applied Physics* **43**, 075501, 2010.

[106] Biehs S.-A., Reddig D. and Holthaus M., Thermal radiation and near-field energy density of thin metallic films, *The European Physical Journal B* **55**, 237-251, 2007.

[107] Biehs S.-A., Thermal heat radiation, near-field energy density and near-field radiative heat transfer of coated materials, *The European Physical Journal B* **58**, 423-431, 2007.

[108] Francoeur M., Mengüç M.P. and Vaillon R., Near-field radiative heat transfer enhancement via surface phonon polaritons coupling in thin films, *Applied Physics Letters* **93**, 043109, 2008.

[109] Ben-Abdallah P., Joulain K., Drevillon J. and Domingues G., Near-field heat transfer mediated by surface wave hybridization between two films, *Journal of Applied Physics* **106**, 044306, 2009.

[110] Fu C.J. and Tan W.C., Near-field radiative heat transfer between two plane surfaces with one having a dielectric coating, *Journal of Quantitative Spectroscopy and Radiative Transfer* **110**, 1027-1036, 2009.

[111] Biehs S.-A., Huth O. and Rüting F., Near-field radiative heat transfer for structured surfaces, *Physical Review B* **78**, 085414, 2008.

[112] Lee B.J., Park K. and Zhang Z.M., Energy pathways in nanoscale thermal radiation, *Applied Physics Letters* **91**, 153101, 2007.

[113] Lee B.J. and Zhang Z.M., Lateral shifts in near-field thermal radiation with surface phonon polaritons, *Nanoscale and Microscale Thermophysical Engineering* **12**(3), 238-250, 2008.

[114] Francoeur M., Mengüç M.P. and Vaillon R., Solution of near-field thermal radiation in one-dimensional layered media using dyadic Green's functions and the scattering matrix method, *Journal of Quantitative Spectroscopy and Radiative Transfer* **110**, 2002-2018, 2009.

[115] Sipe J.E., New Green-function formalism for surface optics, *Journal of the Optical Society of America B* **4**(4), 481-489, 1987.

[116] Auslender M. and Hava S., Scattering-matrix propagation algorithm in full-vectorial optics of multilayer grating structures, *Optics Letters* **21**(21), 1765-1767, 1996.

[117] Basu S. and Zhang Z.M., Ultrasmall penetration depth in nanoscale thermal radiation, *Applied Physics Letters* **95**, 133104, 2009.

[118] Kliewer K.L. and Fuchs R., Optical modes of vibration in an ionic crystal slab including retardation. I. Nonradiative region, *Physical Review* **144**(2), 495-503, 1966.

[119] Kliewer K.L. and Fuchs R., Optical modes of vibration in an ionic crystal slab including retardation. II. Radiative region, *Physical Review* **150**(2), 573-588, 1966.

[120] Kliewer K.L. and Fuchs R., Collective electronic motion in a metallic slab, *Physical Review* **153**(2), 498-512, 1967.

[121] Economou E.N., Surface plasmons in thin films, *Physical Review* **182**(2), 539-554, 1969.

[122] Sarid D., Long-range surface plasma waves on very thin metal films, *Physical Review Letters* **47**(26), 1927-1930, 1981.

[123] Burke J.J., Stegeman G.I. and Tamir T., Surface-polariton-like waves guided by thin, lossy metal films, *Physical Review B* **33**, 5186-5201, 1986.

[124] Joulain K. and Henkel C., The near field correlation spectrum of a metallic film, *Applied Physics B* **93**, 151-158, 2008.

[125] Francoeur M., Mengüç M.P. and Vaillon R., Near-field thermal radiation emission from SiC thin films, *Proceedings of Eurotherm 83: Computational Thermal Radiation in Participating Media III*, Lisbon, Portugal, 2009.

[126] Gilmore M.A. and Johnson B.L., Forbidden guided-wave plasmon polaritons in coupled thin films, *Journal of Applied Physics* **93**, 4497-4504, 2003.

[127] Chen J., Smolyakov G.A., Brueck S.R.J. and K.J. Malloy, Surface Plasmon modes of finite, planar, metal-insulator-metal plasmonic waveguides, *Optics Express* **16** 14902-14909, 2008.

[128] Baxter J. et al., Nanoscale design to enable the revolution in renewable energy, *Energy and Environmental Science* **2**, 559-588, 2009.

[129] Mauk M.G., Survey of thermophotovoltaic (TPV) devices, In: *Mid-Infrared Semiconductor Optoelectronics* **118**, Springer, 2006.

[130] Gonzalez-Cuevas J.A., Refaat T.F., Abedin M.N. and Elsayed-Ali H.E., Calculation of temperature and alloy composition effects on the optical properties of $Al_xGa_{1-x}As_ySb_{1-y}$ and $Ga_xIn_{1-x}As_ySb_{1-y}$ in the spectral range 0.5-6 eV, *Journal of Applied Physics* **102**, 014504, 2007.

[131] Laroche M., Rôle des onde de surfaces dans la modification des propriétés radiatives de matériaux microstructurés. Application à la conception de sources infrarouges et à l'effet thermophotovoltaïque, PhD Thesis (in french), Ecole Centrale Paris, Paris, 2005.

[132] Park K., Thermal characterization of heated microcantilevers and a study on near-field radiation, PhD Thesis, Georgia Institute of Technology, Atlanta, 2007.

[133] Nelson R.E., A brief history of thermophotovoltaic development, *Semiconductor Science and Technology* **18**, S141-S143, 2003.

[134] Kolm H.H., Solar-battery power source, *Quarterly Progress Report Solid State Research Group* **35**, MIT Lincoln Laboratory, Lexington, MA, 1956.

[135] Broman L., Thermophotovoltaics bibliography, *Progress in Photovoltaics: Research and Applications* **3**, 65-74, 1995.

[136] Werth J., Operation of photovoltaic cells at high power densities, *Proc. 3rd PV Specialists Conference*, Vol. II, A.6.1-A.6.3, 1963.

[137] Werth J., Thermophotovoltaic energy conversion, *Proc. 17<sup>th</sup> Power Sources Conference*, 23-27, 1963.

[138] Baldasaro P.F., Raynolds J.E., Charache G.W., DePoy D.M., Ballinger C.T., Dononvan T. and Borrego J.M., Thermodynamic analysis of thermophotovoltaic efficiency and power density tradeoffs, *Journal of Applied Physics* **89**(6), 3319-3327, 2001.

[139] Lin S.Y., Moreno J. and Fleming J.G., Three-dimensional photonic-crystal emitter for thermal photovoltaic power generation, *Applied Physics Letters* **83**(2), 380-382, 2003.

[140] Chen Y.B. and Zhang Z.M., Design of tungsten complex gratings for thermophotovoltaic radiators, *Optics Communications* **269**(2), 411-417, 2007.

[141] Streetman B.G. and Banerjee S.K., *Solid State Electronic Devices*, Pearson Prentice Hall, Upper Saddle River, 2006.

[142] Green M.A., *Solar Cells*, Prentice-Hall, The University of New South Wales, Kensington, 1998.

[143] Vaillon R., Robin L., Muresan C. and Ménézo C., Modeling of coupled spectral radiation, thermal and carrier transport in a silicon photovoltaic cell, *International Journal of Heat and Mass Transfer* **49**, 4454-4468, 2006.

[144] Whale M.D., The influence of interference and heterojunctions on the performance of microscale thermophotovoltaic devices, *Microscale Thermophysical Engineering* **5**, 89-106, 2001.

[145] Pan J.L., Choy H.K.H. and Fonstad Jr C.G., Very large radiative transfer over small distances from a black body for thermophotovoltaic applications, *IEEE Transactions on electron devices* **47**(1), 241-249, 2000.

[146] DiMatteo R.S., Greiff P., Finberg S.L., Young-Waithe K.A., Choy H.K.H., Masaki M.M. and Fonstad C.G., Enhanced photogeneration of carriers in a semiconductor via coupling across a nonisothermmal nanoscale vacuum gap, *Applied Physics Letters* **79**(12), 1894-1896, 2001.

[147] DiMatteo R., Greiff P., Seltzer D., Meulenberg D., Brown E., Carlen E., Kaiser K., Finberg S., Nguyen H., Azarkevich J., Baldasaro P., Beausang J., Danielson L., Dashiell M., DePoy D., Ehsani H., Topper W. and Rahner K., Micron-gap thermophotovoltaics (MTPV), *Proceedings of the 6th Conference on Thermophotovoltaic Generation of Electricity*, 2004.

[148] Hanamura K. and K. Mori, Nano-gap TPV generation of electricity though evanescent wave in near-field above emitter surface, *Proceedings of the 7th Conference on Thermophotovoltaic Generation of Electricity*, American Institute of Physics, 2007.

[149] MTPV: http://www.mtpvcorp.com/. April 17 2010.

[150] Pla J., Barrera M. and Rubinelli F., The influence of the InGaP window layer on the optical and electrical performance of GaAs solar cells, *Semiconductor Science and Technology* **22**, 1122-1130, 2007.

[151] Gonzalez-Cuevas J.A., Refaat T.F., Abedin, M.N. and Elsayed-Ali H.E., Modeling of temperature-dependent spectral response of $In_{1-x}Ga_xSb$ infrared detectors, *Optical Engineering* **45**, 044001, 2006.

[152] Palik E.D., *Handbook of Optical Constants of Solids*, Vol. 1, Academic, San Diego, 1998.

[153] Adachi S., *Optical Constants of Crystalline and Amorphous Semiconductors: Material and Fundamental Principles*, Kluwer Academic Publisher, Norwell, 1999.

[154] Adachi S., Optical dispersion relations for GaP, GaAs, GaSb, InP, InAs, InSb, $Al_xGa_{1-x}As$, and $In_{1-x}Ga_xAs_yP_{1-y}$, *Journal of Applied Physics* **66**, 6030-6040, 1989.

[155] Patrini M., Guizzetti G., Galli M., Ferrini R., Bosacchi A., Franchi S. and Magnanini R., Optical functions of bulk and epitaxial GaSb from 0.0025 to 6 eV, *Solid State Communications* **101**, 93-98, 2007.

[156] Bohren C.F. and Huffman D.R., *Absorption and Scattering of Light by Small Particles*, Wiley, New York, 1983.

[157] Adachi S., *Properties of Group-IV, III-V and II-VI Semiconductors*, John Wiley and Sons, England, 2005.

[158] Physical Properties of Indium Antimonide (InSb): http://www.ioffe.ru/SVA/NSM/Semicond/InSb/index.html. April 17 2010.

[159] Martin D. and Algora C., Temperature-dependent GaSb material parameters for reliable thermophotovoltaic cell modeling, *Semiconductor Science and Technology* **19**, 1040-1052, 2004.

[160] Frank D. and Wherrett B.S., Influence of surface recombination on optically bistable semiconductor devices, *Journal of the Optical Society of America B* **4**, 25-29, 1987.

[161] Patankar S.V., *Numerical Heat Transfer and Fluid Flow*, Hemisphere Publishing Corporation, 1980.

[162] Physical Properties of Gallium Antimonide (GaSb): http://www.ioffe.ru/SVA/NSM/Semicond/GaSb/index.html. April 17 2010.

[163] Incropera F.P. and DeWitt D.P., *Fundamentals of Heat and Mass Transfer*, John Wiley & Sons, New York, 2002.

[164] Mohanraj V.J. and Chen Y., Nanoparticles – A review, *Tropical Journal of Pharmaceutical Research* **5**(1), 561-573, 2006.

[165] Khlebtsov N.G., Optics and biophotonics of nanoparticles with a plasmon resonance, *Quantum Electronics* **38**(6), 504-529, 2008.

[166] Daniel M.-C. and Astruc D., Gold nanoparticles: Assembly, supramolecular chemistry, quantum-size properties, and applications toward biology, catalysis, and nanotechnology, *Chemical Reviews* **104**, 293-346, 2004.

[167] Wang X.-Q. and Mujumdar A.S., Heat transfer characteristics of nanofluids: A review, *International Journal of Thermal Sciences* **46**, 1-19, 2006.

[168] Kunadian I., Andrews R., Mengüç M.P. and Qian D., Multiwalled carbon nanotubes deposition profiles within a CVD reactor: An experimental study, *Chemical Engineering Science* **64**, 1503-1510, 2008.

[169] Kunadian I., Andrews R., Qian D. and Mengüç M.P., Growth kinetic of MWCNTs synthesized by a continuous-feed CVD method, *Carbon* **47**, 384-395, 2009.

[170] Lim S.H., Mar W., Matheu P., Derkacs D. and Yu E.T., Photocurrent spectroscopy of optical absorption enhancement in silicon photodiodes via scattering from surface plasmon polaritons in gold nanoparticles, *Journal of Applied Physics* **101**, 104309, 2007.

[171] Pillai S., Catchpole K.R., Trupke T. and Green M.A., Surface plasmon enhanced silicon solar cells, *Journal of Applied Physics* **101**, 093105, 2007.

[172] Francoeur M., Venkata P.G. and Mengüç M.P., Sensitivity analysis for characterization of gold nanoparticles and agglomerates via surface Plasmon scattering patterns, *Journal of Quantitative Spectroscopy and Radiative Transfer* **106**, 44-55, 2007.

[173] Mishchenko M.I., Travis L.D. and Lacis A.A., *Scattering, Absorption, and Emission of Light by Small Particles*, Cambridge University Press, Cambridge, 2002.

[174] Vaillon R., Polarisation du rayonnement et métrologie des particules, *Ecole de Printemps de Rayonnement Thermique*, Vol. 1, Ile d'Oléron, 2001.

[175] Bhanti D., Manickavasagam S. and Mengüç M.P., Identification of non-homogeneous spherical particles from their scattering matrix elements, *Journal of Quantitative Spectroscopy and Radiative Transfer* **56**, 591-608, 1996.

[176] Manickavasagam S. and Mengüç M.P., Scattering matrix elements of fractal-like soot agglomerates, *Applied Optics* **36**, 1337-1352, 1997.

[177] Manickavasagam S. and Mengüç M.P., Scattering-matrix elements of coated infinite-length cylinders, *Applied Optics* **37**, 2473-2482, 1998.

[178] Mengüç M.P. and Manickavasagam S., Characterization of size and structure of agglomerates and inhomogeneous particles via polarized light, *International Journal of Engineering Science* **36**, 1569-1593, 1998.

[179] Manickavasagam S., Mengüç M.P., Drozdowicz Z. and Ball C., Size shape and structure – Analysis of fine particles, *American Ceramic Society Bulletin* **81**, 29-33, 2002.

[180] Klusek C., Manickavasagam S. and Mengüç M.P., Compendium of scattering matrix element profiles for soot agglomerates, *Journal of Quantitative Spectroscopy and Radiative Transfer* **79**, 839-859, 2003.

[181] Aslan M., Yamada J., Mengüç M.P. and Thomasson J.A., Characterization of individual cotton fibers via light-scattering experiments, *Journal of Thermophysics and Heat Transfer* **17**, 442-449, 2003.

[182] Saltiel C., Chen Q., Manickavasagam S., Schadler L.S., Siegel R.W. and Mengüç M.P., Identification of the dispersion behavior of surface treated nanoscale powders, *Journal of Nanoparticle Research* **6**, 35-46, 2004.

[183] Crofcheck C., Wade J., Swamy J.N. Aslan M.M. and Mengüç M.P., Effect of fat and casein particles in milk on the scattering of elliptically polarized light, *Transactions of the ASAE* **48**, 1147-1155, 2005.

[184] Saltiel C., Manickavasagam S., Mengüç M.P. and Andrews R., Light-scattering and dispersion behavior of multiwalled carbon nanotubes, *Journal of the Optical Society of America A* **22**, 1546-1554, 2005.

[185] Aslan M.M., Crofcheck C., Tao D. and Mengüç M.P., Evaluation of micro-bubble size and gas hold-up in two-phase gas-liquid columns via scattered light measurements, *Journal of Quantitative Spectroscopy and Radiative Transfer* **101**, 527-539, 2006.

[186] Aslan M.M., Mengüç M.P., Manickavasagam S. and Saltiel C., Size and shape prediction of colloidal metal oxide MgBaFeO particles from light scattering measurements, *Journal of Nanoparticle Research* **8**, 981-994, 2006.

[187] Kozan M. and Mengüç M.P., Exploration of fractal nature of WO3 nanowire aggregates, *Journal of Quantitative Spectroscopy and Radiative Transfer* **109**, 327-336, 2008.

[188] Kozan M., Thangala J., Bogale R., Mengüç M.P. and Sunkara M.K., In-situ characterization of dispersion stability of WO3 nanoparticles and nanowires, *Journal of Nanoparticle Research* **10**, 599-612, 2008.

[189] Thomasson J.A., Manickavasagam S. and Mengüç M.P., Cotton fiber quality characterization with light scattering and fourier transform infrared techniques, *Applied Spectroscopy* **63**, 321-330, 2009.

[190] Swamy J.N., Crofcheck C. and Mengüç M.P., Time dependent scattering properties of slow decaying liquid foams, *Colloids and Surfaces A – Physicochemical and Engineering Aspects* **338**, 80-86, 2009.

[191] Mishchenko M.I., Videen G., Babenko V.A. et al., T-matrix theory of electromagnetic scattering by particles and its applications: a comprehensive reference database, *Journal of Quantitative Spectroscopy and Radiative Transfer* **88**, 357-406, 2004.

[192] Mishchenko M.I., Videen G., Babenko V.A. et al., Comprehensive T-matrix reference database: a 2004-2006 update, *Journal of Quantitative Spectroscopy and Radiative Transfer* **106**, 304-324, 2007.

[193] Mishchenko M.I., Videen G., Khlebtsov N.G. et al., Comprehensive T-matrix reference database: a 2006-2007 update, *Journal of Quantitative Spectroscopy and Radiative Transfer* **109**, 1447-1460, 2008.

[194] Mishchenko M.I., Zakharova N.T., Videen G., Khlebtsov N.G. et Wriedt, Comprehensive T-matrix reference database: a 2007-2009 update, *Journal of Quantitative Spectroscopy and Radiative Transfer* **111**, 650-658, 2010.

[195] Videen G., Light scattering from a sphere on or near a surface, *Journal of Optical Society of America A* **8**, 483-489, 1991.

[196] Videen G., Light scattering from a sphere behind a surface, *Journal of Optical Society of America A* **10**, 110-117, 1993.

[197] Videen G., Light scattering from an irregular particle behind a plane interface, *Optics Communications* **128**, 81-90, 1996.

[198] Videen G., Polarized light scattering from surface contaminants, *Optics Communications* **143**, 173-178, 1997.

[199] Videen G. and Ngo D., Reciprocity method for obtaining the far fields generated by a source inside or near a microparticle, *Journal of Optical Society of America A* **14**, 70-78, 1997.

[200] Mackowski D.W., Calculation of total cross sections of multiple-sphere clusters, *Journal of Optical Society of America A* **11**, 2851-2861, 1994.

[201] Mackowski D.W. and Mishchenko M.I., Calculation of the T matrix and the scattering matrix for ensembles of spheres, *Journal of Optical Society of America A* **13**, 2266-2278, 1996.

[202] Mackowski D.W., Exact solution for the scattering and absorption properties of sphere clusters on a plane surface, *Journal of Quantitative Spectroscopy and Radiative Transfer* **109**, 770-788, 2008.

[203] Mackowski D.W., A generalization of image theory to predict the interaction of multipole fields with plane surfaces, *Journal of Quantitative Spectroscopy and Radiative Transfer* **111**, 802-809, 2010.

[204] Beck J.V. and Arnold K.J., *Parameter Estimation in Engineering and Science*, Wiley, New York, 1977.

[205] Charnigo R. and Srinivasan C., Self-consistent estimation of mean response functions and their derivatives, Submitted, 2010.

[206] Charnigo R. and Srinivasan C., On simultaneous estimation of a mean response and its derivatives, Submitted, 2010.

[207] Charnigo R., Francoeur M., Mengüç M.P., Brock A., Leichter M. and Srinivasan C., Derivatives of scattering profiles: tools for nanoparticle characterization, *Journal of the Optical Society of America A* **24**, 2578-2589, 2007.

[208] Charnigo R., Francoeur M., Kenkel P., Mengüç M.P., Hall B. and Srinivasan C., On estimating quantitative features of nanoparticles, Submitted to *Inverse Problems*, 2010.

[209] Govindan R., Manickavasagam S. and Mengüç M.P., On measuring the Mueller matrix elements of soot agglomerates, *Proceedings of the First International Symposium on Radiative Transfer*, Begell House, New York, 280-295, 1995.

[210] Park S., Lee G., Song S.H., Oh C.H. and Kim P.S., Resonant coupling of surface plasmons to radiation modes by use of dielectric gratings, *Optics Express* **28**(20), 1870-1872, 2003.

[211] Byun K.M., Kim S.J. and Kim D., Grating-coupled transmission-type surface plasmon resonance sensors based on dielectric and metallic gratings, *Applied Optics* **46**(23), 5703-5708, 2007.

[212] Eringen A.C., *Nonlocal Continuum Field Theories*, Springer-Verlag, New York, 2002.

[213] Ben-Abdallah P., Joulain K. and Pryamikov A., Surface Bloch waves mediated heat transfer between two photonic crystals, *Applied Physics Letters* **96**, 143117, 2010.

[214] Taflove A. and Hagness S.C., *Computational Electrodynamics: The Finite-Difference Time-Domain Method*, Artech House, Norwood, 2005.

[215] Perez-Madrid A., Lapas L.C. and Rubi J.M., Heat exchange between two interacting nanoparticles beyond the fluctuation-dissipation regime, *Physical Review Letters* **103**(4), 048301, 2009.

[216] Semiconductor Today: http://www.semiconductor-today.com/news_items/2009/FEB/WAFERTECHNOLOGY_170209.htm. April 17 2010.

[217] Francoeur M., Vaillon R. and Mengüç M.P., Cascaded photovoltaic and thermophotovoltaic energy conversion systems with near-field radiation transfer enhancement at nanoscale gaps, US Patent, Application No. 12/534,322, 2009.

[218] Tai C.-T., *Dyadic Green's Functions in Electromagnetic Theory*, IEEE Press, Piscataway, 1994.

[219] Plot Digitizer: http://plotdigitizer.sourceforge.net/. April 17 2010.

# Vita

## PERSONAL INFORMATION

- **Name**: Mathieu Francoeur
- **Nationality**: Canadian
- **Place of birth**: Greenfield Park, PQ, Canada
- **Date of birth**: November 10, 1978

## EDUCATION

| | |
|---|---|
| **M.Sc.** | Department of Mechanical Engineering, Université Laval, Québec, PQ, Canada, 2002-2004. |
| **B.Eng.** | Department of Mechanical Engineering, Université Laval, Québec, PQ, Canada, 1998-2002. |

## PROFESSIONAL EXPERIENCE

- Assistant Professor, Department of Mechanical Engineering, University of Utah, Salt Lake City, UT, 2010-
- Research Assistant, Department of Mechanical Engineering, University of Kentucky, Lexington, KY, 2005-2010.
- Consultant, General Electric Global Research, Niskayuna, NY, 2007-2010.
- Teaching Assistant, Department of Mechanical Engineering, University of Kentucky, Lexington, KY, 2006-2007.
- Research and Teaching Assistant, Department of Mechanical Engineering, Université Laval, Québec, PQ, 2002-2005.
- Mechanical Engineer (Internship), Bombardier Transportation, Lapocatière, PQ, Canada, 2001.

## HONORS AND AWARDS

- Journal of Quantitative Spectroscopy and Radiative Transfer (JQSRT) Young Scientist Award in Radiative Transfer, Category Ph.D. student, 2009.
- Dissertation Year Fellowship, University of Kentucky, 2008-2009.

- ES D3 Ph.D. Scholarship, Natural Sciences and Engineering Research Council of Canada (NSERC), 2005-2008.
- Ph.D. Scholarship, Natural Sciences and Technology Foundation of Quebec (FQRNT), Declined (cannot be combined with NSERC Scholarship), 2005.
- Kentucky Graduate Scholarship, University of Kentucky, 2005-2010.
- Board of Honor of Université Laval for outstanding Master Thesis, 2004-2005.

## BOOK CHAPTER

- M. Francoeur, and M.P. Mengüç, "Chapter 16: Near-field thermal radiation", Upcoming fifth edition of *Thermal Radiation Heat Transfer* by R. Siegel and J. Howell, 2010.

## JOURNAL PUBLICATIONS

- R. Charnigo, M. Francoeur, P. Kenkel, M.P. Mengüç, B. Hall, and C. Srinivasan, "On estimating quantitative features of nanoparticles", *Inverse Problems*, Under review, 2010.
- B.T. Wong, M. Francoeur, and M.P. Mengüç, "A Monte Carlo simulation for phonon transport and heating of silicon at nanoscales due to heat generation", *International Journal of Heat and Mass Transfer*, Under review, 2010.
- M. Francoeur, M.P. Mengüç, and R. Vaillon, "Control of near-field radiative heat transfer via surface phonon-polariton coupling in thin films", *Applied Physics A*, Accepted, 2010.
- M. Francoeur, M.P. Mengüç, and R. Vaillon, "Spectral tuning of near-field radiative heat flux between two thin silicon carbide films", *Journal of Physics D: Applied Physics* **43**, 075501, 2010.
- M. Francoeur, M.P. Mengüç, and R. Vaillon, "Local density of electromagnetic states within a nanometric gap formed between two thin films supporting surface phonon-polaritons", *Journal of Applied Physics* **107**, 034313, 2010.
- M. Francoeur, M.P. Mengüç, and R. Vaillon, "Solution of near-field thermal radiation in one-dimensional layered media using dyadic Green's functions and the scattering matrix method", *Journal of Quantitative Spectroscopy and Radiative Transfer* **110**, 2002-2018, 2009.
- M. Francoeur, M.P. Mengüç, and R. Vaillon, "Near-field radiative heat transfer enhancement via surface phonon polaritons coupling in thin films", *Applied Physics Letters* **93**, 043109, 2008.
- M. Francoeur, and M.P. Mengüç, "Role of fluctuational electrodynamics in near-field radiative heat transfer", *Journal of Quantitative Spectroscopy and Radiative Transfer* **109**(2), 280-293, 2008.

- R. Charnigo, M. Francoeur, M.P. Mengüç, A. Brock., M. Leichter, and C. Srinivasan, "Derivatives of scattering profiles: tools for nanoparticle characterization", *Journal of the Optical Society of America A* **24**(9), 2578-2589, 2007 (Selected for *Virtual Journal of Nanoscale Science and Technology* **16**(16), October 15, 2007).
- M. Francoeur, P.G. Venkata, and M.P. Mengüç, "Sensitivity analysis for characterization of gold nanoparticles and agglomerates via surface plasmon scattering patterns", *Journal of Quantitative Spectroscopy and Radiative Transfer* **106**, 44-55, 2007.
- M. Francoeur, and D.R. Rousse, "Short-pulsed laser transport in absorbing and scattering media: time versus frequency-based approaches", *Journal of Physics D: Applied Physics* **40**, 5733-5742, 2007.
- M. Francoeur, R. Vaillon and D.R. Rousse, "Theoretical analysis of frequency and time domain methods for optical characterization of absorbing and scattering media", *Journal of Quantitative Spectroscopy and Radiative Transfer* **93**, 139-150, 2005.

## CONFERENCE PROCEEDINGS

- M. Francoeur, M.P. Mengüç, and R. Vaillon, "Control of near-field radiative heat transfer via surface phonon-polariton coupling in thin films", *META'10: 2nd International Conference on Metamaterials, Photonic Crystals and Plasmonics*, Cairo, Egypt, February 22-25, 2010 (Paper).
- M. Francoeur, M. Arik, and M.P. Mengüç, "Estimating near-field thermal radiation between two flat silicon wafers with surface roughness", *International Conference on Nanomaterials and Nanosystems*, Istanbul, Turkey, August 10-13, 2009 (Extended Abstract).
- R. Charnigo, M. Francoeur, P. Kenkel, M.P. Mengüç, B. Hall, and C. Srinivasan, "Nonparametric derivative estimation and the computation of posterior probabilities for nanoparticle characteristics", *2009 Joint Statistical Meetings*, Washington DC, USA, August 1-6, 2009 (Paper).
- M. Francoeur, M.P. Mengüç, and R. Vaillon, "Near-field thermal radiation emission from SiC thin films", *Eurotherm Seminar 83: Computational Thermal Radiation in Participating Media III*, Lisbon, Portugal, April 15-17, 2009 (Paper).
- M. Francoeur, M.M. Aslan, and M.P. Mengüç, "Polarized-surface-wave-scattering systems (PSWSS) for characterization of nanoparticles", *11th Electromagnetic and Light Scattering Conference*, University of Hertfordshire, England, September 7-12, 2008 (Extended Abstract).
- M. Francoeur, M.P. Mengüç, and R. Vaillon, "Modeling of surface phonon-polaritons coupling in thin films for near-field thermal radiation", *11th*

*Electromagnetic and Light Scattering Conference*, University of Hertfordshire, England, September 7-12, 2008 (Extended Abstract).

- M. Francoeur, and M.P. Mengüç, “Role of fluctuational electrodynamics in near-field radiative heat transfer”, *Fifth International Symposium on Radiative Transfer*, Bodrum, Turkey, June 2007 (Paper).
- M. Francoeur, P.G. Venkata, M.M. Aslan, and M.P. Mengüç, “Sensitivity analysis for characterization of gold nano-particles via surface wave scattering”, *9th Electromagnetic and Light Scattering Conference*, St.Petersburg, Russia, 47-50, June 5-9, 2006 (Extended Abstract).
- M. Francoeur, and D.R. Rousse, “Unsteady radiative transfer in participating media : a frequency-based numerical approach”, *2nd International Conference on Thermal Engineering Theory and Applications*, Al Ain, United Arab Emirates, January 3-6, 2006 (Paper).
- D.R. Rousse, and M. Francoeur, “Frequency and time-based methods for transient radiative transfer”, *Numerical Heat Transfer 2005*, In Nowak, Bialecki, Weçel, eds, 301-312, Cracovie, 2005 (Invited Paper).
- M. Francoeur, and D.R. Rousse, “Numerical solutions of transient radiative transfer using time and frequency-domain approaches”, *ASME Summer Heat Transfer Conference*, HT2005-72737, San Francisco, USA, July 17-22, 2005 (Paper).
- M. Francoeur,and D.R. Rousse, “Transfert radiatif instationnaire en milieu semi-transparent. Partie A : Résolution dans le domaine temporal”, *VIIe Colloque Interuniversitaire Franco-Québécois : Thermiques des Systèmes*, St-Malo, France, 10-03, 2005 (Paper).
- M. Francoeur, and D.R. Rousse, “Transfert radiatif instationnaire en milieu semi-transparent. Partie B : Résolution dans le domaine fréquentiel”, *VIIe Colloque Interuniversitaire Franco-Québécois : Thermiques des Systèmes*, St-Malo, France, 10-04, 2005 (Paper).
- M. Francoeur, R. Vaillon, and D.R. Rousse, “Theoretical analysis of frequency and time domain methods for optical characterization of absorbing and scattering media”, *Fourth International Symposium on Radiative Transfer*, Istanbul, Turkey, 153-162, 2004 (Paper).
- M. Francoeur, and D.R. Rousse, “Analyse du transfert radiatif instationnaire en milieu semi-transparent absorbant et diffusant: utilisation de limiteurs de flux”, *International Conference on Thermal Engineering Theory and Applications*, ICTEA-HT5-03, Beirut, Lebanon, 2004 (Paper).
- M. Francoeur, D.R. Rousse, and R. Vaillon, “Analyse du transfert radiatif instationnaire en milieu semi-transparent absorbant et diffusant”, *VIe Colloque Interuniversitaire Franco-Québécois : Thermiques des Systèmes*, Québec, Canada, 08-07, 2003 (Paper).

## ORAL AND POSTER PRESENTATIONS

- M.Francoeur, M.P. Mengüç, and R. Vaillon, "Thermal impacts on performances of nanoscale-gap thermophotovoltaic energy conversion devices", *Electromagnetic and Light Scattering Conference XII*, Helsinki, Finland, June 28-July 2, 2010 (Poster).
- M.Francoeur, M.P. Mengüç, and R. Vaillon, "Thermal impacts on performances of nanoscale-gap thermophotovoltaic energy conversion devices", *6th International Symposium on Radiative Transfer*, Antalya, Turkey, June 13-19, 2010 (Poster).
- M.Francoeur, M.P. Mengüç, and R. Vaillon, "On tuning the near-field thermal radiation spectrum emitted by thin films via coupling of surface phonon-polaritons", *2009 ASME Summer Heat Transfer Conference*, San Francisco, USA, July 19-23, 2009 (Oral presentation).
- M. Francoeur, and M.P. Mengüç, "Near-field thermal radiation and potential application for clean energy production", *KYNanomat 2008*, Louisville, KY, March 16-18, 2008 (Poster).
- M. Francoeur, M.M. Aslan, P.G. Venkata, and M.P. Mengüç, "Polarized-surface-wave-scattering system (PSWSS) for *in-situ* and on-line characterization of nanostructures", *KYNanomat 2008*, Louisville, KY, March 16-18, 2008 (Poster).
- M. Francoeur, M.M. Aslan, P.G. Venkata, and M.P. Mengüç, "Polarized-surface-wave-scattering system (PSWSS) for *in-situ* and on-line characterization of nanostructures", *NSF CMMI Engineering Research and Innovation Conference 2008*, Knoxville, TN, January 7-10, 2008 (Poster).
- M. Francoeur, and M.P. Mengüç, "Characterization of nanoparticles via scattering of surface waves", *Thermal Radiation at the Nanoscale: Forces, Heat Transfer, Coherence*, Les Houches, France, May 22-23, 2007 (Poster).
- M. Francoeur, P.G. Venkata, and M.P. Mengüç, "Sensitivity analysis for characterization of gold nanoparticles and 2D-agglomerates via surface plasmon scattering patterns", *2006 International Mechanical Engineering Congress & Exposition*, November 5-10, Chicago, IL, IMECE2006-16390, 2006 (Poster and Oral Presentations).

## INVITED PRESENTATIONS

- M. Francoeur and R. Vaillon, "Compendium of collaborative research activities on particle characterization and photovoltaic systems between RTL and CETHIL", National Research Council (NRC) Canada, Ottawa, Ontario, July 30, 2008.

- M. Francoeur, “Caractérisation de nanoparticules via la diffusion d’ondes de surface”, Institut National des Sciences Appliquées (INSA) de Lyon, May 16, 2007.

## PATENT APPLICATION

- M. Francoeur, R. Vaillon, and M.P. Mengüç, “Cascaded photovoltaic and thermophotovoltaic energy conversion systems with near-field radiation transfer enhancement at nanoscale gaps”, US Patent, Application No. 12/534,322, August 3, 2009.